REPORT DOCUMENTATION PAGE

Form Approved
OMB No. 0704-0188

1. AGENCY USE ONLY *(Leave blank)*	2. REPORT DATE	3. REPORT TYPE AND DATES COVERED
	December 15, 1999	Technical 05/16/94 to12/15/99

4. TITLE AND SUBTITLE: An Experimental Investigation of Pressure Fluctuations in Three-dimensional Turbulent Boundary layers

5. FUNDING NUMBERS
N00014-94-1-0092
N00014-94-1-0802

6. AUTHORS

Michael C. Goody and Roger L. Simpson

7. PERFORMING ORGANIZATION NAME(S) AND ADDRESS(ES)

Department of Aerospace and Ocean Engineering
Virginia Polytechnic Institute and State University
Blacksburg, Virginia 24061-0203

8. PERFORMING ORGANIZATION REPORT NUMBER

VPI-AOE-268

9. SPONSORING/MONITORING AGENCY NAME(S) AND ADDRESS(ES)

Office of Naval Research
800 N. Quincy Street
Arlington, Virginia 22217

10. SPONSORING/MONITORING AGENCY REPORT NUMBER

11. SUPPLEMENTARY NOTES

12a. DISTRIBUTION/AVAILABILITY STATEMENT

Unlimited

DISTRIBUTION STATEMENT A
Approved for Public Release
Distribution Unlimited

12b. DISTRIBUTION CODE

13. ABSTRACT *(Maximum 200 words)* Experimental surface pressure fluctuations measurements over a wide range of Reynolds number ($1400<Re_\theta<23000$) are presented for 3 types of turbulent boundary layers: 1) a zero pressure gradient 2-D turbulent boundary layer, 2) a 3-D pressure-driven turbulent boundary layer that forms away from a wing-body junction, and 3) the separating flow about the leeside of a 6:1 prolate spheroid at angle of attack. The statistics of the fluctuating surface pressure and existing measurements of the velocity field and the covariance of the surface pressure and fluctuating velocity components were studied. The spectral power density of surface pressure fluctuations beneath highly three-dimensional flow contain nearly constant spectral levels within a middle to high frequency range, due to a lack of overlapping frequency structure between the large-scale motions and the viscous-dominated motions. Each of these types of motion have different flow histories due to the three-dimensional flow structure. The resulting RMS surface pressure fluctuation distributions reflect the importance of the high frequency wall region contributions. Scaling parameters for the spectra beneath three-dimensional flows must incorporate local flow structure in order to be successful. An analysis based on the Poisson equation shows that the variation of the high frequency spectral levels is related to the variation of near-wall mean velocity gradients and v^2 structure. In the 6:1 prolate spheroid flow, near regions of crossflow Separation there is a local minimum in RMS surface pressure fluctuations, whereas around reattachments and under the large shed vortices there is a local maximum in RMS surface pressure fluctuations.

14. SUBJECT TERMS	15. NUMBER OF PAGES
Three-dimensional turbulent boundary layers, surface pressure fluctuations, acoustic noise, separated flow, vortical flow	337
	16. PRICE CODE

17. SECURITY CLASSIFICATION OF REPORT	18. SECURITY CLASSIFICATION OF THIS PAGE	19. SECURITY CLASSIFICATION OF ABSTRACT	20. LIMITATION OF ABSTRACT
UNCLASSIFIED	UNCLASSIFIED	UNCLASSIFIED	UNLIMITED

a ..... The speed of sound

d ..... Pressure transducer sensing diameter

d_{LOCAL} ..... Prolate spheroid model diameter at a given axial position

f ..... Frequency, Hz

k_1, k_2, k_3 ..... Wavenumber vector components in the x, y, and z direction, respectively

L ..... Prolate spheroid model length, 1.37 m

P ..... Mean pressure at a point within the flow

p ..... Fluctuation of the surface pressure

Q_e ..... Dynamic pressure at the edge of the boundary layer, $\frac{1}{2}\rho U_e^2$

Q_∞ ..... Dynamic pressure of flow far upstream of the measurement location, $\frac{1}{2}\rho U_\infty^2$

r ..... Distance from the prolate spheroid model surface along a line perpendicular to the model axis

r_S ..... Distance between a point where the surface pressure fluctuations are measured and the point in the flow that is the source of the surface pressure fluctuations

Re_L ..... Model length Reynolds number, $U_\infty L/\nu$

Re_θ ..... Momentum thickness Reynolds number, $U_\infty \theta/\nu$

Re_δ ..... Boundary layer thickness Reynolds number, $u_\tau \delta/\nu$

R_{pu} ..... Correlation coefficient of wall pressure and the fluctuating u-component of velocity

$$R_{pu} = \frac{\overline{p\,u}}{\sqrt{\overline{p^2}}\sqrt{\overline{u^2}}}$$

R_{pv} ..... Correlation coefficient of wall pressure and the fluctuating v-component of velocity

$$R_{pv} = \frac{\overline{p\,v}}{\sqrt{\overline{p^2}}\sqrt{\overline{v^2}}}$$

R_{pw} ..... Correlation coefficient of wall pressure and the fluctuating w-component of velocity

$$R_{pw} = \frac{\overline{p\,w}}{\sqrt{\overline{p^2}}\sqrt{\overline{w^2}}}$$

TKE ..... Turbulent kinetic energy, $\frac{1}{2}\rho(\overline{u^2} + \overline{v^2} + \overline{w^2})$

t ..... Time

t_{max} ..... Maximum thickness of the wing, 7.17 cm

u_τ ..... Friction velocity, $(\tau_W/\rho)^{1/2}$

U, V, W ..... Mean velocity components

U_i ..... Mean velocity component, tensor notation where i = 1, 2, 3 coresponds to U, V, W, respectively.

u, v, w ..... Fluctuating velocity components in the directions of U, V, and W, respectively

u_i ..... Fluctuating velocity component, tensor notation where i = 1, 2, 3 coresponds to u, v, w, respectively.

U_C ..... Magnitude of the convection velocity of pressure fluctuations

U_{C1}, U_{C2}, U_{C3} ... Convection velocity vector components in the x, y, and z direction, respectively

U_∞ ..... Wind-tunnel free-stream velocity

$d\Omega$ ..... Differential volume element

x, y, z ..... Coordinate system axes

x_i ..... Spatial coordinate, tensor notation where i = 1, 2, 3 coresponds to x, y, z, respectively.

α ..... Angle of attack of model relative to the incident flow

β_{FS} ..... Free-stream mean flow angle measured relative to the wind tunnel centerline

β_W ..... Near-wall mean flow angle measured relative to the wind tunnel centerline

δ ..... Boundary layer thickness. Distance from the wall where $(U^2+W^2)^{1/2}/U_e = 0.995$

δ^* ..... Boundary layer magnitude displacement thickness

$$\delta^* = \int_0^{\delta} \left[1 - \frac{\left(U^2 + W^2\right)^{\frac{1}{2}}}{U_e} \right] dr \qquad \text{(Prolate Spheroid)}$$

$$\delta^* = \int_0^{\delta} \left[1 - \frac{\left(U^2 + W^2\right)^{\frac{1}{2}}}{U_e} \right] dy \qquad \text{(Wing - Body Junction)}$$

Δ ..... Boundary layer thickness based on the velocity defect law (from Rotta, 1962)

$$\Delta = \frac{\delta^* U_e}{u_\tau} = \int_0^{\infty} \left(\frac{U_e - U}{u_\tau} \right) dy$$

ν ..... Kinematic viscosity of air

ρ ..... Mass density of air

θ ..... Boundary layer momentum thickness

$$\theta = \int_0^{\delta} \left[1 - \frac{\left(U^2 + W^2\right)^{\frac{1}{2}}}{U_e} \right] \left[\frac{\left(U^2 + W^2\right)^{\frac{1}{2}}}{U_e} \right] dr \qquad \text{(Prolate Spheroid)}$$

$$\theta = \int_0^{\delta} \left[1 - \frac{U}{U_e} \right] \left[\frac{U}{U_e} \right] dy \qquad \text{(Wing - Body Junction)}$$

τ_W ..... Shear-stress magnitude at the wall

τ ..... Reynolds shear stress, $\rho\left[(\overline{uv})^2 + (\overline{vw})^2\right]^{1/2}$

ϕ ..... Circumferential angle coordinate, measured from windward side of prolate spheroid model

Φ ..... Spectral power density of surface pressure fluctuations such that

$$\overline{p^2} = \int_0^{\infty} \Phi(\omega)\, d\omega$$

Φ_{O1} ..... Non-dimensional spectral power density, $\Phi U_e / \tau_W^2 \delta^*$

Φ_{O2} ..... Non-dimensional spectral power density, $\Phi U_e / Q_e^2 \delta^*$

Φ_{O3} ..... Non-dimensional spectral power density, $\Phi u_\tau / \tau_W^2 \delta^*$

Φ_{O4} ..... Non-dimensional spectral power density, $\Phi u_\tau / Q_e^2 \delta^*$

Φ_{O5} ..... Non-dimensional spectral power density, $\Phi u_\tau / \tau_W^2 \delta$

Φ_{O6} ..... Non-dimensional spectral power density, $\Phi u_\tau / Q_e^2 \delta$

Φ_{O7} ..... Non-dimensional spectral power density, $\Phi U_e / \tau_W^2 \delta$

Φ_{O8} ..... Non-dimensional spectral power density, $\Phi U_e / Q_e^2 \delta$

Φ_{O9} ..... Non-dimensional spectral power density, $\Phi u_\tau / \tau_W^2 \Delta$

Φ_{O10} ..... Non-dimensional spectral power density, $\Phi u_\tau / Q_e^2 \Delta$

Φ_{O11} ..... Non-dimensional spectral power density, $\Phi U_e / \tau_W^2 \Delta$

Φ_{O12} ..... Non-dimensional spectral power density, $\Phi U_e / Q_e^2 \Delta$

Φ_{O13} ..... Non-dimensional spectral power density,

$$\frac{\Phi(\omega)\left[U^2 + W^2\right]^{\frac{1}{2}}_{\tau_{max}}}{\tau^2_{max}\ y_{\tau_{max}}}$$

Φ_{O14} ..... Non-dimensional spectral power density,

$$\frac{\Phi(\omega)\left[U^2 + W^2\right]^{\frac{1}{2}}_{W_{max}}}{\left(\frac{1}{2}\rho W^2_{max}\right)^2\ y_{W_{max}}}$$

ω ..... Circular frequency, $(2\pi f)$, rad/s

ω_{O1} ..... Non-dimensional frequency, $\omega\delta^* / U_e$

ω_{O2} ..... Non-dimensional frequency, $\omega\delta^* / u_\tau$

ω_{O3} ..... Non-dimensional frequency, $\omega\delta / u_\tau$

ω_{O4} ..... Non-dimensional frequency, $\omega\delta / U_e$

ω_{O5} ..... Non-dimensional frequency, $\omega\Delta / u_\tau$

ω_{O6} ..... Non-dimensional frequency, $\omega\Delta / U_e$

ω_{O7} ..... Non-dimensional frequency,

$$\frac{\omega\ y_{\tau_{max}}}{\left[U^2 + W^2\right]^{\frac{1}{2}}_{\tau_{max}}}$$

ω_{O8} ..... Non-dimensional frequency,

$$\frac{\omega\ y_{W_{max}}}{\left[U^2+W^2\right]^{\frac{1}{2}}_{W_{max}}}$$

superscript:

( )' ..... The root mean square value of a fluctuating quantity

( )$^+$ ..... Indicates that the variable is made non-dimensional using the viscous scales: τ_W for pressure, u_τ for velocity, and ν/u_τ for length

$(\overline{\ })$ ..... Denotes a long-time averaged quantity

subscript:

( )$_{max}$ ..... The maximum of ( ).

When one variable is the subscript to another variable, the latter variable is evaluated at the condition of the former variable. For example, $y_{\tau_{max}}$ is the y location of τ_{max} (maximum Reynolds shear stress)

Note : This document follows the usual tensor convention that a repeated index (i) within a term indicates summation with respect to the repeated index over the range 1, 2, 3.

1. INTRODUCTION

When fluid moves past a solid surface a *boundary layer* of fluid is formed that is distinct from other parts of the flowfield. The boundary layer is typically a thin region of the flowfield immediately adjacent to the solid surface. Within the boundary layer the velocity of the fluid changes from a *free-stream* value away from the surface to the velocity of the surface. Any interaction between the solid surface and the fluid (e.g. friction) takes place through the boundary layer. Therefore, understanding the flow physics of the boundary layer is important.

Boundary layers are divided into two broad categories, *laminar* and *turbulent*. In laminar boundary layers the acceleration/deceleration occurs in a series of layers or laminates of fluid. Each laminate only interacts with adjacent laminates through molecular viscosity. Most boundary layers of practical concern are turbulent. Turbulent flows are characterized by swirls, or eddies, of fluid that vary in spatial and temporal extent. Flow variables such as pressure and velocity fluctuate in a seemingly random way. These fluctuations enhance the mixing of particles within the flow as well as the mixing of flow properties such as momentum. Rather than having laminates that only interact with their immediate neighbor, large scale fluctuations convect fluid near the free-stream boundary to near the wall. The enhanced mixing can be beneficial. An example is a combustor in which the enhanced mixing of fuel and oxidizer increases combustor efficiency. Enhanced mixing can also be undesirable. Higher momentum fluid close to the solid surface increases the friction between the flow and the surface. This means greater drag force on automobiles, aircraft and marine vehicles and greater pressure drop in pipes. The pressure fluctuations generated within the boundary layer of applications such as helicopters, turbomachinery, aircraft, and marine vehicles can generate significant undesirable noise and induce vibrations that can contribute to accelerated structural fatigue.

Flow-induced pressure fluctuations have proven to be a very complex physical phenomena- difficult to calculate and difficult to measure. They are a *broadband* phenomena which means that they exist over a wide range of frequencies. This is because they are produced

by turbulent eddies that have many sizes. The broadband nature of turbulence limits the calculation of pressure fluctuations using direct numerical simulation (DNS) of the governing equation to low Reynolds number flows. *Reynolds number* (= (velocity scale)(length scale) / (kinematic viscosity)) is a certain ratio of flow parameters that is often used as a measure of turbulence. A higher Reynolds number is indicative of a more turbulent flow. Most flows of engineering interest are at high Reynolds number.

It is not currently possible to directly measure the pressure fluctuations *within* the boundary layer because placing a pressure probe within the boundary layer alters the flowfield too greatly. Therefore, pressure fluctuation measurements can only be made at the solid surface beneath the boundary layer. Initially this seems simple- just cut a hole in the surface, place a pressure transducer in the hole and make measurements. However, the turbulent eddies that produce pressure fluctuations extend to very small sizes. Contributions of sources that are smaller than the transducer sensing area are spatially integrated, and thereby attenuated. In the present study a miniature pressure transducer was used along with a pinhole to reduce spatial averaging (attenuation). Another difficulty arises in isolating the pressure fluctuations due to turbulence from the fluctuations due to other sources. Measured pressure signals are usually contaminated by coherent, facility-related acoustic inputs and external vibration of the transducer. Turbulent pressure fluctuations have a relatively small coherence in time and space. A noise cancellation technique originally developed by other researchers was adapted to the present study and used to isolate surface pressure fluctuations due to turbulence. The broadband nature of turbulent pressure fluctuations also requires accurate calibration of the pressure transducer over a wide frequency range. This issue was also dealt with in the present study.

1.1. Motivation

Pressure fluctuations in turbulent boundary layers are a source of noise, through the wake of a vehicle and through large turbulent motions that can cause disturbances in the free-stream flow which propagate away as sound. Pressure fluctuations are also a source of vibrations that can accelerate structural fatigue. Additionally, pressure fluctuations and their correlation with velocity fluctuations is an important diffusive mechanism in turbulence transport. Most fundamental investigations of surface pressure fluctuations have been confined to zero pressure

gradient, two-dimensional, turbulent boundary layers. This is the simple case of a boundary layer on a flat plate that is aligned with the flow. Some empirical relationships with some theoretical basis have been developed to describe surface pressure fluctuations beneath two-dimensional, turbulent boundary layers. The theoretical basis for these relationships is not disputed in the literature, however, there is some discrepancy in their measured behavior. Though studied extensively, the pressure fluctuations beneath the simple case of a zero-pressure-gradient, two-dimensional, turbulent boundary layer is still the subject of current research. Other studies have been done to investigate the effect of pressure gradient and boundary layer separation on surface pressure fluctuations. However, such studies are typically highly idealized laboratory flows that yield some insight on the behavior of surface pressure fluctuations. Researchers have also made measurements on real-world flows such as gliders and aircraft. However, such measurements are difficult to reproduce and only limited measurements of the velocity field were made. The present research seeks to bridge this gap. Accurate surface pressure measurements were carried out and related to extensive velocity field measurements in complex flows of practical interest.

1.2. Background

1.2.1. Coherent Structures

The concept of *coherent structures*, sometimes called *turbulent eddies* or just *eddies*, play an important role in the understanding of turbulence. Therefore, a brief description of coherent structures is warranted here. Many papers have been written on the subject. Recent reviews are given by Hussain (1986) and Robinson (1991). Robinson defines a coherent structure as "a three-dimensional region of flow over which at least on fundamental flow variable (velocity component, density, temperature, etc.) exhibits significant correlation with itself or with another variable over a range of space and/or time that is significantly larger than the smallest local scales of the flow."

Recent investigations of surface pressure fluctuations in two-dimensional turbulent boundary layers have related them to the coherent structures or *organized motions* known to exist in wall-bounded turbulent flows (Kammeyer, 1995; Russell, 1997). Ha (1993) and Lewis (1996) studied coherent structures in the boundary layer of a wing-body junction and Madden (1997) studied coherent structures in the boundary layer of a 6:1 prolate spheroid.

1.2.2. Pressure Fluctuations

The motion of a fluid is described by the Navier-Stokes and mass continuity equations. For an incompressible fluid with constant density and constant viscosity the governing equations may be expressed as,

$$\frac{\partial \vec{U}}{\partial t} + \left(\vec{U}\cdot\nabla\right)\vec{U} = -\frac{\nabla P}{\rho} + \nu\nabla^2\vec{U} \tag{1}$$

$$\nabla\cdot\vec{U} = 0 \tag{2}$$

The divergence of equation 1 is

$$\nabla\cdot\frac{\partial \vec{U}}{\partial t} + \nabla\cdot\left(\vec{U}\cdot\nabla\right)\vec{U} = -\frac{\nabla^2 P}{\rho} + \nu\nabla\cdot\nabla^2\vec{U} \tag{3}$$

which may be written as

$$\frac{\partial\left(\nabla\cdot\vec{U}\right)}{\partial t} + \nabla\cdot\left(\vec{U}\cdot\nabla\right)\vec{U} = -\frac{\nabla^2 P}{\rho} + \nu\nabla\cdot\left(\nabla\left(\nabla\cdot\vec{U}\right)\right) - \nu\nabla\cdot\left(\nabla\times\left(\nabla\times\vec{U}\right)\right) \tag{4}$$

The first and fourth terms of equation 4 are identically zero due to mass conservation (equation 2). The last term of equation 4 is zero since it is the divergence of the curl of a vector. Therefore, equation 4 is equal to

$$\nabla\cdot\left(\vec{U}\cdot\nabla\right)\vec{U} = -\frac{\nabla^2 P}{\rho} \tag{5}$$

which may be expressed as

$$\nabla^2 P = -\rho\frac{\partial^2}{\partial x_i\,\partial x_j}\left(U_i U_j\right) \tag{6}$$

which follows the usual tensor convention that a repeated index in a term indicates summation with respect to the repeated index over the range 1, 2, 3. If the terms on the right-hand side of equation 6 are known then equation 6 is a Poisson equation for the pressure. An equation for the fluctuating pressure may be obtained by expressing P and U_i as the sum of a mean and fluctuating part (Reynolds decomposition),

$$P = \overline{P} + p \tag{7}$$

$$U_i = \overline{U}_i + u_i \tag{8}$$

Note that p is used in this section to represent the fluctuating pressure in general, not just the fluctuating surface pressure. Substituting equations 7 and 8 into equation 6 gives

$$\nabla^2 \overline{P} + \nabla^2 p = -\rho \frac{\partial^2}{\partial x_i \partial x_j} \left(\overline{U}_i \overline{U}_j + \overline{U}_i u_j + u_i \overline{U}_j + u_i u_j \right) \tag{9}$$

Averaging equation 9 over time leaves

$$\nabla^2 \overline{P} = -\rho \frac{\partial^2}{\partial x_i \partial x_j} \left(\overline{U}_i \overline{U}_j + \overline{u_i u_j} \right) \tag{10}$$

Subtracting equation 10 from equation 9 gives

$$\nabla^2 p = -\rho \left[2 \frac{\partial \overline{U}_i}{\partial x_j} \frac{\partial u_j}{\partial x_i} + \frac{\partial^2}{\partial x_i \partial x_j} \left(u_i u_j - \overline{u_i u_j} \right) \right] \tag{11}$$

which is a Poisson equation for the fluctuating pressure. Note that the p in equation 11 represents the fluctuating pressure in general. Equation 11 is valid for all points within the flow. The first term on the right-hand side of equation 11 represents the turbulence-mean-shear interaction. It is linear with respect to the velocity fluctuations and is sometimes called the *rapid* term because it responds quicker to changes in the mean flow. The second term on the right-hand side of equation 11 represents the turbulence interaction with itself. It is non-linear with respect to the velocity fluctuations and is sometimes called the *slow* term because it responds to changes in the mean flow only after the mean flow alters the turbulence.

In order to obtain an equation for the *surface* pressure fluctuation at a point *on the wall* (point O, figure 1), equation 11 is integrated over the half-space above the wall through the use of the symmetric form of Green's theorem,

$$\oint_{\Omega} \left(\Psi \nabla^2 \Theta - \Theta \nabla^2 \Psi \right) d\Omega = \oint_{\Sigma} \left(\Psi \frac{\partial \Theta}{\partial n} - \Theta \frac{\partial \Psi}{\partial n} \right) d\Sigma \tag{12}$$

where $\partial/\partial n$ is the derivative in the direction normal to Σ and pointing away from Ω (figure 1). The integration may be performed by making substitutions $\Theta = p$ and $\Psi = 1/r_S$, using spherical coordinates to describe the position of sources of surface pressure fluctuations $\vec{r}_s = (r_S, \vartheta_S, \varphi_S)$, and dividing the surface, Σ, bounding the half-space, Ω, as shown in figure 1,

$$\oint_{\Omega}\left[\frac{1}{r_S}\nabla^2 p - p\nabla^2\left(\frac{1}{r_S}\right)\right]d\Omega = \oint_{\Sigma_1}\left[\frac{1}{r_S}\frac{\partial p}{\partial n} - p\frac{\partial}{\partial n}\left(\frac{1}{r_S}\right)\right]d\Sigma_1 + \lim_{r_S\to 0}\oint_{\Sigma_2}\left[\frac{1}{r_S}\frac{\partial p}{\partial n} - p\frac{\partial}{\partial n}\left(\frac{1}{r_S}\right)\right]d\Sigma_2 + \lim_{r_S\to\infty}\oint_{\Sigma_3}\left[\frac{1}{r_S}\frac{\partial p}{\partial n} - p\frac{\partial}{\partial n}\left(\frac{1}{r_S}\right)\right]d\Sigma_3 \tag{13}$$

The second term of the integrand on the left hand side is zero because

$$\nabla^2\left(\frac{1}{r_S}\right) = 0 \tag{14}$$

and the last integral on the right hand side is zero since

$$\lim_{r_S\to\infty}\left(\frac{1}{r_S}\right) = 0 \tag{15}$$

$$\lim_{r_S\to\infty}(p) = 0 \tag{16}$$

Equation 16 is a boundary condition. The pressure fluctuations are assumed zero far from the boundary layer. Also, the second term of the integrand over Σ_1 is zero because at all points on Σ_1 the position vector, $\vec{r}_s = (r_S, \vartheta_S, \varphi_S)$, is parallel to Σ_1. Therefore, for all points on Σ_1,

$$\frac{\partial}{\partial n}\left(\frac{1}{r_S}\right) = 0 \tag{17}$$

Substituting equations 14 - 17 into equation 13 leaves

$$\oint_{\Omega}\left[\frac{1}{r_S}\nabla^2 p\right]d\Omega = \oint_{\Sigma_1}\left[\frac{1}{r_S}\frac{\partial p}{\partial n}\right]d\Sigma_1 + \lim_{r_S\to 0}\oint_{\Sigma_2}\left[\frac{1}{r_S}\frac{\partial p}{\partial n} - p\frac{\partial}{\partial n}\left(\frac{1}{r_S}\right)\right]d\Sigma_2 \tag{18}$$

For the integral over Σ_2, r_S is constant. Therefore,

$$\partial n = -\partial r_S$$

$$d\Sigma_2 = r_S^2 \sin\vartheta_S \, d\vartheta_S \, d\varphi_S$$

and the integral over Σ_2 becomes

$$\lim_{r_S \to 0} \oint_{\Sigma_2} \left[\frac{1}{r_S} \frac{\partial p}{\partial n} - p \frac{\partial}{\partial n} \left(\frac{1}{r_S} \right) \right] d\Sigma_2 = \lim_{r_S \to 0} \oint_{\Sigma_2} - \left[\frac{1}{r_S} \frac{\partial p}{\partial r_S} - p \frac{\partial}{\partial r} \left(\frac{1}{r_S} \right) \right] r_S^2 \sin\vartheta_S \, d\vartheta_S \, d\varphi_S$$

$$= \lim_{r_S \to 0} \oint_{\Sigma_2} - \left[r_S \frac{\partial p}{\partial r_S} + p \left(\frac{1}{r_S^2} \right) r_S^2 \right] \sin\vartheta_S \, d\vartheta_S \, d\varphi_S \qquad (19)$$

$$= \lim_{r_S \to 0} \oint_{\Sigma_2} - \left[r_S \frac{\partial p}{\partial r_S} + p \right] \sin\vartheta_S \, d\vartheta_S \, d\varphi_S$$

Since $\partial p / \partial r_S$ remains finite as $r_S \to 0$,

$$\lim_{r_S \to 0} \left(r_S \frac{\partial p}{\partial r_S} \right) = 0 \qquad (20)$$

which leaves

$$\lim_{r_S \to 0} \oint_{\Sigma_2} \left[\frac{1}{r_S} \frac{\partial p}{\partial n} - p \frac{\partial}{\partial n} \left(\frac{1}{r_S} \right) \right] d\Sigma_2 = \lim_{r_S \to 0} \oint_{\Sigma_2} - \left[r_S \frac{\partial p}{\partial r_S} + p \right] \sin\vartheta_S \, d\vartheta_S \, d\varphi_S$$

$$= \lim_{r_S \to 0} \oint_{\Sigma_2} (-p) \sin\vartheta_S \, d\vartheta_S \, d\varphi_S$$

$$= \int_0^{\pi} \int_0^{\pi} (-p_O) \sin\vartheta_S \, d\vartheta_S \, d\varphi_S \qquad (21)$$

$$= \int_0^{\pi} \left(p_O \cos\vartheta_S \right)_0^{\pi} d\varphi_S$$

$$= \int_0^{\pi} (-2 p_O) \, d\varphi_S$$

$$= -2\pi p_O$$

The surface Σ_2 has become point O (figure 1) through the limit $r_S \to 0$. Therefore p_O denotes the fluctuating pressure at point O, on the wall. In fact, p_O is quantity of interest in the present development. Substituting equation 21 into equation 18 yields

$$\oint_{\Omega} \left[\frac{1}{r_S} \nabla^2 p \right] d\Omega = \oint_{\Sigma_1} \left[\frac{1}{r_S} \frac{\partial p}{\partial n} \right] d\Sigma_1 - 2\pi p_O \qquad (22)$$

Evaluation of the integral over Σ_1 is not straightforward and requires consideration of the physical situation. In the limit as $r \to 0$, the surface Σ_1 consists of all points on the wall except point O (figure 1). Also, on Σ_1 $\partial p / \partial n$ is equivalent to $-\partial p / \partial y$ at $y = 0$ in a Cartesian (x, y, z) coordinate

system (figure 1). The pressure gradient is related to the velocity field through equation 1. Since $\vec{U} = (U, V, W)$, equation 1 consists of three scalar equations for momentum transport. By doing a Reynolds decomposition of the V-momentum equation, subtracting the mean V-momentum equation, applying the continuity equation (equation 2) and requiring that all velocity components, both mean and fluctuating, are zero at $y = 0$ (the "no-slip" condition) one is left with

$$\left.\frac{\partial p}{\partial y}\right|_{y=0} = \upsilon \left.\frac{\partial^2 v}{\partial y^2}\right|_{y=0} \tag{23}$$

where υ is the kinematic viscosity. Kim (1989), using a direct numerical simulation database of a channel flow (Kim *et al.*, 1987; $Re_\theta = 283$), kept equation 23 as a boundary condition in his calculation of p and referred to the solution of $\partial p/\partial y$ at $y = 0$ as the "Stokes" pressure. In his calculation, the Stokes pressure contributed less than 10% to the total p' at the wall, which he concluded was insignificant. In the present development, the integral over Σ_1 is assumed insignificant, and neglected. Therefore, the solution to equation 22 may be written as

$$\begin{aligned} p_O &= -\frac{\rho}{2\pi}\oint_\Omega \left[\frac{1}{r_S}\nabla^2 p\right] d\Omega \\ &= \frac{\rho}{2\pi}\oint_\Omega \left[2\frac{\partial \overline{U}_i}{\partial x_j}\frac{\partial u_j}{\partial x_i} + \frac{\partial^2}{\partial x_i \partial x_j}\left(u_i u_j - \overline{u_i u_j}\right)\right]\frac{d\Omega}{r_S} \end{aligned} \tag{24}$$

As with equation 11, equation 24 can be split into a *rapid* pressure that describes the mean shear-turbulence interaction and a *slow* pressure which describes the turbulence-turbulence interaction. Since the remainder of this document deals with surface pressure fluctuations, the subscript "O" is dropped with the understanding that p is the fluctuating pressure at a point on the wall. Equation 24 is rewritten with these considerations as the *Poisson Integral*,

$$p = \frac{\rho}{\pi}\oint_\Omega \left[\frac{\partial \overline{U}_i}{\partial x_j}\frac{\partial u_j}{\partial x_i}\right]\frac{d\Omega}{r_S} + \frac{\rho}{2\pi}\oint_\Omega \left[\frac{\partial^2}{\partial x_i \partial x_j}\left(u_i u_j - \overline{u_i u_j}\right)\right]\frac{d\Omega}{r_S} \tag{25}$$

1.3. Literature Review

1.3.1. Pressure Fluctuations

Pressure fluctuations generated by turbulent flow has received considerable attention over the past 45 years. A review of knowledge about pressure fluctuations beneath turbulent boundary

layers is given by Willmarth (1975). Blake (1986) gives a comprehensive review of experimental research and theory. The review of Eckelmann (1990) covers the period from 1975 to 1987. It focusses mainly on low Reynolds number direct numerical simulations and experiments that used conditional sampling/averaging techniques to investigate the role of coherent structures in the relationship between velocity fluctuations within the turbulent boundary layer and pressure fluctuations at the surface beneath the turbulent boundary layer. The comprehensive review of Bull (1996) covers theoretical and experimental research from the 1950s up to 1992.

Some of the earliest research on turbulent pressure fluctuations is the theoretical work of Lighthill (1952, 1954). His formulation followed an analogy approach. Rather than solve for a turbulent flow directly, he considered an equivalent system of a uniform acoustic medium at rest that is subjected to an external fluctuating stress. The external fluctuating stress is the difference between the momentum fluctuation of the turbulent flow and the hydrostatic pressure of the uniform acoustic medium. This approach is often referred to as *Lighthill's analogy* and is fundamental to modern aeroacoustic theory.

The theoretical work of Kraichnan (1956) and Phillips (1956) focussed on pressure fluctuations within an incompressible, zero pressure gradient, turbulent boundary layer. Their analyses were based directly on the Navier-Stokes equation and assumed that the turbulence was homogeneous in planes parallel to an infinite plane boundary. This assumption allowed them to calculate the wavenumber-frequency spectrum using a partial Fourier transform. Their analysis showed that the wavenumber-frequency spectrum is zero at zero wavenumber independent of frequency. This result is often referred to as the *Kraichnan-Phillips theorem.* Ffowcs-Williams (1982) later showed that the Kraichnan-Phillips theorem is only true in the limit as Mach number goes to zero.

Willmarth and Wooldridge (1962) measured one of the first high quality data sets of surface pressure fluctuations. Measurements of the mean square and power spectrum of pressure, the space-time correlation of pressure in the streamwise direction, and the spatial correlation of pressure in the lateral direction were carried out beneath a thick boundary layer ($Re_\theta = 29000$, 38000). Their analysis showed that pressure-producing turbulent structures are convected

downstream at a speed that varies with wavelength. Long wavelength disturbances are convected downstream faster than short wavelength disturbances. They also showed that pressure-producing turbulent structures decay and vanish after traveling a distance of approximately six wavelengths. The lateral and streamwise length scales of the fluctuating pressure were found to be the same– on the order of the boundary layer thickness.

Corcos (1963) used the measurements of Willmarth and Wooldridge (1962) to develop a correction for measured power spectra that accounts for the attenuation of high frequency spectral levels due to finite (non-zero) transducer size. Corcos (1963) assumed that the cross-spectrum of surface pressure fluctuations was separable in the streamwise and lateral directions. Using this assumption he was able to numerically integrate the spatial correlation data of Willmarth and Wooldridge (1962). The Corcos (1963) correction and spectral attenuation due to finite transducer size is discussed in more detail in §2.3.2.

Schloemer (1967) measured the power spectrum, and the magnitude of the streamwise and lateral cross-spectrum of surface pressure fluctuations. The measurements were carried out in mild adverse, mild favorable, and zero pressure gradient flows. The adverse pressure gradient increased low frequency spectral levels with little effect on the high frequency spectral levels. Decreased high frequency spectral levels were measured in the favorable pressure gradient flow. The decay of a given turbulent structure in the streamwise direction was more rapid in the adverse pressure gradient flow and slower in the favorable pressure gradient flow. The lateral cross-spectral levels were unaffected by the pressure gradient.

Bradshaw (1967) measured power spectra of surface pressure and surface pressure-velocity correlations in a turbulent boundary layer with equilibrium, adverse pressure gradient. His results were presented in the context of "active" shear stress producing motions and "inactive" irrotational motions that contribute little to the production of shear stresses. The concept that the inner turbulent boundary layer consists of active and inactive motions was attributed to Townsend (1961) and the data of Bradshaw (1967) support this concept. Bradshaw (1967) also used dimensional analysis to show that the contribution of the active motions to the wavenumber spectrum of surface pressure fluctuations decays as τ_W^2/k_1 up to a

wavenumber that is proportional to the thickness of the viscous sublayer. Using arguments relating the existence of an inner boundary layer variable scaling and an outer boundary layer variable scaling, he proposed that an overlap region exists in the p spectrum beneath two-dimensional, turbulent boundary layers at high Reynolds number. Both inner and outer variable scalings should collapse the p spectrum within the overlap region and the spectrum should decay as ω^{-1}.

Blake (1970) measured the pressure fluctuations beneath several high Reynolds number ($8210 < Re_\theta < 29800$) zero-pressure gradient smooth-wall boundary layers and several rough wall boundary layers in which the height and separation of the rough elements were independently varied. Power spectra and broadband spatial correlations of p in both the streamwise and lateral directions were presented. The smooth-wall p spectra showed the overlap region proposed by Bradshaw (1967), however, the observed spectral decay was $\omega^{-0.75}$. His smooth-wall spatial correlation data was in agreement with the earlier measurements of Willmarth and Wooldridge (1962) and his smooth-wall cross-spectral data exhibited the longitudinal and lateral similarity proposed by Corcos (1963). The high frequency spectral levels of surface pressure on the rough walls collapsed when normalized using the roughness height, friction velocity, and wall shear stress. The roughness separation affected the large-scale turbulent motions and the roughness height was the main influence on the medium and small-scale turbulence.

Fricke (1971) presented measurements of the power spectrum and spatial correlation of surface pressure fluctuations in the streamwise direction in the separated flow behind a boundary layer fence. His results show that root-mean-square of surface pressure fluctuations beneath subsonic, separated flows are an order of magnitude higher than the value measured beneath an attached boundary layer. He also formulated a model for the root-mean-square of surface pressure fluctuations beneath the separated flow behind a boundary layer fence that agreed well with his data. His model was a modified form of Kraichnan's (1956) analysis.

Panton and Linebarger (1974) calculated the one-dimensional wavenumber spectrum of surface pressure fluctuations in the streamwise direction beneath an equilibrium boundary layer. They used the formulation of Kraichnan (1956) and only included the mean shear-wall-normal

fluctuating velocity term of the Poisson integral (equation 25). They assumed functional forms for the mean velocity and wall-normal velocity fluctuations. The form of the spatial correlation of wall-normal velocity fluctuations that they used included a scale-anisotropy factor. They show the contribution of the inner, middle, and outer layer to different parts of the wavenumber spectrum. They also show the variation of different parts of the wavenumber spectrum with equilibrium pressure gradient and their scale-anisotropy parameter.

Schewe (1983) measured the surface pressure fluctuations beneath a zero pressure gradient, turbulent boundary layer with transducers of various size and an array of four small transducers. He showed that the probability distribution measured with a large transducer does not resolve the large amplitude pressure events. As the transducer size increases the probability distribution function, skewness, and flatness factor approach a Gaussian distribution. It was shown that a transducer diameter of $d^+ = 19$ is sufficient to resolve the essential structures of the turbulent boundary layer fluctuations. Schewe used his data and the data of selected previous investigations (with higher d^+) to show a trend of increasing measured values of p'/Q_e as d^+ increases.

Simpson *et al.* (1987) measured the power spectrum and convective wave speed of surface pressure fluctuations at several locations beneath a two-dimensional separating boundary layer. The root-mean-square pressure fluctuations increased monotonically through the adverse pressure gradient attached-flow region and the detached-flow region and was proportional to the ratio of the streamwise length scale to the length scale in other directions. The power spectra at several locations that span the development of boundary layer separation collapsed at high frequencies when normalized using δ^*/U_∞ as the time scale and the maximum shearing stress as the pressure scale. The p spectra showed an ω^{-3} decay at the higher frequencies of the separating flow which is in agreement with the earlier investigations of Bradshaw (1967) and Schloemer (1967) of p beneath two-dimensional, adverse-pressure-gradient, boundary layers. The convective wave speed of surface pressure fluctuations at high frequencies decreased downstream of the onset of the separation process. The decrease was attributed to intermittent backflow.

McGrath and Simpson (1987) measured the power spectrum, coherence, and convective wave speeds of surface pressure fluctuations beneath turbulent boundary layers with zero and favorable pressure gradient that covered a range of Re_θ from 3000 to 18800. The power spectra beneath the zero pressure gradient boundary layer collapsed at low frequencies when normalized using δ^*/U_e as the time scale and τ_W as the pressure scale and collapsed at high frequencies when normalized using ν/u_τ^2 as the time scale and τ_W as the pressure scale. An overlap region in which both the high frequency scaling and low frequency scaling collapse the power spectra was observed in the zero pressure gradient boundary layers with $Re_\theta > 5000$. The p spectra within the overlap region decayed as $\omega^{-0.7}$ rather than ω^{-1} as proposed by Bradshaw (1967). The lateral coherence in the zero pressure gradient flow decayed faster than in the favorable pressure gradient flow which is in agreement with the earlier investigation of Schloemer (1967). Also, the convective wave speed normalized by the free-stream velocity was faster in the favorable pressure gradient flow which is in agreement with the earlier investigation of Schloemer (1967).

Kim (1989) calculated the pressure fluctuations in a turbulent channel flow using the direct numerical simulation database of Kim *et al.* (1987). He retained the slow pressure term of the Poisson equation (equation 11). He found that the contribution of the slow pressure term to the pressure fluctuations was larger than the rapid pressure contribution throughout the channel except very near the wall, where they were approximately the same. This contradicts the earlier arguments of Kraichnan (1956) and Panton and Linebarger (1974) that the contribution of the slow pressure term to the Poisson equation (equation 11) is negligible. Probability density distributions, power spectra, and spatial correlations of the pressure fluctuations throughout the flow field were also calculated and discussed.

Farabee and Casarella (1991) measured power spectra and cross-spectra of surface pressure fluctuations beneath several two-dimensional, zero pressure gradient, turbulent boundary layers that covered a range of Re_θ from 3386 to 6025. They present experimentally measured power spectra that extend to among the lowest frequencies ever reported. Though not shown, they report that the low frequency spectral levels collapse when normalized using δ^*/U_e as the time scale and Q_e as the pressure scale and follow an ω^2 frequency dependence. They also use the observed scaling behavior of the power spectrum to develop an equation for the mean-square

surface pressure fluctuations that increases as the natural logarithm of the Reynolds number, Re_δ. Their data does not support the streamwise cross-spectral similarity proposed by Corcos (1963). Their convective wave speed data show that sources within the outer and inner boundary layer produce the low and high wavenumber spectrum, respectively.

Keith *et al.* (1992) present power spectra of surface pressure fluctuations from various experimental and numerical studies normalized using several different scaling laws. The attenuation of high frequency spectral levels caused by inadequate transducer spatial resolution is discussed. Dimensional analysis is used to relate various scaling laws to one another and show the Reynolds number (Re_θ) dependence of each of the scaling laws.

Gravante *et al.* (1998) measured power spectra of surface pressure fluctuations beneath several two-dimensional, zero pressure gradient, turbulent boundary layer that cover a Re_θ from 1577 to 7076. Measurements were carried out using transducers with pinhole masks of various sizes ($2 \le d^+ \le 27$) in order to investigate the effect of transducer spatial resolution on measured high frequency spectral levels. They concluded that a transducer sensing diameter in the range $12 \le d^+ < 18$ was required in order to avoid spectral attenuation for frequencies up to $f^+ \equiv fv/u_\tau^2 = 1$. However, the reduction in measured values of the root-mean-square surface pressure was barely noticeable for transducers with a diameter $d^+ < 27$.

1.3.2. Wing-Body Junction Flow

The flowfield around a wing-body junction is well documented for a variety of wing shapes and a wide range of Reynolds number. As a turbulent boundary layer on a flat wall flows around a wing mounted normal to the wall, the lateral mean vorticity generated within the boundary layer is stretched around the wing and, in this way, a significant component of vorticity forms in the streamwise direction. A horseshoe vortex that is wrapped around the wing and has legs that extend downstream of the junction is characteristic of a wing-body junction flow (figure 2). Most previous studies have focussed on the complex, highly unsteady flow just upstream of the nose of the wing. Pierce and Tree (1990) conducted an oil flow visualization, measured the mean surface pressure, and used a LDV to measure the streamwise and wall-normal mean velocity components in the nose region of a symmetric wing. The wing section used in their

study had a circular nose and the approach Re_θ= 12500. The focus of their study was to determine a vortex model for the mean flow. Devenport and Simpson (1990) used oil flow visualization, mean pressure measurements on the test wall and wing surface, single-component (streamwise) hot-wire anemometer measurements, and three-component LDV measurements to document the time-averaged and time-dependent turbulent structure in the plane of symmetry just upstream of a wing-body junction. Their study was conducted using the same wing model as used in the present study (3:2 elliptic nose, NACA 0020 tail). The approach Re_θ was 6700. The measurements of the mean velocity and Reynolds stress tensor were used to compute spatial correlations and the turbulent kinetic energy balance. They were the first to report bimodal probability distribution functions of the streamwise and wall-normal velocity at some measurement locations. The bimodal probability distribution functions cause high levels of turbulence intensity. Further references to research concerning the wing-body junction flow are given by Ha (1993), Simpson (1996), Lewis (1996), and Fleming (1997).

Hasan *et al.* (1985) present the mean and fluctuating streamwise component and correlations between the streamwise and wall-normal velocity fluctuations measured with a hot-wire anemometer and surface pressure power spectra and RMS pressure distributions around a wing-body junction. Their measurements were made on irregularly spaced grid of locations that extended from 6.0 times the wing thickness upstream of the wing nose to 2.5 times the wing thickness downstream and laterally from the plane of symmetry to 1.5 times the wing thickness to the side of the wing. The wing cross-section consisted of a 3:1 elliptic nose, parallel mid-body, and a NACA 0020 tail. The free-stream velocity of the approach flow was 30 m/s. The power spectra of wall-pressure show a consistent trend of low frequency spectral levels at locations near the wing that are high as compared to the low frequency spectra at locations away from the wing. They attribute the elevated spectral levels to low frequency organized motions associated with the wing-body junction vortex.

Previous studies of the fluctuating surface pressure in a wing-body junction flow are confined mainly to the unsteady nose region just upstream of the wing. Rife *et al.* (1992) and Shinpaugh (1994) examined the relationship between the bimodal velocity and surface pressure fluctuations in the nose region. Rife *et al.* (1992) measured the streamwise and wall-normal

velocity components and surface pressure simultaneously in a flow with an approach $Re_\theta = 6900$. They presented power spectra and probability distribution functions of the surface pressure along with conditionally averaged correlations between the surface pressure fluctuations and each of the velocity components that they measured. Shinpaugh (1994) measured the streamwise and wall-normal velocity components and surface pressure simultaneously in a flow with an approach $Re_\theta = 6700$. He presented probability distribution functions of the surface pressure and conditionally averaged correlations between the surface pressure fluctuations and each of the velocity components that he measured. Ölçmen and Simpson (1994) studied the effect of wing shape on surface pressure fluctuations just upstream of a wing-body junction. They studied six different shapes, including the geometry used in the present investigation. They used oil flow visualizations of the near-wall flow and probability distributions and power spectra of the surface pressure fluctuations in their analysis. They were able to empirically relate a fluctuating pressure force to the momentum rate in the streamwise and wall-normal direction.

The velocity field at the measurement stations used in the present study (figure 3) have been extensively documented by Ölçmen and Simpson (1995a, 1996) and Ölçmen *et al.* (1998). The LDV measurements of the complete velocity vector, Reynolds stress tensor and triple products, mean surface pressure measurements, and oil flow visualizations that were performed in conjunction with the above studies were used directly in the present investigation.

1.3.3. Flow Around a 6:1 Prolate Spheroid

The flow about a 6:1 prolate spheroid exhibits open separation phenomena of three-dimensional flow (figure 4). It is reflected by the convergence of skin friction lines (Wetzel *et al.*, 1998). The flow separating from the lee-side rolls up into a strong vortex on each side of the body. This primary vortex may be accompanied by one or more smaller vortices, each of which is associated with a separation and reattachment line. The complex interactions between vortices result in a highly skewed three-dimensional shear layer. Kreplin *et al.* (1985, 1993) Meier *et al.* (1984, 1985) and Vollmers *et al.* (1983) have documented the surface flow, mean surface pressure, skin friction, and mean velocity at several Reynolds numbers and angles of attack. The leeside flow has proven difficult for turbulence models to calculate (Chesnakas and Simpson, 1996; AGARD, 1991; Gee *et al.*, 1992; Sung *et al.*, 1993).

The current study is part of an ongoing effort to extensively measure this flowfield in order to increase the understanding of the flow physics and to provide an experimental data base for comparison with computations. The effects of Reynolds number and angle of attack on boundary layer transition and separation location were studied by Ahn and Simpson (1992). Barber and Simpson (1991) documented the mean and turbulent velocities in the cross-flow separation region, but the use of five-hole pressure probes and crossed hot wires precluded them from obtaining data within the inner boundary layer. Previous studies of a tripped flow at a length Reynolds number $Re_L = 4.2\times10^6$ by Chesnakas *et al.* (1993) and Chesnakas and Simpson (1994, 1996, 1997) did not suffer this limitation and have documented the turbulence structure, including all Reynolds stresses and velocity triple products, from y^+ closer than 7. This was possible through the use of the specially designed, miniature fiber-optic LDV probe described in Chesnakas and Simpson (1994). The data of Chesnakas et al (1993) and Chesnakas and Simpson (1994, 1996, 1997) were used directly in the present study. Simpson (1989, 1995, 1996) reviewed three-dimensional turbulent separation in detail. Wetzel, *et al.* (1998) focussed on the measurement and quantitative description of three-dimensional crossflow separation.

Much analysis of surface pressure fluctuations beneath equilibrium, 2-D boundary layers exist in the literature. The present study extends this knowledge to the analysis of a complex, 3-D, separating boundary layer of practical interest. Additionally, the flows of the present study cover a large range of Reynolds number. Surface pressure-velocity spatial correlations and the extensive data on the turbulent velocity field are used to explain features of p and p'.

1.4. Outline of Dissertation

This dissertation presents experimental measurements of the surface pressure fluctuations beneath a two-dimensional boundary layer and two three-dimensional turbulent boundary layers of practical interest. The goals of this research were (1) to characterize the surface pressure fluctuations beneath three-dimensional turbulent boundary layers of practical interest, (2) to gain understanding of the effect of flow three-dimensionality on surface pressure fluctuations, and (3) to investigate the relationship between surface pressure fluctuations and the complex, three-dimensional structure of the turbulent velocity field. The approach was to study the statistics of both the surface pressure and the velocity field through new measurements of the fluctuating

surface pressure and existing measurements of the velocity field and the covariance of the surface pressure and fluctuating velocity components. Chapter 2 describes the experimental method used in the present investigation. Chapter 3 presents the measurements of the fluctuating surface pressure beneath two-dimensional boundary layers that serve as a baseline for comparison to the measurements of the fluctuating surface pressure beneath three-dimensional boundary layers. Chapter 4 presents measurements of the root mean square (RMS) and spectral power density of the fluctuating surface pressure at 10 locations beneath the turbulent boundary layer away from a wing-body junction. Some scaling issues are also discussed. Chapter 5 presents measurements of the root mean square (RMS) and spectral power density of the fluctuating surface pressure and surface pressure-velocity correlations about a 6:1 prolate spheroid. Conclusions drawn from this research and suggestions for further research are the subject of Chapter 6.

2. EXPERIMENTAL APPARATUS AND TECHNIQUES

2.1. Test Facilities

2.1.1. Virginia Tech Boundary Layer Wind Tunnel

The Virginia Tech Boundary Layer Wind Tunnel is an open circuit, subsonic wind tunnel. The tunnel test section is 8 m long with a rectangular cross section that is 0.91 m wide with variable height in order to adjust the streamwise pressure gradient (figure 5). Test flows are generated by a 19 kW centrifugal blower that draws air through an air filter and blows the air through a fixed-setting flow damper that is used to control flow speed. Downstream of the blower, a section of honeycomb, a two-dimensional 4:1 contraction ratio, and seven wire-mesh screens reduce the free-stream turbulence intensity to 0.2% at a nominal flow speed of 27 m/s (Devenport and Simpson, 1990). The maximum nominal flow velocity is 32 m/s. As the flow enters the test section, the boundary layer is tripped by a 6.3 mm high step after which it passes through an additional 1.5:1 contraction and reaches a throat where the test section height is 25.1 cm. The nominal flow velocity and temperature are measured at the throat which is 1.63 m downstream of the test section entrance. An additional roughness plate is secured to the test section floor 1.35 m downstream of the test section entrance in order to thicken the boundary layer and thereby produce higher Reynolds number flows (e.g. $Re_\theta = 23400$). The roughness plate is 61 cm long and consists of 3.2 mm high, 3.2 mm wide, square ribs that extend the width of the test section and are spaced 12.7 mm apart in the streamwise direction (Ölçmen *et al.*, 1998). The roughness plate is not required to produce the lower Re_θ (= 7300) flow. The height of the test section gradually increases downstream of the throat in order to allow for the growth of the boundary layer and maintain a very nearly zero streamwise pressure gradient. Hot-wire traverses show that the potential core is uniform within +3%/-1.5% in the streamwise direction and ±2% in the lateral direction (Ölçmen *et al.*, 1998). The wind tunnel is fully contained within an indoor laboratory and the flow temperature is regulated to within ±1°C by a Carrier brand A/C unit. Further information may be found on the Internet at http://www.aoe.vt.edu/aoe/physical/bllab.html.

2.1.2. Virginia Tech Stability Wind Tunnel

The Virginia Tech Stability Wind Tunnel is a continuous, closed jet, single return, subsonic wind tunnel with a 7.3 m long test section that has a 1.8 m square cross section (figure 6). The tunnel was acquired by Virginia Tech in 1958 from the NACA Langley Aeronautical Laboratory where it was originally constructed in 1940. Test flows are generated by a 4.3 m propeller which is driven by a by a 450 kW d.c. motor. The maximum flow velocity is 84 m/s. Tunnel speed is regulated by a custom designed Emerson VIP ES-6600 SCR Drive and the flow temperature is stabilized through the continuous entrainment of atmospheric air by an air exchange tower. The regulated power supply, turning vanes, a 9:1 contraction, and seven wire-mesh screens provide low free-stream turbulence levels — of the order of 0.03% (Choi and Simpson, 1987). A comprehensive discussion of the Virginia Tech Stability Wind Tunnel is given by Simpson (1997). Further information may be found on the Internet at http://www.aoe.vt.edu/aoe/physical/tunnel_descrip.htm.

2.2. Test Flows

2.2.1. Two-Dimensional Boundary Layer

The measurements of p beneath two zero-pressure-gradient, two-dimensional boundary layers (Re_θ = 7300, 23400) were carried out in the Virginia Tech Boundary Layer Wind Tunnel (§2.1.1). For the Re_θ = 7300 flow, the nominal free-stream air speed was 27.5 m/s and measurements were made 303 cm downstream of the test section entrance. The velocity field has been documented by Ölçmen and Simpson (1996) and is discussed further in chapter 3. For the Re_θ = 23400 flow, the nominal free-stream air speed was 32.0 m/s and measurements were made 696 cm downstream of the test section entrance. The velocity field has been documented by Ölçmen *et al.* (1998) and is discussed further in chapter 3. All measurements were carried out at ambient pressure and the flow temperature was 25°C ± 1°C.

2.2.2. Wing-Body Junction Flow

The measurements of p in two pressure driven, three dimensional turbulent boundary layers that are each produced by a wing-body junction geometry were carried out in the Virginia Tech Boundary Layer Wind Tunnel (§2.1.1: figure 7). For one of the flows, the nominal air speed was 27.5 m/s and Re_θ = 5940 based on the momentum thickness at 0.75 chord lengths upstream

of the nose of the wing on the tunnel centerline. For the other flow, the nominal air speed was 32.0 m/s and $Re_\theta = 23200$ based on the momentum thickness in the 2-D flow produced by removing the wing. All measurements were carried out at ambient pressure and the flow temperature was 25°C ± 1°C.

In each flow, measurements of p were carried out at 10 *stations* that traverse one side of the wing (figure 3) and are away from the horseshoe vortex that forms about the wing-body junction (figure 2). These flows are referred to as "wing-body junction" flows only to distinguish them from the other pressure-driven, three-dimensional turbulent boundary layer that is produced by the flow about a 6:1 prolate spheroid and is also part of the present investigation. The measurement stations were chosen based on the existence of previously documented mean velocity, Reynolds stress, triple products, and skin friction measurements (Ölçmen *et al.*, 1999b; $Re_\theta = 5940$: Ölçmen and Simpson, 1995a, 1996; $Re_\theta = 23200$: Ölçmen *et al.*, 1998, 1999b). The existing velocity measurements were carried out using a three-orthogonal-velocity-component, fiber-optic laser-Doppler velocimeter (LDV) probe (Ölçmen and Simpson, 1995b).

The same wing model was used for both Re_θ flows. It has a maximum thickness of 7.17 cm, chord length of 30.5 cm, and a height of 22.9 cm. The wing cross-section is a 3:2 elliptical nose, with the major axis aligned with the chord, and a NACA 0020 tail joined at the maximum thickness. The wing was mounted at zero angle of attack with the leading edge 302 cm downstream of the test section entrance in the $Re_\theta = 5940$ flow and 707 cm downstream of the test section entrance in the $Re_\theta = 23200$ flow. A 3.7 mm gap was left between the ceiling of the test section and the top of the wing model in order to prevent the formation of a second horseshoe vortex. The mean surface pressure measurements and oil flow visualizations conducted on the test section floor by Ölçmen and Simpson (1995a: $Re_\theta = 5940$) and Ölçmen *et al.* (1998: $Re_\theta = 23200$) confirmed that the wing was mounted at zero angle of attack and showed that blockage effects, due to the test section side walls, are negligible when the test section is configured in the manner used for the present study.

2.2.3. Flow Around a 6:1 Prolate Spheroid

The measurements of p beneath the pressure driven, three dimensional turbulent boundary layer that is produced by flow about a 6:1 prolate spheroid were carried out in the Virginia Tech Stability Wind Tunnel (§2.1.2). Measurements were carried out at $\alpha = 10°$, 20° and $x/L = 0.600$,

0.772. At each of these four measurement *stations*, p was measured at 5° increments of ϕ in the range $90° \leq \phi \leq 180°$ where $\phi = 0°$ is the most windward ϕ *location* and $\phi = 180°$ is the most leeward ϕ location on the model. All measurements were conducted at a constant Reynolds number, $Re_L = 4.20 \times 10^6$ (50.73 m/s < U_∞ < 55.25 m/s), and ambient temperature. The velocity field at the present measurement stations has been documented by Chesnakas and Simpson (1994, 1996, 1997) and is discussed further in chapter 5.

The 6:1 prolate spheroid that was used for these measurements is 1.37 m long and was constructed of a machined fiberglass skin bonded to an aluminum frame. A circumferential trip, consisting of posts 1.2 mm in diameter, 0.7 mm high and spaced 2.5 mm apart, was placed around the model circumference at $x/L = 0.2$. This fixed the location of transition. Windows of size 30 mm × 150 mm × 0.75 mm (figure 8) were placed in the skin of the model for optical access to the flow (Chesnakas and Simpson, 1994, 1996, 1997). The windows were molded to the curvature of the model and mounted flush with the model surface in order to alleviate flow disturbances. Wax was used to fill any small gaps in the model surface. The model was supported with a rear-mounted, 0.75 m long sting aligned along the model axis and connected to a vertical post extending through the wind tunnel floor.

2.3. Some Measurement Issues

2.3.1. Low Frequency Spectral Contamination

Measured pressure signals are usually contaminated by coherent, facility-related acoustic pressures and external vibration of the transducer. This contamination takes the form of additional spectral energy that is superimposed upon the spectral energy produced by the turbulence and is generally confined to the low frequency end of the spectrum. Low frequency spectral contamination has long been recognized as a source of error in the measurement of turbulent surface pressure fluctuations. Wills (1970) use spatial correlation measurements of p to calculate the spectral contribution due to extraneous sound and vibration. Then, these spectral levels were removed from his measured spectral levels, leaving only the spectral contribution due to the turbulence. Most present day investigations either use an acoustically quiet wind tunnel and accept the experimental uncertainty due to acoustic sources still present or use some type of noise cancellation technique.

Noise cancellation techniques take advantage of the fact that p due to external sound and vibration remain coherent over a larger distance and a longer time as compared to p due to turbulence. Lauchle and Daniels (1987), Simpson *et al.* (1987), Agarwal and Simpson (1989), and Helal *et al.* (1989) each give a comprehensive review of noise cancellation techniques.

Lauchle and Daniels (1987) carried out measurement of p in a pipe flow of glycerine. The glycerine was used to allow for the resolution of the highest frequency p by decreasing the d^+ of their transducer through the high viscosity of glycerine (see §2.3.2). They measured p using three transducer assemblies equally spaced along the circumference of the pipe at a given axial location. The pipe acts as a waveguide. Facility-related acoustic waves travel through the pipe as plane waves normal to the center axis of the pipe. In this way, the contribution to p from to external sound is circumferentially coherent. Each transducer assembly contained a pressure transducer and an accelerometer. Values of p were extracted through a combination of subtracting the measured signal from different pressure transducers, subtracting the measured signal from different accelerometers, and computing cross-spectra.

McGrath and Simpson (1987) used two pressure transducers separated by a lateral distance greater than 4 boundary layer thicknesses to measure p beneath a 2-D boundary layer. Their measurements were carried out in the Virginia Tech Boundary Layer Wind Tunnel test section which acts like a waveguide to facility-related acoustic waves. Their analysis shows that subtracting the two transducer signals from one another left only the p produced by turbulence. The part of the signal measured by each transducer due to external sound and flow unsteadiness produced by the wind tunnel was correlated laterally across the test section. Due to the large transducer spacing, the part of the signal due to turbulence was uncorrelated, but statistically the same since the mean flow was two dimensional. Contamination of the measured signal by external vibration was accounted for by mechanically isolating the pressure transducers from the wind tunnel such as was done in the present study.

Agarwal and Simpson (1989) used two transducers separated by a lateral distance that is slightly less than one-third of the boundary layer thickness. Their measurements were carried out in the Virginia Tech Stability Wind Tunnel test section which acts as a waveguide to facility-

related acoustic waves. Their analysis shows that the method of McGrath and Simpson (1987) removes part of the turbulent p in addition to p from external sources when the microphone spacing is small. However, they show that by time-delaying one of the transducer signal and then subtracting it from the other transducer signal, the p due to turbulence can be recovered, provided that the time delay is longer than δ/U_C. They also show that for the technique to work properly the two transducers must be mechanically coupled. Otherwise the p due to external sound and vibration measured by the two transducers will not necessarily be correlated to one another.

Ölçmen and Simpson (1994) applied the technique of Agarwal and Simpson (1989) using only one transducer to measure p near the nose of a wing-body junction. The time-delay noise cancellation technique of Ölçmen and Simpson (1994) was used in the present study and is described below. In the present study, vibrational contamination of the measured signal was eliminated by mechanically isolating the transducer from the wind tunnel. The signal from a single transducer was delayed by the period of a given frequency and subtracted from the original signal, canceling the contributions from coherent sources at that frequency and higher harmonics.

Consider the pressure signal (mean zero) at two different parts of the measured record, $p(t)$ and $p(t+\Delta t)$, where Δt is the time delay. Each part of the measured signal may be decomposed into a turbulent contribution, p_T, and a contribution due to coherent external sources p_C. It is assumed here that there is no incoherent contribution from external sources.

$$p(t) = p_T(t) + p_C(t) \tag{26}$$

$$p(t+\Delta t) = p_T(t+\Delta t) + p_C(t+\Delta t) \tag{27}$$

Now consider two sub-records where each sub-record is long enough to be stationary. One sub-record starts at $p(t)$ and the other sub-record starts at $p(t+\Delta t)$. The mean square of the sub-record that starts at $p(t)$ subtracted from the sub-record that starts at $p(t+\Delta t)$ is

$$\begin{aligned}\overline{\left[p(t+\Delta t)-p(t)\right]^2} &= \overline{\left[p_T(t+\Delta t)+p_C(t+\Delta t)-p_T(t)-p_C(t)\right]^2} \\ &= \overline{p_T^2(t+\Delta t)} + \overline{p_T^2(t)} + \overline{p_C^2(t+\Delta t)} + \overline{p_C^2(t)} \\ &+ 2\overline{p_T(t+\Delta t)p_C(t+\Delta t)} - 2\overline{p_T(t+\Delta t)p_T(t)} - 2\overline{p_T(t+\Delta t)p_C(t)} \\ &- 2\overline{p_C(t+\Delta t)p_T(t)} - 2\overline{p_C(t+\Delta t)p_C(t)} + 2\overline{p_T(t)p_C(t)}\end{aligned} \tag{28}$$

If Δt is short enough such that $p_C(t)$ and $p_C(t+\Delta t)$ are correlated[†], then

$$\overline{p_C^2(t+\Delta t)} + \overline{p_C^2(t)} = 2\overline{p_C(t+\Delta t)p_C(t)} \tag{29}$$

If Δt is long enough such that $p_T(t)$ and $p_T(t+\Delta t)$ are not correlated, then

$$\overline{p_T(t+\Delta t)p_T(t)} = 0 \tag{30}$$

Since, by definition, p_T and p_C are from independent sources, it follows that

$$\overline{p_T(t+\Delta t)p_C(t+\Delta t)} = 2\overline{p_T(t+\Delta t)p_C(t)} = 2\overline{p_C(t+\Delta t)p_T(t)} = 2\overline{p_T(t)p_C(t)} = 0 \tag{31}$$

Substituting equations 29 - 31 into equation 28 leaves

$$\overline{\left[p(t+\Delta t)-p(t)\right]^2} = \overline{p_T^2(t+\Delta t)} + \overline{p_T^2(t)} \tag{32}$$

But, being that both sub-records are stationary,

$$\overline{p_T^2(t+\Delta t)} = \overline{p_T^2(t)} \tag{33}$$

Therefore,

$$\frac{1}{2}\left(\overline{\left[p(t+\Delta t)-p(t)\right]^2}\right) = \overline{p_T^2(t)} \tag{34}$$

The above analysis, which is done in the time domain, is directly applicable to the spectral power density[‡] through Parseval's theorem. Parseval's theorem states that the mean square may be calculated by integrating the square of the time series (mean zero) over all time or, equivalently, integrating the square of the constituent Fourier components over all frequencies. Therefore, the square of the Fourier components at a particular frequency, which is the spectral power estimate at that frequency, is, in effect, the mean square contribution of fluctuations at that particular frequency. So, through equation 34, the power spectrum of a composite signal that is formed by subtracting a sub-record that starts at $p(t)$ from the sub-record that starts at $p(t+\Delta t)$ will contain only the contribution from the turbulence at the frequency $1/\Delta t$ and higher harmonics.

---

† The sub-record that starts at $p(t)$ and the sub-record that starts at $p(t+\Delta t)$ must be taken from a larger single record of contiguous data in order for equation 29 to be valid.

‡ Also referred to as the power spectrum in the present document

The choice of time-delay is crucial to the success of this noise cancellation technique. The time-delay must be short enough so that equation 29 is valid and long enough so that equation 30 is valid. In practice, most background spectral energy is confined to $f < 100$ Hz, but the results of Agarwal and Simpson suggest that a more conservative estimate would be $f < 1$ kHz. The longest time-delay used for the present measurements was 246 ms[¶]. Since the period of a 1 kHz signal is 1 ms, the highest frequency background spectral energy would need to be coherent for at least 246 periods in order for the constraint imposed by equation 29 to be satisfied. This was assumed to be true in the present study.

In order to satisfy the constraint imposed by equation 30 a long time delay was used. The selection of the time-delay was also influenced by details of the calculation of the power spectrum and follows the development of Ölçmen and Simpson (1994). In the present study, the Fast Fourier Transform (FFT) algorithm of Press *et al.* (1994) was used. This is an algorithm that is based on the Cooley-Tukey Algorithm (1965) which has been optimized for memory usage. It computes the FFT of a discrete time series of N samples that are sampled at a rate of one sample per s seconds where N must be a power of 2. Multiplying the resulting FFT with its complex conjugate yields $N/2$ estimates of the power spectrum that are equally spaced within the frequency range $0 \le f < 1/(2s)$. The frequency resolution of each power spectral estimate is given by the bin width, $\Delta f = 1/(Ns)$. So, in the end, the power spectrum is estimated at the discrete frequencies $f_n = n/(Ns)$ where $n = 0,1,2,\ldots, (N/2 - 1)$. By Parseval's theorem, the spectral value at f_n is an estimate of the contribution to the mean square from fluctuations in the frequency range $(n - \frac{1}{2})/(Ns) \le f_n < (n + \frac{1}{2})/(Ns)$[§]. In the present study, the time-delay $\Delta t = Ns$ was used. The time-delay subtraction removes the contribution from coherent sources at the frequency $1/\Delta t$ and higher harmonics. The calculated power spectrum consists of spectral estimates of the

---

[¶] This time delay was used for the two-dimensional boundary layer and wing-body junction flow data.

[§] Note that the power spectral estimate at f_0 contains energy from the mean of the time series and is usually discarded, as was done in the present study. Each measured time series was made to have zero mean value before computing the FFT in order to insure that any remaining spectral energy from frequencies close to the mean value did not *leak* into (contaminate) adjacent, low frequency spectral estimates (side-lobe leakage is discussed by Bendat and Piersol, 1986, pp. 393-400).

contribution to the mean square from fluctuations at the frequency Δf and higher harmonics. Therefore, by using $\Delta t = 1/\Delta f$, the contributions to from coherent sources were subtracted from each spectral estimate that constitutes the calculated power spectrum.

If the time-delay $\Delta t = 1/\Delta f$ is too short to avoid subtracting some of the turbulent contribution, then the record length, N, is too small and should be increased. Otherwise, the resulting Δf will be too large and will not sufficiently resolve the low frequency power spectrum[††]. In the present study, the shortest sub-record is has a period of 29 ms[‡‡]. Therefore, contributions to p that are at frequencies less than 35 Hz are not resolved. However, the contribution to p' from such sources is negligible in the flows of the present study.

2.3.2. High Frequency Spectral Attenuation

In order to accurately measure the pressure fluctuations at a point one would need an infinitely small transducer. However, commercially available transducers have a finite size. The pressure measured by transducers of finite size is the average pressure applied across the transducer sensing area. Pressure fluctuations smaller than the transducer sensing area are spatially integrated, and thereby attenuated. This causes the measured power spectrum of surface pressure fluctuations to be attenuated at high frequencies.

2.3.2.1. Required Transducer Size

While theoretically an infinitely small transducer is required to accurately measure the full spectrum of wall-pressure fluctuations, experiments have shown that a small, but finite, transducer is sufficient. Schewe (1983) determined that a transducer diameter $d^+ < 19$ is sufficient to resolve all essential wall-pressure fluctuations. Gravante *et al.* (1998) report that the maximum allowable sensing diameter to avoid spectral attenuation at high frequencies is in the range $12 < d^+ < 18$, and for $d^+ < 27$ the reduction in p' was "barely observable". The studies of Schewe (1983) and Gravante *et al.* (1998) show that the required sensing diameter depends on the viscous scales of

---

[††] The analysis of Agarwal and Simpson (1989) show that Δt must be greater than δ / U_C in order to avoid subtracting part of the turbulent contribution to p.

[‡‡] This time delay was used for the 6:1 prolate spheroid flow data.

the flow to be measured. For flows of interest, particularly high Reynolds number flows, the viscous scales are typically smaller than the diameter of commercially available transducers with sufficiently high sensitivity. Often a pinhole mask is used to decrease the effective sensing area of the pressure transducer in order to resolve this issue (Blake, 1970; McGrath and Simpson 1987; Farabee and Casarella, 1991; Gravante *et al.*, 1998). Bull and Thomas (1976) assert that the discontinuity in the wall due to the presence of a pinhole disturbs the flow and leads to a significant error in the measured wall pressure spectrum at high frequencies. However, their assertion is not supported by the favorable comparison of the data of other researchers. For example, the data of Gravante *et al.* (1998) taken using a pinhole ($d^+ = 12$) and the data of Schewe (1983) taken with a flush-mounted transducer ($d^+ = 19$) show nearly identical spectral levels at high frequencies when normalized using viscous scales. It should be noted that the transducer sensing diameter used by Schewe and Gravante *et al.* was more than 4 times smaller than that used by Bull and Thomas. Additionally, Bull (1996) noted in a recent review of knowledge about wall-pressure fluctuations that the error due to the presence of the pinhole may "tend to zero as pinhole diameter is reduced" (p. 308).

A pinhole mask with a diameter of 0.5 mm was used in the present measurement system to reduce spatial averaging. The pinhole mask and transducer dead volume can be approximated as a Helmholtz resonator. The frequency response of a Helmholtz resonator is governed by (as given by Holman, 1989)

$$\frac{p_{TRUE}}{p_{MEASURED}} = \sqrt{\left[1-\left(\frac{\omega}{\omega_n}\right)^2\right]^2 + 4\zeta^2\left(\frac{\omega}{\omega_n}\right)^2} \tag{35}$$

$$\phi_H = tan^{-1}\left(\frac{2\zeta}{\frac{\omega}{\omega_n}-\frac{\omega_n}{\omega}}\right) \tag{36}$$

where

$$\zeta = \frac{16\nu}{d^3 a}\sqrt{\frac{3L_H V_H}{\pi}} \tag{37}$$

and

$$\omega_n = \sqrt{\frac{3\pi d^2 a^2}{16 L_H V_H}} \tag{38}$$

Figure 9 shows the notation used in equations 37 and 38.

2.3.2.2. Correction Methods

The effects of transducer size, shape and sensitivity has been investigated both theoretically and experimentally (Blake, 1986). Initial investigations of this issue sought to characterize the effect of finite transducer size. Corcos (1963, 1967) estimated the attenuation due to finite transducer size for square and circular transducer shapes and provided a correction in terms a similarity parameter, $\omega d/2U_C$. Corcos (1963, 1967) developed the correction assuming that the transducer sensitivity was uniform over the transducer sensing area and by asserting that the cross-spectral density of pressure fluctuations is separable in the streamwise and spanwise direction based on measurements by Willmarth and Wooldridge (1962). Others have extended the analysis of Corcos (1963, 1967) to consider transducers of different shape and sensitivity (Gilchrist and Strawderman, 1965; White, 1967; Geib, 1969; Chase, 1969) Willmarth and Roos (1965) questioned the validity of the Corcos (1963, 1967) correction by questioning the separability and similarity of the cross-spectral density for small spatial separation. More recent experiments by Farabee and Casarella (1991) and Abraham and Keith (1998) showed that the streamwise cross-spectral similarity proposed by Corcos (1963, 1967) does not agree with their data at small spatial separation and low frequency. Singer (1997) proposed a different form of Corcos' similarity hypothesis that compares better with large-eddy simulation results (Singer, 1996) at mixed streamwise and spanwise, or off-axis, separations.

Despite questions concerning the underlying assumptions of the Corcos (1963, 1967) correction, direct examination has shown that the Corcos correction recovers the true pressure spectrum within limits. Schewe (1983) experimentally determined the Corcos correction to be adequate for $\omega d/U_C < 4$. More recently, Lueptow (1995) used a direct numerical simulation of channel flow (Kim *et al.*, 1987) to investigate the effect of transducer size, shape, and sensitivity on the resolution of high frequency pressure fluctuations. Lueptow reported that the Corcos correction recovers the true wall pressure spectrum for $\omega d/U_C < 11$ for a circular deflection-type

transducer such as was used in the present study. The correction given by Corcos (1963) is the method most commonly used to correct experimental wall pressure spectra.

2.4. Pressure Transducer

The Endevco model 8507-C2 pressure transducer (figure 10) was used for the present measurements. It is a high sensitivity piezoresistive, circular-deflection-type, pressure transducer that has a nominally flat frequency response from 0-70 kHz with a rated sensitivity of 130 mV/psi and a full scale output of 300 mV. The transducer contains an active four-arm strain gage bridge that operates with a nominal 10.0 V excitation voltage and is diffused into a sculpted silicon diaphragm.

2.5. Measurements in a Two-Dimensional Boundary Layer and a Wing-Body Junction Flow

The calibration, data acquisition and reduction, and measurement uncertainty of the measurements in the two-dimensional boundary layers is identical to that of the measurements in the wing-body junction flow. Therefore, the description of these procedures for both sets of measurements are grouped together in this section.

2.5.1. Calibration

The nominally flat frequency response (0 kHz $< f <$ 70 kHz) of the Endevco model 8507-C2 pressure transducer is degraded by the response of the pinhole mask that is necessary in order to resolve small-scale pressure fluctuations. Whether or not the degree of degradation is significant depends on flow conditions such as pressure and temperature (equations 35 - 38). The power spectrum of pressure fluctuations beneath the 2-D, $Re_\theta = 23400$ flow without any calibration applied is shown in figure 11. This power spectrum is typical of the power spectra measured in the two-dimensional and wing-body junction flows. The resonant peak due to the pinhole is near 28 kHz. Figure 12 shows the expected amplitude and phase response of the pinhole mask. The amplitude response shown in figure 12 is that of a Helmholtz resonator (equation 35) that is attenuated at high frequencies using the values given by Corcos (1963), assuming that $U_C = 14u_\tau$ (Ha, 1993), in order to account for the finite pinhole size (§2.3.2). The

phase response shown in figure 12 is that of a Helmholtz resonator (equation 36). The maximum deviation of the expected amplitude response, within the frequency range of interest here (0 Hz $< f <$ 20 kHz), is 17% (0.7 dB). The maximum phase shift, within the frequency range of interest here, is 0.8°. Since these values are within acceptable uncertainties of p spectral values, only a static (0 Hz) calibration was performed.

All of the power spectral levels measured in the two-dimensional and wing-body junction flows follow a well defined power law decay at the highest frequencies. Therefore, upward deviations of the high frequency spectral levels from the power law decay are due only to the dynamic response of the pinhole mask. The frequency at which the spectral level starts to deviate from the high frequency spectral power law-type decay is the upper limit of valid spectral levels. Spectral levels calculated at frequencies higher than this upper limit were discarded in the present study.

The static calibration was done using a beaker-tubing arrangement (figure 13). The basic principle is to apply both positive and negative pressures to the beaker using the input tube. The water inside the beaker holds the applied pressure field in the beaker. One of the output tubes is connected to a Datametrics Barocel pressure transducer type 590D-100T-3Q8-H5X-4D (range = 100 torr) which has a known sensitivity and measures the applied pressure. The other output tube is connected to the pressure transducer back-pressure vent tube (figure 13). The static sensitivity of the transducer was 0.0237 mV/Pa during the measurements in the higher Re_θ flows (Re_θ = 23400(2-D), 23200(3-D)). During the measurements in the lower Re_θ flows (Re_θ = 7300(2-D), 5940(3-D)), the static sensitivity of the transducer-amplifier system was 0.0243 mV/Pa.

2.5.2. Data Acquisition and Reduction

The pressure transducer was mounted within a housing unit designed for these experiments (figure 14). Access to the flow field was provided through a 0.5 mm diameter pinhole (figure 15) which was used to decrease spatial averaging (§2.3). The housing unit was mounted flush with the surface of the test section and rigidly supported from the laboratory floor beneath the wind tunnel. The diameter of the housing unit was 1.55 cm while the hole in the test

surface was 1.65 cm in diameter. The resulting gap between the housing unit and the test surface mechanically isolated the housing unit from the wind tunnel which prevented tunnel vibration from contaminating the surface pressure measurements. The gap was covered with 0.03 mm thick cellophane tape in order to provide continuity of the surface while maintaining mechanical isolation of the housing unit. The tape did not significantly contribute to surface roughness because the thickness of the tape is smaller than the viscous sublayer ($\leq 2.3\,\nu/u_\tau$).

The transducer signal was amplified by a Measurements Group model 2310 strain gage conditioning amplifier and stored to 12-bit precision by an IBM-type PC using a RC Electronics ISC-16 A/D converter. The surface pressure fluctuations were sampled at 67 kHz. At each measurement station, 512 records of 32768 contiguous samples per record were acquired. The total sampling period at each measurement station was at least 16 minutes in order to insure the stationary of the measured signal[¶¶]. During post-processing, each of the contiguous records was divided into 2 sub-records and the time-delay subtraction was carried out. The time-delayed power spectra were calculated using a C program called TIM-DLY.C (appendix A) which uses the FFT algorithm given by Press *et al.* (1994). Additional bin averaging (Bendat and Piersol, 1986) was performed to produce the final spectrum using a C program called BIN-AV.C (appendix B). The final spectral values were calculated using at least 1024 averages. The Poisson Equation Term Ratio which is discussed in chapter 4 was computed using a C program called P-TERM.C (appendix C) and the data of Ölçmen and Simpson (1996: $Re_\theta = 5940, 7300$) and the data of Ölçmen *et al.* (1998: $Re_\theta = 23200, 23400$). The normalization of the p spectra was done using Microsoft Excel v5.0. Also, the values of p' were calculated by integrating each p spectrum using Microsoft Excel v5.0. Numerical integrations were calculated using the composite trapezoidal rule.

2.5.3. Measurement Uncertainty

The experimental uncertainty for the spectral power density of surface pressure fluctuations is primarily due to the statistical convergence uncertainty and the uncertainty

---

[¶¶] A time interval was allowed to elapse in between the acquisition of each contiguous record of data in order to lengthen the total sample period. These time intervals were not necessarily equal to one another.

introduced by assuming that the transfer function of the pressure transducer-pinhole combination is equal to 1 within the frequency range of interest in the present study. Following the analysis of Bendat and Piersol (1986), the normalized statistical convergence uncertainty is

$$\varepsilon_{\text{convergence}} = \frac{1}{\sqrt{\text{Number of ensembles averaged}}} \tag{39}$$

The p spectra presented here were calculated by averaging at least 1024 ensembles. Therefore, the upper limit of $\varepsilon_{\text{convergence}} = \pm 3\%$. The maximum deviation of the expected amplitude response of the pressure transducer-pinhole combination (figure 12) is a conservative estimate of the uncertainty due to the assumption of a transfer function equal to 1 within the frequency range of interest. This value is $\varepsilon_{\text{transfer}} = \pm 17\%$. Following the analysis of Kline and McClintock (1953), the combined uncertainty due to the statistical convergence uncertainty and the uncertainty due to the transfer function is

$$\varepsilon_{\text{spectral value}} = \sqrt{\varepsilon^2_{\text{convergence}} + \varepsilon^2_{\text{transfer}}} \tag{40}$$

The uncertainty of the p spectral values is estimated to be $\pm 17.3\%$ using equation 40. Values of p' were calculated as the square root of $\overline{p^2}$. Each value of $\overline{p^2}$ was calculated by numerically integrating the spectral power density of p using the composite trapezoidal rule. Therefore, the uncertainty of p' and $\overline{p^2}$ is due to the uncertainty of the individual p spectral values that were integrated. Following the analysis of Kline and McClintock (1953), the uncertainty of $\overline{p^2}$ is

$$\varepsilon_{\overline{p^2}} = \varepsilon_{\text{spectral value}} \frac{\sqrt{\sum_{i=1}^{N} \left(\Phi_i(\omega_i)\right)^2 (\Delta\omega_i)^2}}{\sum_{i=1}^{N} \left(\Phi_i(\omega_i)\right)(\Delta\omega_i)} \tag{41}$$

where $\Phi_i(\omega_i)$ and $\Delta\omega_i$ are each individual spectral value and corresponding bin width, respectively. The uncertainty of $\overline{p^2}$ is estimated to be $\pm 14.3\%$ using equation 40. Following the analysis of Kline and McClintock (1953), the uncertainty of p' is

$$\varepsilon_{p'} = \sqrt{\frac{1}{2}\varepsilon^2_{\overline{p^2}}} \tag{42}$$

The uncertainty of p' is estimated to be $\pm 10.1\%$ using equation 42.

2.6. Measurements in Flow Around a 6:1 Prolate Spheroid

2.6.1. Calibration

The static calibration was performed using the procedure described in §2.5.1. The sensitivity of the pressure transducer was 0.0233 mV/Pa. A coarse dynamic calibration was done using a GenRad model 1986 Omnical Sound Level Calibrator. The calibration was done using a sound pressure level (SPL) of 114 dB at 125 Hz, 250 Hz, 500 Hz, 1 kHz, 2 kHz, and 4 kHz. A Hewlett-Packard model HP 3478A true-RMS multimeter was used to measure the output AC voltage of each pressure transducer. The results of the coarse dynamic calibration are shown in figure 16. Note that the coarse dynamic calibration was performed on the pressure transducer alone, without the pinhole mask. The purpose of the coarse dynamic calibration on the pressure transducer alone was to verify that the frequency response of transducer alone is constant.

The pinhole mask used to reduce spatial averaging (Corcos, 1963) significantly affected the dynamic response of the pressure transducer system. For the conditions of the prolate spheroid flow, the theoretical estimate of the resonant frequency (equation 38) is 11.28-11.54 kHz and the theoretical estimate of the damping factor (equation 37) is 0.0115-0.0122 depending on ϕ location. Figure 17 shows a representative power spectrum ($\alpha = 10°$, $x/L = 0.772$, $\phi = 150°$) of the pressure transducer signal with a time-delay subtraction ($\Delta t = 29$ ms) and the static calibration applied. Figure 18 shows this power spectrum corrected assuming the theoretical transducer frequency response. Clearly the theoretical correction is insufficient. The source of the high frequency ($\approx$33 kHz) spike in the power spectrum (figure 18) is unknown. Such a spike was observed in all of the p spectra in the prolate spheroid flow. The spike must be due to some measurement error since there is no natural phenomenon present to cause it. Therefore, for each spectrum, the minimum high frequency spectral estimate (before the spike) was located. All spectral estimates at higher frequencies than where this minimum occurred were discarded.

The frequency response of the transducer-pinhole mask system that was used for the p measurements on a prolate spheroid was modeled after the theoretical frequency response of a Helmholtz resonator (equation 35). The velocity data at $\alpha = 10°$, $x/L = 0.772$, $\phi = 150°$ show that $\overline{v^2}/u_\tau^2$ (figure 19) is similar to that in a two-dimensional boundary layer. Additionally,

Chesnakas and Simpson (1997) show that the mean velocity profile is collateral near the wall which suggests that the structure of the boundary layer is nearly two-dimensional near the wall. McGrath and Simpson (1987) showed that the pressure spectrum beneath 2-D boundary layers collapse at high frequencies when normalized using viscous scales. Their normalized p spectra can be approximated by the four curves shown in figure 20. It is assumed here that, near the resonant frequency of the transducer-pinhole mask, the pressure spectrum at $\alpha = 10°$, $x/L = 0.772$, $\phi = 150°$ follows the curves in figure 20 when normalized using viscous scales based on the behavior of $\overline{v^2}/u_\tau^2$ and the mean velocity at this location. It is also assumed here that the frequency response of the pinhole mask is constant below 1 kHz and equal to the static sensitivity. These two assumptions were used along with the mathematical form of the Helmholtz resonator to construct a transfer function for the transducer-pinhole combination. Therefore, the resulting transfer function will produce a p spectrum (at $\alpha = 10°$, $x/L = 0.772$, $\phi = 150°$) that is similar to that of McGrath and Simpson (1987) near the resonant frequency of the transducer-pinhole mask.

The initial approximation of the transfer function for the transducer-pinhole system at $\alpha = 10°$, $x/L = 0.772$, $\phi = 150°$ is illustrated in figure 21. The transfer function is defined such that the measured signal multiplied by the static sensitivity divided by the transfer function yields the true pressure fluctuation. The approximate transfer function is unity from 0-1 kHz. The approximate transfer function is given by the uncorrected pressure spectrum, normalized using viscous scales, divided by the curves that fit the data of McGrath and Simpson (1987) for frequencies higher than 6 kHz. The low frequency variation is blended to the high frequency variation in the range 1-6 kHz. This procedure yields a table of values that approximate the transfer function. The initial approximation (figure 21) was used only to determine the likely variation of the transfer function near resonance being that it is not adequately described by the theoretical response of a Helmholtz resonator.

The center frequency of the resonant peak of the uncorrected pressure spectra varies with azimuthal position. Table 1 shows this variation at $\alpha = 10°$. A table of values for the transfer function would require adjustment at each measurement location due to the variation of resonance frequency with azimuthal position. Such an adjustment would have a large number of degrees of freedom which would degrade the validity of such a procedure. Therefore, it is desirable to

describe the frequency response with a function that has limited degrees of freedom. The approximate transfer function shown in figure 21 can be described by

$$\left(\frac{p_{\text{MEASURED}}}{p_{\text{TRUE}}}\right)^2 = \frac{2\left(\frac{f}{f_n}\right) + 1}{\left[1-\left(\frac{f}{f_n}\right)^2\right]^2 + 4\zeta^2\left(\frac{f}{f_n}\right)^2} \tag{43}$$

where f_n and ζ are determined by fitting the curve (figure 22). Equation 22 was modeled after the theoretical curve for a Helmholtz resonator and can be adjusted to fit the data at other azimuthal locations with only 2 degrees of freedom.

The data at each measurement station were taken at different times. Also, the transducer was removed from the model and moved to another physical location in order to switch from measuring p at $x/L = 0.600$ to measuring p at $x/L = 0.722$. The values of f_n ($=\omega_n/2\pi$) and ζ for a theoretical Helmholtz resonator do not adequately model the observed spectral behavior. Therefore, the values of f_n and ζ were determined by inspection for each spectrum. The variation of f_n and ζ with azimuthal position is not large. The peak in the uncorrected spectrum is centered about the actual resonant frequency. The resonance of the transducer-pinhole system is the most likely cause for this sharp peak. The damping factor (ζ) was determined such that the pressure spectrum varies smoothly at frequencies near resonance. It was assumed that any "waviness" in the pressure spectrum at frequencies near resonance is most likely due to the resonance of the transducer-pinhole system.

While it is not standard to vary the transfer function from measurement to measurement, the variation of the transfer function is not large and it was done judiciously in order to decrease the likelihood of discarding valid data. Tables 1 and 2 show the values of f_n and ζ used for each pressure spectrum. Figure 23 shows representative transfer functions that bound the transfer functions that were used for the p data at $x/L = 0.600$. The maximum difference between the functions shown in figure 23 is 1.2 dB at $f = 8500$ Hz. Figure 24 shows representative transfer functions that bound the transfer functions that were used for the p data at $x/L = 0.772$. The maximum difference between the functions shown in figure 24 is 1.2 dB at $f = 20$ kHz. The measurement uncertainty due to this calibration procedure is the subject of §2.6.3.

2.6.2. Data Acquisition and Reduction

The pressure transducer was mounted to the optical access window (figure 8). Access to the flow field was provided through a 0.5 mm diameter pinhole (figure 25) which was used to decrease spatial averaging (§2.3). The Corcos correction (Corcos, 1963) was applied to the power spectra to account for the spatial resolution issues discussed in §2.3.2. Figure 26 shows the correction that was applied to the power spectra at $\alpha = 20°$, $x/L = 0.772$ which extend through the full range of d^+ used here ($38 < d^+ < 92$). Gravante *et al.* (1998) report that the maximum allowable sensing diameter to avoid spectral attenuation at high frequencies is in the range $12 < d^+ < 18$. In order to have $d^+ \leq 18$ here would require a pinhole of 0.09 mm which, in turn, would lower the Helmholtz resonant frequency of the pinhole to 1860 Hz. Such a low resonant frequency would cause significant attenuation of the high frequency spectral values, thus offsetting any benefit of better spatial resolution. Since the Corcos correction has been found to recover the true pressure spectrum for the flow conditions here (Schewe, 1983; Lueptow, 1995), it was used here rather than a smaller d^+ pinhole.

The surface pressure fluctuations were sampled at 71 kHz and stored to 12-bit precision by an IBM-type PC using a RC Electronics ISC-16 A/D converter. At each measurement location, 25 records of 16384 contiguous samples per record were acquired. The total sampling period at each measurement station was at least 5 minutes in order to insure the stationary of the measured signal[§§]. During post-processing, each contiguous record was divided into 8 sub-records and the time-delay subtraction was carried out. The time-delayed power spectra were calculated using a C program called TIM-DLY.C (appendix A) which uses the FFT algorithm given by Press *et al.* (1994). Additional bin averaging (Bendat and Piersol, 1986) was performed to produce the final spectrum using a C program called BIN-AV.C (appendix B). The final spectral values were calculated using at least 500 averages. The application of the pressure transducer frequency response function and the normalization of the p spectra was done using Microsoft Excel v5.0. Also, the values of p' were calculated by integrating each p spectrum using

---

[§§] A time interval was allowed to elapse in between the acquisition of each contiguous record of data in order to lengthen the total sample period. These time intervals were not necessarily equal to one another.

Microsoft Excel v5.0. Numerical integrations were calculated using the composite trapezoidal rule.

The surface pressure-velocity covariance measurements acquired by the author that are presented in chapter 5 are part of the data set of Chesnakas and Simpson (1997), but have not been published. Since these measurements are presented in this dissertation for the first time, some details of the associated data acquisition and reduction are included here. Velocity measurements for the surface pressure-velocity covariance were made radially and 1 mm windward of the pressure pinhole using a three-orthogonal-velocity-component, fiber-optic LDV probe. The LDV probe was mounted inside the model with all laser beams passing through a window (figure 8). The probe can be remotely traversed ±2.5 cm in both the axial direction and normal to the major axis of the model. Positioning in the circumferential direction (ϕ) was achieved by rotating the model about its major axis on the sting. The Doppler frequency of each of the LDV signals was analyzed using 3 Macrodyne model FDP3100 frequency domain signal processors operating in coincidence mode. The flow was seeded using polystyrene latex spheres 0.7 μm in diameter. The particle velocity and the pressure at the window pressure tap were sampled simultaneously and stored with 16-bit precision. The sample rate varied from 40 samples/sec near the surface to 250 samples/sec in the outer part of the measurement region. Boundary layer velocity profiles were measured at 10-14 circumferential locations in the range $90° \leq \phi \leq 180°$. Each profile consisted of 17-19 radial locations from 0.007 cm above the model surface out to 2.5-3.0 cm. At each of these locations 16384 coincident 3-D velocity-surface pressure realizations were acquired.

The surface pressure data acquired simultaneously with the 3-D velocity data were used to compute the surface pressure-velocity covariance. They were not used to compute pressure spectra. Separate surface pressure measurements were carried out at a higher sampling rate (71 kHz) and used to compute the pressure spectra. Pressure fluctuations due to acoustics and vibration do not affect the surface pressure-velocity covariance since only p contributions due to turbulence correlate with the turbulent velocity fluctuations.

The outer layer/free-stream velocity measurements presented in chapter 5 are part of the data set of Goody *et al.* (1998), but some have not been published. Since these measurements are presented in this dissertation for the first time, some detail of the associated data acquisition and reduction are included here. Measurements of the mean velocity, Reynolds stresses, and triple products were made by Goody *et al.* (1998) in the outer boundary layer and free-stream using a miniature 4-sensor hot-wire probe that consists of two orthogonal X-wire arrays (Auspex Corp. AVOP-4-100). The *quad-wire* probe has 5 μm tungsten sensors 0.8 mm in length and a measurement volume of 0.5 mm^3 (figure 27). The quad-wire sensors were operated separately, each using a Dantec 56C17/56C01 anemometer unit. Anemometer outputs were read by an IBM-type PC through an Analogic 12-bit HSDAS-12 A/D converter buffered by four ×10 buck-and-gain amplifiers. A traversing gear mounted in the wind tunnel allowed the horizontal and vertical position of the probe to be controlled from the computer. A probe holder positioned the tip of the probe well upstream of the traverse gear. The probe was held parallel to the free-stream direction for all velocity measurements. A detailed description of the quad-wire measurement system in addition to related calibration and reduction procedures is given by Devenport *et al.* (1997), and Wittmer *et al.* (1998). Profiles of the complete flow velocity vector were measured at 5° ϕ increments (circumferential) from $\phi = 130°$, 140° to $\phi = 180°$. Each profile consisted of 11-13 radial locations from 0.60-0.75 cm to 8-12 cm above the model surface.

2.6.3. Measurement Uncertainty

The experimental uncertainty for the spectral power density of surface pressure fluctuations is primarily due to the statistical convergence uncertainty and the uncertainty of the transfer function of the pressure transducer-pinhole combination. Following the analysis of Bendat and Piersol (1986), the normalized statistical convergence uncertainty is given by equation 39. The p spectra presented here were calculated by averaging at least 500 ensembles. Therefore, the upper limit of $\varepsilon_{convergence} = \pm 4.5\%$. The uncertainty of the transfer function of the pressure transducer-pinhole combination has two parts. The first part is the uncertainty of the p spectrum of McGrath and Simpson (1987) which was used to determine the shape of the transfer function near resonance. The uncertainty given by McGrath and Simpson (1987) is $\varepsilon_{\text{McGrath and Simpson (1987)}} = \pm 1.5$ dB (±41%). The second part is conservatively estimated as the maximum difference among the transfer functions used at a particular axial (x/L) location which is

$\varepsilon_{\text{max difference}} = \pm 1.2$ dB (32%). Following the analysis of Kline and McClintock (1953), the combined uncertainty due to the statistical convergence uncertainty and the uncertainty due to the transfer function is

$$\varepsilon_{\text{spectral value}} = \sqrt{\varepsilon^2_{\text{convergence}} + \varepsilon^2_{\text{McGrath and Simpson (1987)}} + \varepsilon^2_{\text{max difference}}} \tag{44}$$

The uncertainty of the p spectral values is estimated to be $\varepsilon_{\text{spectral value}} = \pm 52.2\%$ (± 1.8 dB) using equation 44.

Values of p' were calculated as the square root of $\overline{p^2}$. Each value of $\overline{p^2}$ was calculated by numerically integrating the spectral power density of p using the composite trapezoidal rule and adding an Analytical Integral Contribution (AIC). The AIC is described in §5.4.1 where it is noted that the AIC gives a lower bound on the true value of $\overline{p^2}$. The uncertainty of $\overline{p^2}$ due to the AIC was determined, using a "jitter" analysis (Moffat, 1982), to be $\varepsilon_{\text{AIC}} = +8\%$. Since the uncertainty of $\overline{p^2}$ due to the AIC is only positive, the lower bound of the uncertainty of $\overline{p^2}$ is only due to $\varepsilon_{\text{spectral value}}$. The lower bound of the uncertainty of $\overline{p^2}$ is estimated to be -15.1% using equation 40. The upper bound of the uncertainty of $\overline{p^2}$ is due to $\varepsilon_{\text{spectral value}}$ and ε_{AIC}. Following the analysis of Kline and McClintock (1953), the upper bound of the uncertainty of $\overline{p^2}$ is

$$\varepsilon_{\overline{p^2}}(\text{upper bound}) = \sqrt{\varepsilon^2_{\text{AIC}} + \varepsilon^2_{\text{spectral value}} \frac{\sum_{i=1}^{N} \left(\left(\Phi_i(\omega_i) \right) \Delta\omega_i \right)^2}{\left(\sum_{i=1}^{N} \left(\Phi_i(\omega_i) \right) \Delta\omega_i \right)^2}} \tag{45}$$

where $\Phi_i(\omega_i)$ and $\Delta\omega_i$ are each individual spectral value and corresponding bin width, respectively. The upper bound of the uncertainty of $\overline{p^2}$ is estimated to be +17%. Therefore, the uncertainty of $\overline{p^2}$ is estimated to be +17% / -15%. The uncertainty of p' is estimated to be +12% / -10.7% using equation 42.

The p measurements made simultaneously with velocity were not adjusted for the response of the pressure transducer at high frequencies. In consideration of the rapid decay of the p spectrum with frequency and the loss of correlation between surface and interior fluctuations as

frequency increases, the uncertainty that this introduces in the surface pressure-velocity covariance is very small. Using the definition of R_{pu}, R_{pv}, and R_{pw} given in the List of Symbols and neglecting the uncertainty of the surface pressure-velocity covariances, the uncertainty of R_{pu}, R_{pv}, and R_{pw} is due to the uncertainty of p', u', v', and w'. The uncertainty of p' is estimated above as $\varepsilon_{p'} = +12\% / -10.7\%$. The uncertainty of u', v', and w' is given by Chesnakas and Simpson (1997) as $\varepsilon_{u'} = \varepsilon_{v'} = \varepsilon_{w'} = \pm 1.5\%$. Therefore, following the analysis of Kline and McClintock (1953), the uncertainty in the correlation coefficients is equal and is calculated using

$$\begin{aligned} \varepsilon_{R_{pu}, R_{pv}, R_{pw}} &= \sqrt{\varepsilon_{p'}^2 + \varepsilon_{u', v', w'}^2} \\ &= +12.1\% / -10.8\% \end{aligned} \tag{46}$$

3. TWO-DIMENSIONAL BOUNDARY LAYER RESULTS

The two-dimensional boundary layers discussed in this chapter mainly serve as a baseline upon which to compare the more complex three-dimensional boundary layers discussed in subsequent chapters. They are of comparable Reynolds number to the wing-body junction flows discussed in chapter 4. An understanding of p beneath a two-dimensional boundary layer is necessary in order to appreciate the features of p beneath three-dimensional boundary layers. Relevant boundary layer flow parameters are given in table 3. The velocity field measurements of the lower Re_θ (= 7300) 2-D boundary layer are reported by Ölçmen and Simpson (1996). The velocity field measurements of the higher Re_θ (= 23400) 2-D boundary layer are reported by Ölçmen *et al.* (1998). The U^+ (figure 28) profiles exhibit law-of-the-wall similarity,

$$U^+ = \frac{1}{\kappa} ln(y^+) + C \tag{47}$$

where κ and C are constants. Ölçmen and Simpson (1996) calculated u_τ in the lower Reynolds number flow by fitting the U data to equation 47 using Coles' (1956) constants, $\kappa = 0.41$ and $C = 5$. Ölçmen *et al.* (1998) calculated u_τ in the higher Reynolds number flow by averaging the u_τ determined by fitting the U data to equation 47 using Coles' (1956) constants with the u_τ determined by fitting the U data to a near-wall approximation of Spalding's (1961) law-of-the-wall,

$$U^+ = y^+ - \frac{\kappa^4}{24\, e^{\kappa C}} (y^+)^4 \tag{48}$$

where κ and C are Coles' constants. The Reynolds normal stresses are shown in figure 29.

3.1. Spectral Scaling of Surface Pressure Fluctuations

There is not a universal scaling that collapses the p spectra of different Reynolds number flows at all frequencies. However, scaling characteristics of the power density spectrum of p show which turbulent structures are dominant for a given frequency range. The high frequency end ($\omega^+ > 0.15$) of the p spectra collapse to within measurement uncertainties when normalized

using τ_W as the pressure scale and ν/u_τ^2 as the time scale and agree with the previous investigations (figure 30). The collapse of the p spectra when normalized on inner boundary layers indicates that the high frequency p is due to inner layer turbulent motions near the wall. Additionally, at $\omega^+ > 0.8$, the p spectra decay as ω^{-5} which is in agreement with the analytical analysis of Blake (1986). It should be noted that no spatial resolution correction (i.e. Corcos (1963) correction) has been applied to the p spectra presented here. The favorable comparison with other data (figure 30), particularly the low d^+ data of Schewe (1983) and Gravante *et al.* (1998), indicate that a correction is not required. The discrepancy between the inner-scaled spectra for $\omega^+ > 0.5$ can be attributed to transducer resolution limitations. For $\omega^+ > 0.5$ the lower spectral values are reported by Blake (1970; $d^+ > 43$) and the higher spectral values are the present data at $Re_\theta = 23400$ ($d^+ = 31$) and the data of Schewe (1983) ($d^+ = 19$). A lower value of d^+ indicates better transducer resolution of small-scale, high-frequency fluctuations. Contributions to p from sources that are smaller than the transducer sensing area are spatially integrated, and thereby attenuated (§2.3.2).

The spectra presented here are single-sided. The p spectra of McGrath and Simpson (1987), Farabee and Casarella (1991), and Blake (1970) shown here were multiplied by 2 in order to make them consistent with the definition of Φ used here. Some relevant boundary layer parameters for the comparison p spectra are given in table 3. The data of McGrath and Simpson (1987) presented here is an unpublished re-reduction of the original data by Shinpaugh and Simpson that corrected for the low frequency response (< 100 Hz) of their transducer.

There is general agreement in the literature on the proper pressure and time scales for the p spectrum at high frequencies. The same is not true for the p spectrum in the low and middle frequency ranges. Many researchers such as Blake (1970) and Keith *et al.* (1992) have shown the p spectrum to collapse at low frequencies using an outer boundary layer variable scaling of Q_e as the pressure scale and δ^*/U_e as the time scale in addition to a mixed inner-outer variable scaling which uses τ_W as the pressure scale and δ^*/U_e as the time scale. Farabee and Casarella (1991) reported that the former (outer variable) scaling only collapse p spectra at very low frequencies, $\omega\delta^*/U_e \leq 0.03$. Farabee and Casarella (1991) and Gravante *et al.* (1998) used τ_W as the pressure scale and δ/u_τ as the time scale to collapse p spectra at middle frequencies.

In the present study, the p spectra for various investigations which cover a wide range of Reynolds number ($1400 < Re_\theta < 23400$) were normalized using the time scales δ^*/U_e, δ^*/u_τ, δ/u_τ, and δ/U_e, and pressure scales τ_W and Q_e (figures 31 - 38). None of the eight possible scaling combinations successfully collapsed the p spectra at the lowest frequencies presented here, which do not extend into the very low frequency range of Farabee and Casarella (1991). In a middle frequency range the p spectra collapse when normalized using τ_W as the pressure scale independent of the time scale used. The p spectra collapse at $0.7 < \omega_{O1} < 2.5$ with δ^*/U_e as the time scale (figure 31), at $20 < \omega_{O3} < 70$ with δ^*/u_τ as the time scale (figure 33), at $100 < \omega_{O5} < 500$ with δ/u_τ as the time scale (figure 35), and at $4 < \omega_{O7} < 20$ with δ/U_e as the time scale (figure 37). Since the recent studies of Farabee and Casarella (1991) and Gravante *et al.* (1998) favor δ/u_τ as the time scale, the following discussion will illustrate the relationship between inner layer and outer layer scaling using figure 35.

It has been postulated (Bradshaw, 1967; Panton and Linebarger, 1974; Blake, 1986), using arguments relating the existence of an inner scaling and an outer scaling, that an overlap region exists in the p spectrum beneath 2-D boundary layers at high Reynolds number. Both inner and outer boundary layer scaling collapse the power spectrum in this overlap region. Using dimensional analysis, Bradshaw (1967) argued that the p spectrum in this region decreases as ω^{-1} and is due to "universal" turbulent motions within the log layer where the convection velocity approaches the local mean velocity. The size/existence of this region increases as Re_δ increases and is related to Kolmogorov's hypothesis (Batchelor, 1953) of an energy cascade.

The p spectrum for the higher Re_θ flows ($Re_\theta > 18800$) exhibit an overlap region. For the present data at $Re_\theta = 23400$ the frequency range $0.03 < \omega^+ < 0.06$ corresponds to $250 < \omega_{O3} < 500$. Examination of figures 30 and 35 reveals that both scalings collapse the p spectra and follow a power law decay within this range. An ω^{-1} decay is included in figures 30 - 38 since an ω^{-1} decay has a theoretical basis. However, the observed spectral decay is closer to $\omega^{-0.8}$. Blake (1970) observed an $\omega^{-0.75}$ decay and McGrath and Simpson (1987) observed an $\omega^{-0.7}$ decay within the overlap region. It should be noted that exact slopes are difficult to measure. The size of the middle frequency range in which the p spectra exhibit an $\omega^{-0.8}$ decay increases with Reynolds number. The low Re_θ (= 1400) p data of Schewe (1983) only

tangentially approach a power law decay while the high Re_θ (=23400) p data of the present study decay as $\omega^{-0.8}$ for $30 < \omega_{O3} < 2000$ (figure 35).

3.2. Root Mean Square of Surface Pressure Fluctuations

Each of the p spectra were integrated to obtain $\overline{p^2}$ values. Figure 39 shows p'/τ_w as a function of Re_δ. Although there is scatter in p'/τ_w values due to transducer resolution limitations and accumulated experimental errors in individual frequency-spectral values, there is a general trend of increasing p'/τ_w with Re_δ, albeit with a moderate correlation coefficient (= 0.66). A trend of increasing p' with Re_δ is in agreement with previous investigations (Bradshaw, 1967; Panton and Linebarger, 1974; Farabee and Casarella, 1991; Bull, 1996). The source of the increasing trend in p' with Reynolds number is the overlap region of the p spectrum. The logarithmically spaced ordinate in figures 30 - 38 makes it difficult to judge what features of the p spectrum significantly affect the $\overline{p^2}$ integral. However, since

$$\frac{\overline{p^2}}{\tau_W^2} = \int_0^\infty \left[\frac{\omega\Phi(\omega)}{\tau_W^2}\right] d\left(ln(\omega)\right) \tag{49}$$

figure 40 shows $\omega\Phi/\tau_W^2$ so that contributions to the $\overline{p^2}/\tau_W^2$ integral are evenly spaced along the logarithmically spaced ω_{O3} axis. The Reynolds number trend is clearly visible at high frequencies. As Reynolds number increases so does the area under the $\omega\Phi/\tau_W^2$ curve due to increased high frequency p content. The increased high frequency p content follows directly from the overlap region extending to higher frequencies as Reynolds number increases.

Bradshaw (1967) and Panton and Linebarger (1974) analytically show that the energy within the overlap range of the p spectrum is proportional to $\ln(Re_\delta)$. Farabee and Cassarella (1991) propose an equation for $\overline{p^2}/\tau_W^2$ (solid line in figure 39),

$$\frac{\overline{p^2}}{\tau_W^2} = \begin{cases} 6.5 & \left(Re_\delta \le 333\right) \\ 6.5 + 1.86\, ln\left(\dfrac{Re_\delta}{333}\right) & \left(Re_\delta > 333\right) \end{cases} \tag{50}$$

by numerically integrating their measured spectra over the range $\omega_{O3} < 100$, integrating the equation proposed by Bull (1979)

$$\Phi^+ = \frac{2.5}{\omega^+} exp\left[-1.45\left(ln\left(\frac{\omega^+}{\omega_V}\right)\right)^2\right] \tag{51}$$

over the range $\omega^+ > \omega_V = 0.3$[¶¶], and assuming that Φ^+ decays as ω^{-1} in the range $100 \leq \omega_{O3} \leq 0.3Re_\delta$. Note that $\omega_{O3} = Re_\delta \omega^+$. Therefore, $\omega_{O3} = 0.3Re_\delta$ is equivalent to $\omega^+ = 0.3$. The trend shown in figure 39 is consistent with a logarithmic increase in p'/τ_w with Reynolds number, however, the level proposed by Farabee and Casarella (1991) is lower than most of the data shown in figure 39. Note the use of Re_δ to characterize the overlap region. Panton (1990) calls Re_δ the "preferred" Reynolds number in his general discussion of turbulent boundary layer scaling since Re_δ is the ratio of the outer length scale to inner length scale.

[¶¶] Bull (1979) proposed that $\omega_V = 0.375$.

4. WING-BODY JUNCTION RESULTS

This chapter discusses measurements of p beneath the three-dimensional flow *away* from a wing-body junction. All measurement stations are outside the horseshoe vortex that forms about the wing-body junction. The present flow is referred to as a "wing-body junction" flow only to distinguish it from the flow about a 6:1 prolate spheroid that is the subject of chapter 5.

The complexity of the skewed 3-D boundary layer (figure 3) necessitates the use of multiple coordinate systems. The Tunnel coordinate system is right-handed with the x-axis parallel to the tunnel centerline pointing downstream and the y-axis perpendicular to the tunnel floor pointing up. The Wall-Shear-Stress coordinate system is right-handed with the x-axis in the shear-stress direction at the wall as approximated by the measured mean-flow angle closest to the wall (Ölçmen and Simpson, 1995a; Ölçmen *et al.*, 1996, 1999b). The y-axis is normal to the wall, pointing up.

Relevant boundary layer parameters of the present flow are given in tables 4 and 5. For comparison, data measured in 2-D, zero-pressure gradient boundary layers with a Reynolds number comparable to the present flows are also included in tables 4 and 5. The velocity field measurements of the lower Re_θ (= 5940) boundary layer are reported by Ölçmen and Simpson (1996). The velocity field measurements of the higher Re_θ (= 23200) boundary layer are reported by Ölçmen *et al.* (1998). The u_τ at each measurement station was calculated by fitting the U data in Wall-Shear-Stress coordinates to a near-wall approximation of Spalding's (1961) law-of-the-wall (equation 48). Profiles of the mean velocity components are shown in figures 41 - 44 and profiles of the Reynolds normal stresses are shown in figures 45 - 50. Details of the velocity field are given in the following sections as they relate to p.

4.1. RMS Surface Pressure Fluctuations and Features of the Velocity Field

Each of the p spectra was integrated to obtain the $\overline{p^2}$ values given in table 6. For the lower Re_θ flow (table 6) p'/τ_w and p'/Q_e are higher than beneath a 2-D flow and increase with station number for stations 0-3 due to adverse pressure gradient effects on the lower frequencies (Simpson *et al.*, 1987). Also, table 6 indicates that most of the p' is due to low frequency ($f < 1$ kHz) fluctuations which increase in magnitude with station number. The $\overline{p^2}$ from low frequencies at station 3 is double the low frequency $\overline{p^2}$ at station 0. The high frequency ($f > 1$ kHz) contribution to p' at stations 0-3 is nearly constant.

The lateral pressure gradient in wall-shear-stress coordinates (table 4) pushes the flow away from the wing at stations 0-3. Ölçmen and Simpson (1996) report that at stations 0-3 the mean flow angle changes monotonically from near the wall to the free stream by $4.4° < |\beta_{FS} - \beta_W| < 25°$ (figure 3). Examination of table 6 and the dimensional p spectra (figure 51) suggest that the monotonic (in y) turning of the mean flow at stations 0-3 has little effect on high frequency p (which have a lower spectral level than the 2-D at comparable Re_θ), but increase the low frequency p substantially.

The lateral pressure gradient in wall-shear-stress coordinates (table 4) changes sign between stations 3 and 4. At stations 4-9 the lateral pressure gradient pushes the mean flow back toward the wing. Ölçmen and Simpson (1996, p. 7) observed that "At station 4 the W/u_τ values are close to zero up to $y^+ \approx 40$. Above this y location, values monotonically increase. At stations further downstream the effect of the sign change of the lateral pressure gradient is felt most near the wall. This results in negative W/u_τ values ... The pressure force is most effective on the near-wall flow where the momentum of the flow is lowest." Figures 43 and 44 show the W/u_τ mean velocity profiles in wall-shear-stress coordinates. Note that the location of maximum W propagates outward from the wall at successive downstream stations.

For stations 4-8 the mean velocity at the boundary layer edge accelerates (table 4). The magnitude displacement thickness, δ^*, decreases as well as the $\overline{p^2}$ contribution from low frequency fluctuations ($f < 1$ kHz) (table 6). While the details of the above $\overline{p^2}$ discussion is confined to the $Re_\theta = 5940$ flow, similar trends are present in the $Re_\theta = 23200$ data.

4.2. Features of the Dimensional Power Spectra

The most significant feature of the spectral power density spectrum of surface pressure fluctuations (figures 51 and 52) at stations 4-9 is the constant (or nearly constant) spectral levels in the frequency range 2 kHz $< f <$ 5 kHz. A flat mid-frequency spectral region has also been observed in the 3-D flow on the lee-side of a prolate spheroid at angle of attack (chapter 4). In that flow the flat mid-frequency spectral region is believed to due to the lack of overlapping frequency structure between the large-scale motions of the outer layer and the viscous-dominated near-wall region. A similar situation exists in the present flow. The lateral pressure gradient imposed by the presence of the wing skews the near-wall, low momentum mean flow. The larger near-wall velocity gradients associated with the skewed flow presumably produce high frequency pressure fluctuations as prescribed by the Poisson integral (equation 25).

The effect of the flat spectral region on $\overline{p^2}$ is significant. Table 6 shows the effect on $\overline{p^2}$ of removing the spectral contribution that makes the region flat. Figure 53 shows the p spectrum at station 8, $Re_\theta = 23200$ as an example. At station 8 the flat spectral region accounts for 40% of the $\overline{p^2}$ integral (table 6). The method used to remove the flat spectral region was to first find the frequency at which the p spectrum departs from a constant power law decay. At station 8 this frequency is 889 Hz (figure 53). Then, the power law was determined. At station 8, 20 spectral values (166 Hz $< f <$ 889 Hz) were used to determine that the power law, $\Phi(f) = 2.332 f^{-0.928}$. Next, the end of the flat spectral region was located. Here, the end of the flat spectral region is defined as the frequency at which the p spectrum is parallel to the power law just determined. At station 8 this frequency is 6456 Hz. Finally, the spectral levels at higher frequencies ($f >$ 6456 Hz) were attenuated by a constant factor in order to match up with the spectral level given by the previously determined power law at the end of the flat spectral region. At station 8, $Re_\theta = 23200$, the three parts of the "non-flat" p spectrum (Φ_{NF}) are,

$$\Phi_{NF} = \text{data} \qquad \text{for } f < 889 \text{ Hz}$$

$$\Phi_{NF} = 2.332 f^{-0.928} \qquad \text{for } 889 \text{ Hz} \le f < 6456 \text{ Hz}$$

$$\Phi_{NF} = 0.3(\text{data}) \qquad \text{for } f \ge 6456 \text{ Hz}$$

The physical mechanism that produces the flat spectral region appears to be independent of, or at least slowly varying with, Reynolds number. As station number increases from 0-3 the p

spectral level beneath the lower Re_θ flow approaches the p spectral level beneath the higher Re_θ flow at middle frequencies. The p spectra generally overlap at stations 4-9 for 300 Hz $< f <$ 3 kHz. An example of this is station 7 (figure 53) where the overlap extends to 7 kHz. Ölçmen *et al.* (1999b) discuss Reynolds number effects for the flows studied here. They found that while the magnitude of the shear stresses (normalized on u_τ) increase with Reynolds number, below $y^+ = 100$ the stresses tend to overlap. The sources of high frequency p are located within the near-wall flow.

4.3. Spectral Scaling of Surface Pressure Fluctuations

The p spectra of the present study do not collapse when normalized using boundary layer scales that collapse the p spectra in 2-D flows. The p spectra were normalized using the candidate boundary layer scales given in table 7. The first nine candidate scaling combinations in table 7 (figures 54 - 71) are all permutations of the boundary layer scales that have been shown to scale the p spectra beneath equilibrium flows within various frequency ranges. The motivation for the next four candidate scaling combinations in table 7 (figures 72 - 79), which use Δ as the length scale, was the assertion of Rotta (1962) which is supported by Fernholtz and Finley (1995a) that Δ is the proper length scale for the outer layer. The last two scaling combinations in table 7 (figures 80 - 83) were attempted based on the assumption that the source of unique features in the p spectra (i.e. the flat spectral region) are unique features in the velocity field. The only scalings which even remotely collapse the p spectra in any frequency range are the time and pressure scale combinations: δ^*/U_e, Q_e at $\omega_{O1} > 25$ (figure 59); δ^*/u_τ, Q_e at $\omega_{O2} > 700$ (figure 63); and Δ/U_e, Q_e at $\omega_{O6} > 600$ (figure 79). Each scaling combination was only successful for the higher Re_θ flow. However, a scaling combination based on outer boundary layer variables that collapses the p spectra at high frequency does not make physical sense since the source of high frequency p is small-scale, near-wall turbulence.

The lack of scaling parameters that collapse the p spectra is not surprising given the complexity of these 3-D flows. In 2-D equilibrium boundary layers similarity parameters exist that scale the velocity (e.g. law-of-the-wall, defect law). In the 3-D flows of the present study, the only scaling which collapses any part of the velocity profile is $U^+ = y^+$ near the wall ($y^+ < 5$) when the velocity is expressed in wall-shear-stress coordinates. Additionally, the

frequency/wavenumber dependence of the wave speed of p is exacerbated in this 3-D flow because turbulent structures travel in different directions depending on the distance from the wall (Ha and Simpson, 1993). In order to be successful, scaling parameters for p beneath 3-D flows must incorporate more detailed velocity field information through the Poisson equation.

Previous analysis of 2-D flows (Bradshaw, 1967; Panton and Linebarger, 1974; Blake, 1986) have shown that the Poisson integral is dominated by the mean-shear-turbulence term in the form

$$p \approx \frac{\rho}{\pi} \oint_{\Omega} \left[\frac{\partial U}{\partial y} \frac{\partial v}{\partial x} \right] \frac{d\Omega}{r_S} \tag{52}$$

For the present flow, it is assumed that the high frequency p is generated by small-scale velocity fluctuations near the wall. In a study of three-dimensional boundary layers, Ölçmen and Simpson (1992) showed that the near-wall mean region of the boundary layer follows a two-dimensional wall law reasonably well. Therefore, it is assumed here that, as with 2-D boundary layers, high frequency contributions to the Poisson integral are dominated by the mean-shear-turbulence term and that derivatives of the mean velocity in the x- and z-direction are negligible. Since the y-derivative of the W-component of velocity is not always negligible in the present flow, the 2-D approximation of the Poisson integral (equation 52) is modified here, in the form

$$p \approx \frac{\rho}{\pi} \oint_{\Omega} \left[\frac{\partial U}{\partial y} \frac{\partial v}{\partial x} + \frac{\partial W}{\partial y} \frac{\partial v}{\partial z} \right] \frac{d\Omega}{r_S} \tag{53}$$

Consider the variation of equation (53) from station to station with the goal of collapsing the high frequency end of the p spectra beneath the 3-D flows of the present study.

Some simplifying assumptions must be made in order to evaluate equation (53) with the data available. Similar to a recent model for the p spectrum under a 3-D boundary layer that was proposed by Panton (1998), it is assumed that the small-scale turbulent structures near the wall are homogenous in planes parallel to the wall and behave as traveling waves. Therefore,

$v = v \cos(\omega t - k_1 x - k_3 z)$, where $k_1 = \omega/U_{c1}$ and $k_3 = \omega/U_{c3}$ are the wavenumbers in the x- and z-direction, respectively. The traveling wave model results in

$$\frac{\partial v}{\partial x} = k_1 v \sin(\omega t - k_1 x - k_3 z) \quad \text{which varies like} \quad k_1 v_\omega$$

$$\frac{\partial v}{\partial z} = k_3 v \sin(\omega t - k_1 x - k_3 z) \quad \text{which varies like} \quad k_3 v_\omega \tag{54}$$

where v_ω is v at a particular frequency. High frequency contributions to the p spectrum primarily originate in the near-wall region where the flow roughly scales on the wall variables ν/u_τ and u_τ. Rewriting equation (53) with the above considerations in mind results in

$$\frac{p}{\tau_W} = \frac{1}{\pi} \oint_\Omega \left(k_1^+ v_\omega^+ \frac{\partial U^+}{\partial y^+} + k_3^+ v_\omega^+ \frac{\partial W^+}{\partial y^+} \right) \frac{d\Omega^+}{r_S^+} \tag{55}$$

Since near-wall turbulent structures have small spatial extent and in light of the $1/r_S^+$ dependence of equation (55), it is assumed that the variation of p/τ_W at a particular high frequency results mainly from the variation of the integrand of equation (55). Furthermore, it is assumed that the variation of the integrand of equation (55) at a particular frequency may be approximated by the variation of $\overline{v^{+2}}(\partial U^+/\partial y^+ + \partial W^+/\partial y^+)^2$ at a particular distance from the wall.

Modification of the inner variable scaling shown in figures 54 and 55 is required to account for the variation of the Poisson integrand (approximated by $\overline{v^{+2}}(\partial U^+/\partial y^+ + \partial W^+/\partial y^+)^2$) near the wall from station to station. To this end, a *Poisson Equation Term Ratio* (Π_R) is formed as

$$\Pi_R = \frac{\left[\overline{v^{+2}} \left(\frac{\partial U^+}{\partial y^+} + \frac{\partial W^+}{\partial y^+} \right)^2 \right]_{3\text{-D}}}{\left[\overline{v^{+2}} \left(\frac{\partial U^+}{\partial y^+} \right)^2 \right]_{2\text{-D}}} \tag{56}$$

Two issues must be addressed in order to evaluate Π_R with velocity data. First is the coordinate system to use to express the velocity terms. Ideally, Π_R would be coordinate system independent, however, Π_R is not. In the present study, the wall-shear-stress coordinate system was used since it is aligned with the near wall flow. Therefore, phase errors that are introduced by the approximations of the turbulent velocity structure in the x and z-direction are minimized. The

second issue is where (distance from the wall) to evaluate the velocity terms. In the present study, a spectral ratio (Φ_R) of $\Phi^+(\omega^+=1)$ at each measurement station in the 3-D flow to $\Phi^+(\omega^+=1)$ in the 2-D flow at comparable Re_θ is used as a measure of the variation of the high frequency pressure spectral levels. The variation of Π_R closely tracks the change in Φ_R from station to station. Figures 84 and 85 show Π_R as a function of Φ_R with each ratio expressed in decibels. The candidate y^+ locations shown in figures 84 and 85 where selected based on the following criteria. The locations $10 \le y^+ \le 50$ where selected because they are near the wall. Small-scale fluctuations that are near the wall are sources of high frequency p. The locations $y^+ \ge 50$ were selected by assuming several values for the convection velocity, $10 \le (U_C^+ = U_C/u_\tau) \le 18$ and using

$$\omega^+ = k^+ U_C^+ = \left(\frac{2\pi}{y^+}\right) U_C^+ \tag{57}$$

to calculate the y^+ values at $\omega^+ = 1$ for the various U_C^+ values. If Π_R at some y^+ tracked the variation of Φ_R from station to station perfectly, all points in figures 84 and 85 for that y^+ would lie along a line with a slope of 1 and passing through the origin (solid line in figures 84 and 85).

Two quantities are used to measure which $\Pi_R(y^+)$ best fit the ideal linear relationship with $\Phi_R(\omega^+)$. The first measure is the range of $\Phi_R(\omega^+=1) / \Pi_R(y^+)$ at the different stations. In other words the scatter in values of $10 \log_{10}[\Phi^+ / \Pi_R]$ at $\omega^+ = 1$ with Π_R evaluated at the various candidate y^+ locations (figures 86 and 87). The second measure is the correlation coefficient between Φ_R / Π_R and y^+. The correlation coefficient is unity if a linear relationship exists between the two, but gives no information concerning the slope. Figures 86 and 87 indicate that the best fit is at $y^+ = 50$ for both Re_θ. The high frequency p spectral collapse (figures 88 and 89), where Π_R is evaluated at $y^+=50$, show that the variation of the high frequency spectra in the present non-equilibrium 3-D flows result from features of the near-wall velocity field which change Π_R from station to station. It is significant that the complex variations in the high frequency p spectrum are tracked by a relatively simple term (Π_R) which only requires mean velocity and Reynolds stress data.

5. PROLATE SPHEROID RESULTS

5.1. Mean Flow

The velocity components are presented here as U, V, W in the Body Surface coordinate system. This is different from the Body Axis coordinate system which uses x, r, ϕ to define a position. The difference is shown in figure 90. The transformation from the Body Axis coordinate system to the Body Surface coordinate system involves a rotation about the ϕ axis. The rotations required are 1.948° and 6.167° at $x/L = 0.600$ and $x/L = 0.772$, respectively. There is also some mention of the Wall-Shear-Stress coordinate system in the following sections. In the Wall-Shear-Stress coordinate system, the U component of velocity is aligned with the wall-shear-stress (nearest wall velocity). The V component of velocity is normal to the model surface and the W component of velocity is normal to U and W forming a right-handed coordinate system. The Wall-Shear-Stress coordinate system is used to scale the mean velocity profile near the wall (Chesnakas and Simpson, 1997). The axial locations $x/L = 0.600$ and $x/L = 0.772$ were chosen for the present study because detailed LDV measurements of the 3-D, crossflow separation are available at these x/L locations (Wetzel *et al.*, 1998; Chesnakas and Simpson, 1993, 1994, 1996, 1997; Goody *et al.*, 1998).

The mean flow and Reynolds-averaged turbulence stresses have been previously discussed (Chesnakas and Simpson, 1994, 1996, 1997). Some key features which are relevant to the present discussion are given here. Tables 8 - 11 give some boundary layer parameters of the present flows. The values of ρ, ν, u_τ, and U_∞ given in tables 8 - 11 were calculated using the pressure, temperature, and U_∞ during the measurements of p and the C_f measurements of Chesnakas and Simpson (1997). Mean velocity profiles from LDV measurements (Chesnakas and Simpson, 1997) and outer layer hot-wire anemometer data (Goody *et al.*, 1998) were used to calculate δ^*, θ, and U_e/U_∞. Figure 91 shows distributions of u_τ, δ^*, and Re_θ. The nearest wall region ($y^+ < 50$) of the present flow follows the law-of-the-wall mean velocity profile when expressed in wall shearing stress coordinates (Chesnakas and Simpson, 1994, 1996, 1997).

Figures 92 - 107 show secondary flow streamlines interpolated from the V, W data for each station. Figures 92, 93, 96, 97, 100, 101, 104, and 105 also contain contours of the mean velocity magnitude and figures 94, 95, 98, 99, 102, 103, 106, and 107 contain contours of the turbulent kinetic energy (*TKE*) to show qualitatively how the mean flow field and the turbulence field are related. Additionally, figures 93 - 107 (even) have a logarithmic *r*-axis in order to highlight the near-wall flow.

5.1.1. 10° Angle of Attack

The secondary flow field at $\alpha = 10°$, $x/L = 0.600$, is shown in figures 92-95. Mean-flow separation, as indicated by a minimum in skin friction magnitude (Wetzel *et al.*, 1998), is at $\phi = 145°$, with a vortex center (zero secondary flow velocity) at $\phi = 162°$ approximately 0.375 cm above the surface. Figure 93 indicates that the weak separation at this measurement station thickens the boundary layer while figure 95 shows that near-wall *TKE* is suppressed at $120° < \phi < 160°$. Figures 96-99 show the flow field at $\alpha = 10°$, $x/L = 0.772$. Mean-flow separation (Wetzel *et al.*, 1998) is at $\phi = 137°$, with a vortex approximately 1.25 cm above the surface at $\phi = 165°$. Like at $x/L = 0.600$, the boundary layer is thickest (figure 93) and near-wall *TKE* is suppressed (figure 99) within the middle range of ϕ ($120° < \phi < 150°$). However, at $x/L = 0.772$ there is a local maximum in *TKE* (along lines of constant ϕ) away from the wall within the middle range of ϕ ($120° < \phi < 150°$). The locus of these local maxima are nearly aligned with the convergence of secondary streamlines associated with separation. It bears repeating that these maxima are only local maxima. For each of the $\alpha = 10°$ cases, the *TKE* near the wall is maximum at $\phi = 90°$ and $\phi = 180°$ because of large production due to large mean velocity gradients and turbulent shear stresses. The *TKE* decreases in the middle range of ϕ (120° - 150°). However, at any given ϕ location the maximum *TKE* remains in the near-wall region.

5.1.2. 20° Angle of Attack

The flow field at $\alpha = 20°$, $x/L = 0.600$, is shown in figures 100-103. Mean flow separation (Wetzel *et al.*, 1998) occurs at $\phi = 131°$. The separation sheet rolls into a vortex centered at $\phi = 158°$ approximately 1.8 cm from the surface. The boundary layer is thickest near separation and there is a local minimum in the velocity magnitude within the secondary vortex (figure 101).

There are kinks in the streamlines at $\phi = 145°$ and high *TKE* contours extend out into the flow with a local maximum near $r = 2.0$ cm (figure 103). Flow visualization shows a secondary separation to be incipient at $\phi = 140°$ (Wetzel *et al.*, 1998).

Figures 104-107 show the flow field at $\alpha = 20°$, $x/L = 0.772$. This case has the highest degree of three-dimensionality of those considered here. The primary separation (Wetzel *et al.*, 1998) location is at $\phi = 115°$ and the primary vortex is outside the LDV measurement region. Hot-wire data show this vortex center to be at $r = 3$ cm, $\phi = 155°$ (figure 100) (Goody *et al.*, 1998). In addition, there is a fully-formed secondary vortex at $\phi = 140°$ approximately 0.6 cm from the surface. Associated with the secondary vortex is separation ($\phi = 145°$), and reattachment at $\phi = 135°$. It should be noted that near-wall velocity measurements were not carried out at $\phi = 135°$ which is why the secondary streamlines in figures 104 - 107 do not converge at $\phi = 135°$ like they do at the primary and secondary separation, where near-wall velocity measurements were carried out. The boundary layer is thickest near the separations (figure 105) and the mean velocity magnitude exceeds the tunnel flow velocity beneath the primary vortex (figures 104 and 105). The vortices away from the wall have relatively low mean velocity gradients and bring fluid with relatively low *TKE* from the outer layer toward the wall at the most leeward (highest) ϕ locations (figures 106 and 107). Figures 104 and 105 show the low velocity trough, first reported by Chesnakas and Simpson (1997), between the primary separation location and the primary vortex. The trough extends out a significant distance from the wall. Diminished mean flow gradients and Reynolds shear stresses within the trough cause *TKE* to be lower there, due to diminished *TKE* production (figures 106 and 107). However, at the edges of the trough mean velocity gradients are higher. Higher mean velocity gradients combined with elevated Reynolds stresses increase *TKE* production. This is most evident at the top of the low velocity trough ($\phi = 140°$, $r = 2.75$ cm, $r^+ = 3990$) where the highest *TKE* ($= 0.022\rho U_\infty^2$) was measured. The main contribution to this high *TKE* is $\overline{w^2}$ ($= 0.022U_\infty^2$) as compared to $\overline{u^2}$ ($= 0.012U_\infty^2$) and $\overline{v^2}$ ($= 0.009U_\infty^2$). Also notable is that the Reynolds shear stresses are maximum at this location.

The mean flow at the $\alpha = 20°$ measurement stations has a stronger effect on the turbulence field than the mean flow at the $\alpha = 10°$ measurement stations. High *TKE* is not confined to the

near-wall region. There are small regions of highly turbulent fluid away from the wall due to the separations. Additionally, each of the separations is followed by low *TKE* levels near the wall. The *TKE* levels are higher where reattachment is present.

The outward secondary flow streamlines near regions of separation in figures 92-107 do not appear to agree with the separation locations given above. The apparent discrepancy is due to the coordinate system used to represent velocity components and is discussed in depth by Wetzel *et al.* (1998). In a coordinate system locally aligned with the separation line, the LDV data show zero cross-flow velocity very close to the local minimum in skin friction magnitude (Wetzel *et al.*, 1998). While this coordinate system is useful to determine the precise location of flow separation, the orientation of this coordinate system changes in space. Therefore, such a coordinate system is not appropriate for the global, field-type plots shown here.

5.2. Surface Pressure Spectra

Surface pressure measurements were carried out at 5° increments of ϕ. The p spectra are divided into two groups in this section- first, the p spectra at $\alpha = 10°$ and second, the p spectra at $\alpha = 20°$. The p spectra are presented in this manner because the p spectra at $\alpha = 10°$ are similar to the p spectra beneath equilibrium boundary layers, whereas the p spectra at $\alpha = 20°$ are not, as will be shown later. For each group, features of the dimensional p spectra are discussed, then several boundary layer scalings are presented.

5.2.1. 10° Angle of Attack

The p spectra at $\alpha = 10°$, $x/L = 0.600$ are shown in figure 108. In general, the spectral level within a given frequency range is highest at $\phi = 90°$ and lowest at $\phi = 145°$. Recall that at $\alpha = 10°$, $x/L = 0.600$ the boundary layer separates at $\phi = 145°$. The range of spectral levels among different ϕ locations is largest (~ 13 dB) at the highest frequencies. The range of spectral levels within 600 Hz $< f <$ 1 kHz is nearly equal to the measurement uncertainty. The p spectra at $\alpha = 10°$, $x/L = 0.772$ are shown in figure 109. At the lowest frequencies ($f <$ 400 Hz), the spectral level of p is highest at $\phi = 110°$ and lowest is at $170° < \phi < 180°$. At the highest frequencies, the spectral level of p is highest at $\phi = 90°$ and is lowest where the flow is separating, at $135° < \phi < 140°$. At $\alpha = 10°$, $x/L = 0.772$, boundary layer separation is at $\phi = 137°$. Like at

$x/L = 0.600$, the range of spectral levels of p at a given frequency is greatest (~ 19 dB) at the highest frequencies.

Scalings characteristics of the p spectrum show which turbulent structures are dominant for a given frequency range. Figure 110 shows the p spectra at $\alpha = 10°$, $x/L = 0.600$ using τ_W as the pressure scale and ν/u_τ^2 as the time scale. These inner layer scales are equivalent to using u_τ as a velocity scale and ν/u_τ as a length scale which are the scales used for the familiar law-of-the-wall mean velocity profile that holds nearest the wall in these flows when the velocity is expressed in wall-shear-stress coordinates (Chesnakas and Simpson, 1997). The spectra collapse at the highest frequencies, $\omega^+ > 0.2$, and approach the ω^{-5} decay that exists beneath equilibrium boundary layers (Blake, 1986; McGrath and Simpson, 1987; Keith *et al.*, 1992; Gravante *et al.*, 1998). The p spectra at $\alpha = 10°$, $x/L = 0.772$ also collapse to an ω^{-5} decay at high frequencies when non-dimensionalized using inner variables (figure 111). The ϕ locations with an ω^{-5} region are those at which τ_W is smallest and ν/u_τ^2 is largest. The source of the ω^{-5} region of the p spectrum is the smallest turbulent structures nearest the wall.

The present flows contain separations and are complex and 3-D — definitely non-equilibrium. Therefore, it is significant that the high frequency p spectra of the present flows ($\alpha = 10°$) compare well with the p spectrum beneath a 2-D, zero pressure gradient boundary layer (figures 112 and 113). The favorable comparison indicates that the near-wall structure of p in the present flows at $\alpha = 10°$ is similar to that in a 2-D, zero pressure gradient boundary layer.

The spectra presented here are single-sided. The p spectra of McGrath and Simpson (1987), Farabee and Casarella (1991), and Blake (1970) shown here were multiplied by 2 in order to make them consistent with the definition of Φ used here. Some relevant boundary layer parameters for the comparison p spectra are given in table 3. The data of McGrath and Simpson (1987) presented here is an unpublished re-reduction of the original data that corrected for the low frequency response (< 100 Hz) of their transducer.

Figure 114 shows the spectra at $\alpha = 10°$, $x/L = 0.600$ non-dimensionalized using mixed inner and outer variables. The pressure scale is τ_W and δ^*/U_e is the time scale. The p spectra

leeward of separation ($\phi > 145°$) collapse for $0.8 < \omega_{01} < 3$ and decay nearly as $\omega^{-0.6}$. The p spectra windward of separation ($\phi < 145°$) also collapse for $0.8 < \omega_{01} < 2$, however, do not follow a discernable power law decay. The p spectra for all ϕ collapse for $\omega_{01} > 4$ and decay nearly as $\omega^{-7/3}$, but note that only the p spectra at $\phi > 110°$ extend to $\omega_{01} > 4$. The spectra at $\alpha = 10°$, $x/L = 0.772$, $\phi \leq 140°$ collapse at middle frequencies ($1 < \omega_{01} < 6$) when normalized using mixed variables (figure 115), but they do not follow a discernable power law decay. The collapse of the p spectra at $\alpha = 10°$ normalized using mixed variables is limited to specific ranges of ϕ.

It has been postulated (Bradshaw, 1967; Panton and Linebarger, 1974; Keith *et al.*, 1992), using arguments relating the existence of an inner (viscous region) scaling and an outer (largest eddy) scaling within the boundary layer, that an overlap region exists in the p spectrum beneath 2-D boundary layers at high Reynolds number. Both inner layer and outer layer scaling hold in this overlap region. Bradshaw (1967) argued that the p spectrum in this region decreases as ω^{-1}. The low frequency p spectra at $\alpha = 10°$, $x/L = 0.600$ (figure 116) vary about as ω^{-1} for $0.07 < \omega_{01} < 0.3$ when normalized using Q_e as a pressure scale and δ^*/U_e as a time scale. The p spectra in the same range at $x/L = 0.772$ do not scale as well using these variables (figure 117). Although this flow differs from a 2-D adverse-pressure-gradient separation, the spectral levels are comparable to those upstream of detachment reported by Simpson *et al.* (1987) (figures 116 and 117). In the mid-frequency range, around $\omega_{01} = 2$, the $\omega^{-0.5}$ variation observed by Simpson *et al.* (1987) is also present.

The variation of the p spectra in the mid-frequency range may be a Reynolds number effect. The low frequency spectral contributions are from the largest shear layer structures. The power spectral contribution of these large structures increases with Reynolds number. The high frequency scaling is Reynolds number independent. This requires a greater decay in the power spectrum within the mid-frequency range as Reynolds number increases.

5.2.2. 20° Angle of Attack

The spectral level at low frequencies ($f < 300$ Hz) at $\alpha = 20°$, $x/L = 0.600$ is highest at $\phi = 150°$ and is lowest at $\phi = 105°$ (figure 118). The spectral value at 1 kHz has three local

maxima: one at $\phi = 130°$ which is near primary separation; one at $\phi = 145°$ which is near incipient secondary separation; and one at $\phi = 160°$ which is near the ϕ location of the center of the shed vortex. The spectral value increases with increasing ϕ to primary separation, and decreases with increasing ϕ for $160° \leq \phi \leq 180°$. At the highest frequencies ($f \approx 25$ kHz) the range of spectral levels among different ϕ locations is 28 dB. The largest high frequency spectral level is at $\phi = 160°$ (under the shed vortex) and is over 75 dB — significant high frequency content. The smallest high frequency spectral level is at $\phi = 130°$ which is very near boundary layer separation ($\phi = 131°$). The p spectra at $\alpha = 20°$, $x/L = 0.772$ are shown in figure 119. The range of spectral levels among different ϕ locations at the lowest frequencies ($f < 300$ Hz) is nearly 10 dB. The highest spectral level within this frequency range is at $\phi = 150°$ and the lowest is at $\phi = 175°$. The spectral level at 1 kHz increases with ϕ to reattachment near $\phi = 135°$ and then decreases toward the leeward plane of symmetry ($\phi = 180°$). The range of spectral levels among different ϕ locations at the highest frequencies is nearly 25 dB. The highest spectral level within this frequency range is 76 dB at $\phi = 150°$. The lowest spectral level is at the primary boundary layer separation ($\phi = 115°$) like the other measurement stations.

None of the boundary layer variable scalings mentioned above collapse the p spectra at $\alpha = 20°$ as well as they roughly do for the p spectra at $\alpha = 10°$ (figures 120-127). However, around the primary separation and at windward ϕ locations, at $110° < \phi < 130°$, the p spectra collapse at $2 < \omega_{01}$ with an ω^{-3} variation when normalized using τ_W as the pressure scale and δ^*/U_e as the time scale (figures 123 and 125). Simpson *et al.* (1987) also observed an ω^{-3} variation during 2-D detachment and downstream.

Even though the $\alpha = 20°$ case is a highly non-equilibrium flow, there are some p spectral features that can be consistently related to the flow above. As the flow moves from the windward to leeward sides ($\phi = 90°$), there is low level low-frequency large-scaled turbulence content due to the thin accelerating boundary layer with low mean velocity gradients in the outer layer. Substantial high frequency ($\omega \sim u_\tau^2 / \nu$) content is produced by the nearest wall-layer structure with a relatively large u_τ. The mid-frequencies (4 kHz $< f <$ 10 kHz) have nearly constant, or flat, spectral values.

At more leeward locations the low frequency content increases because of the thickening boundary layer and the separation with large-scale structures while the high frequency content is much lower because of much lower u_τ. Further leeward under the large vortex, the low frequency content decreases because there are low mean velocity gradients in the outer layer while much larger u_τ values increase the high frequency content. Again, the mid-frequencies have nearly constant spectral values.

5.3. Surface Pressure-Velocity Correlations

In order to examine the locations of turbulent flow that strongly influence p, simultaneous p and velocity fluctuation measurements were made for three of the stations; $\alpha = 10°$, $x/L = 0.772$; $\alpha = 20°$, $x/L = 0.600$ and $x/L = 0.772$. Although the Reynolds stresses are discussed by Chesnakas and Simpson (1997), they are presented here as they relate to the surface pressure-velocity correlation coefficient. The correlation coefficients and Reynolds stresses are presented in this section with a logarithmic radial (r) coordinate in order to emphasize the near-wall turbulent structures. The surface pressure-velocity covariances measured in the vicinity of $y^+ = 10$ are expected to be low because of attenuation of higher frequency surface pressure fluctuations by the pinhole that is much larger ($38 < d^+ < 92$) than the near wall coherent structures ($12\,\nu/u_\tau$). Two-point correlation coefficients are presented in this section. When evaluating the magnitude of the correlation coefficients presented here, it should be kept in mind that the single-point correlation coefficient of the uv-stress in a 2-D, zero pressure gradient boundary layer is -0.3 to -0.5.

5.3.1. $\alpha = 10°$, $x/L = 0.772$

At $\alpha = 10°$, $x/L = 0.772$, there is substantial R_{pu} ($\approx$ -0.07) at $r \approx 1$ cm ($r^+ \approx 1200$), $90° < \phi < 120°$ (figure 128). This r^+ corresponds to the wake region in which free-stream flow is entrained into the boundary layer. Relatively high correlation coefficient in the outer layer is also significant because pressure fluctuation sources that interact with the free-stream are radiated away as sound. There are two regions of significant positive R_{pu}. The first region is at $r \approx 0.13$ cm ($r^+ \approx 125$), $120° < \phi < 135°$ and $R_{pu} \approx 0.09$. This r^+ is the outer edge of the semi-logarithmic part of the mean velocity profile in wall-shear-stress coordinates (log layer). The

second region is at $r \approx 0.2$ cm ($r^+ \approx 240$), $170° < \phi < 180°$ and $R_{pu} \approx 0.12$. None the regions of high R_{pu} correspond to regions of particularly high $\overline{u^2}$ (figure 129).

Figures 130 and 131 show R_{pv} and the fluctuating v-velocity component, respectively, at $\alpha = 10°$, $x/L = 0.772$. The maximum negative correlation is $-0.08 > R_{pv} > -0.11$ at $160° < \phi < 120°$, 0.1 cm $< r <$ 0.2 cm, which is roughly at $r^+ \approx 100 - 250$. Highly turbulent fluid in this case is present mainly near the wall. This maximum negative R_{pv} occurs at the outer edge of the mean velocity profile semi-logarithmic region. Bradshaw (1967) showed that in 2-D boundary layers, with both zero and equilibrium adverse pressure gradients, the semi-logarithmic region of the mean flow velocity profile is the source of the overlap region of the pressure spectrum. The correlation magnitude is high at this radial location because the overlap region of the spectrum is the main contribution to the $\overline{p^2}$ integral for high enough Re_θ (Bradshaw, 1967).

The maximum in R_{pv} in the semi-logarithmic region of the mean flow velocity profile can be seen through the solution to the Poisson equation relating surface pressure fluctuations to velocity fluctuations within the boundary layer (§1.2.2). Although the solution is an integral over all of space, the influence of any individual source decreases as $1/r_S$. In contrast, the magnitude of the v' source terms are small for small r_S, where they are constrained by the wall. They increase to a maximum toward the middle of the boundary layer. The combined effect is that the semi-logarithmic region is where the strength of source terms are high, and $1/r_S$ is still high enough that these sources influence the pressure at the wall.

Returning to figure 130, the high R_{pv} magnitude at the edge of the log layer is not evident at all ϕ positions. In the separation region, $120° < \phi < 160°$, R_{pv} remains low for all r. However, by considering the behavior of $\overline{v^2}$ (figure 131), this is to be expected. The band of maximum v' is farther away from the wall in the separation region. Pressure fluctuation sources located farther from the wall have less influence on p through the $1/r_S$ term in the Poisson integral (equation 25).

There are two regions of significant negative R_{pw} (≈ -0.08). One is centered about $r = 0.2$ cm ($r^+ = 180$), $\phi = 140°$, the other is at $r = 0.5$ cm ($r^+ = 600$), $\phi = 170°$ (figure 132). Values of $\overline{w^2}$ are low in both of these regions (figure 133). There are two regions with high

positive R_{pw}. One is at 0.02 cm < r < 0.04 cm (20 < r^+ < 40), 90° < ϕ < 120° where 0.08 < R_{pw} < 0.10. The other region is at 0.02 cm < r < 0.07 cm (20 < r^+ < 80), 160° < ϕ < 180° where 0.10 < R_{pw} < 0.16. Values of $\overline{w^2}$ are highest in both regions of high R_{pw} (figure 133).

5.3.2. $\alpha = 20°$, $x/L = 0.600$

There is significant R_{pu} at $\alpha = 20°$, $x/L = 0.600$ (figure 134) in the same regions as at $\alpha = 10°$, $x/L = 0.772$ (figure 128). At 1 cm < r < 1.5 cm (1000 < r^+ < 1500), 90° < ϕ < 120°, R_{pu} reaches -0.1 and 0.10 < R_{pu} < 0.16 at 0.15 cm < r < 0.4 cm (200 < r^+ < 700), 170° < ϕ < 180°. Also there is high positive R_{pu} (= 0.1) at r = 0.1 cm (r^+ = 100), 120° < ϕ < 130°. However, these regions do not appear as prominent in figure 134 as they are in figure 128 due to other regions of higher correlation associated with a stronger shed vortex and the incipient formation of a secondary vortex. At ϕ = 140°, R_{pu} is high from r = 0.02 cm (r^+ = 20) where R_{pu} = 0.085 to r = 0.3 cm (r^+ = 340) where R_{pu} = 0.11 reaching a maximum of R_{pu} = 0.16 at r = 0.2 cm (r^+ = 230). It is also interesting that at ϕ = 140° R_{pu} goes from R_{pu} = +0.16 at r = 0.2 cm (r^+ = 230) to R_{pu} = -0.20 at r = 0.6 cm (r^+ = 680), and then positive again (R_{pu} = +0.09) at r = 1.5 cm (r^+ = 1700). There is a secondary vortex at r = 0.6 cm, ϕ = 140° downstream, at $\alpha = 20°$, $x/L = 0.772$ (figure 105). There is also a region of high negative R_{pu} at 0.1 cm < r < 1.0 cm, 150° < ϕ < 170° where R_{pu} goes from -0.1 to a maximum (magnitude) of -0.3 at r = 0.2 cm (r^+ = 550), ϕ = 160°. The only region of the flowfield in which both R_{pu} (figure 134) and $\overline{u^2}$ (figure 135) are high is at r = 1.5 cm (1700 < r^+ < 2200), 140° < ϕ < 150° where R_{pu} = 0.1.

Like at $\alpha = 10°$, $x/L = 0.772$ (figure 130), there is significant negative R_{pv} at r = 0.125 cm (100 < r^+ < 170), 100° < ϕ < 125° where -0.07 > R_{pv} > -0.11 and at 0.125 cm < r < 1 cm (200 < r^+ < 1800), 155° < ϕ < 180° where -0.1 > R_{pv} > -0.18 (figure 136). Unlike at $\alpha = 10°$, $x/L = 0.772$, there is a region of small spatial extent centered at r = 0.5 cm (r^+ = 570), ϕ = 140° in which R_{pv} is highly negative ($R_{pv} \approx$ -0.18). Again, the secondary vortex at $\alpha = 20°$, $x/L = 0.772$, r = 0.6 cm, ϕ = 140° (figure 105) is probably incipient at this location. Also unlike $\alpha = 10°$, $x/L = 0.772$ there is high positive R_{pv} in the outer layer at most ϕ locations. At 1.5 cm < r < 3 cm, 110° < ϕ < 150° and 165° < ϕ < 180°, 0.07 < R_{pv} < 0.19. Only regions of negative R_{pv} correspond to regions in which $\overline{v^2}$ is high (figure 137).

Figure 138 is especially interesting due to the topological structure present in R_{pw} that is not associated with the mean flow and only weakly associated with $\overline{w^2}$ (figure 139) at $x/L = 0.600$. There is an arch-shaped region of negative R_{pw} (figure 138). The legs of this arch are at $\phi = 130°$ and $\phi = 150°$ and extend from measurement locations closest to the wall ($r \approx 0.008$ cm, $r^+ \leq 11$) out to $r = 0.3$ cm ($r^+ = 235, 440$ at $\phi = 130°, 150°$, respectively). At $\phi = 130°$, R_{pw} ranges from -0.06 to -0.11 and at $\phi = 150°$, R_{pw} ranges from -0.05 to -0.10. The legs of the arch-like structure are connected at $130° < \phi < 150°$, 0.2 cm $< r <$ 0.6 cm where $-0.06 > R_{pw} > -0.21$. Within this region, R_{pw} is maximum (magnitude) at $\phi = 140°$, $r = 0.6$ cm ($r^+ = 690$). However, closer to the wall at $\phi = 140°$ (0.007 cm $< r <$ 0.125 cm, $8 < r^+ < 144$), R_{pw} is highly positive ($0.08 < R_{pw} < 0.20$). Between these regions of positive R_{pw} and negative R_{pw}, R_{pw} is necessarily zero. It is interesting that R_{pw} is near zero at $\phi = 135°$ and $\phi = 145°$ since downstream, at $x/L = 0.772$, there is a reattachment at $\phi = 135°$ and a secondary separation at $\phi = 147°$. At $\phi = 170°$, there is another region of high, negative R_{pw} ($-0.10 > R_{pw} > -0.18$) from $r = 0.08$ cm ($r^+ = 138$) to $r = 1.0$ cm ($r^+ = 1690$).

There are two region of significant positive R_{pw}. One region is at ϕ near 180°, 0.022 cm $< r <$ 0.06 cm ($35 < r^+ < 95$) where $0.09 < R_{pw} < 0.11$. The other region is in the outer layer, 1 cm $< r <$ 3 cm ($975 < r^+ < 3500$), at $120° < \phi < 140°$ where $0.14 < R_{pw} < 0.26$. None of the regions of significant R_{pw} correspond to any regions of high $\overline{w^2}$ (figure 139). In fact, R_{pw} is near zero at the ϕ location where $\overline{w^2}$ is highest (near $\phi = 160°$, figure 139)

5.3.3. $\alpha = 20°$, $x/L = 0.772$

Like at both $\alpha = 10°$, $x/L = 0.772$ and $\alpha = 20°$, $x/L = 0.600$, there is a region of high negative R_{pu} in the outer layer at $90° < \phi < 110°$ (figure 140). At 0.4 cm $< r <$ 2.75 cm ($350 < r^+ < 3100$), $-0.1 > R_{pu} > -0.35$. Also like the other measurement stations, there is high positive R_{pu} in the middle ϕ range, $110° < \phi < 145°$. Between the primary separation ($\phi = 115°$) and reattachment ($\phi = 135°$), $0.07 < R_{pu} < 0.16$ at 0.1 cm $< r <$ 0.4 cm ($10 < r^+ < 340$). Within the middle range of ϕ ($110° < \phi < 145°$), $\overline{u^2}$ is only relatively high near reattachment at $130° < \phi < 140°$ (figure 141).

Just windward of the secondary separation at $\phi = 145°$, $0.07 < R_{pu} < 0.19$ at $0.009 \text{ cm} < r < 0.3 \text{ cm}$ ($10 < r^+ < 300$). The value $R_{pu} = 0.19$ was measured at $r = 0.2$ cm ($r^+ = 200$). Just leeward of the secondary separation, $150° < \phi < 155°$, the magnitude of R_{pu} is exceptionally high ($-0.1 > R_{pu} > -0.5$) at $0.009 \text{ cm} < r < 0.3 \text{ cm}$ ($10 < r^+ < 1800$). The value $R_{pu} = 0.5$ was measured at $r = 0.3$ cm ($r^+ = 500$), $\phi = 155°$. The magnitude of R_{pu} remains high away from the wall ($0.2 \text{ cm} < r < 1.5 \text{ cm}$, $360 < r^+ < 2600$) in a region extending leeward to $\phi = 170°$ (figure 140). It is also notable that R_{pu} is near zero along the convergence of streamlines indicative of the secondary separation at $\phi = 147°$.

The behavior of R_{pu} is particularly interesting at $\phi = 140°$ along a line of constant ϕ. Near the wall at $r = 0.008$ cm ($r^+ = 12$), $R_{pu} = 0.1$. As r increases, R_{pu} becomes negative and reaches $R_{pu} = -0.1$ at $r = 0.124$ cm ($r^+ = 180$). As r increases more, R_{pu} becomes positive again and reaches $R_{pu} = 0.34$ at $r = 0.6$ cm ($r^+ = 870$) which is the approximate center of the secondary vortex (figure 140). There is similar behavior of R_{pu} near the center of the primary vortex ($r = 3$ cm, $\phi = 155°$). Measurements of R_{pu} were limited to $r < 2.75$ cm, however, at $r = 2.75$ cm, $\phi = 155°$, $R_{pu} = 0.22$ which is significant.

Like at both $\alpha = 10°$, $x/L = 0.772$ and $\alpha = 20°$, $x/L = 0.600$, there is significant negative R_{pv} at the middle r locations windward of $\phi = 115°$ and leeward of $\phi = 160°$ (figure 142). At $0.08 \text{ cm} < r < 0.12 \text{ cm}$ ($62 < r^+ < 132$), $105° < \phi < 115°$, $-0.09 > R_{pv} > -0.12$ with a local maximum R_{pv} at $r = 0.08$ cm ($r^+ = 90$), $\phi = 105°$. At $0.12 \text{ cm} < r < 0.6 \text{ cm}$ ($216 < r^+ < 1050$), $160° < \phi < 170°$, $-0.10 > R_{pv} > -0.17$ with a local maximum R_{pv} at $r = 0.3$ cm ($r^+ = 520$), $\phi = 105°$. However, these regions of high negative R_{pv} are overshadowed by the presence of a localized source of p. The localized source is associated with the secondary vortex present at $x/L = 0.772$, r = 0.6 cm, $\phi = 140°$. Here the term *localized source* is used to describe a small range of r and ϕ in which the correlation is high. This particular source is where the secondary flow streamlines have high curvature and the streamwise flow is rapidly decelerating. There is a small region of high $\overline{v^2}$ at $\alpha = 20°$, $x/L = 0.772$ near $r = 1.5$ cm, $\phi = 140°$ (figure 143) which is also a localized source of p. While this localized source is away from the wall ($r^+ \approx 2200$) the presence of reattachment causes pressure fluctuations associated with this source to be convected

to the surface. High negative R_{pv} is observed near this region where high $\overline{v^2}$ and reattachment is present.

Also like at both $\alpha = 10°$, $x/L = 0.772$ and $\alpha = 20°$, $x/L = 0.600$, there is significant positive R_{pv} in the outer layer at $90° < \phi < 120°$ (figure 142). At 1 cm $< r <$ 2.75 cm ($1000 < r^+ < 3000$), $0.10 < R_{pv} < 0.33$ with a local maximum R_{pv} at $r = 2.0$ cm ($r^+ = 1700$), $\phi = 120°$. There is another region of high R_{pv} in the outer layer between the primary and secondary vortex (figure 142). At 0.4 cm $< r <$ 2.75 cm ($490 < r^+ < 4700$), $145° < \phi < 155°$, $0.10 < R_{pv} < 0.30$ with a local maximum R_{pv} at $r = 2.0$ cm ($r^+ = 2000$), $\phi = 145°$.

The correlation, R_{pw}, is positive at the windward ϕ locations, $\phi = 100°$, 105° (figure 144). At 0.008 cm $< r <$ 0.05 cm ($9 < r^+ < 230$), $0.09 < R_{pw} < 0.18$ with a local maximum R_{pw} at $r = 0.023$ cm ($r^+ = 25$), $\phi = 100°$. Between the primary separation and reattachment, R_{pw} is negative and low. At $\phi = 140°$, R_{pw} is high from close to the wall ($r = 0.006$ cm, $r^+ = 9$) where $R_{pw} = 0.34$ out to $r = 0.2$ cm ($r^+ = 290$) where $R_{pw} = 0.13$ reaching a local maximum of $R_{pw} = 0.45$ at $r = 0.02$ cm ($r^+ = 30$). Similar to R_{pu} and R_{pv}, R_{pw} is nearly zero along the convergence of streamlines indicative of secondary separation ($\phi = 147°$, figure 144).

Leeward of the secondary separation, at $\phi = 150°$, R_{pw} is negative near the wall ($r = 0.006$ cm, $r^+ = 7$) where $R_{pw} = -0.15$. It remains high and negative well out into the flow ($r = 1$ cm, $r^+ = 1225$, $R_{pw} = -0.23$). At $\phi = 150°$, R_{pw} reaches a local maximum of $R_{pw} = -0.39$ at $r = 0.6$ cm ($r^+ = 730$). This region of high negative R_{pw} away from the wall extends windward to $\phi = 140°$. At 0.2 cm $< r <$ 2 cm ($200 < r^+ < 2900$), $-0.15 > R_{pw} > -0.46$ with a maximum $R_{pw} = -0.46$ at $r = 1$ cm ($r^+ = 1450$), $\phi = 140°$. This r, ϕ location is just above the secondary vortex (figure 144) where the secondary streamlines associated with the primary vortex show large curvature as they extend over the secondary vortex. There are also high levels of $\overline{w^2}$ at $\phi = 140°$, however, farther away from the wall than the high, negative R_{pw} (figure 145).

At the leeward ϕ locations, $160° < \phi < 170°$, R_{pw} is low and positive near the wall, however, away from the wall R_{pw} is high and negative. At 0.12 cm $< r <$ 1.5 cm ($220 < r^+ < 2750$), $160° < \phi < 170°$, $-0.10 > R_{pw} > -0.15$ (figure 144). Away from the wall, R_{pw} is

high and positive at most ϕ locations. At $100° < \phi < 130°$, 0.4 cm $< r <$ 2.75 cm ($300 < r^+ < 3500$), $0.09 < R_{pw} < 0.41$ and at $130° < \phi < 155°$, 2.0 cm $< r <$ 2.75 cm ($2030 < r^+ < 4690$), $0.11 < R_{pw} < 0.27$.

5.4. Mean Square of Surface Pressure Fluctuations

Each of the p spectra were integrated to obtain $\overline{p^2}$ values. In order to use a more complete spectrum, a high frequency contribution to the mean square integral was added to the numerically integrated experimental spectral estimates. At $\alpha = 10°$, the p spectra collapse at the highest frequencies when scaled on inner variables. Therefore, the high frequency behavior can be described by a single curve. At $\alpha = 20°$, most of the measured p spectra do not extend to frequencies that are high enough to exhibit inner variable scaling, despite the high sampling rate and high frequency spectral correction used here. It is clear that an additional high frequency contribution to the $\overline{p^2}$ integral is required, especially at $\alpha = 20°$ (figures 120 and 121).

5.4.1. The Calculation Method

The procedure used here to calculate $\overline{p^2}$ was to first numerically integrate the experimental spectral estimates. Then, the last spectral estimate (highest frequency), was scaled on inner variables. This non-dimensional estimate served as the lower limit of an analytical integral contribution (AIC). For p spectra that extended to frequencies that are high enough to exhibit an ω^{-5} spectral decay, the integrand of the AIC was proportional to ω^{-5} (figure 146). For p spectra that did not extend to frequencies that are high enough to exhibit an ω^{-5} spectral decay, the integrand of the AIC consisted of two parts. The first part is an extrapolation of the observed spectral decay of p. The second part of the AIC was proportional to ω^{-5} (figure 147). The highest frequency AIC integrand was $\Phi^+ = 0.50(\omega^+)^{-5}$ (the ω^{-5} line in figures 110 and 111) for the p spectra at $\alpha = 10°$ and $\Phi^+ = 2.00(\omega^+)^{-5}$ (the ω^{-5} line in figures 120 and 121) for the p spectra at $\alpha = 20°$. Once made dimensional, the value of the AIC yields the high frequency contribution to $\overline{p^2}$.

For the data at $\alpha = 10°$, the AIC is generally within 10% of the total $\overline{p^2}$ (tables 12 and 13). However, it reaches 22% at $x/L = 0.600$, $\phi = 90°$ (table 12). For $\alpha = 20°$, the AIC varies from less than 1% of the total $\overline{p^2}$ near separation, where $\overline{p^2}$ is lowest, to 73% of the total

$\overline{p^2}$ at $x/L = 0.600$ (table 14) and 75% at $x/L = 0.772$ (table 15) at ϕ locations under the vortex, where $\overline{p^2}$ is large. While the AIC to $\overline{p^2}$ is large for some ϕ locations at $\alpha = 20°$, it must be noted that the values presented here are a lower bound on the true $\overline{p^2}$ values. Therefore, the variation of $\overline{p^2}$ with ϕ that is presented here is accurate. At ϕ locations where $\overline{p^2}$ is small, the AIC is small. At ϕ locations where $\overline{p^2}$ is large, the AIC is large, however, the true $\overline{p^2}$, if different, is higher than the values presented here. Additionally, the p spectrum at ϕ locations where the AIC is large are nearly flat in the middle to high frequency range. The large AIC at these ϕ locations emphasizes the large contribution of the p spectrum at high frequencies to the $\overline{p^2}$ integral.

5.4.2. Results

The p' estimates are presented here normalized using the far upstream dynamic pressure, Q_∞, and the wall shear stress, τ_w (figure 148). Since Q_∞ is nearly constant, p'/Q_∞ closely approximates the true variation of p' with ϕ. Recall that Re_L, rather than Q_∞, was kept constant during these measurements. The recent review of Bull (1995) concluded that p'/τ_W was the most appropriate parameter for consideration of p' beneath 2-D flows. Also, τ_w is a local minimum at separation (Wetzel *et al.*, 1998).

At $\alpha = 10°$, the values of p'/Q_∞ and p'/τ_W are in the range observed beneath 2-D flows (Blake, 1970; Simpson *et al.*, 1987). The value of p'/Q_∞ is largest at $\phi = 90°$ and $\phi = 180°$ and smallest very near separation (figure 148). The decrease in p'/Q_∞ at middle ϕ locations is almost entirely a result of the minimum in high frequency p very near separation (tables 12 and 13). The low frequency contribution to p'/Q_∞ is nearly constant with ϕ (tables 12 and 13). Values of p'/τ_W are largest at the middle ϕ locations near separation (figure 148). However, the maximum in p'/τ_W does not correlate with the separation location as well as the minimum in p'/Q_∞.

At $\alpha = 20°$, p'/Q_∞ is a local minimum very near separation due to decreased high frequency spectral values (figures 118 and 119 tables 14 and 15). The maximum p'/Q_∞ is near the ϕ location of the center of the primary vortex (figure 148) and is mostly due to the AIC (tables 14 and 15). The large AIC here is a result of the measured spectral values at high frequency which are nearly constant or even increasing at some ϕ locations (figures 110 and 111). Although the AIC is a model, it most likely follows p' accurately since the application of the AIC was

consistent for each ϕ location. At $x/L = 0.772$, there is also local maximum in p'/Q_∞ at reattachment. This local maximum occurs in the contribution to $\overline{p^2}$ from all frequencies (tables 14 and 15). A local maximum in p'/τ_W occurs at both the primary and secondary separations (figure 148). The p'/τ_w value magnifies the effect of the separation (through u_τ) and follows the relative contribution of the outer layer and low frequency spectral contribution as compared to the viscous wall layer high frequency contribution (tables 14 and 15). Around the separation locations larger values of p'/τ_w occur because low frequency contributions are relatively large while τ_w is much lower with a lower contribution from the viscous region.

6. CONCLUSIONS

6.1. Two-Dimensional Boundary Layer

Surface pressure fluctuation measurements beneath two zero pressure gradient, 2-D turbulent boundary layers, each at a different Reynolds number, were presented. There is not a universal scaling that collapses the p spectra of different Reynolds number flows at all frequencies. However, the p spectra collapse at high frequencies ($\omega^+ > 0.15$) and decay as ω^{-5} when normalized using τ_W as the pressure scale and ν/u_τ^2 as the time scale. Since τ_W and ν/u_τ^2 are inner boundary layer scales, the collapse of the p spectra using these scales indicates that sources of high frequency p are small scale turbulent motions near the wall. The present analysis was not designed to address the effects of transducer size on spatial resolution in detail. Nevertheless, high frequency spectral levels of p that were measured using transducers with a small sensing area were consistently greater than the spectral levels that were measured using larger transducers.

The p spectra collapse within a middle frequency range ($0.7 < \omega_{O1} < 2.5$; $20 < \omega_{O3} < 70$; $100 < \omega_{O5} < 500$; $4 < \omega_{O7} < 20$) when normalized using τ_W as the pressure scale independent of the time scale used. The middle frequency region of p spectral collapse overlaps (in frequency) the high frequency region of p spectral collapse and decays as $\omega^{-0.8}$. None of the pressure- time scale combinations used in the present study collapsed the p spectra at low frequencies. However, p spectra have been shown by others (Farabee and Casarella, 1991) to collapse when normalized on outer boundary layer variables within a frequency range lower than presented here.

The p spectrum within the middle frequency range, also called the *overlap* frequency range, was shown to be the largest contribution to p' through the $\overline{p^2}$ integral. The size of the overlap frequency range was shown to increase with Reynolds number. Therefore, the increase in p' with Reynolds number is due to an increase in the size of the overlap frequency range within which the p spectrum decays slowly. Dimensionally, the Reynolds number Re_δ is the most appropriate measure of the size of the overlap region since Re_δ is the ratio of the outer layer

length scale to the inner length scale. As this ratio increases, so does the size of the overlap region. The data presented here is consistent with a logarithmic increase of $\overline{p^2}/\tau_w^2$ with Re_δ. Also, the favorable comparison of the present investigation with the previous work of other researchers on two-dimensional, turbulent, boundary layers confirms the quality of the experimental apparatus and supports the validity of the experimental techniques used in the present investigation.

6.2. Wing-Body Junction Flow

Surface pressure fluctuation measurements at 10 locations beneath two 3-D turbulent boundary layers *away* from a wing-body junction, each at a different Reynolds number, were presented. Scaling parameters that collapse the pressure spectra within a given frequency range beneath 2-D flows do not collapse the pressure spectra beneath the present 3-D flows. However, the p spectra decay as ω^{-5} at the highest frequencies ($f > 10$ kHz) and decay as ω^n within the frequency range 100 Hz $< f <$ 900 Hz. The exponent, n, changes with measurement station ($-0.6 < n < -1.3$).

At both Reynolds numbers, the flow decelerates at measurement stations upstream of the wing which increases the magnitude of low frequency p significantly, but has little effect on the high frequency p. The flow turns and accelerates at stations to the side of the wing which decreases the magnitude of low frequency p and increases the magnitude of high frequency p. Spectral levels of p at these measurement stations are nearly constant and do not change appreciably with Reynolds number within a middle frequency range (1 kHz $< f <$ 5 kHz). Analysis based on the Poisson integral (equation 25) shows that the variation of high frequency p from measurement station to measurement station is tracked by the variation of mean velocity gradients and $\overline{v^2}$ structure near the wall. The increased spectral levels at high frequencies due to the near constant spectral levels at middle frequencies increases p' significantly. Therefore, accurate measurement of p' requires the accurate measurement of high frequency p particularly when large changes in near-wall mean velocity gradients and $\overline{v^2}$ structure is present.

6.3. Flow Around a 6:1 Prolate Spheroid

The flow around a 6:1 prolate spheroid is complex and three-dimensional. It contains crossflow separations and shed vortices. The wall-shear-stress magnitude decreases to a local minimum at crossflow separation locations and a local maximum at reattachment and under the shed vortices. The *TKE* levels near the wall follow these same trends. The updrafts around regions of separation carry *TKE* away from the wall while secondary reattachments bring some *TKE* back toward the wall. Outer region mean velocities on the windward side of the primary separation increase monotonically to the inviscid free-stream, but increase and then decrease as r increases within the vortices.

Despite the three-dimensional nature of the mean flow, the p spectra and p' at low angle of attack are comparable to that beneath an equilibrium boundary layer. The p spectra at $\alpha = 10°$ collapse at high frequencies when normalized on inner boundary layer variables. The p spectra do not collapse as well when normalized on outer boundary layer variables, however, the p spectral levels are comparable to those beneath a 2-D, separating boundary layer. When normalized on mixed inner and outer boundary layer variables, the spectral collapse of the p spectra is confined to select ranges of ϕ.

The three-dimensionality of the flow is readily apparent in the p spectra at $\alpha = 20°$. High p spectral levels extend to high frequencies underneath the shed vortex and at the most leeward ϕ locations (near $\phi = 90°$). The elevated p spectral levels at high frequencies are due to the nearly constant p spectral levels at middle frequencies.

The flat mid-frequency spectral region is believed to occur because of (1) the lack of overlapping frequency structure between the larger-scale motions and the viscous-dominated region and (2) the decrease of low frequency content with a substantial increase in the high frequency levels. The first reason may be due to the three-dimensional flow structure where the near-wall and outer layer flows have different flow histories and low spatial correlations. The second reason just reflects the need for a flatter spectrum to connect the low and high frequency contributions.

The p spectra at $\alpha = 20°$ does not collapse when normalized on inner boundary layer variables. However, only the p spectra near separation (where u_τ is low) were measured at non-dimensional frequencies (ω^+) high enough in order to exhibit an ω^{-5} decay, which is where spectral collapse would occur. There is p spectral collapse at high frequency near primary separation and windward of primary separation at both $\alpha = 10°$ and $\alpha = 20°$ when the p spectra are normalized using τ_W as the pressure scale and δ^*/U_e as the time scale. The success of this scaling combination, albeit limited, suggests that the high frequency p spectra are affected by both the inner and outer layer flow, however, this scaling combination (τ_W, δ^*/U_e) is not sufficient to fully capture the effect.

The correlation coefficient, R_{pv}, shows the strong relationship between p and v within the log layer that has been theorized and observed beneath equilibrium boundary layers. Windward of the primary separation and leeward of the primary vortex, relatively large negative levels of R_{pv} occur around $100 < r^+ < 250$ and indicate the strong influence of v in this region. In the outermost part of the measured flowfield, relatively positive values of R_{pv} occur, especially in the updraft of the primary separation. Negative R_{pv} is large upstream of the formation of the secondary separation and within the secondary separation and reattachment. Deceleration of the flow are also a source of p through w' near $\phi = 90°$ and $\phi = 180°$.

The topological structure of the surface pressure-velocity correlation coefficient at $\alpha = 20°$, $x/L = 0.600$ is especially interesting. It is very similar topological structure at $\alpha = 20°$, $x/L = 0.772$ near the separations, reattachment, and secondary vortex even though these mean flow features are not present at $\alpha = 20°$, $x/L = 0.600$. Zero R_{pu} and R_{pw} along a line of constant ϕ out to $r^+ \sim 200$ at $\phi = 145°$, $x/L = 0.600$ appears to be a precursor to the secondary separation at $\phi = 145°$, $x/L = 0.772$. It is unclear whether the correlations are low because sources of p are convected away from the surface by the secondary separation, or sources of p that are leeward of the secondary separation are out of phase with sources of p that are windward of the secondary separation, thereby canceling each other. Near the secondary vortex at $r = 0.6$ cm, $\phi = 140°$, $x/L = 0.772$, all three correlation coefficients (R_{pu}, R_{pv}, and R_{pw}) are high at both $x/L = 0.600$ and $x/L = 0.772$ even though the secondary vortex is only present at $x/L = 0.772$. This suggests that

the secondary vortex is due to the pressure fluctuations and Reynolds stresses rather than the other way around.

The p at low angle of attack is comparable to measurements in equilibrium flows. Around separations, where τ_W is low, the high frequency spectral content of p is small, while low frequency contributions from the outer layer are relatively large. In regions with large τ_W, the wall region produces strong high frequency spectral content. There are smaller low frequency contributions at locations with relatively small gradients in the outer region mean velocity distribution. Both of these features occur around $\phi = 90°$ and under the large vortices. Therefore, at these locations spectral values are nearly constant at middle and high frequencies. The resulting p' distributions over the surface reflect the importance of the high frequency wall region contributions. Around separations there is a local minimum in p'. Around reattachments and under the large vortices there is a local maximum in p'.

6.5. General Conclusions

Two data sets have been measured in three-dimensional flows of practical interest. The data show features of p unique to three-dimensional flow. In that regard, the present data base can serve as a test case for the computational investigations of others.

Three-dimensional, skewed flows can have nearly constant p spectral levels within a middle frequency range that significantly increases p'. The nearly constant spectral levels are due to a lack of overlapping frequency structure between the large-scale motions and the viscous-dominated motions since each of these types of motion may have different flow histories due to the three-dimensional flow structure. This effect amplifies the importance of the middle frequency range to p' as compared to two-dimensional flows. Also, from an instrumentation point of view, accurate p' measurements in a three-dimensional flow require accurate high frequency ($f > 20$ kHz) p measurements.

Scaling parameters for the p spectra beneath three-dimensional flows must incorporate local flow structure, through the Poisson integral, in order to be successful. Analysis based on the

Poisson integral shows that high frequency p is mainly due to the mean velocity gradients and $\overline{v^2}$ structure near the wall.

Measurements of the correlation coefficient between surface pressure and velocity fluctuations show that there can be sources of p away from the wall in three-dimensional flows. Sources of p away from the wall are significant in terms of fluid-structure interaction since they contribute low frequency fluctuations. Structures typically have low resonant frequencies. Sources of p away from the wall are also significant in terms of radiated sound since they are likely to interact with the free-stream and be radiated away as sound.

6.6. Suggestions for Future Work

Spectral power densities of p, p' values, and some surface pressure-velocity correlation coefficients beneath three-dimensional flows of practical interest were presented and discussed in the present study. The logical next step is to obtain more detailed information, such as wave speeds and length scales of p in three-dimensional flows of practical interest as has been done beneath two-dimensional boundary layers (Willmarth and Roos, 1965; McGrath and Simpson, 1987; Farabee and Casarella, 1991). Such data can be best acquired using multiple pressure transducers that are spatially separated and simultaneously sample the fluctuating surface pressure. The use of multiple transducers in this way is also known as *wave-vector filtering* and is discussed in detail by Blake (1986). A wave-vector filter can be used to calculate the wavenumber-frequency spectrum, from which the wave speed can be determined. Also, spatial coherence length scales can be calculated using the p data from a wave-vector filter.

The success of the Poisson Equation Term Ratio presented in §4.3 highlights the value of identifying sources of p within the fluctuating velocity field. Correlation coefficients between surface pressure and velocity were presented here. The logical next step is to obtain more detailed information through surface pressure-velocity cross-spectra. Cross-spectra between the surface pressure and velocity fluctuations at various points within the flow will show the locations within the fluctuating velocity field that are the dominant source of pressure fluctuations within a given frequency range. This type of data and the wave speed data mentioned above can be used, along

with the Poisson equation, to further the understanding of, and possibly model, the pressure fluctuations in three-dimensional, turbulent, boundary layers.

Abraham, B. M., and Keith, W. L., 1998, "Direct Measurements of Turbulent Boundary Layer Wall Pressure Wavenumber-Frequency Spectra," *Journal of Fluids Engineering*, Vol. 120, pp. 29-39.

AGARD, 1991, "Calculation of 3D Separated Turbulent Flows in Boundary Layer Limit," AGARD-AR-255, Neuilly sur Seine, France.

Agarwal, N. K., and Simpson, R. L., 1989, "A New Technique for Obtaining the Turbulent Pressure Spectrum from the Surface Pressure Spectrum," *Journal of Sound and Vibration*, Vol. 135, No. 2, pp. 346-350.

Ahn, S., and Simpson, R. L., 1992, "Cross-flow Separation on a Prolate Spheroid at Angles of Attack," AIAA Paper 92-0428.

Barber, K. M., and Simpson, R. L., 1991, "Mean Velocity and Turbulence Measurements of Flow Around a 6:1 Prolate Spheroid," AIAA Paper 91-0255.

Batchelor, G. K., 1953, *The Theory of Homogenous Turbulence*, Cambridge University Press.

Bendat, J. S., and Piersol, A. G., 1986, *Random Data: Analysis and Measurement*, 2nd ed., Wiley, New York, pp. 252-290.

Blake, W. K., 1970, "Turbulent Boundary-Layer Wall-Pressure Fluctuations on Smooth and Rough Walls," *Journal of Fluid Mechanics*, Vol. 44, Part 4, pp. 637-660.

Blake, W. K., 1986, *Mechanics of Flow-Induced Sound and Vibration*, Academic, New York, pp. 497-595.

Bradshaw, P., 1967, "'Inactive' Motion and Pressure Fluctuations in Turbulent Boundary Layers," *Journal of Fluid Mechanics*, Vol. 30, No. 2, pp. 241-258.

Bull, M. K., and Thomas, A. S. W., 1976, "High Frequency Wall-Pressure Fluctuations in Turbulent Boundary Layers," *The Physics of Fluids*, Vol. 19, No. 4, pp. 597-599.

Bull, M. K., 1979, "On the Form of the Wall-Pressure Spectrum in a Turbulent Boundary Layer in Relation to Noise Generation by Boundary Layer-Surface Interactions," *Mechanics of Sound Generation in Flows*, IUTAM Conference, Springer-Verlag, Berlin, pp. 210-216.

Bull, M. K., 1996, "Wall-Pressure Fluctuations Beneath Turbulent Boundary Layers: Some Reflections on Forty Years of Research," *Journal of Sound and Vibration*, Vol. 190, No. 3, pp. 299-315.

Chase, D. M., 1969, "Turbulent-Boundary-Layer Pressure Fluctuations and Wavenumber Filtering by Nonuniform Spatial Averaging," *Journal of the Acoustical Society of America*, Vol. 46, No. 5, Part 2, pp. 1350-1365.

Chesnakas, C. J., Simpson, R. L., and Madden, M. M., 1993, "Three Dimensional Velocity Measurements on a 6:1 Prolate Spheroid at Angle of Attack," Data Report VPI-AOE-202, *Dept. of Aero & Ocean Engr, VPI&SU*, Blacksburg, VA.

Chesnakas, C. J., and Simpson, R. L., 1994, "Full Three-Dimensional Measurements of the Cross-flow Separation Region of a 6:1 Prolate Spheroid," *Experiments in Fluids*, Vol. 17, pp. 68-74.

Chesnakas, C. J., and Simpson, R. L., 1996, "Measurements of the Turbulence Structure in the Vicinity of a 3-D Separation," *Journal of Fluids Engineering*, Vol. 118, No. 1, pp. 268-275.

Chesnakas, C. J., and Simpson, R. L., 1997, "A Detailed Investigation of the 3-D Separation about a 6:1 Prolate Spheroid at Angle of Attack," *AIAA Journal*, Vol. 35, No. 6, pp. 990-999.

Choi, K., and Simpson, R. L., 1987, "Some Mean Velocity, Turbulence, and Unsteadiness Characteristics of the VPI&SU Stability Wind Tunnel," Data Report VPI-AOE-161, *Dept of Aero & Ocean Engr, VPI&SU*, Blacksburg, VA.

Coles, D., 1956, "The Law of the Wake in the Turbulent Boundary Layer," *Journal of Fluid Mechanics*, Vol. 1, Part 2, pp. 191-226.

Cooley, J. W., and Tukey, J. W., 1965, "An Algorithm for the Machine Calculation of Complex Fourier Series," *Mathematics of Computation*, Vol. 19, No. 90, pp. 297-301.

Corcos, G. M., 1963, "Resolution of Pressure in Turbulence," *Journal of the Acoustical Society of America*, Vol. 35, No. 2, pp. 192-199.

Corcos, G. M., 1967, "The Resolution of Turbulent Pressures at the Wall of a Boundary Layer," *Journal of Sound and Vibration*, Vol. 6, No. 1, pp. 59-70.

Devenport, W. J., and Simpson, R. L., 1990, "Time-Dependent and Time-Averaged Turbulence Structure Near the Nose of a Wing-Body Junction," *Journal of Fluid Mechanics*, Vol. 210, pp. 23-55.

Devenport, W. J., Rife, M. C., Liapis, S. I., and Follin, G. J., 1997, "The Structure and Development of a Wing-Tip Vortex," *Journal of Fluid Mechanics*, Vol. 332, pp. 71-104.

Eckelmann, H., 1990, "A Review of Knowledge on Pressure Fluctuations," *Near Wall Turbulence: Proceedings of the 1988 Zoran Zaric Memorial Conference*, ed. S. J. Kline and N. H. Afgan, pp. 328-347.

Farabee, T. M., and Casarella, M. J., 1991, "Spectral Features of Wall Pressure Fluctuations Beneath Turbulent Boundary Layers," *Physics of Fluids A*, Vol. 3, No. 10, pp. 2410-2420.

Ffowcs-Williams, J. E., 1982, "Boundary-Layer Pressures and the Corcos Model: A Development to Incorporate Low-Wavenumber Constraints," *Journal of Fluid Mechanics*, Vol. 125, pp. 9-25.

Fleming, J. L., and Simpson, R. L., 1997, "Experimental Investigation of the Near Wall Flow Structure of a Low Reynolds Number 3-D Turbulent Boundary Layer," Data Report VPI-AOE-247, *Dept. of Aero & Ocean Engr, VPI&SU*, Blacksburg, VA.

Fricke, F. R., 1971, "Pressure Fluctuations in Separated Flows," *Journal of Sound and Vibration*, Vol. 17, No. 1, pp. 113-123.

Gee, K., Cummings, R. M., and Schiff, L. B., 1992, "Turbulence Model Effects on Separated Flow about a Prolate Spheroid," *AIAA Journal*, Vol. 30, No. 3, pp. 655-664.

Geib, F. E., 1969, "Measurements on the Effect of Transducer Size on the Resolution of Boundary-Layer Pressure Fluctuations," *Journal of the Acoustical Society of America*, Vol. 46, No.1, Part 2, pp. 253-261.

Gilchrist, R. B., and Strawderman, 1965, "Experimental Hydrophone-Size Correction Factor for Boundary-Layer Pressure Fluctuations," *Journal of the Acoustical Society of America*, Vol. 38, pp. 298-302.

Goody, M. C., Simpson, R. L., Engel M., Chesnakas, C. J., and Devenport, W. J., 1998, "Mean Velocity and Pressure and Velocity Spectral Measurements within a Separated Flow Around a Prolate Spheroid at Incidence", AIAA Paper 98-0630.

Gravante, S. P., Naguib, A. M., Wark, C. E., and Nagib, H. M., 1998, "Characterization of the Pressure Fluctuations Under a Fully Developed Turbulent Boundary Layer," *AIAA Journal*, Vol. 36, No. 10, pp. 1808-1816.

Ha, S., 1993, "An Experimental Study of Coherent Structures in a Three-Dimensional Turbulent Boundary Layer," Ph.D. Dissertation, *Dept of Aerospace and Ocean Engr, VPI&SU.*

Hasan, M. A. Z., Casarella, M. J., and Rood, E. P., 1985, "An Experimental Study of the Flow and Wall-Pressure Field Around a Wing Body Junction," *Shear Flow-Structure Interaction Phenomena*, (ed. A. Akay and M. Reischman), ASME NCA-1, pp. 89-95.

Helal, H. M., Casarella, M. J., and Farabee, T. M., 1989, "An Application of Noise Cancellation Techniques to the Measurement of Wall Pressure Fluctuations in a Wind Tunnel," Report No. H00563, NCA 5, *ASME Winter Annual Meeting*, pp. 49-59.

Hussain, A. K. M. F., 1986, "Coherent Structures and Turbulence," *Journal of Fluid Mechanics*, Vol. 173, pp. 303-356.

Kammeyer, M., 1995, "An Experimental Investigation of Organized Turbulent Motions and Wall-Pressure Fluctuations in Complex Flows," Data Report NSWCCD-TR-95/222, Bethesda, MD.

Keith, W. L., Hurdis, D. A., and Abraham, B. M., 1992, "A Comparison of Turbulent Boundary Layer Wall-Pressure Spectra," *Journal of Fluids Engineering*, Vol. 114, No. 2, pp. 338-347.

Kim, J., Moin, P., and Moser, R., 1987, "Turbulence Statistics in Fully Developed Channel Flow at Low Reynolds Number," *Journal of Fluid Mechanics*, Vol. 177, pp. 133-166.

Kim, J., 1989, "On the Structure of Pressure Fluctuations in Simulated Turbulent Channel Flow," NASA TM-101084.

Kline, S. J., and McClintock, F. A., "Describing Uncertainties in Single Sample Experiments," *Mechanical Engineering*, Vol. 75, Jan. 1953, pp. 3-8.

Kraichnan, R. H., 1956, "Pressure Fluctuations in Turbulent Flow over a Flat Plate," *Journal of the Acoustical Society of America*, Vol. 28, No. 3, pp. 378-390.

Kreplin, H. P., Vollmers, H., Meier, H. U., 1985, "Wall Shear Stress Measurements on an Inclined Prolate Spheroid in the DFVLR 3m×3m Low Speed Wind Tunnel," Data Report DFVLR 1B 222-84/A33, Göttingen, Germany.

Kreplin, H. P., and Stäger, R., 1993, "Measurements of the Reynolds Stress Tensor in the Three-Dimensional Turbulent Boundary Layer of an Inclined Body of Revolution," Paper 2-4, *9th Symposium on Turbulent Shear Flow*, Kyoto, Japan.

Lauchle, G. C., and Daniels, M. A., 1987, "Wall-Pressure Fluctuations in Turbulent Pipe Flow," *Physics of Fluids*, Vol. 30, No. 10, pp. 3019-3024.

Lewis, D. J., 1996, "An Experimental Investigation of Heat Transfer in Three-Dimensional and Separating Turbulent Boundary Layers," Ph.D. Dissertation, *Dept of Aerospace and Ocean Engr, VPI&SU*.

Lighthill, M. J., 1952, "On Sound Generated Aerodynamically: I. General Theory," *Proceedings of the Royal Society of London. Series A*, Vol. 211, pp. 564-587.

Lighthill, M. J., 1954, "On Sound Generated Aerodynamically: II. Turbulence as a Source of Sound," *Proceedings of the Royal Society of London. Series A*, Vol. 222, pp. 1-32.

Lueptow, R. M., 1995, "Transducer Resolution and the Turbulent Wall Pressure Spectrum," *Journal of the Acoustic Society of America*, Vol. 97, No. 1, pp. 370-378.

Madden, M. M., 1997, "Octant Analysis of the Reynolds Stresses in the Three-Dimensional Turbulent Boundary Layer of a Prolate Spheroid," M.S. Thesis, *Dept of Aerospace and Ocean Engr, VPI&SU.*

McGrath, B. E., and Simpson, R. L., 1987, "Some Features of Surface Pressure Fluctuations in Turbulent Boundary Layers with Zero and Favorable Pressure Gradients," NASA CR-4051.

Meier, H. U., Kreplin, H. P., Ländaußer, A., and Baumgarten, D., 1984, "Mean Velocity Distributions in Three-Dimensional Boundary Layers Developing on a 1:6 Prolate Spheroid with Natural Transition", Data Report DFVLR 1B 222-86/A10, Göttingen, Germany.

Meier, H. U., Kreplin, H. P., and Ländaußer, A., 1985, "Wall Pressure Measurements on a 1:6 Prolate Spheroid in the DFVLR 3m×3m Low Speed Wind Tunnel (α=10°, U_∞=55 m/s, Artificial Transition)," Data Report DFVLR 1B 222-86/A04, Göttingen, Germany.

Moffat, R. J., 1982, "Contributions to the Theory of Single-Sample Uncertainty Analysis," *Journal of Fluids Engineering*, Vol. 104, pp. 250-260.

Ölçmen, M. S., and Simpson, R. L., 1994, "Influence of Wing Shapes on Surface Pressure Fluctuations at Wing-Body Junctions," *AIAA Journal*, Vol. 32, No. 1, pp. 6-15.

Ölçmen, M. S. and Simpson, R. L., 1995a, "An Experimental Study of a Three-Dimensional Pressure-Driven Turbulent Boundary Layer", *Journal of Fluid Mechanics*, Vol. 290, pp. 225-262.

Ölçmen, M. S. and Simpson, R. L., 1995b, "A Five-Velocity-Component Laser-Doppler Velocimeter for Measurements of a Three-Dimensional Turbulent Boundary Layer," *Measurement Science and Technology*, Vol. 6, pp. 1-15.

Ölçmen, M. S. and Simpson, R. L., 1996, "Higher Order Turbulence Results for a Three-Dimensional Pressure-Driven Turbulent Boundary Layer", Data Report VPI-AOE-237, *Dept. Of Aero & Ocean Engr, VPI&SU*, Blacksburg, VA; submitted to DTIC.

Ölçmen, M. S., Simpson, R. L., George, J., and Whitfield, C., 1998, "Experimental Study of High Reynolds Number (Re=23000) Two and Three-Dimensional Turbulent Boundary Layers", Data Report VPI-AOE-260, *Dept. Of Aero & Ocean Engr, VPI&SU*, Blacksburg, VA; submitted to DTIC.

Ölçmen, M. S., Simpson, R. L. and George, J., 1999a, "Experimental Study of High Reynolds Number (Re_θ = 23200) Two and Three-Dimensional Turbulent Boundary Layers", AIAA paper 99-0553.

Ölçmen, M. S., Simpson, R. L. and George, J., 1999b, "Some Reynolds Number Effects on a Three-Dimensional Turbulent Boundary Layer", AIAA paper 99-0554.

Panton, R. L., and Linebarger, J. H., 1974, "Wall Pressure Spectra Calculations for Equilibrium Boundary Layers," *Journal of Fluid Mechanics*, Vol. 65, No. 2, pp. 261-287.

Panton, R. L., 1990, "Scaling Turbulent Wall Layers," *Journal of Fluids Engineering*, Vol. 112, pp. 425-432.

Panton, R. L., 1998, "On the Wall-Pressure Spectrum Under a Three-Dimensional Boundary Layer," *Journal of Fluids Engineering*, Vol. 120, pp. 407-410.

Phillips, O. M., 1956, "On the Aerodynamic Surface Sound from a Plane Turbulent Boundary Layer," *Proceedings of the Royal Society of London. Series A*, Vol. 234, pp. 327-335.

Pierce, F. J., and Tree, I. K., 1990, "The Mean Flow Structure on the Symmetry Plane of a Turbulent Junction Vortex," *Journal of Fluids Engineering*, Vol. 112, pp. 16-22.

Press, W. H., Teulolsky, S. A., Vetterling, W. T., and Flannery, B. P., 1994, *Numerical Recipes in C: The Art of Scientific Computing*, 2nd ed., Cambridge University Press. (FFT algorithm on pp. 513-514)

Rife, M. C., Devenport, W. J., and Simpson, R. L., 1992, "An Experimental Study of the Relationship Between Velocity and Pressure Fluctuations in a Wing-Body Junction," Data Report VPI-AOE-188, *Dept. of Aero & Ocean Engr, VPI&SU*, Blacksburg, VA.

Robinson, S. K., 1991, "Coherent Motions in the Turbulent Boundary Layer," *Annual Review of Fluid Mechanics*, Vol. 23, pp. 601-639.

Rotta, J. C., 1962, "Turbulent Boundary Layers in Incompressible Flow," *Progress in Aeronautical Sciences*, Vol. 2, Pergamon, pp. 10-11.

Russell, S. J., 1997, "Wall Pressure Signatures of Organized Turbulent Motions," Data Report MSWCCD-TR-97/009, Bethesda, MD.

Schewe, G., 1983, "On the Structure and Resolution of Wall-Pressure Fluctuations Associated with Turbulent Boundary-Layer Flow," *Journal of Fluid Mechanics*, Vol. 134, pp. 311-328.

Schloemer, H. H., 1967, "Effects of Pressure Gradient on Turbulent-Boundary-Layer Wall-Pressure Fluctuations," *Journal of the Acoustical Society of America*, Vol. 42, No. 1, pp. 93-113.

Shinpaugh, K. A., 1994, "Measurements in the Bimodal Region of a Wing-Body Junction Flow with a Rapidly-Scanning Two-Velocity-Component Laser-Doppler Velocimeter," Ph.D. Dissertation, *Dept of Aerospace and Ocean Engr, VPI&SU*, Blacksburg, VA.

Simpson, R. L., 1989, "Turbulent Boundary-Layer Separation," *Annual Review of Fluid Mechanics*, Vol. 21, pp. 205-234.

Simpson, R. L., 1995, "Three-Dimensional Turbulent Boundary Layers and Separation," AIAA Paper 95-0226.

Simpson, R. L., 1996, "Aspects of Turbulent Boundary-Layer Separation," *Progress in Aerospace Sciences*, Vol. 32, Pergamon, pp. 457-521.

Simpson, R. L., 1997, "Unsteady Aero/Hydrodynamics for Maneuvering Aircraft, Submarines, and Automobiles," data Report VPI-AOE-253, *Dept of Aero and Ocean Engr, VPI&SU*, Blacksburg, VA.

Simpson, R. L., Ghodbane, M., and McGrath, B. E., 1987, "Surface Pressure Fluctuations in a Separating Turbulent Boundary Layer," *Journal of Fluid Mechanics*, Vol. 177, pp. 167-186.

Simpson, R. L., Strickland, J. H., and Barr, P. W., 1977, "Features of a Separating Turbulent Boundary Layer in the Vicinity of Separation," *Journal of Fluid Mechanics*, Vol. 79, No. 3, pp. 553-594.

Singer, B. A., 1996, "Large-Eddy Simulation of Turbulent Wall-Pressure Fluctuations," NASA CR-198276.

Singer, B. A., 1997, "Turbulent Wall-Pressure Fluctuations: A New Model for Off-Axis Cross-Spectral Density," *Journal of Fluids Engineering*, Vol. 119, pp. 277-280.

Spalding, D. B., 1961, "A Single Formula for the Law of the Wall," Conference on Internal Developments in Heat Transfer, Part 2, Boulder, CO., *American Society of Mechanical Engineers*, pp. 439-446.

Sung, C. H., Griffin, M. J., Tsai, J. F., and Huang, T. T., 1993, "Incompressible Flow Computation of Forces and Moments on Bodies of Revolution at Incidence," AIAA Paper 93-0787.

Townsend, A. A., 1961, "Equilibrium Layers and Wall Turbulence," *Journal of Fluid Mechanics*, Vol. 11, pp. 97-120.

Vollmers, H., Kreplin, H. P., and Meier, H. U., 1983, "Separation and Vortical-Type Flow Around a Prolate Spheroid - Evaluation of Relevant Parameters," Paper 14, AGARD-CP-342.

Wetzel, T. G., Simpson, R. L., and Chesnakas, C. J., 1998, "Measurement of Three-Dimensional Crossflow Separation," *AIAA Journal*, Vol. 36, No. 4, pp. 557-564.

White, P. H., 1967, "Effects of Transducer Size, Shape, and Surface Sensitivity on the Measurement of Boundary-Layer Pressures," *Journal of the Acoustical Society of America*, Vol. 41, pp. 1358-1363.

Willmarth, W. W., and Roos, F. W., 1965, "Resolution and Structure of the Wall Pressure Field Beneath a Turbulent Boundary Layer," *Journal of Fluid Mechanics*, Vol. 22, Part 1, pp. 81-94.

Willmarth, W. W., and Wooldridge, C. E., 1962, "Measurements of the Fluctuating Pressure at the Wall Beneath a Thick Turbulent Boundary Layer," *Journal of Fluid Mechanics*, Vol. 14, pp. 187-210.

Willmarth, W. W., 1975, "Pressure Fluctuations Beneath Turbulent Boundary Layers," *Annual Review of Fluid Mechanics*, Vol. 7, pp. 13-38.

Wittmer, K. S., Devenport, W. J., and Zoldos, J. S., 1998, "A Four-Sensor Hot-Wire Probe System for Three-Component Velocity Measurement," *Experiments in Fluids*, Vol. 24, pp. 769-786.

TABLES

Table 1. The variation of calibration curve parameters and transducer diameter (in viscous units) with measurement location on a 6:1 prolate spheroid at $\alpha = 10°$.

	$x/L = 0.600$			$x/L = 0.772$		
ϕ	ζ	f_n (Hz)	d^+	ζ	f_n (Hz)	d^+
90°	0.090	9950	68	0.085	12100	63
95°	0.090	9950	67	0.085	12100	62
100°	0.090	9950	65	0.085	12100	61
105°	0.085	9950	64	0.085	12000	58
110°	0.080	9950	62	0.085	12000	55
115°	0.080	9830	61	0.085	11800	52
120°	0.080	9830	60	0.085	11775	49
125°	0.080	9650	57	0.090	11675	47
130°	0.070	9600	55	0.090	11600	43
135°	0.070	9600	53	0.090	11550	42
140°	0.070	9500	51	0.090	11550	43
145°	0.070	9600	51	0.087	11700	46
150°	0.070	9600	51	0.087	11900	49
155°	0.070	9600	52	0.087	11900	53
160°	0.070	9600	53	0.085	11900	57
165°	0.070	9600	55	0.085	11900	59
170°	0.070	9600	56	0.085	11900	62
175°	0.070	9600	57	0.083	11900	61
180°	0.070	9600	58	0.080	11900	60

Table 2. The variation of calibration curve parameters and transducer diameter (in viscous units) with measurement location on a 6:1 prolate spheroid at $\alpha = 20°$.

	$x/L = 0.600$			$x/L = 0.772$		
ϕ	ζ	f_n (Hz)	d^+	ζ	f_n (Hz)	d^+
90°	0.095	9850	77	0.095	12110	68
95°	0.095	9850	74	0.090	12100	62
100°	0.090	9750	71	0.085	12050	56
105°	0.085	9700	67	0.083	11700	51
110°	0.085	9700	63	0.085	11660	44
115°	0.075	9650	56	0.088	11570	38
120°	0.075	9600	49	0.089	11750	43
125°	0.070	9500	42	0.088	12000	54
130°	0.070	9500	39	0.088	12150	64
135°	0.065	9500	51	0.085	12250	68
140°	0.065	9650	57	0.083	12000	73
145°	0.070	9650	57	0.084	12000	51
150°	0.085	9710	73	0.088	12250	61
155°	0.100	9800	87	0.100	12400	85
160°	0.100	9900	92	0.105	12400	92
165°	0.100	9900	88	0.105	12350	90
170°	0.100	9900	84	0.104	12325	88
175°	0.100	9900	81	0.103	12300	84
180°	0.100	9900	78	0.103	12310	79

Table 3. Boundary layer parameters for the present flows and for some previous studies of zero pressure gradient, two-dimensional boundary layers.

Author	Re_θ	Re_δ	d^+	U_e m/s	u_τ m/s	δ mm	δ^* mm	$\nu(\times 10^5)$ m²/s	ρ kg/m³
Present Study	7300	2268	29	27.1	0.98	39.1	6.20	1.69	1.09
	23400	8327	31	31.3	1.03	134.2	15.8	1.66	1.11
Blake (1970)	8210	2480	43	22.25	0.85	45.7	7.85	1.58	N/A
	10200	2791	51	28.75	1.06	43.2	7.24	1.63	N/A
	13200	3420	63	37.94	1.33	42.9	7.19	1.65	N/A
	17000	4154	78	49.98	1.65	42.4	7.11	1.67	N/A
Farabee and Casarella (1991)	3386	1169	33	15.5	0.63	27.9	4.50	1.49	N/A
	4487	1535	44	21.3	0.83	27.4	4.29	1.49	N/A
	6025	2010	57	28.3	1.07	27.8	4.29	1.48	N/A
Gravante *et al.* (1998)	4972	1706	12	15.7	0.58	44.9	6.50†	1.52	N/A
	6241	2012	12	15.7	0.57	53.9	8.06†	1.52	N/A
	7076	2348	12	15.3	0.57	62.9	9.10†	1.52	N/A
McGrath and Simpson (1987)	7010	2317	27	22.34	0.84	43.2	6.58	1.56	1.19
	18820	5531	35	32.48	1.09	79.2	11.88	1.56	1.19
Schewe (1983)	1400	556	19	6.3	0.28	30.0	4.60	1.51	1.15

† Calculated using the θ given and assumming that $H \equiv \delta^*/\theta = 1.3$

Table 4. Outer boundary layer parameters. Pressure gradients are in wall-shear-stress coordinates. Lower Re_θ flow data (Re_θ = 7300 (2-D), 5940 (3-D)) of Ölçmen and Simpson (1996). Higher Re_θ flow data (Re_θ = 23400 (2-D), 23200 (3-D)) of Ölçmen *et al.* (1998).

Station	U_e m/s	δ mm	δ^* mm	Q_e Pa	$\left(\frac{\partial C_p}{\partial\left(\frac{x}{t_{max}}\right)}\right)_{WC}$	$\left(\frac{\partial C_p}{\partial\left(\frac{z}{t_{max}}\right)}\right)_{WC}$	β_W deg	β_{FS} deg
Re_θ = 7300 (2-D), 5940 (3-D)								
2D	27.1	39.1	6.20	399	—	—	—	—
0	26.4	N/A	N/A	379	N/A	N/A	-6.1	-4.9
1	24.9	39.2	6.90	340	0.069	0.112	-11.5	-8.5
2	24.8	40.2	7.54	337	-0.054	0.208	-24.0	-21.5
3	25.3	39.3	6.86	351	-0.378	0.146	-33.7	-18.0
4	27.3	39.0	5.53	409	-0.449	-0.097	-30.6	-30.2
5	29.5	39.6	5.37	477	-0.416	-0.218	-19.7	-25.3
6	30.5	39.2	5.24	511	-0.287	-0.400	-7.2	-20.8
7	31.0	38.8	5.20	528	0.042	-0.480	-3.5	-10.9
8	30.9	38.4	5.08	524	0.085	-0.320	2.6	0.9
9	30.5	40.7	5.68	511	0.080	-0.159	4.7	4.7
Re_θ = 23400 (2-D), 23200 (3-D)								
2D	31.3	134.2	15.8	543	—	—	—	—
0	31.0	N/A	N/A	532	N/A	N/A	N/A	N/A
1	29.3	136.4	22.8	470	0.049	0.100	-10.8	-2.2
2	28.7	135.1	18.4	451	-0.049	0.168	-23.1	-4.7
3	29.0	136.8	16.8	462	-0.320	0.131	-31.2	-7.7
4	31.1	131.9	17.3	530	-0.391	0.020	-25.7	-8.8
5	33.0	123.3	13.7	598	-0.336	-0.159	-16.3	-8.0
6	34.7	128.6	17.2	660	-0.268	-0.317	-10.3	-5.7
7	35.5	129.0	12.9	694	0.007	-0.255	-3.8	-2.7
8	35.2	133.5	13.0	682	0.028	-0.162	4.2	0.6
9	34.3	134.6	13.5	650	0.061	-0.117	6.6	2.3

Table 5. Inner boundary layer parameters. Lower Re_θ data taken from Ölçmen and Simpson (1996). Higher Re_θ data taken from Ölçmen *et al.* (1998).

	Re_θ = 7300 (2-D), 5940 (3-D)				Re_θ = 23400 (2-D), 23200 (3-D)			
Station	u_τ, m/s	ν, m²/s ($\times 10^5$)	τ_w, Pa	d^+	u_τ, m/s	ν, m²/s ($\times 10^5$)	τ_w, Pa	d^+
2D	0.98	1.69	1.04	29.5	1.03	1.66	1.17	31.5
0	1.15	1.69	1.44	34.6	N/A	1.66	N/A	30.6
1	0.86	1.68	0.818	26.2	0.91	1.68	0.906	27.5
2	0.87	1.68	0.821	26.2	0.92	1.68	0.918	27.7
3	0.96	1.68	1.00	29.0	1.09	1.68	1.31	33.2
4	1.11	1.67	1.35	33.7	1.24	1.68	1.68	37.5
5	1.15	1.67	1.45	34.9	1.21	1.67	1.60	36.7
6	1.16	1.67	1.48	35.3	1.21	1.67	1.60	36.7
7	1.20	1.67	1.58	36.5	1.30	1.67	1.88	39.8
8	1.02	1.67	1.15	31.1	1.13	1.67	1.40	34.4
9	1.01	1.67	1.12	30.7	1.10	1.66	1.35	33.8

Table 6. Variation of $\overline{p^2}$ and p' for the lower Re_θ flows, Re_θ = 7300 (2-D), 5940 (3-D) and the low and the high frequency contributions to the $\overline{p^2}$ integral. The values of $\overline{p^2}$ presented here were calculated by integrating the p spectra.

		Contribution to $\overline{p^2}$ integral, Pa²							
Station	$\overline{p^2}$, Pa²	< 1 kHz		> 1 kHz		p'/τ_W	p'/Q_e	"Non-flat" $\overline{p^2}$, Pa²	
				Re_θ = 7300 (2-D), 5940 (3-D)					
2D	12.9	5.4	42%	7.5	58%	3.44	0.0090		
0	13.7	7.3	53%	6.4	47%	2.57	0.0098		
1	14.8	8.3	56%	6.5	44%	4.71	0.0114		
2	17.5	10.8	62%	6.7	38%	5.10	0.0124		
3	21.4	14.7	69%	6.7	31%	4.61	0.0132		
4	27.7	13.1	47%	14.6	53%	3.90	0.0129	21.9	79%
5	17.6	10.1	57%	7.5	43%	2.89	0.0088	15.8	90%
6	20.7	8.2	40%	12.5	60%	3.08	0.0089	17.1	82%
7	28.7	8.1	28%	20.6	72%	3.39	0.0102	20.2	70%
8	30.6	7.9	26%	22.7	74%	4.80	0.0106	23.2	76%
9	33.0	9.5	29%	23.5	71%	5.12	0.0113	23.2	70%
				Re_θ = 23400 (2-D), 23200 (3-D)					
2D	25.8	11.4	44%	14.4	56%	4.32	0.0094		
0	26.8	15.4	57%	11.4	43%	4.67	0.0097		
1	27.8	17.3	62%	10.5	38%	5.81	0.0112		
2	33.8	23.6	70%	10.2	30%	6.34	0.0129		
3	40.1	30.2	75%	9.9	25%	4.82	0.0137		
4	34.2	24.6	72%	9.6	28%	3.48	0.0110		
5	29.5	18.7	63%	10.8	37%	3.39	0.0091	26.2	89%
6	30.2	15.2	50%	15.0	50%	3.43	0.0083	23.3	77%
7	36.1	13.6	38%	22.5	62%	3.20	0.0087	24.2	67%
8	38.8	12.6	32%	26.2	68%	4.44	0.0091	23.3	60%
9	41.3	13.2	32%	28.1	68%	4.77	0.0099	28.3	68%

Table 7. Candidate length (L_S), velocity (V_S), and pressure scales (P_S) used to normalize the p spectra, in the form $\Phi(\omega)V_S/P_S^2 L_S$, and frequency, in the form $\omega L_S/V_S$.

Length scale	Velocity scale	Pressure scale
ν/u_τ	u_τ	τ_W
δ^*	U_e	τ_W
δ^*	U_e	Q_e
δ^*	u_τ	τ_W
δ^*	u_τ	Q_e
δ	u_τ	τ_W
δ	u_τ	Q_e
δ	U_e	τ_W
δ	U_e	Q_e
Δ	u_τ	τ_W
Δ	u_τ	Q_e
Δ	U_e	τ_W
Δ	U_e	Q_e
The velocities below are in the tunnel coordinate system		
y at τ_{MAX}	$(U^2+W^2)^{1/2}$ at τ_{MAX}	τ_{MAX}
y at W_{MAX}	$(U^2+W^2)^{1/2}$ at W_{MAX}	$\frac{1}{2}\rho W_{MAX}^2$

Table 8. Some boundary layer parameters of the flow at $\alpha = 10°$, $x/L = 0.600$.

ϕ deg	ρ kg/m^3	$\nu(\times 10^5)$ m^2/s	u_τ † m/s	U_e ‡ m/s	U_∞ m/s	δ^* ‡ mm	d^+ †	Re_θ ‡
90	1.05	1.79	2.45	54.8	54.7	1.16	68	2483
95	1.05	1.80	2.42	55.3	55.2	1.25	67	2673
100	1.05	1.80	2.36	55.3	55.2	1.35	65	2863
105	1.05	1.80	2.31	55.3	55.2	1.45	64	3073
110	1.06	1.78	2.23	54.8	54.6	1.56	62	3283
115	1.06	1.78	2.17	54.7	54.4	1.79	61	3739
120	1.06	1.76	2.10	54.2	53.9	2.01	60	4195
125	1.10	1.67	1.91	51.3	51.1	2.34	57	4797
130	1.10	1.66	1.82	51.1	50.9	2.66	55	5399
135	1.10	1.66	1.76	50.9	50.7	3.03	53	6084
140	1.10	1.66	1.70	50.9	50.7	3.40	51	6770
145	1.10	1.66	1.70	50.9	50.7	3.58	51	7182
150	1.10	1.65	1.70	50.8	50.6	3.76	51	7594
155	1.10	1.66	1.74	51.0	50.8	3.65	52	7501
160	1.10	1.66	1.77	51.0	50.8	3.55	53	7407
165	1.10	1.66	1.82	51.2	50.8	3.30	55	7031
170	1.10	1.66	1.88	51.6	51.0	3.05	56	6654
175	1.10	1.66	1.90	51.6	51.0	2.86	57	6254
180	1.10	1.66	1.92	51.5	51.0	2.67	58	5855

† Calculated using the C_f measurements of Chesnakas and Simpson (1997)

‡ Calculated using the δ^*, θ, and U_e/U_∞ measurements of Goody *et al.* (1998)

Table 9. Some boundary layer parameters of the flow at $\alpha = 10°$, $x/L = 0.772$.

ϕ deg	ρ kg/m^3	$\nu(\times 10^5)$ m^2/s	u_τ † m/s	U_e ‡ m/s	U_∞ m/s	δ^* ‡ mm	d^+ †	Re_θ ‡
90	1.06	1.79	2.25	58.0	54.7	1.47	63	3145
95	1.05	1.80	2.23	58.0	55.0	1.59	62	3368
100	1.05	1.79	2.19	57.3	54.8	1.70	61	3592
105	1.06	1.79	2.07	56.8	54.7	1.99	58	4122
110	1.06	1.77	1.94	55.9	54.1	2.28	55	4651
115	1.07	1.76	1.82	55.3	53.8	2.79	52	5555
120	1.07	1.75	1.70	54.9	53.6	3.31	49	6458
125	1.07	1.74	1.65	54.6	53.4	4.06	47	7716
130	1.07	1.74	1.50	56.2	53.2	5.62	43	10417
135	1.07	1.73	1.47	55.6	53.1	6.39	42	11636
140	1.07	1.74	1.50	55.2	53.2	7.33	43	13394
145	1.07	1.74	1.61	54.4	53.2	7.24	46	14016
150	1.07	1.73	1.71	53.5	53.1	7.16	49	14637
155	1.08	1.73	1.84	52.5	52.9	5.81	53	12549
160	1.08	1.72	1.95	51.3	52.6	4.47	57	10640
165	1.09	1.70	2.01	51.2	52.0	3.57	59	8430
170	1.09	1.69	2.08	51.4	51.7	2.67	62	6400
175	1.09	1.68	2.06	51.3	51.5	2.25	61	5307
180	1.10	1.67	2.02	50.9	51.0	1.83	61	4213

† Calculated using the C_f measurements of Chesnakas and Simpson (1997)

‡ Calculated using the δ^*, θ, and U_e/U_∞ measurements of Goody *et al.* (1998)

Table 10. Some boundary layer parameters of the flow at $\alpha = 20°$, $x/L = 0.600$.

ϕ deg	ρ kg/m^3	ν ($\times 10^5$) m^2/s	u_τ † m/s	U_e ‡ m/s	U_∞ m/s	δ^* ‡ mm	d^+ †	Re_θ ‡
90	1.10	1.66	2.55	51.0	50.9	0.67	77	1406
95	1.10	1.66	2.47	51.0	50.9	0.76	74	1586
100	1.10	1.66	2.38	50.9	50.9	0.85	71	1767
105	1.10	1.66	2.24	50.9	50.9	1.01	67	2056
110	1.10	1.66	2.10	50.9	50.9	1.18	63	2346
115	1.10	1.66	1.88	50.8	50.9	1.80	56	3358
120	1.10	1.66	1.62	50.8	50.9	2.42	49	4370
125	1.10	1.66	1.41	50.6	50.9	3.5	43	5790
130	1.10	1.66	1.29	50.4	50.9	4.98	39	10827
135	1.10	1.66	1.70	50.2	50.9	5.94	51	10546
140	1.10	1.66	1.91	50.0	50.9	6.24	57	12940
145	1.10	1.66	1.88	56.1	50.9	5.47	57	12242
150	1.10	1.66	2.44	54.8	50.9	4.57	73	10889
155	1.10	1.66	2.88	51.8	50.9	4.34	87	10405
160	1.10	1.66	3.04	49.5	50.9	4.00	92	9493
165	1.10	1.66	2.93	49.9	50.9	2.14	88	5045
170	1.10	1.66	2.80	50.4	50.9	0.28	84	597
175	1.10	1.66	2.71	50.7	50.9	0.37	81	781
180	1.10	1.66	2.61	51.0	50.9	0.45	78	965

† Calculated using the C_f measurements of Chesnakas and Simpson (1997)

‡ Calculated using the δ^*, θ, and U_e/U_∞ measurements of Goody *et al.* (1998)

Table 11. Some boundary layer parameters of the flow at $\alpha = 20°$, $x/L = 0.772$.

ϕ deg	ρ kg/m^3	$\nu(\times 10^5)$ m^2/s	u_τ † m/s	U_e ‡ m/s	U_∞ m/s	δ^* ‡ mm	d^+ †	Re_θ ‡
90	1.07	1.74	2.36	59.4	53.3	0.82	68	1647
95	1.06	1.77	2.21	64.7	54.3	1.05	62	2055
100	1.06	1.77	2.00	68.8	54.3	1.28	56	2462
105	1.06	1.77	1.82	57.6	54.2	1.75	51	3249
110	1.05	1.79	1.56	57.5	54.9	2.60	44	4458
115	1.05	1.79	1.35	56.8	54.9	3.80	38	5910
120	1.06	1.78	1.53	55.7	54.5	5.19	43	8136
125	1.05	1.80	1.96	57.1	55.3	6.23	54	11434
130	1.05	1.80	2.29	57.7	55.1	7.28	64	14732
135	1.05	1.79	2.45	53.7	54.9	6.08	68	13550
140	1.05	1.80	2.62	50.2	55.3	4.88	73	12368
145	1.05	1.80	1.83	56.4	55.3	6.40	51	14625
150	1.05	1.80	2.21	57.3	55.1	5.29	61	13406
155	1.05	1.80	3.08	56.2	55.3	3.52	85	8935
160	1.05	1.79	3.29	55.5	54.9	2.60	92	6348
165	1.06	1.78	3.20	56.8	54.5	1.44	90	3474
170	1.05	1.80	3.15	58.9	55.0	0.28	88	600
175	1.05	1.79	2.99	58.0	54.8	0.34	84	727
180	1.05	1.79	2.83	57.2	54.8	0.39	79	854

† Calculated using the C_f measurements of Chesnakas and Simpson (1997)

‡ Calculated using the δ^*, θ, and U_e/U_∞ measurements of Goody *et al.* (1998)

Table 12. Variation of $\overline{p^2}/Q_\infty^2$ with ϕ at $\alpha = 10°$, $x/L = 0.600$ showing the contribution of various frequency ranges to the $\overline{p^2}$ integral including the Analytical Integral Contribution (AIC). The values presented here were calculated by integrating the p spectra.

ϕ	Total $\overline{p^2}/Q_\infty^2$	Contribution to $\overline{p^2}/Q_\infty^2$ ($\times 10^5$)					
deg	($\times 10^5$)	$f \le 994$ Hz		994 Hz $< f \le 25$ kHz		$f > 25$ kHz (AIC)	
90	14.5	2.5	17%	8.7	60%	3.3	23%
95	13.2	2.4	18%	8.1	61%	2.7	21%
100	12.2	2.3	19%	7.8	64%	2.1	17%
105	11.1	2.2	20%	7.2	65%	1.7	15%
110	10.4	2.3	22%	6.9	66%	1.2	12%
115	9.6	2.3	24%	6.4	67%	0.9	9%
120	9.3	2.5	28%	6.1	65%	0.7	7%
125	7.9	2.1	26%	5.5	70%	0.3	4%
130	7.1	2.1	29%	4.8	68%	0.2	3%
135	6.4	2.1	32%	4.2	66%	0.1	2%
140	6.1	2.2	36%	3.8	63%	0.09	1%
145	5.4	1.9	35%	3.4	63%	0.09	2%
150	5.5	2.0	36%	3.4	63%	0.09	1%
155	5.7	2.0	34%	3.6	64%	0.1	2%
160	6.1	2.0	33%	4.0	65%	0.1	2%
165	6.8	2.0	30%	4.6	67%	0.2	3%
170	7.5	2.0	27%	5.2	69%	0.3	4%
175	7.9	2.1	26%	5.5	70%	0.3	4%
180	8.0	2.0	25%	5.6	70%	0.4	5%

Table 13. Variation of $\overline{p^2}/Q_\infty^2$ with ϕ at $\alpha = 10°$, $x/L = 0.772$ showing the contribution of various frequency ranges to the $\overline{p^2}$ integral including the Analytical Integral Contribution (AIC). The values presented here were calculated by integrating the p spectra.

ϕ	Total $\overline{p^2}/Q_\infty^2$	Contribution to $\overline{p^2}/Q_\infty^2$ ($\times 10^5$)					
deg	($\times 10^5$)	$f \le 994$ Hz		994 Hz $< f \le 25$ kHz		$f > 25$ kHz (AIC)	
90	11.9	2.3	19%	8.2	69%	1.4	12%
95	11.0	2.3	21%	7.6	68%	1.2	11%
100	10.4	2.4	24%	7.0	67%	1.0	9%
105	9.3	2.4	25%	6.4	69%	0.5	6%
110	8.9	3.0	34%	5.6	63%	0.3	3%
115	7.9	3.0	37%	4.8	61%	0.1	2%
120	6.6	2.7	41%	3.8	58%	0.06	1%
125	5.8	2.8	47%	3.0	52%	0.04	1%
130	5.0	2.6	53%	2.4	47%	0.01	0%
135	4.5	2.7	60%	1.8	40%	0.01	0%
140	4.1	2.5	60%	1.6	40%	0.01	0%
145	4.5	2.3	51%	2.2	48%	0.03	1%
150	5.6	2.4	43%	3.1	56%	0.07	1%
155	6.7	2.3	35%	4.2	63%	0.2	2%
160	8.1	2.2	27%	5.6	69%	0.3	4%
165	9.6	2.3	24%	6.8	71%	0.5	5%
170	10.3	2.0	19%	7.5	73%	0.8	8%
175	10.5	2.0	20%	7.7	73%	0.8	7%
180	10.7	2.2	21%	7.8	73%	0.7	6%

Table 14. Variation of $\overline{p^2}/Q_\infty^2$ with ϕ at $\alpha = 20°$, $x/L = 0.600$ showing the contribution of various frequency ranges to the $\overline{p^2}$ integral including the Analytical Integral Contribution (AIC). The values presented here were calculated by integrating the p spectra.

ϕ	Total $\overline{p^2}/Q_\infty^2$	Contribution to $\overline{p^2}/Q_\infty^2$ ($\times 10^5$)					
deg	($\times 10^5$)	$f \le 994$ Hz		994 Hz $< f \le 25$ kHz		$f > 25$ kHz (AIC)	
90	26.8	1.9	7%	11.4	43%	13.5	50%
95	24.4	1.9	8%	11.4	46%	11.1	46%
100	21.3	2.0	9%	11.1	52%	8.2	39%
105	17.9	2.0	11%	10.5	59%	5.4	30%
110	14.7	2.2	15%	9.7	66%	2.8	19%
115	11.5	2.4	20%	8.4	73%	0.7	7%
120	10.1	2.8	28%	7.1	70%	0.2	2%
125	8.2	3.3	41%	4.9	59%	0.03	0%
130	6.1	3.5	58%	2.6	42%	0.01	0%
135	5.5	3.1	57%	2.3	42%	0.07	1%
140	9.2	4.1	44%	4.7	51%	0.4	5%
145	12.3	3.9	32%	7.3	59%	1.1	9%
150	24.9	4.0	16%	9.9	40%	11.0	44%
155	45.2	4.2	9%	10.9	24%	30.1	67%
160	58.3	4.0	7%	11.8	20%	42.5	73%
165	46.8	3.2	7%	11.9	25%	31.7	68%
170	38.0	2.7	7%	12.0	32%	23.3	61%
175	30.5	2.0	7%	11.1	36%	17.4	57%
180	27.1	2.1	8%	10.8	40%	14.2	52%

Table 15. Variation of $\overline{p^2}/Q_\infty^2$ with ϕ at $\alpha = 20°$, $x/L = 0.772$ showing the contribution of various frequency ranges to the $\overline{p^2}$ integral including the Analytical Integral Contribution (AIC). The values presented here were calculated by integrating the p spectra.

ϕ	Total $\overline{p^2}/Q_\infty^2$	Contribution to $\overline{p^2}/Q_\infty^2$ ($\times 10^5$)					
deg	($\times 10^5$)	$f \le 994$ Hz		994 Hz $< f \le$ 23 kHz		$f >$ 23 kHz (AIC)	
90	22.4	3.1	14%	11.2	50%	8.1	36%
95	18.7	3.3	18%	10.8	58%	4.6	24%
100	15.6	3.8	24%	10.0	65%	1.8	11%
105	12.9	4.1	32%	8.3	64%	0.5	4%
110	10.5	4.5	43%	5.9	56%	0.07	1%
115	8.2	5.4	66%	2.8	34%	0.006	0%
120	9.9	6.1	62%	3.7	37%	0.08	1%
125	14.9	6.6	45%	7.2	48%	1.1	7%
130	27.4	9.6	35%	13.7	50%	4.1	15%
135	44.9	22.0	49%	17.2	38%	5.7	13%
140	18.2	9.0	50%	6.8	37%	2.4	13%
145	23.9	10.0	42%	13.3	55%	0.6	3%
150	35.8	18.3	51%	11.7	33%	5.8	16%
155	59.5	8.0	14%	10.2	17%	41.3	69%
160	66.8	4.4	7%	11.0	16%	51.4	77%
165	54.9	2.7	5%	11.0	20%	41.2	75%
170	47.5	2.6	6%	10.5	22%	34.4	72%
175	40.2	2.3	6%	10.6	26%	27.3	68%
180	34.7	2.4	7%	10.1	29%	22.2	64%

FIGURES

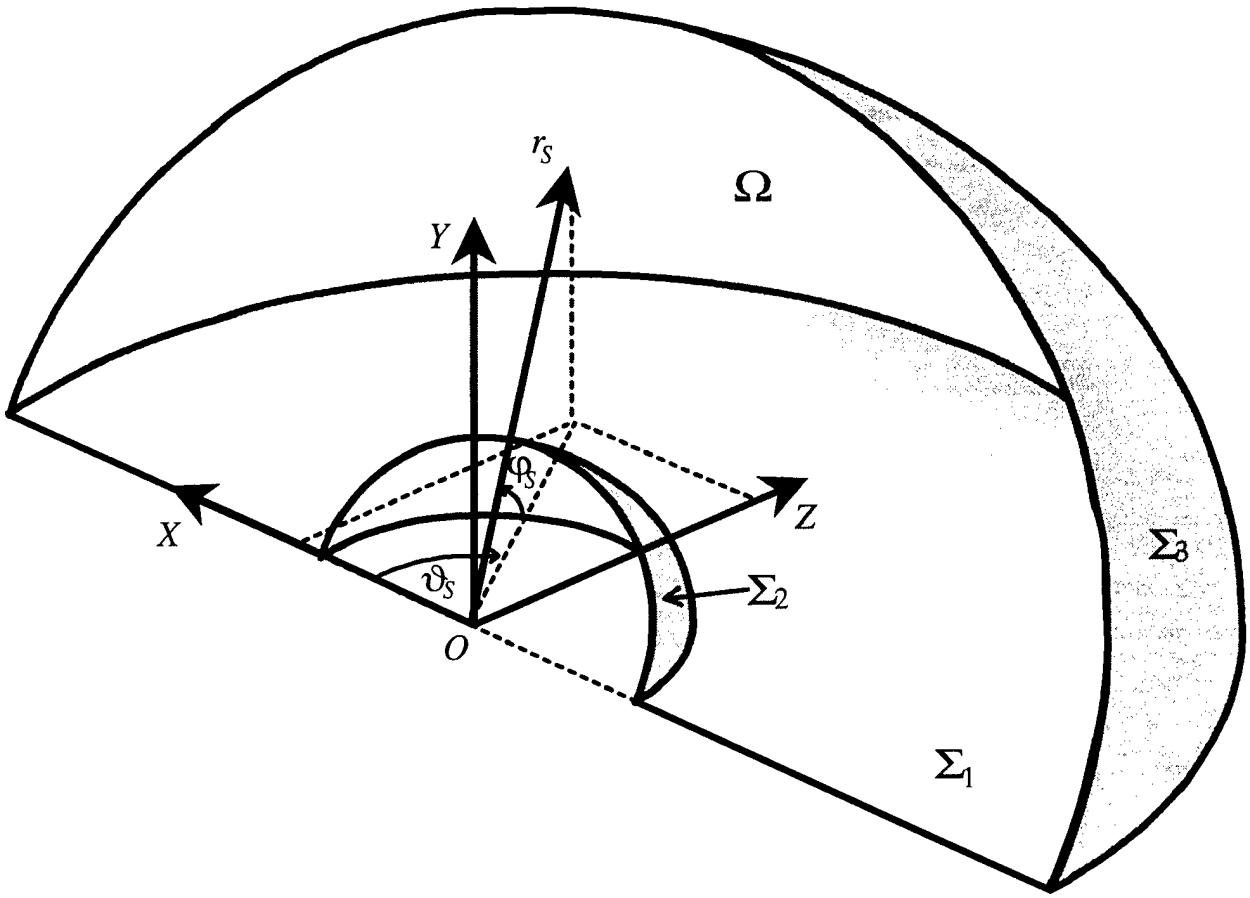

Figure 1. Sketch showing the nomenclature and coordinate system used to integrate the Poisson differential equation that relates pressure fluctuations to velocity fluctuations.

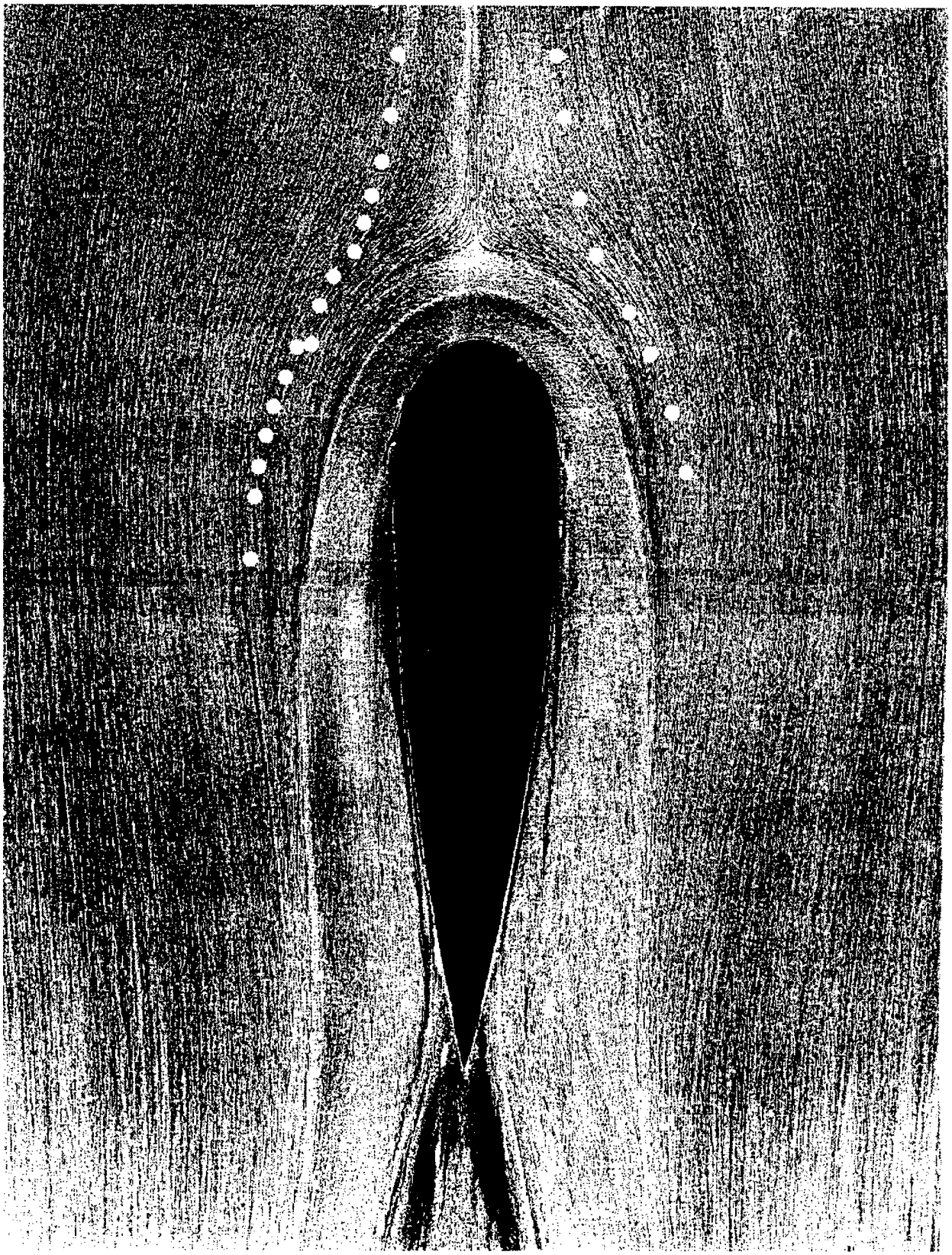

Figure 2. Oil flow visualization of the flow near the test wall. The nominal free stream velocity is 27.5 m/s ($Re_\theta = 5940$). The white dots on the right of the wing show measurement locations 0-7 (starting from the top of the figure). Figure 2 of Ölçmen and Simpson (1995a).

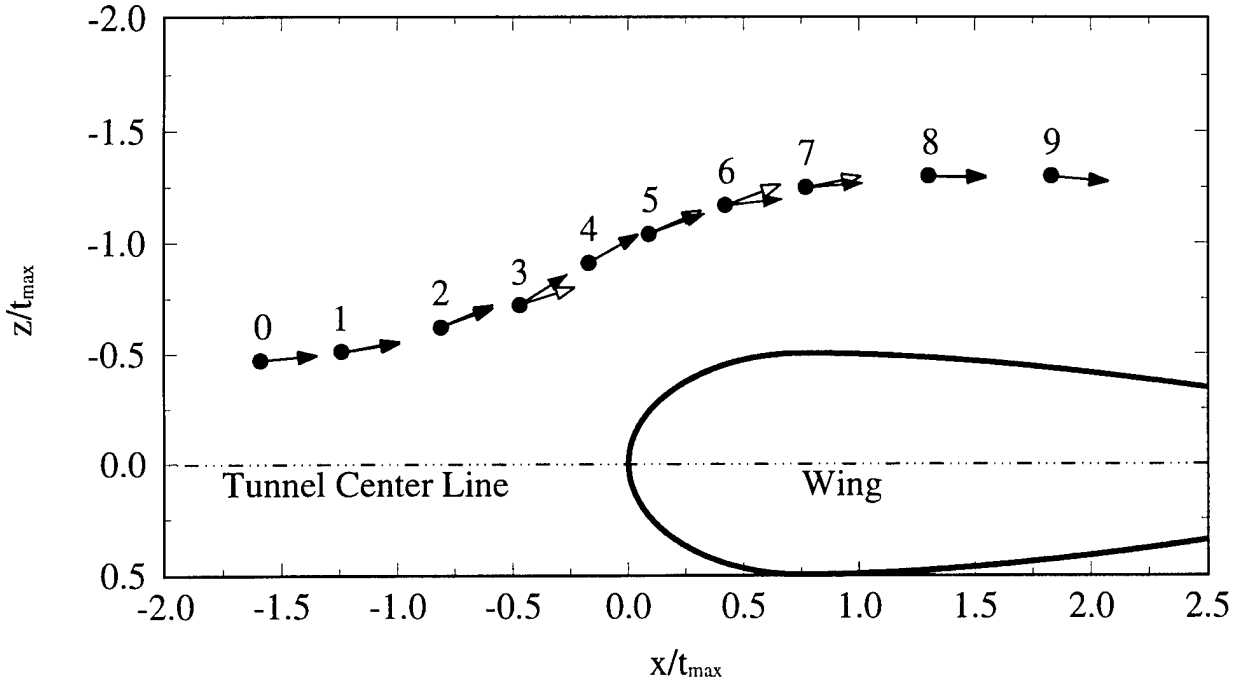

Figure 3. Wing shape and measurement stations. Full arrows show the wall-shear-stress direction in the $Re_\theta = 5940$ flow (β_W in table 4). The empty arrows show the free-stream direction in the $Re_\theta = 5940$ flow (β_{FS} in table 4). The y coordinate is normal to the paper, pointing out, forming a right-handed coordinate system.

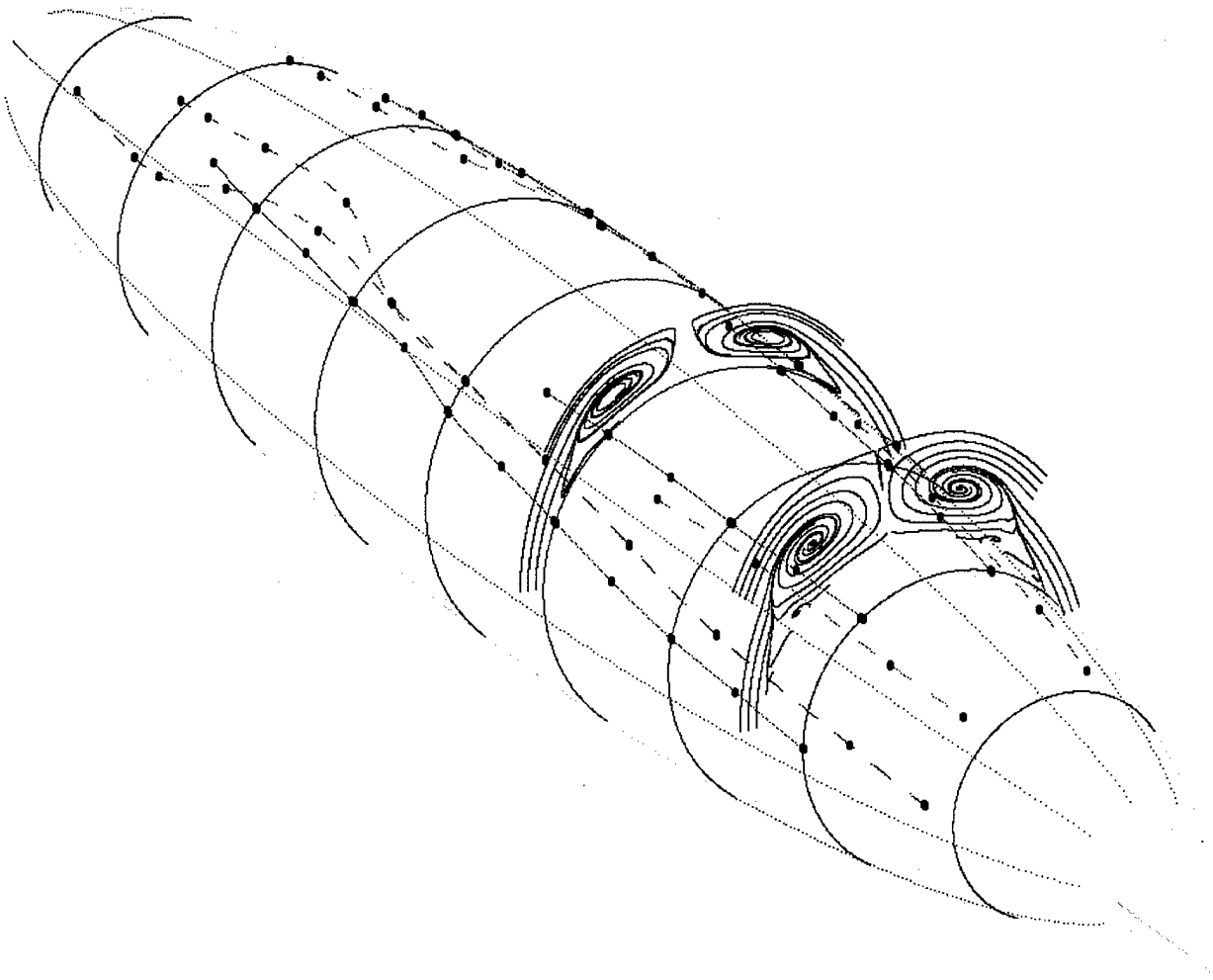

Figure 4. Mean secondary flow about a 6:1 prolate spheroid at $\alpha = 20°$, $x/L = 0.600$ and $x/L = 0.772$. Solid lines on the model surface denote separation lines as indicated by oil-flow visualization. Dashed lines denote the locus of minima in skin friction magnitude. Figure 1 of Wetzel *et al.* (1998).

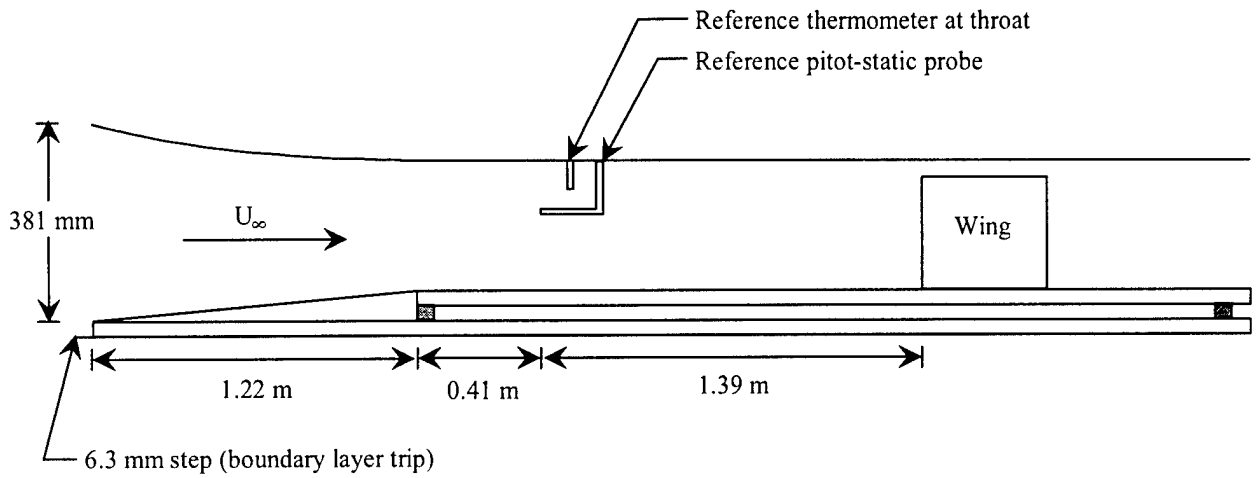

Figure 5. Sketch of the Virginia Tech Boundary Layer Wind Tunnel. The wing position shown here corresponds to the $Re_\theta = 5940$ flow.

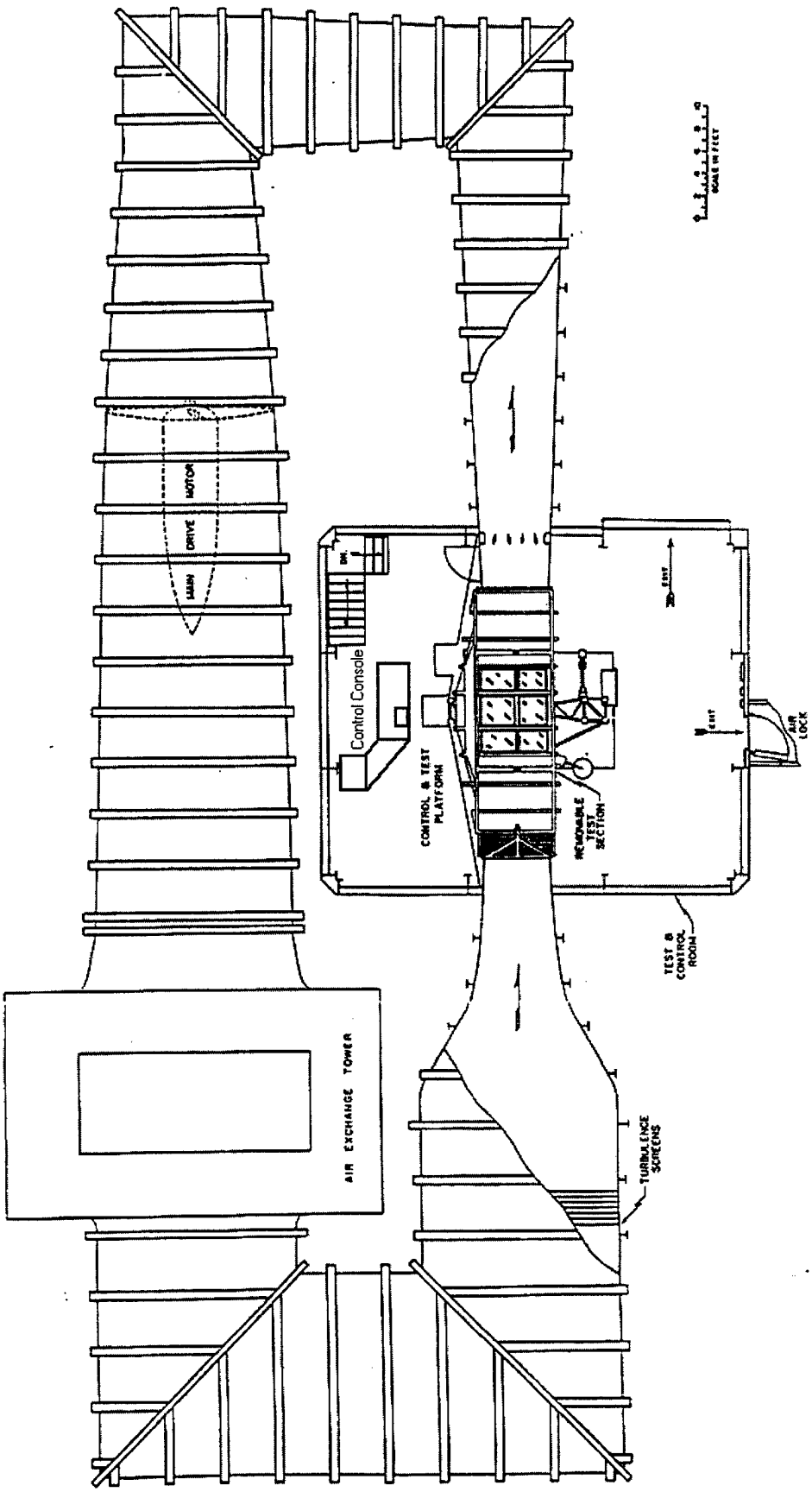

Figure 6. Schematic of the Virginia Tech Stability Wind Tunnel.

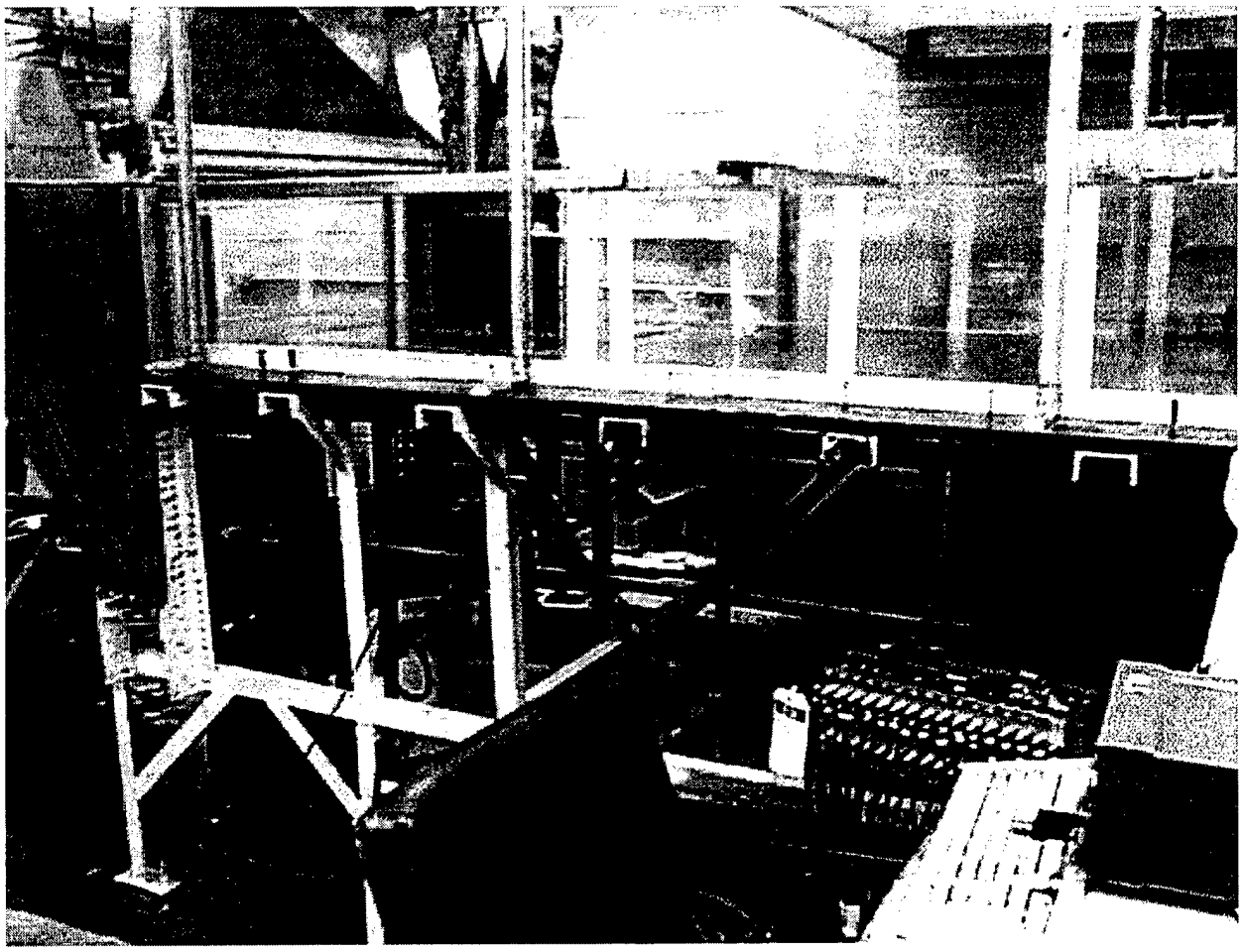

Figure 7. The test section of the Virginia Tech Boundary Layer Wind Tunnel configured for the $Re_\theta = 5940$, wing-body junction flow.

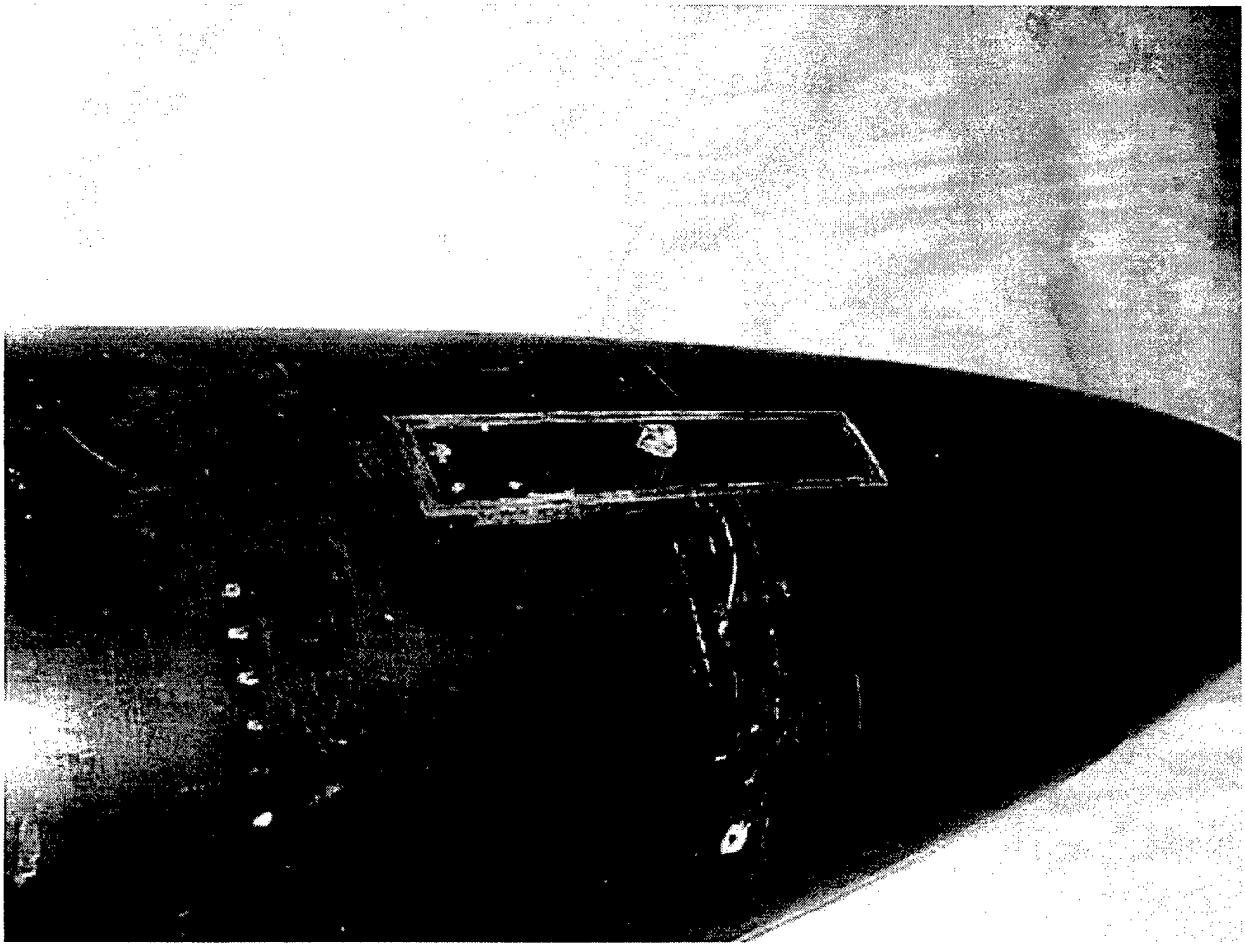

Figure 8. The window that is molded to the curvature of the 6:1 prolate spheroid model at $x/L = 0.600$. The window provides optical access to the flow field for the LDV laser beams.

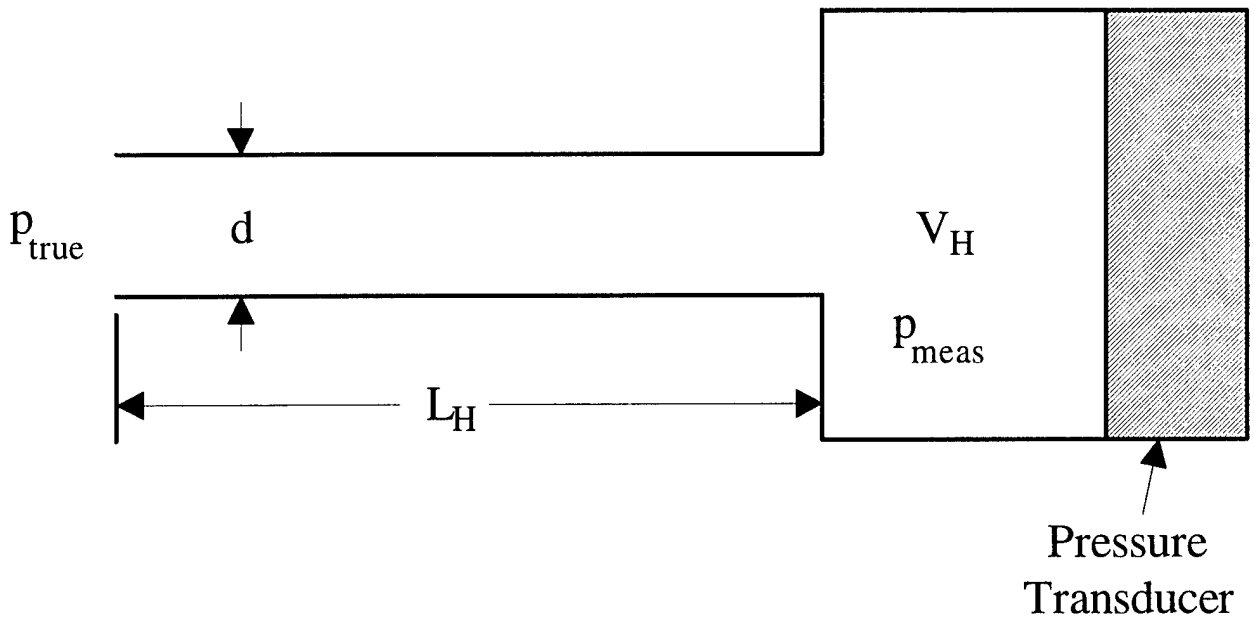

Figure 9. Sketch of an ideal Helmholtz resonator.

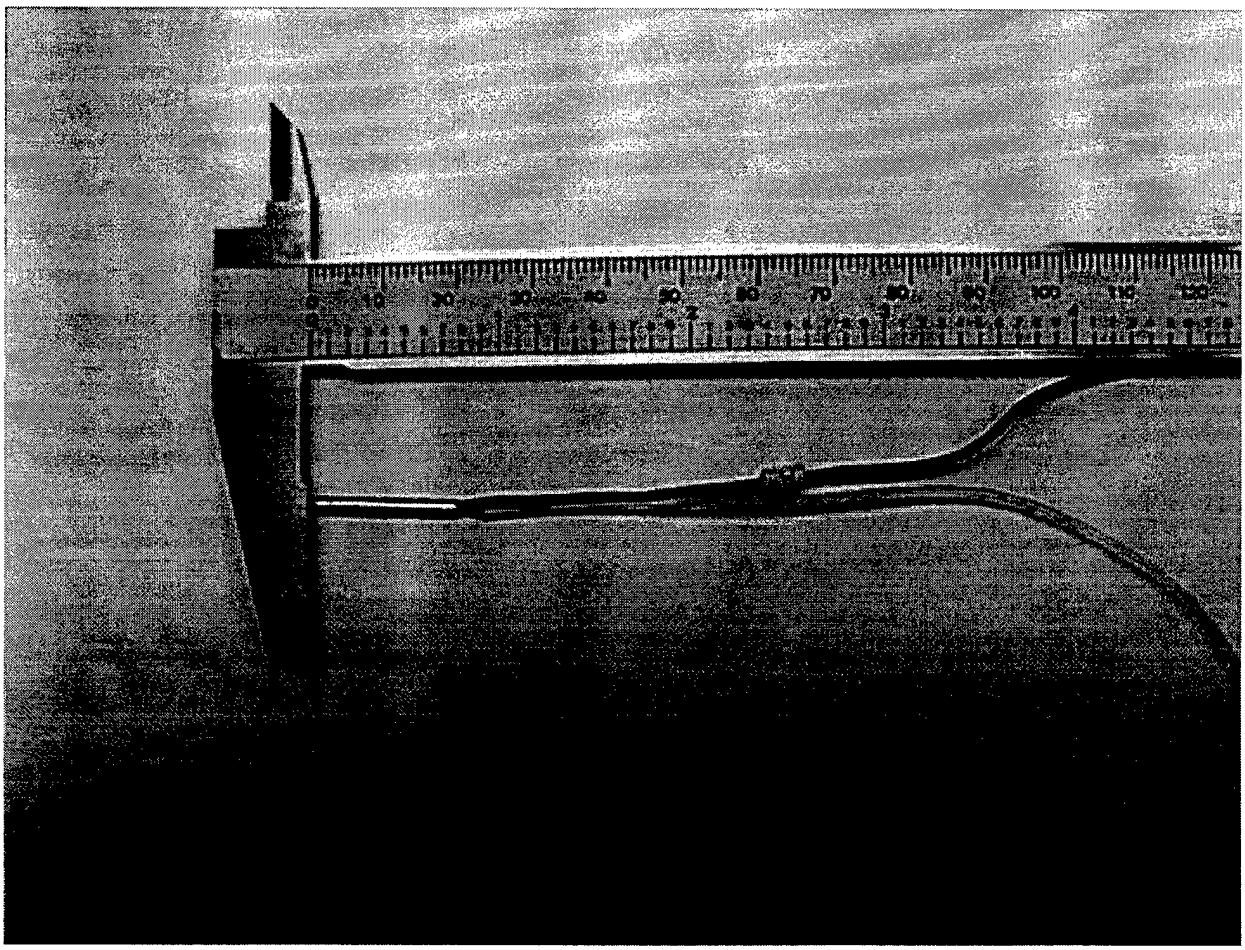

Figure 10. The Endevco model 8507-C2 pressure transducer.

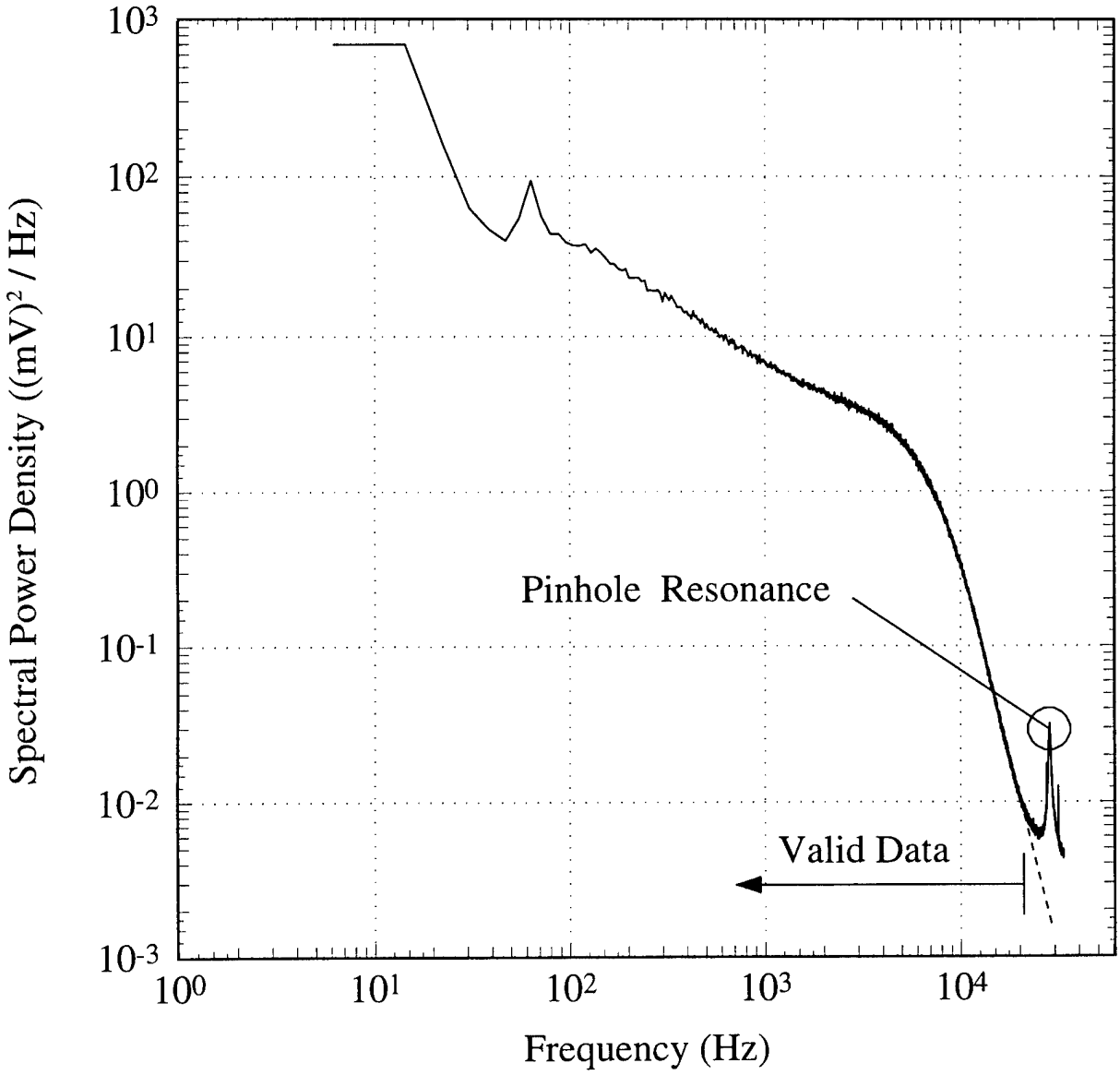

Figure 11. The spectral power density of the uncalibrated pressure transducer signal measured beneath a two-dimensional boundary layer ($Re_\theta = 23400$). The dashed line shows a power law decay with a constant exponent.

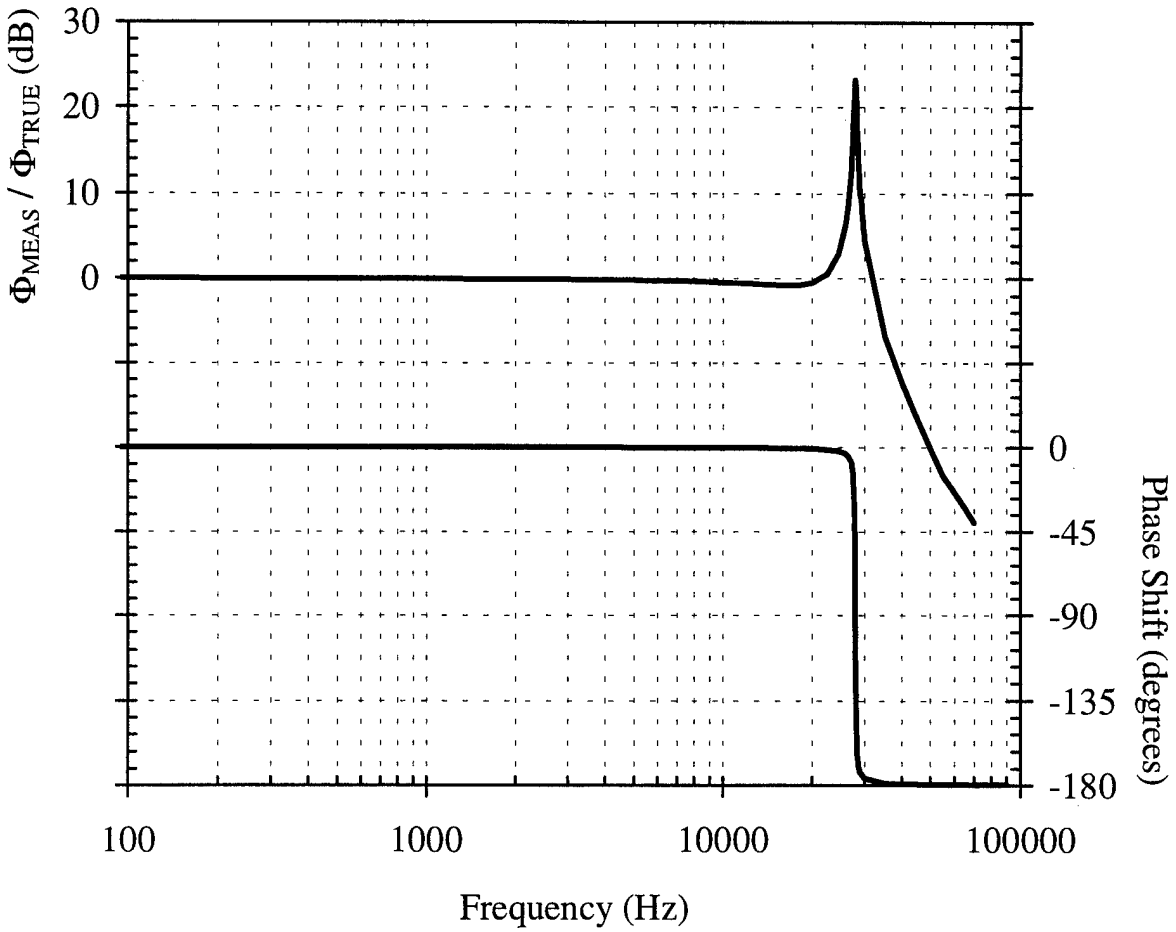

Figure 12. The amplitude and phase response of the pinhole mask that was used in conjunction with the p measurements in the two-dimensional and wing-body junction flows. The amplitude response shown is that of a Helmholtz resonator (equation 35) that is attenuated at high frequencies using the values given by Corcos (1963), assuming $U_C = 14u_\tau$, in order to account for finite pinhole size. The phase response shown is that of a Helmholtz resonator (equation 36).

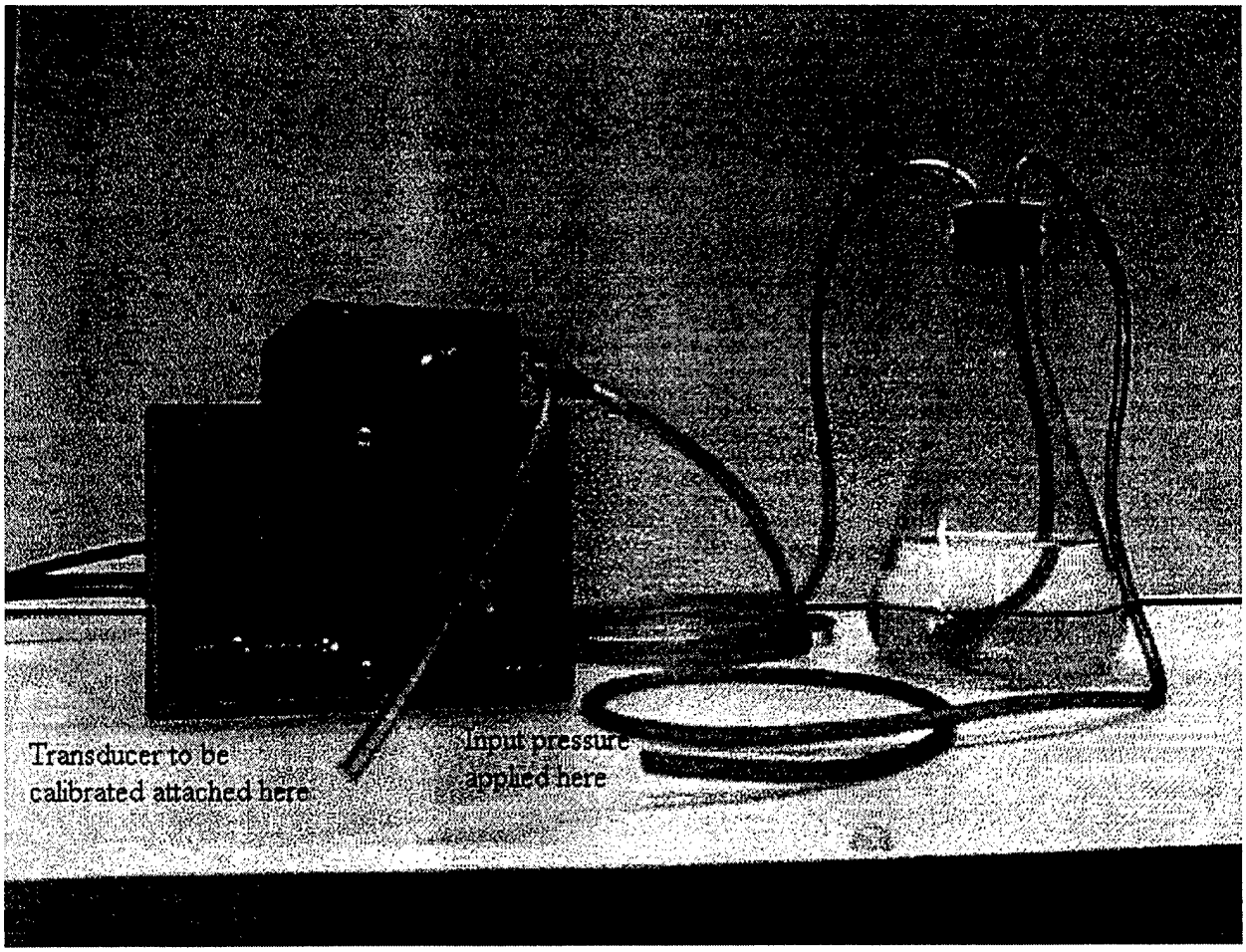

Figure 13. The beaker-tubing arrangement that was used to perform the static calibration of the Endevco pressure transducer.

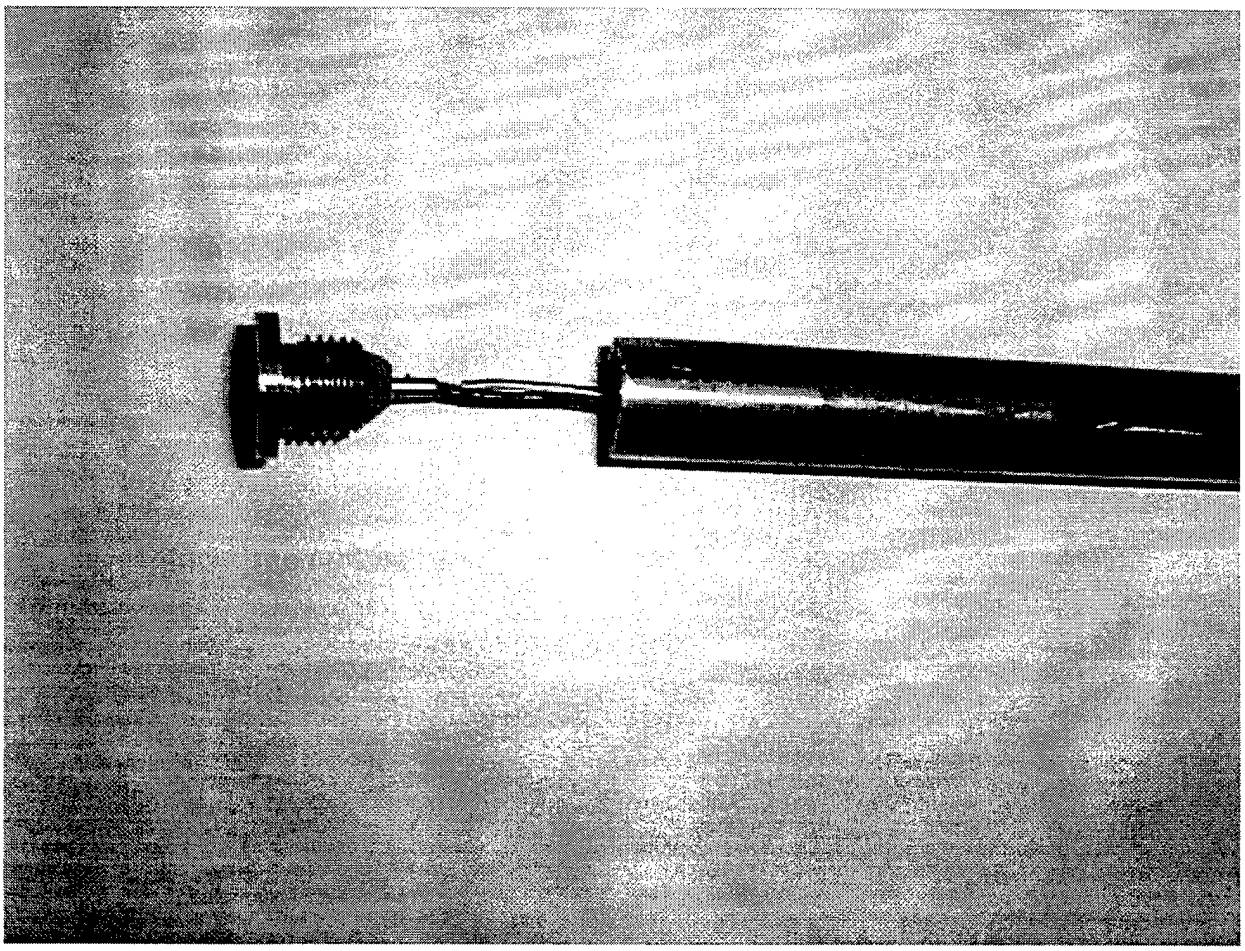

Figure 14. The pressure transducer housing unit used to measure p beneath the two-dimensional boundary layer and wing-body junction flow. The pressure transducer is held inside the cap (left) with clay. The outer diameter of the shaft of the housing unit is 0.537 inches.

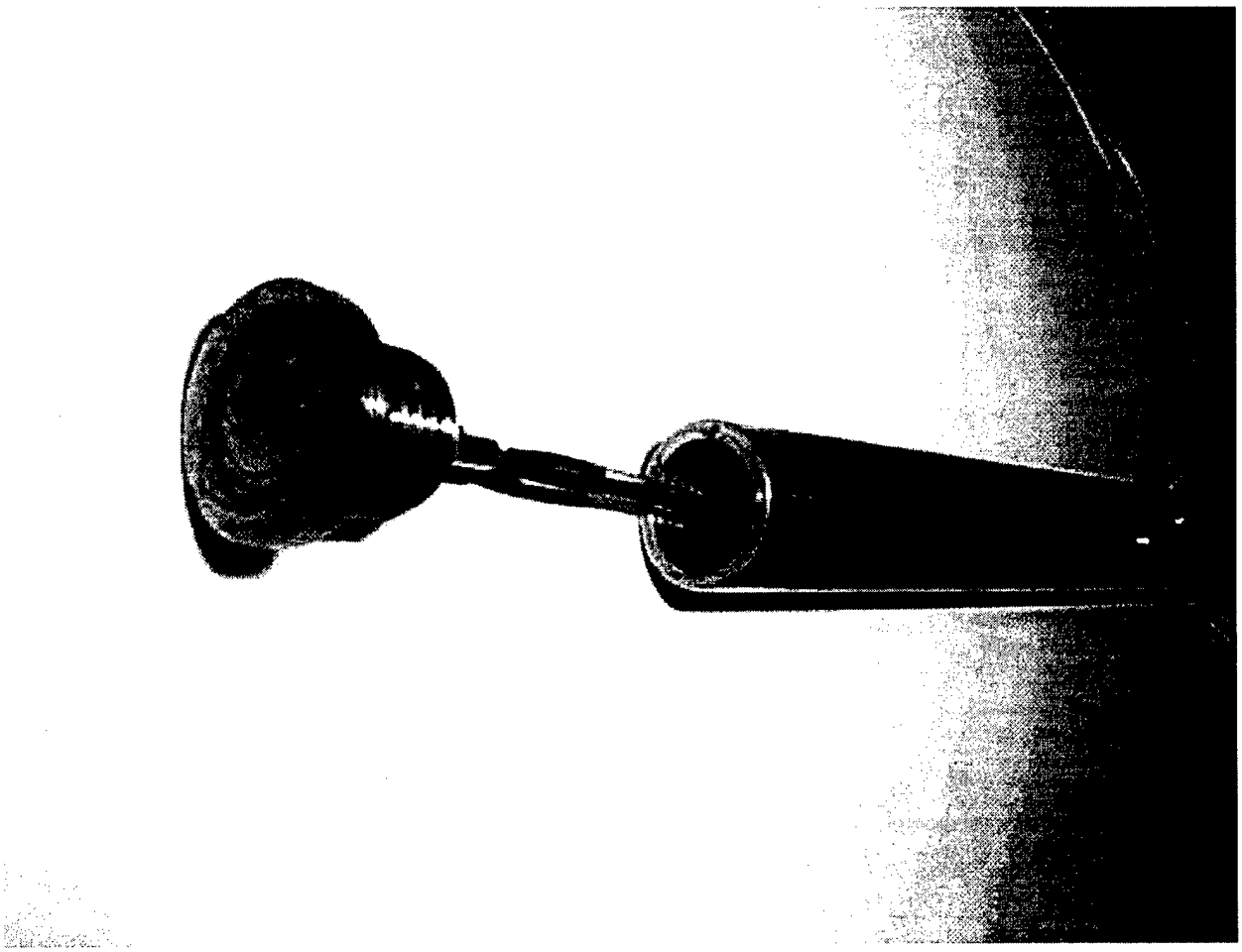

Figure 15. Close-up view of the pressure transducer housing unit in figure 14 showing details of the 0.5 mm pinhole mask.

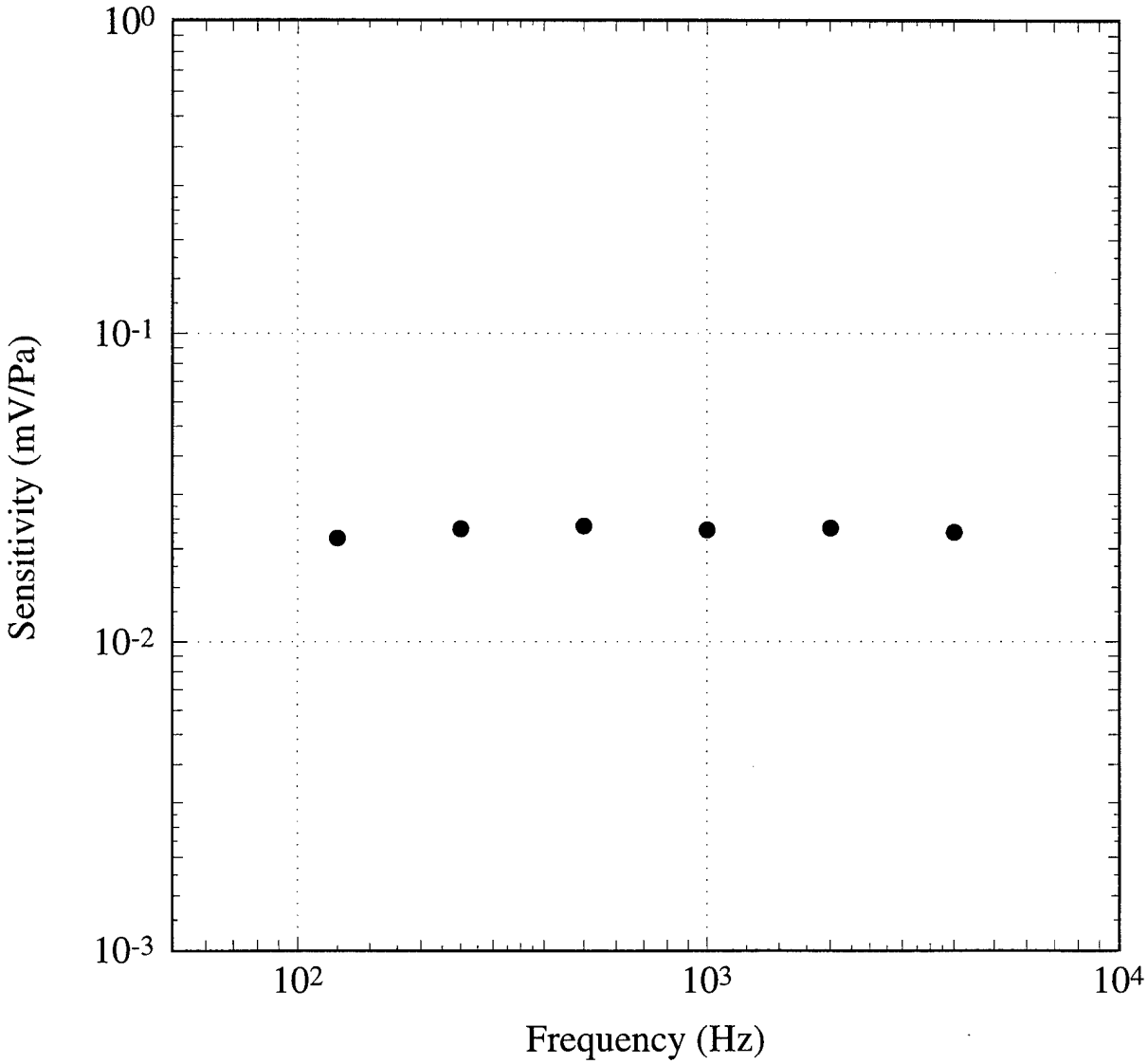

Figure 16. The frequency response of the Endevco 8507-C2 pressure transducer as measured by a GenRad model 1986 Omnical Sound Level Calibrator.

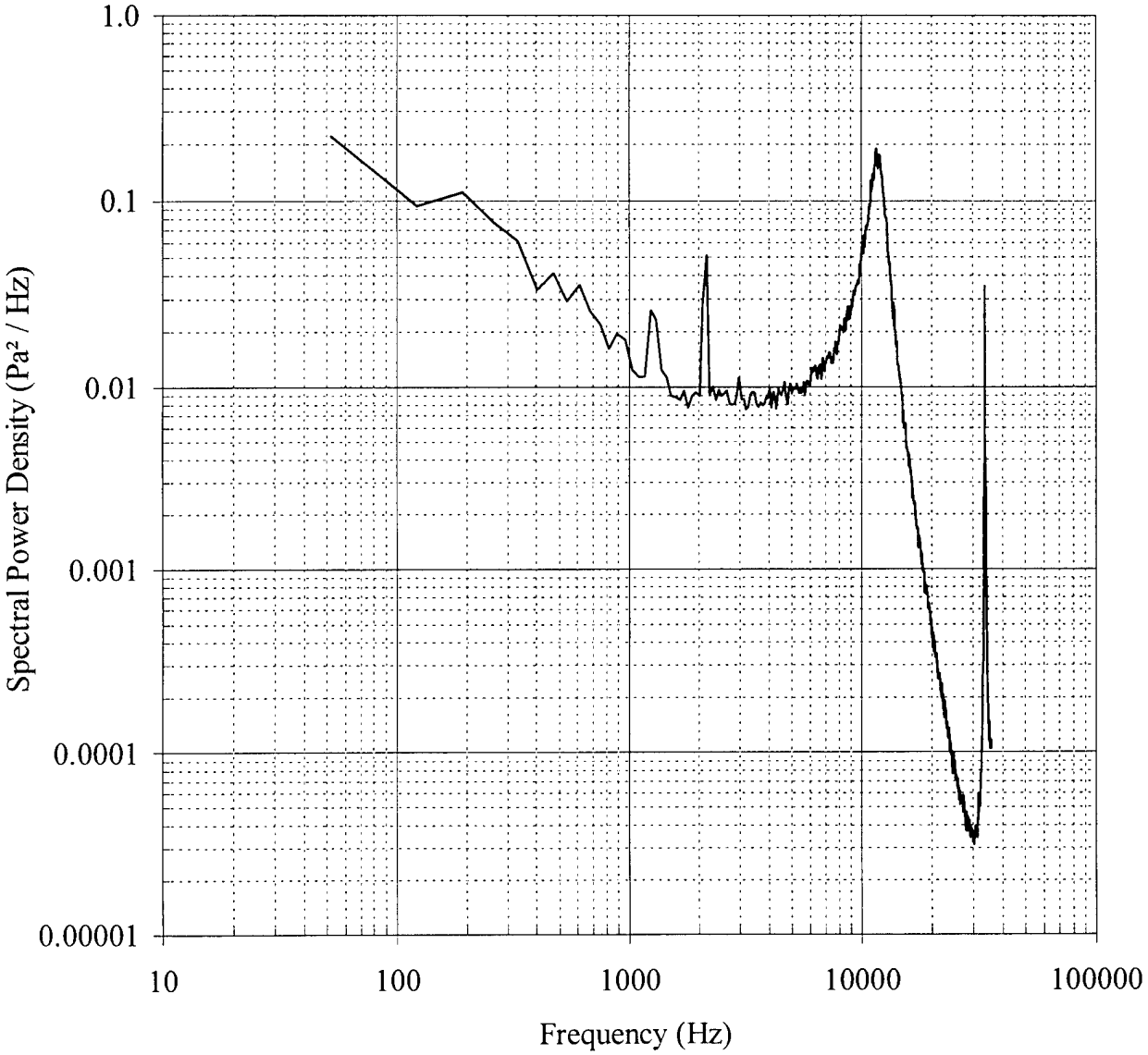

Figure 17. The spectral power density of the pressure transducer signal measured at $x/L = 0.772$, $\phi = 150°$ on a 6:1 prolate spheroid at $\alpha = 10°$ with only the static calibration applied.

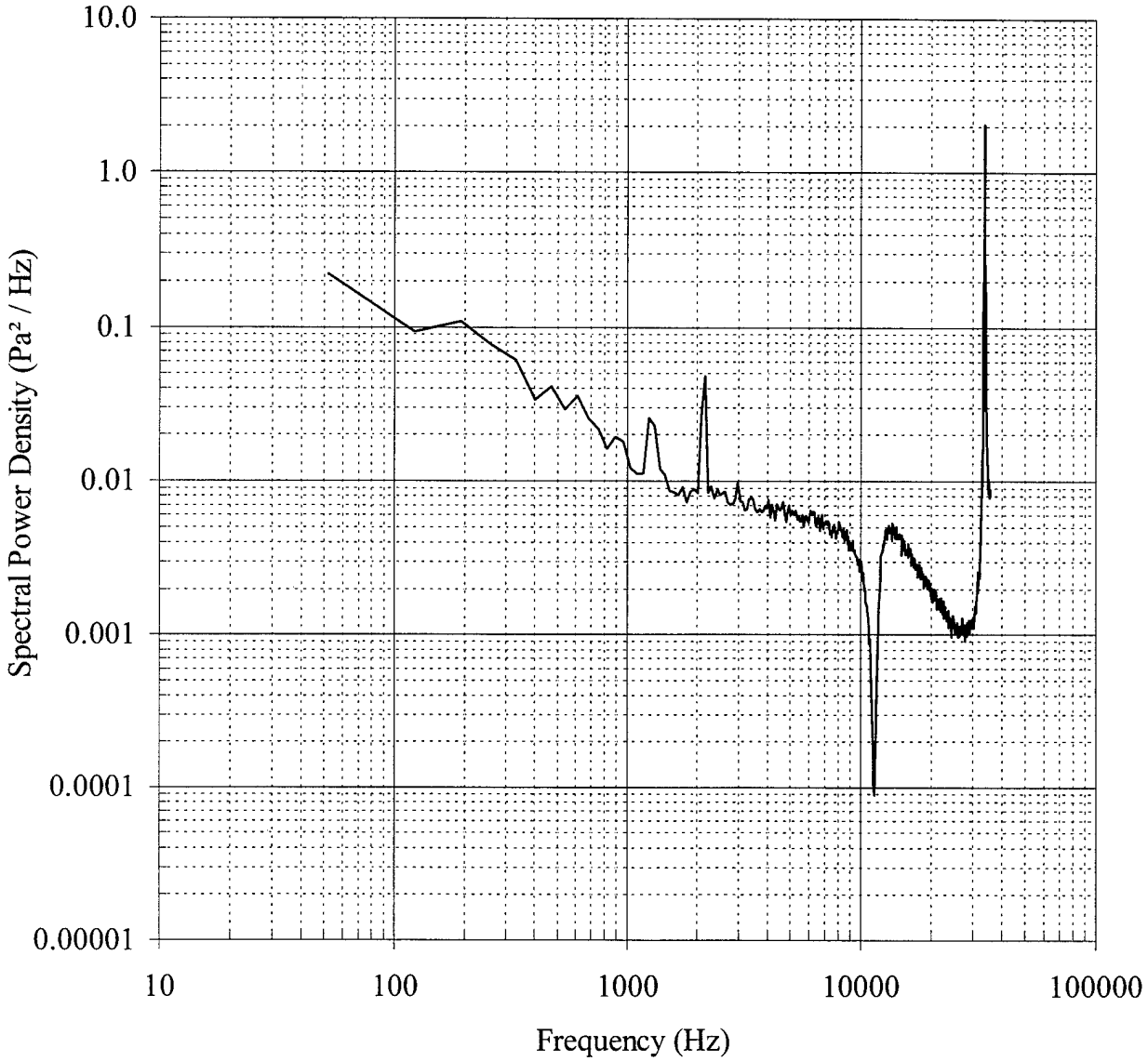

Figure 18. The spectral power density of the pressure transducer signal measured at $x/L = 0.772$, $\phi = 150°$ on a 6:1 prolate spheroid at $\alpha = 10°$ with the static calibration and the Helmholtz resonator theoretical correction applied.

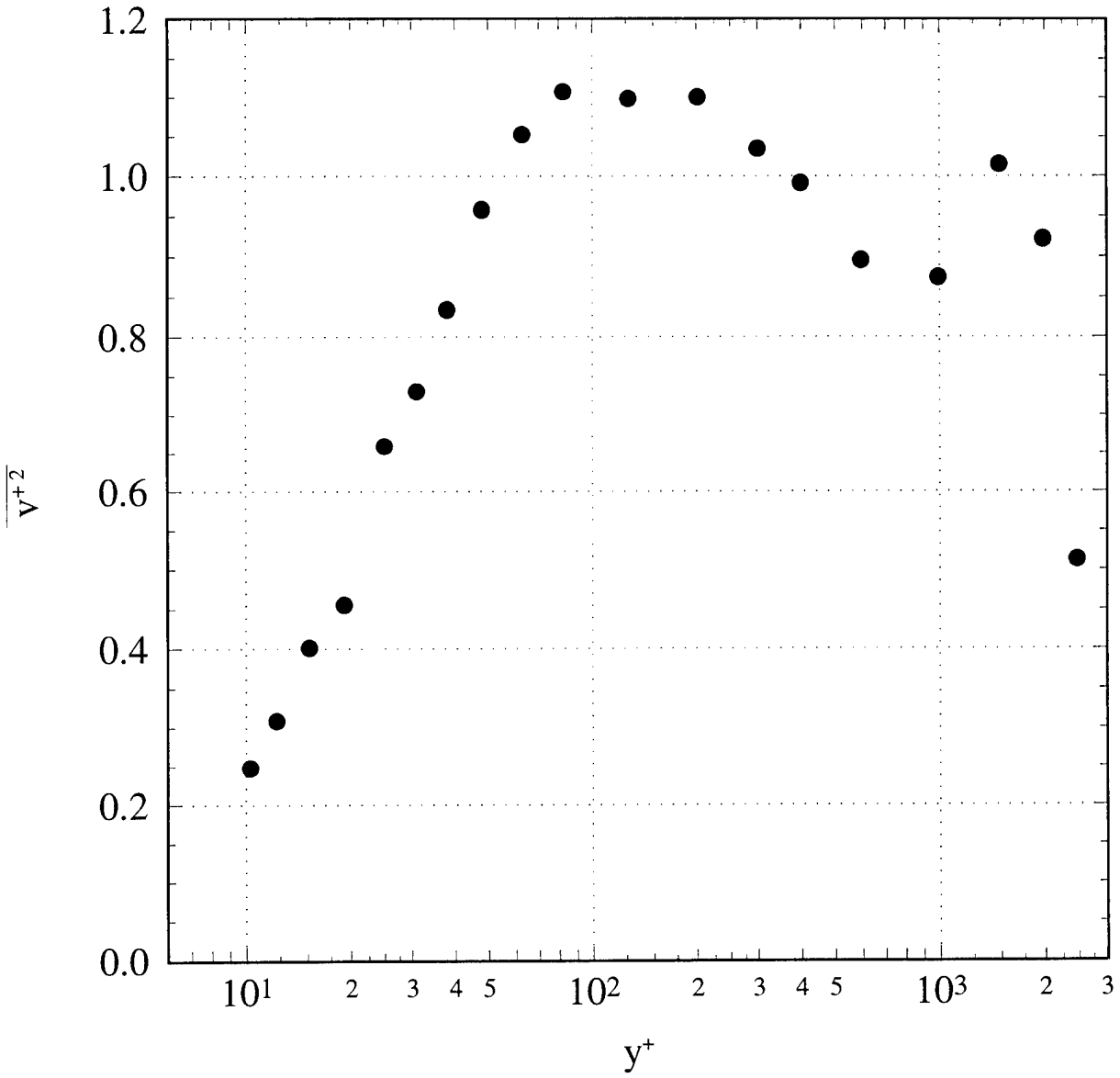

Figure 19. Profile of the $\overline{v'^2}/u_\tau^2$ Reynolds normal stress in body-surface coordinates at $x/L = 0.772$, $\phi = 150°$ on a 6:1 prolate spheroid at $\alpha = 10°$. Data of Chesnakas and Simpson (1997).

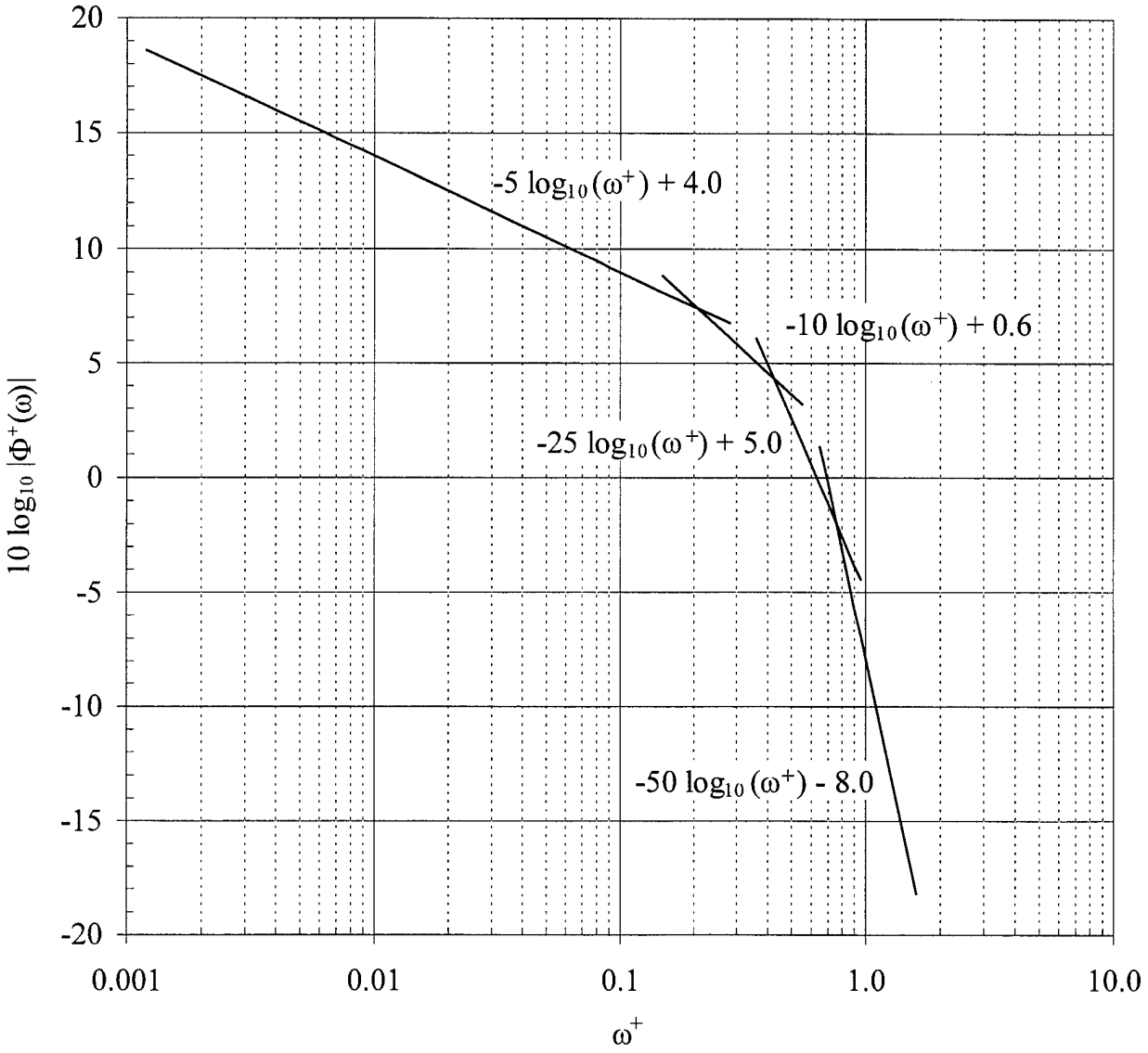

Figure 20. Curves fit to the *p* spectrum beneath a two-dimensional boundary layer with favorable pressure gradient normalized using viscous scales. These curves fit the data of McGrath and Simpson (1987).

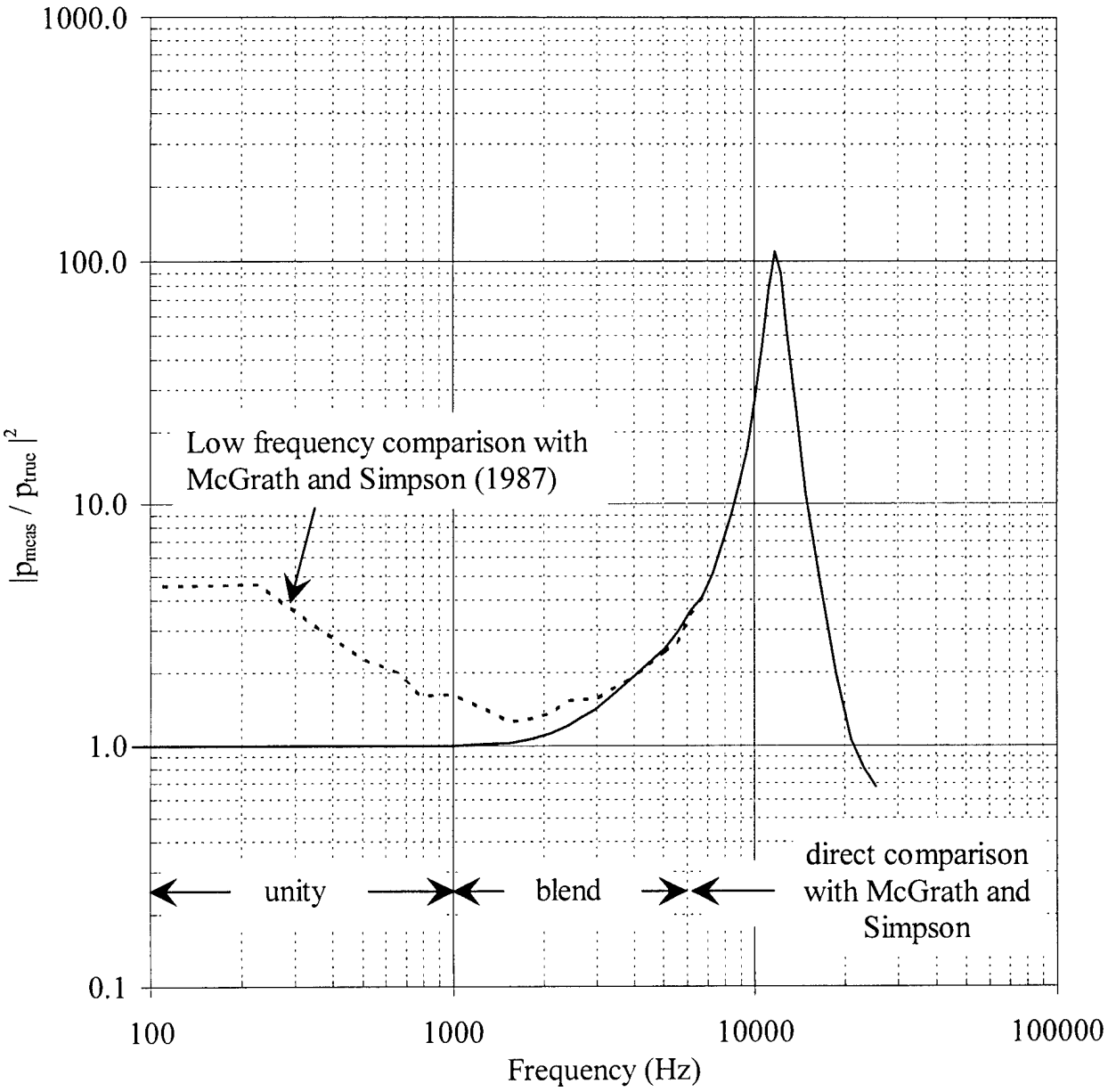

Figure 21. Construction of the approximate transfer function for the Endevco pressure transducer mounted at $x/L = 0.772$, $\phi = 150°$ on a 6:1 prolate spheroid at $\alpha = 10°$.

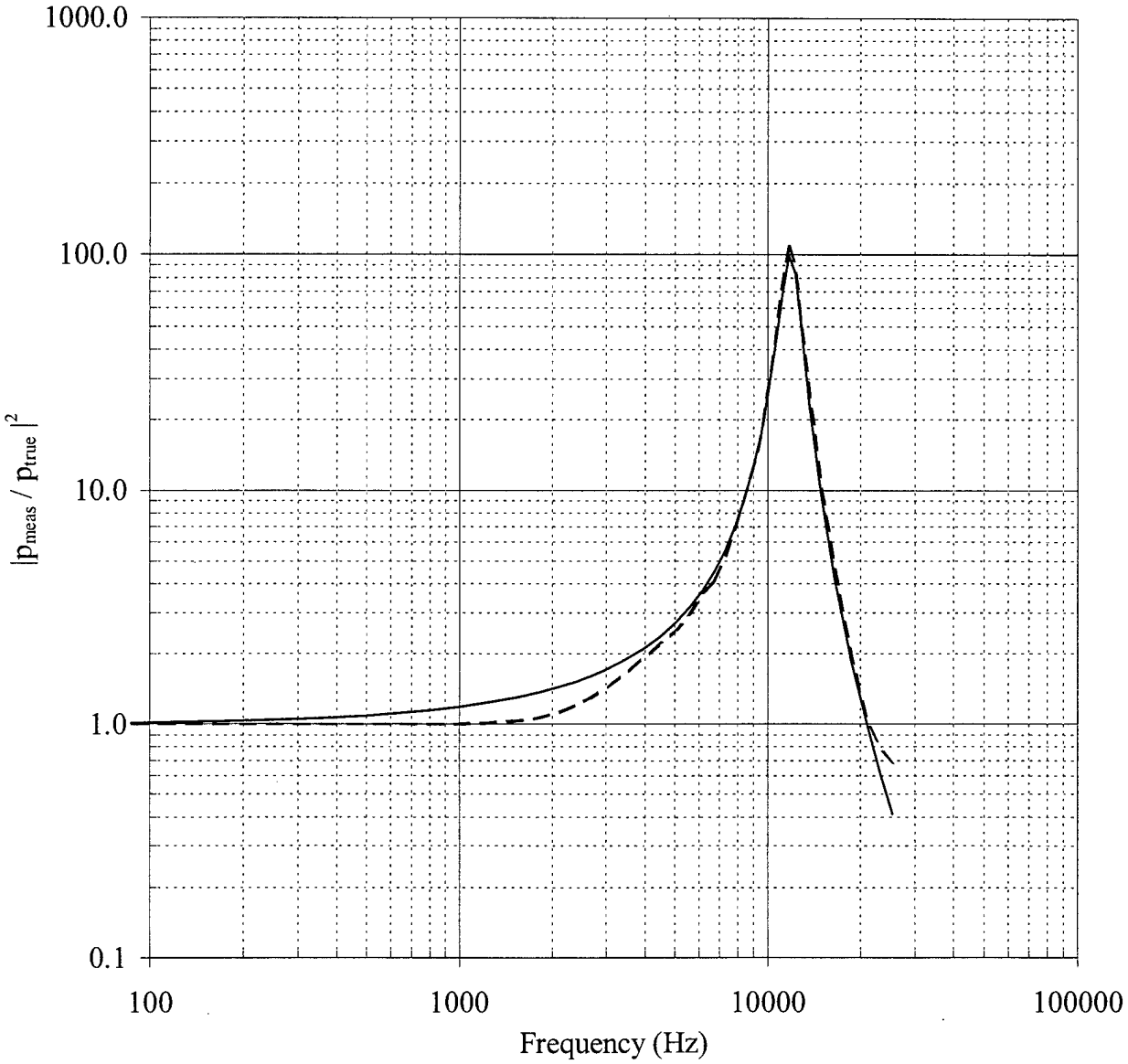

Figure 22. The transfer function used for the p spectrum at $\alpha = 10°$, $x/L = 0.772$, $\phi = 150°$ (solid line, equation 43) and the approximate transfer function shown in figure 21 (dashed line).

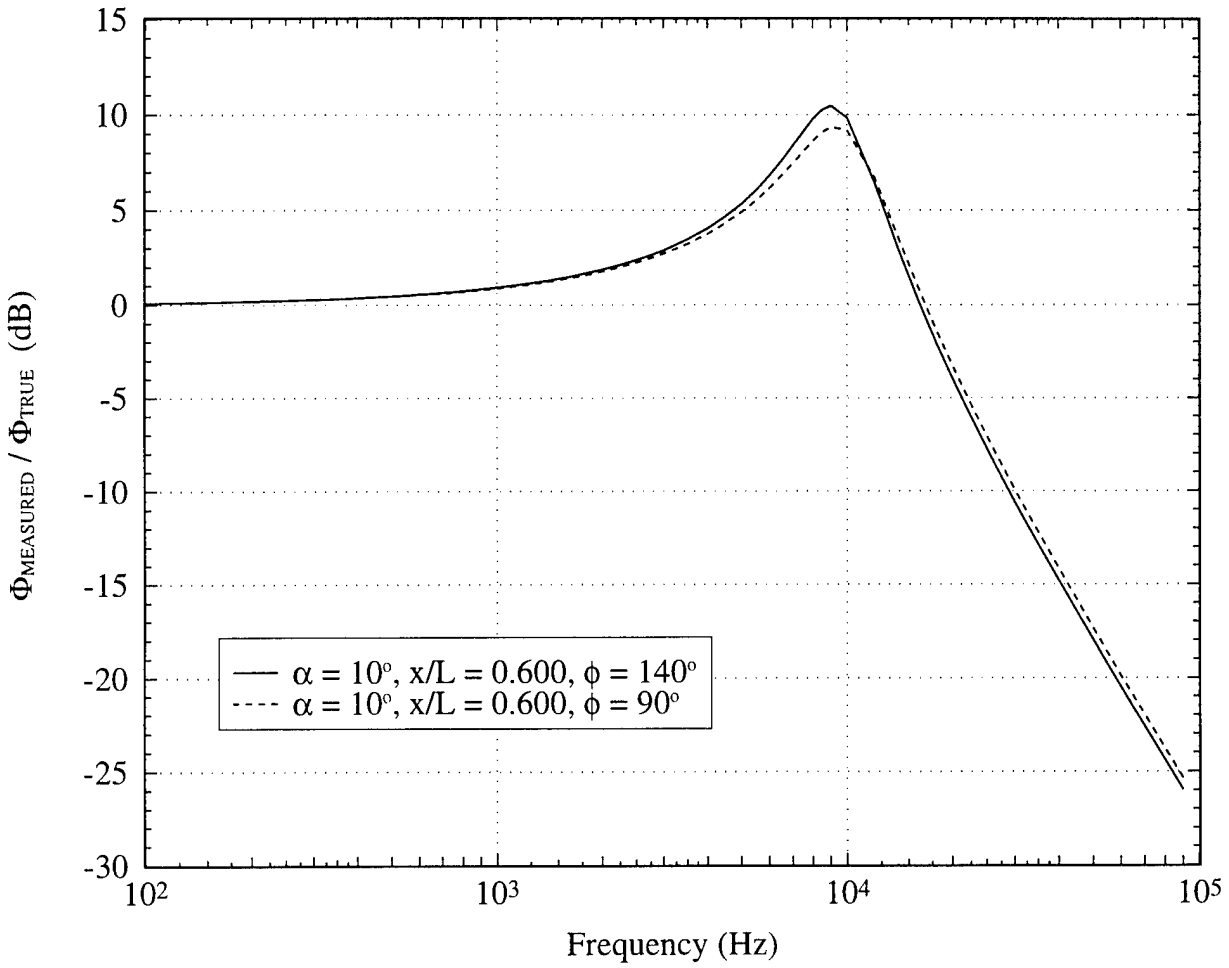

Figure 23. Representative transfer functions that bound the transfer functions that were used for the *p* data at *x/L* = 0.600.

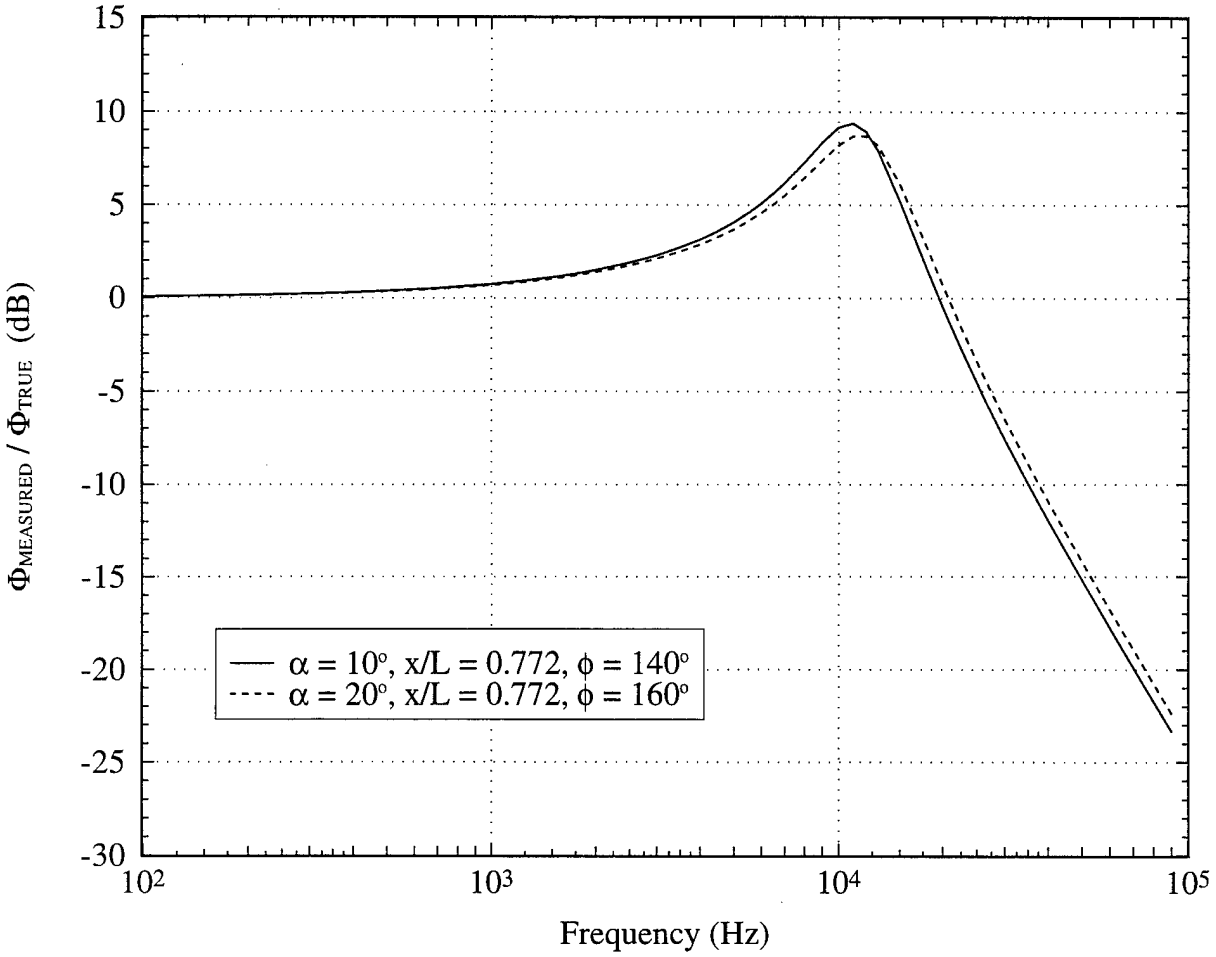

Figure 24. Representative transfer functions that bound the transfer functions that were used for the *p* data at *x/L* = 0.772.

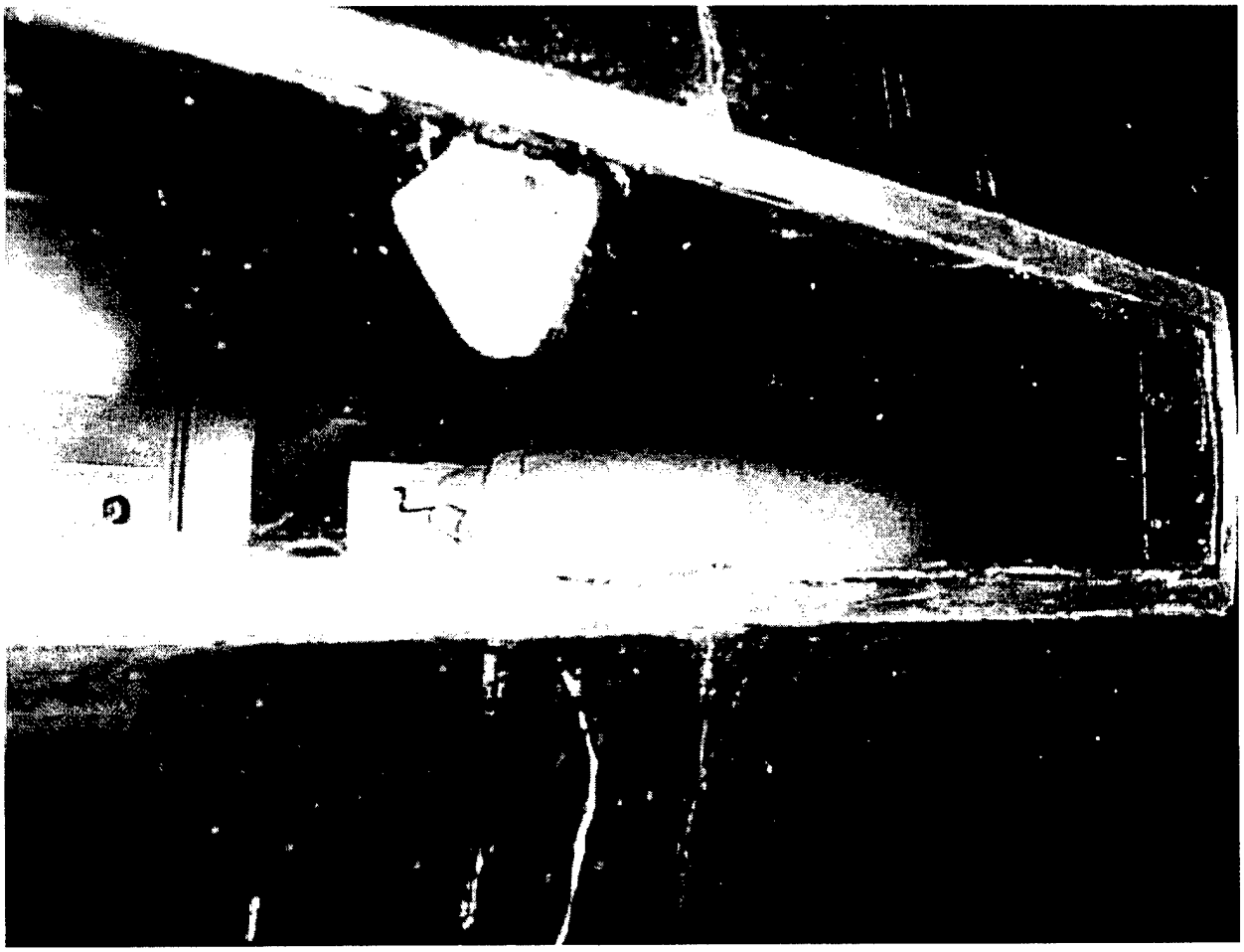

Figure 25. The window that is molded to the curvature of the 6:1 prolate spheroid model at $x/L = 0.600$. The window provides optical access to the flow field for the LDV laser beams. This view shows detail of the pressure transducer mount.

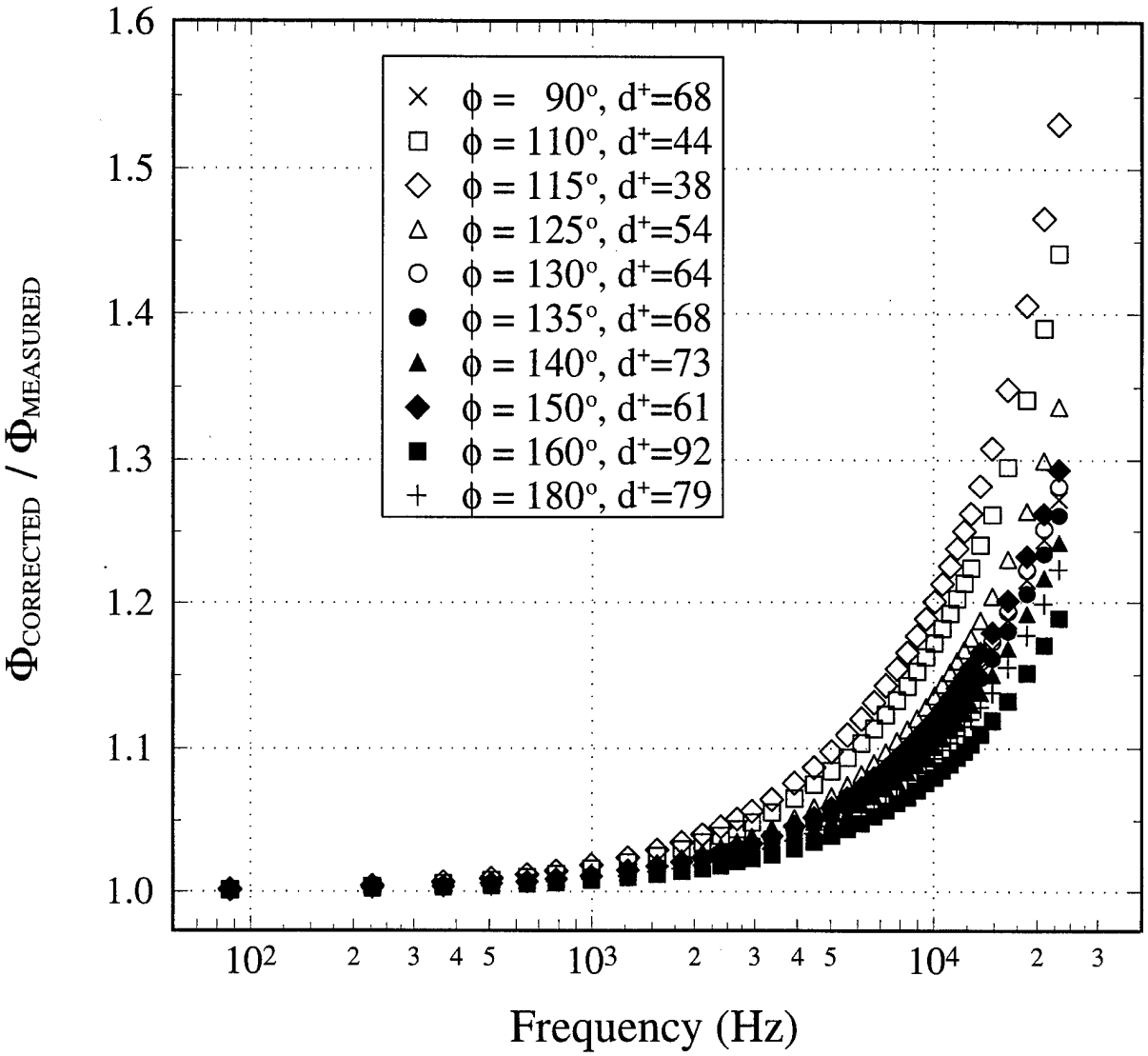

Figure 26. The Corcos (1963) correction applied to the *p* spectra measured on a 6:1 prolate spheroid at $\alpha = 20°$, $x/L = 0.772$.

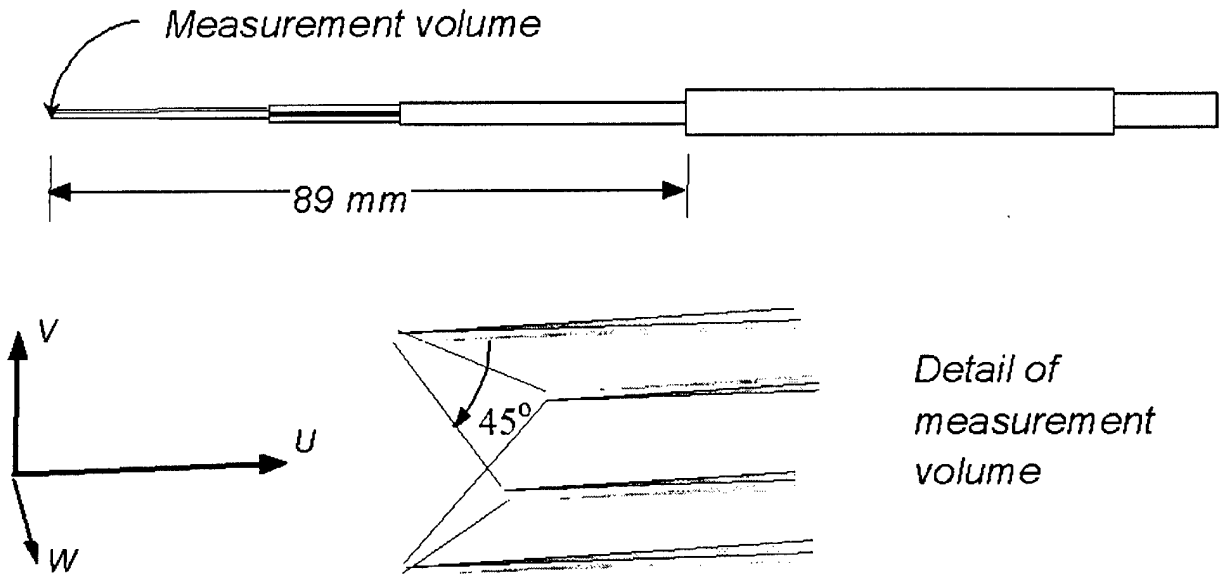

Figure 27. The Auspex Corporation model AVOP-4-100 miniature, four-sensor, hot-wire probe.

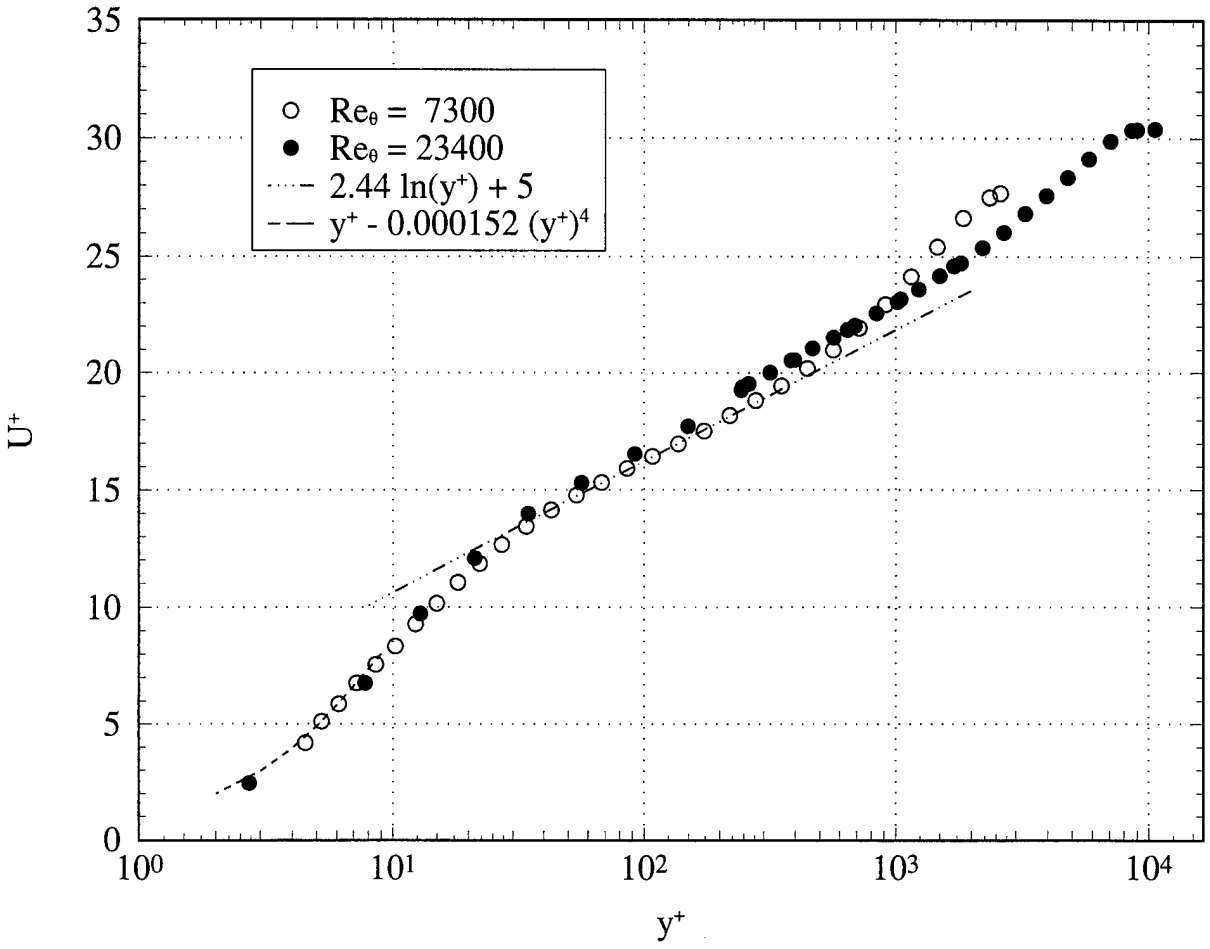

Figure 28. U^+ mean velocity profiles along with the wall laws used to calculate the shear stress at the wall. The empty symbols denote quantities measured by Ölçmen and Simpson (1996) in the $Re_\theta = 7300$ flow. The solid symbols denote quantities measured by Ölçmen *et al.* (1998) in the $Re_\theta = 23400$ flow.

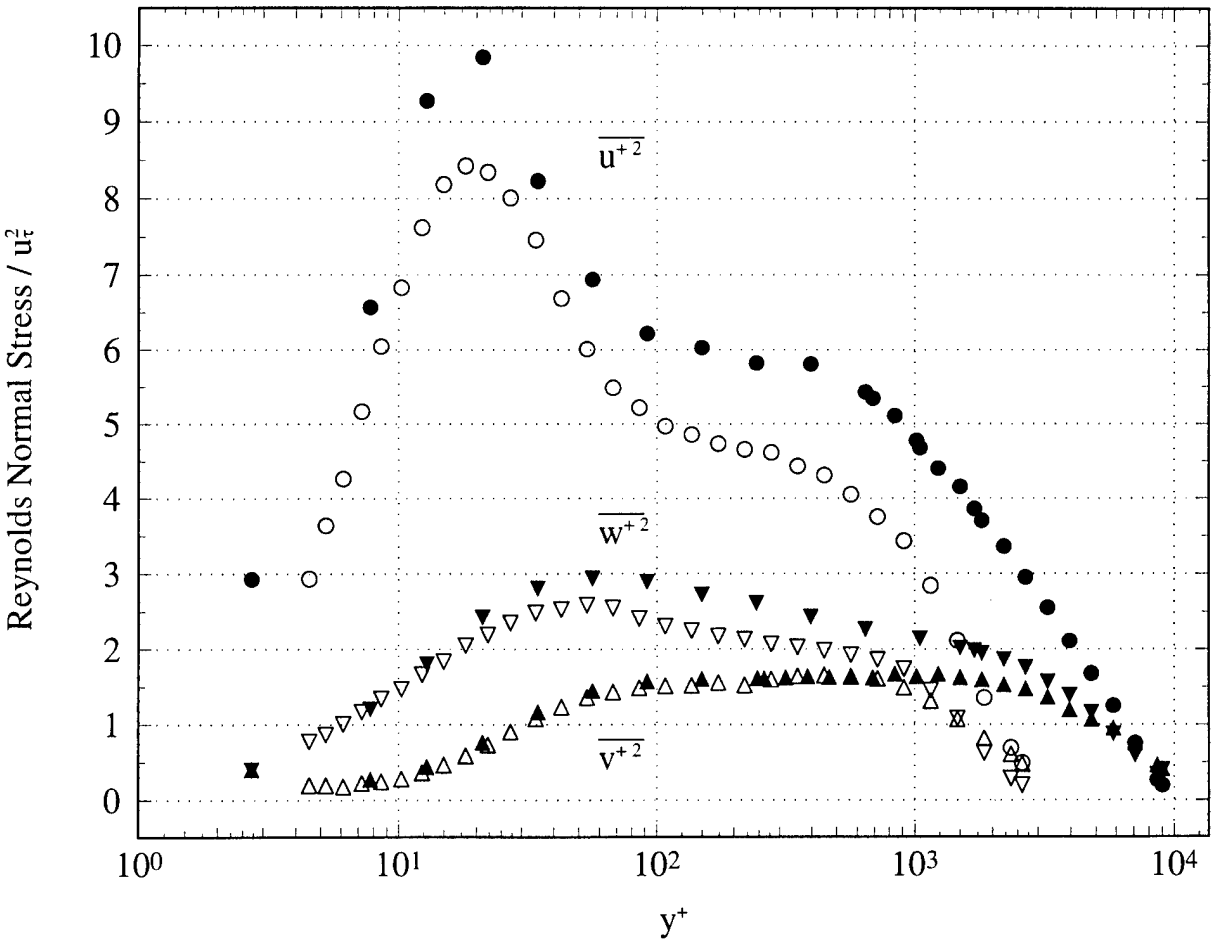

Figure 29. The Reynolds normal stress profiles. The empty symbols denote quantities measured by Ölçmen and Simpson (1996) in the $Re_\theta = 7300$ flow. The solid symbols denote quantities measured by Ölçmen *et al.* (1998) in the $Re_\theta = 23400$ flow.

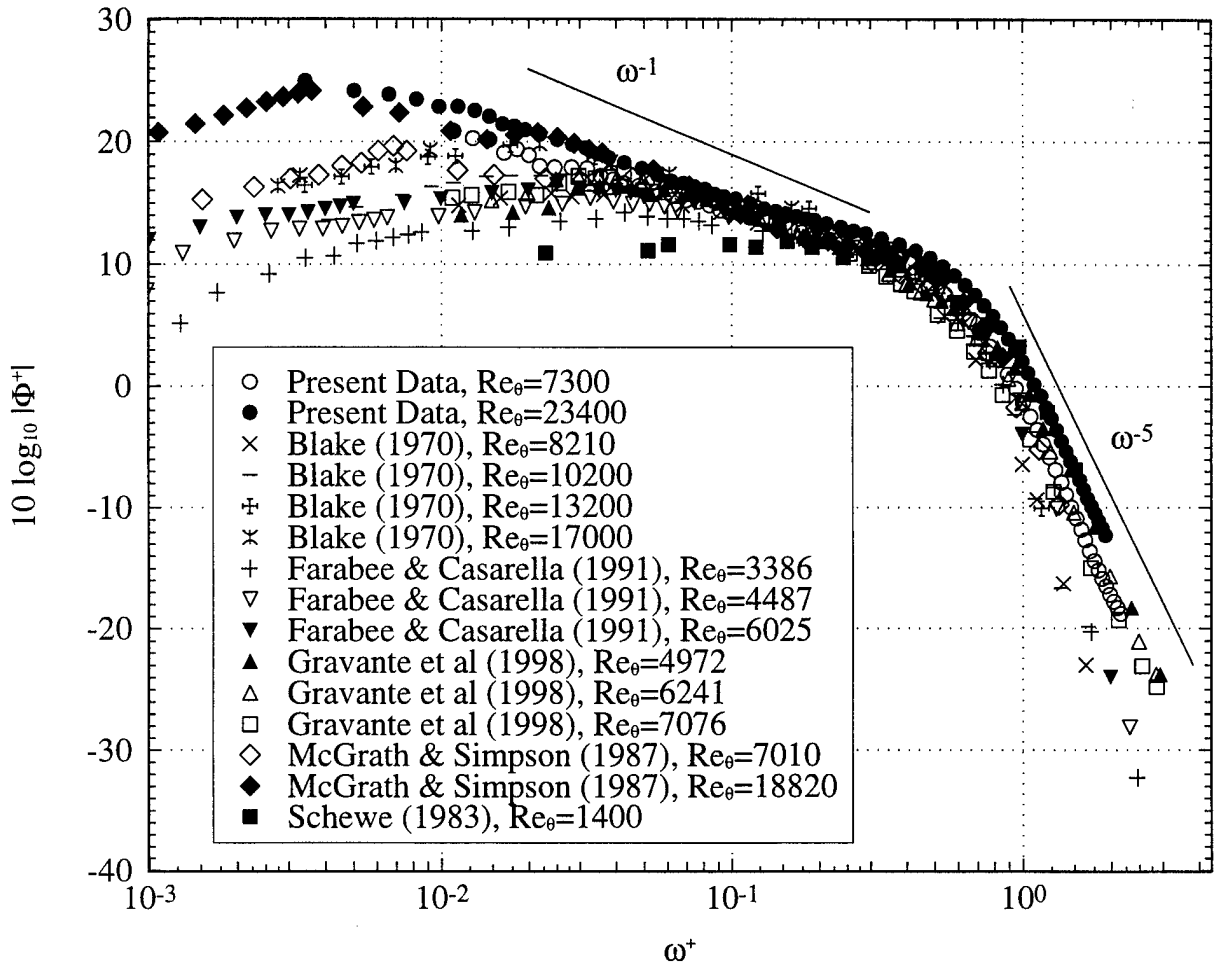

Figure 30. Spectral power density of p beneath the two-dimensional, zero-pressure-gradient, turbulent boundary layers of various investigations normalized using τ_w as the pressure scale and ν/u_τ^2 as the time scale.

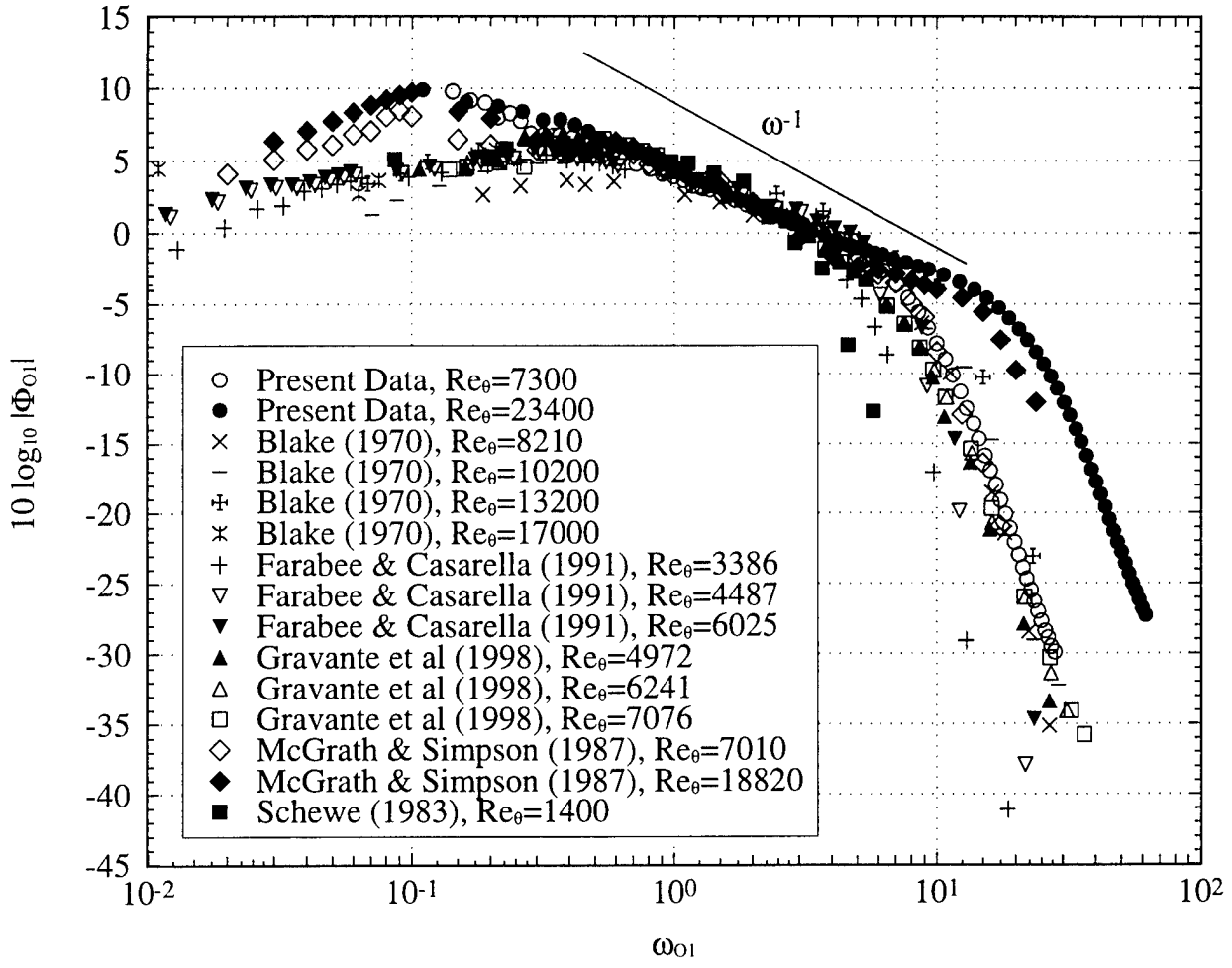

Figure 31. Spectral power density of p beneath the two-dimensional, zero-pressure-gradient, turbulent boundary layers of various investigations normalized using τ_w as the pressure scale and δ^*/U_e as the time scale.

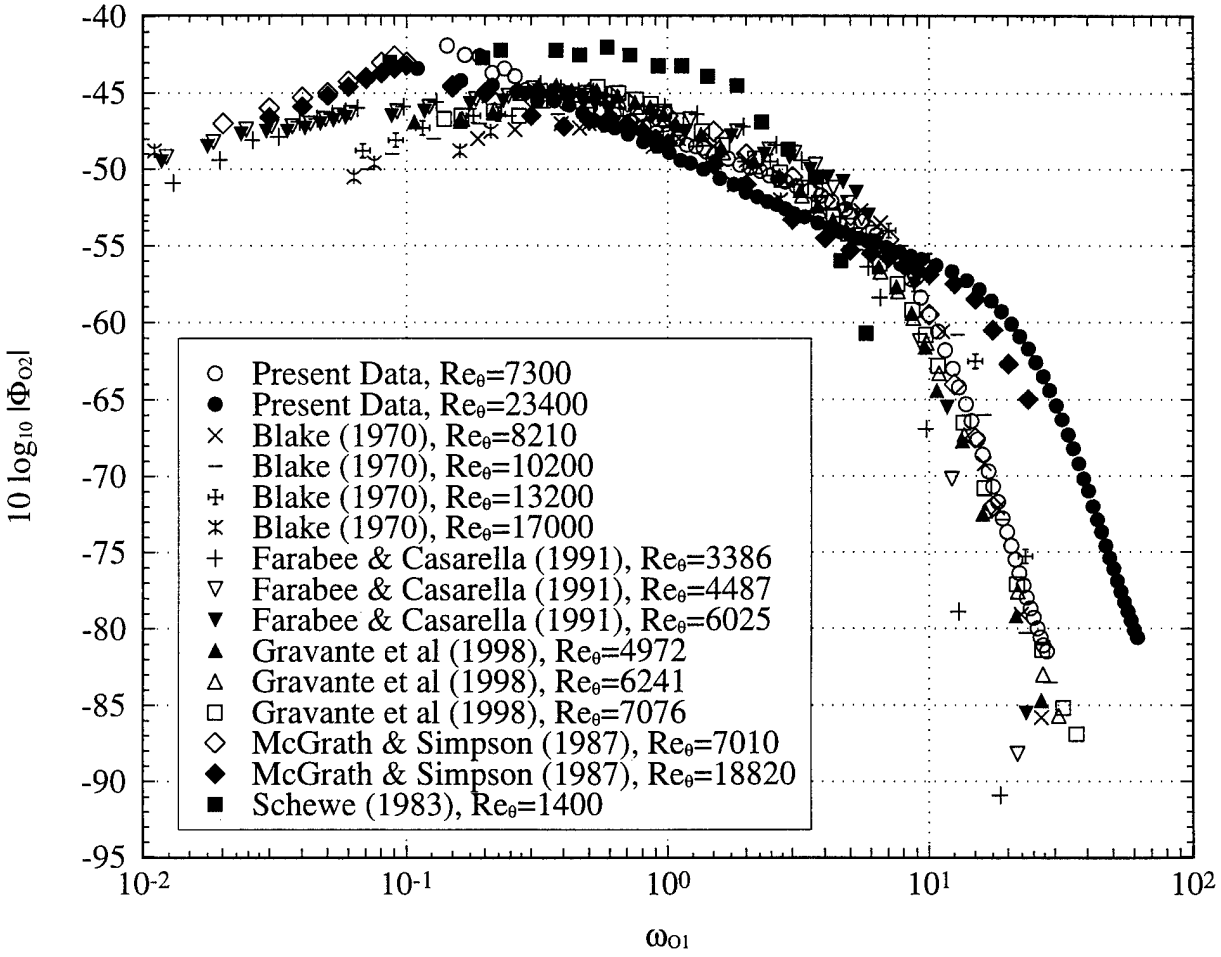

Figure 32. Spectral power density of p beneath the two-dimensional, zero-pressure-gradient, turbulent boundary layers of various investigations normalized using Q_e as the pressure scale and δ^*/U_e as the time scale.

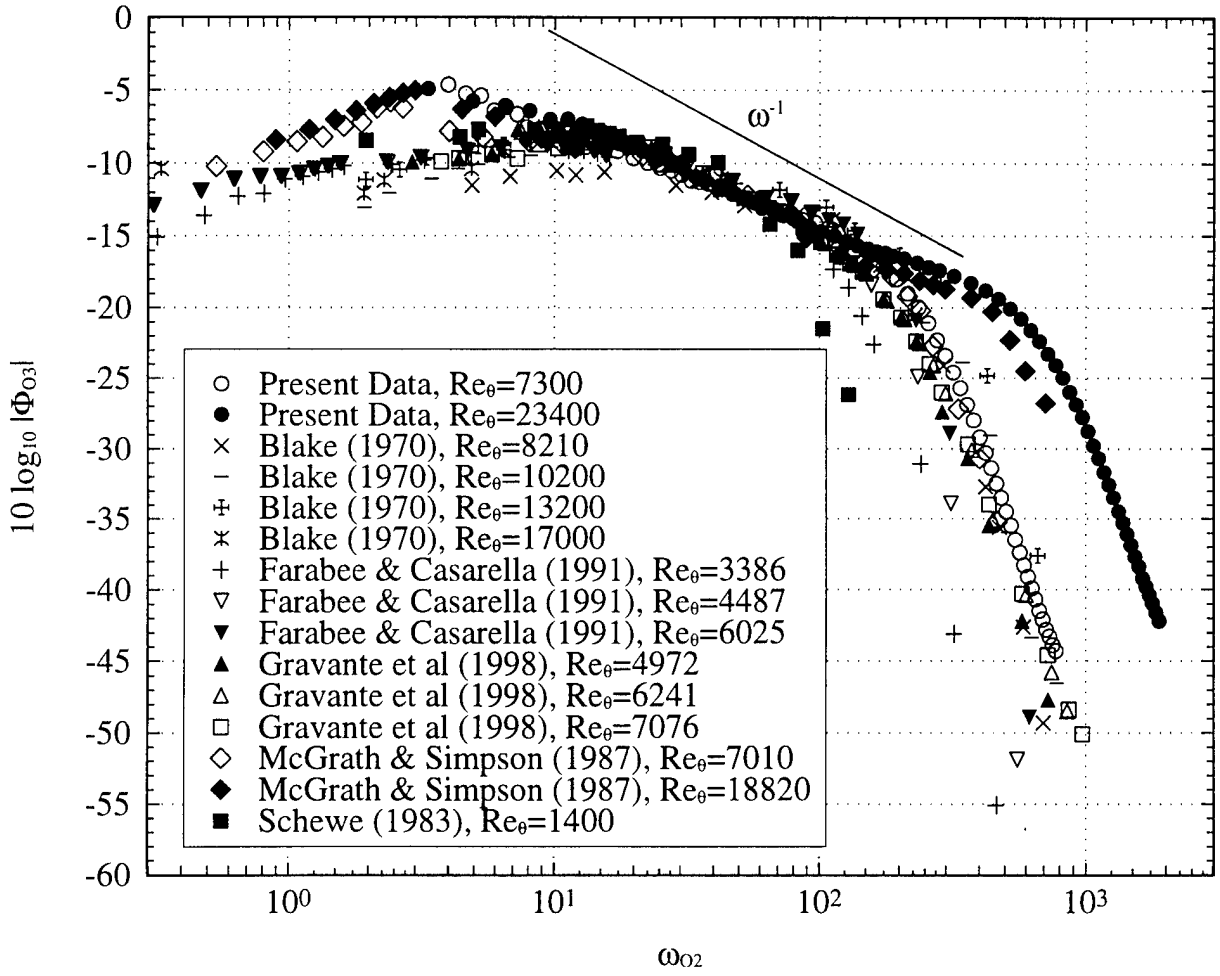

Figure 33. Spectral power density of p beneath the two-dimensional, zero-pressure-gradient, turbulent boundary layers of various investigations normalized using τ_W as the pressure scale and δ^*/u_τ as the time scale.

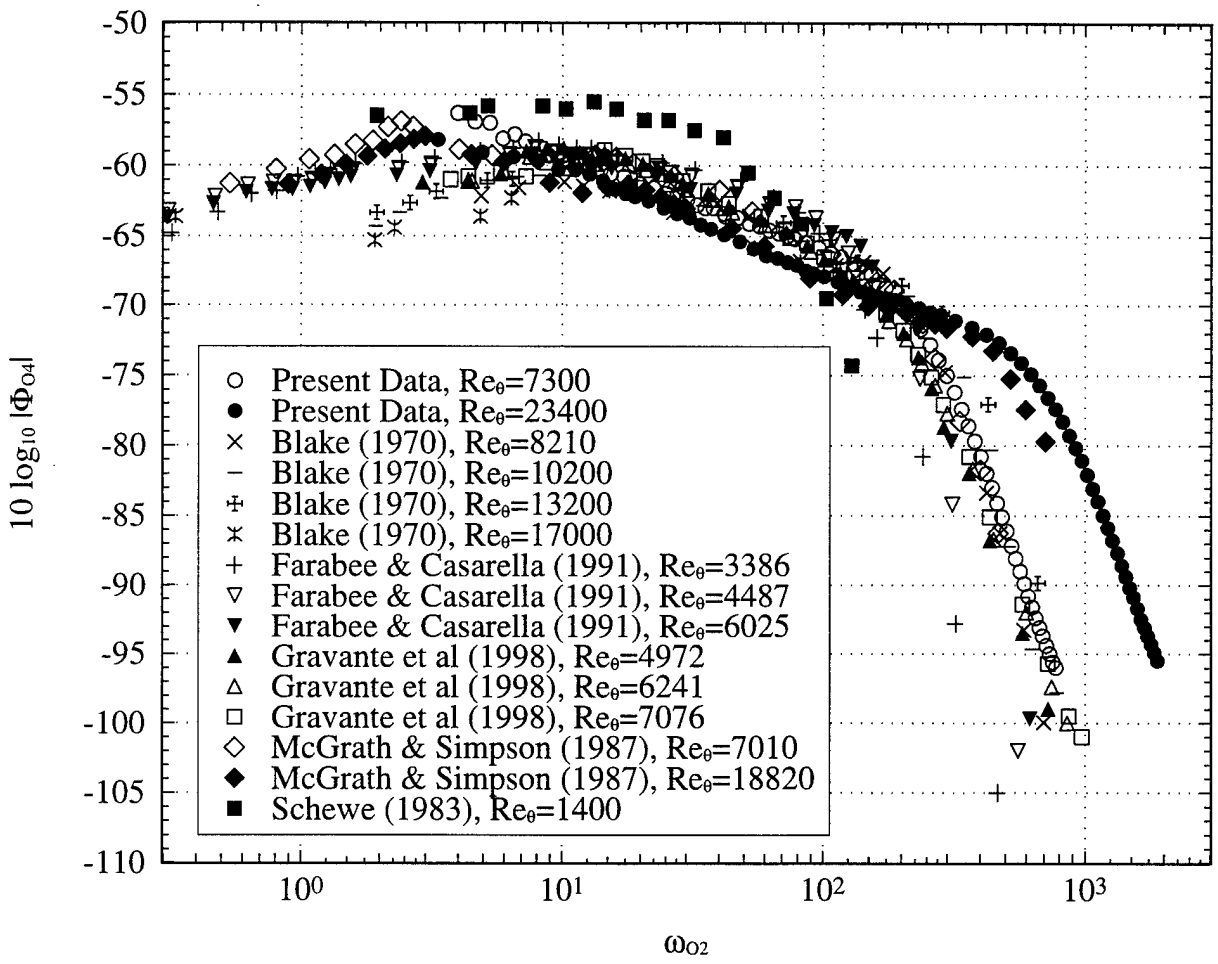

Figure 34. Spectral power density of p beneath the two-dimensional, zero-pressure-gradient, turbulent boundary layers of various investigations normalized using Q_e as the pressure scale and δ^*/u_τ as the time scale.

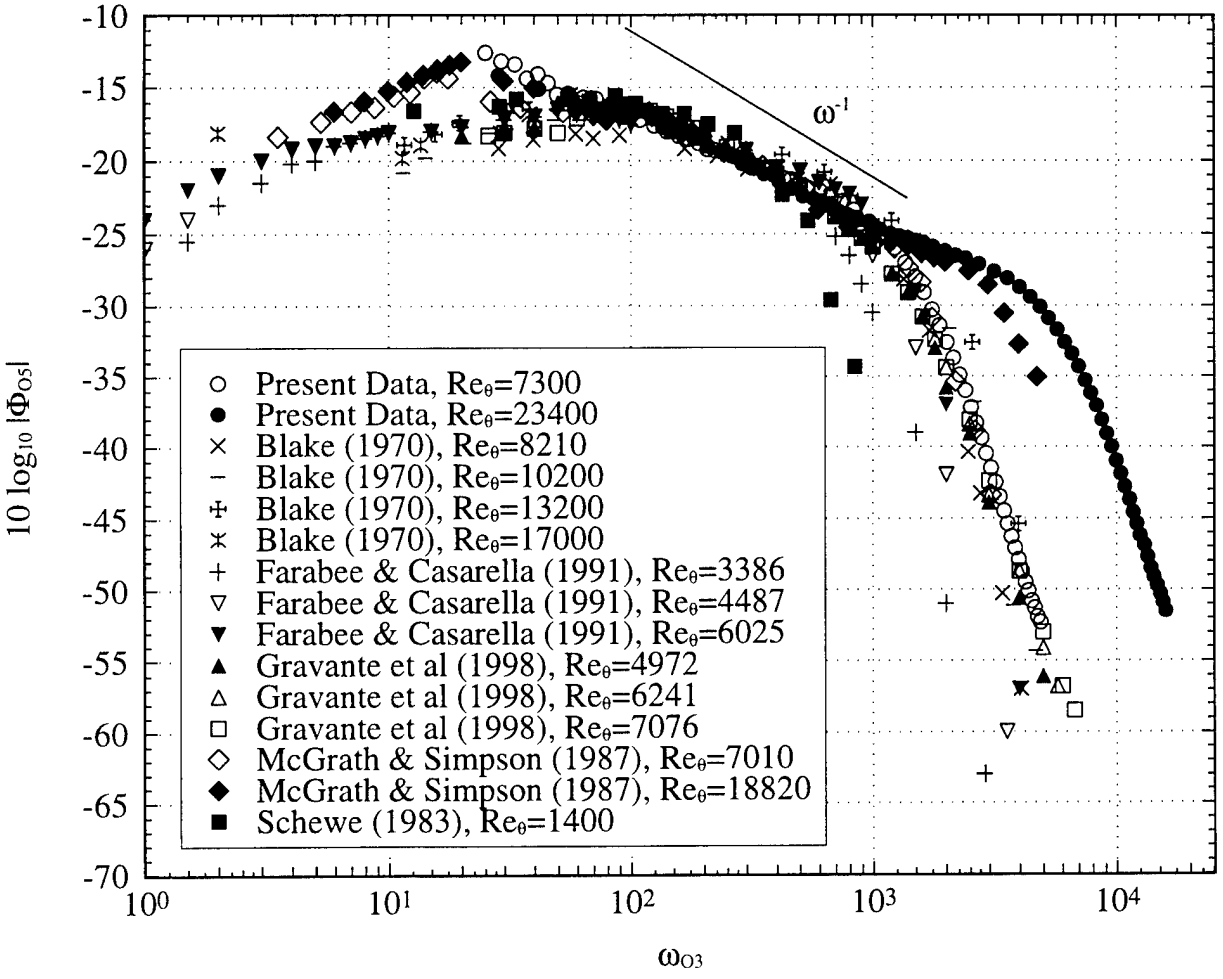

Figure 35. Spectral power density of p beneath the two-dimensional, zero-pressure-gradient, turbulent boundary layers of various investigations normalized using τ_W as the pressure scale and δ/u_τ as the time scale.

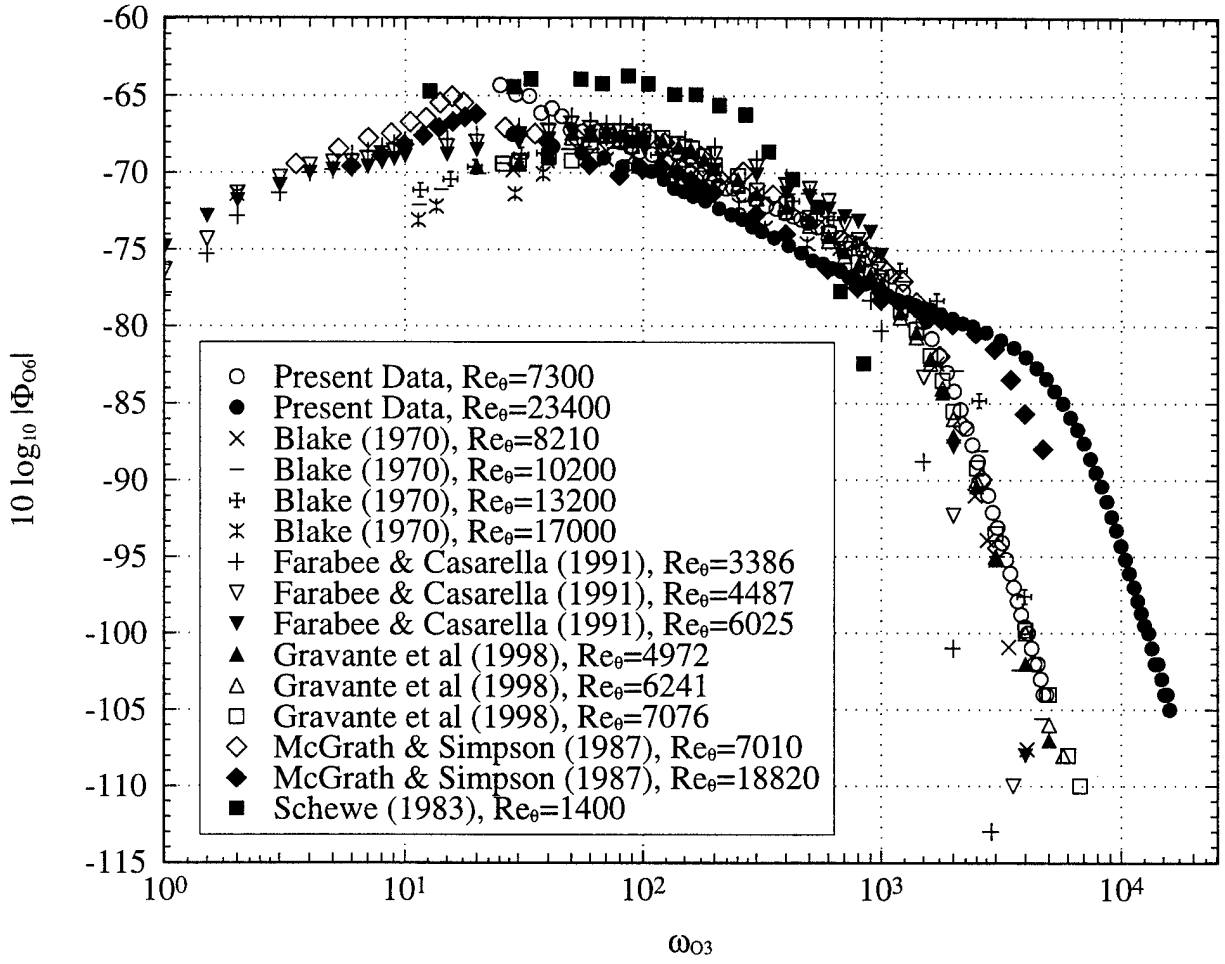

Figure 36. Spectral power density of p beneath the two-dimensional, zero-pressure-gradient, turbulent boundary layers of various investigations normalized using Q_e as the pressure scale and δ/u_τ as the time scale.

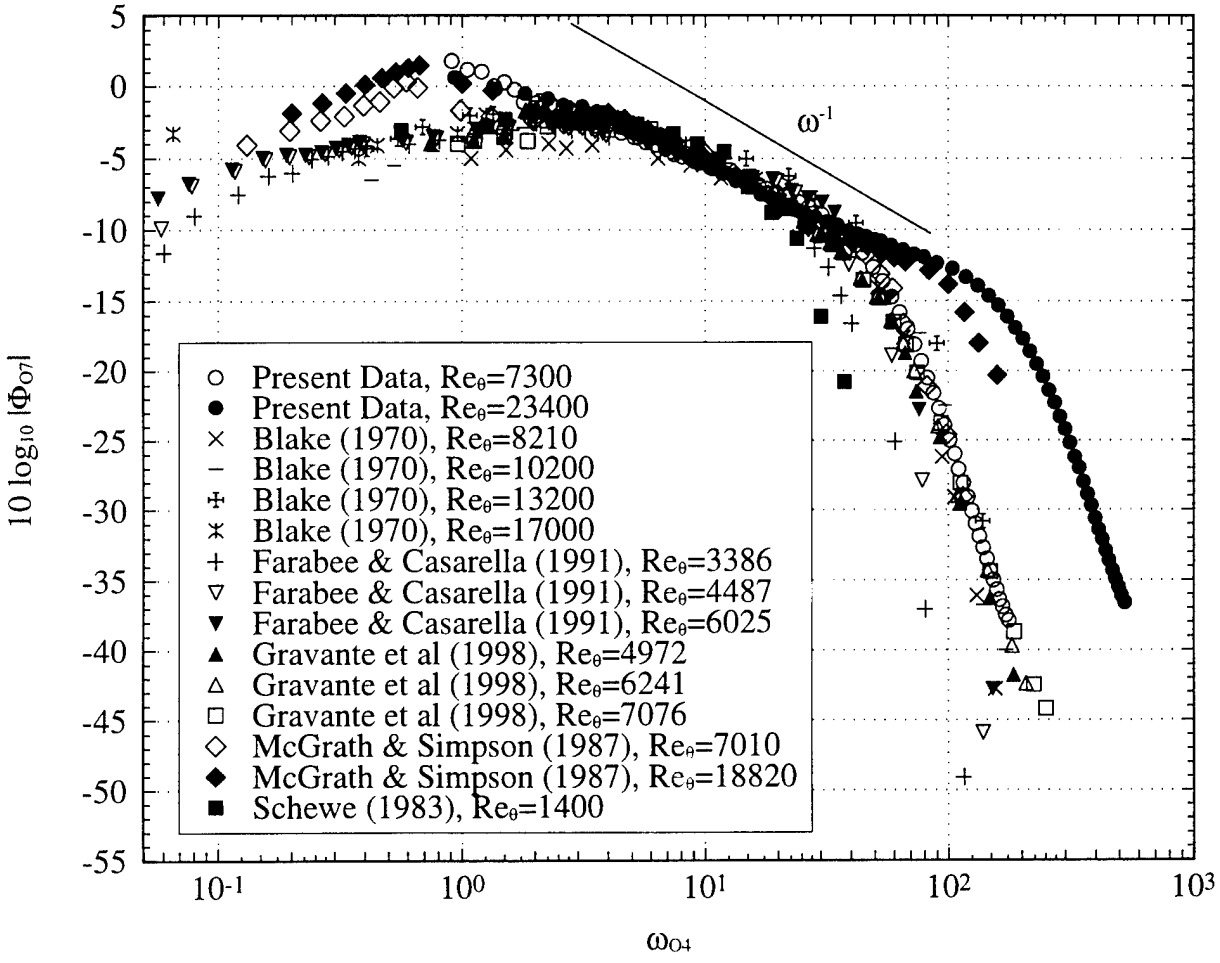

Figure 37. Spectral power density of p beneath the two-dimensional, zero-pressure-gradient, turbulent boundary layers of various investigations normalized using τ_W as the pressure scale and δ/U_e as the time scale.

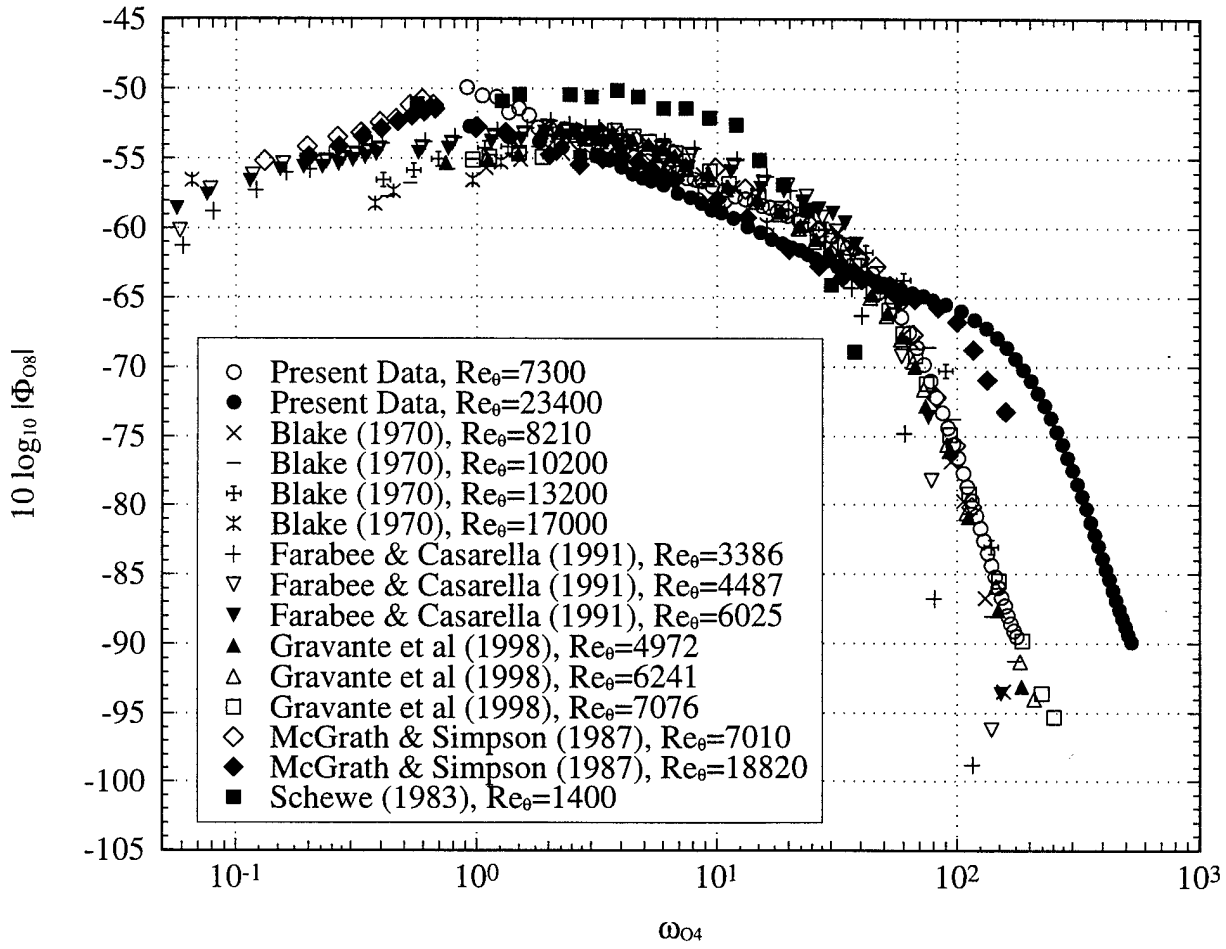

Figure 38. Spectral power density of p beneath the two-dimensional, zero-pressure-gradient, turbulent boundary layers of various investigations normalized using Q_e as the pressure scale and δ/U_e as the time scale.

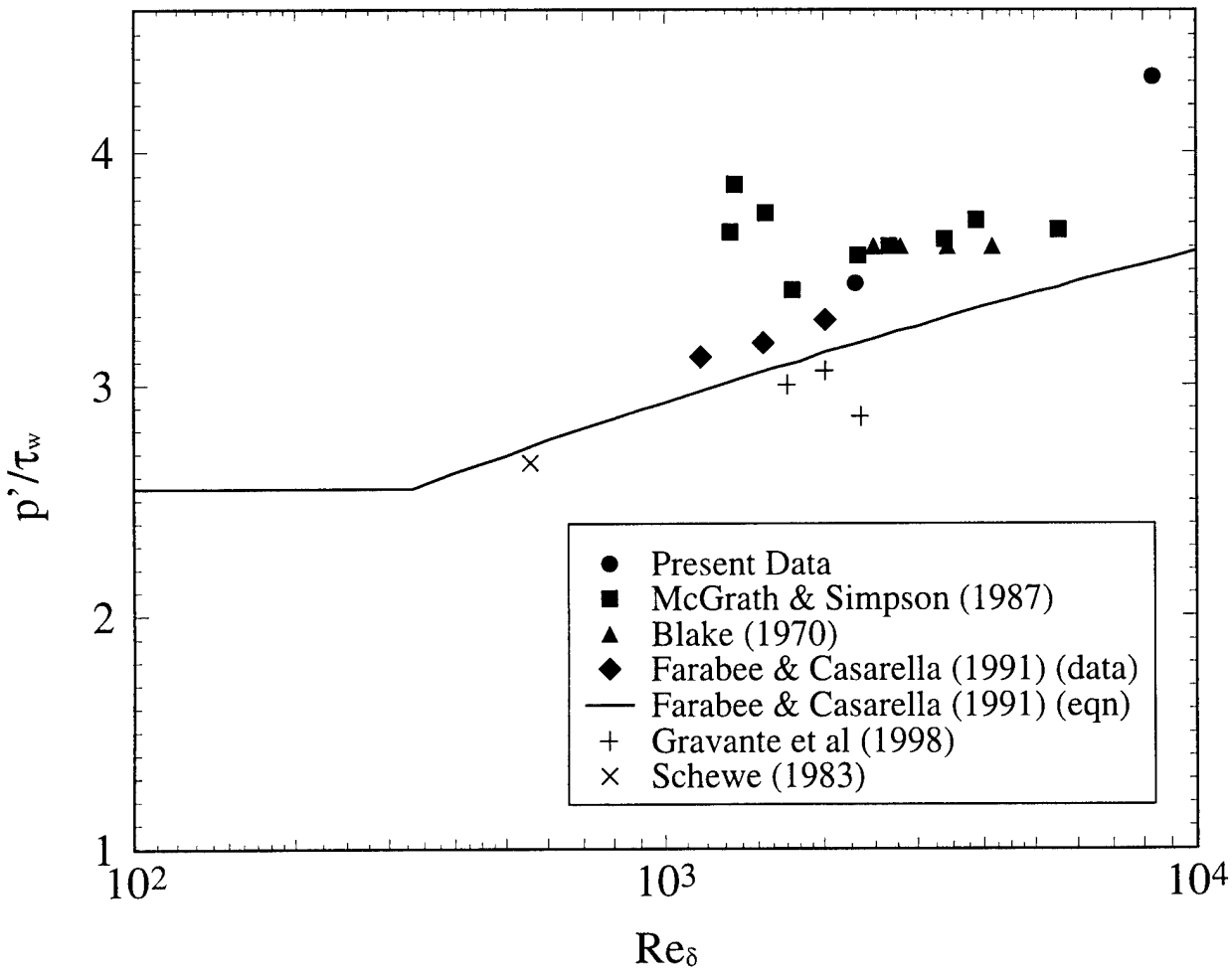

Figure 39. The root mean square of p beneath the two-dimensional, zero-pressure-gradient, turbulent boundary layers of various investigations as a function of Reynolds number based on boundary layer thickness.

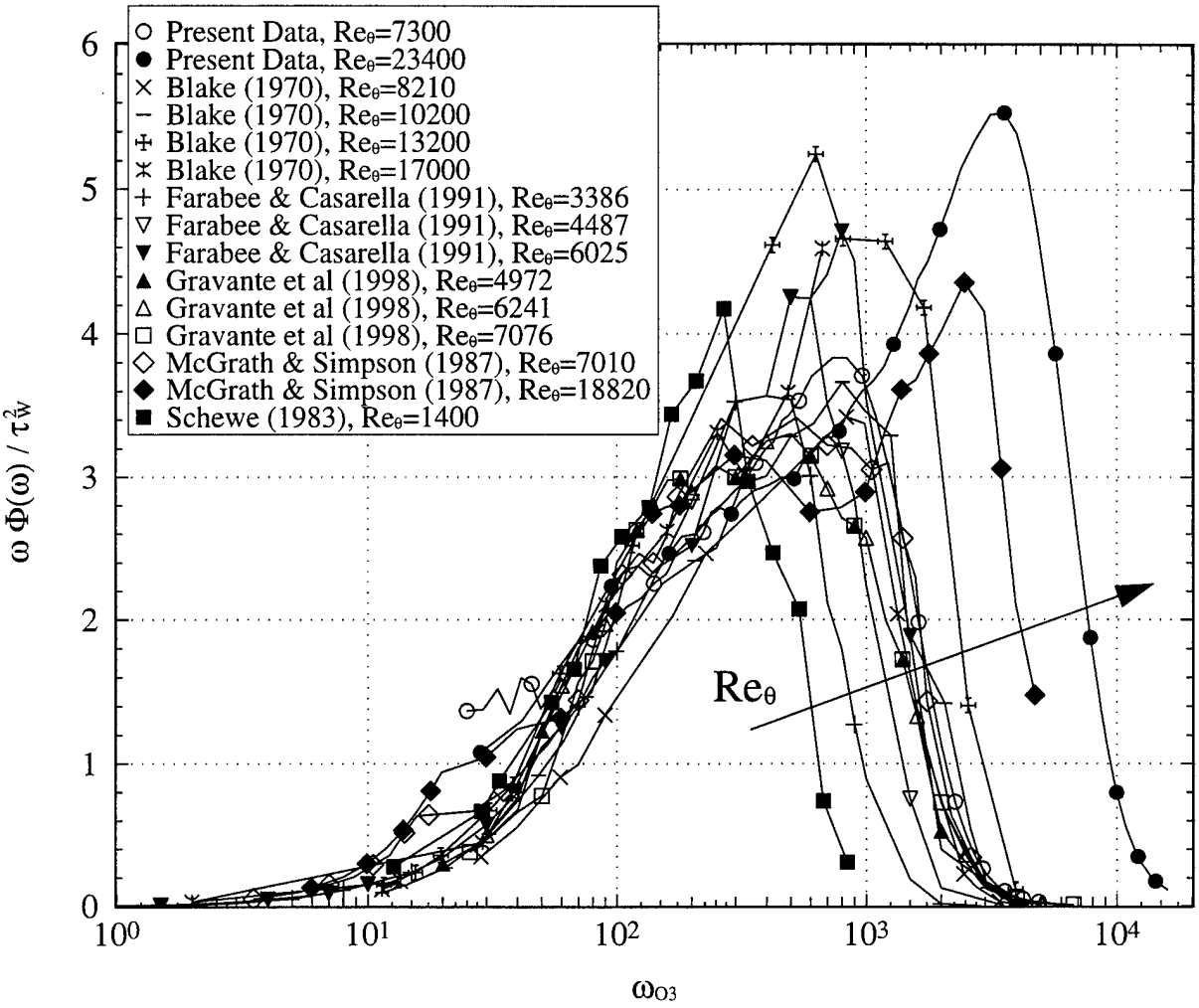

Figure 40. The quantity $\omega\Phi/\tau_w^2$ beneath the two-dimensional, zero-pressure-gradient, turbulent boundary layers of various investigations as a function of ω_{O3} in order to illustrate the contributions of different frequency ranges to the $\overline{p^2}/\tau_w^2$ integral.

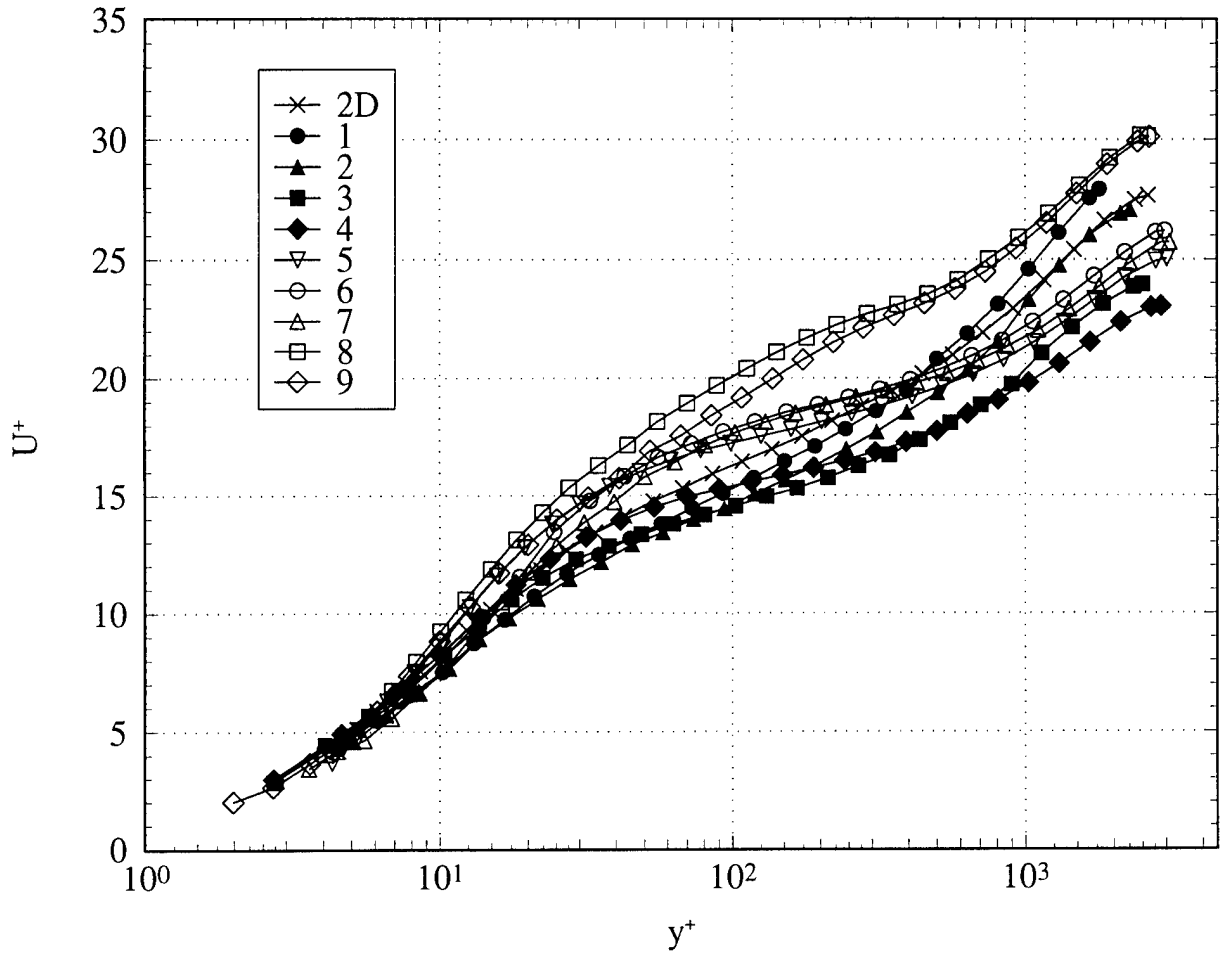

Figure 41. Profiles of the U^+ mean velocity in wall-shear-stress coordinates (Re_θ = 7300 (2-D); 5940 (3-D)). The numbers in the legend denote the measurement station. Data taken from Ölçmen and Simpson (1996).

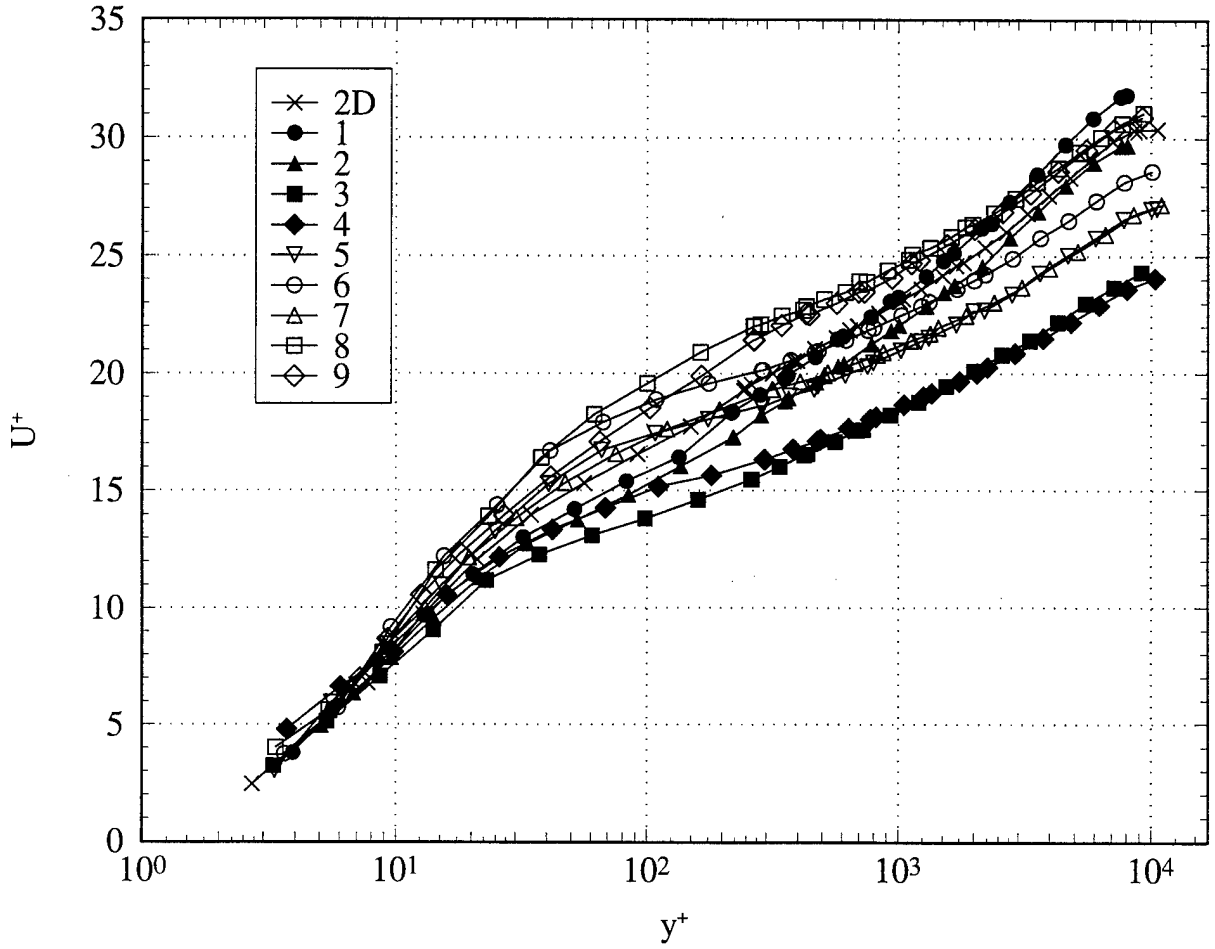

Figure 42. Profiles of the U^+ mean velocity in wall-shear-stress coordinates ($Re_\theta = 23400$ (2-D); 23200 (3-D)). The numbers in the legend denote the measurement station. Data taken from Ölçmen *et al.* (1998).

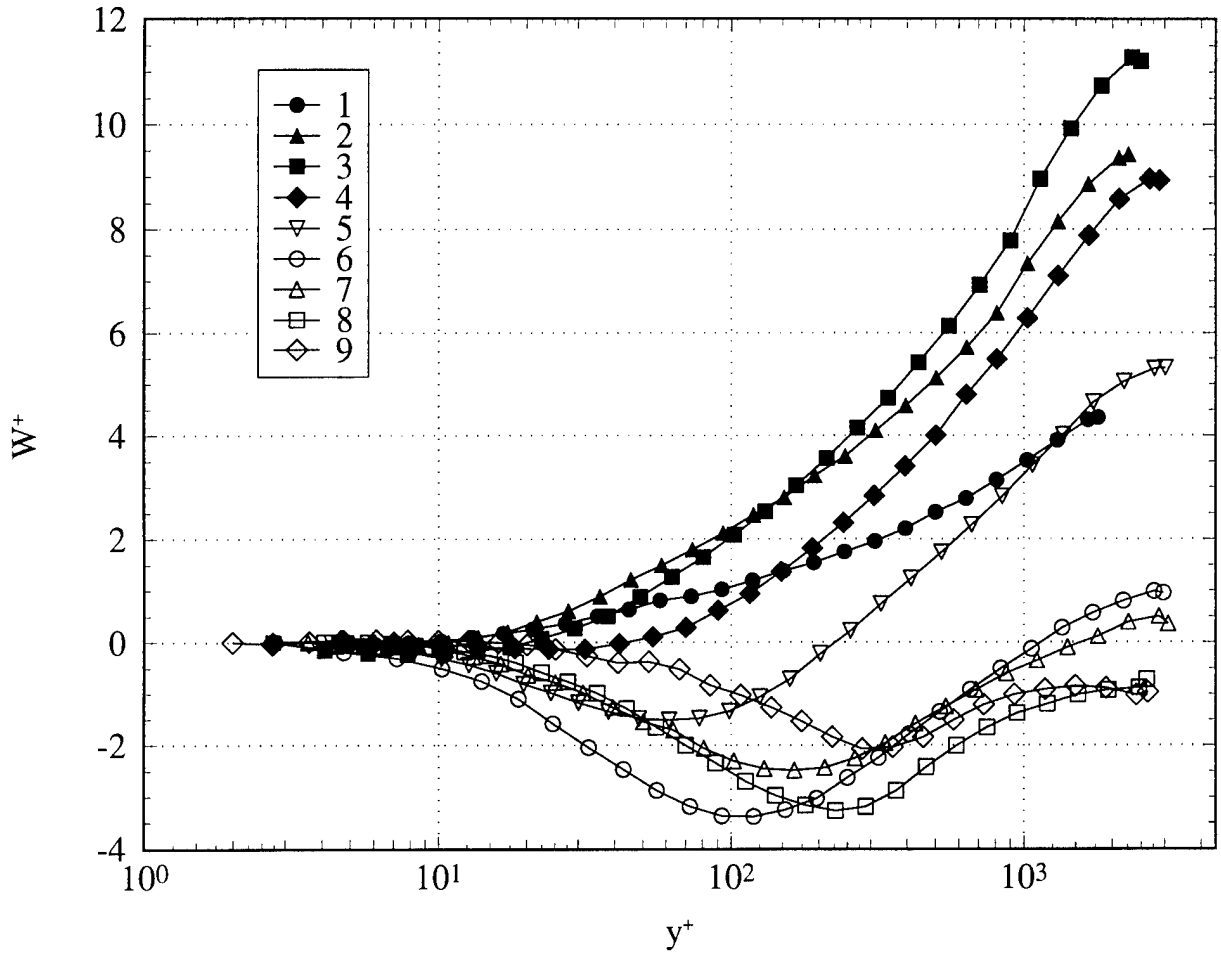

Figure 43. Profiles of the W^+ mean velocity in wall-shear-stress coordinates (Re_θ = 7300 (2-D); 5940 (3-D)). The numbers in the legend denote the measurement station. Data taken from Ölçmen and Simpson (1996).

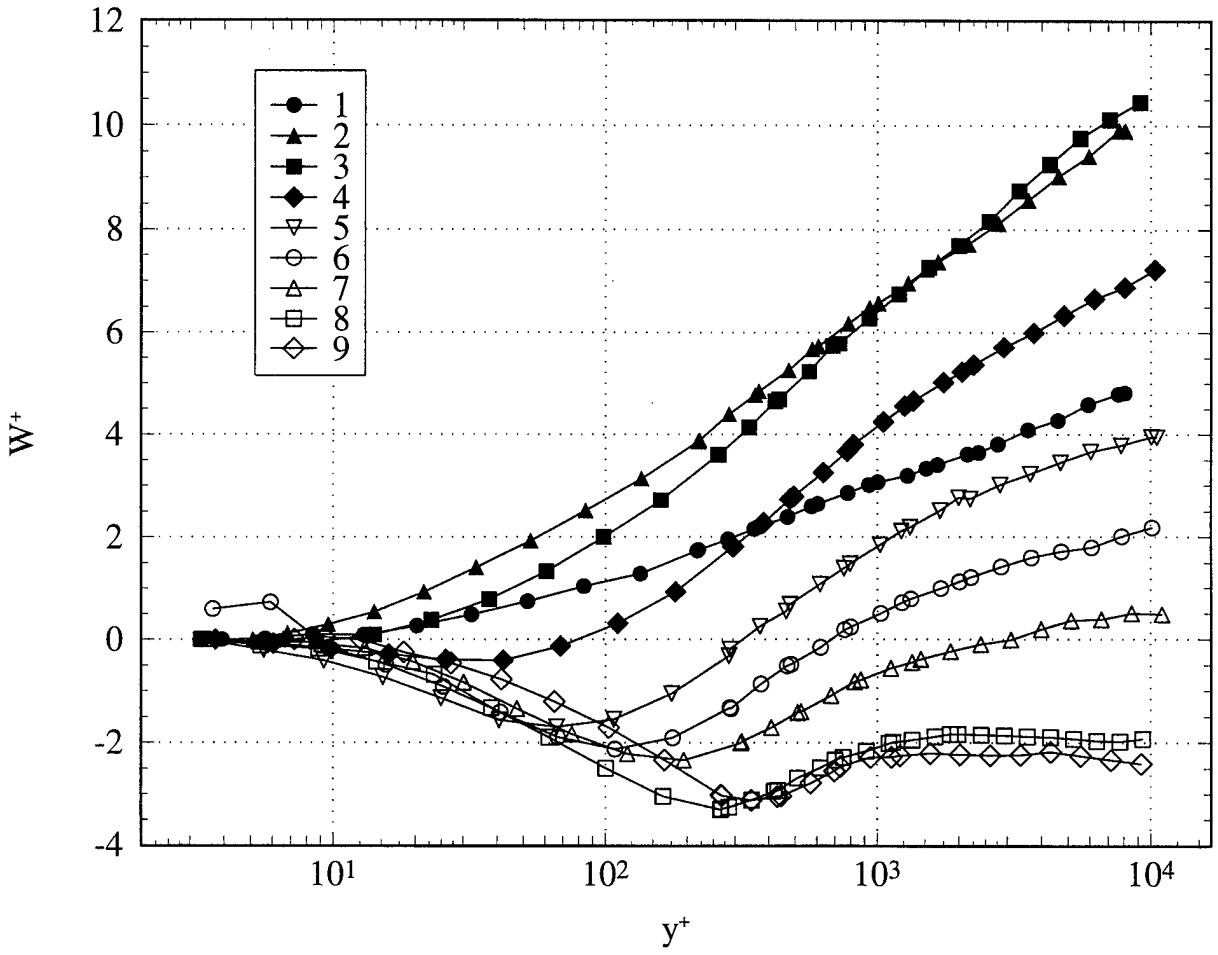

Figure 44. Profiles of the W^+ mean velocity in wall-shear-stress coordinates (Re_θ = 23400 (2-D); 23200 (3-D)). The numbers in the legend denote the measurement station. Data taken from Ölçmen *et al.* (1998).

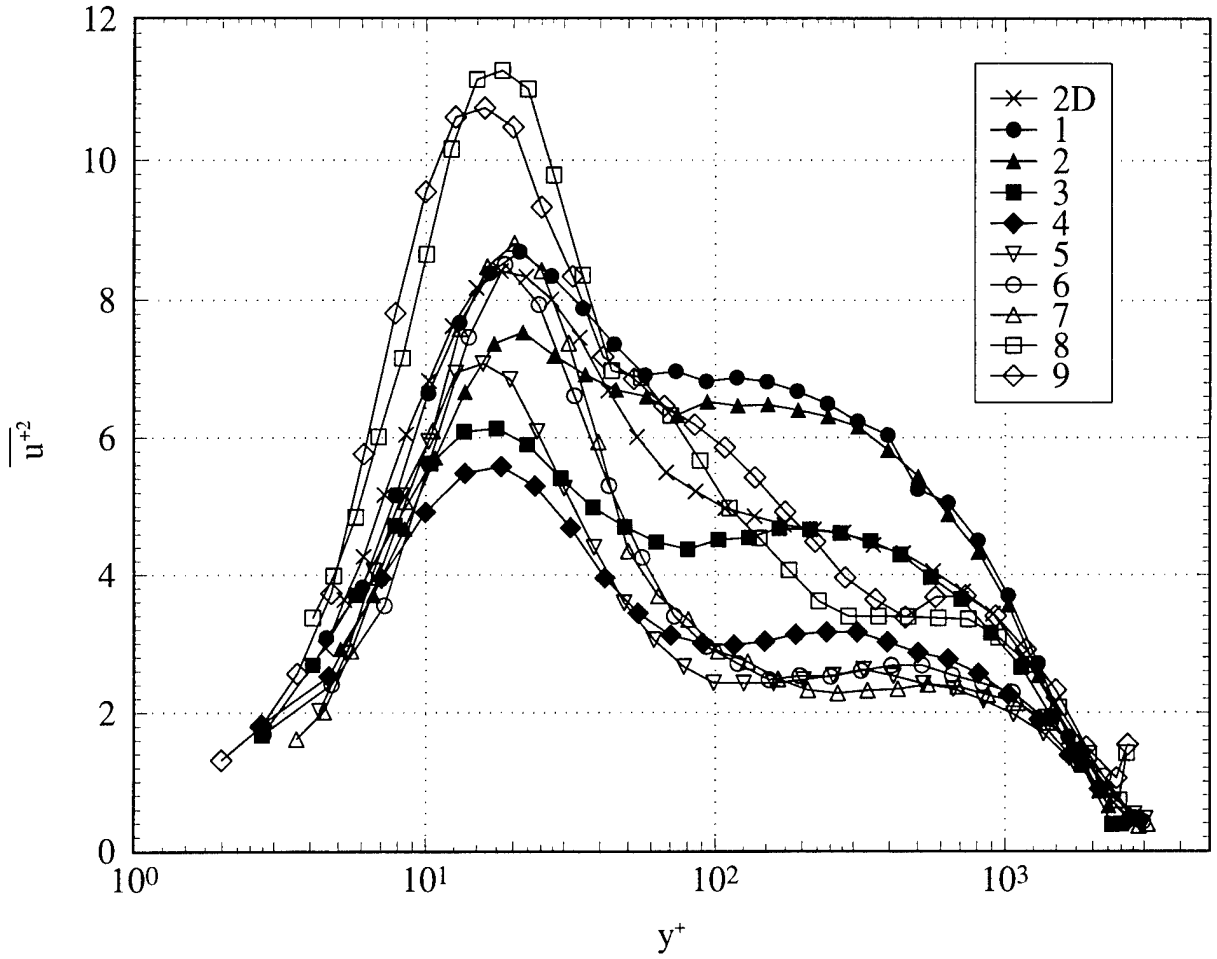

Figure 45. Profiles of the $\overline{u^{+2}}$ Reynolds normal stress in wall-shear-stress coordinates (Re_θ = 7300 (2-D); 5940 (3-D)). The numbers in the legend denote the measurement station. Data taken from Ölçmen and Simpson (1996).

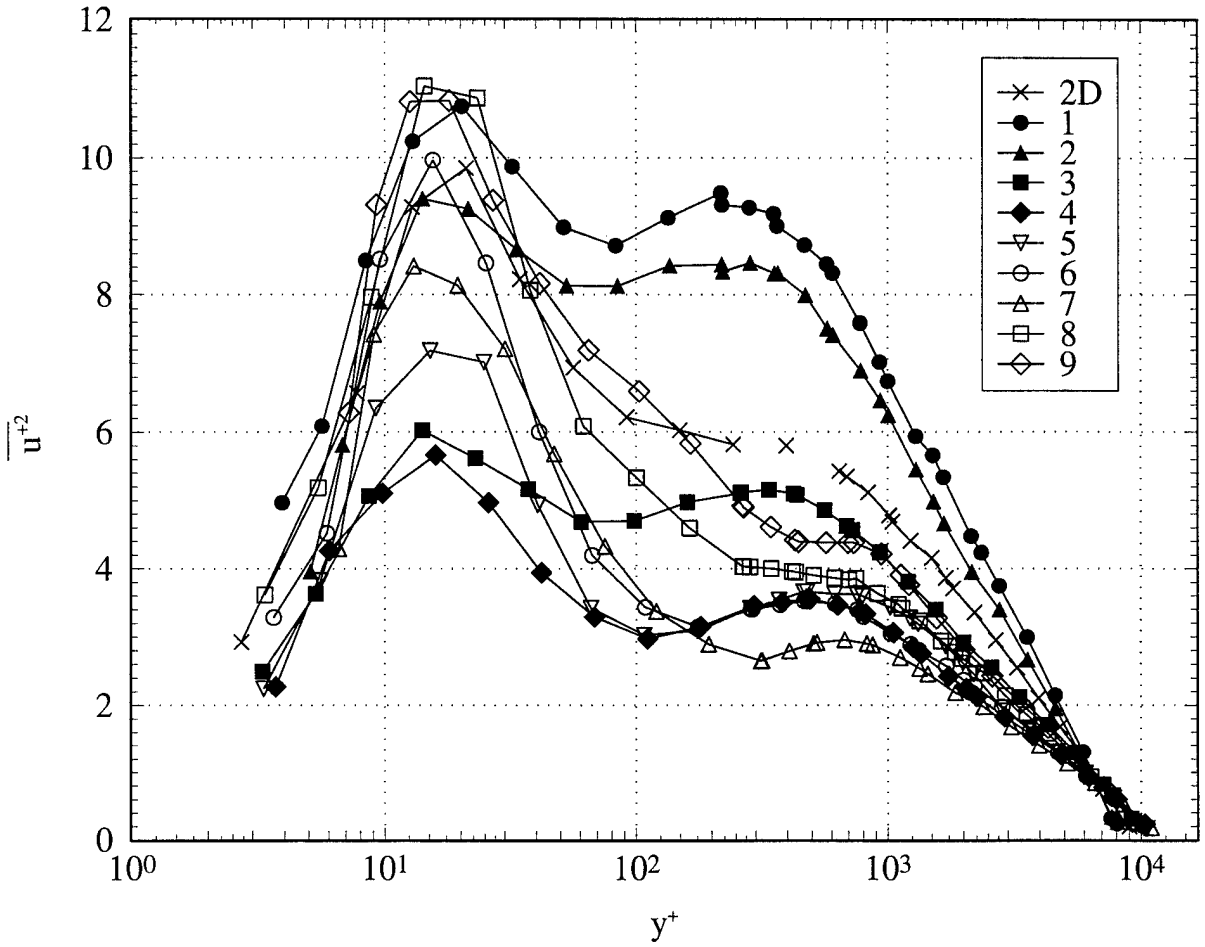

Figure 46. Profiles of the $\overline{u^{+2}}$ Reynolds normal stress in wall-shear-stress coordinates ($Re_\theta = 23400$ (2-D); 23200 (3-D)). The numbers in the legend denote the measurement station. Data taken from Ölçmen *et al.* (1998).

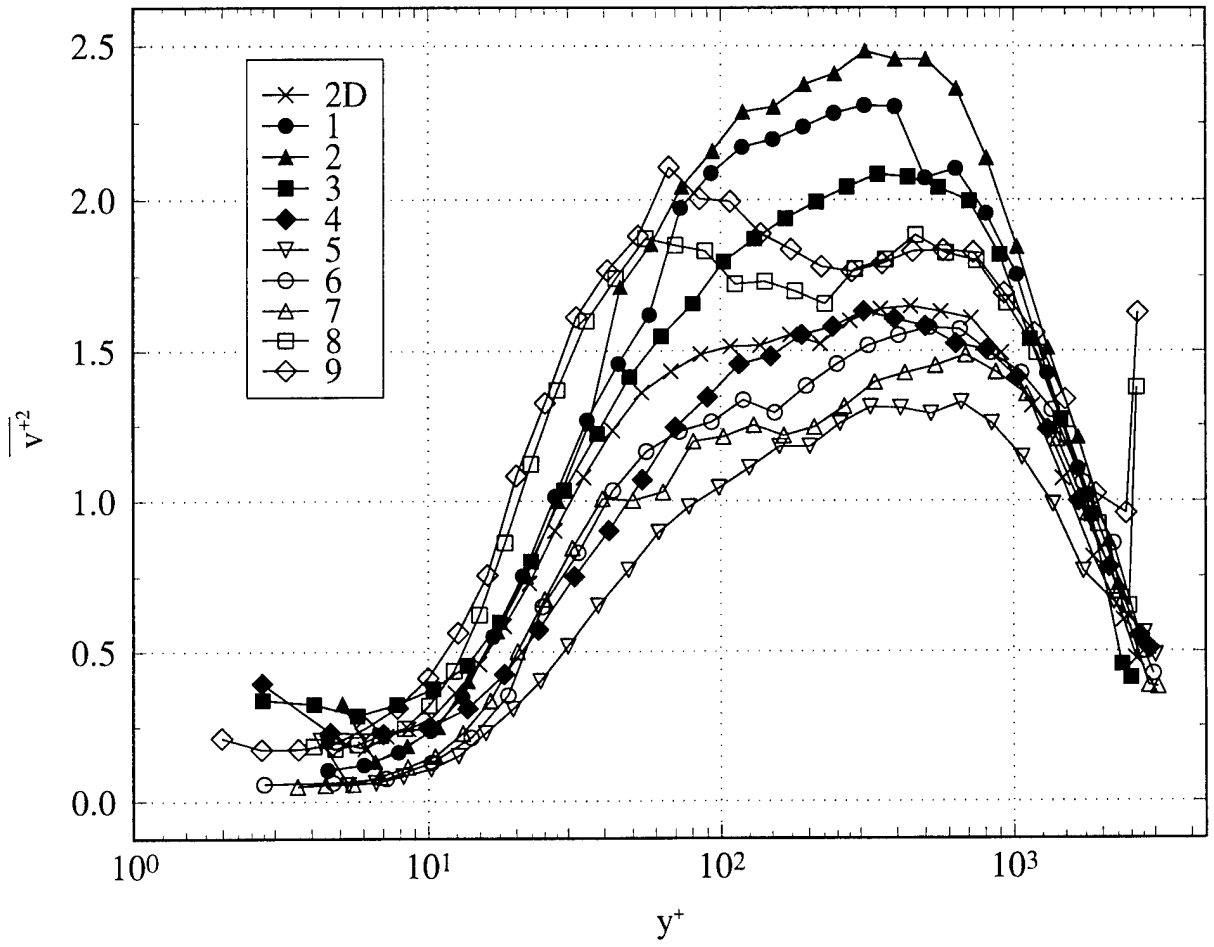

Figure 47. Profiles of the $\overline{v^{+2}}$ Reynolds normal stress in wall-shear-stress coordinates (Re_θ = 7300 (2-D); 5940 (3-D)). The numbers in the legend denote the measurement station. Data taken from Ölçmen and Simpson (1996).

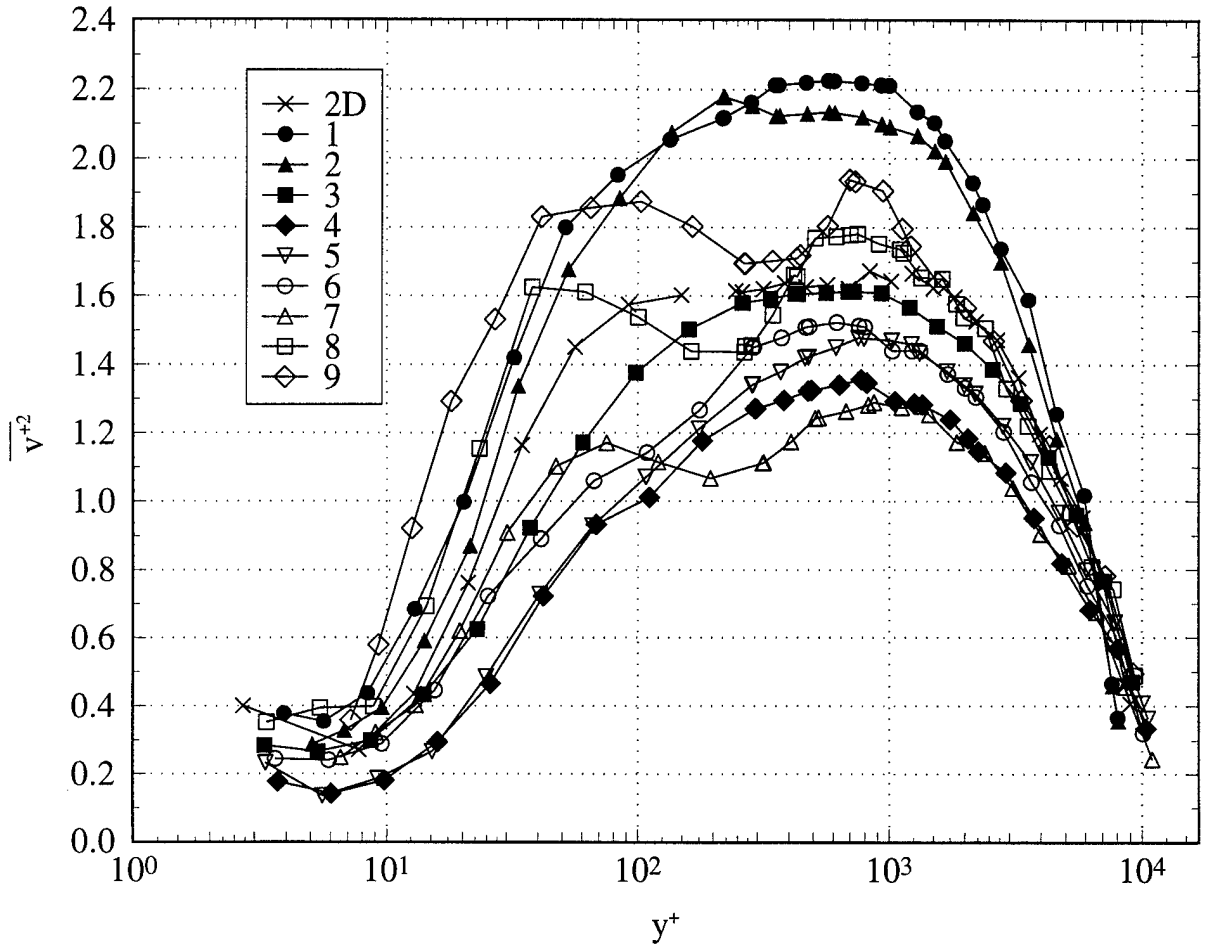

Figure 48. Profiles of the $\overline{v^{+2}}$ Reynolds normal stress in wall-shear-stress coordinates (Re_θ = 23400 (2-D); 23200 (3-D)). The numbers in the legend denote the measurement station. Data taken from Ölçmen *et al.* (1998).

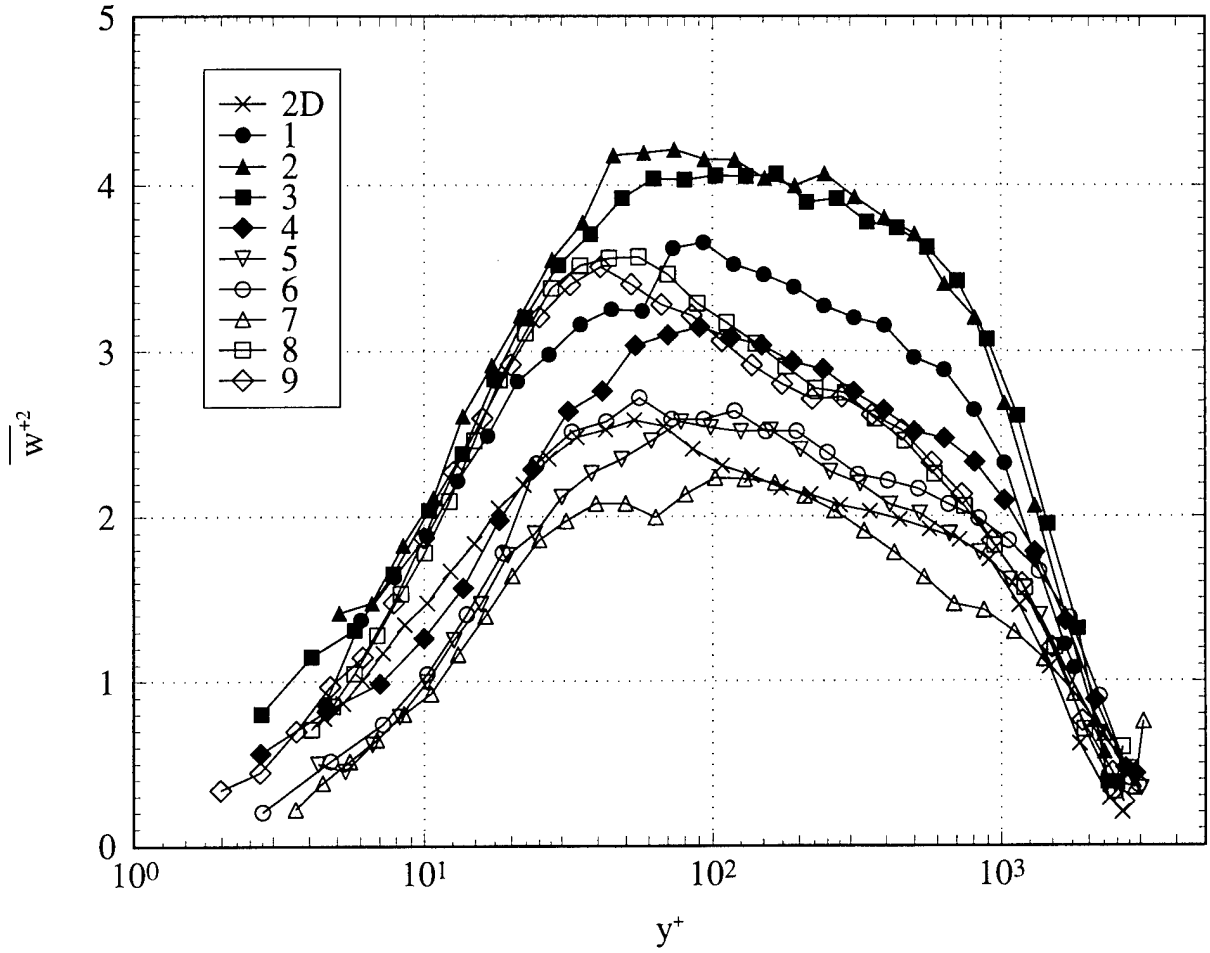

Figure 49. Profiles of the $\overline{w^{+2}}$ Reynolds normal stress in wall-shear-stress coordinates (Re_θ = 7300 (2-D); 5940 (3-D)). The numbers in the legend denote the measurement station. Data taken from Ölçmen and Simpson (1996).

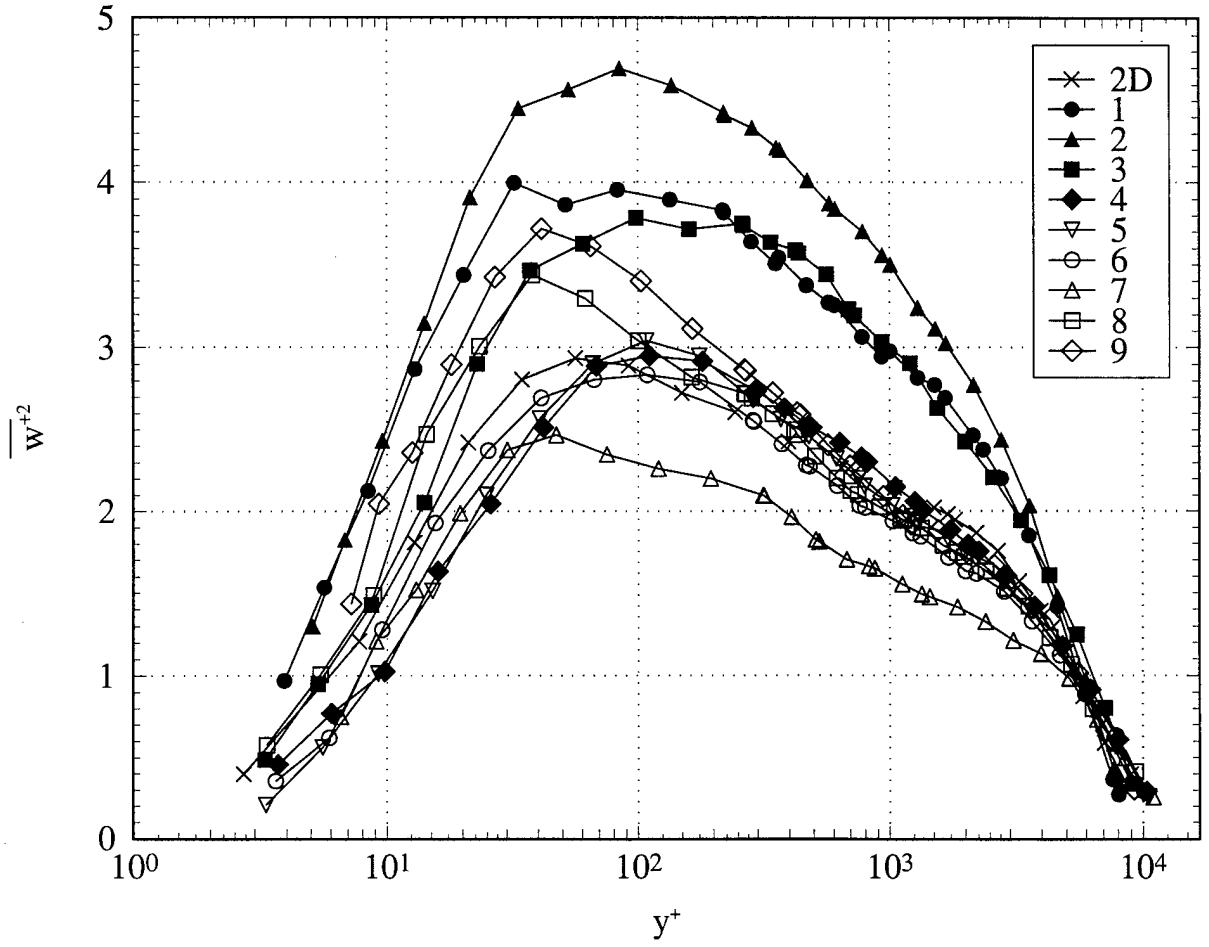

Figure 50. Profiles of the $\overline{w^{+2}}$ Reynolds normal stress in wall-shear-stress coordinates (Re_θ = 23400 (2-D); 23200 (3-D)). The numbers in the legend denote the measurement station. Data taken from Ölçmen *et al.* (1998).

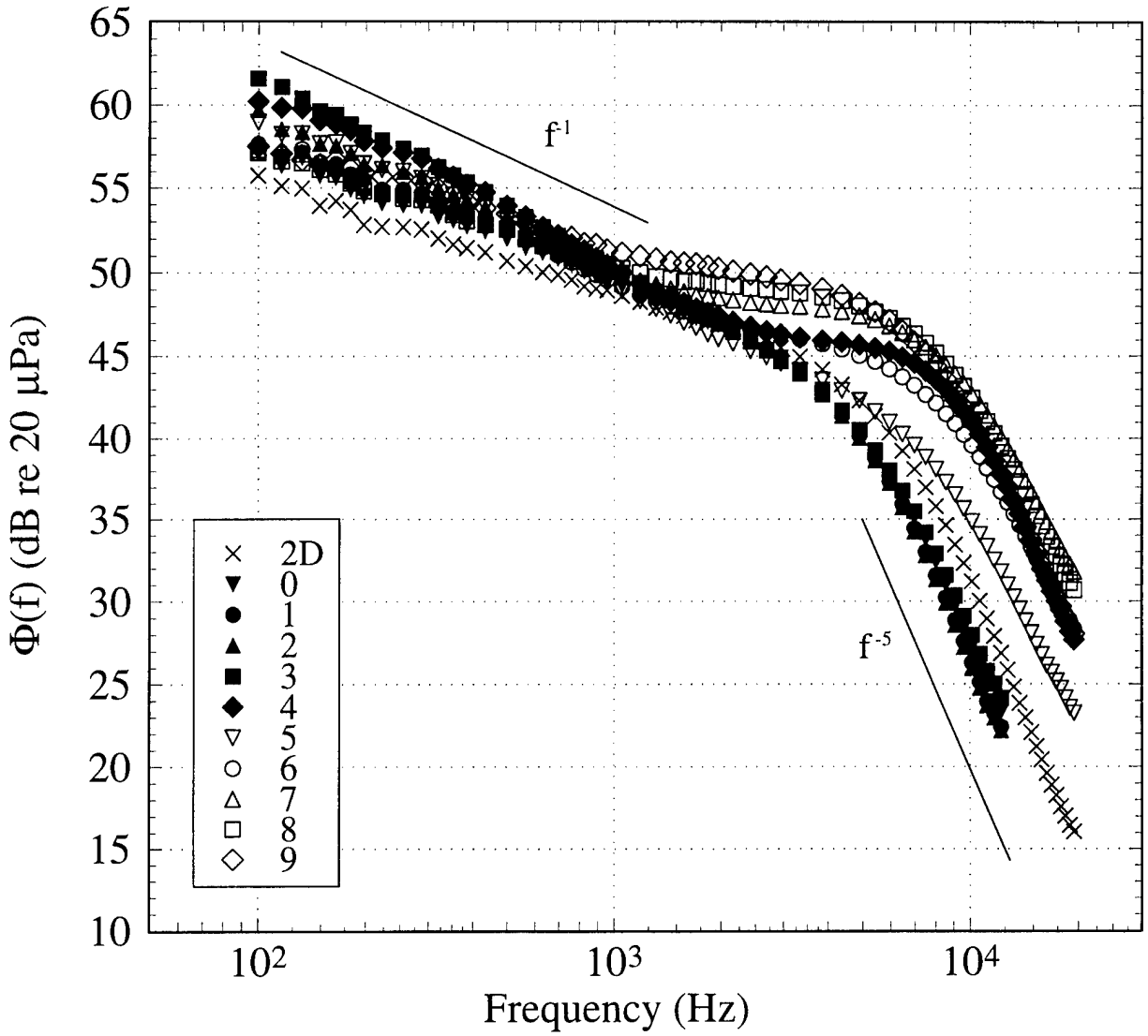

Figure 51. Spectral power density of p (Re_θ = 7300 (2-D); 5940 (3-D)). The numbers in the legend denote the measurement station.

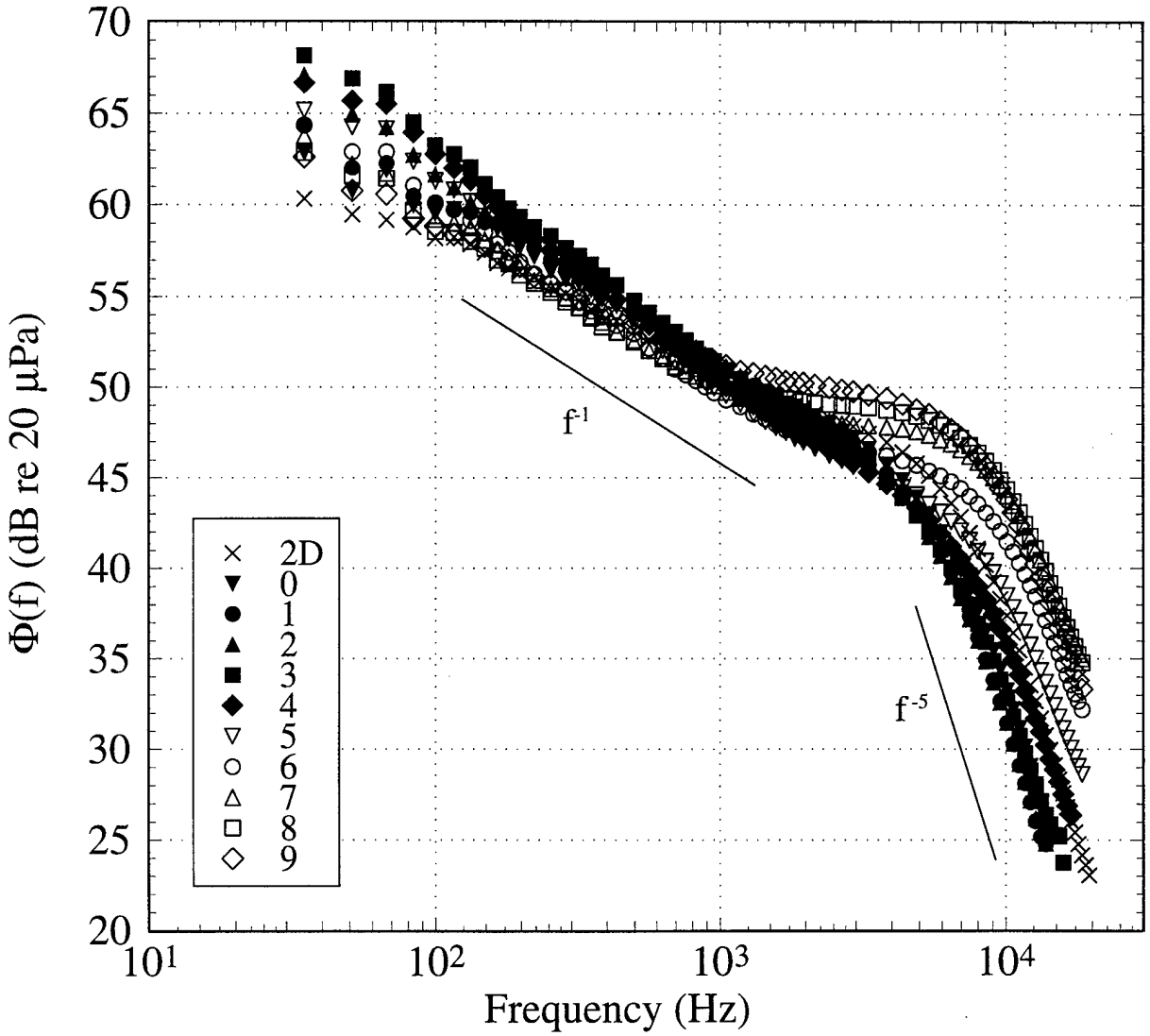

Figure 52. Spectral power density of p (Re_θ = 23400 (2-D); 23200 (3-D)). The numbers in the legend denote the measurement station.

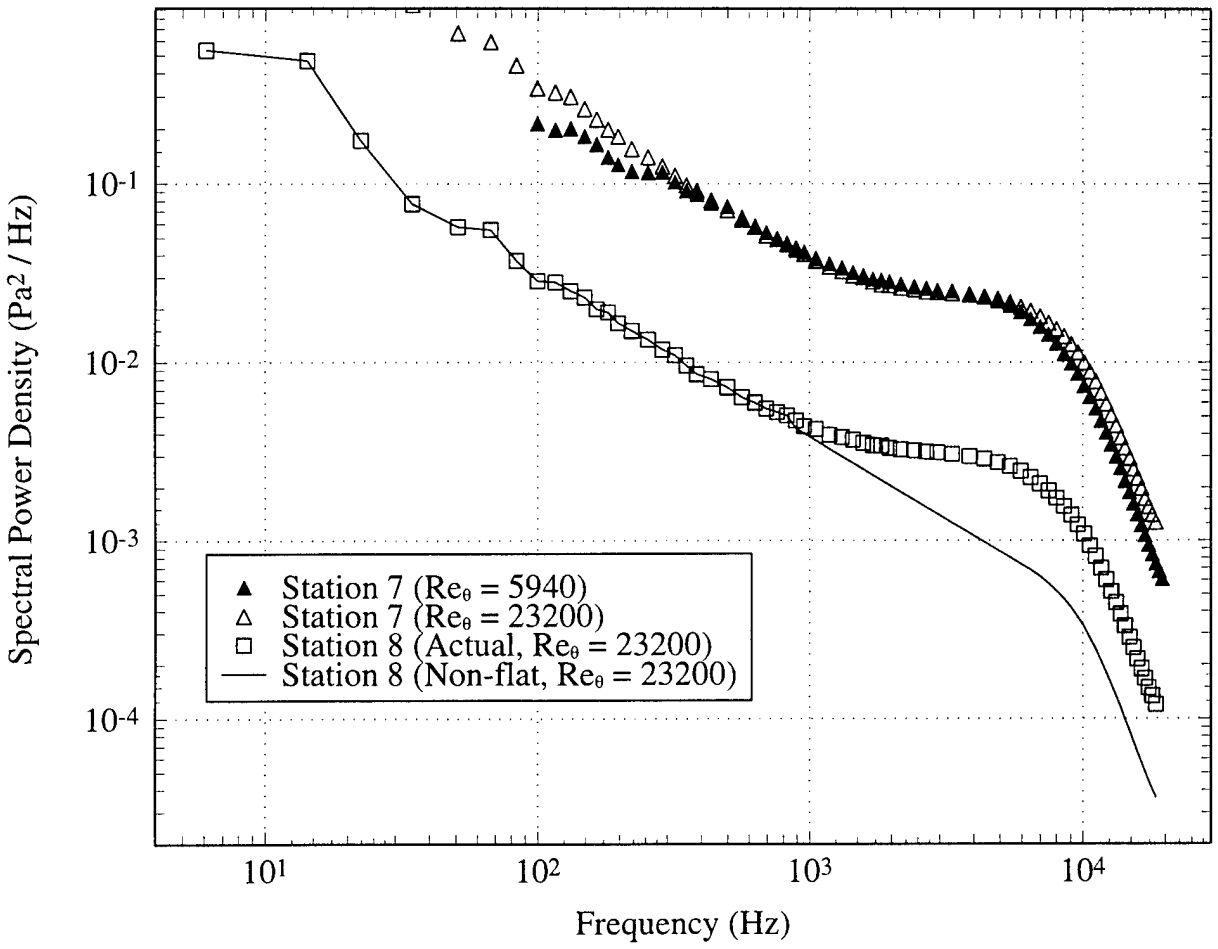

Figure 53. Spectral power density of p at measurement stations 7 and 8. The station 7 data are multiplied by 10 in this figure in order to produce the offset for clarity.

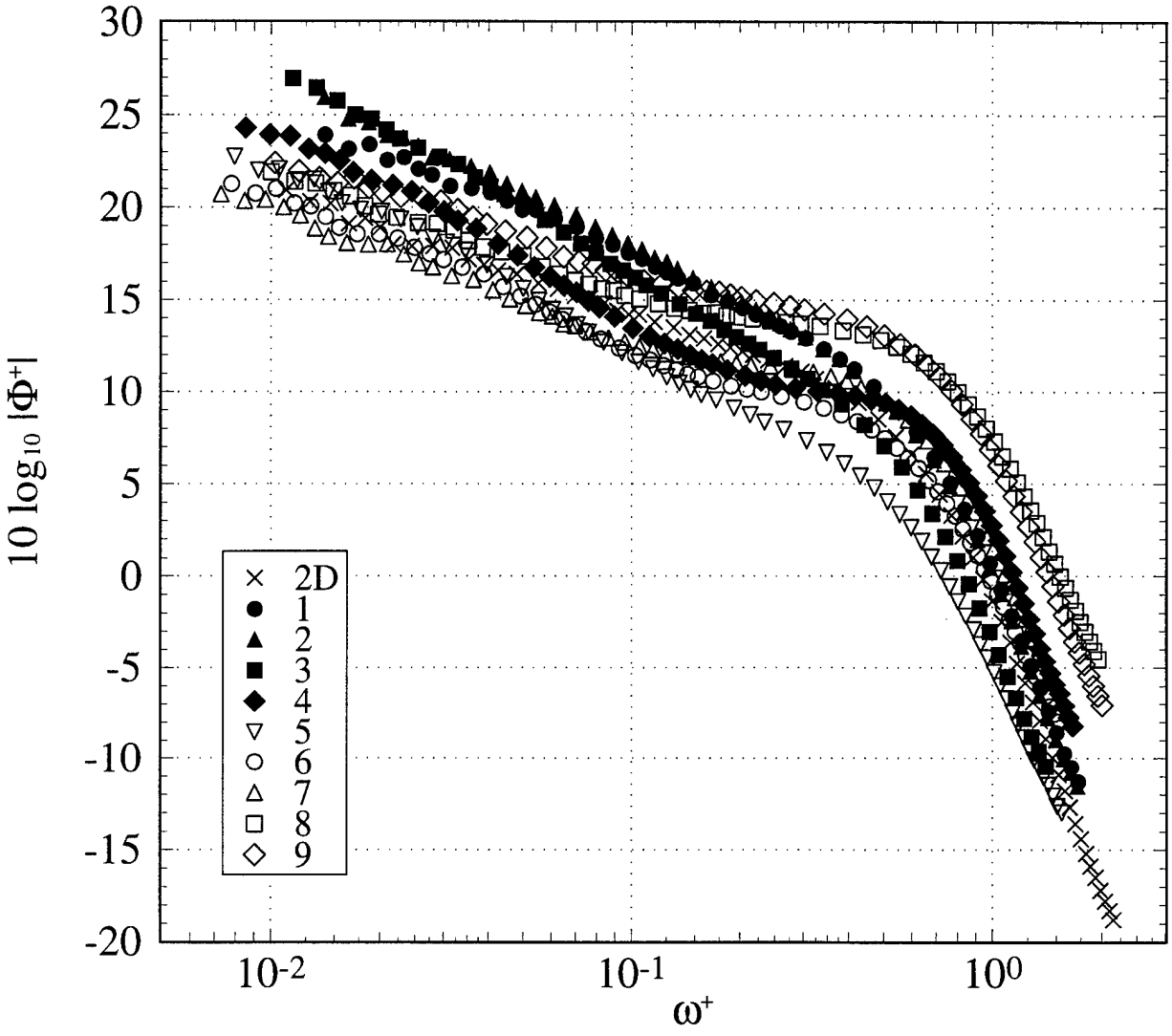

Figure 54. Spectral power density of p (Re_θ = 7300 (2-D); 5940 (3-D)) normalized using τ_W as the pressure scale and ν/u_τ^2 as the time scale. The numbers in the legend denote the measurement station.

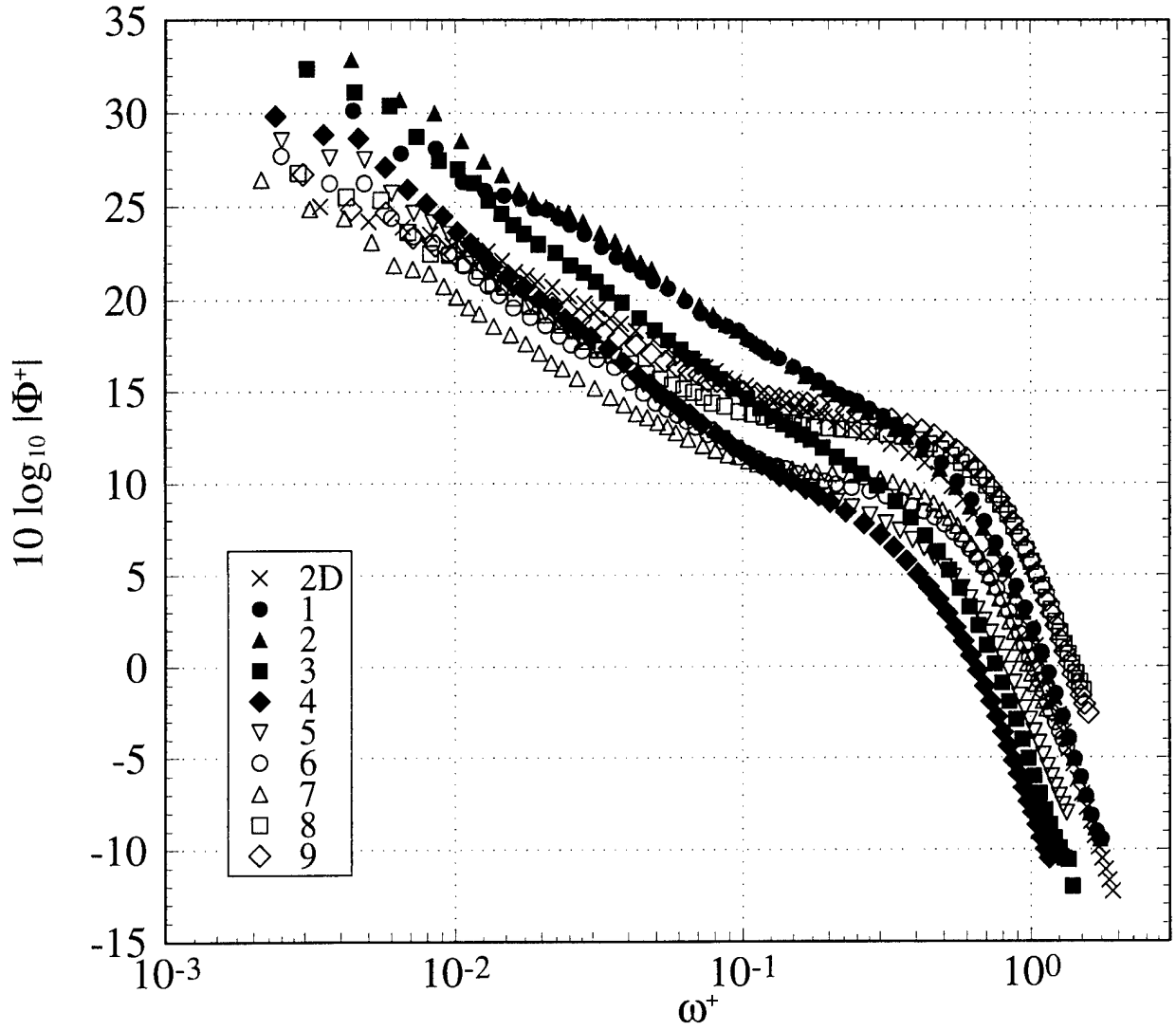

Figure 55. Spectral power density of p (Re_θ = 23400 (2-D); 23200 (3-D)) normalized using τ_W as the pressure scale and ν/u_τ^2 as the time scale. The numbers in the legend denote the measurement station.

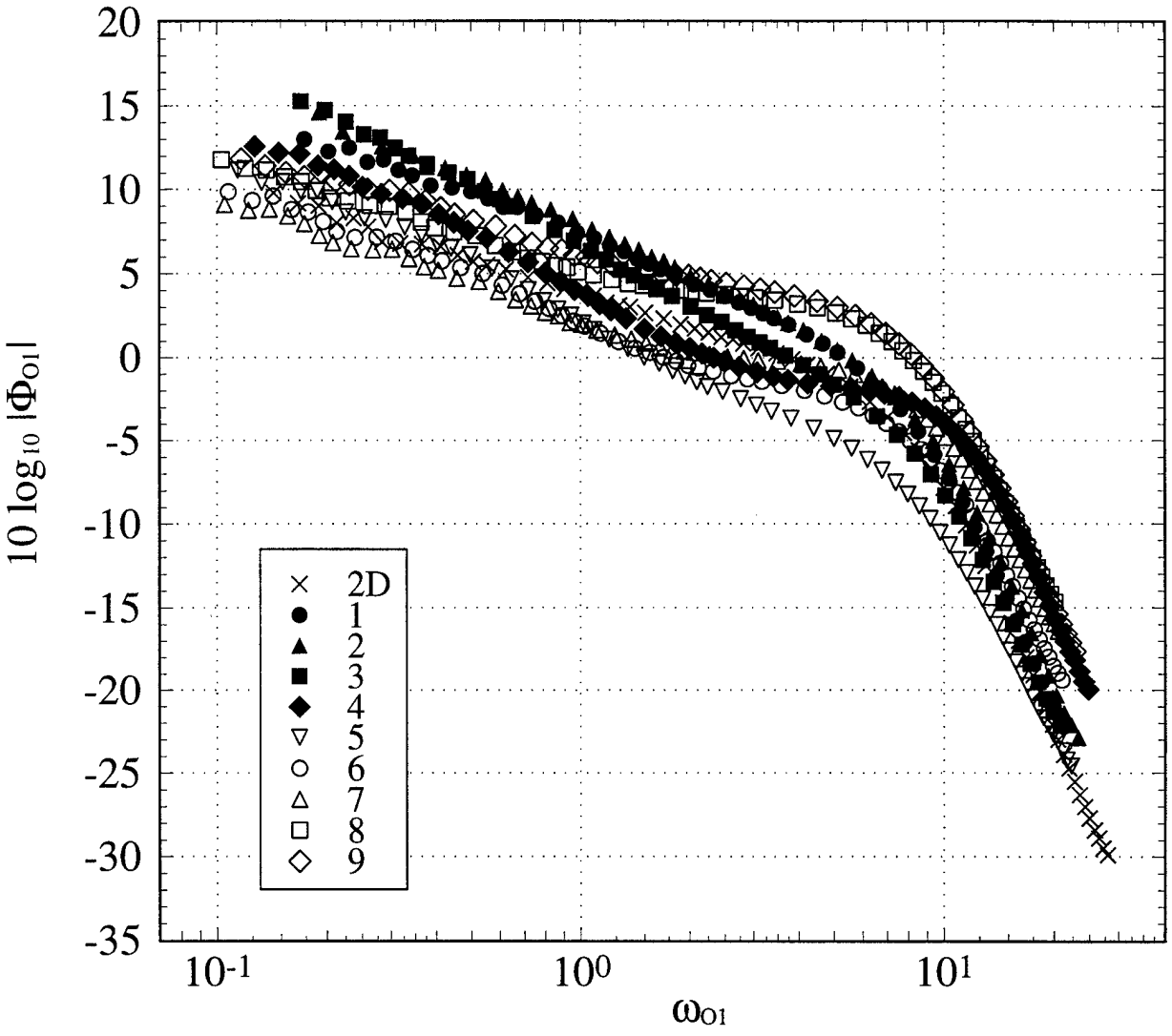

Figure 56. Spectral power density of p (Re_θ = 7300 (2-D); 5940 (3-D)) normalized using τ_W as the pressure scale and δ^*/U_e as the time scale. The numbers in the legend denote the measurement station.

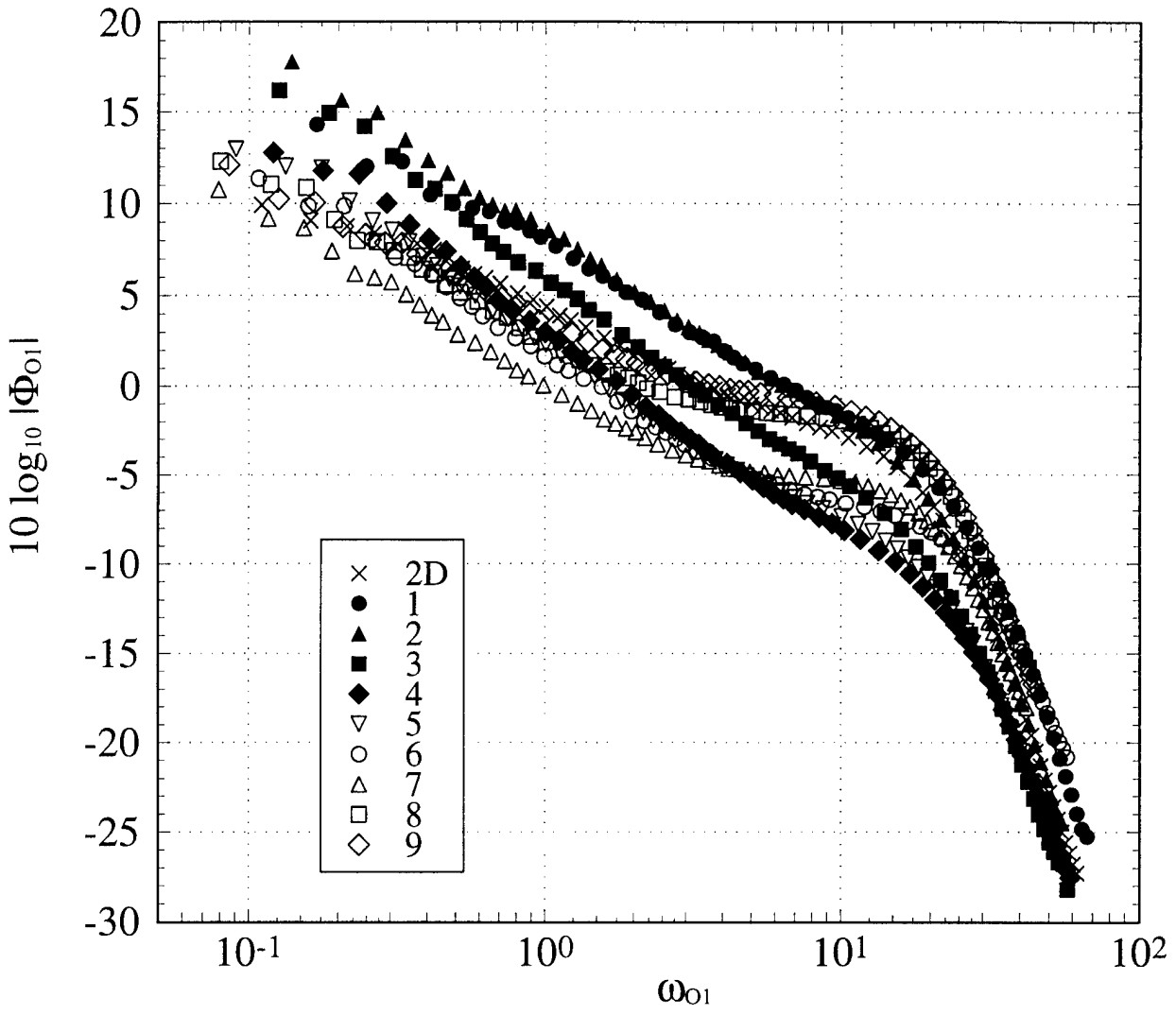

Figure 57. Spectral power density of p (Re_θ = 23400 (2-D); 23200 (3-D)) normalized using τ_W as the pressure scale and δ^*/U_e as the time scale. The numbers in the legend denote the measurement station.

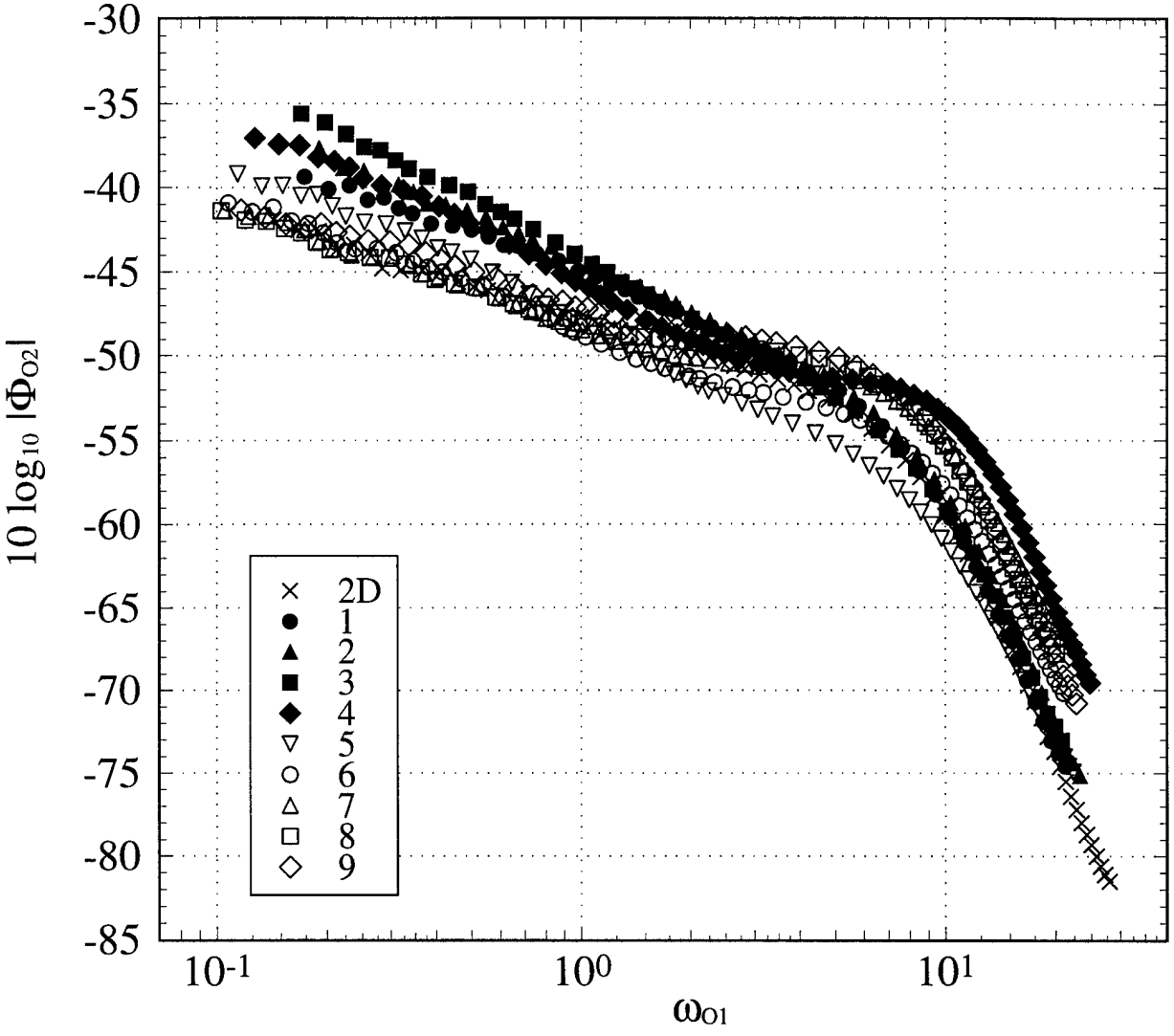

Figure 58. Spectral power density of p ($Re_\theta = 7300$ (2-D); 5940 (3-D)) normalized using Q_e as the pressure scale and δ^*/U_e as the time scale. The numbers in the legend denote the measurement station.

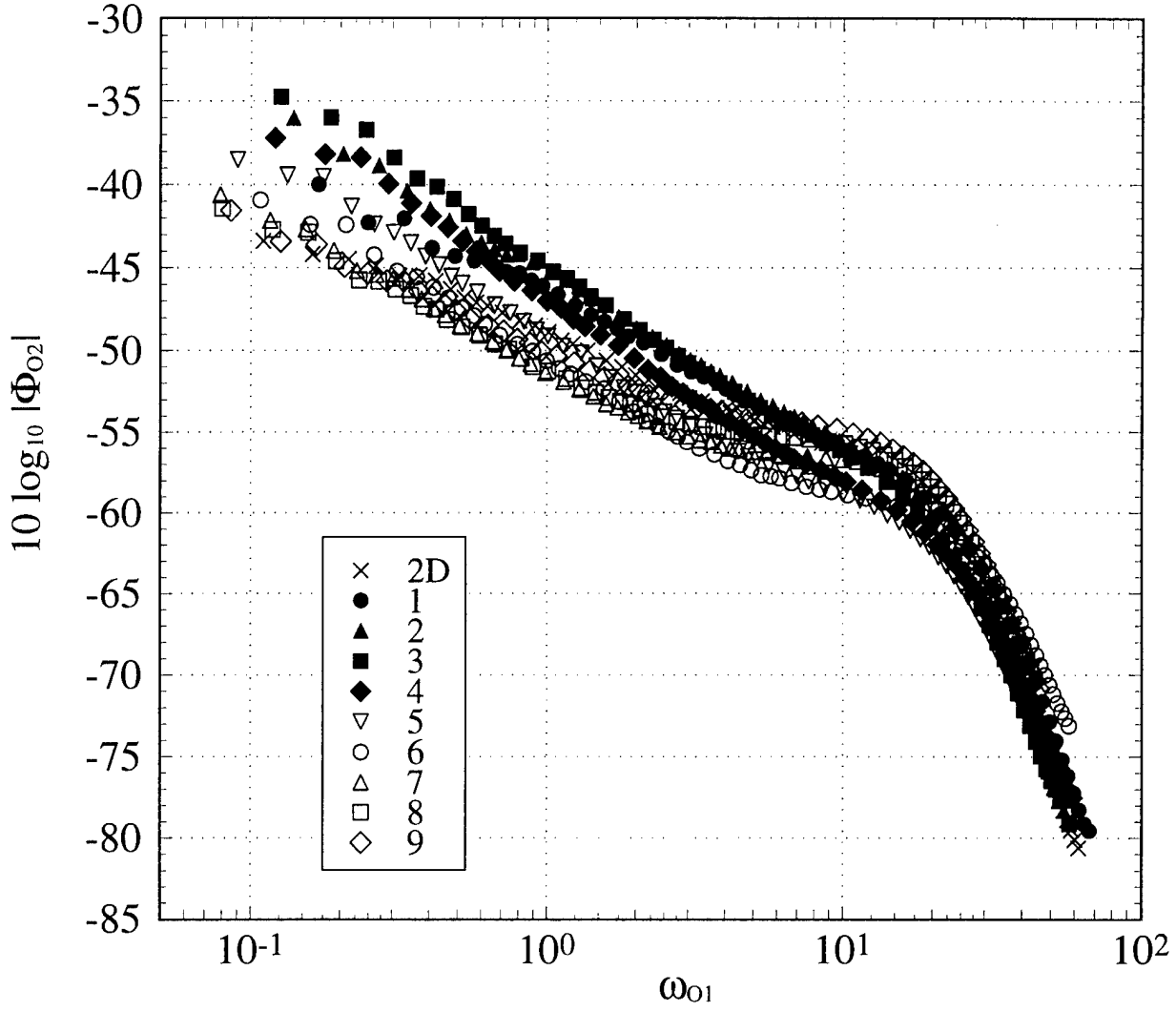

Figure 59. Spectral power density of p (Re_θ = 23400 (2-D); 23200 (3-D)) normalized using Q_e as the pressure scale and δ^*/U_e as the time scale. The numbers in the legend denote the measurement station.

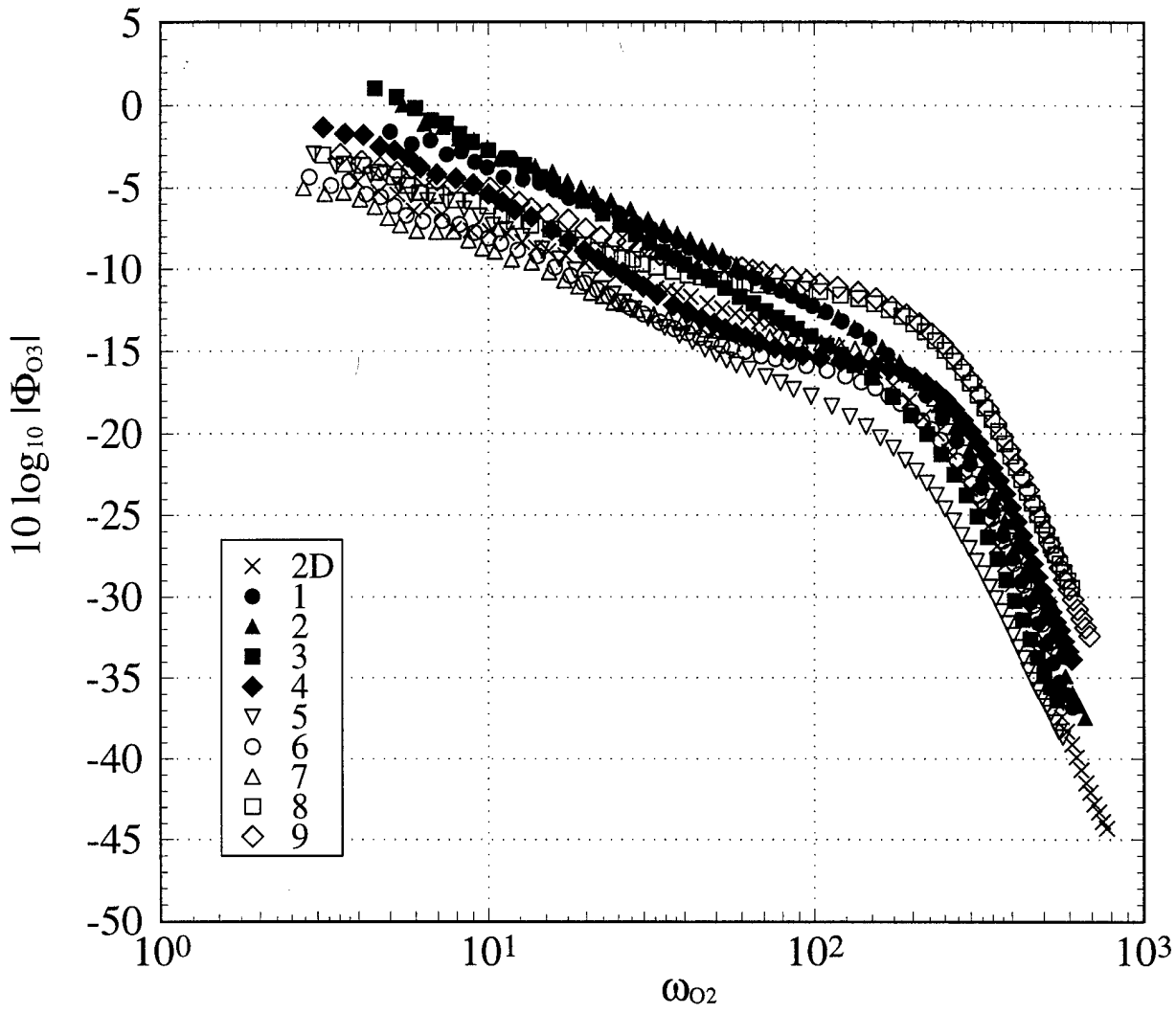

Figure 60. Spectral power density of p (Re_θ = 7300 (2-D); 5940 (3-D)) normalized using τ_W as the pressure scale and δ^* / u_τ as the time scale. The numbers in the legend denote the measurement station.

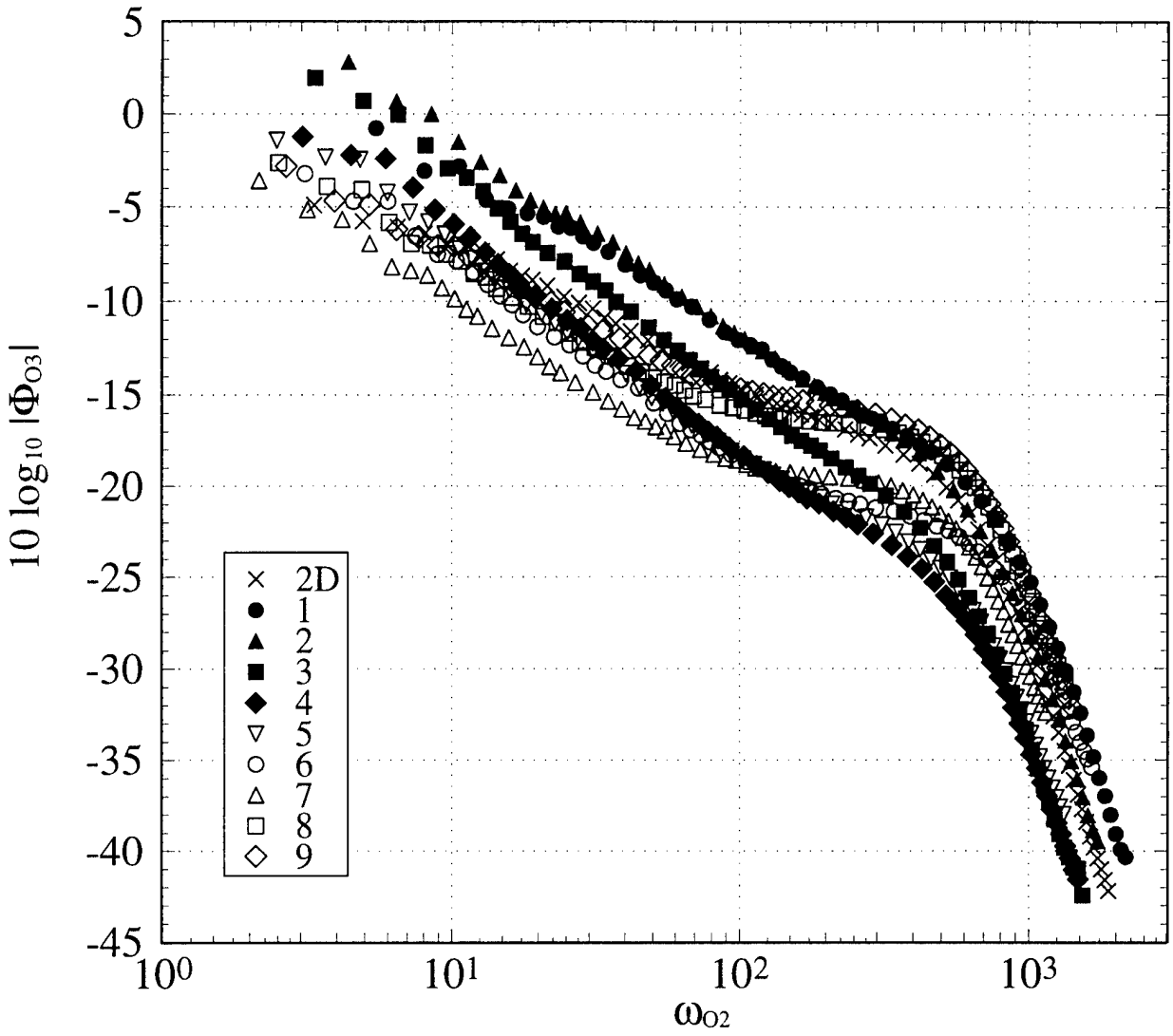

Figure 61. Spectral power density of p (Re_θ = 23400 (2-D); 23200 (3-D)) normalized using τ_w as the pressure scale and δ^*/u_τ as the time scale. The numbers in the legend denote the measurement station.

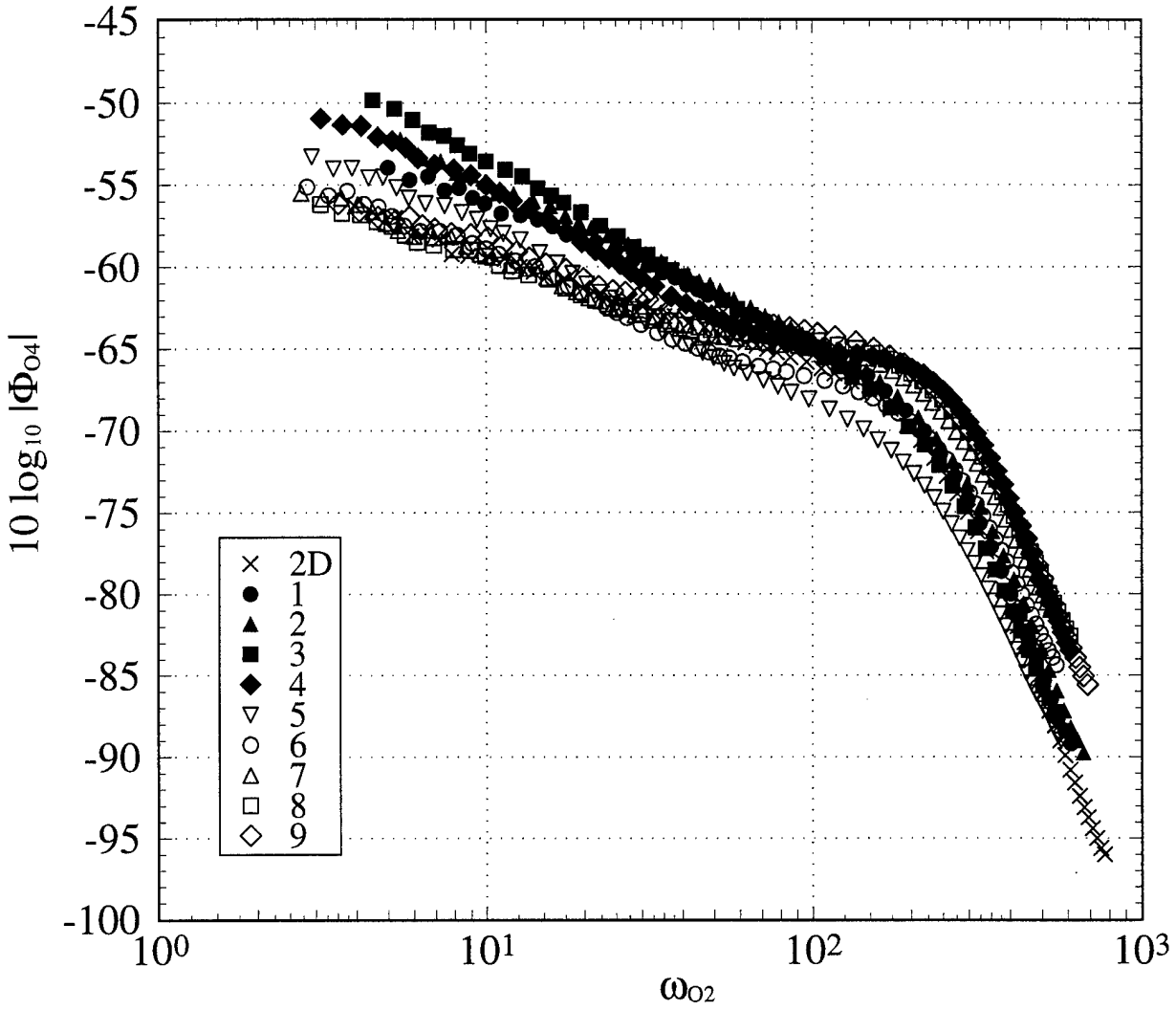

Figure 62. Spectral power density of p (Re_θ= 7300 (2-D); 5940 (3-D)) normalized using Q_e as the pressure scale and δ^*/u_τ as the time scale. The numbers in the legend denote the measurement station.

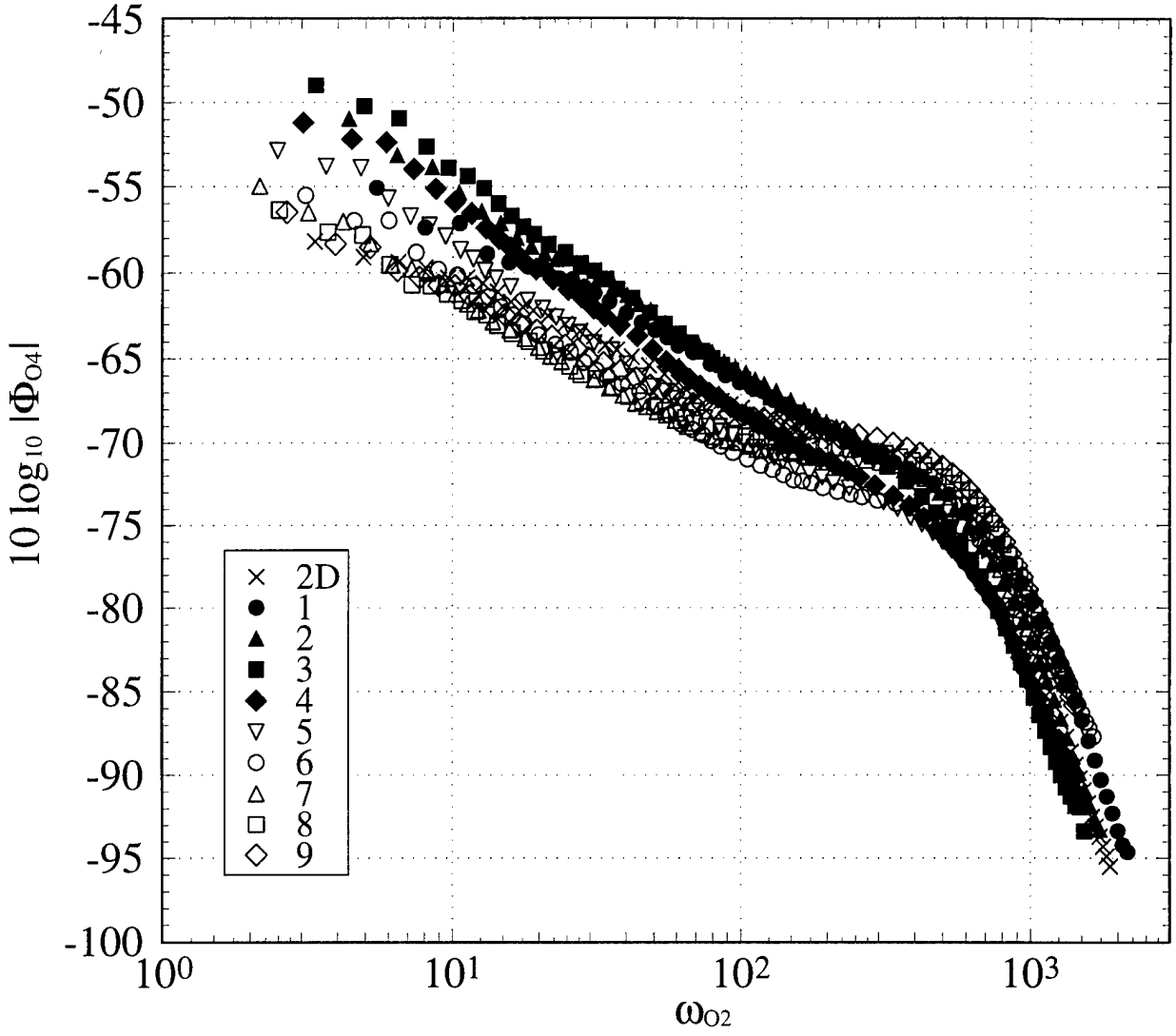

Figure 63. Spectral power density of p (Re_θ = 23400 (2-D); 23200 (3-D)) normalized using Q_e as the pressure scale and δ^* / u_τ as the time scale. The numbers in the legend denote the measurement station.

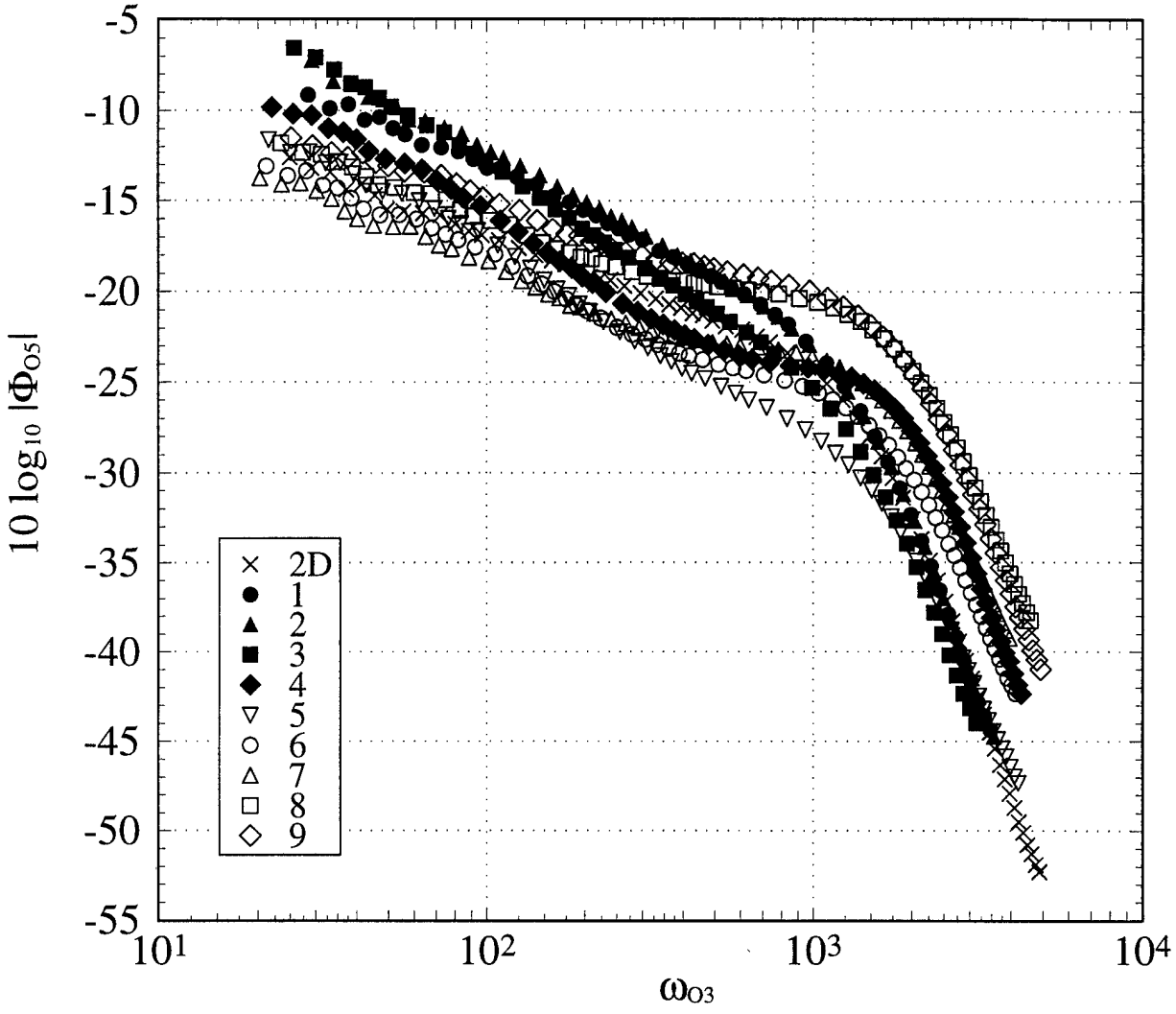

Figure 64. Spectral power density of p (Re_θ= 7300 (2-D); 5940 (3-D)) normalized using τ_w as the pressure scale and δ / u_τ as the time scale. The numbers in the legend denote the measurement station.

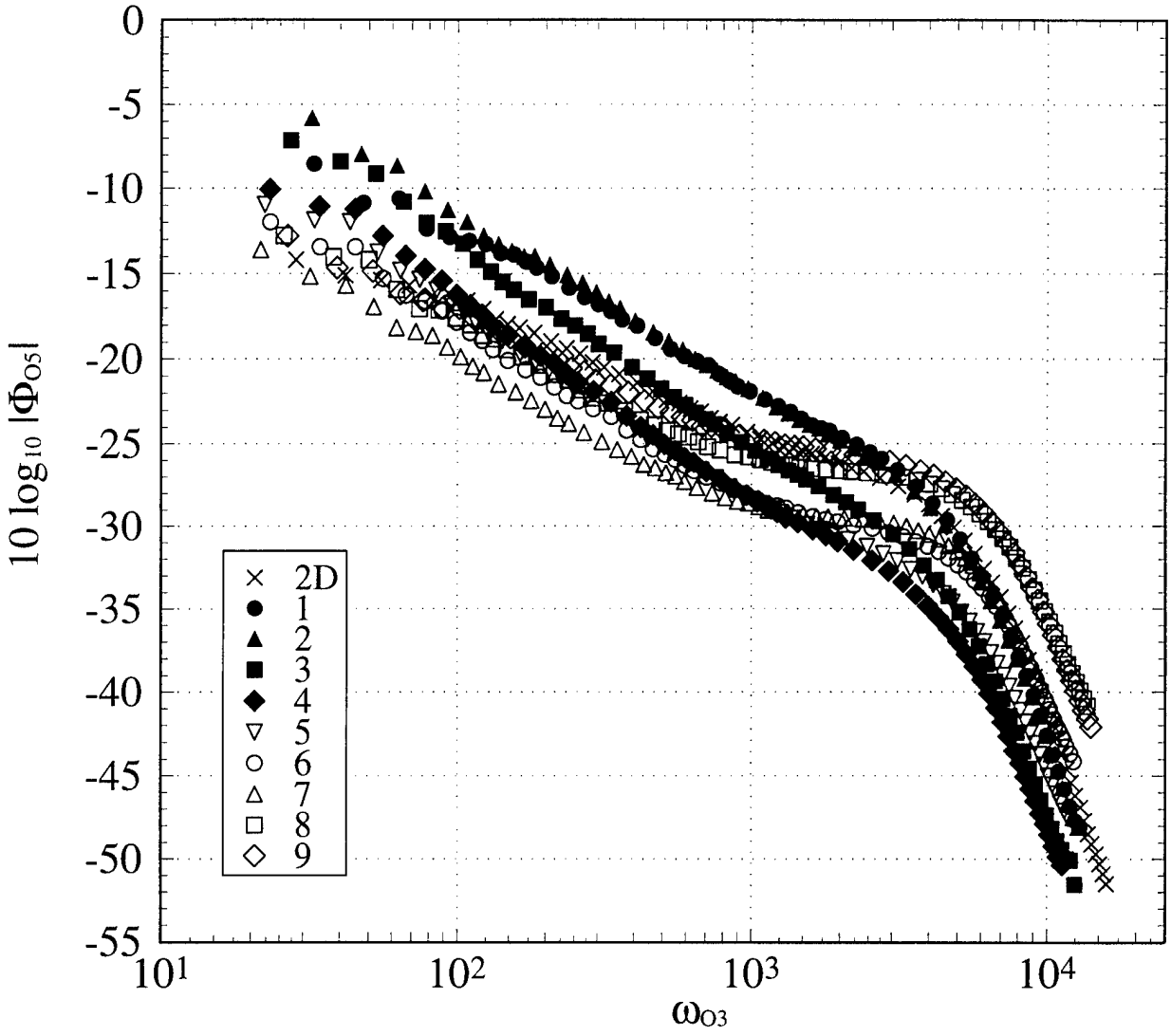

Figure 65. Spectral power density of p (Re_θ = 23400 (2-D); 23200 (3-D)) normalized using τ_W as the pressure scale and δ / u_τ as the time scale. The numbers in the legend denote the measurement station.

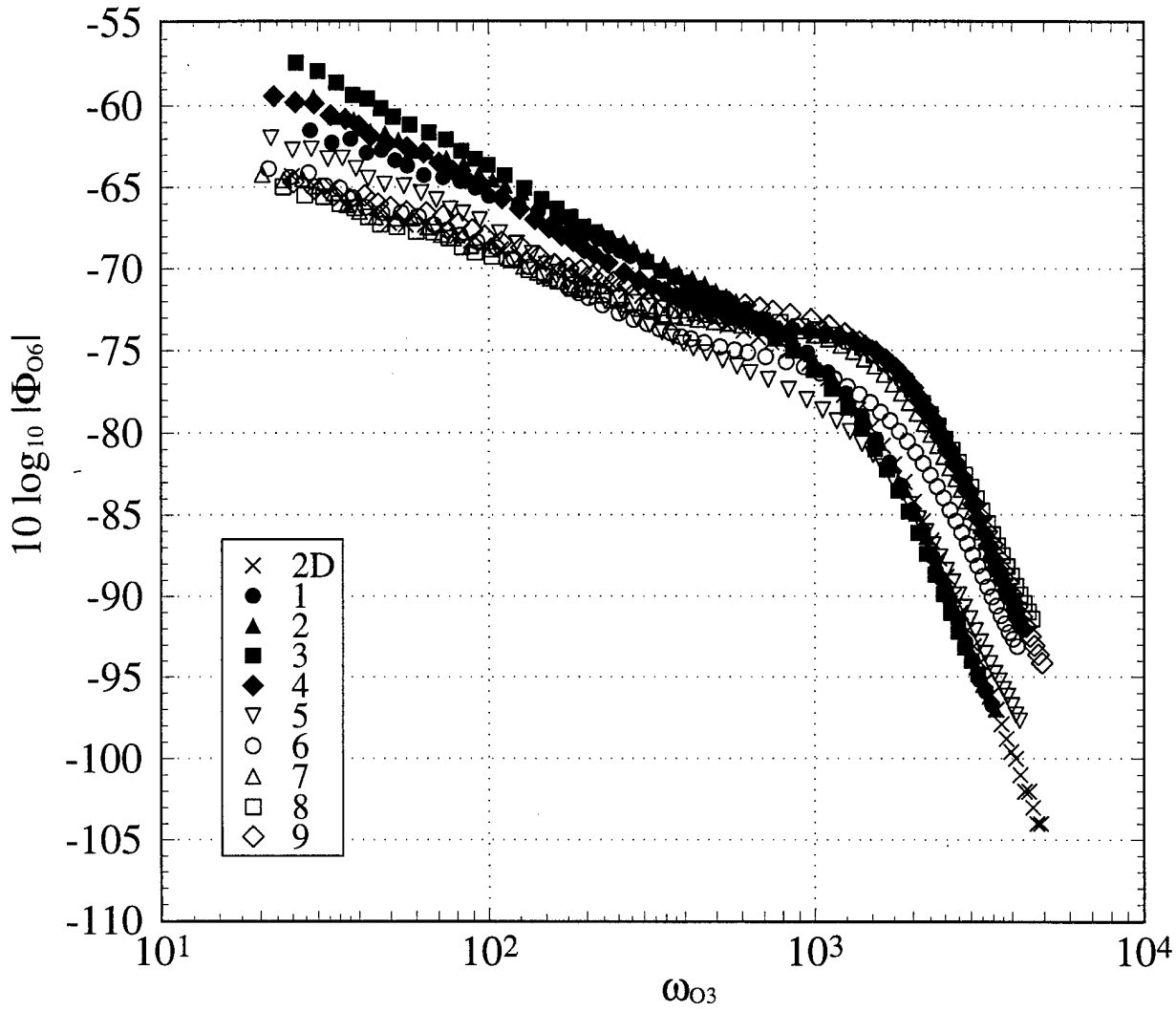

Figure 66. Spectral power density of p ($Re_\theta = 7300$ (2-D); 5940 (3-D)) normalized using Q_e as the pressure scale and δ / u_τ as the time scale. The numbers in the legend denote the measurement station.

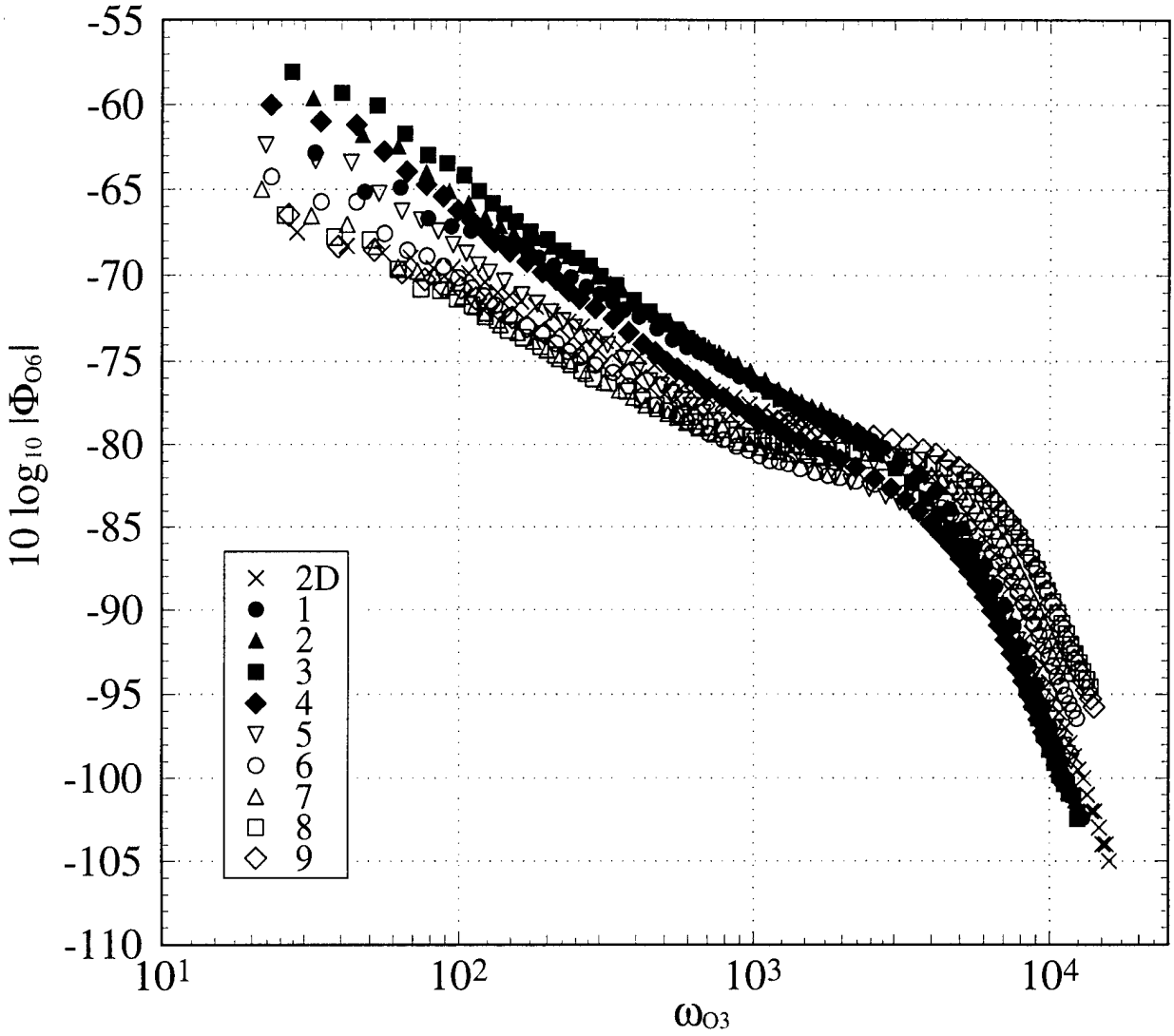

Figure 67. Spectral power density of p (Re_θ= 23400 (2-D); 23200 (3-D)) normalized using Q_e as the pressure scale and δ / u_τ as the time scale. The numbers in the legend denote the measurement station.

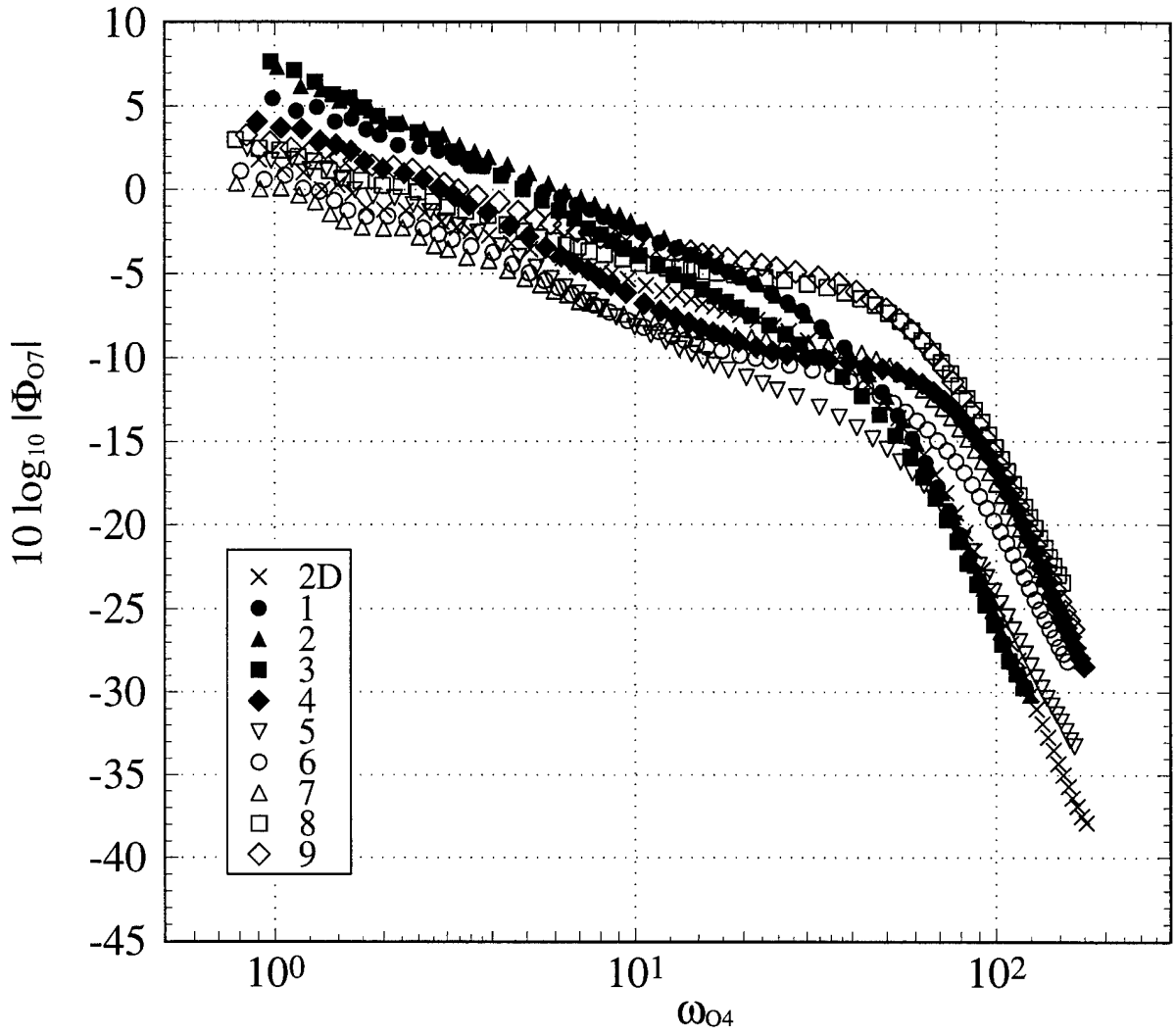

Figure 68. Spectral power density of p ($Re_\theta = 7300$ (2-D); 5940 (3-D)) normalized using τ_W as the pressure scale and δ / U_e as the time scale. The numbers in the legend denote the measurement station.

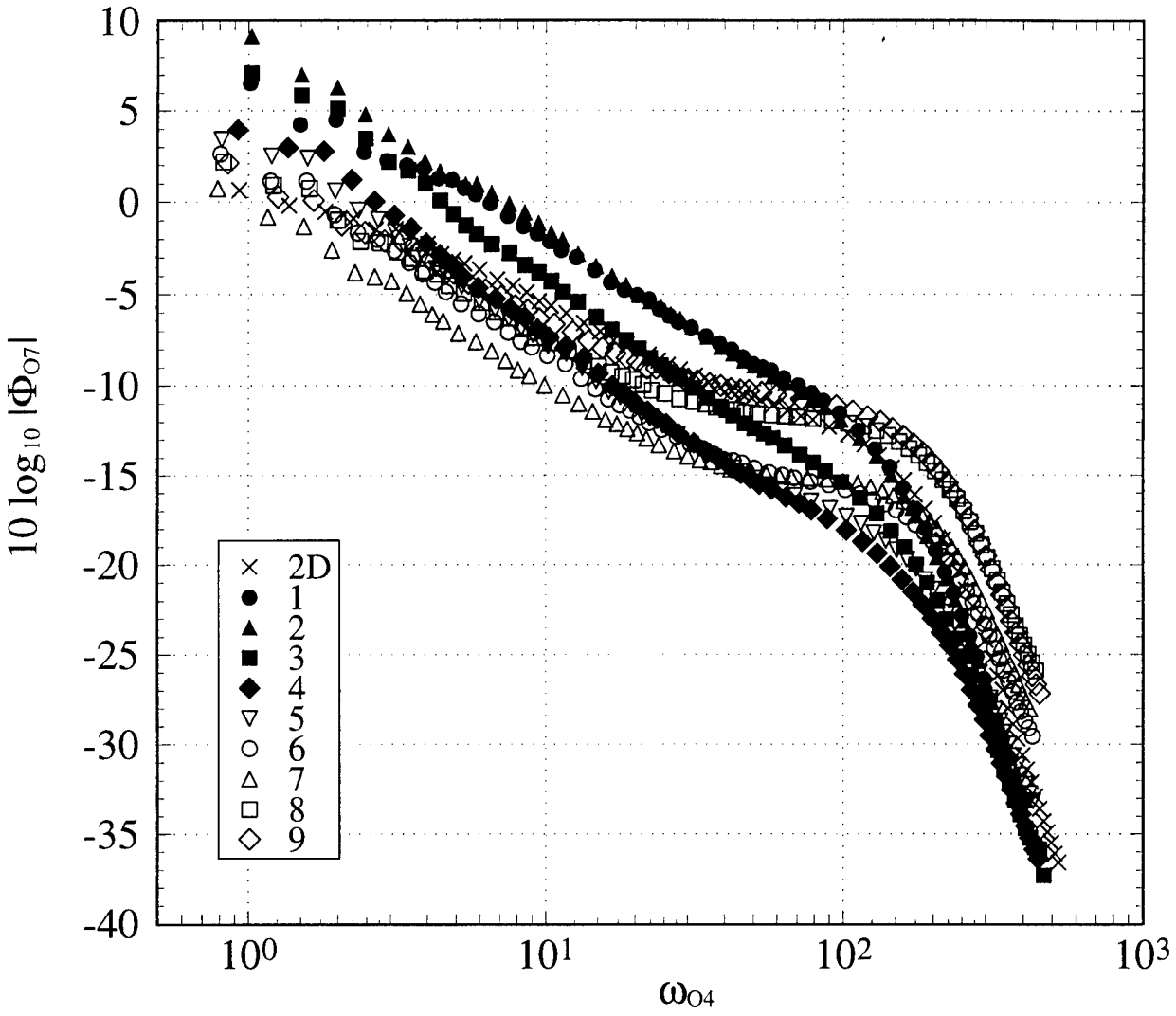

Figure 69. Spectral power density of p (Re_θ= 23400 (2-D); 23200 (3-D)) normalized using τ_W as the pressure scale and δ / U_e as the time scale. The numbers in the legend denote the measurement station.

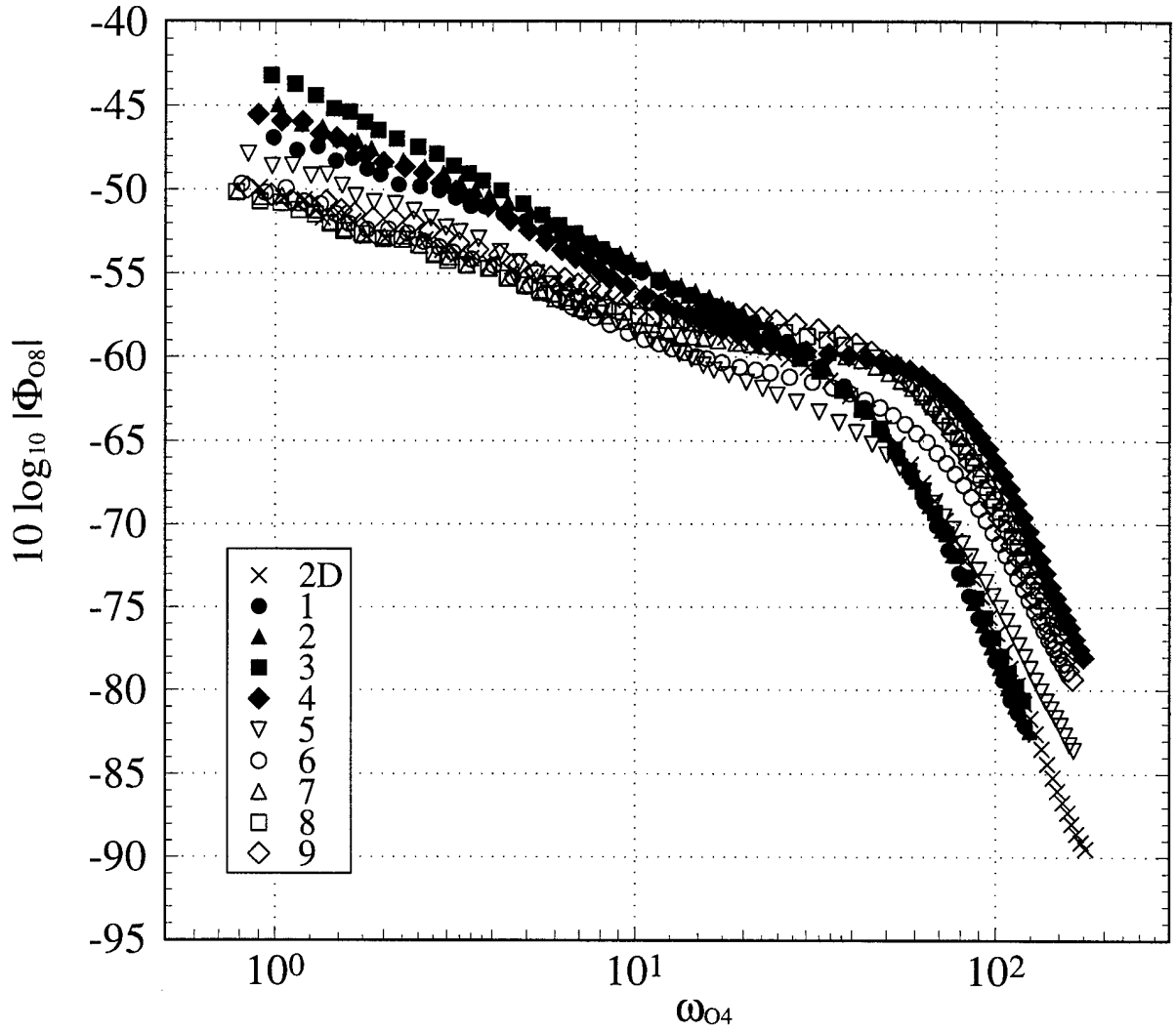

Figure 70. Spectral power density of p ($Re_\theta = 7300$ (2-D); 5940 (3-D)) normalized using Q_e as the pressure scale and δ / U_e as the time scale. The numbers in the legend denote the measurement station.

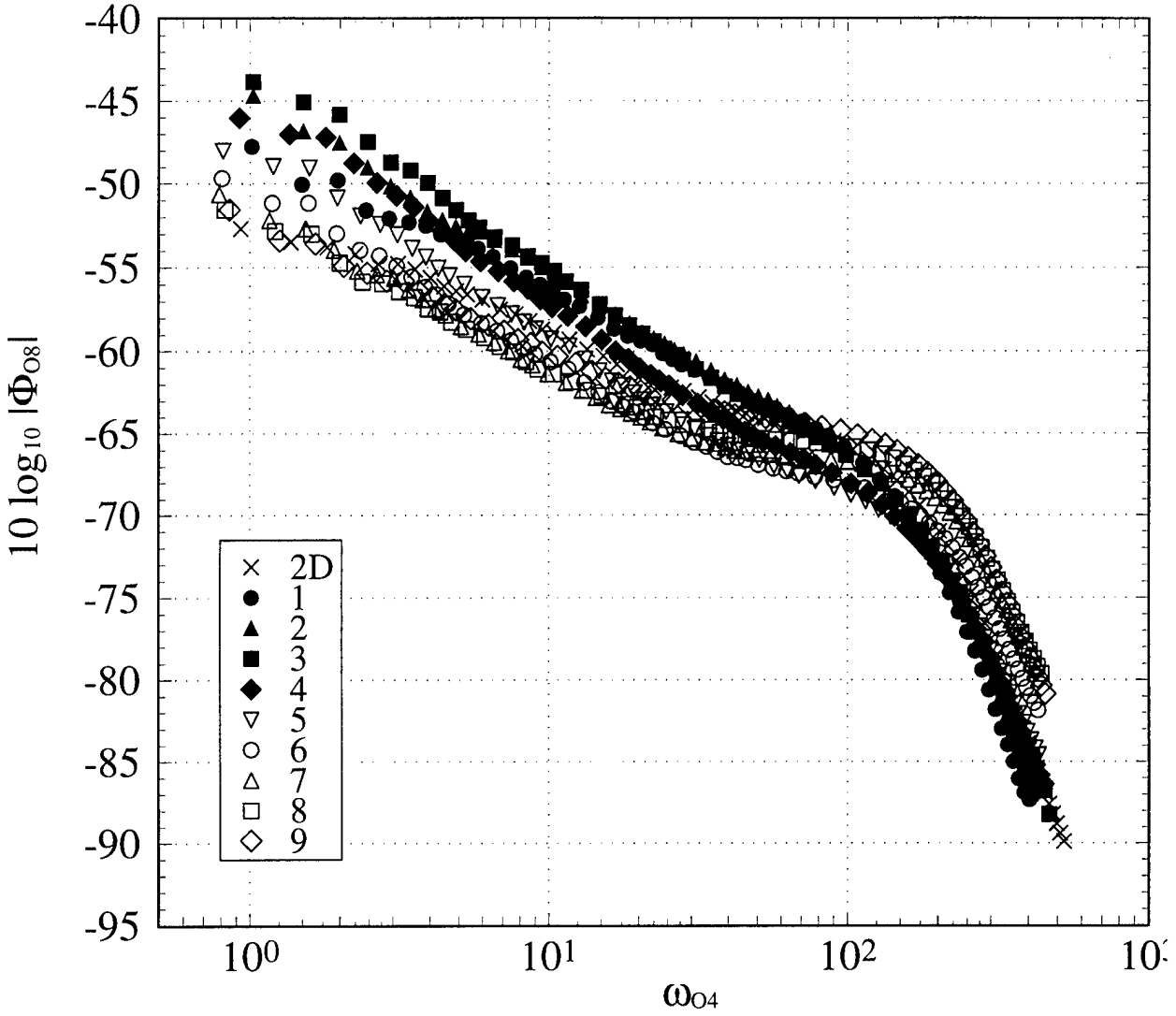

Figure 71. Spectral power density of p (Re_θ = 23400 (2-D); 23200 (3-D)) normalized using Q_e as the pressure scale and δ / U_e as the time scale. The numbers in the legend denote the measurement station.

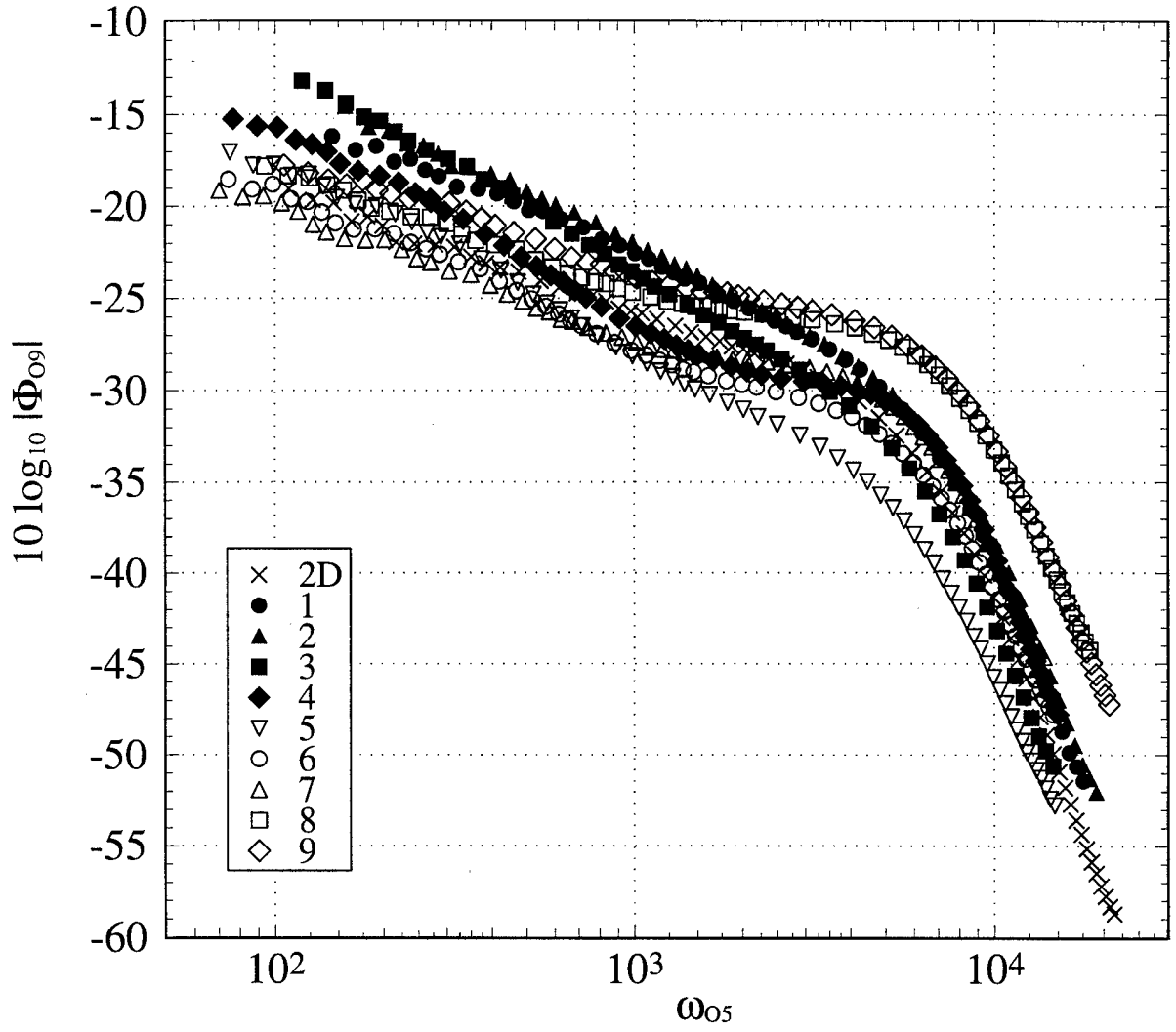

Figure 72. Spectral power density of p (Re_θ= 7300 (2-D); 5940 (3-D)) normalized using τ_W as the pressure scale and Δ / u_τ as the time scale. The numbers in the legend denote the measurement station.

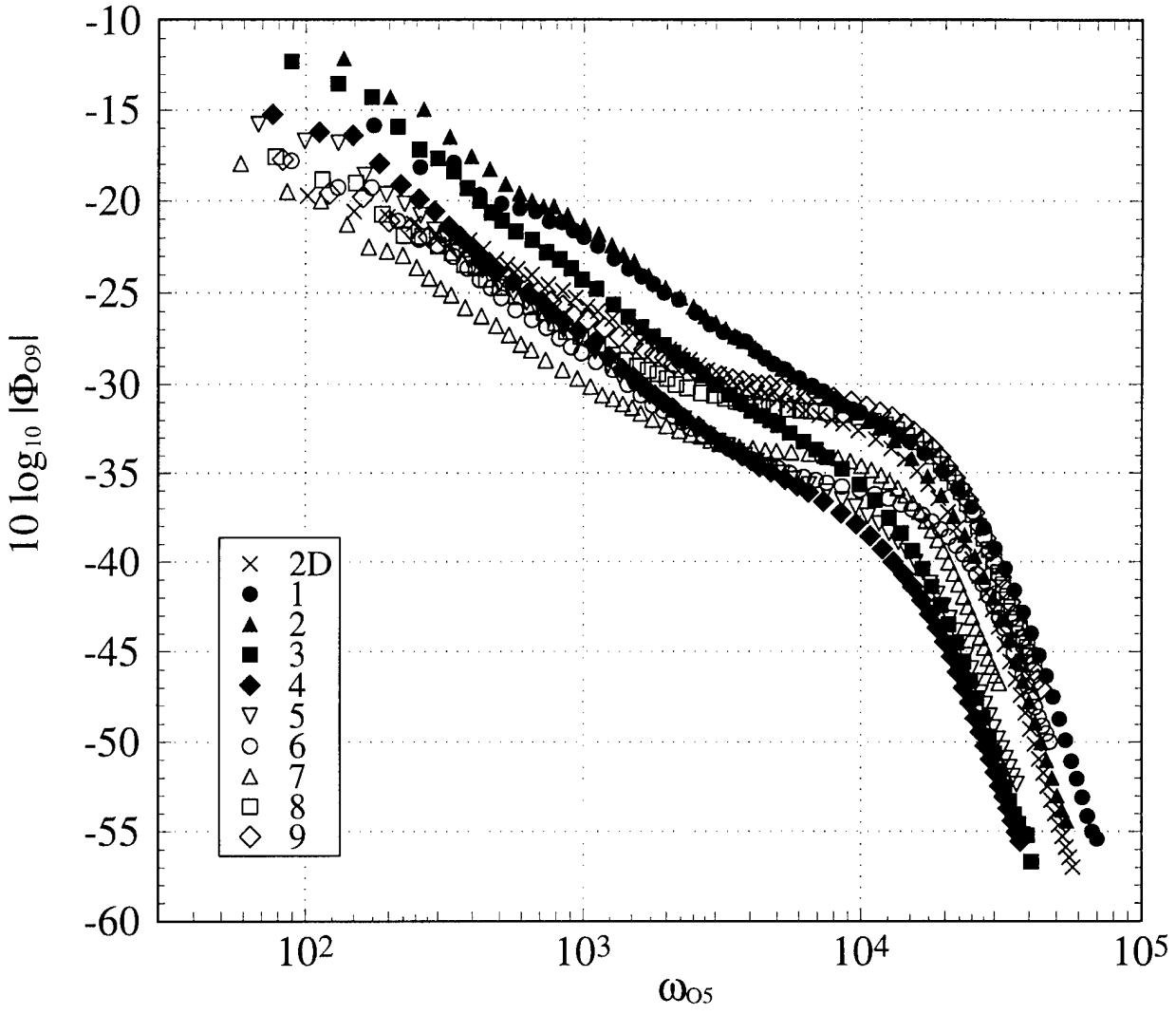

Figure 73. Spectral power density of p (Re_θ = 23400 (2-D); 23200 (3-D)) normalized using τ_w as the pressure scale and Δ / u_τ as the time scale. The numbers in the legend denote the measurement station.

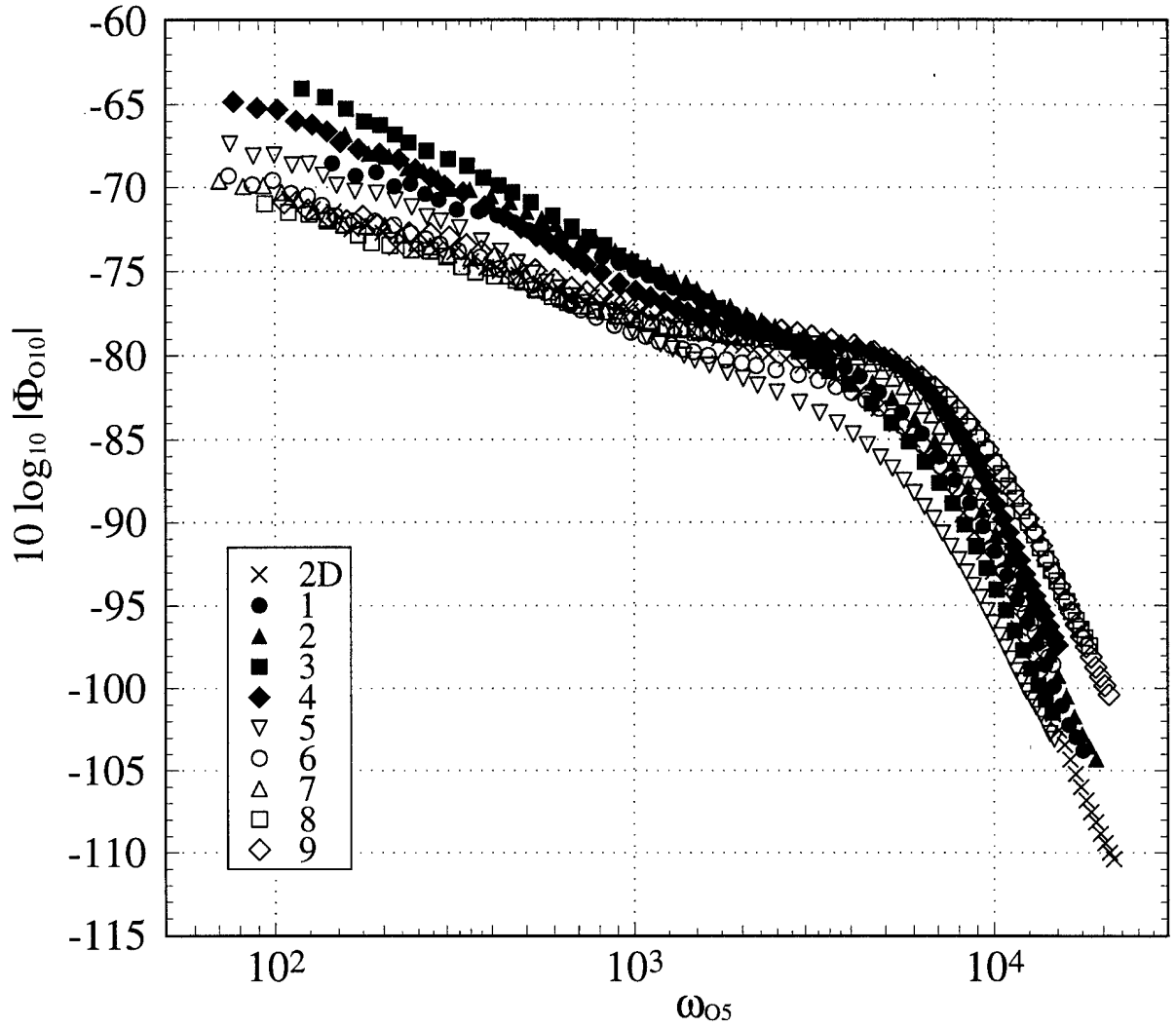

Figure 74. Spectral power density of p (Re_θ = 7300 (2-D); 5940 (3-D)) normalized using Q_e as the pressure scale and Δ / u_τ as the time scale. The numbers in the legend denote the measurement station.

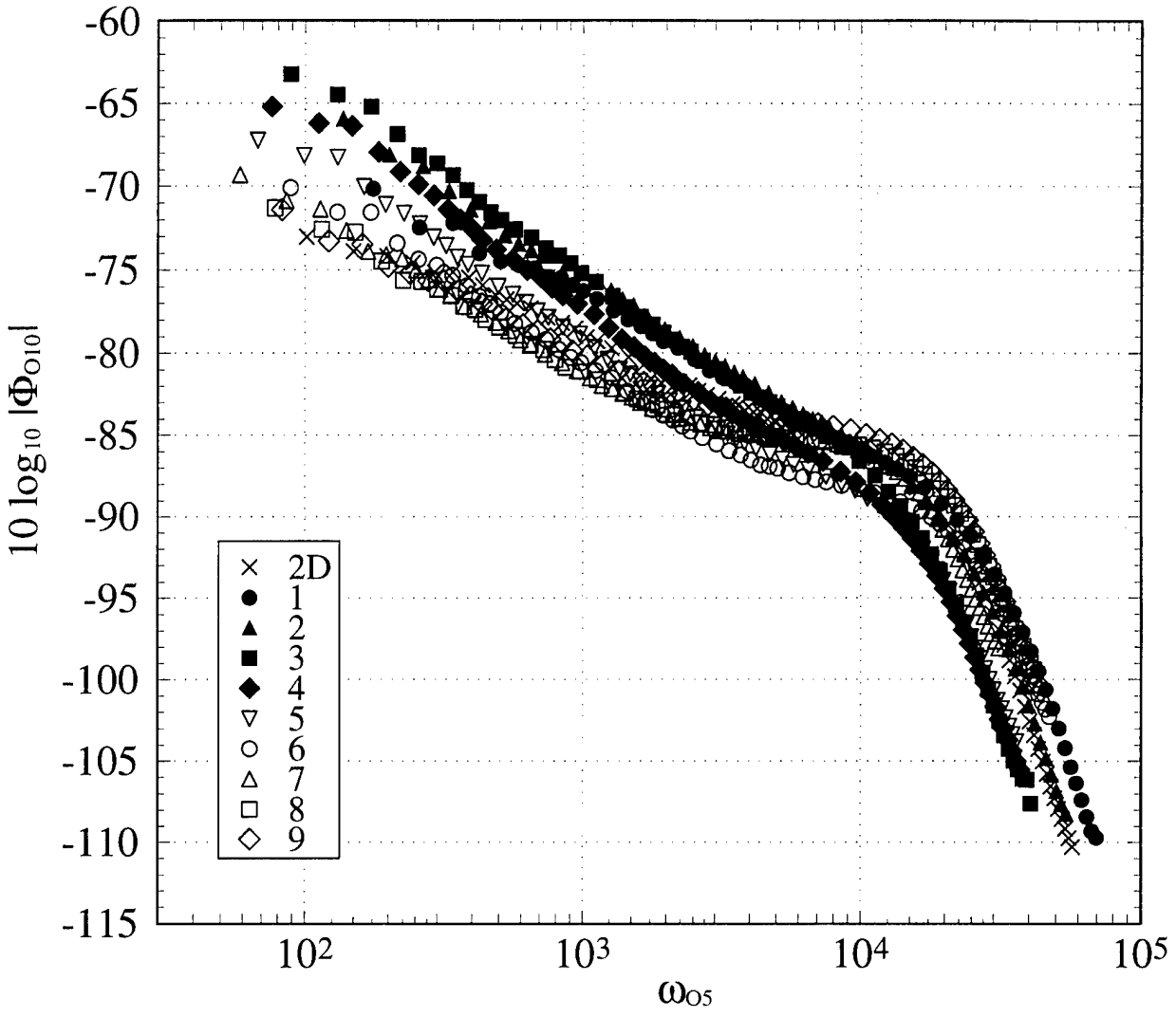

Figure 75. Spectral power density of p (Re_θ = 23400 (2-D); 23200 (3-D)) normalized using Q_e as the pressure scale and Δ / u_τ as the time scale. The numbers in the legend denote the measurement station.

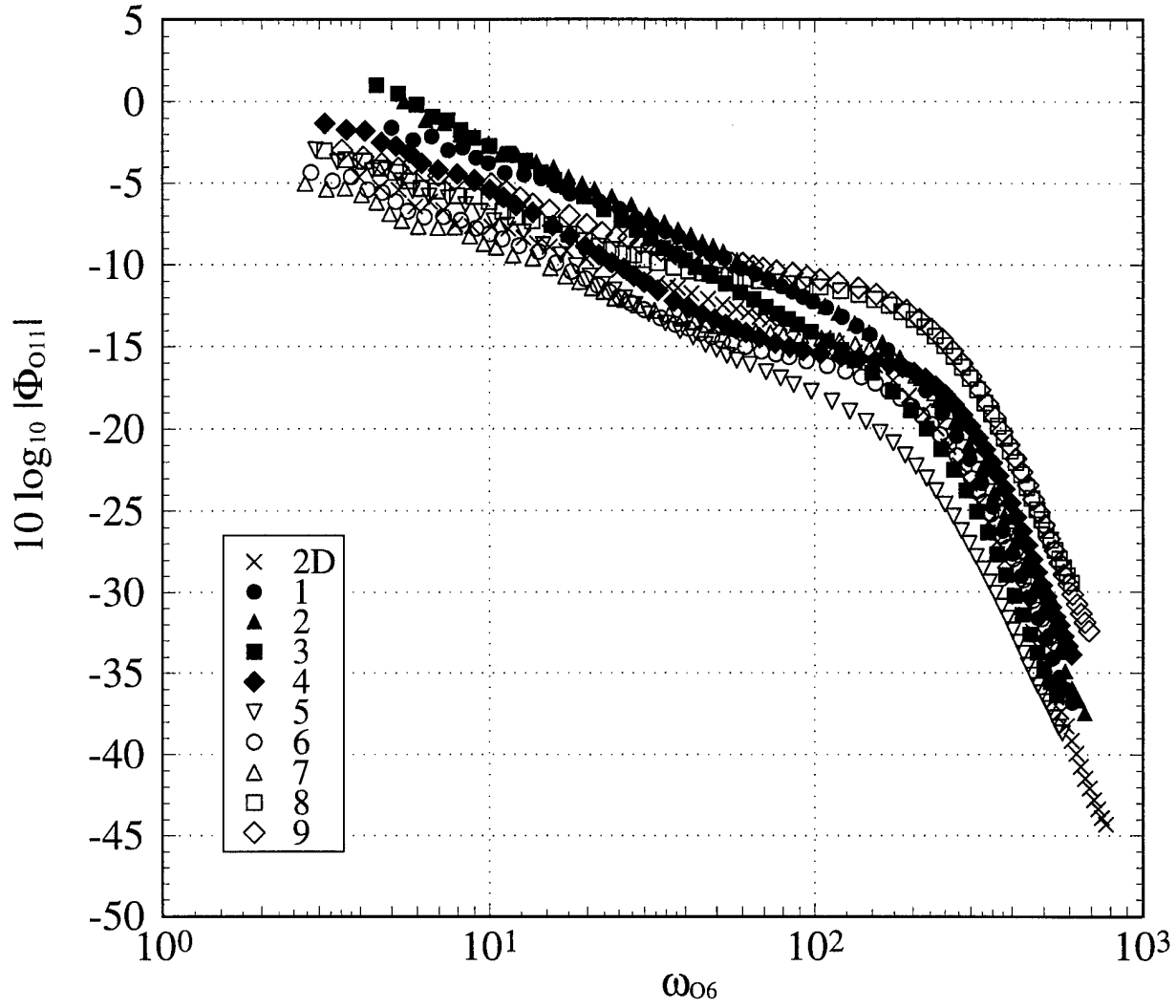

Figure 76. Spectral power density of p (Re_θ = 7300 (2-D); 5940 (3-D)) normalized using τ_W as the pressure scale and Δ / U_e as the time scale. The numbers in the legend denote the measurement station.

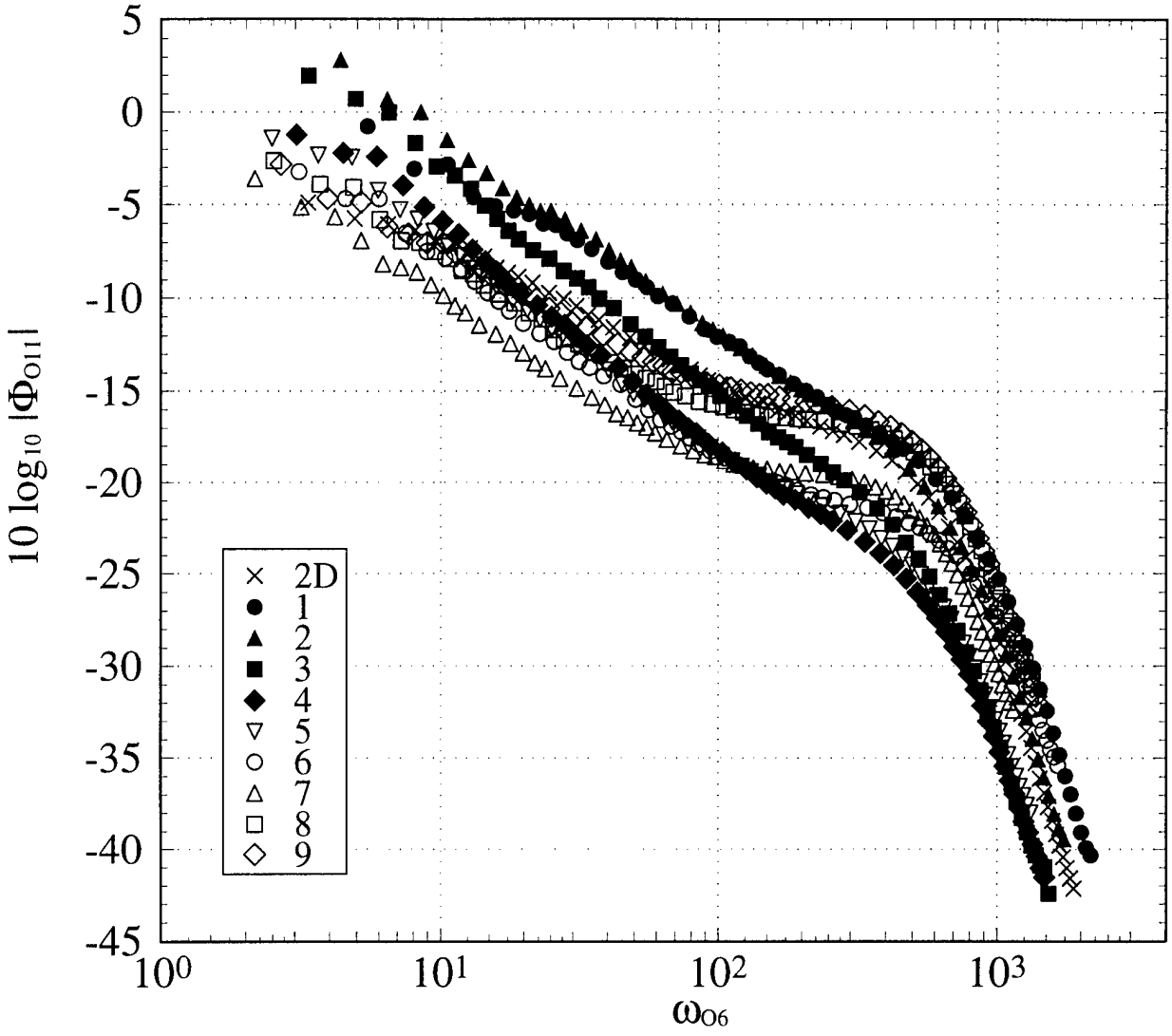

Figure 77. Spectral power density of p (Re_θ = 23400 (2-D); 23200 (3-D)) normalized using τ_W as the pressure scale and Δ / U_e as the time scale. The numbers in the legend denote the measurement station.

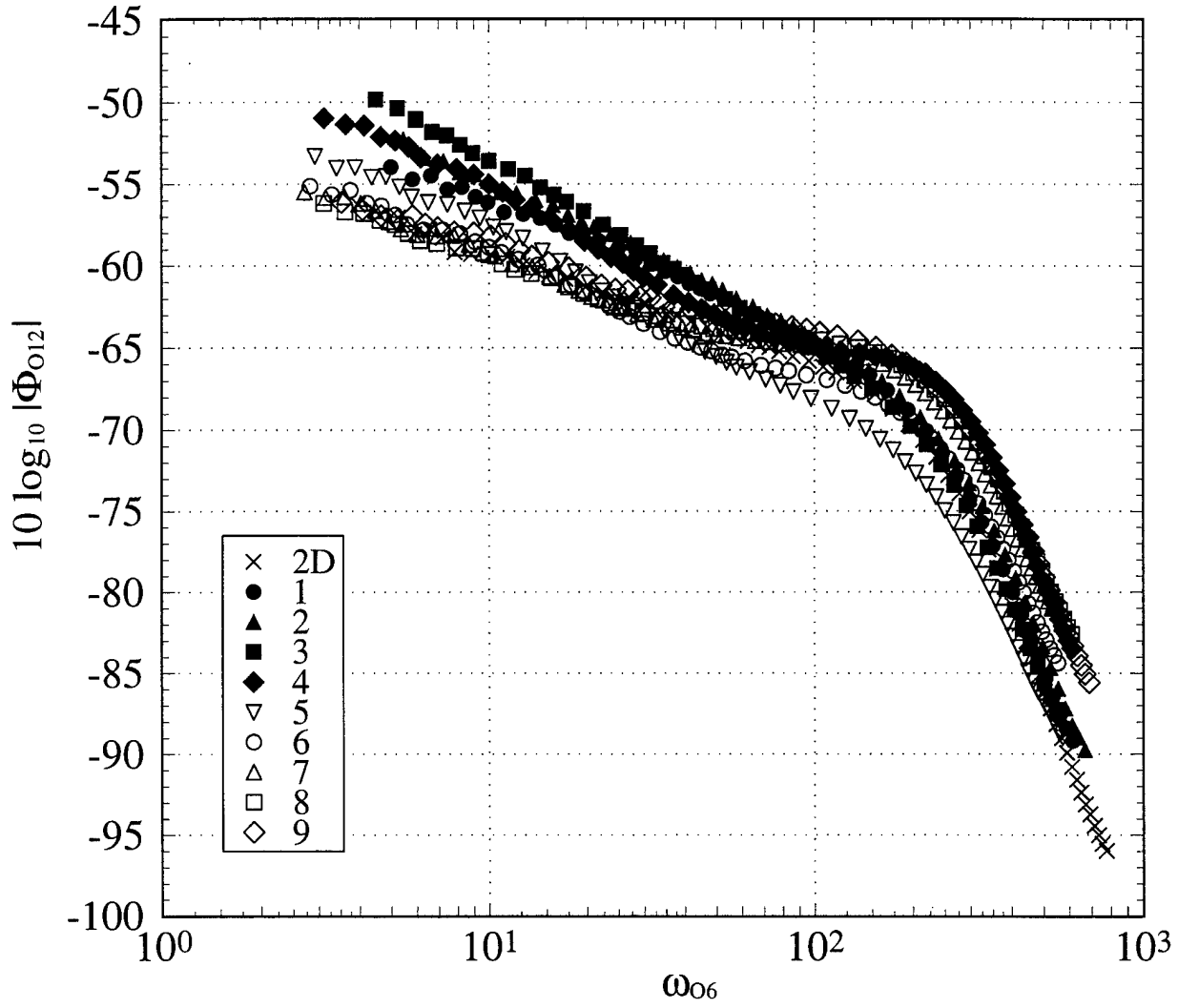

Figure 78. Spectral power density of p (Re_θ = 7300 (2-D); 5940 (3-D)) normalized using Q_e as the pressure scale and Δ / U_e as the time scale. The numbers in the legend denote the measurement station.

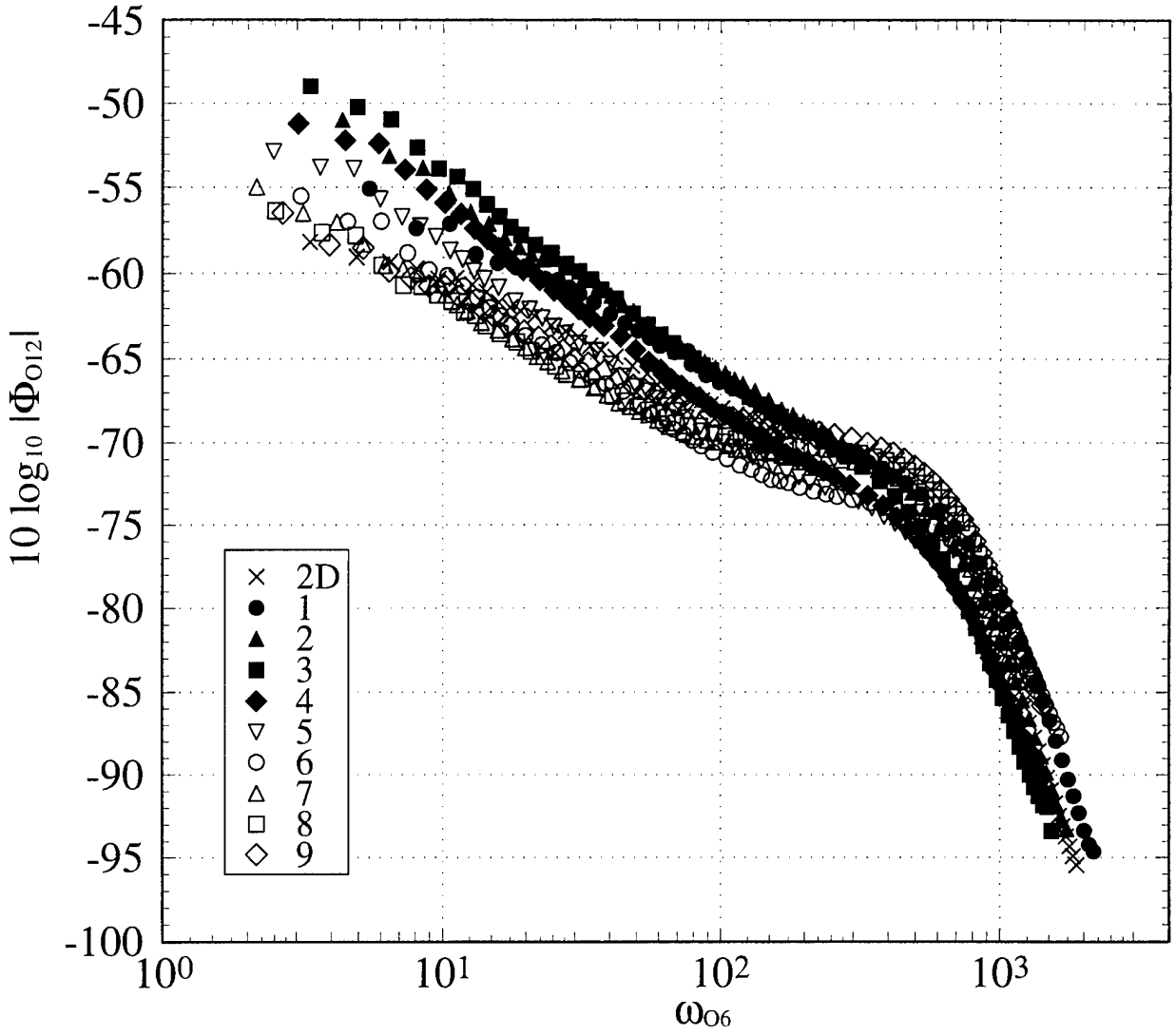

Figure 79. Spectral power density of p (Re_θ = 23400 (2-D); 23200 (3-D)) normalized using Q_e as the pressure scale and Δ / U_e as the time scale. The numbers in the legend denote the measurement station.

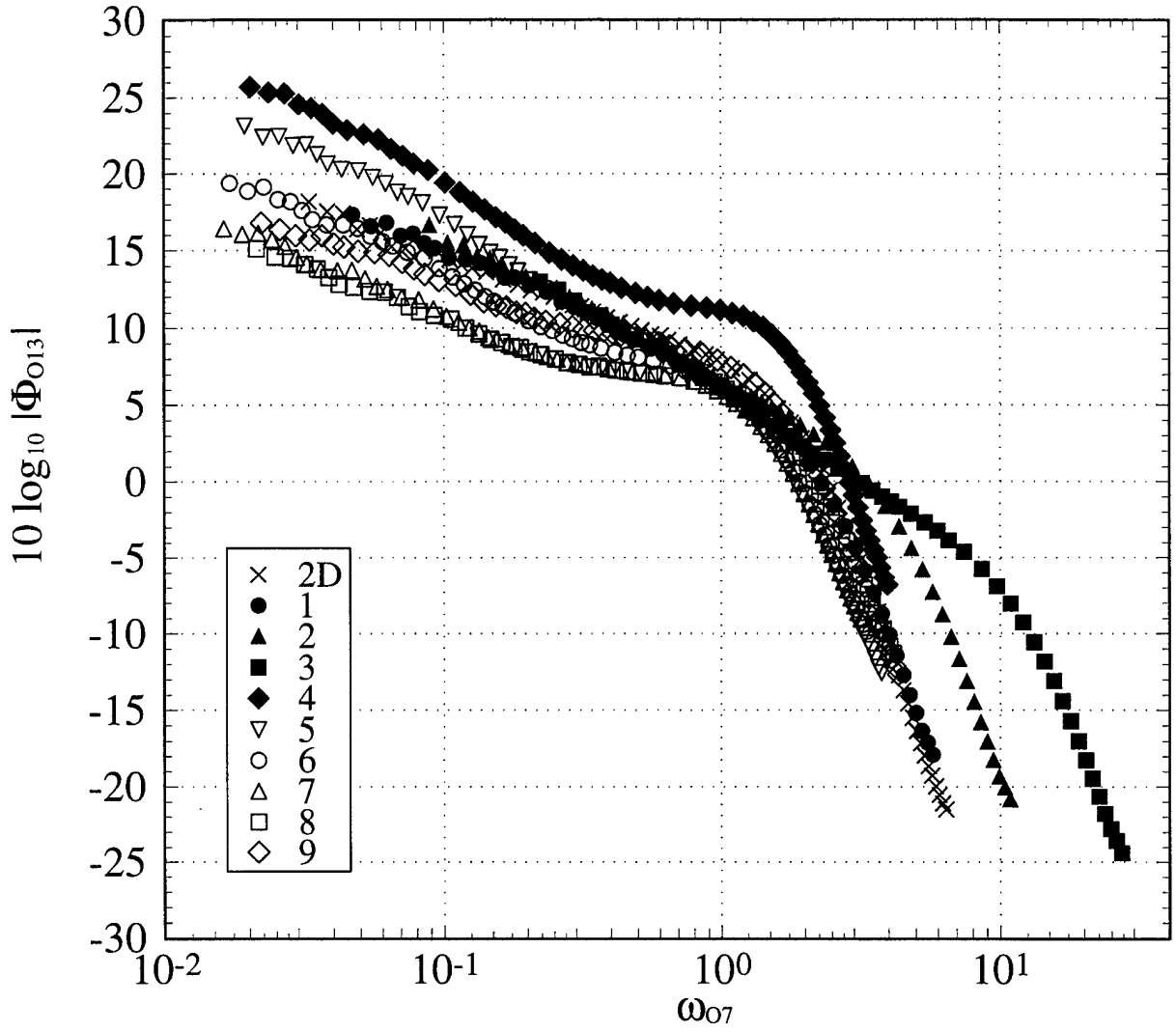

Figure 80. Spectral power density of p (Re_θ = 7300 (2-D); 5940 (3-D)) normalized using τ_{MAX} as the pressure scale and $y / (U^2+W^2)^{1/2}$ at the y location of τ_{MAX} as the time scale. The numbers in the legend denote the measurement station.

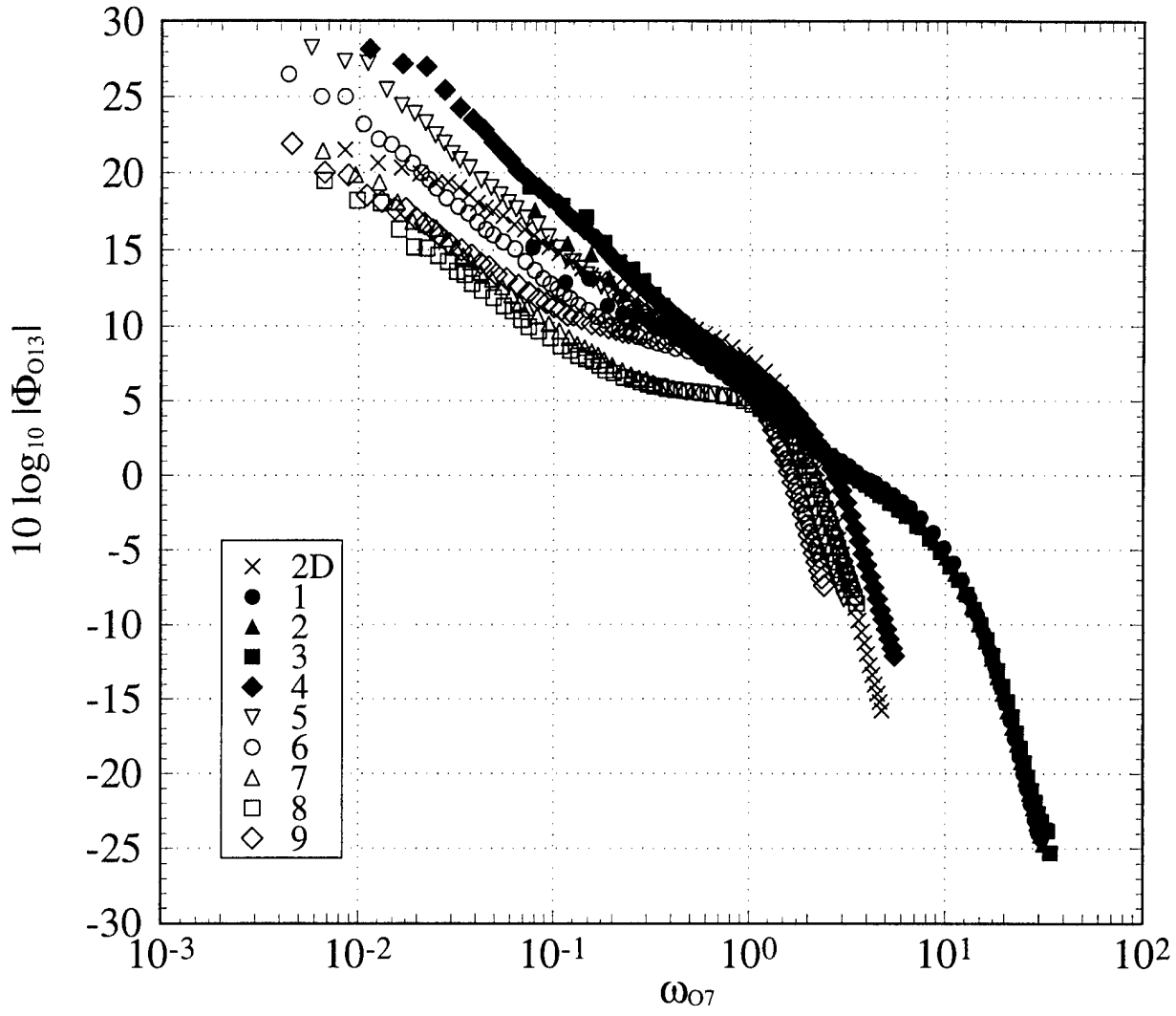

Figure 81. Spectral power density of p (Re_θ = 23400 (2-D); 23200 (3-D)) normalized using τ_{MAX} as the pressure scale and $y / (U^2+W^2)^{1/2}$ at the y location of τ_{MAX} as the time scale. The numbers in the legend denote the measurement station.

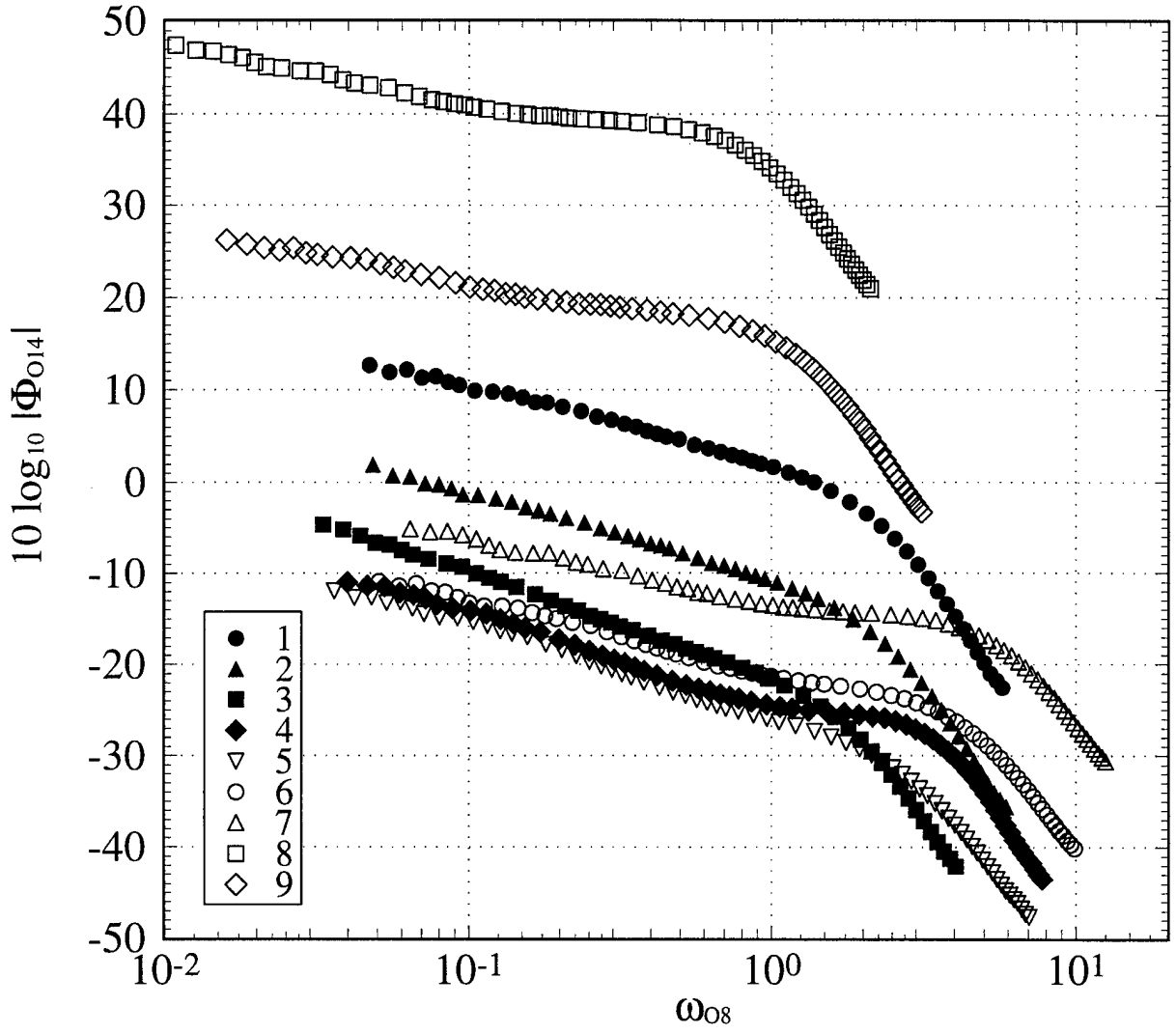

Figure 82. Spectral power density of p ($Re_\theta = 5940$) normalized using $\frac{1}{2}\rho W_{MAX}^2$ as the pressure scale and $y / (U^2+W^2)^{\frac{1}{2}}$ at the y location of W_{MAX} as the time scale. The numbers in the legend denote the measurement station.

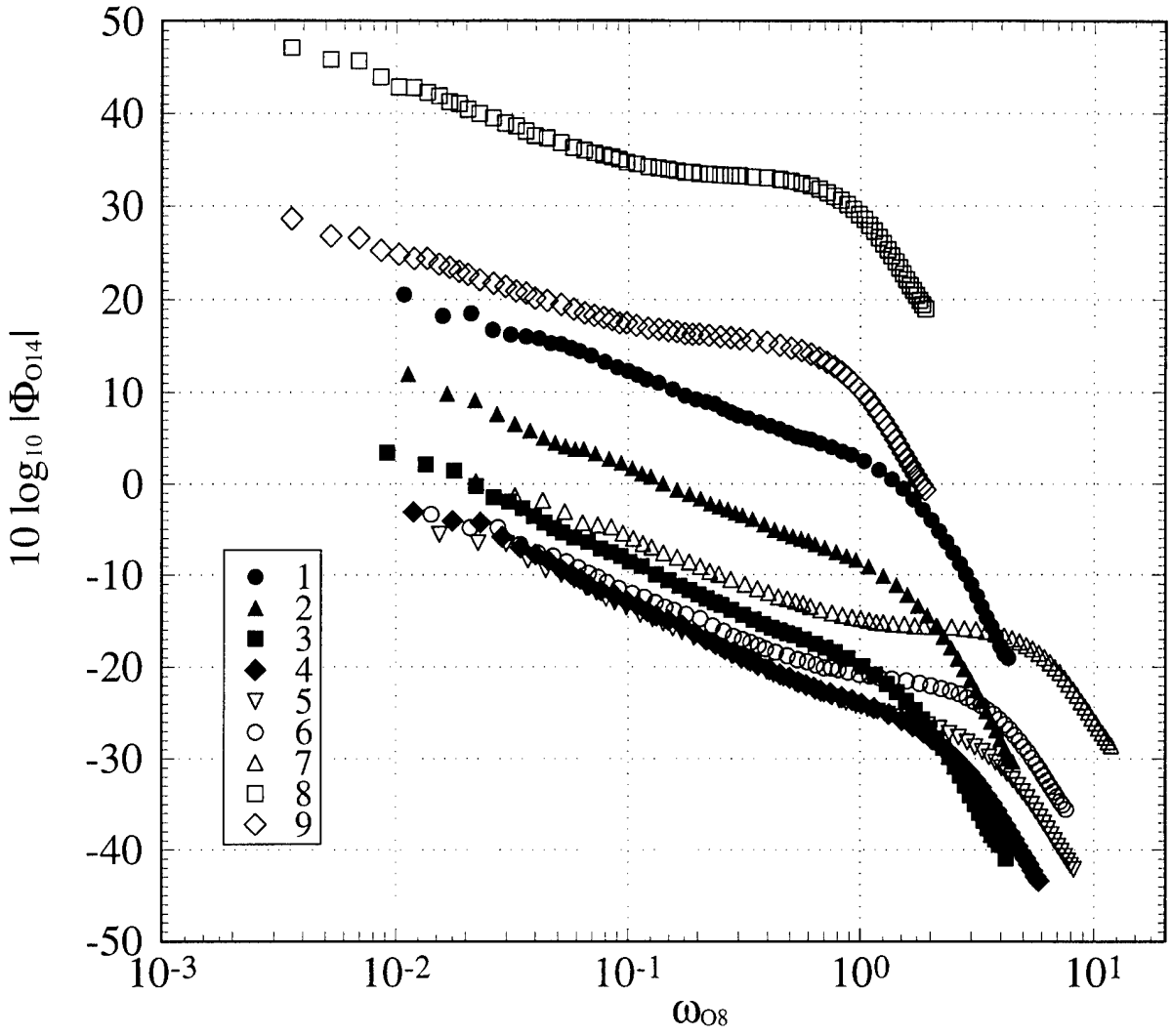

Figure 83. Spectral power density of p ($Re_\theta = 23200$) normalized using $\frac{1}{2}\rho W_{MAX}^2$ as the pressure scale and $y / (U^2+W^2)^{1/2}$ at the y location of W_{MAX} as the time scale. The numbers in the legend denote the measurement station.

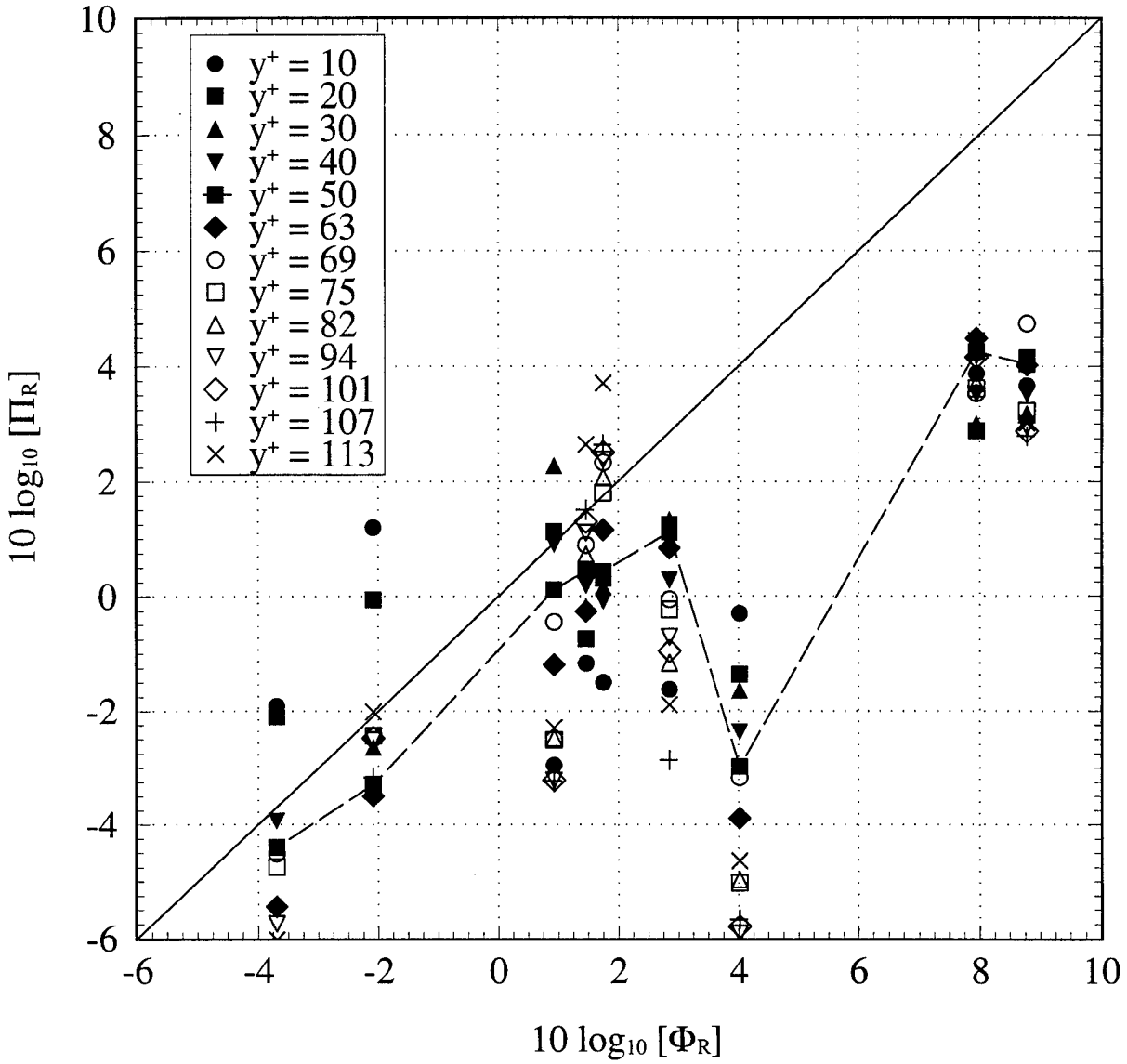

Figure 84. The *Poisson ratio* (Π_R) evaluated at the y^+ locations given in the legend at all of measurement stations in the $Re_\theta = 5940$ flow as a function of the *spectral ratio* (Φ_R). The dashed lines connects the values of Π_R evaluated at $y^+ = 50$ at all of the measurement stations. The solid line shows one-to-one correlation.

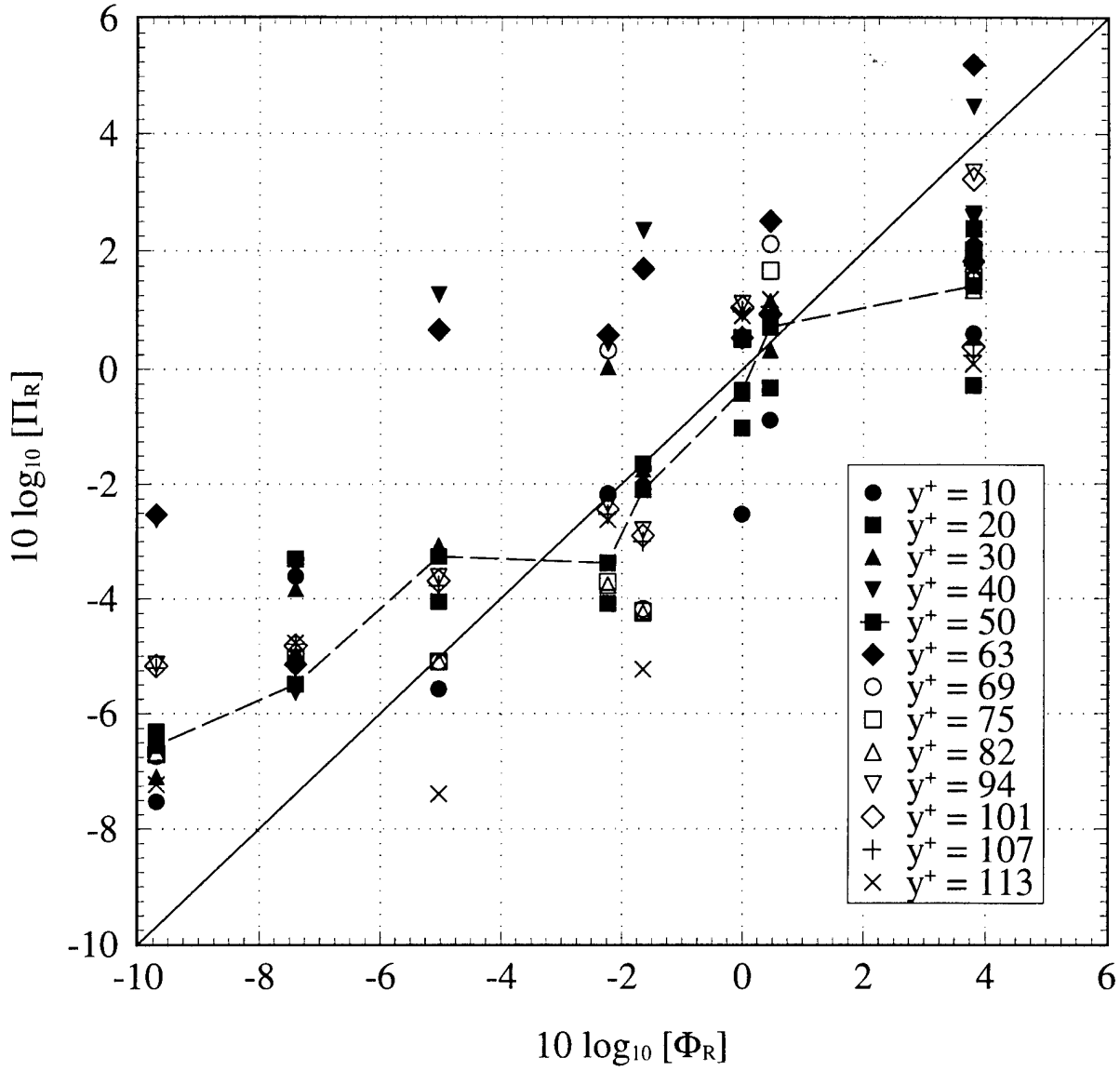

Figure 85. The *Poisson ratio* (Π_R) evaluated at the y^+ locations given in the legend at all of measurement stations in the $Re_\theta = 23200$ flow as a function of the *spectral ratio* (Φ_R). The dashed lines connects the values of Π_R evaluated at $y^+ = 50$ at all of the measurement stations. The solid line shows one-to-one correlation.

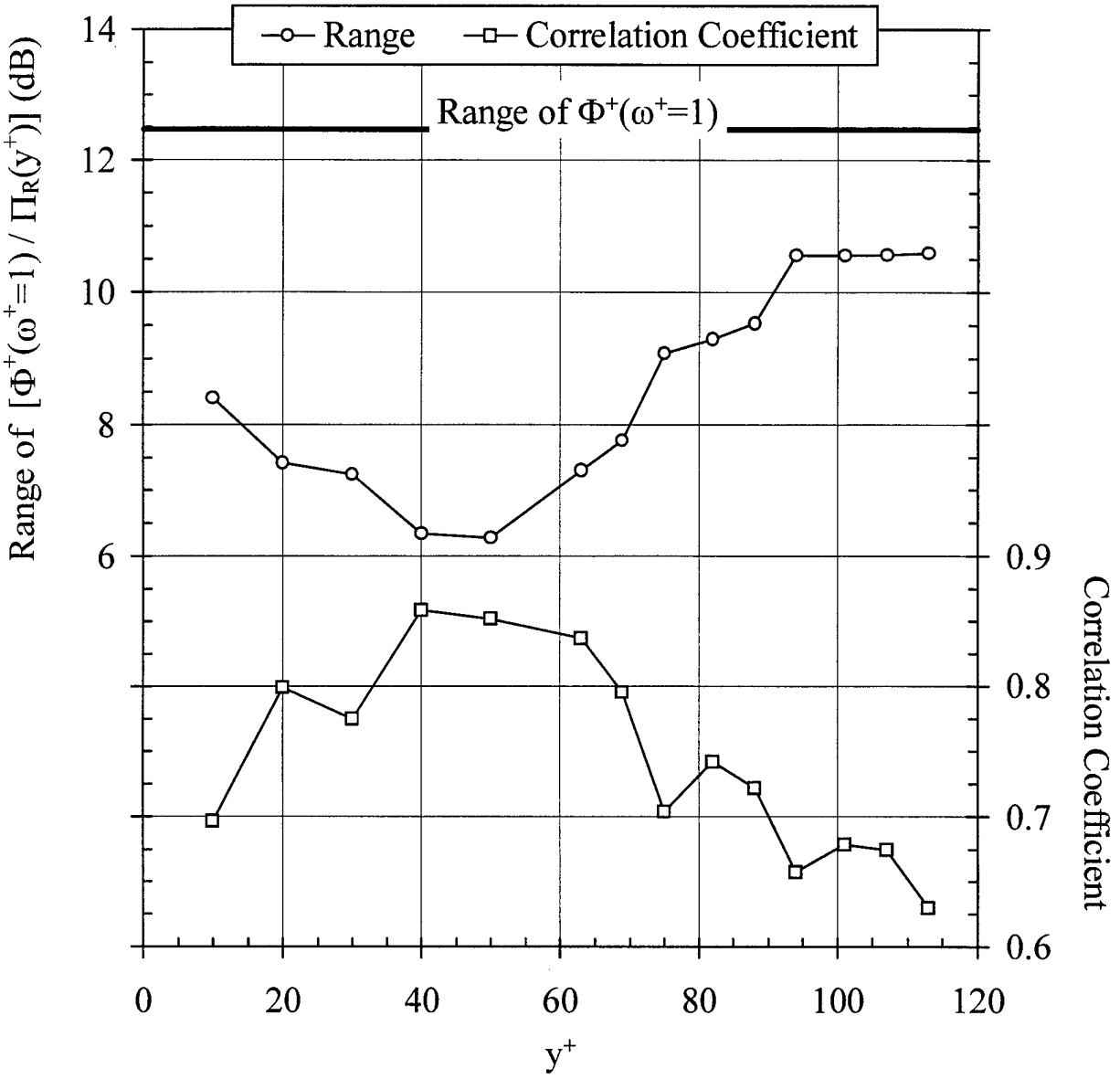

Figure 86. The "best fit" parameters used to measure the degree of high frequency spectral collapse with Π_R evaluated at various y^+ locations within the $Re_\theta = 5940$ flow — (1) The correlation coefficient between $\Phi_R / \Pi_R(y^+)$ and y^+, and (2) The range of spectral values (Φ^+ / Π_R) at $\omega^+ = 1$ among the measurement stations. The solid line shows the range of Φ^+ at $\omega^+ = 1$ among the measurement stations *without* Π_R applied.

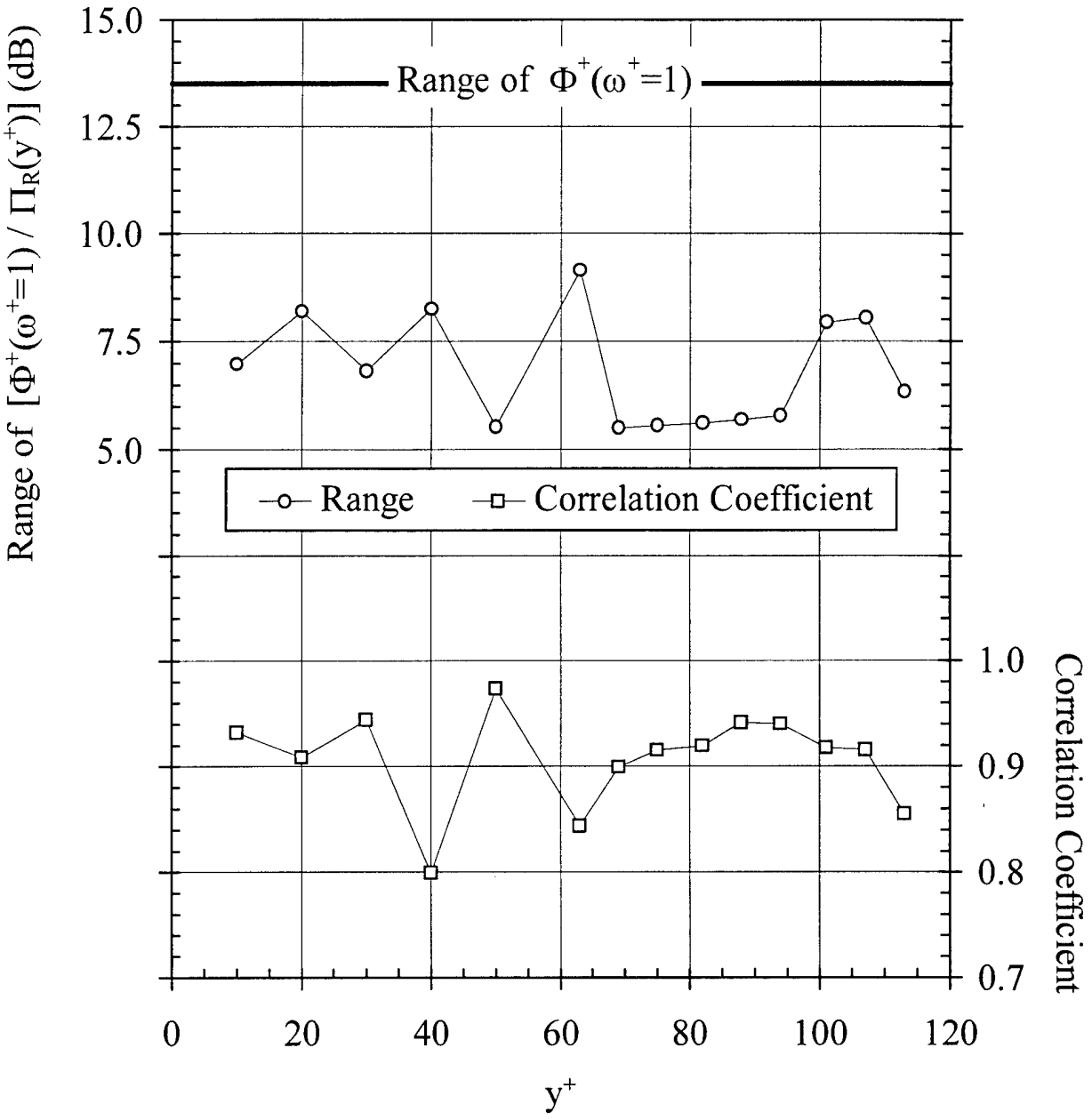

Figure 87. The "best fit" parameters used to measure the degree of high frequency spectral collapse with Π_R evaluated at various y^+ locations within the $Re_\theta = 23200$ flow — (1) The correlation coefficient between $\Phi_R / \Pi_R(y^+)$ and y^+, and (2) The range of spectral values (Φ^+ / Π_R) at $\omega^+ = 1$ among the measurement stations. The solid line shows the range of Φ^+ at $\omega^+ = 1$ among the measurement stations *without* Π_R applied.

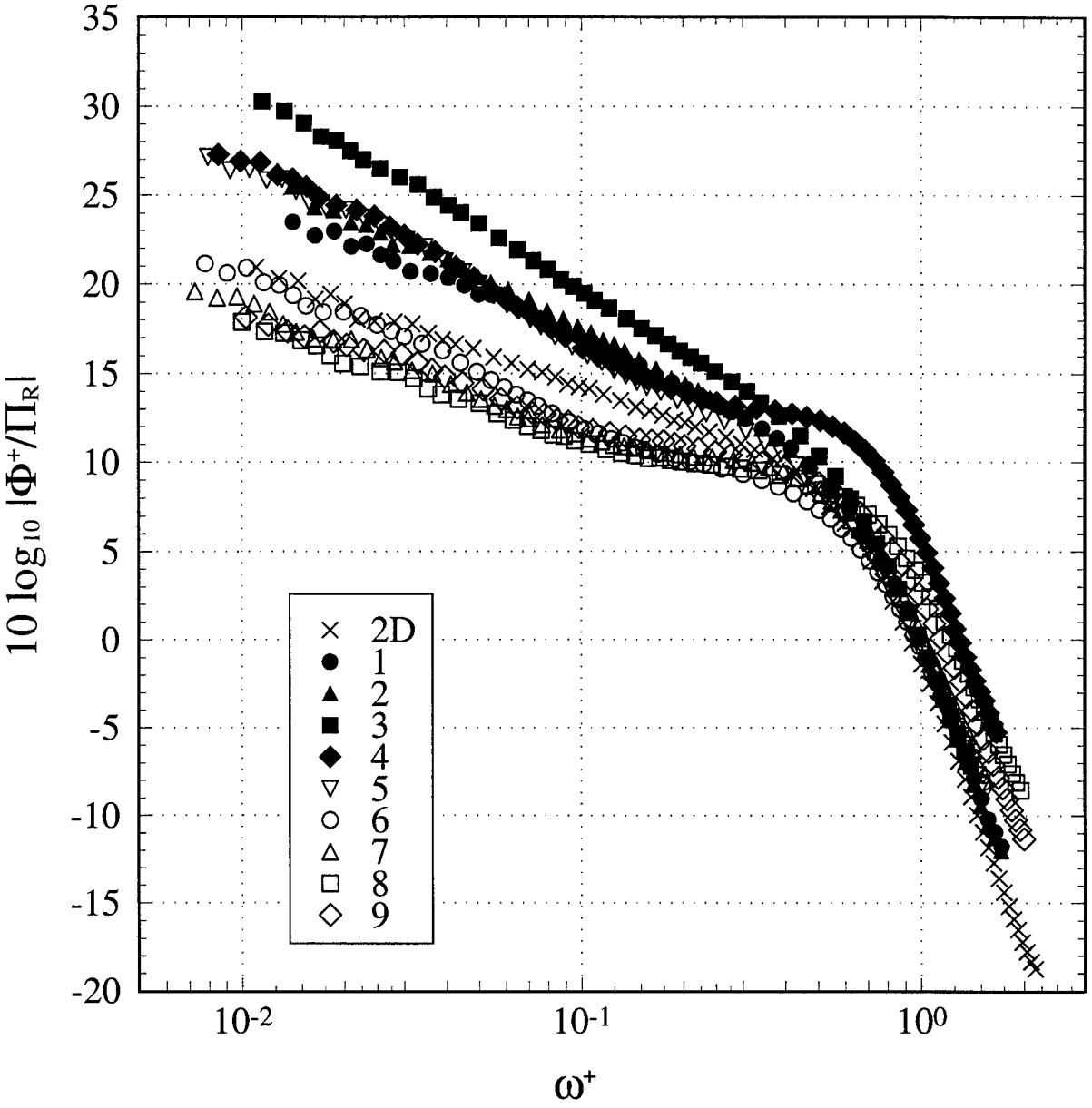

Figure 88. Spectral power density of p (Re_θ = 7300 (2-D); 5940 (3-D)) normalized using τ_W as the pressure scale, ν/u_τ^2 as the time scale, and Π_R evaluated at $y^+ = 50$. The numbers in the legend denote the measurement station. Note that $\Pi_R = 1$ for 2-D flow.

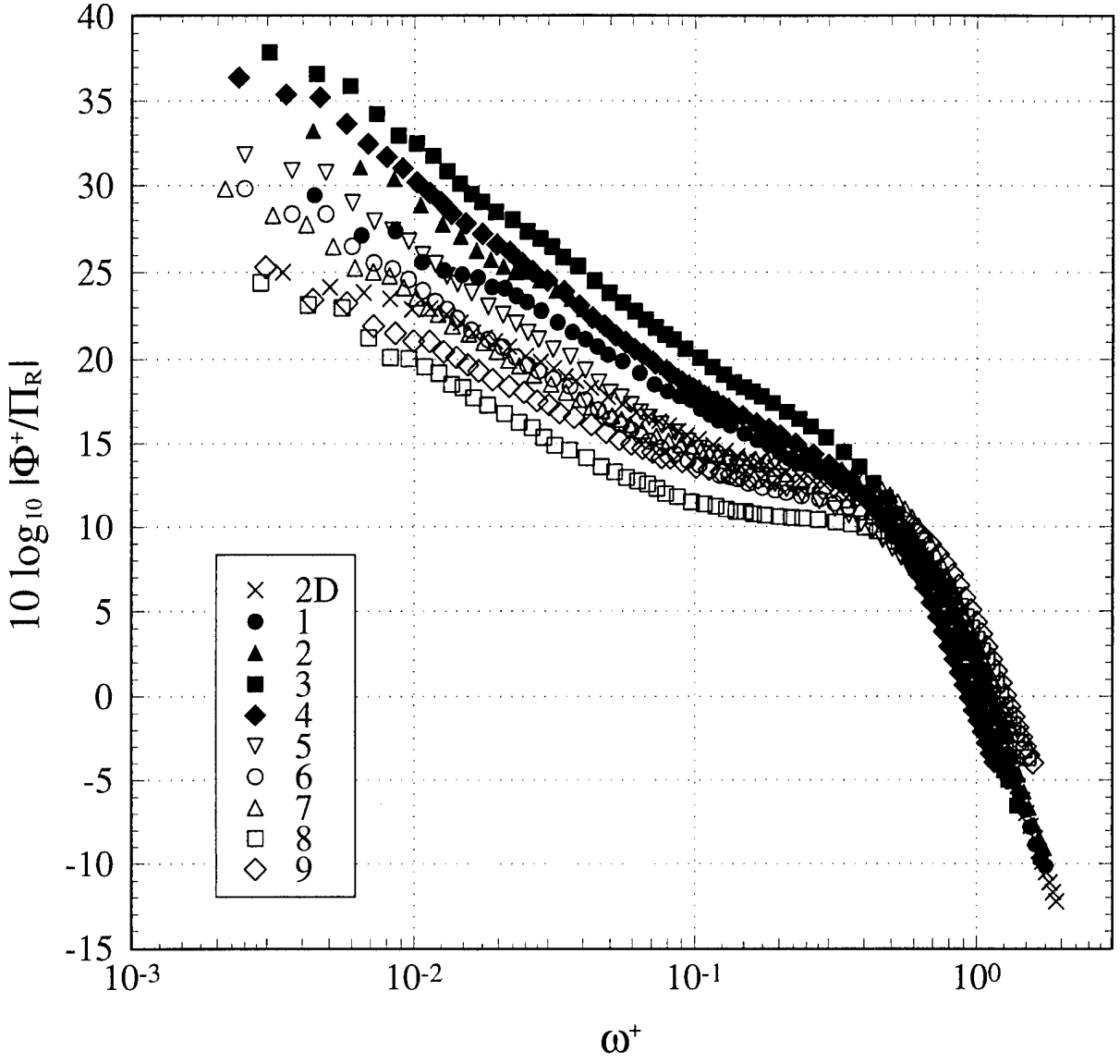

Figure 89. Spectral power density of p (Re_θ = 23400 (2-D); 23200 (3-D)) normalized using τ_w as the pressure scale, ν/u_τ^2 as the time scale, and Π_R evaluated at $y^+ = 50$. The numbers in the legend denote the measurement station. Note that $\Pi_R = 1$ for 2-D flow.

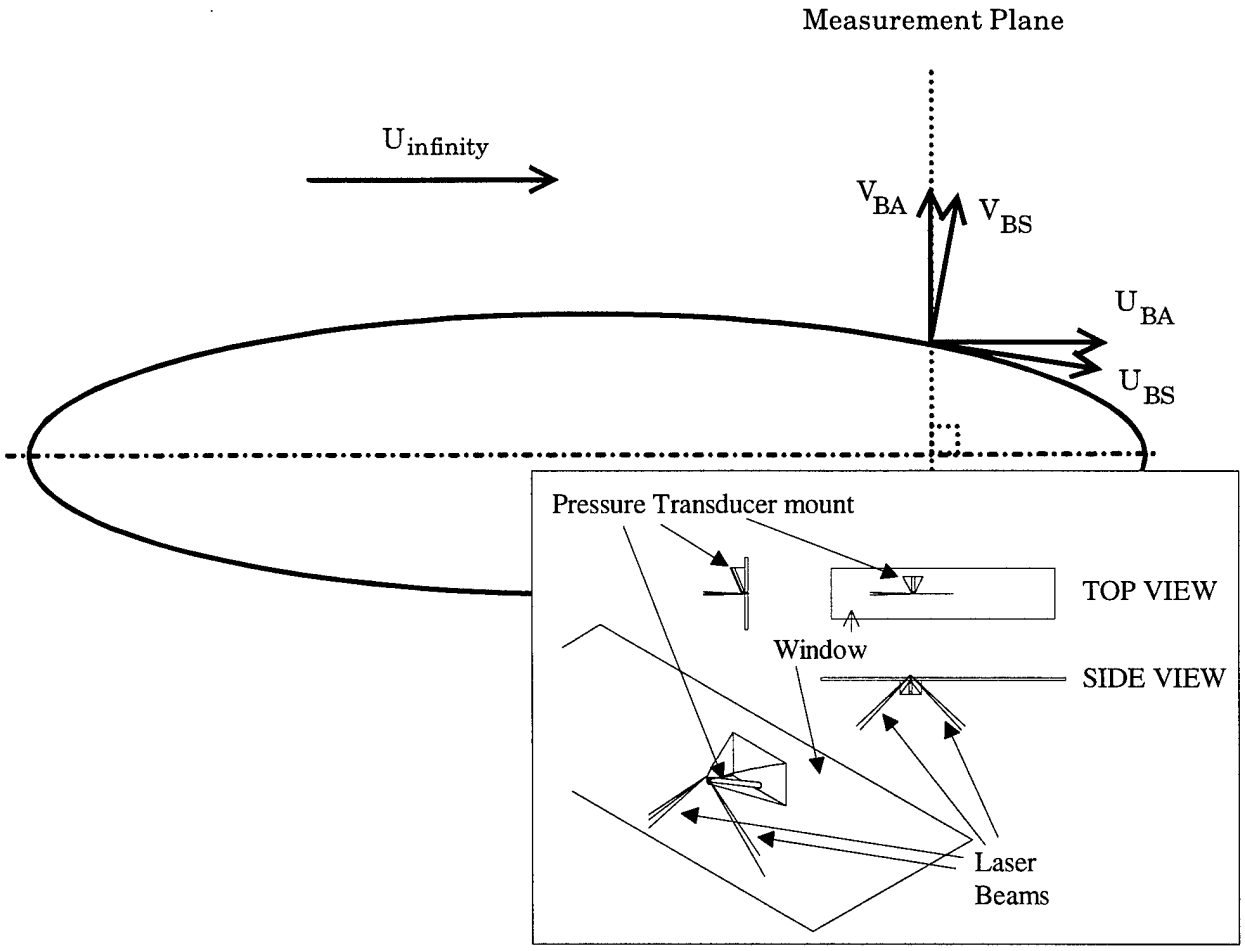

Figure 90. Relationship between Body Axis (BA) coordinate system and Body Surface (BS) coordinate system. Insert : Schematics of pinhole and cylindrical pressure transducer mount attached to double-convex curvature LDV window.

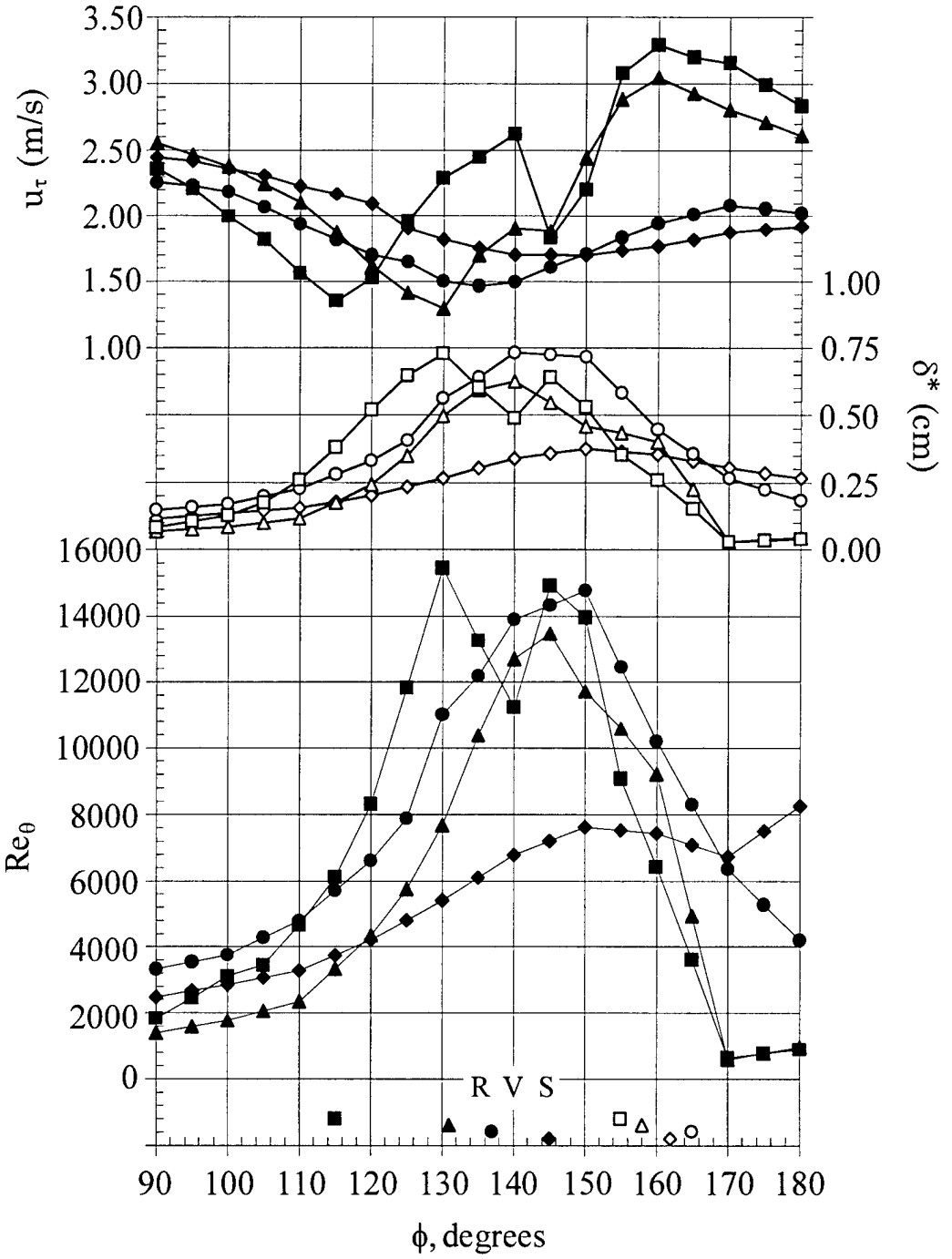

Figure 91. . Variation of displacement thickness (δ^*), friction velocity (u_τ), and Reynolds number (Re_θ) with ϕ position: ◇, $\alpha = 10°$, $x/L = 0.600$; ○, $\alpha = 10°$, $x/L = 0.772$; Δ , $\alpha = 20°$, $x/L = 0.600$; □, $\alpha = 20°$, $x/L = 0.772$. The solid symbols immediately above the ϕ-axis denote the location of primary separation (Wetzel *et al.*, 1998). The open symbols immediately above the ϕ-axis denote the approximate location of the shed vortex core. The letters R, V, and S denote the location of reattachment, secondary vortex core, and secondary separation, respectively, for $\alpha = 20°$, $x/L = 0.772$.

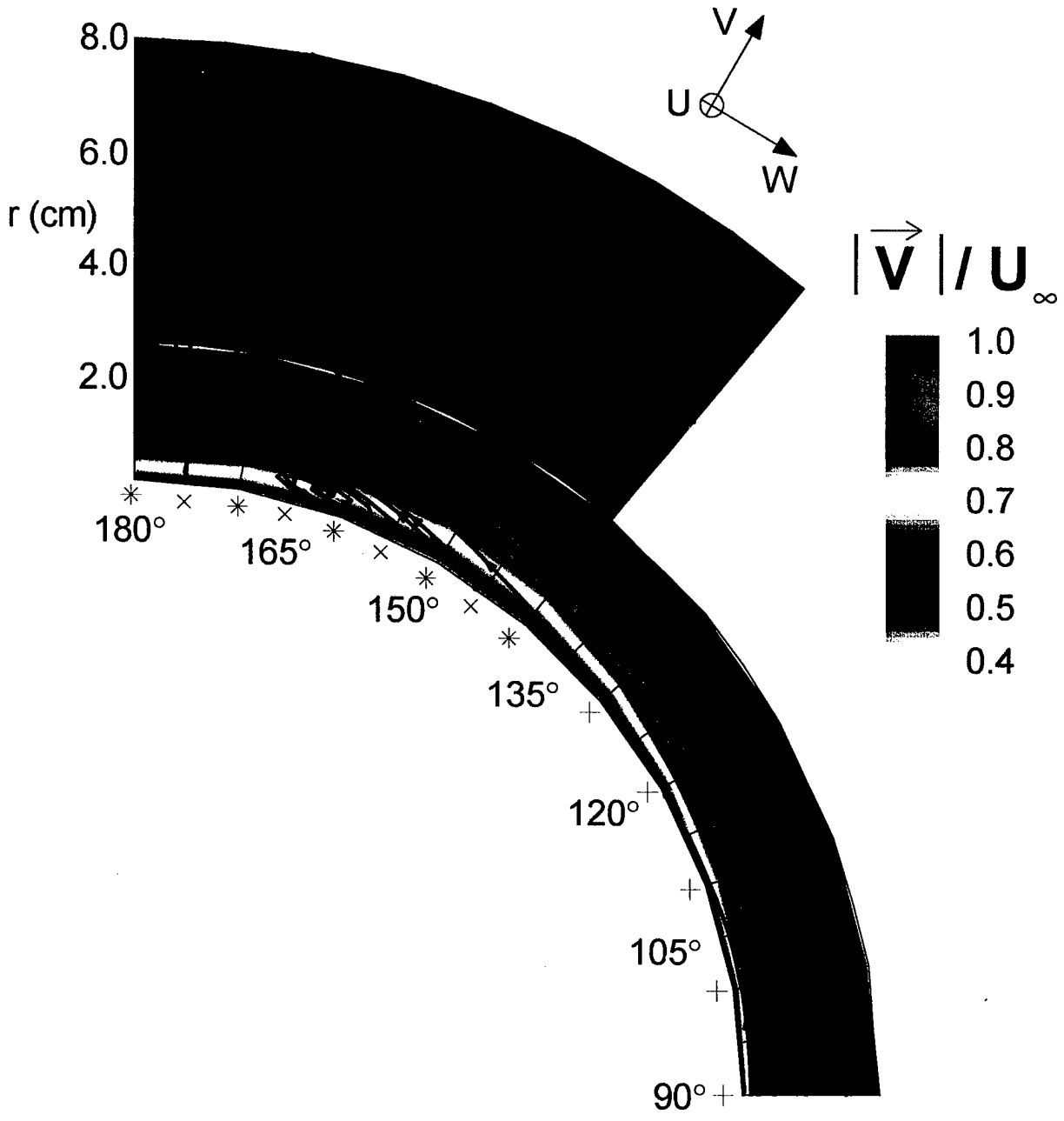

Figure 92. Secondary streamlines with contour levels of mean velocity magnitude, $\alpha = 10°$, $x/L = 0.600$. The pluses (+) along the ϕ-axis denote the ϕ locations at which radial profiles of simultaneous velocity (LDV) and surface pressure measurements were carried out. The Xs (×) along the ϕ-axis denote the ϕ locations at which radial profiles of velocity were carried out using a 4-hot-wire probe. The asterisks (*) denote ϕ-locations at which velocity profiles were carried using both LDV and the 4-hot-wire probe.

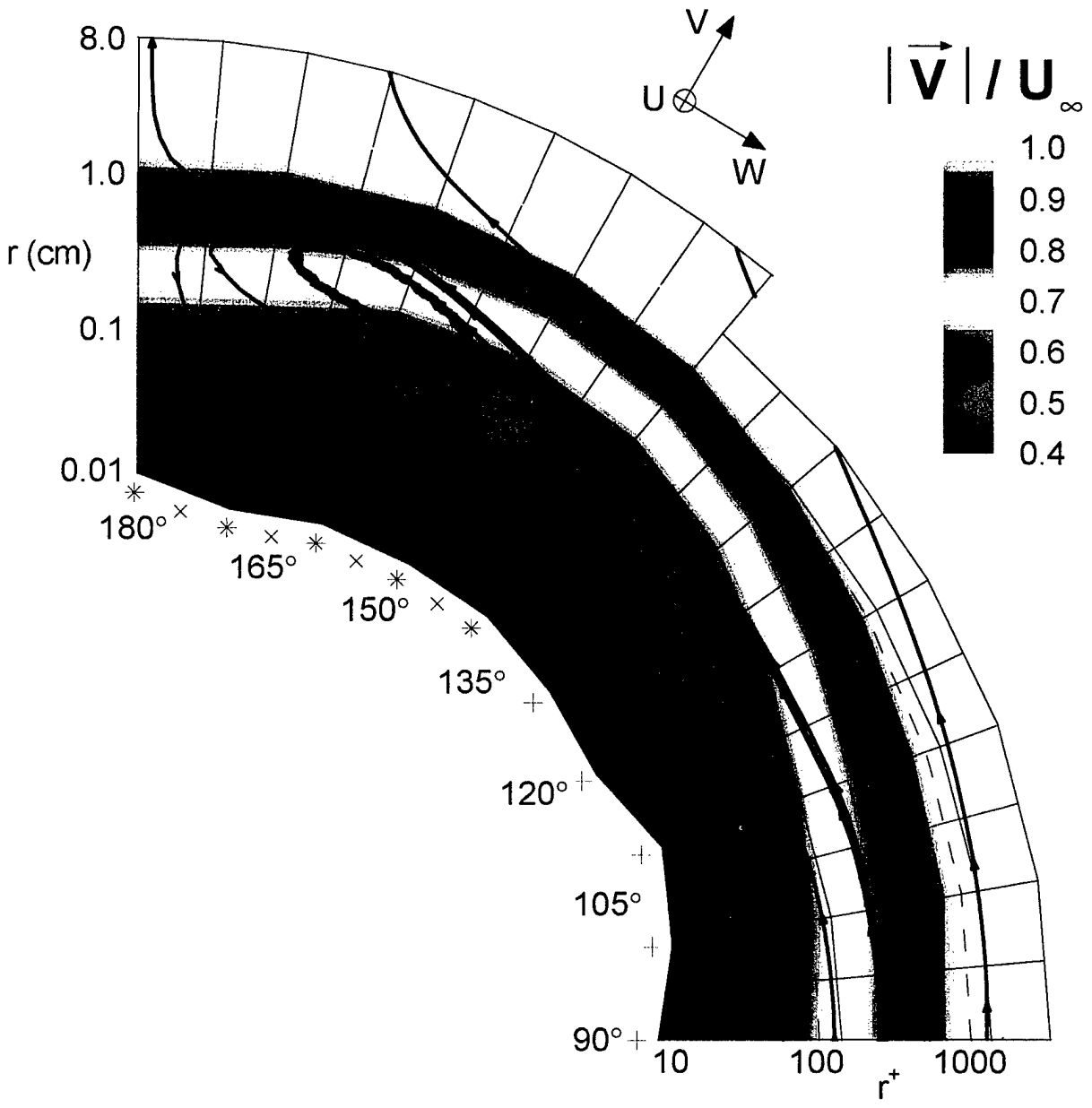

Figure 93. Secondary streamlines with contour levels of the mean velocity magnitude, $\alpha = 10°$, $x/L = 0.600$. The pluses (+) along the ϕ-axis denote the ϕ locations at which radial profiles of simultaneous velocity (LDV) and surface pressure measurements were carried out. The Xs (×) along the ϕ-axis denote the ϕ locations at which radial profiles of velocity were carried out using a 4-hot-wire probe. The asterisks (*) denote ϕ-locations at which velocity profiles were carried using both LDV and the 4-hot-wire probe. The radial coordinate (r) is plotted on a logarithmic scale and the dashed lines show lines of constant r^+. The irregular shape of the inner boundary is defined by the measurement locations nearest the model surface.

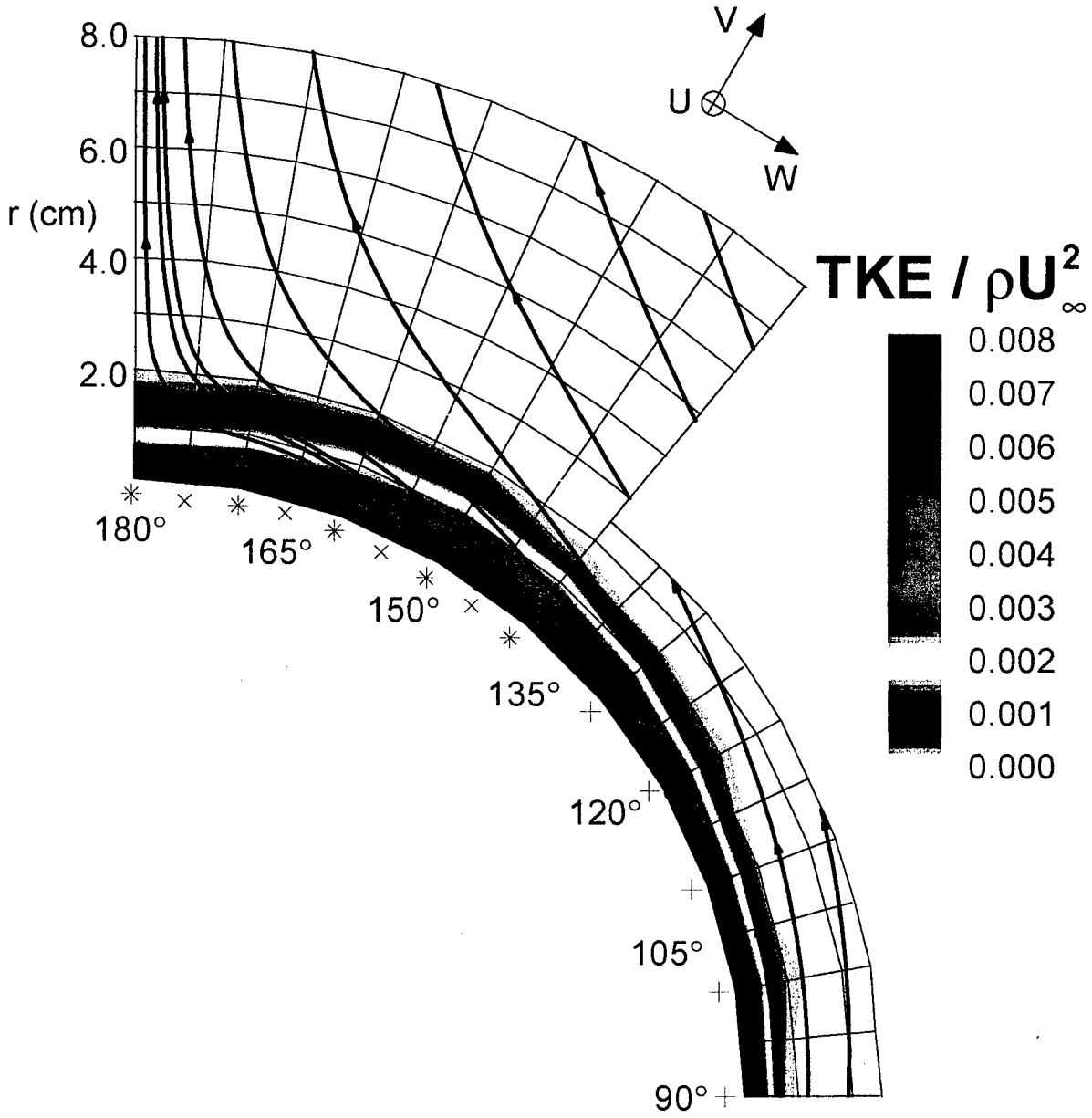

Figure 94. Secondary streamlines with contour levels of *TKE*, $\alpha = 10°$, $x/L = 0.600$. The pluses (+) along the ϕ-axis denote the ϕ locations at which radial profiles of simultaneous velocity (LDV) and surface pressure measurements were carried out. The Xs (×) along the ϕ-axis denote the ϕ locations at which radial profiles of velocity were carried out using a 4-hot-wire probe. The asterisks (*) denote ϕ-locations at which velocity profiles were carried using both LDV and the 4-hot-wire probe.

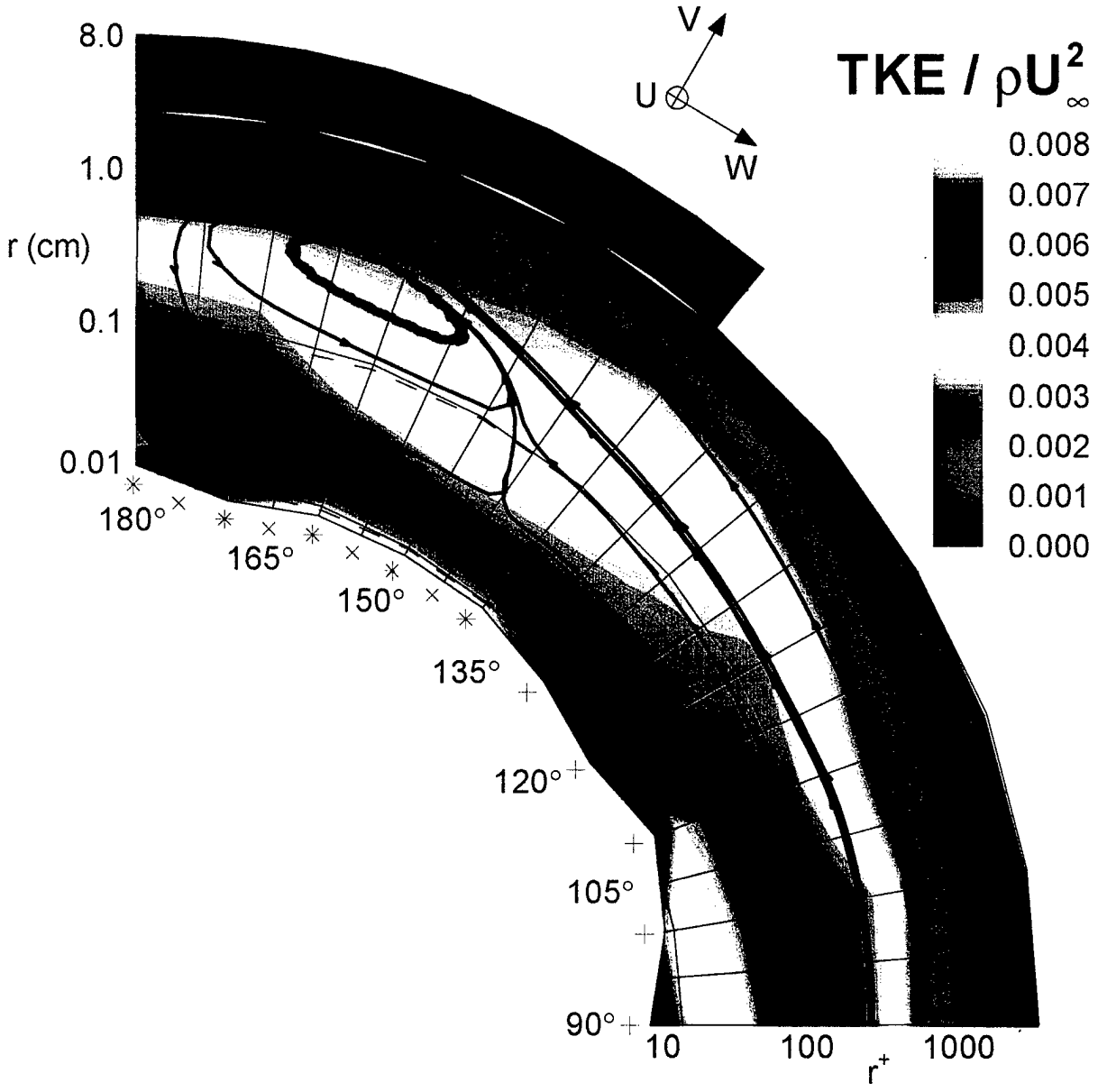

Figure 95. Secondary streamlines with contour levels of *TKE*, $\alpha = 10°$, $x/L = 0.600$. The pluses (+) along the ϕ-axis denote the ϕ locations at which radial profiles of simultaneous velocity (LDV) and surface pressure measurements were carried out. The Xs (×) along the ϕ-axis denote the ϕ locations at which radial profiles of velocity were carried out using a 4-hot-wire probe. The asterisks (*) denote ϕ-locations at which velocity profiles were carried using both LDV and the 4-hot-wire probe. The radial coordinate (r) is plotted on a logarithmic scale and the dashed lines show lines of constant r^+. The irregular shape of the inner boundary is defined by the measurement locations nearest the model surface.

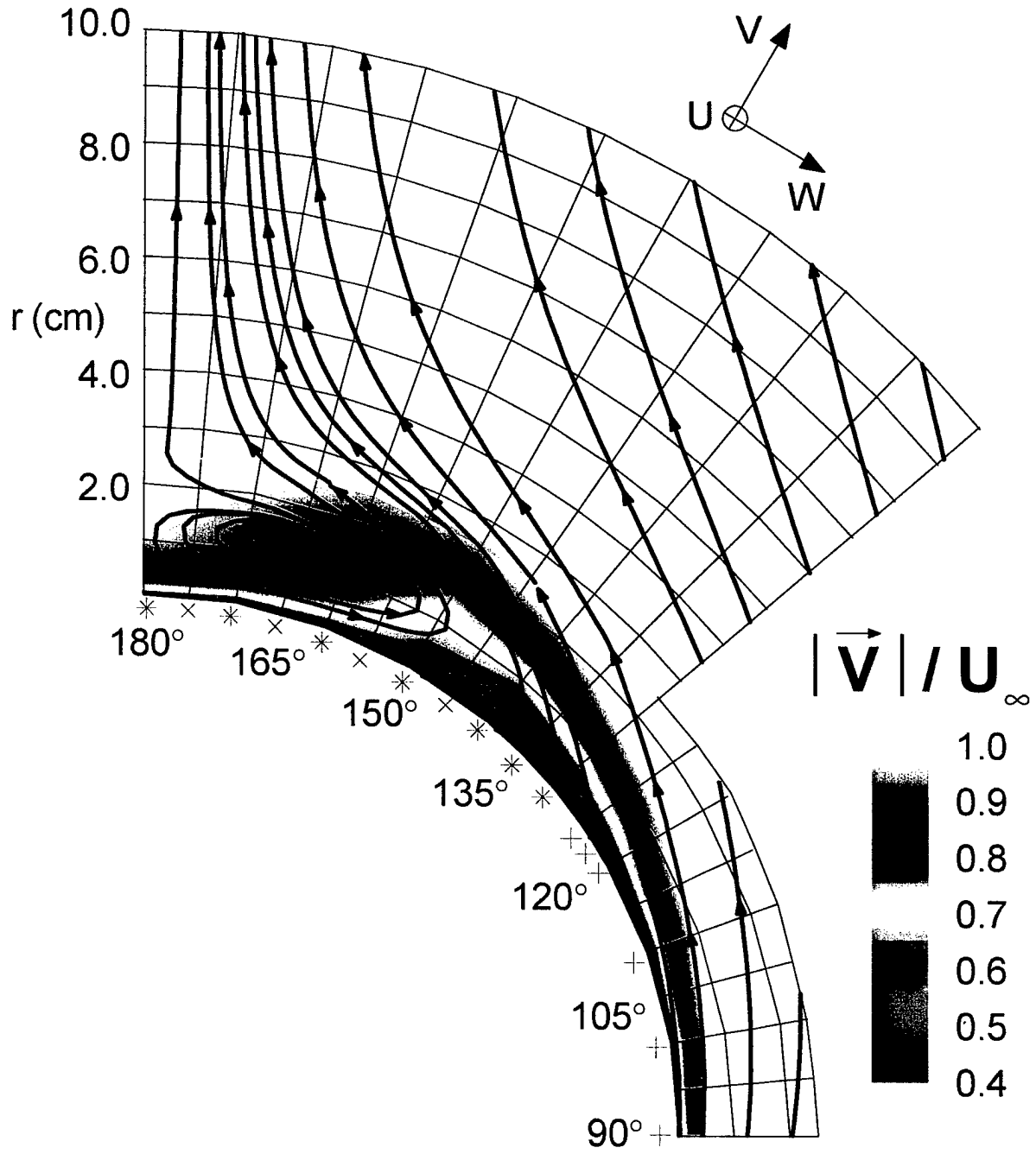

Figure 96. Secondary streamlines with contour levels of mean velocity magnitude, $\alpha = 10°$, $x/L = 0.772$. The pluses (+) along the ϕ-axis denote the ϕ locations at which radial profiles of simultaneous velocity (LDV) and surface pressure measurements were carried out. The Xs (×) along the ϕ-axis denote the ϕ locations at which radial profiles of velocity were carried out using a 4-hot-wire probe. The asterisks (*) denote ϕ-locations at which velocity profiles were carried using both LDV and the 4-hot-wire probe.

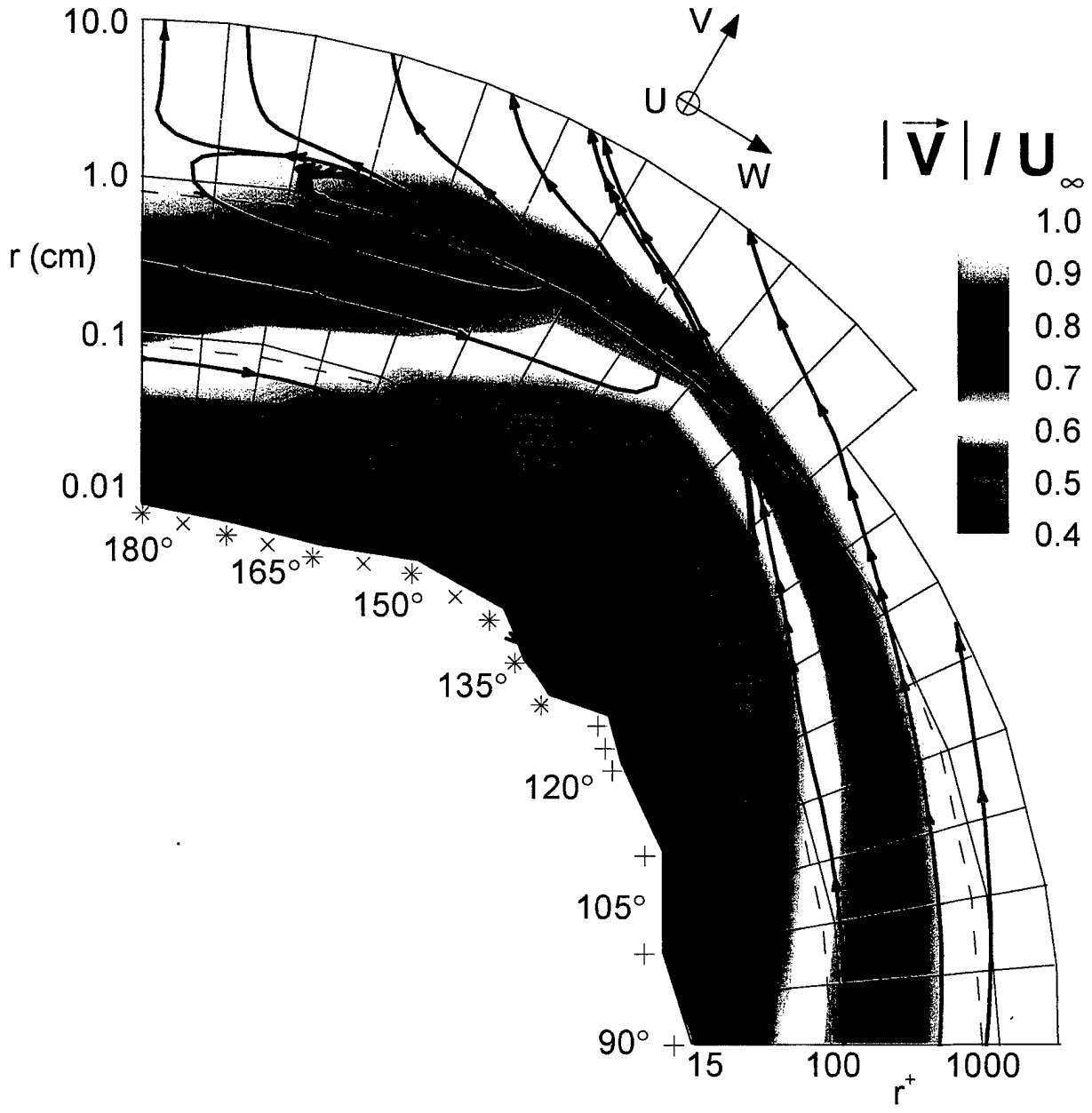

Figure 97. Secondary streamlines with contour levels of the mean velocity magnitude, $\alpha = 10°$, $x/L = 0.772$. The pluses (+) along the ϕ-axis denote the ϕ locations at which radial profiles of simultaneous velocity (LDV) and surface pressure measurements were carried out. The Xs (×) along the ϕ-axis denote the ϕ locations at which radial profiles of velocity were carried out using a 4-hot-wire probe. The asterisks (*) denote ϕ-locations at which velocity profiles were carried using both LDV and the 4-hot-wire probe. The radial coordinate (r) is plotted on a logarithmic scale and the dashed lines show lines of constant r^+. The irregular shape of the inner boundary is defined by the measurement locations nearest the model surface.

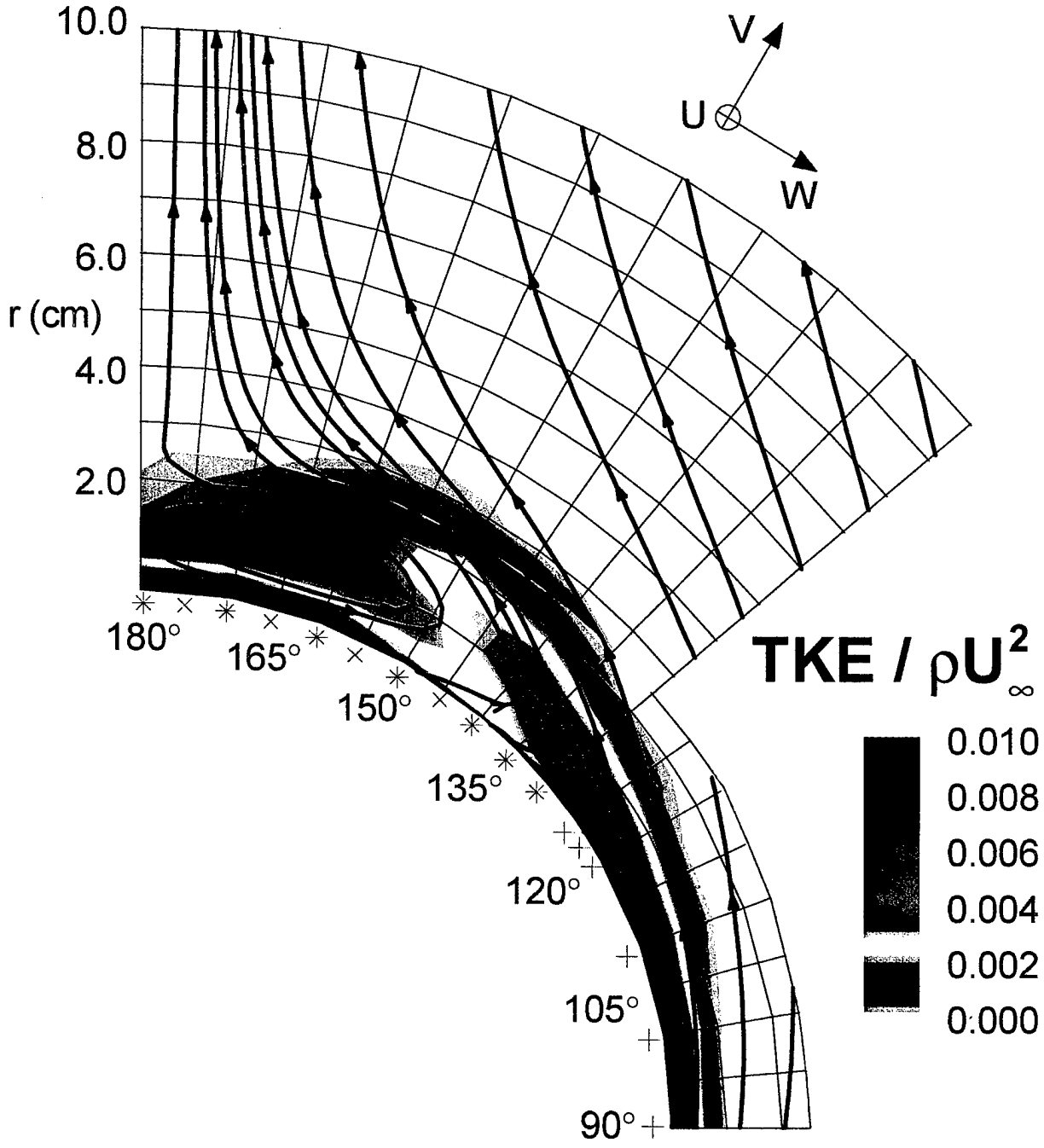

Figure 98. Secondary streamlines with contour levels of *TKE*, $\alpha = 10°$, $x/L = 0.772$. The pluses (+) along the ϕ-axis denote the ϕ locations at which radial profiles of simultaneous velocity (LDV) and surface pressure measurements were carried out. The Xs (×) along the ϕ-axis denote the ϕ locations at which radial profiles of velocity were carried out using a 4-hot-wire probe. The asterisks (*) denote ϕ-locations at which velocity profiles were carried using both LDV and the 4-hot-wire probe.

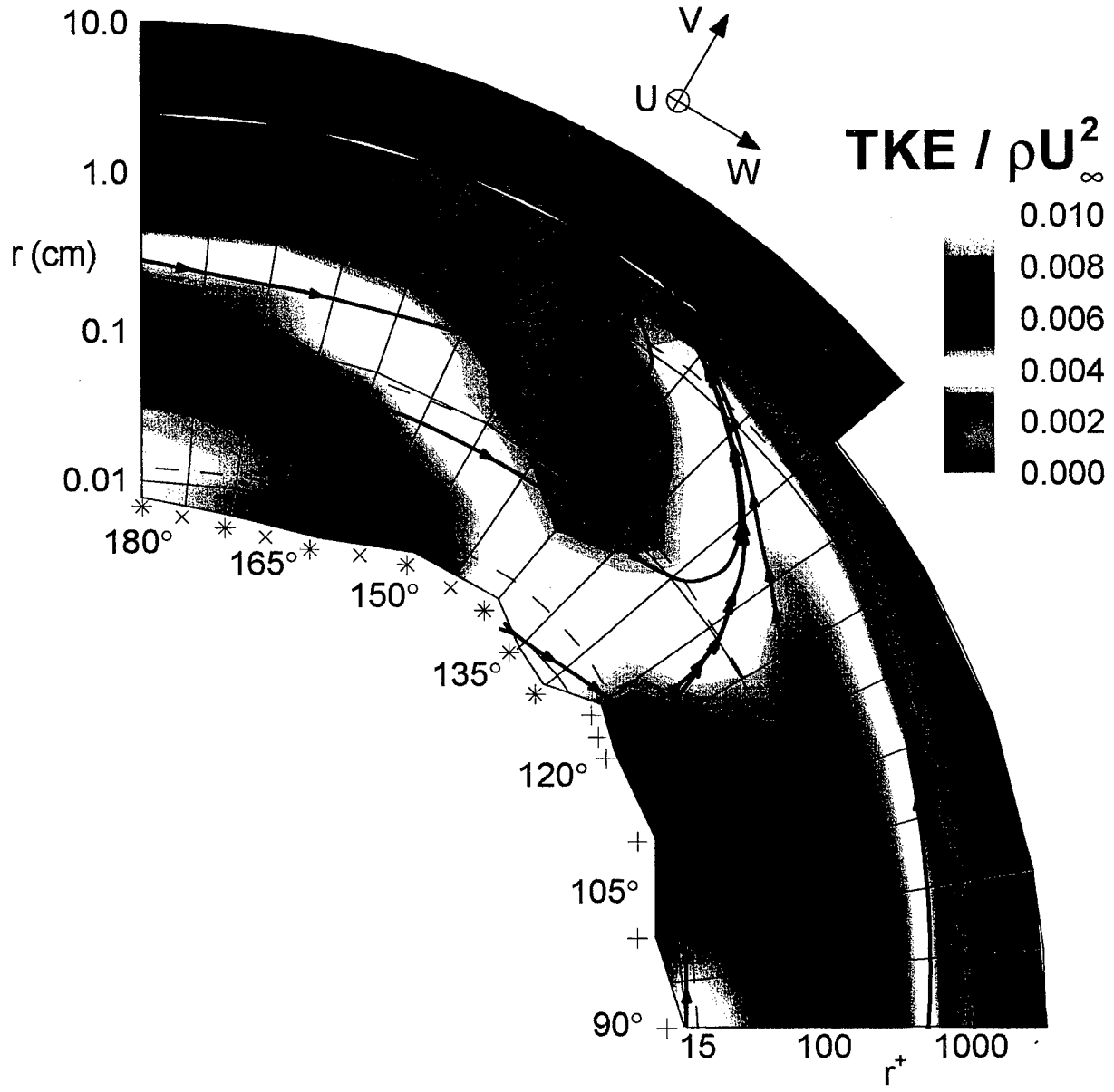

Figure 99. Secondary streamlines with contour levels of *TKE*, $\alpha = 10°$, $x/L = 0.772$. The pluses (+) along the ϕ-axis denote the ϕ locations at which radial profiles of simultaneous velocity (LDV) and surface pressure measurements were carried out. The Xs (×) along the ϕ-axis denote the ϕ locations at which radial profiles of velocity were carried out using a 4-hot-wire probe. The asterisks (*) denote ϕ-locations at which velocity profiles were carried using both LDV and the 4-hot-wire probe. The radial coordinate (r) is plotted on a logarithmic scale and the dashed lines show lines of constant r^+. The irregular shape of the inner boundary is defined by the measurement locations nearest the model surface.

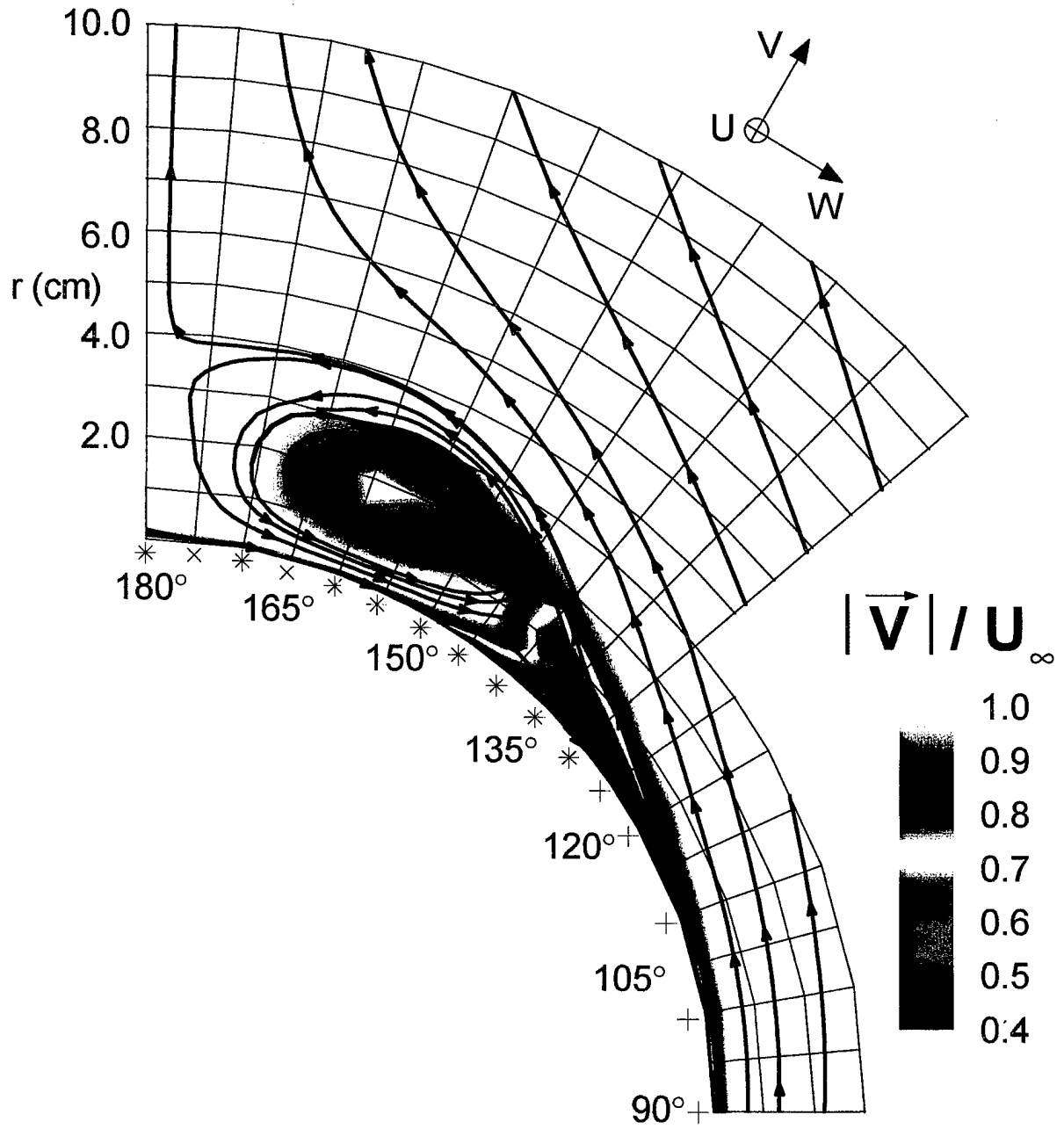

Figure 100. Secondary streamlines with contour levels of mean velocity magnitude, $\alpha = 20°$, $x/L = 0.600$. The pluses (+) along the ϕ-axis denote the ϕ locations at which radial profiles of simultaneous velocity (LDV) and surface pressure measurements were carried out. The Xs (×) along the ϕ-axis denote the ϕ locations at which radial profiles of velocity were carried out using a 4-hot-wire probe. The asterisks (*) denote ϕ-locations at which velocity profiles were carried using both LDV and the 4-hot-wire probe.

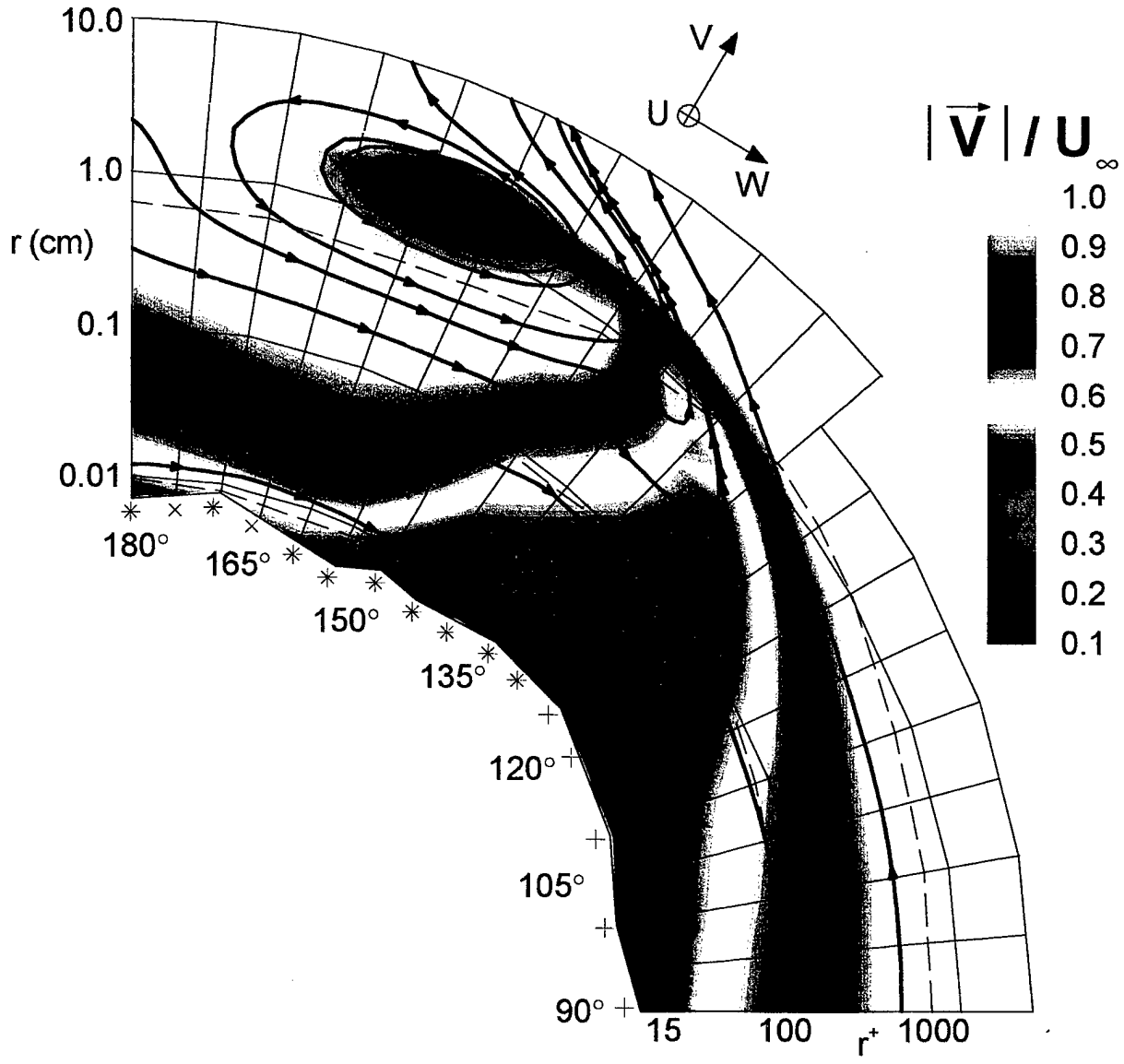

Figure 101. Secondary streamlines with contour levels of the mean velocity magnitude, $\alpha = 20°$, $x/L = 0.600$. The pluses (+) along the ϕ-axis denote the ϕ locations at which radial profiles of simultaneous velocity (LDV) and surface pressure measurements were carried out. The Xs (×) along the ϕ-axis denote the ϕ locations at which radial profiles of velocity were carried out using a 4-hot-wire probe. The asterisks (*) denote ϕ-locations at which velocity profiles were carried using both LDV and the 4-hot-wire probe. The radial coordinate (r) is plotted on a logarithmic scale and the dashed lines show lines of constant r^+. The irregular shape of the inner boundary is defined by the measurement locations nearest the model surface.

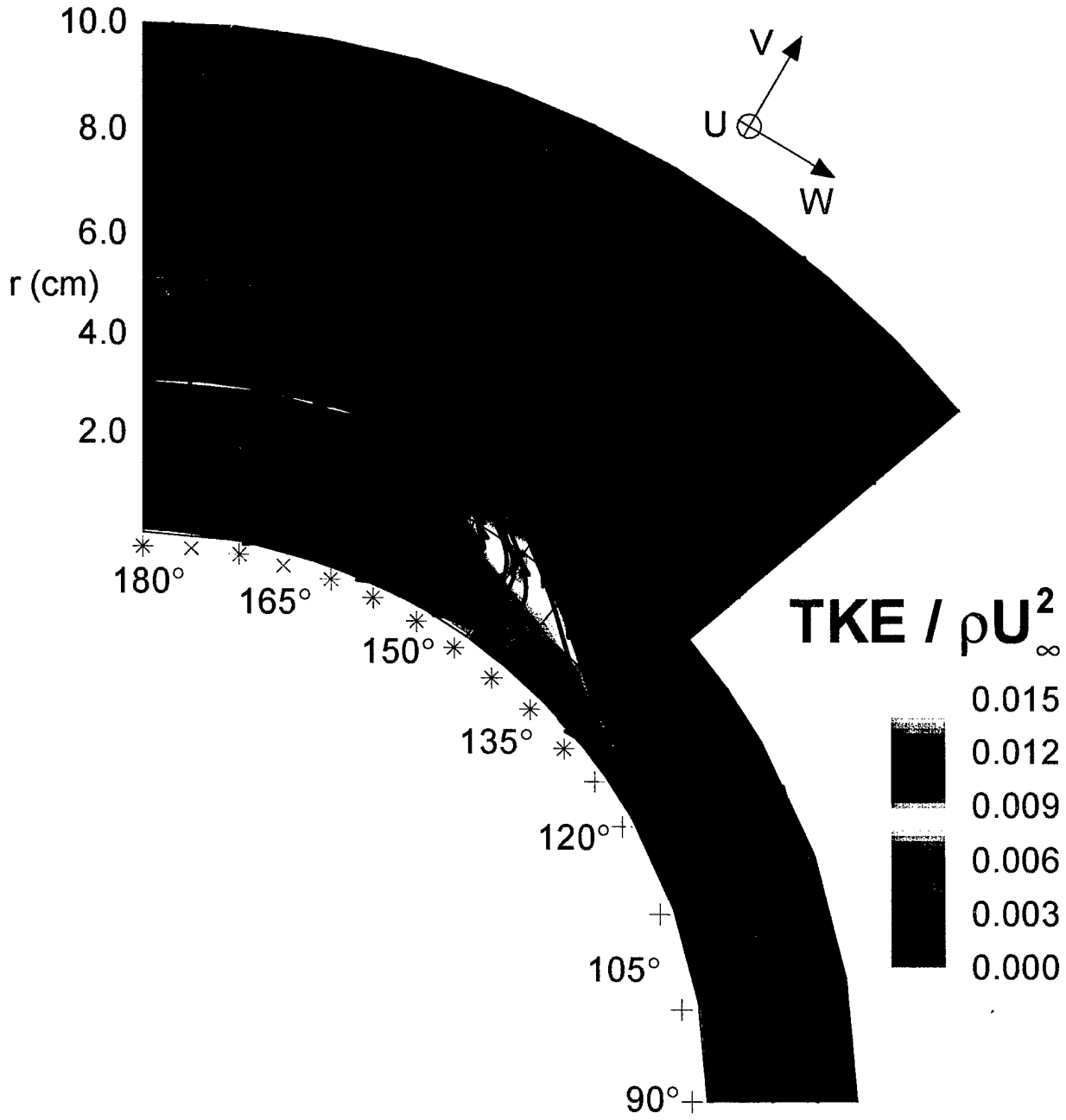

Figure 102. Secondary streamlines with contour levels of *TKE*, $\alpha = 20°$, $x/L = 0.600$. The pluses (+) along the ϕ-axis denote the ϕ locations at which radial profiles of simultaneous velocity (LDV) and surface pressure measurements were carried out. The Xs (×) along the ϕ-axis denote the ϕ locations at which radial profiles of velocity were carried out using a 4-hot-wire probe. The asterisks (*) denote ϕ-locations at which velocity profiles were carried using both LDV and the 4-hot-wire probe.

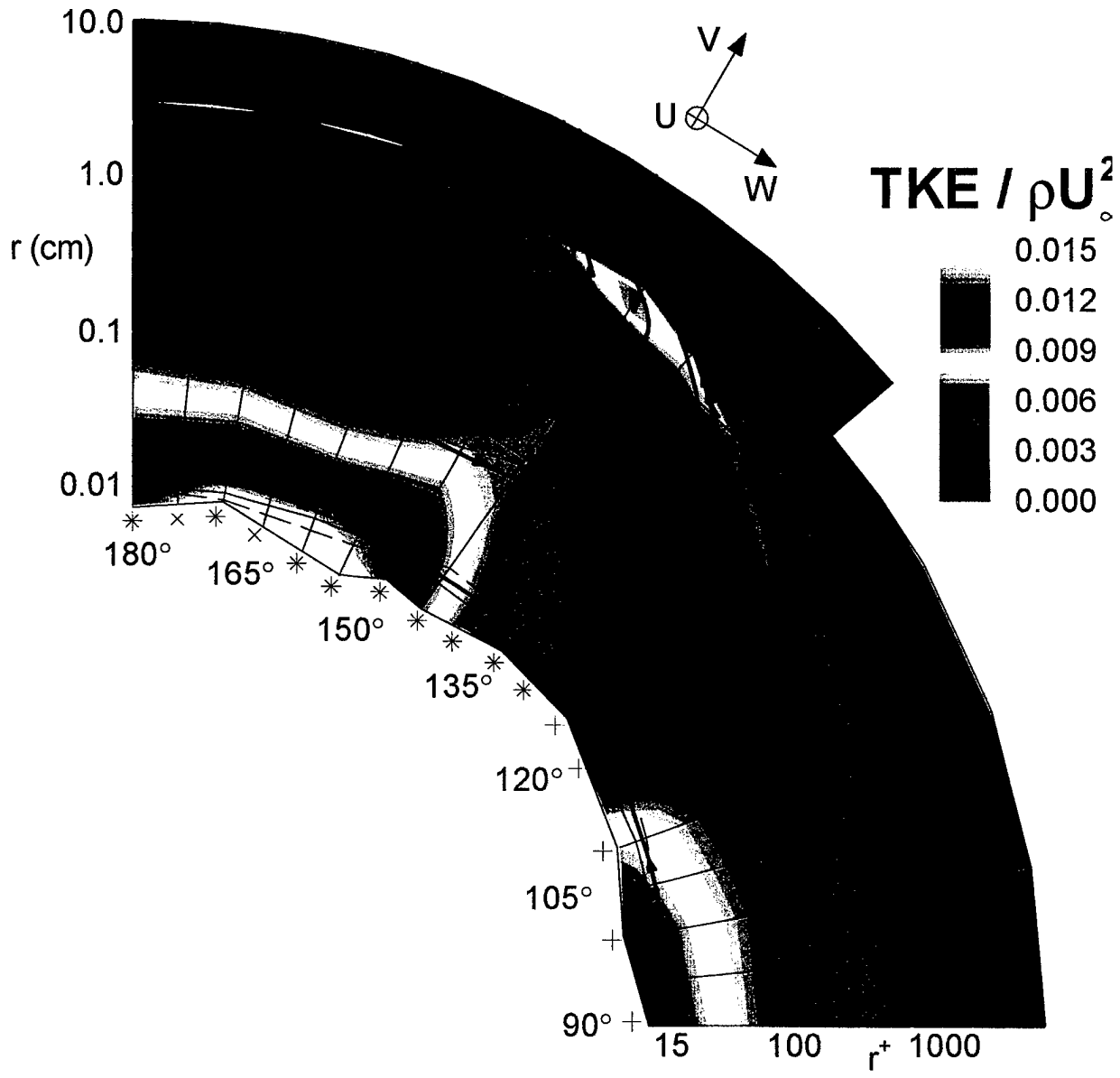

Figure 103. Secondary streamlines with contour levels of *TKE*, $\alpha = 20°$, $x/L = 0.600$. The pluses (+) along the ϕ-axis denote the ϕ locations at which radial profiles of simultaneous velocity (LDV) and surface pressure measurements were carried out. The Xs (×) along the ϕ-axis denote the ϕ locations at which radial profiles of velocity were carried out using a 4-hot-wire probe. The asterisks (*) denote ϕ-locations at which velocity profiles were carried using both LDV and the 4-hot-wire probe. The radial coordinate (r) is plotted on a logarithmic scale and the dashed lines show lines of constant r^+. The irregular shape of the inner boundary is defined by the measurement locations nearest the model surface.

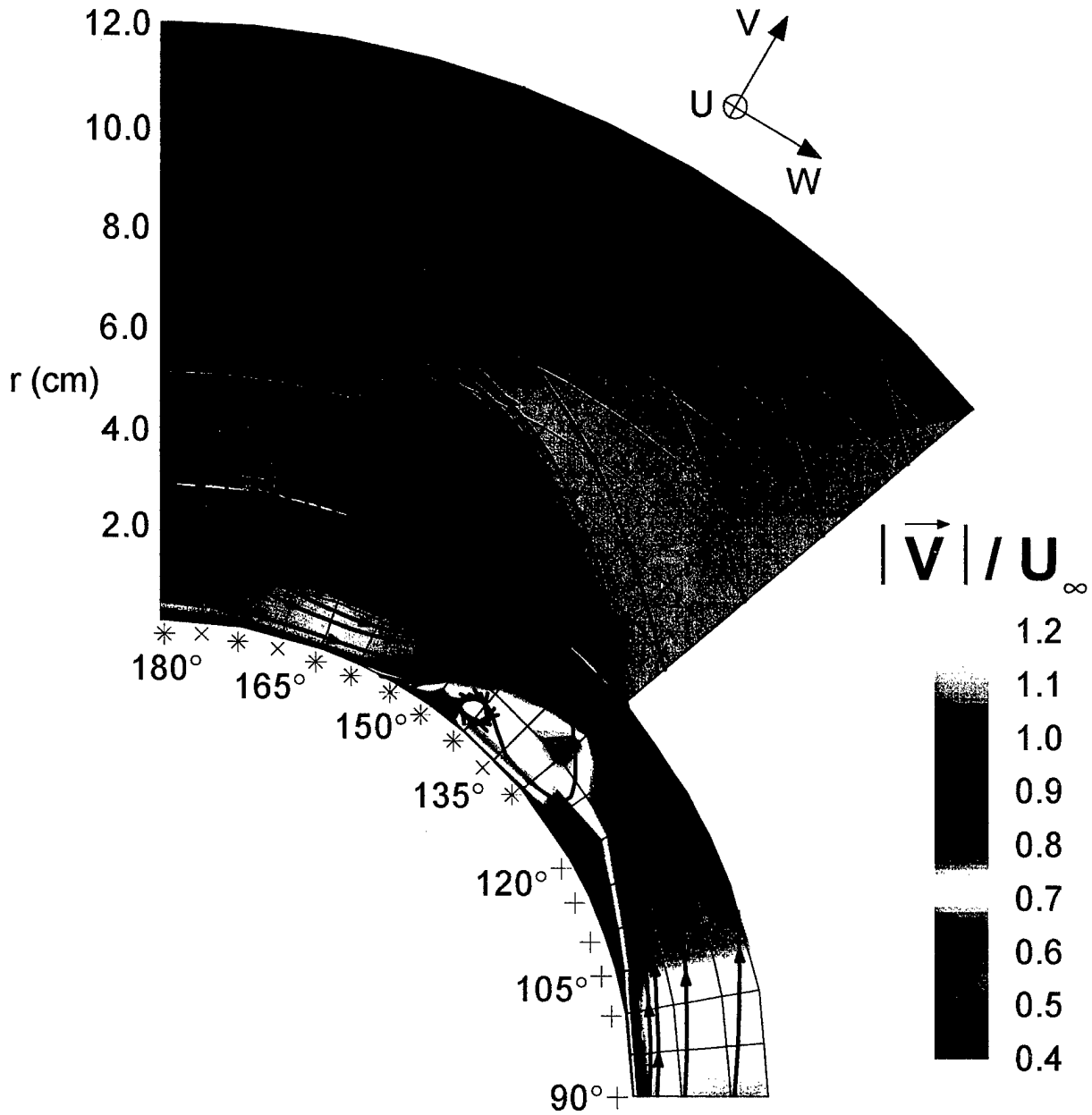

Figure 104. Secondary streamlines with contour levels of mean velocity magnitude, $\alpha = 20°$, $x/L = 0.772$. The pluses (+) along the ϕ-axis denote the ϕ locations at which radial profiles of simultaneous velocity (LDV) and surface pressure measurements were carried out. The Xs (×) along the ϕ-axis denote the ϕ locations at which radial profiles of velocity were carried out using a 4-hot-wire probe. The asterisks (*) denote ϕ-locations at which velocity profiles were carried using both LDV and the 4-hot-wire probe.

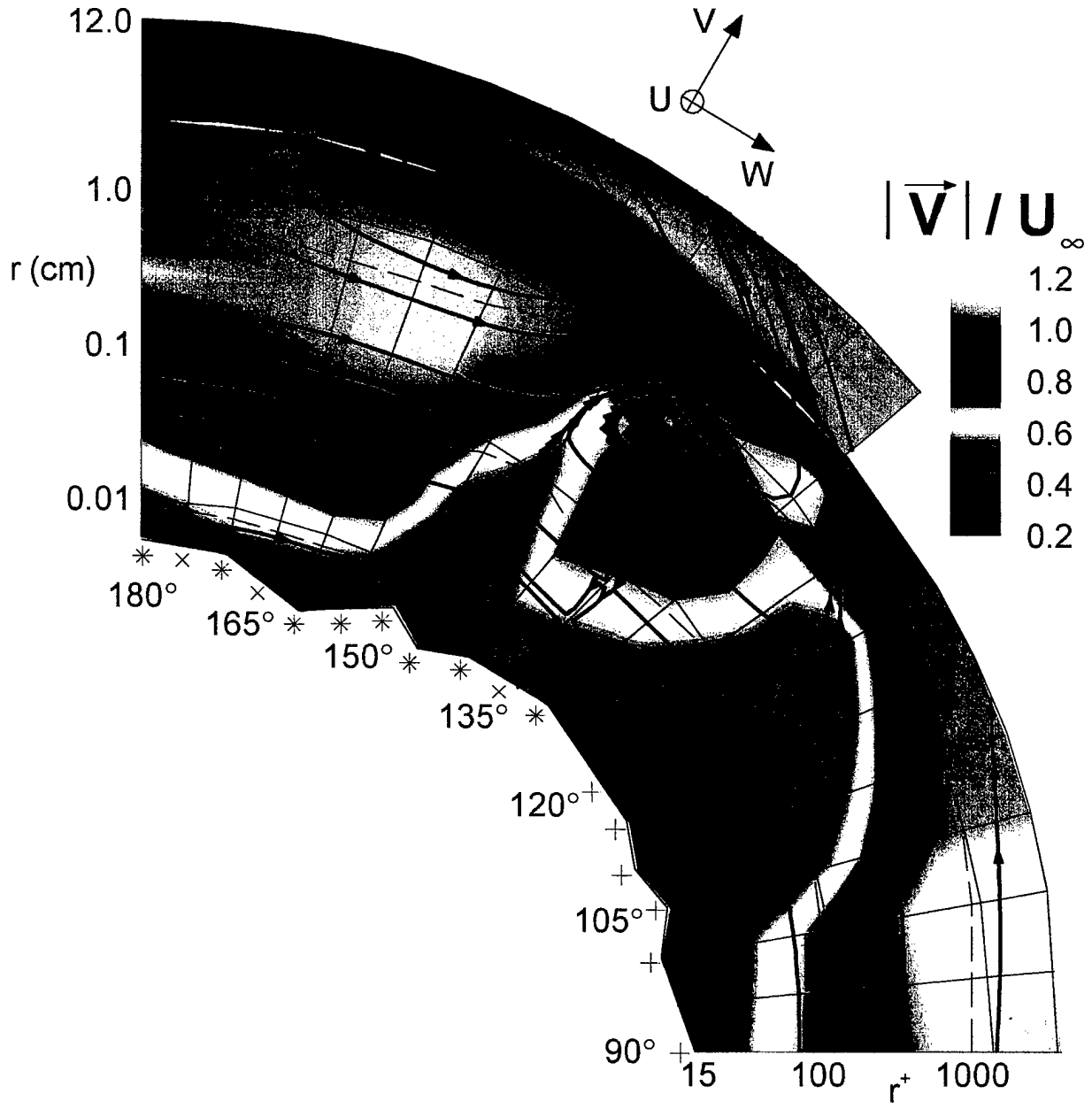

Figure 105. Secondary streamlines with contour levels of the mean velocity magnitude, $\alpha = 20°$, $x/L = 0.772$. The pluses (+) along the ϕ-axis denote the ϕ locations at which radial profiles of simultaneous velocity (LDV) and surface pressure measurements were carried out. The Xs (×) along the ϕ-axis denote the ϕ locations at which radial profiles of velocity were carried out using a 4-hot-wire probe. The asterisks (*) denote ϕ-locations at which velocity profiles were carried using both LDV and the 4-hot-wire probe. The radial coordinate (r) is plotted on a logarithmic scale and the dashed lines show lines of constant r^+. The irregular shape of the inner boundary is defined by the measurement locations nearest the model surface.

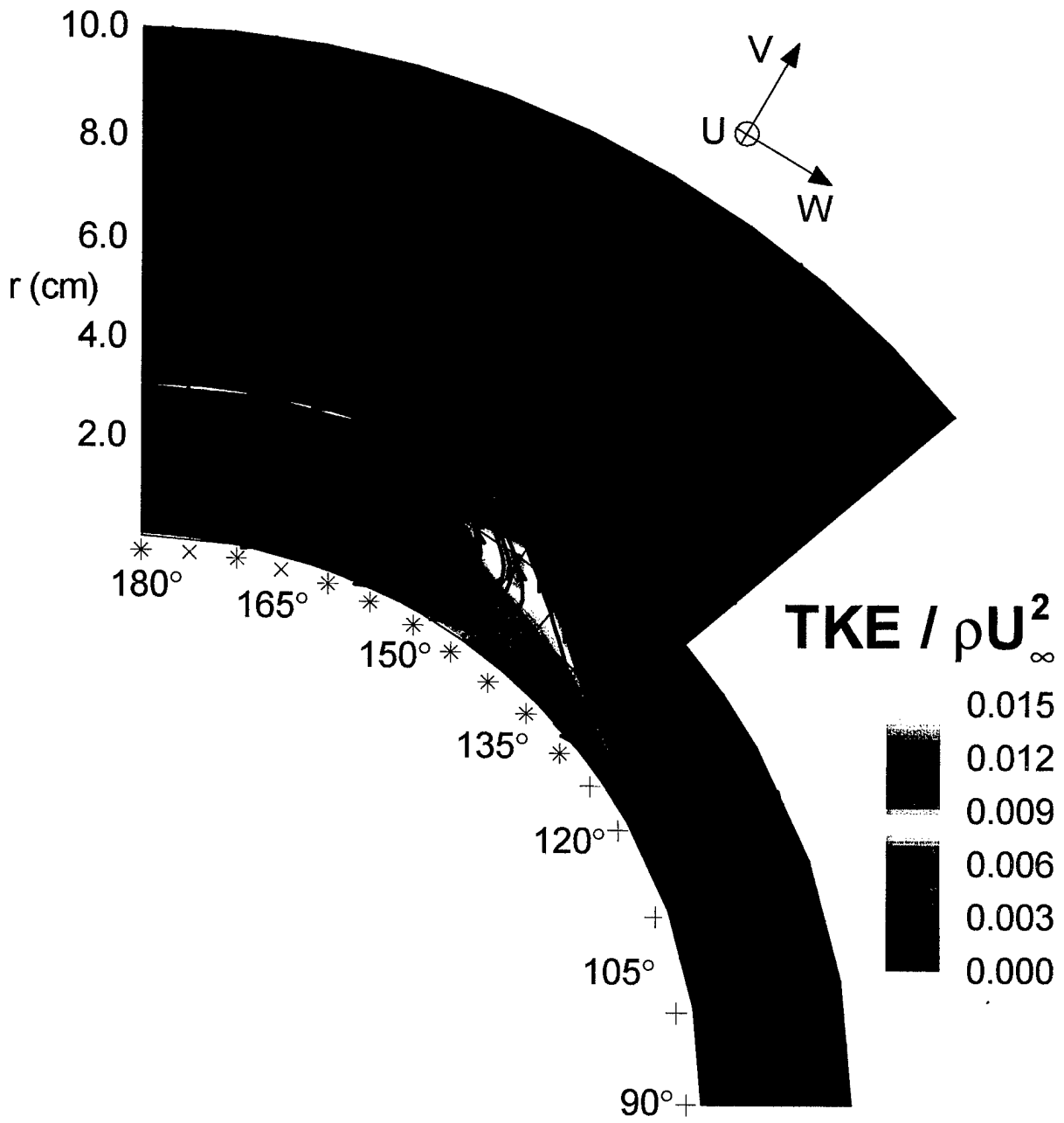

Figure 106. Secondary streamlines with contour levels of *TKE*, $\alpha = 20°$, $x/L = 0.772$. The pluses (+) along the ϕ-axis denote the ϕ locations at which radial profiles of simultaneous velocity (LDV) and surface pressure measurements were carried out. The Xs (×) along the ϕ-axis denote the ϕ locations at which radial profiles of velocity were carried out using a 4-hot-wire probe. The asterisks (*) denote ϕ-locations at which velocity profiles were carried using both LDV and the 4-hot-wire probe.

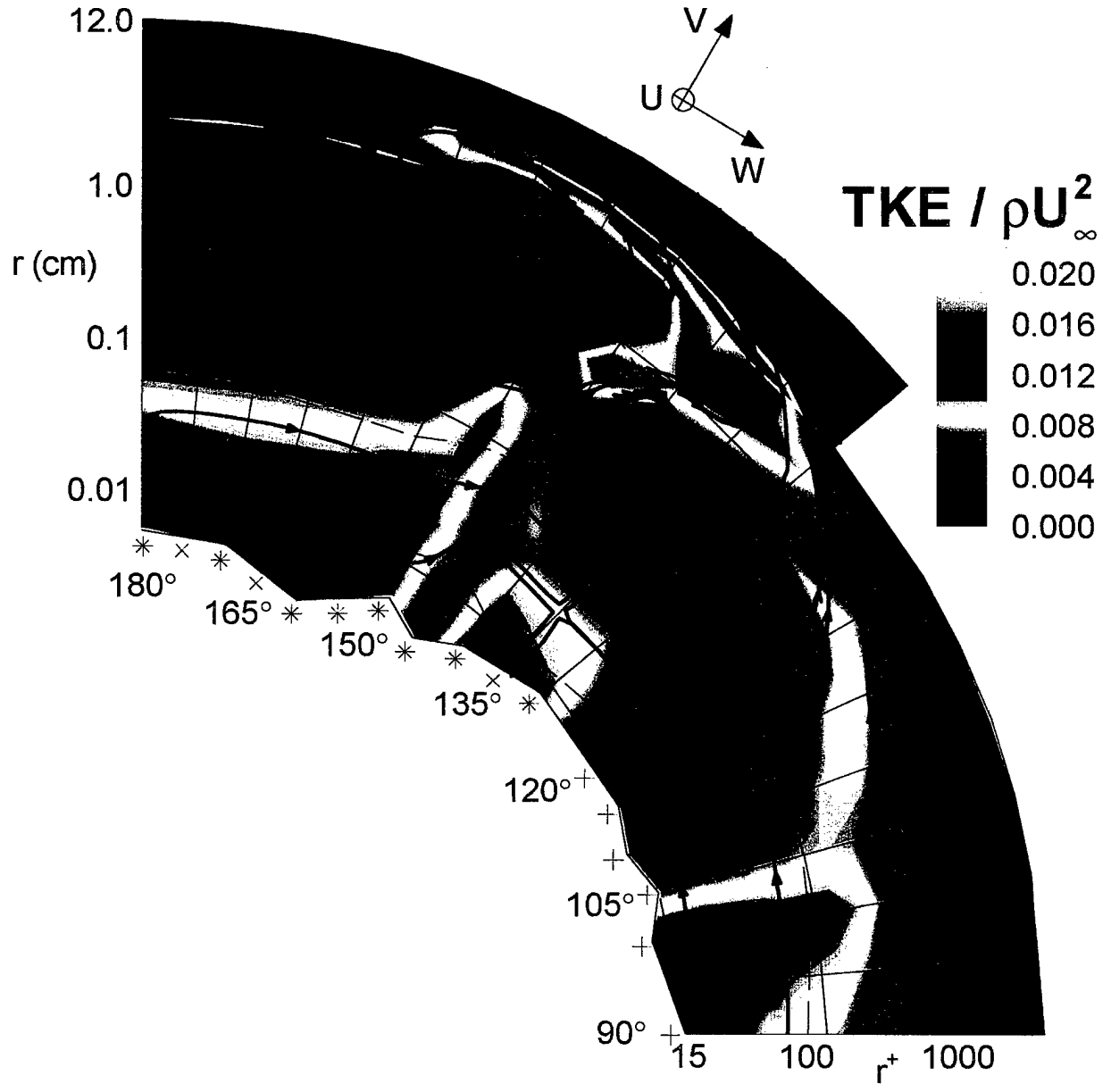

Figure 107. Secondary streamlines with contour levels of *TKE*, $\alpha = 20°$, $x/L = 0.772$. The pluses (+) along the ϕ-axis denote the ϕ locations at which radial profiles of simultaneous velocity (LDV) and surface pressure measurements were carried out. The Xs (×) along the ϕ-axis denote the ϕ locations at which radial profiles of velocity were carried out using a 4-hot-wire probe. The asterisks (*) denote ϕ-locations at which velocity profiles were carried using both LDV and the 4-hot-wire probe. The radial coordinate (r) is plotted on a logarithmic scale and the dashed lines show lines of constant r^+. The irregular shape of the inner boundary is defined by the measurement locations nearest the model surface.

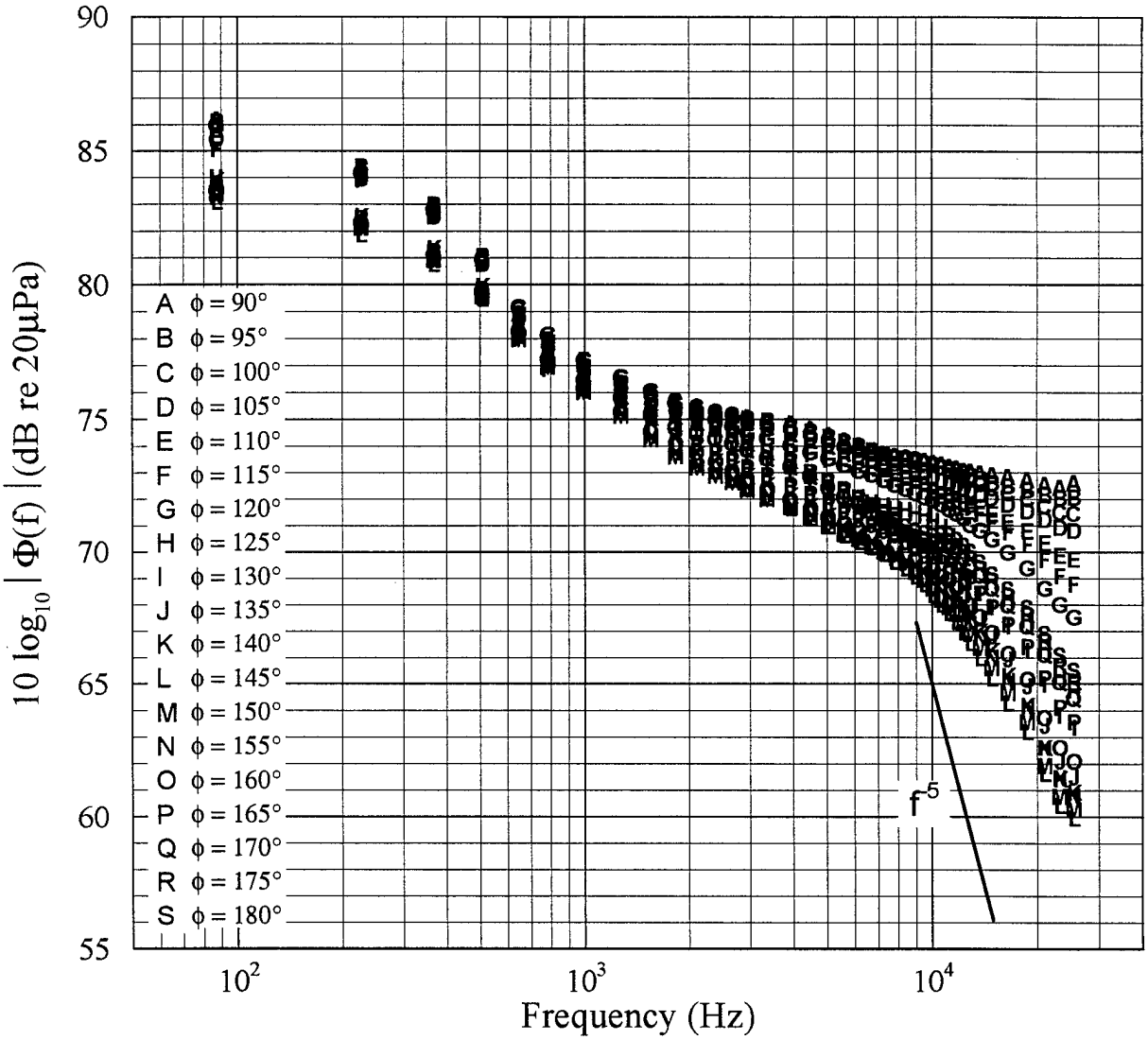

Figure 108. Power spectra of surface pressure fluctuations at $\alpha = 10°$, $x/L = 0.600$.

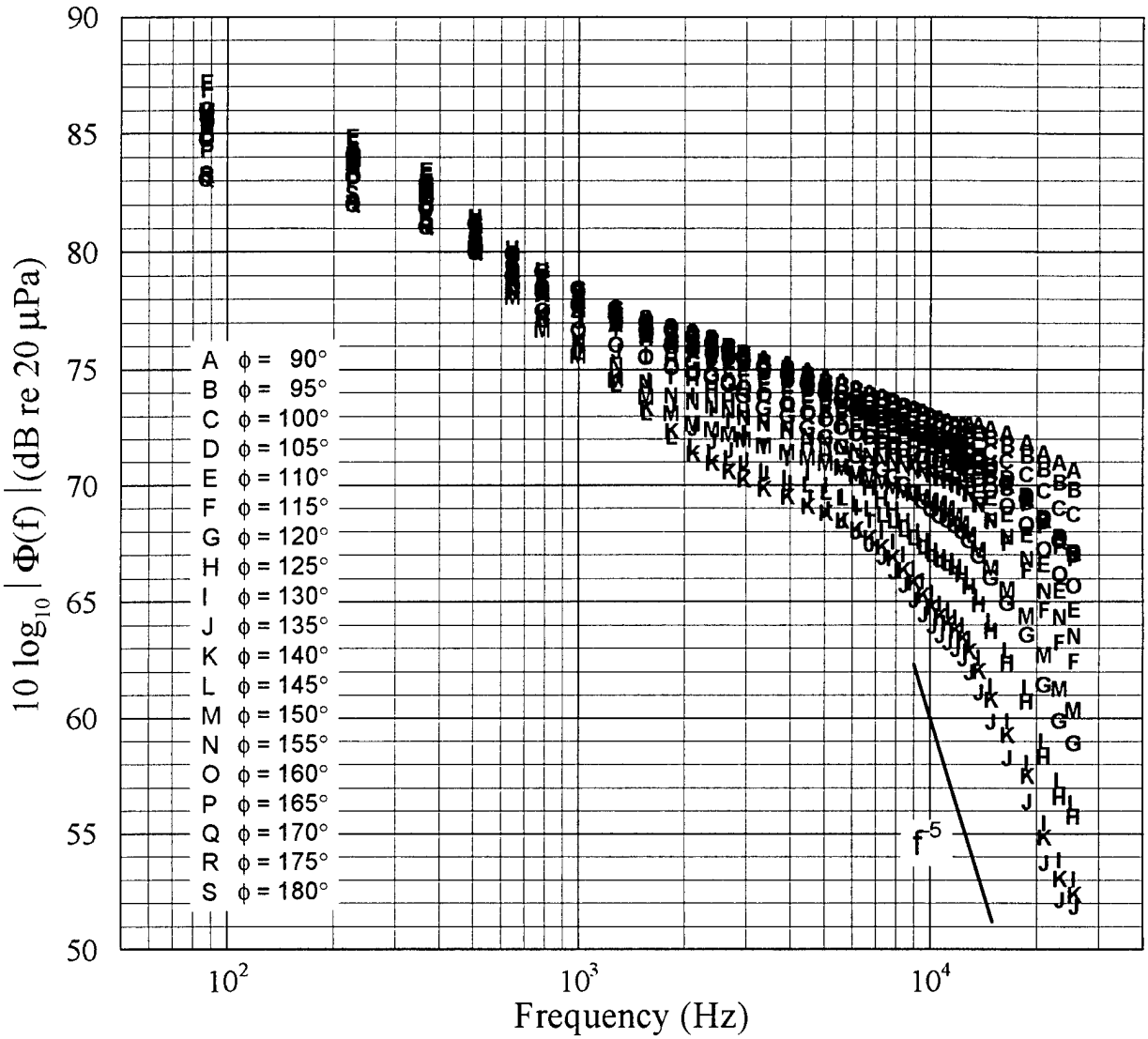

Figure 109. Power spectra of surface pressure fluctuations at $\alpha = 10°$, $x/L = 0.772$.

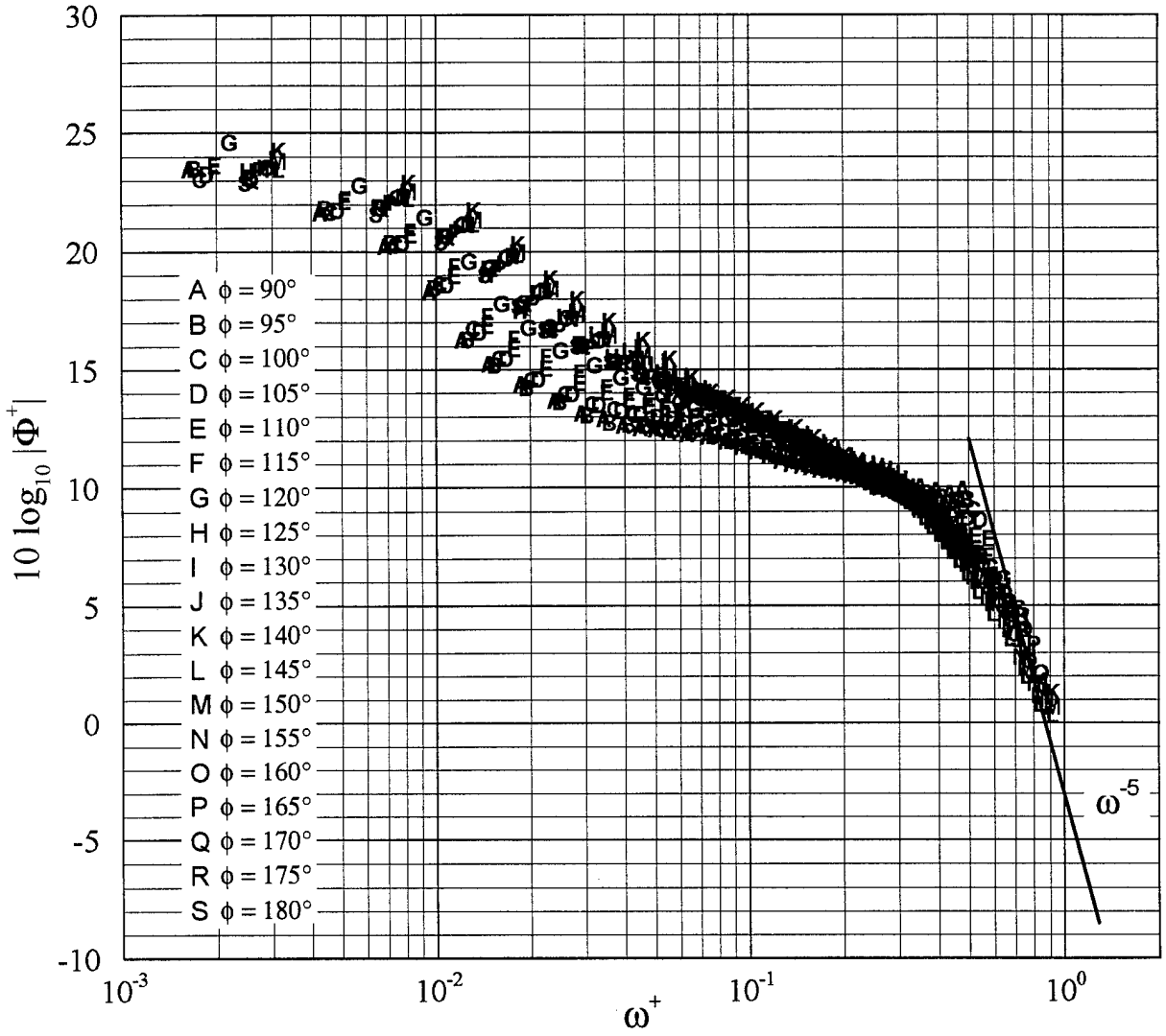

Figure 110. Power spectra of surface pressure fluctuations at $\alpha = 10°$, $x/L = 0.600$ normalized using ν/u_τ^2 as the time scale and τ_W as the pressure scale.

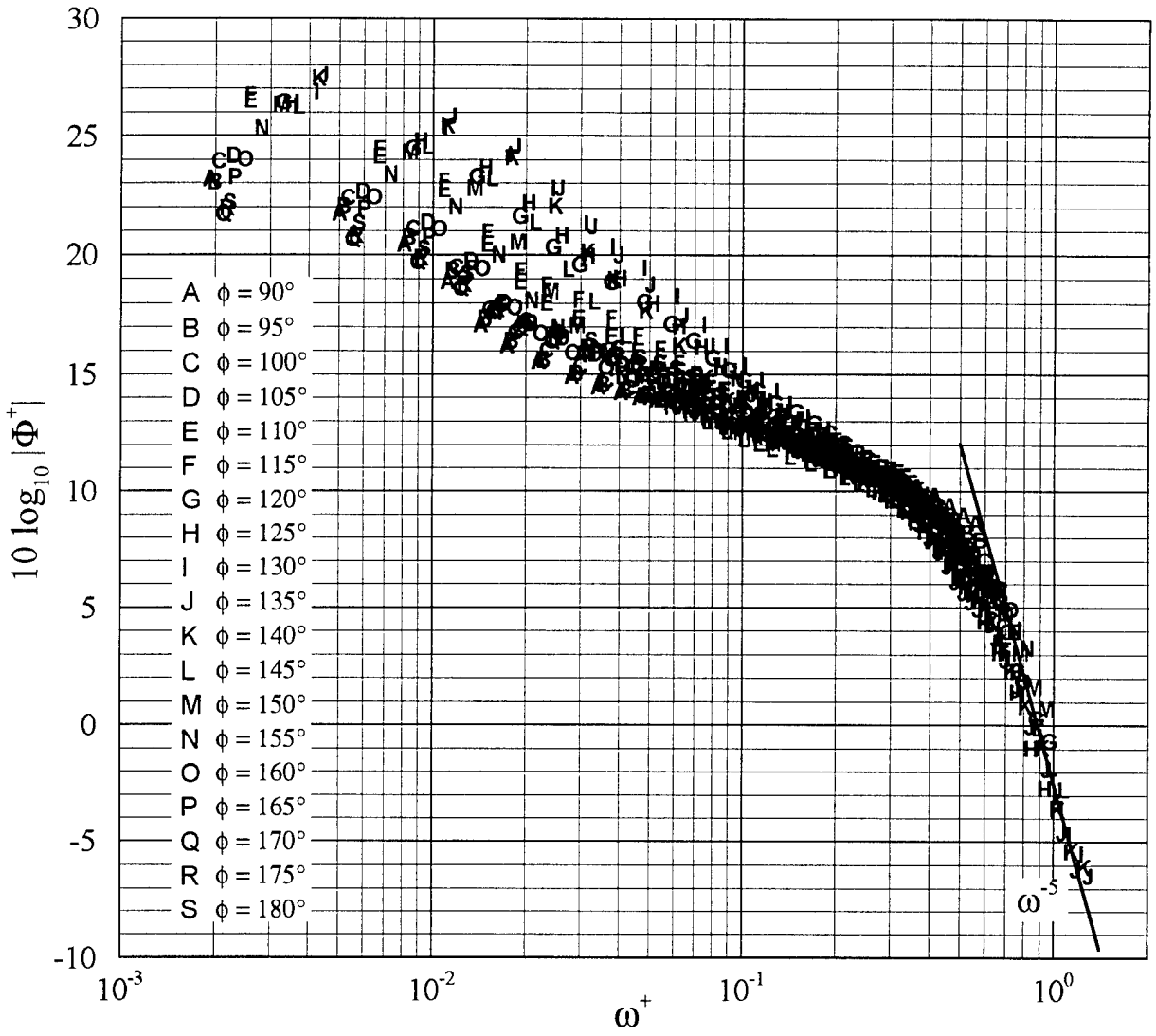

Figure 111. Power spectra of surface pressure fluctuations at $\alpha = 10°$, $x/L = 0.772$ normalized using ν/u_τ^2 as the time scale and τ_W as the pressure scale.

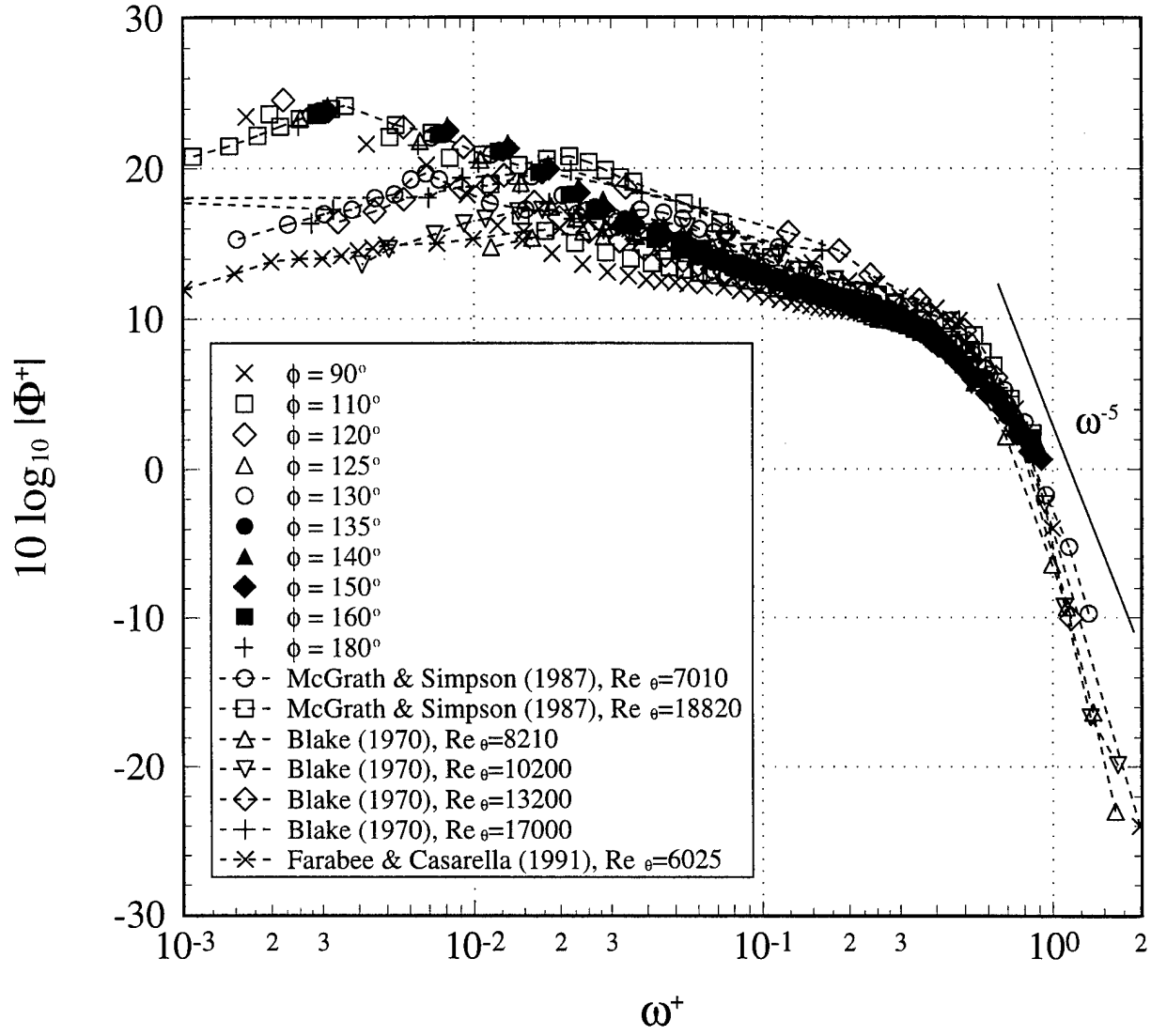

Figure 112. Power spectra of surface pressure fluctuations at $\alpha = 10°$, $x/L = 0.600$ and beneath 2-D, zero pressure gradient boundary layers normalized using ν/u_τ^2 as the time scale and τ_W as the pressure scale.

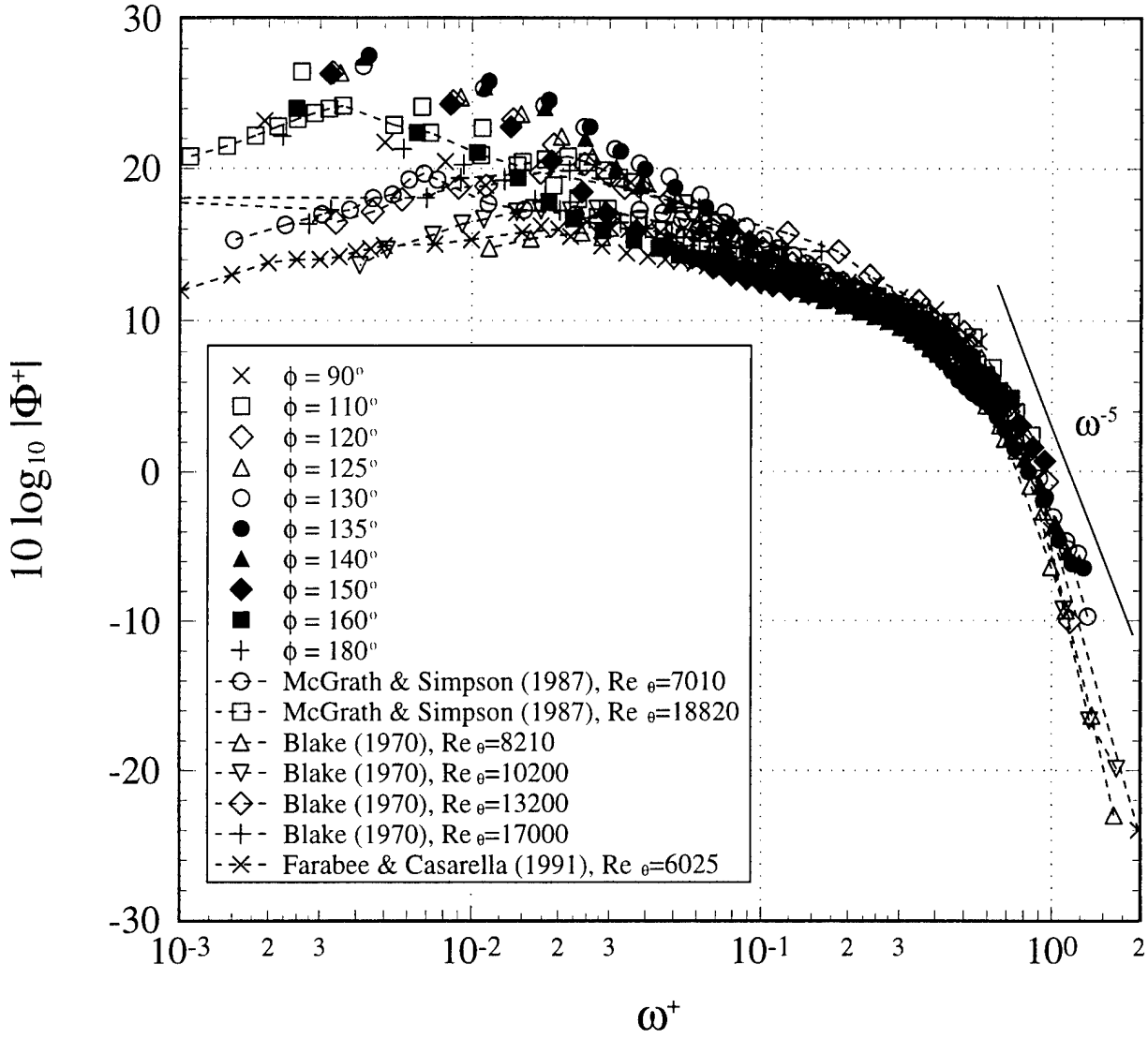

Figure 113. Power spectra of surface pressure fluctuations at $\alpha = 10°$, $x/L = 0.772$ and beneath 2-D, zero pressure gradient boundary layers normalized using ν/u_τ^2 as the time scale and τ_W as the pressure scale.

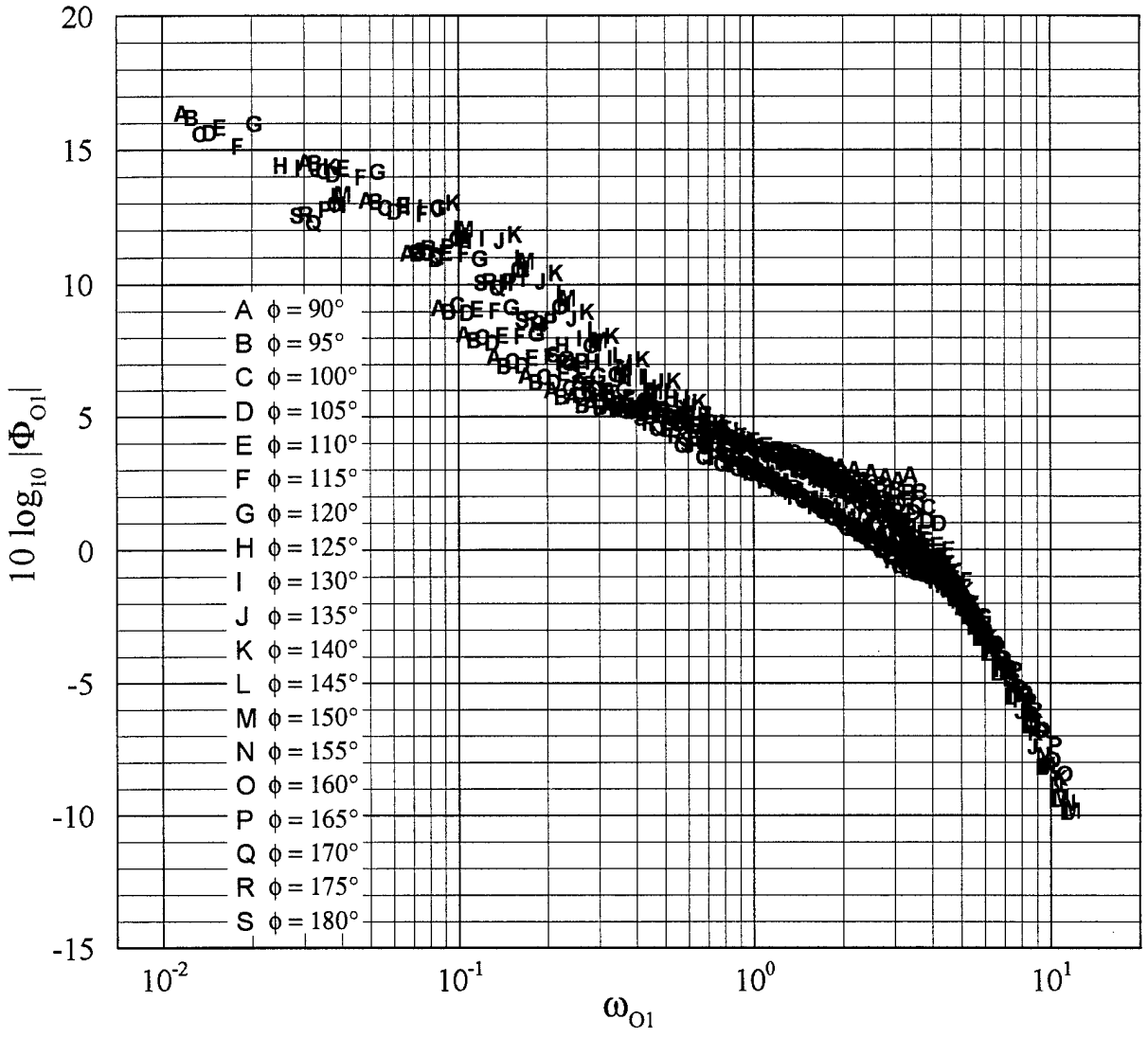

Figure 114. Power spectra of surface pressure fluctuations at $\alpha = 10°$, $x/L = 0.600$ normalized using δ^*/U_e as the time scale and τ_W as the pressure scale.

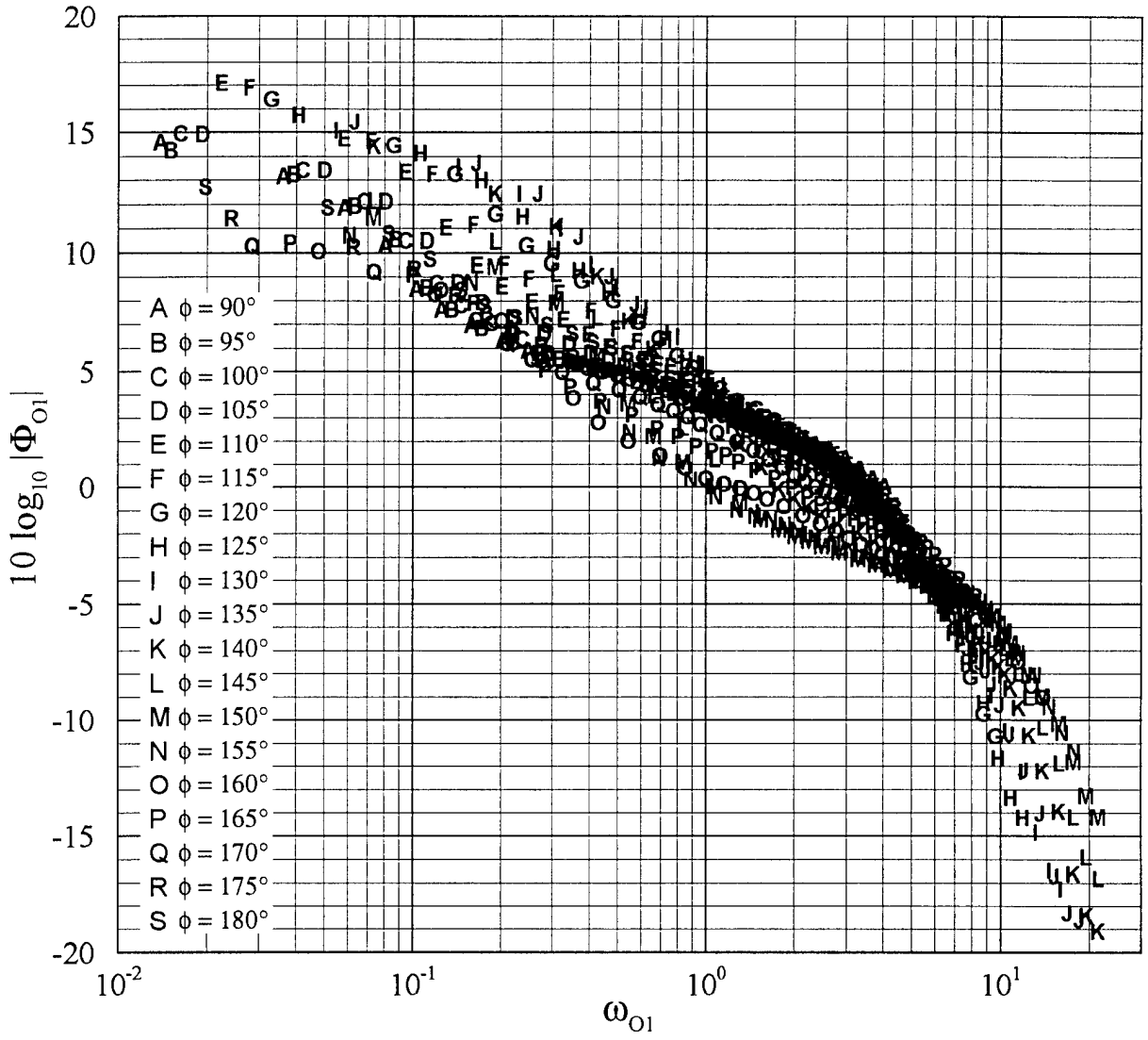

Figure 115. Power spectra of surface pressure fluctuations at $\alpha = 10°$, $x/L = 0.772$ normalized using δ^*/U_e as the time scale and τ_W as the pressure scale.

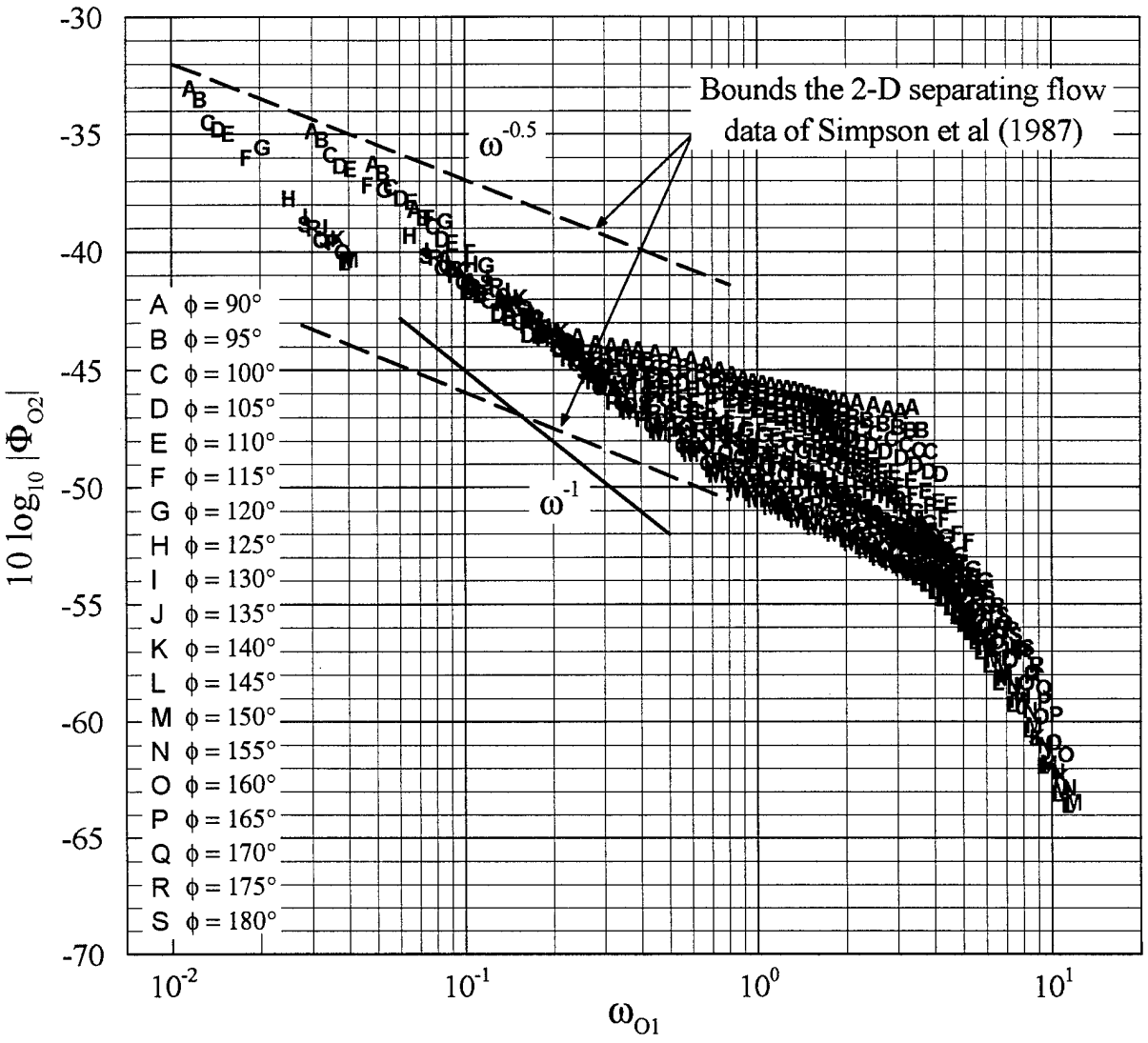

Figure 116. Power spectra of surface pressure fluctuations at $\alpha = 10°$, $x/L = 0.600$ normalized using δ^*/U_e as the time scale and Q_e as the pressure scale.

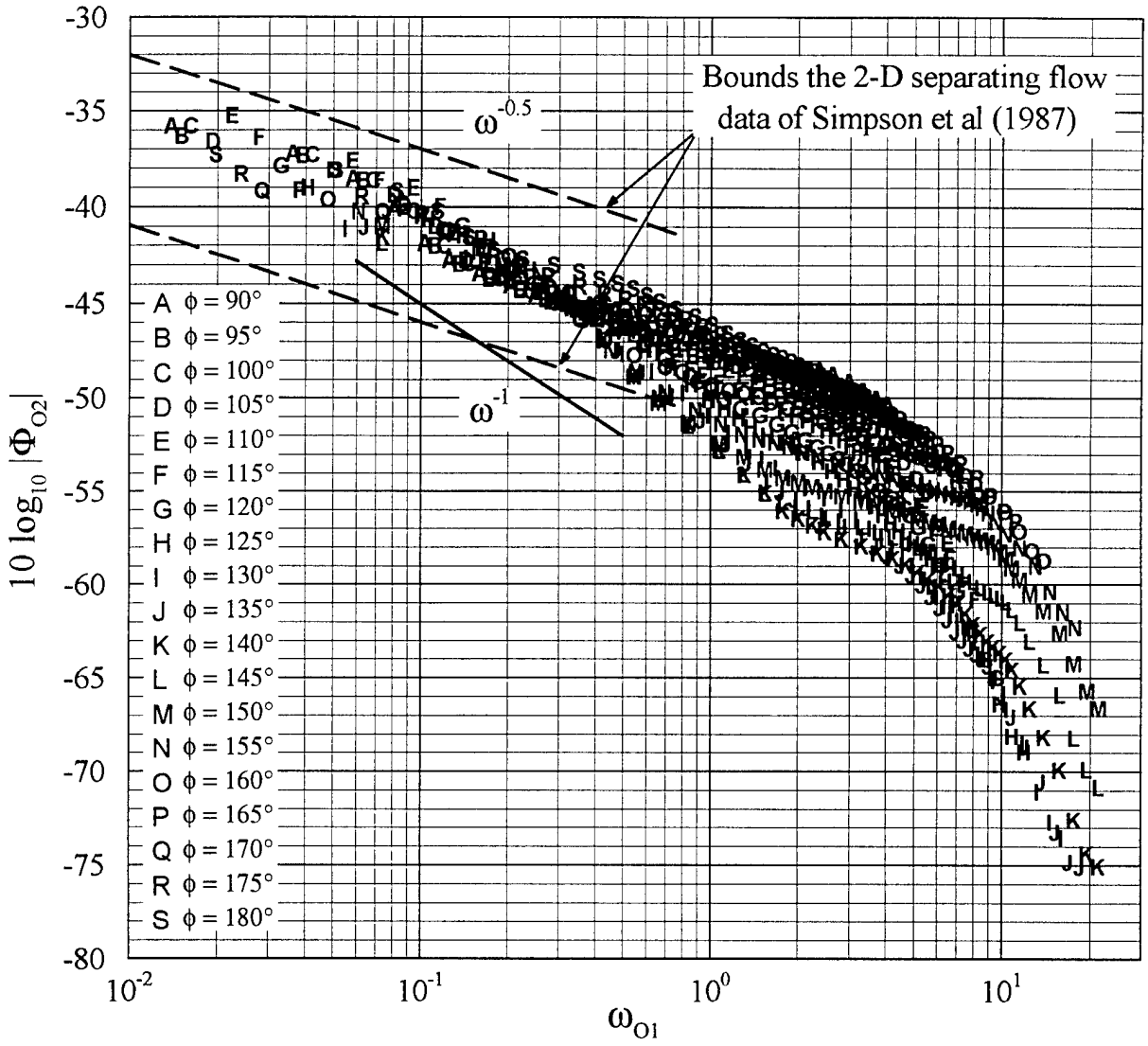

Figure 117. Power spectra of surface pressure fluctuations at $\alpha = 10°$, $x/L = 0.772$ normalized using δ^*/U_e as the time scale and Q_e as the pressure scale.

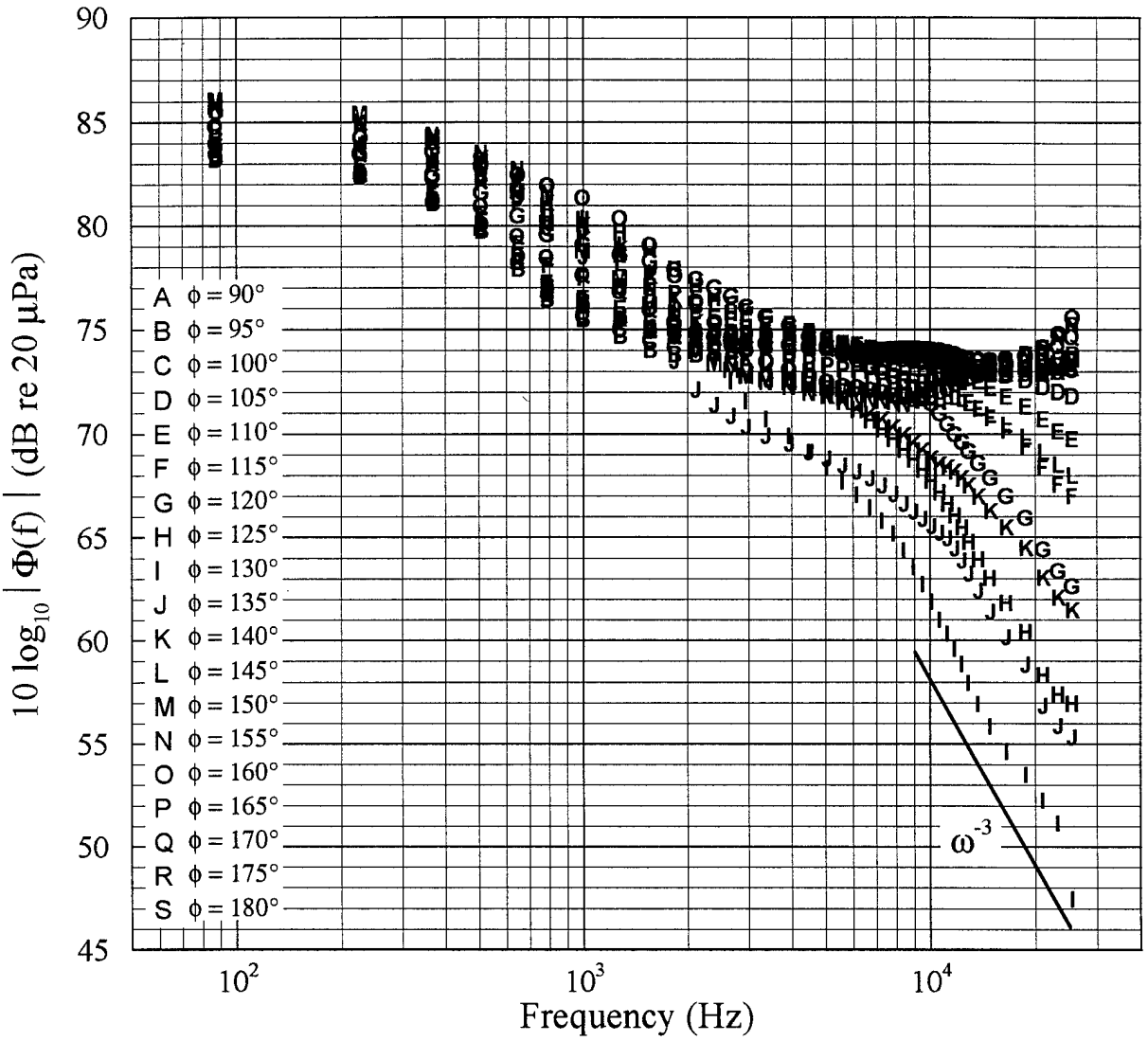

Figure 118. Power spectra of surface pressure fluctuations at $\alpha = 20°$, $x/L = 0.600$.

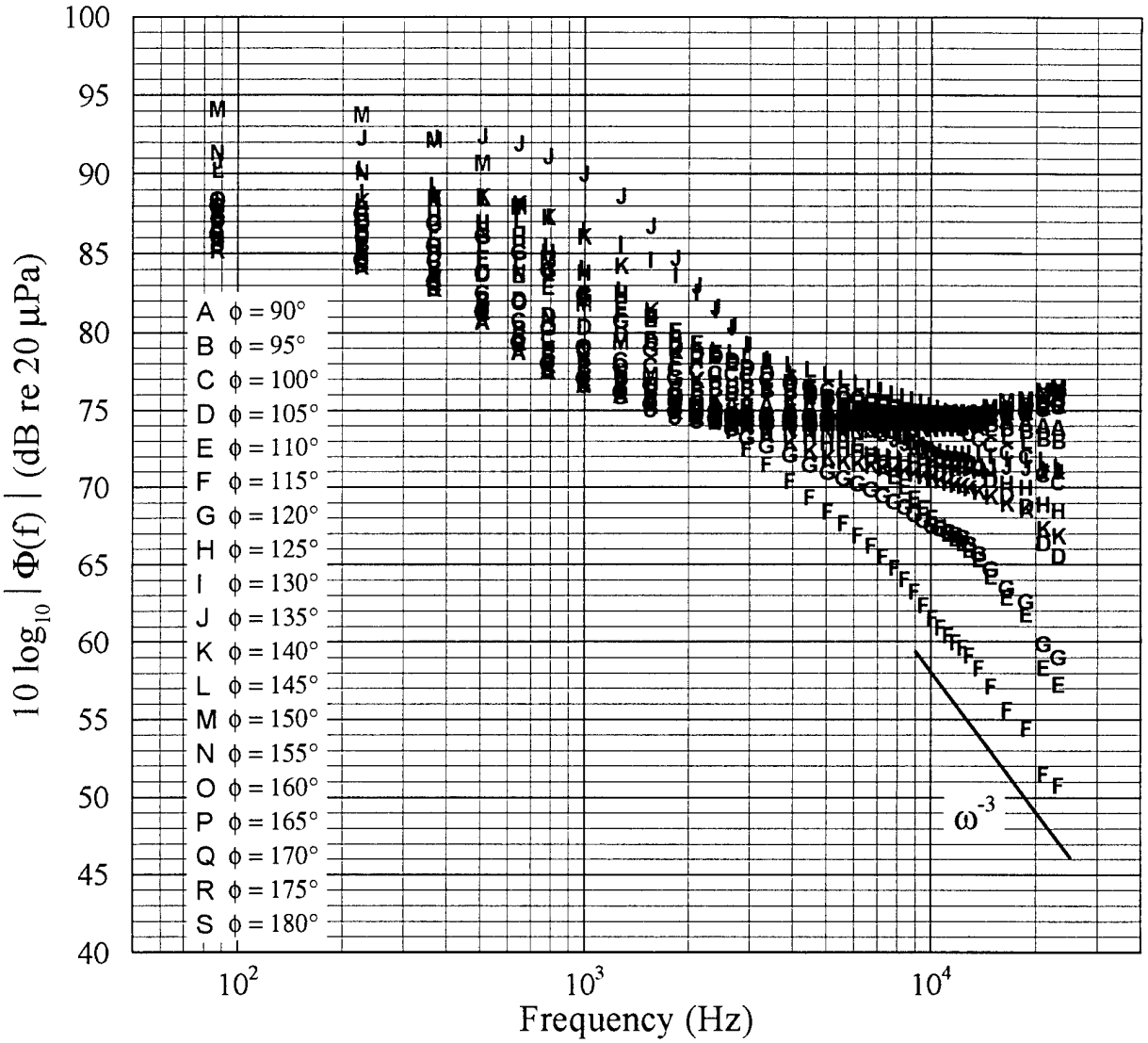

Figure 119. Power spectra of surface pressure fluctuations at $\alpha = 20°$, $x/L = 0.772$.

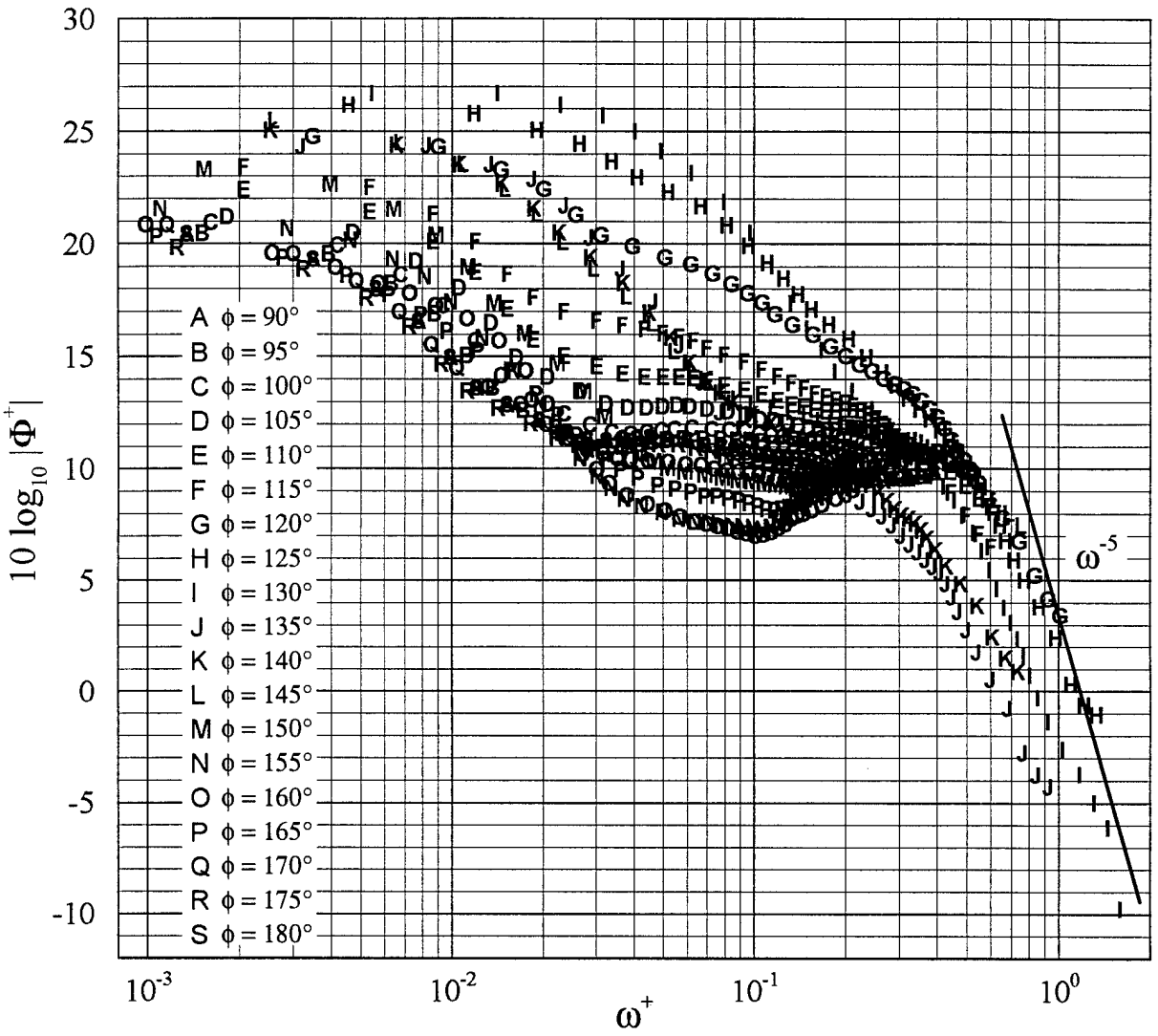

Figure 120. Power spectra of surface pressure fluctuations at $\alpha = 20°$, $x/L = 0.600$ normalized using ν/u_τ^2 as the time scale and τ_W as the pressure scale.

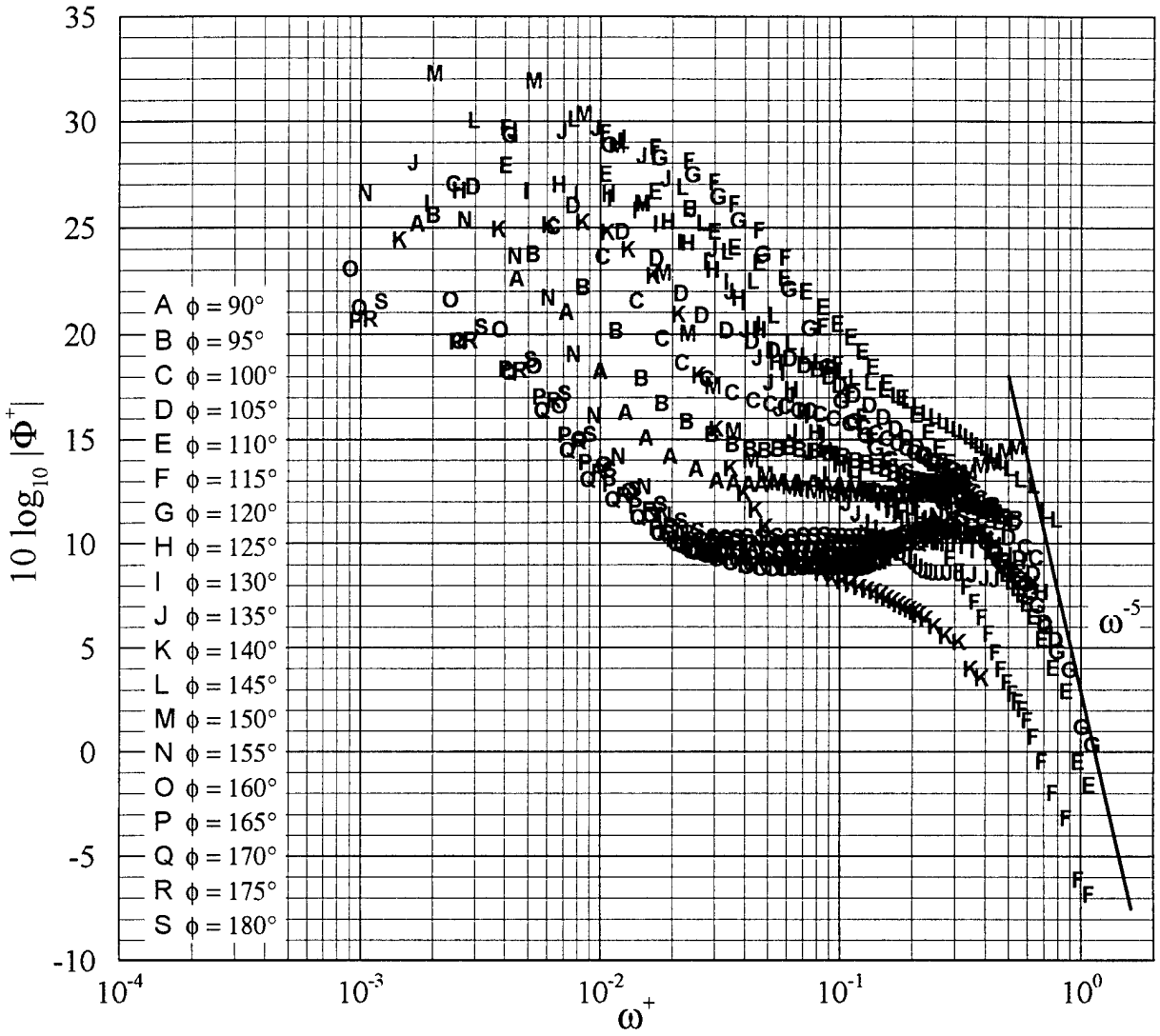

Figure 121. Power spectra of surface pressure fluctuations at $\alpha = 20°$, $x/L = 0.772$ normalized using ν/u_τ^2 as the time scale and τ_W as the pressure scale.

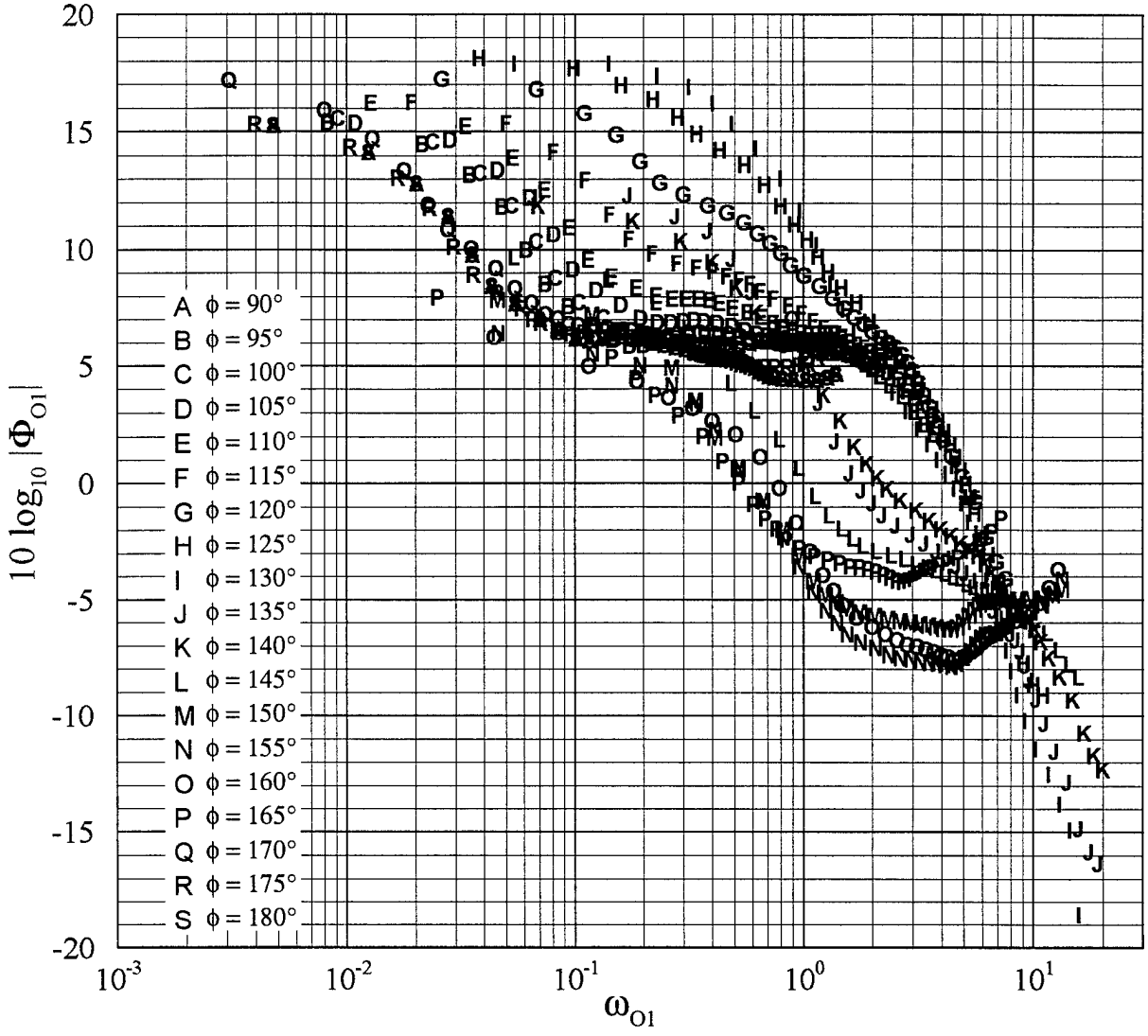

Figure 122. Power spectra of surface pressure fluctuations at $\alpha = 20°$, $x/L = 0.600$ normalized using δ^*/U_e as the time scale and τ_W as the pressure scale.

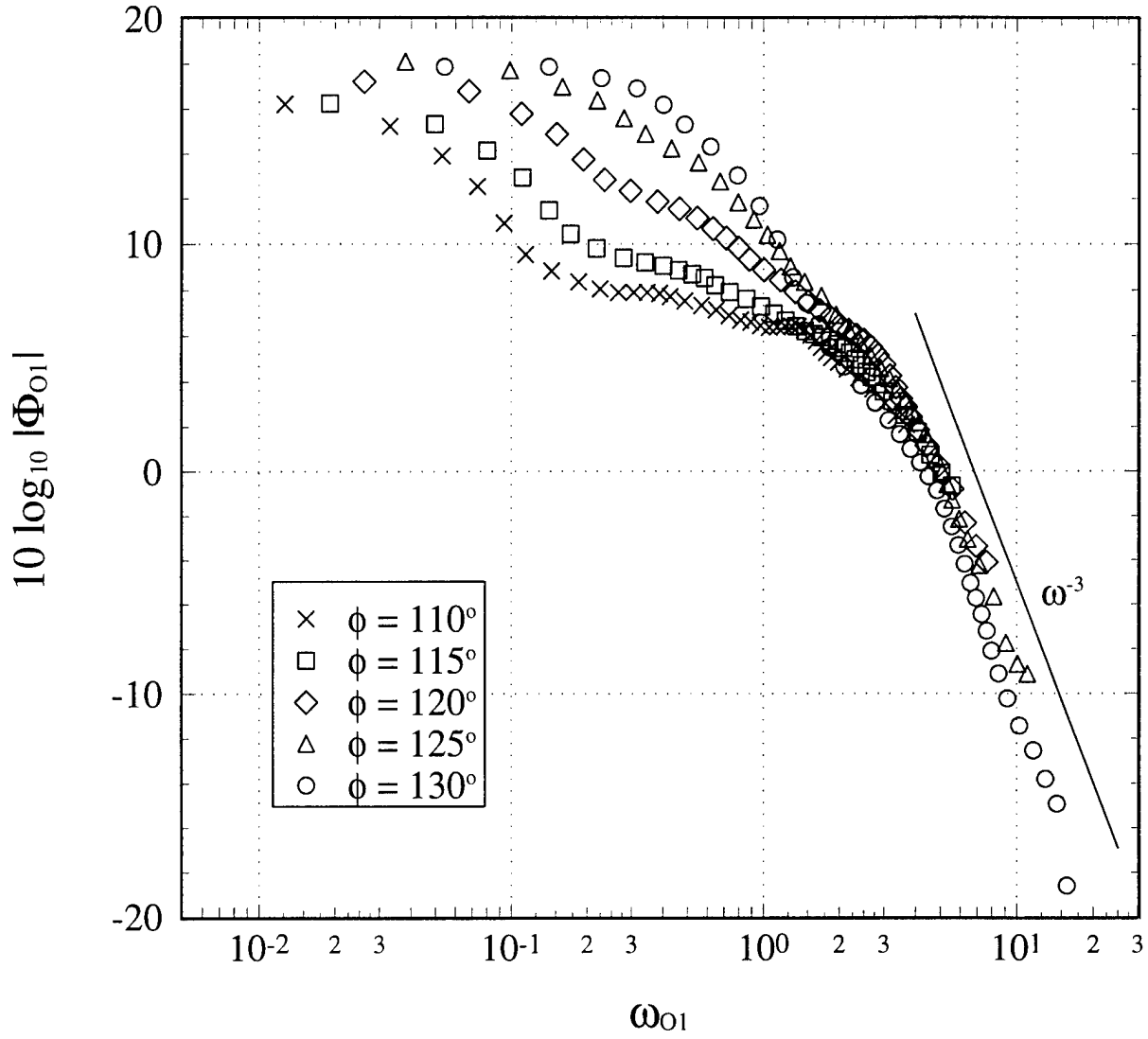

Figure 123. Power spectra of surface pressure fluctuations at $\alpha = 20°$, $x/L = 0.600$, $110° \leq \phi \leq 135°$ normalized using δ^*/U_e as the time scale and τ_W as the pressure scale.

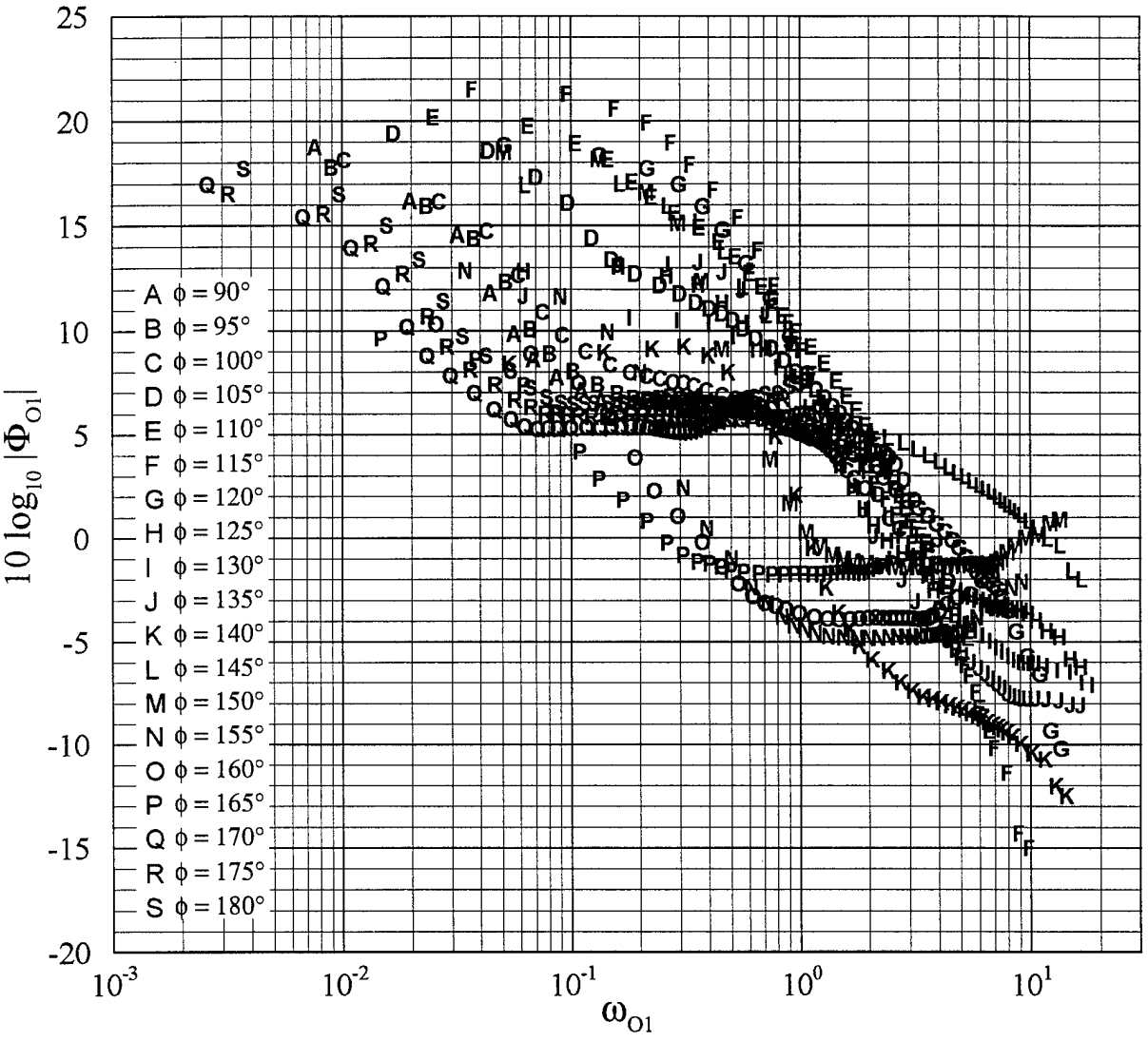

Figure 124. Power spectra of surface pressure fluctuations at $\alpha = 20°$, $x/L = 0.772$ normalized using δ^*/U_e as the time scale and τ_W as the pressure scale.

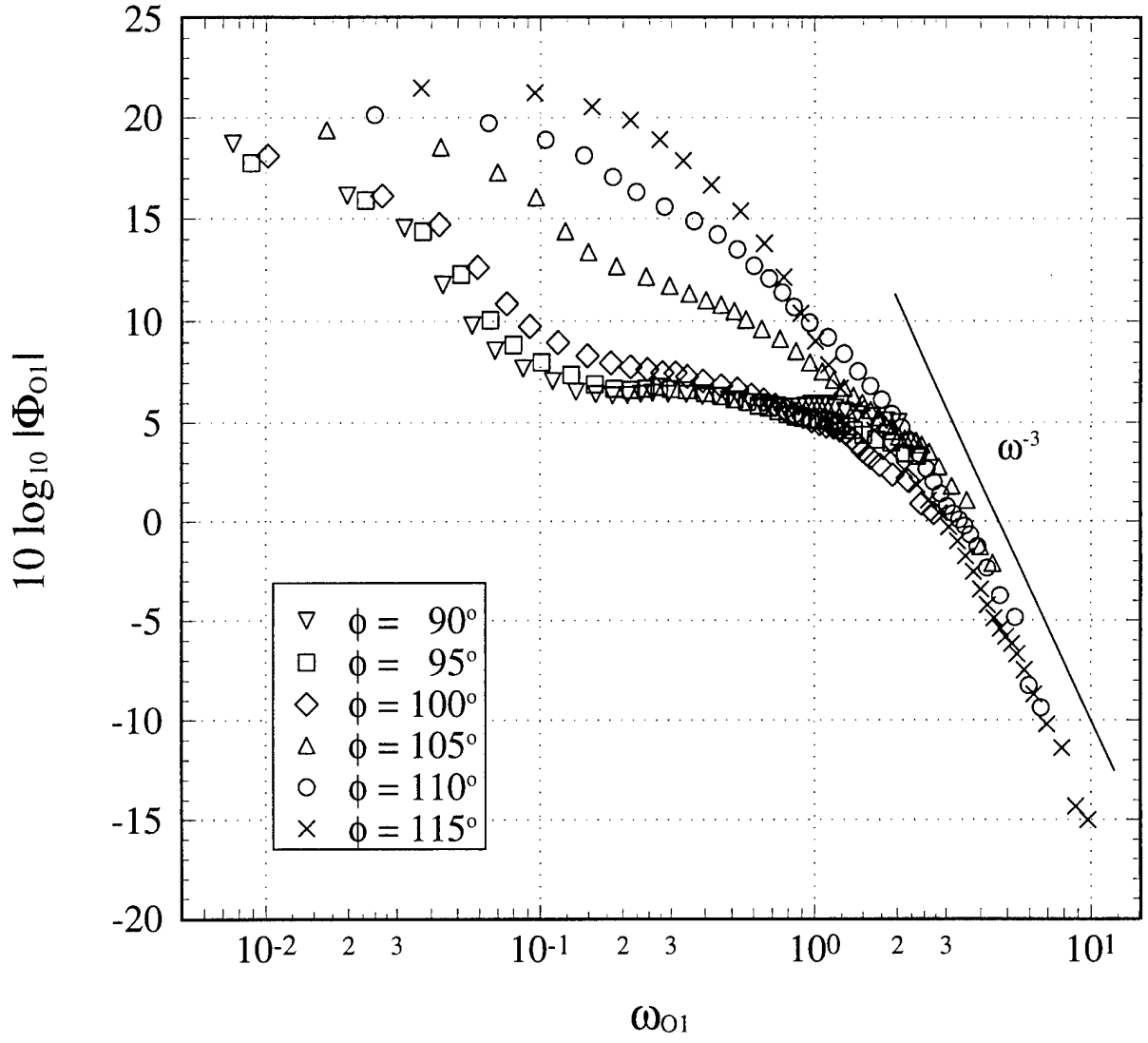

Figure 125. Power spectra of surface pressure fluctuations at $\alpha = 20°$, $x/L = 0772$, $\phi \leq 115°$ normalized using δ^*/U_e as the time scale and τ_W as the pressure scale.

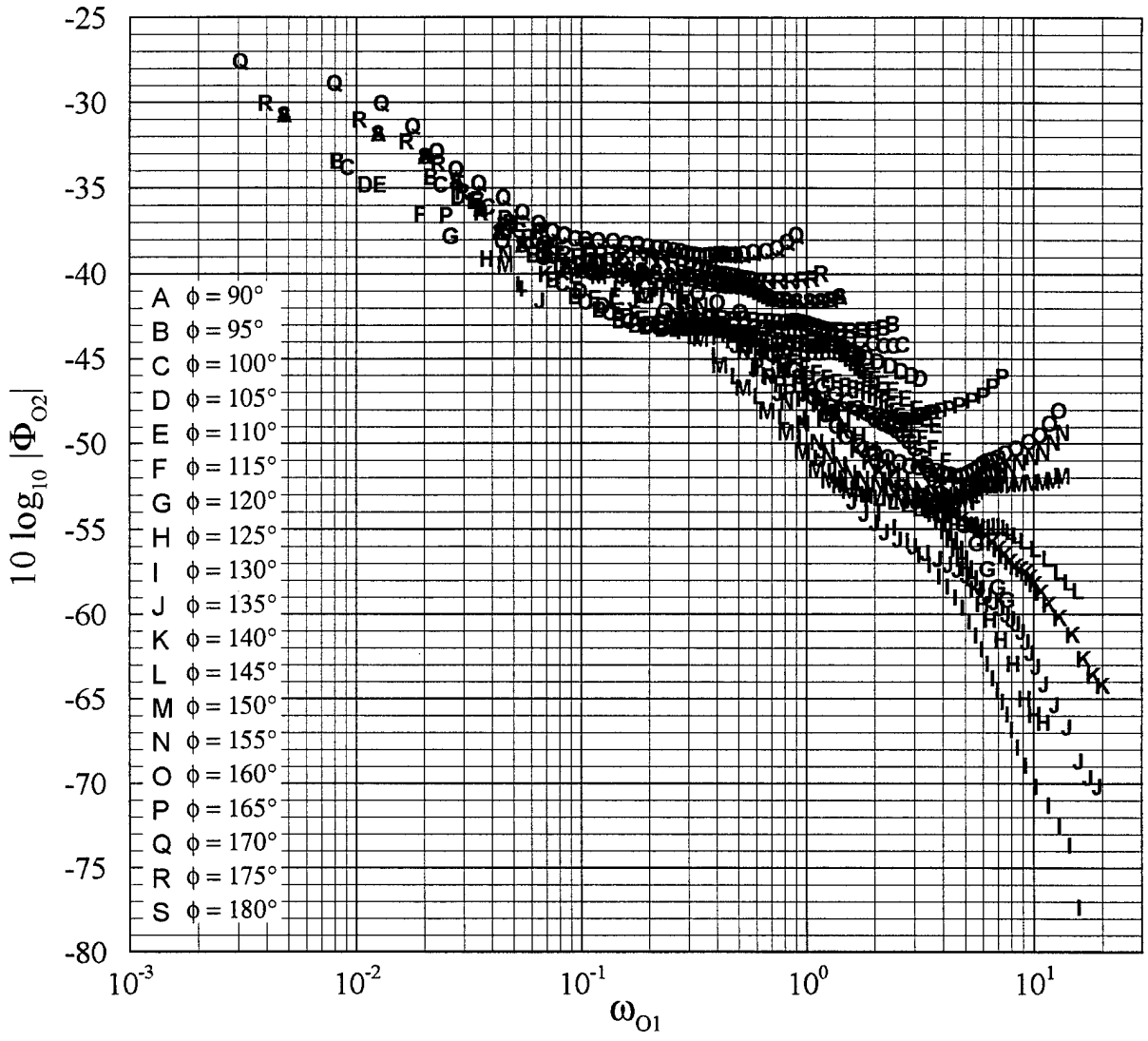

Figure 126. Power spectra of surface pressure fluctuations at $\alpha = 20°$, $x/L = 0.600$ normalized using δ^*/U_e as the time scale and Q_e as the pressure scale.

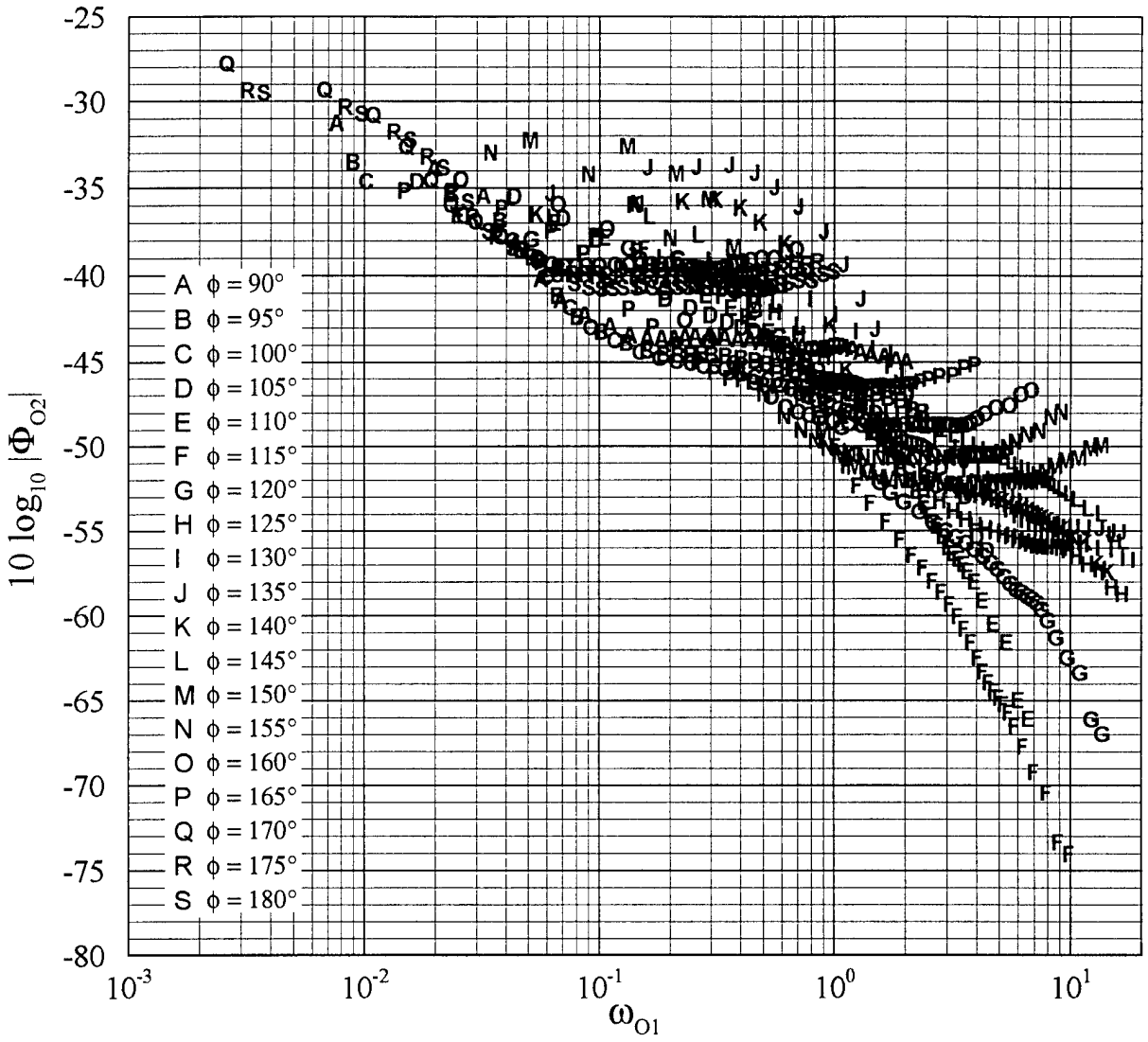

Figure 127. Power spectra of surface pressure fluctuations at $\alpha = 20°$, $x/L = 0.772$ normalized using δ^*/U_e as the time scale and Q_e as the pressure scale.

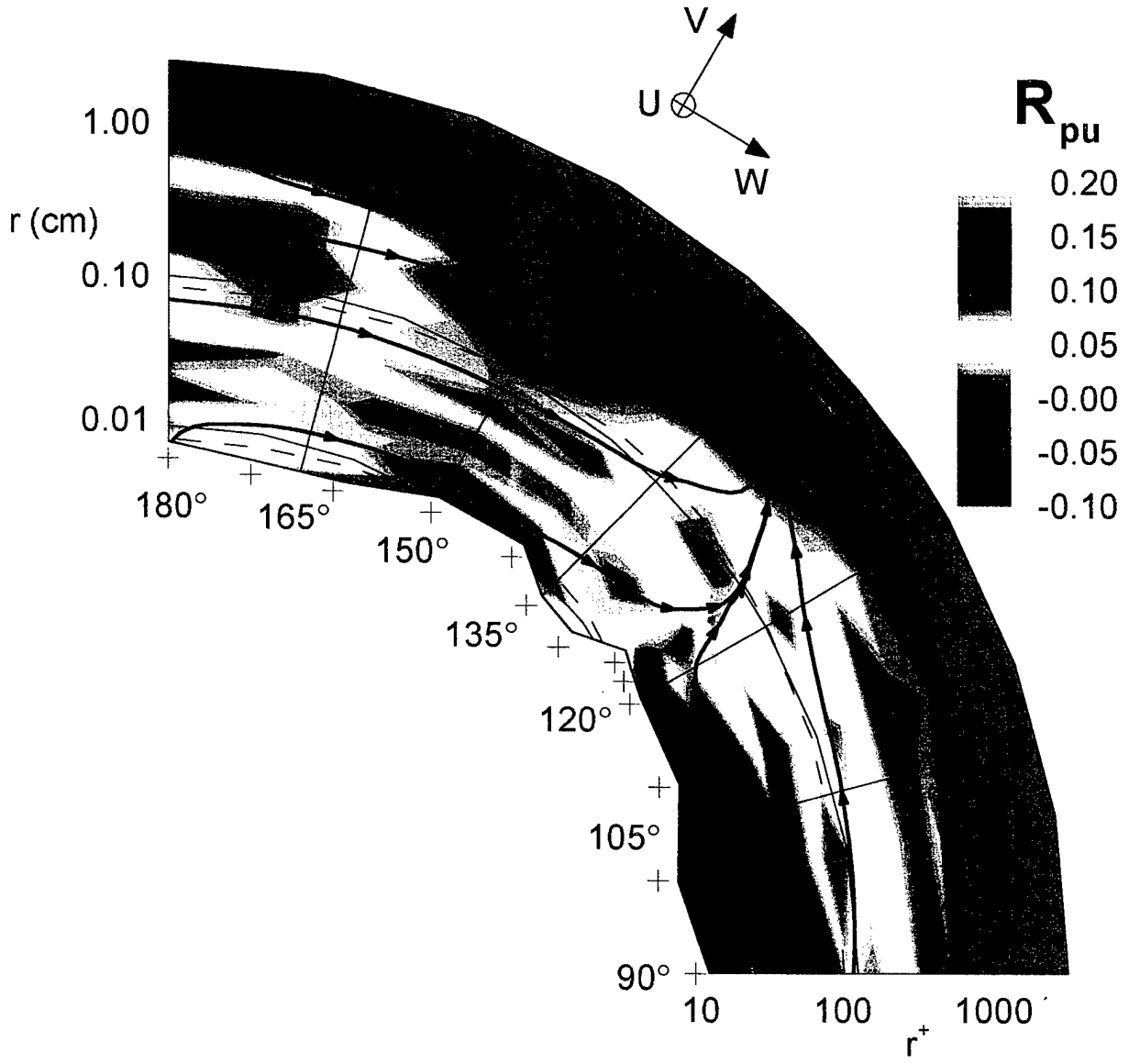

Figure 128. Secondary streamlines with contour levels of the correlation coefficient (R_{pu}) between the surface pressure and the fluctuating u-velocity component, $\alpha = 10°$, $x/L = 0.772$. The pluses (+) along the ϕ-axis denote the ϕ locations at which radial profiles of simultaneous velocity (LDV) and surface pressure measurements were carried out. The radial coordinate (r) is plotted on a logarithmic scale and the dashed lines show lines of constant r^+. The irregular shape of the inner boundary is defined by the measurement locations nearest the model surface.

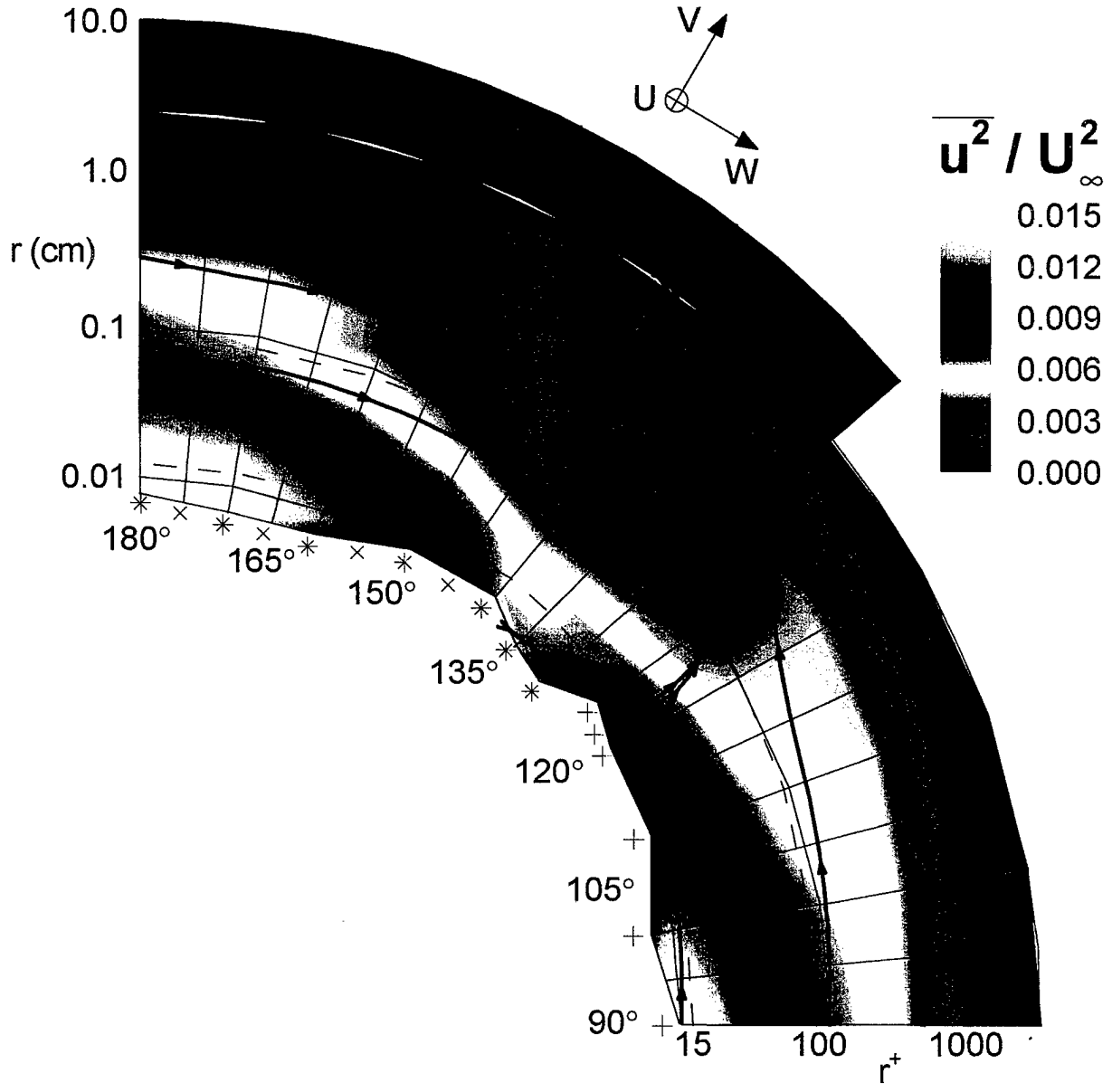

Figure 129. Secondary streamlines with contour levels of the fluctuating u-velocity component, $\alpha = 10°$, $x/L = 0.772$. The pluses (+) along the ϕ-axis denote the ϕ locations at which radial profiles of simultaneous velocity (LDV) and surface pressure measurements were carried out. The Xs (×) along the ϕ-axis denote the ϕ locations at which radial profiles of velocity were carried out using a 4-hot-wire probe. The asterisks (*) denote ϕ-locations at which velocity profiles were carried using both LDV and the 4-hot-wire probe. The radial coordinate (r) is plotted on a logarithmic scale and the dashed lines show lines of constant r^+. The irregular shape of the inner boundary is defined by the measurement locations nearest the model surface.

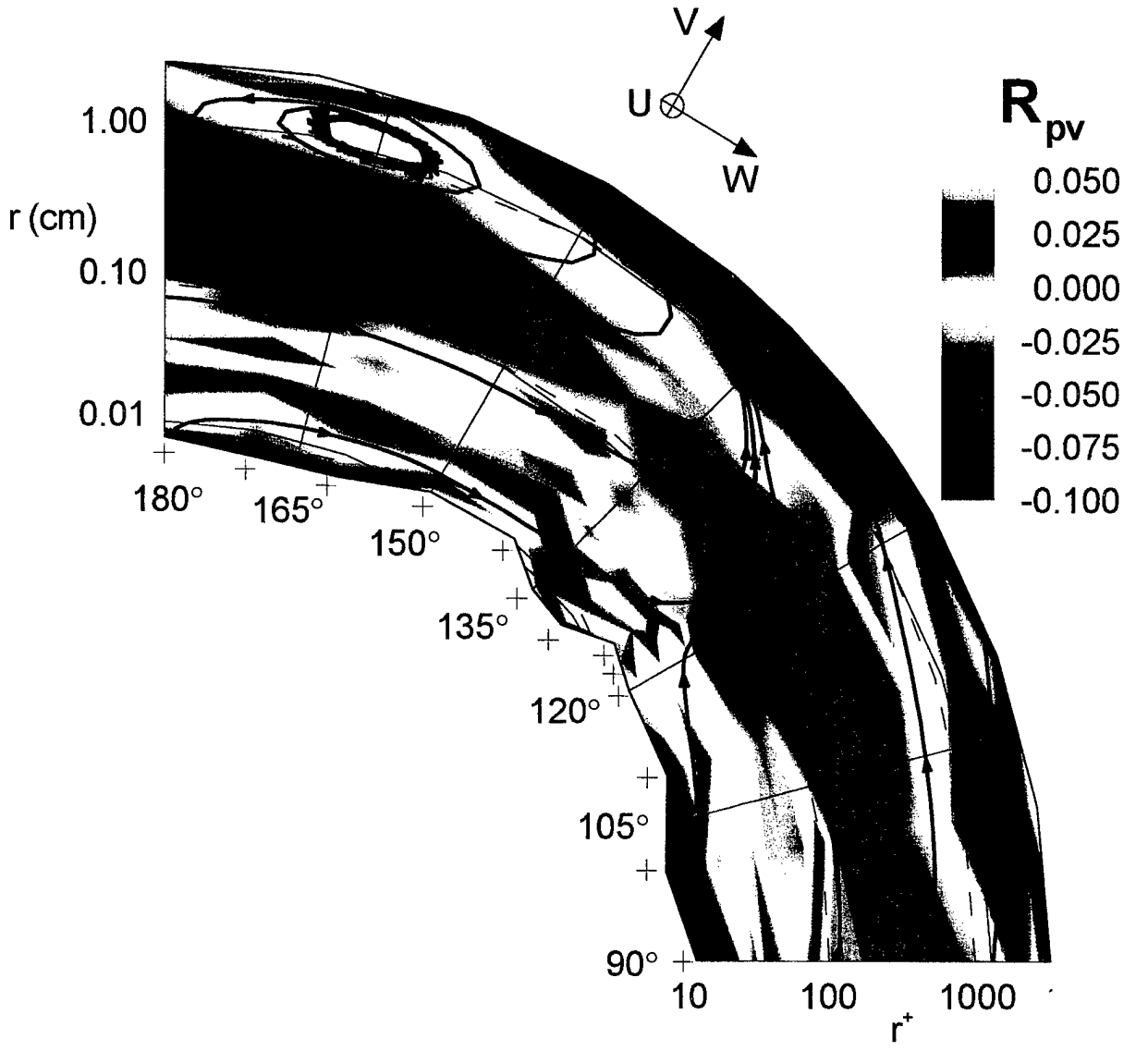

Figure 130. Secondary streamlines with contour levels of the correlation coefficient (R_{pv}) between the surface pressure and the fluctuating v-velocity component, $\alpha = 10°$, $x/L = 0.772$. The pluses (+) along the ϕ-axis denote the ϕ locations at which radial profiles of simultaneous velocity (LDV) and surface pressure measurements were carried out. The radial coordinate (r) is plotted on a logarithmic scale and the dashed lines show lines of constant r^+. The irregular shape of the inner boundary is defined by the measurement locations nearest the model surface.

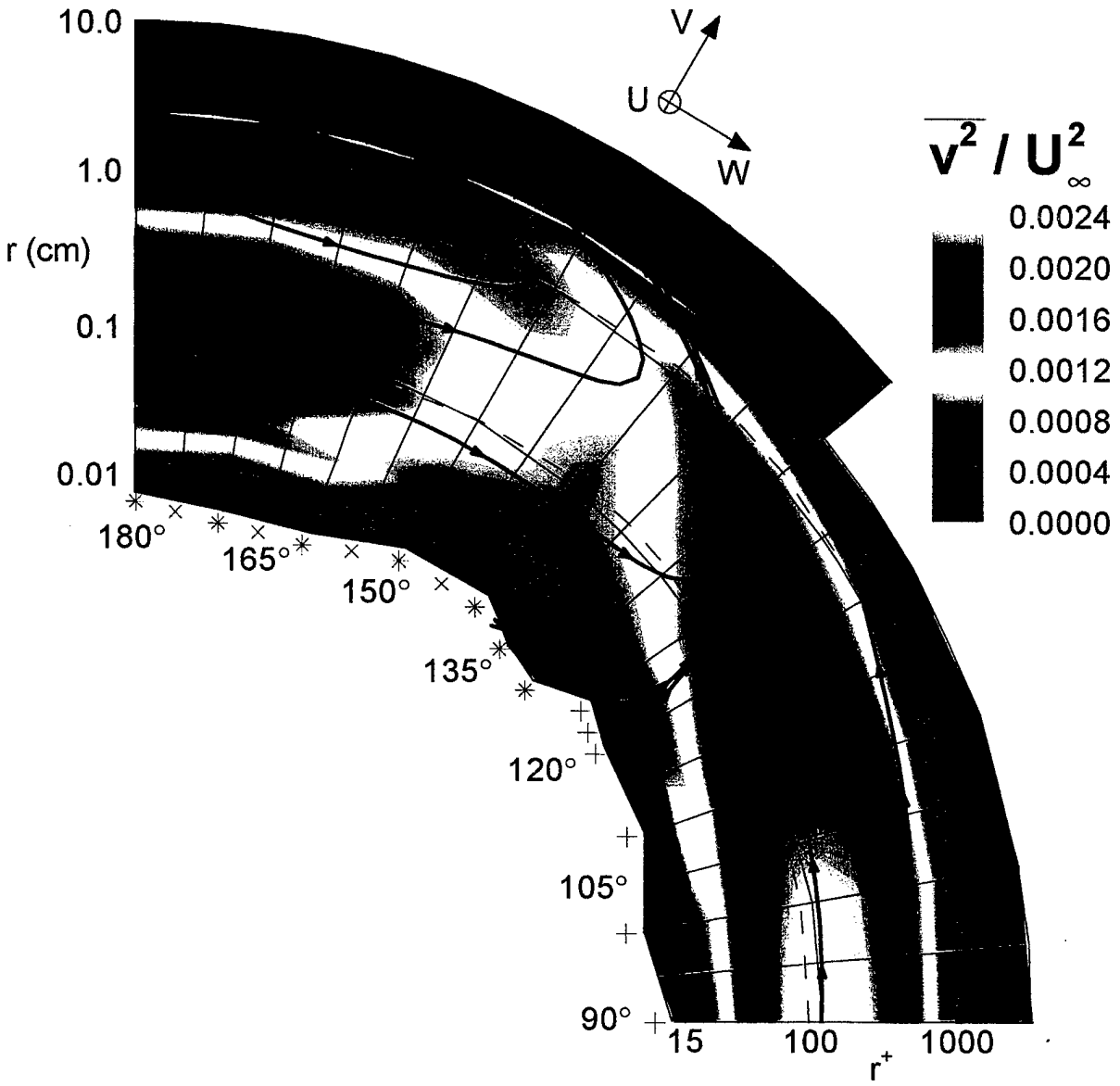

Figure 131. Secondary streamlines with contour levels of the fluctuating v-velocity component, $\alpha = 10°$, $x/L = 0.772$. The pluses (+) along the ϕ-axis denote the ϕ locations at which radial profiles of simultaneous velocity (LDV) and surface pressure measurements were carried out. The Xs (×) along the ϕ-axis denote the ϕ locations at which radial profiles of velocity were carried out using a 4-hot-wire probe. The asterisks (*) denote ϕ-locations at which velocity profiles were carried using both LDV and the 4-hot-wire probe. The radial coordinate (r) is plotted on a logarithmic scale and the dashed lines show lines of constant r^+. The irregular shape of the inner boundary is defined by the measurement locations nearest the model surface.

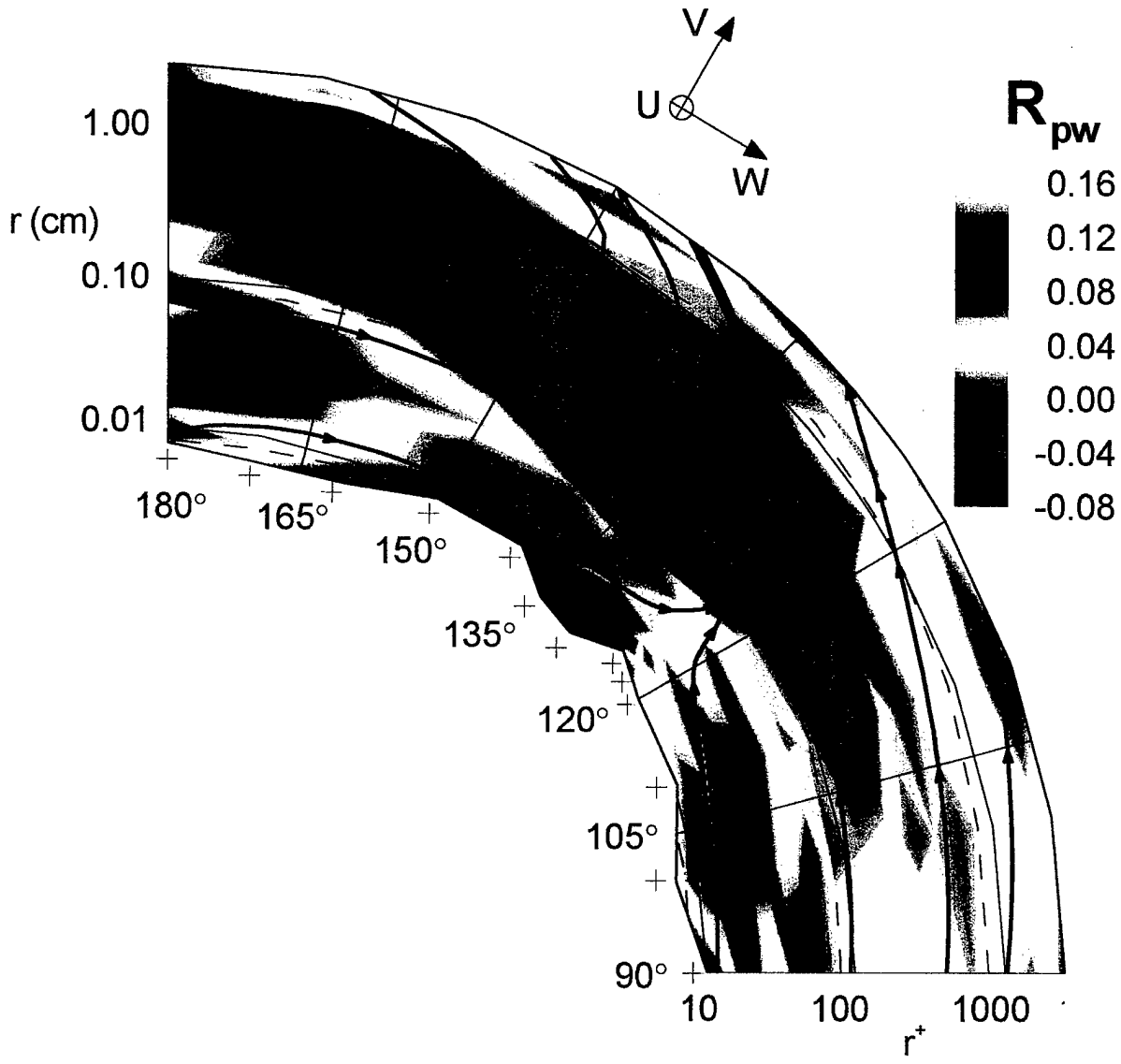

Figure 132. Secondary streamlines with contour levels of the correlation coefficient (R_{pw}) between the surface pressure and the fluctuating w-velocity component, $\alpha = 10°$, $x/L = 0.772$. The pluses (+) along the ϕ-axis denote the ϕ locations at which radial profiles of simultaneous velocity (LDV) and surface pressure measurements were carried out. The radial coordinate (r) is plotted on a logarithmic scale and the dashed lines show lines of constant r^+. The irregular shape of the inner boundary is defined by the measurement locations nearest the model surface.

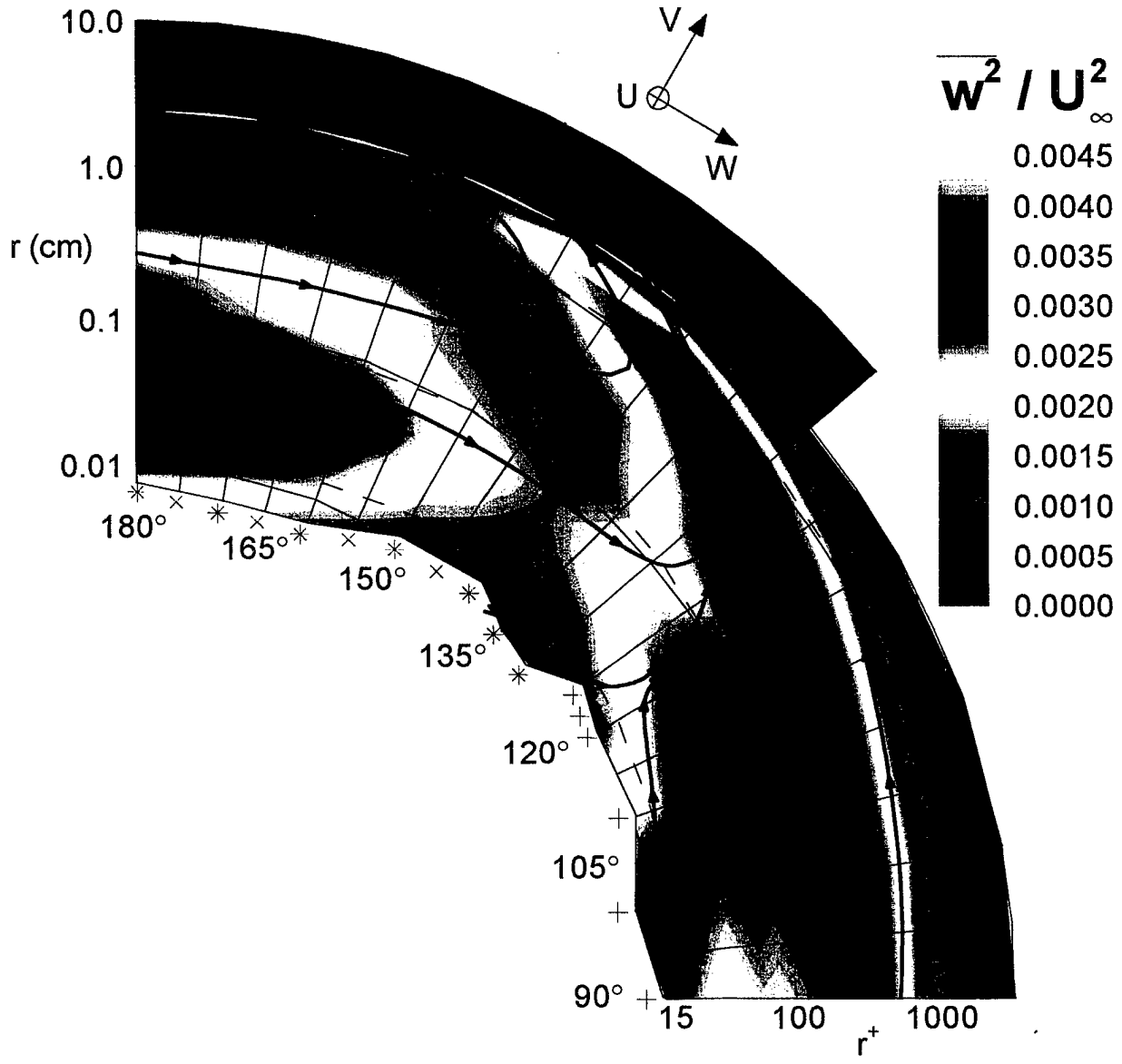

Figure 133. Secondary streamlines with contour levels of the fluctuating w-velocity component, $\alpha = 10°$, $x/L = 0.772$. The pluses (+) along the ϕ-axis denote the ϕ locations at which radial profiles of simultaneous velocity (LDV) and surface pressure measurements were carried out. The Xs (×) along the ϕ-axis denote the ϕ locations at which radial profiles of velocity were carried out using a 4-hot-wire probe. The asterisks (*) denote ϕ-locations at which velocity profiles were carried using both LDV and the 4-hot-wire probe. The radial coordinate (r) is plotted on a logarithmic scale and the dashed lines show lines of constant r^+. The irregular shape of the inner boundary is defined by the measurement locations nearest the model surface.

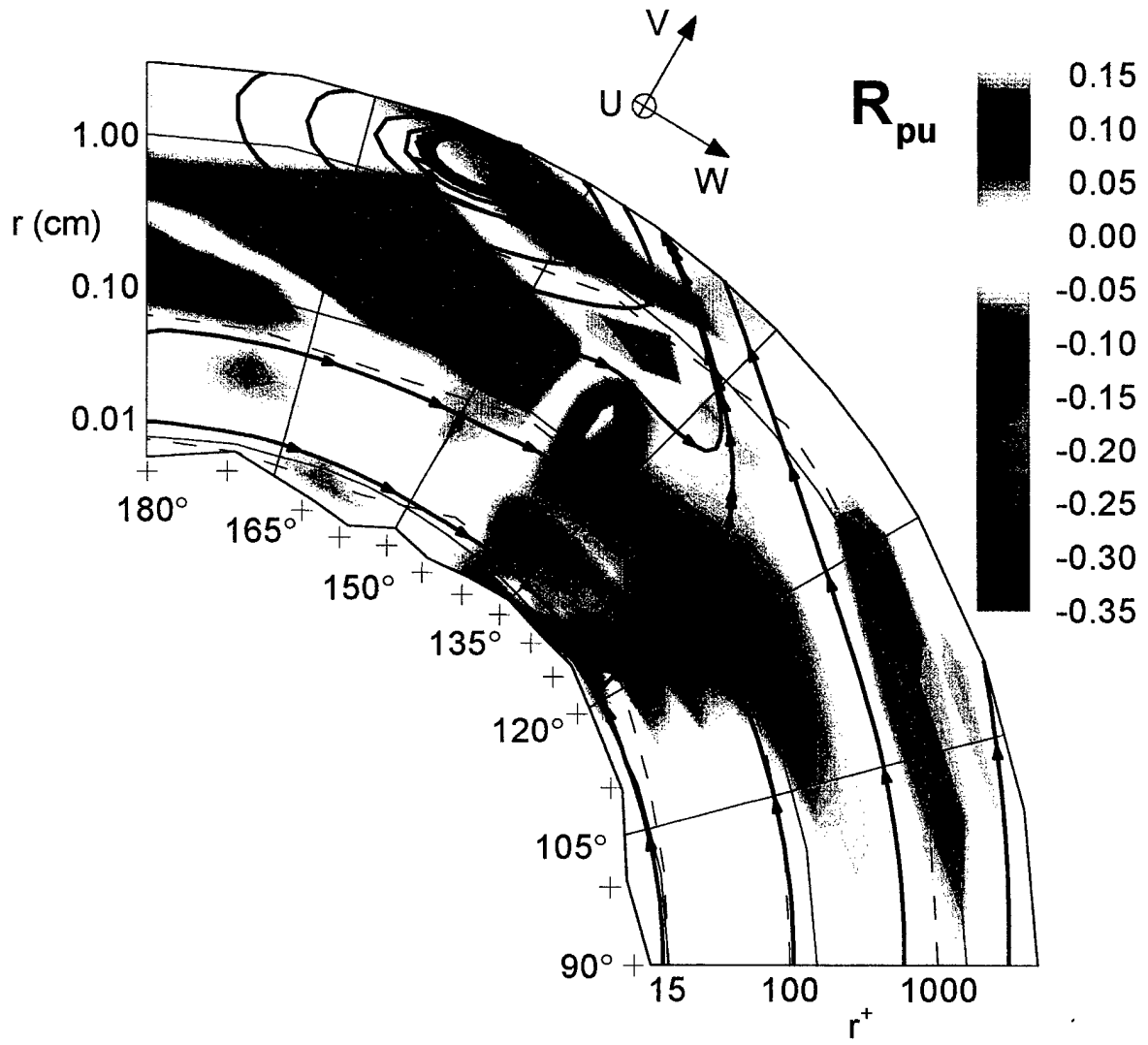

Figure 134. Secondary streamlines with contour levels of the correlation coefficient (R_{pu}) between the surface pressure and the fluctuating u-velocity component, $\alpha = 20°$, $x/L = 0.600$. The pluses (+) along the ϕ-axis denote the ϕ locations at which radial profiles of simultaneous velocity (LDV) and surface pressure measurements were carried out. The radial coordinate (r) is plotted on a logarithmic scale and the dashed lines show lines of constant r^+. The irregular shape of the inner boundary is defined by the measurement locations nearest the model surface.

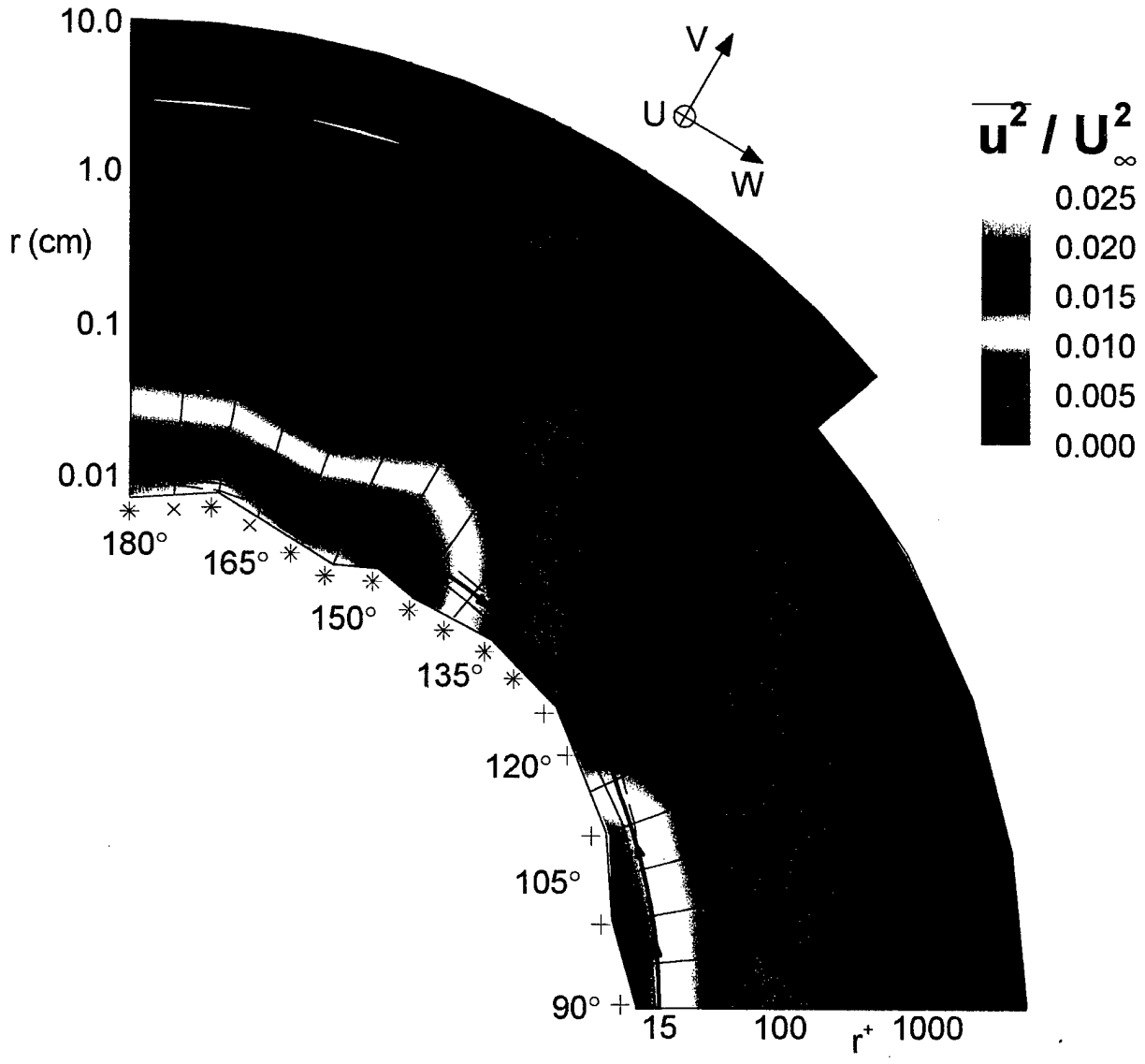

Figure 135. Secondary streamlines with contour levels of the fluctuating u-velocity component, $\alpha = 20°$, $x/L = 0.600$. The pluses (+) along the ϕ-axis denote the ϕ locations at which radial profiles of simultaneous velocity (LDV) and surface pressure measurements were carried out. The Xs (×) along the ϕ-axis denote the ϕ locations at which radial profiles of velocity were carried out using a 4-hot-wire probe. The asterisks (*) denote ϕ-locations at which velocity profiles were carried using both LDV and the 4-hot-wire probe. The radial coordinate (r) is plotted on a logarithmic scale and the dashed lines show lines of constant r^+. The irregular shape of the inner boundary is defined by the measurement locations nearest the model surface.

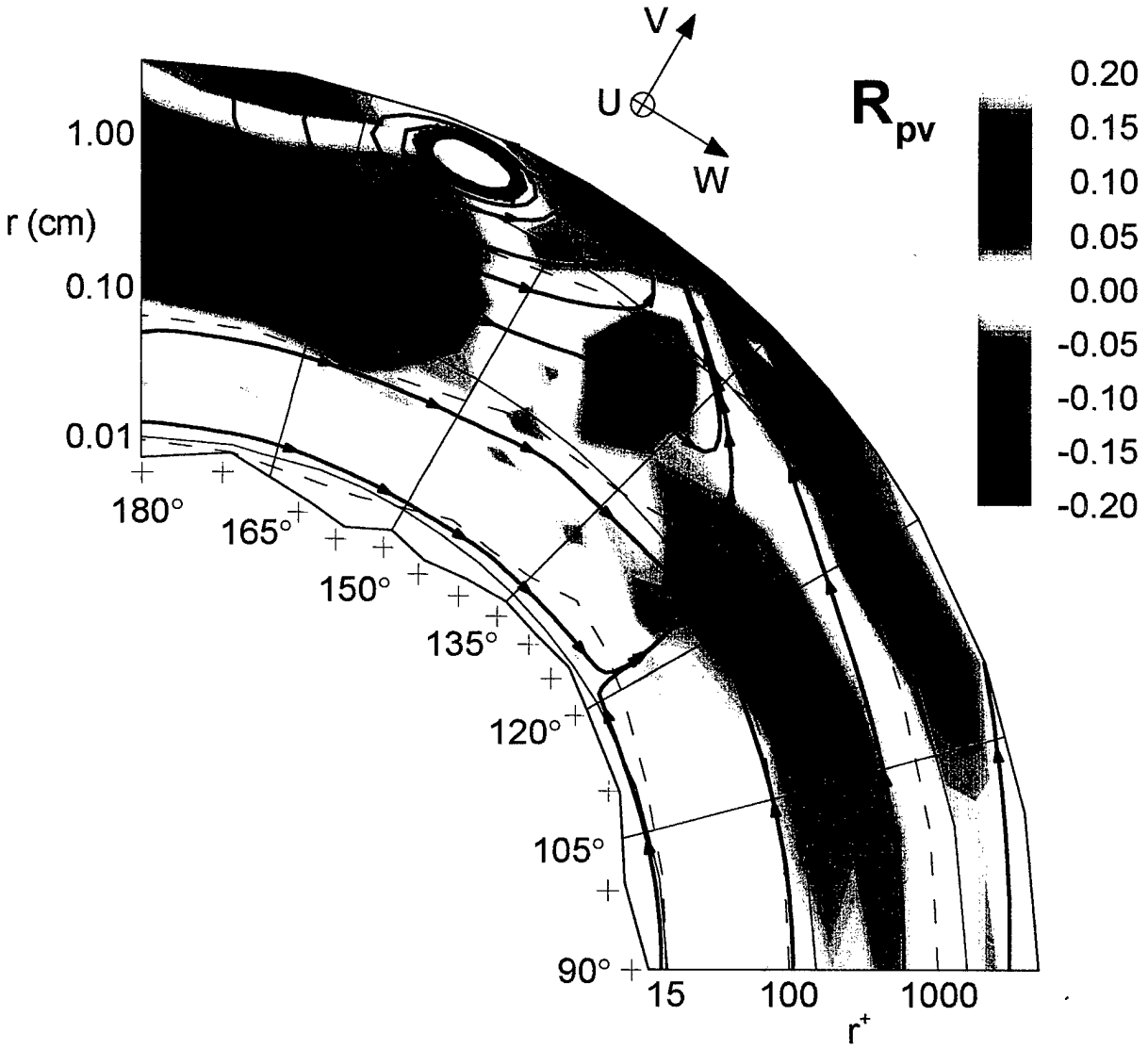

Figure 136. Secondary streamlines with contour levels of the correlation coefficient (R_{pv}) between the surface pressure and the fluctuating v-velocity component, $\alpha = 20°$, $x/L = 0.600$. The pluses (+) along the ϕ-axis denote the ϕ locations at which radial profiles of simultaneous velocity (LDV) and surface pressure measurements were carried out. The radial coordinate (r) is plotted on a logarithmic scale and the dashed lines show lines of constant r^+. The irregular shape of the inner boundary is defined by the measurement locations nearest the model surface.

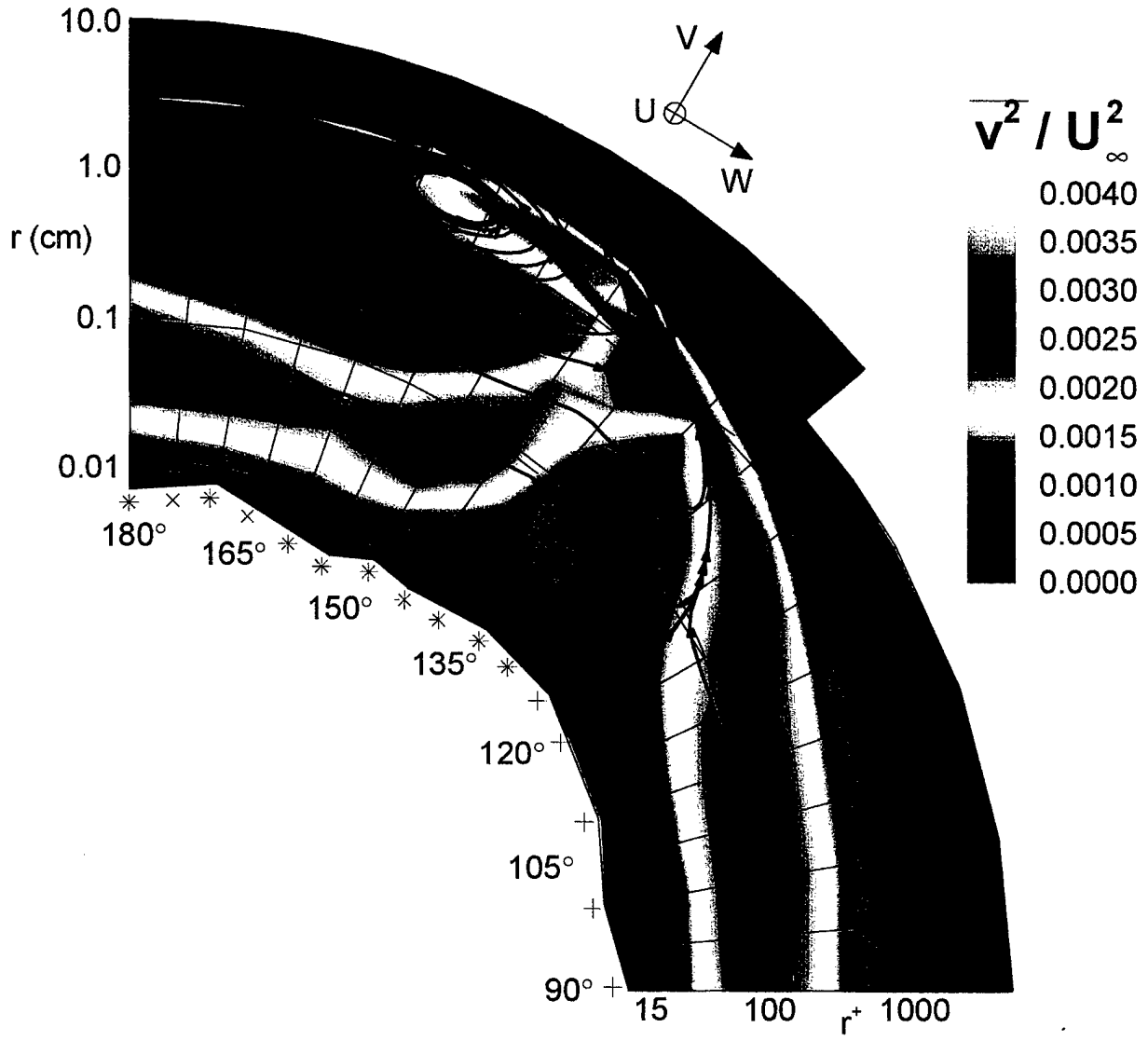

Figure 137. Secondary streamlines with contour levels of the fluctuating v-velocity component, $\alpha = 20°$, $x/L = 0.600$. The pluses (+) along the ϕ-axis denote the ϕ locations at which radial profiles of simultaneous velocity (LDV) and surface pressure measurements were carried out. The Xs (×) along the ϕ-axis denote the ϕ locations at which radial profiles of velocity were carried out using a 4-hot-wire probe. The asterisks (*) denote ϕ-locations at which velocity profiles were carried using both LDV and the 4-hot-wire probe. The radial coordinate (r) is plotted on a logarithmic scale and the dashed lines show lines of constant r^+. The irregular shape of the inner boundary is defined by the measurement locations nearest the model surface.

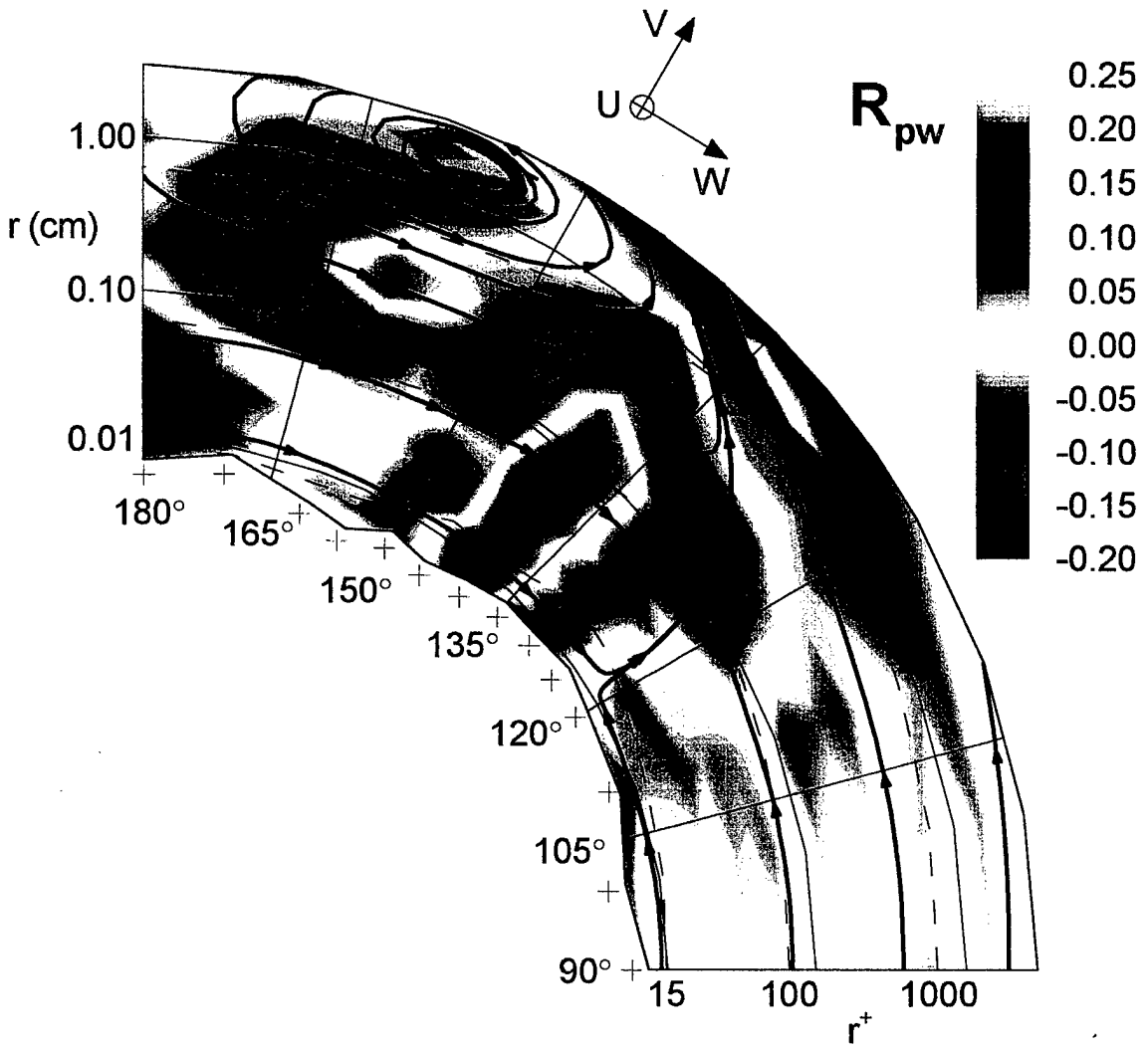

Figure 138. Secondary streamlines with contour levels of the correlation coefficient (R_{pw}) between the surface pressure and the fluctuating w-velocity component, $\alpha = 20°$, $x/L = 0.600$. The pluses (+) along the ϕ-axis denote the ϕ locations at which radial profiles of simultaneous velocity (LDV) and surface pressure measurements were carried out. The radial coordinate (r) is plotted on a logarithmic scale and the dashed lines show lines of constant r^+. The irregular shape of the inner boundary is defined by the measurement locations nearest the model surface.

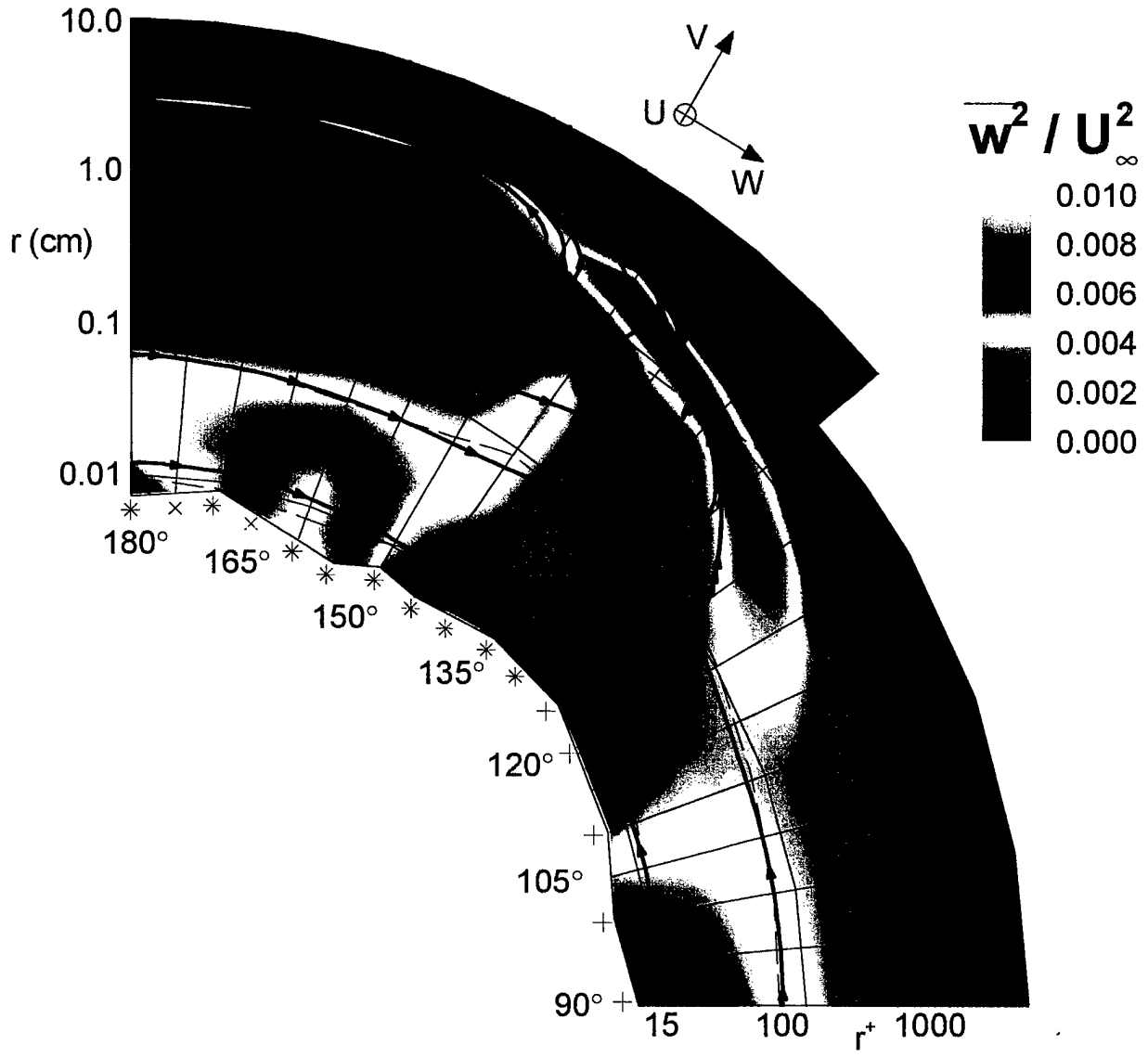

Figure 139. Secondary streamlines with contour levels of the fluctuating w-velocity component, $\alpha = 20°$, $x/L = 0.600$. The pluses (+) along the ϕ-axis denote the ϕ locations at which radial profiles of simultaneous velocity (LDV) and surface pressure measurements were carried out. The Xs (×) along the ϕ-axis denote the ϕ locations at which radial profiles of velocity were carried out using a 4-hot-wire probe. The asterisks (*) denote ϕ-locations at which velocity profiles were carried using both LDV and the 4-hot-wire probe. The radial coordinate (r) is plotted on a logarithmic scale and the dashed lines show lines of constant r^+. The irregular shape of the inner boundary is defined by the measurement locations nearest the model surface.

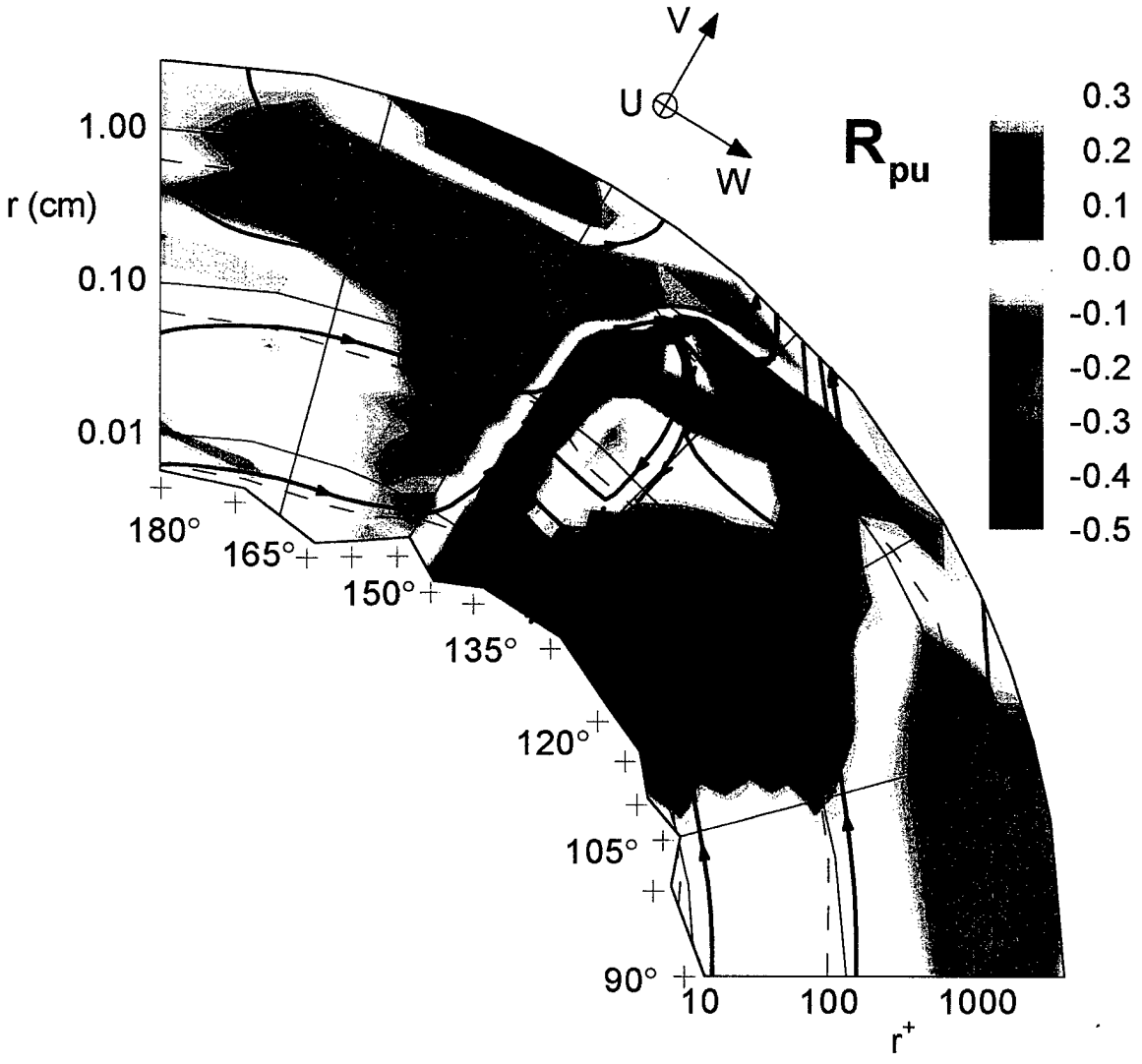

Figure 140. Secondary streamlines with contour levels of the correlation coefficient (R_{pu}) between the surface pressure and the fluctuating u-velocity component, $\alpha = 20°$, $x/L = 0.772$. The pluses (+) along the ϕ-axis denote the ϕ locations at which radial profiles of simultaneous velocity (LDV) and surface pressure measurements were carried out. The radial coordinate (r) is plotted on a logarithmic scale and the dashed lines show lines of constant r^+. The irregular shape of the inner boundary is defined by the measurement locations nearest the model surface.

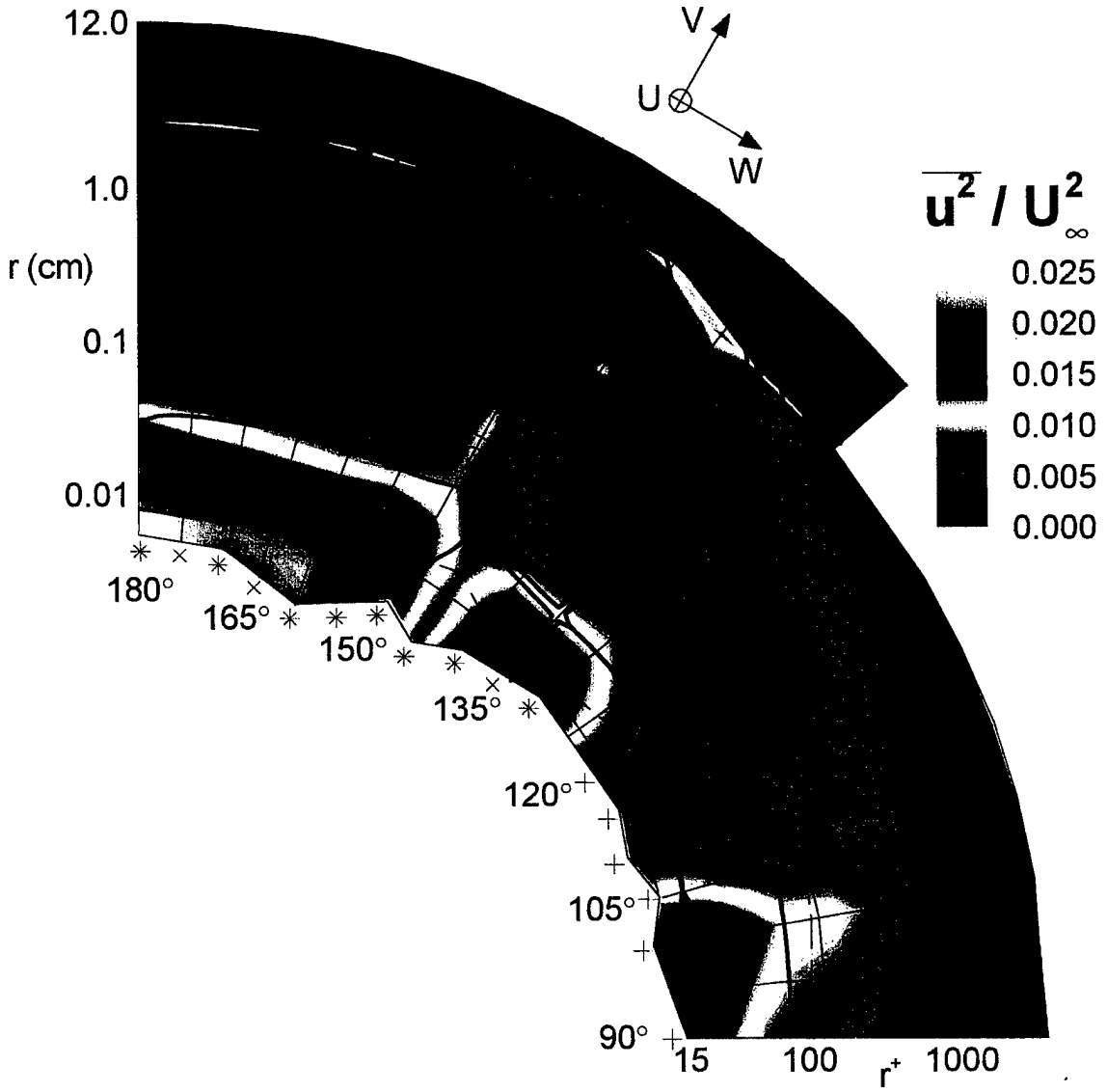

Figure 141. Secondary streamlines with contour levels of the fluctuating u-velocity component, $\alpha = 20°$, $x/L = 0.772$. The pluses (+) along the ϕ-axis denote the ϕ locations at which radial profiles of simultaneous velocity (LDV) and surface pressure measurements were carried out. The Xs (×) along the ϕ-axis denote the ϕ locations at which radial profiles of velocity were carried out using a 4-hot-wire probe. The asterisks (*) denote ϕ-locations at which velocity profiles were carried using both LDV and the 4-hot-wire probe. The radial coordinate (r) is plotted on a logarithmic scale and the dashed lines show lines of constant r^+. The irregular shape of the inner boundary is defined by the measurement locations nearest the model surface.

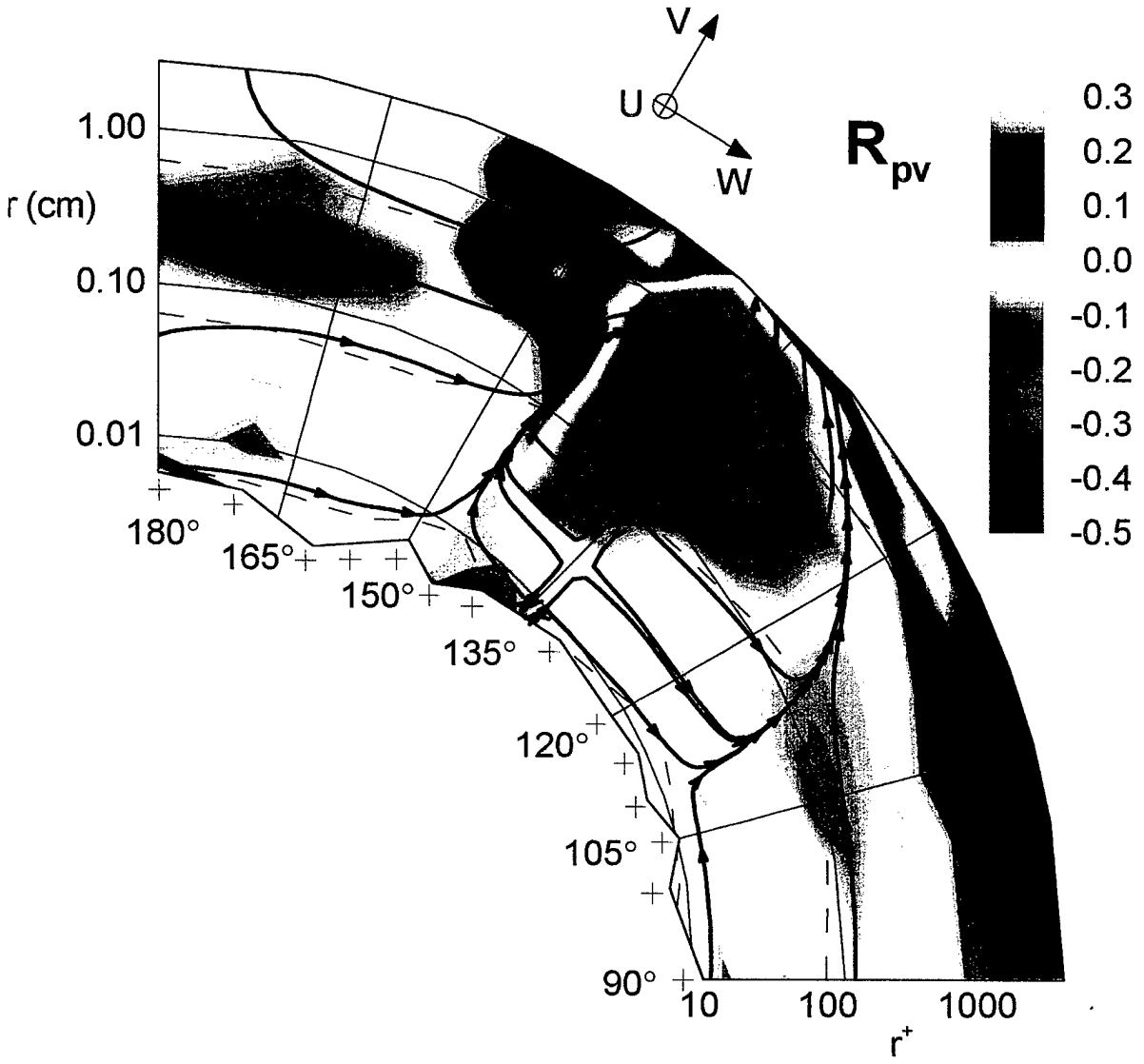

Figure 142. Secondary streamlines with contour levels of the correlation coefficient (R_{pv}) between the surface pressure and the fluctuating v-velocity component, $\alpha = 20°$, $x/L = 0.772$. The pluses (+) along the ϕ-axis denote the ϕ locations at which radial profiles of simultaneous velocity (LDV) and surface pressure measurements were carried out. The radial coordinate (r) is plotted on a logarithmic scale and the dashed lines show lines of constant r^+. The irregular shape of the inner boundary is defined by the measurement locations nearest the model surface.

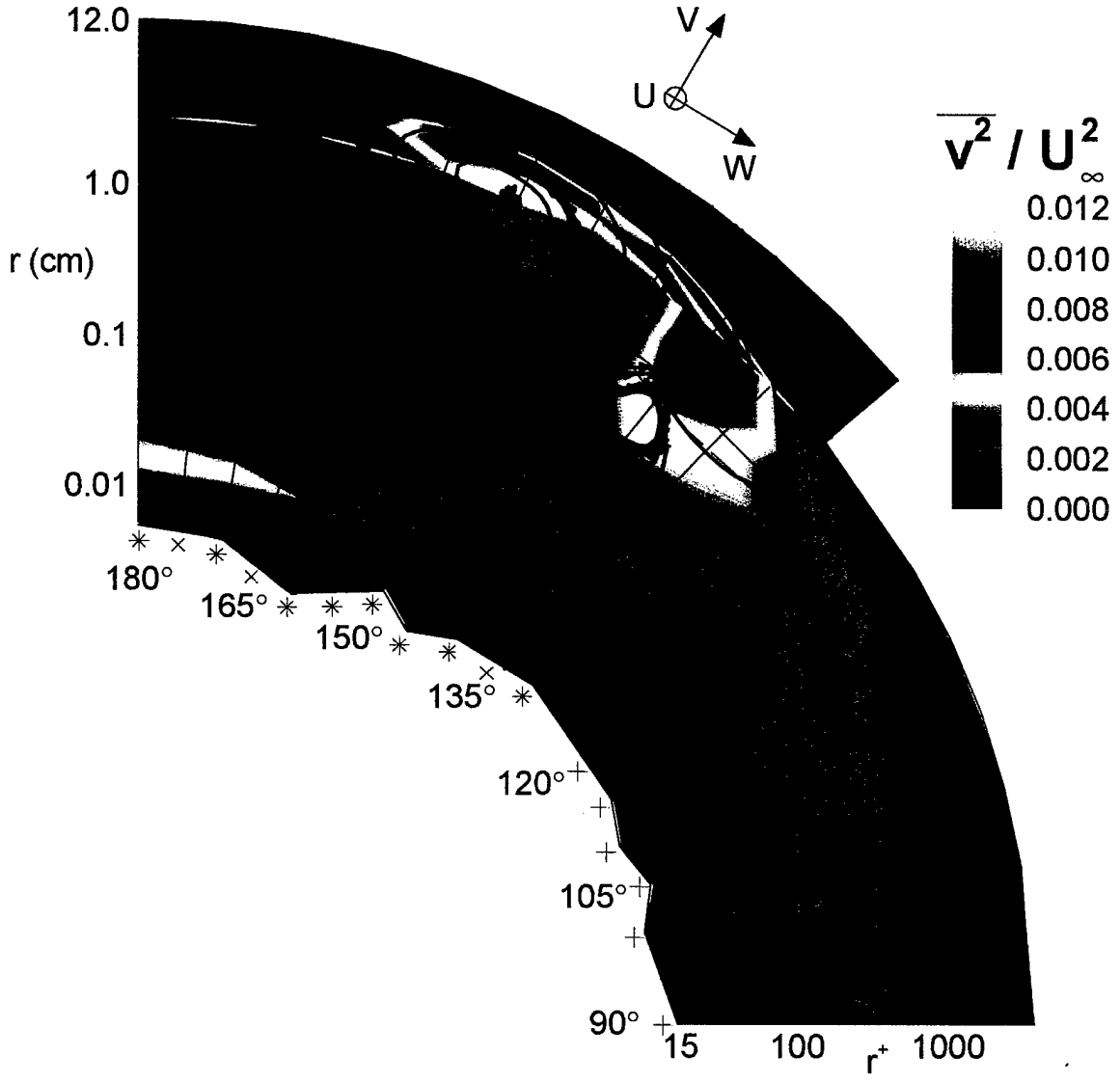

Figure 143. Secondary streamlines with contour levels of the fluctuating v-velocity component, $\alpha = 20°$, $x/L = 0.772$. The pluses (+) along the ϕ-axis denote the ϕ locations at which radial profiles of simultaneous velocity (LDV) and surface pressure measurements were carried out. The Xs (×) along the ϕ-axis denote the ϕ locations at which radial profiles of velocity were carried out using a 4-hot-wire probe. The asterisks (*) denote ϕ-locations at which velocity profiles were carried using both LDV and the 4-hot-wire probe. The radial coordinate (r) is plotted on a logarithmic scale and the dashed lines show lines of constant r^+. The irregular shape of the inner boundary is defined by the measurement locations nearest the model surface.

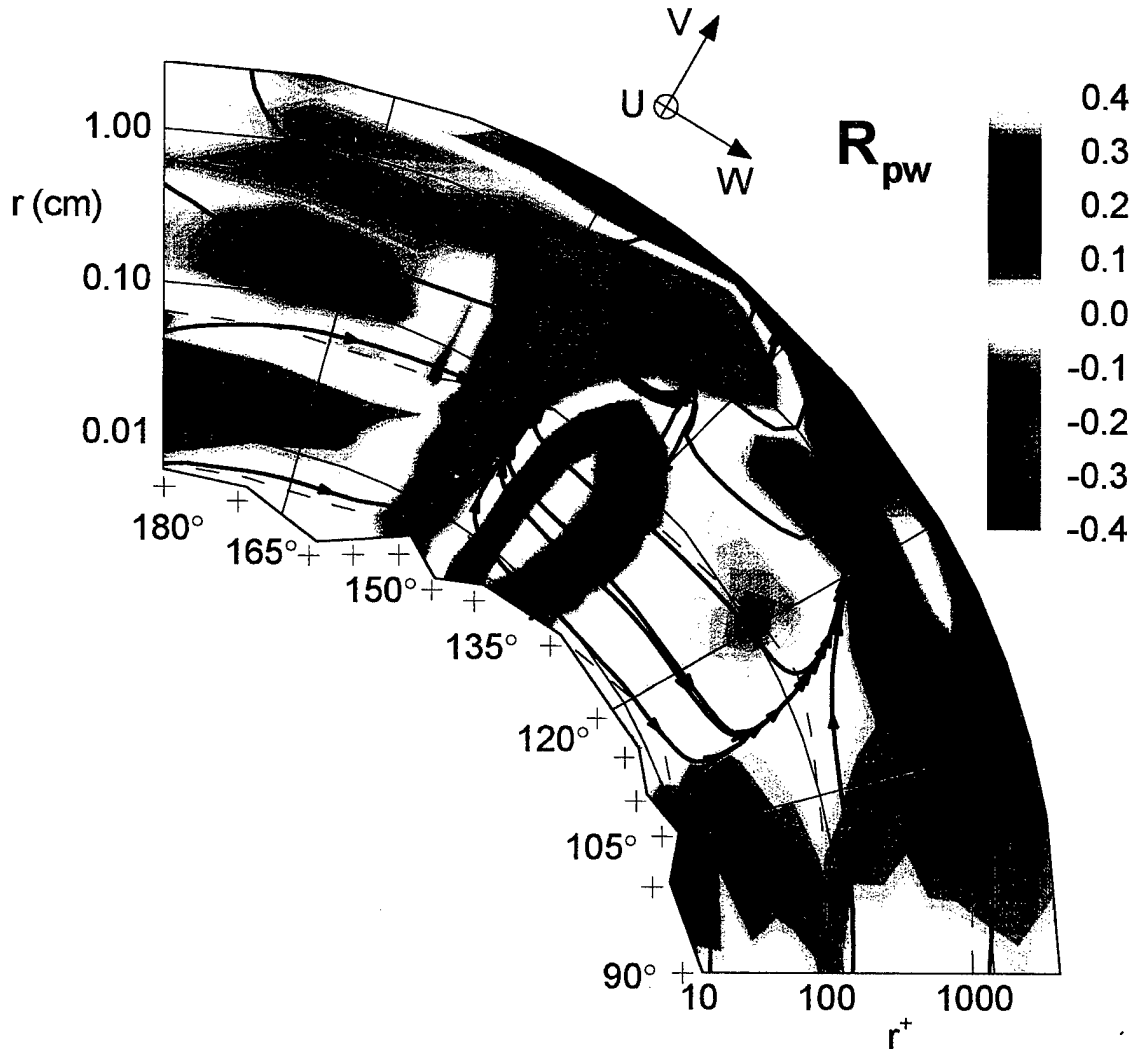

Figure 144. Secondary streamlines with contour levels of the correlation coefficient (R_{pw}) between the surface pressure and the fluctuating w-velocity component, $\alpha = 20°$, $x/L = 0.772$. The pluses (+) along the ϕ-axis denote the ϕ locations at which radial profiles of simultaneous velocity (LDV) and surface pressure measurements were carried out. The radial coordinate (r) is plotted on a logarithmic scale and the dashed lines show lines of constant r^+. The irregular shape of the inner boundary is defined by the measurement locations nearest the model surface.

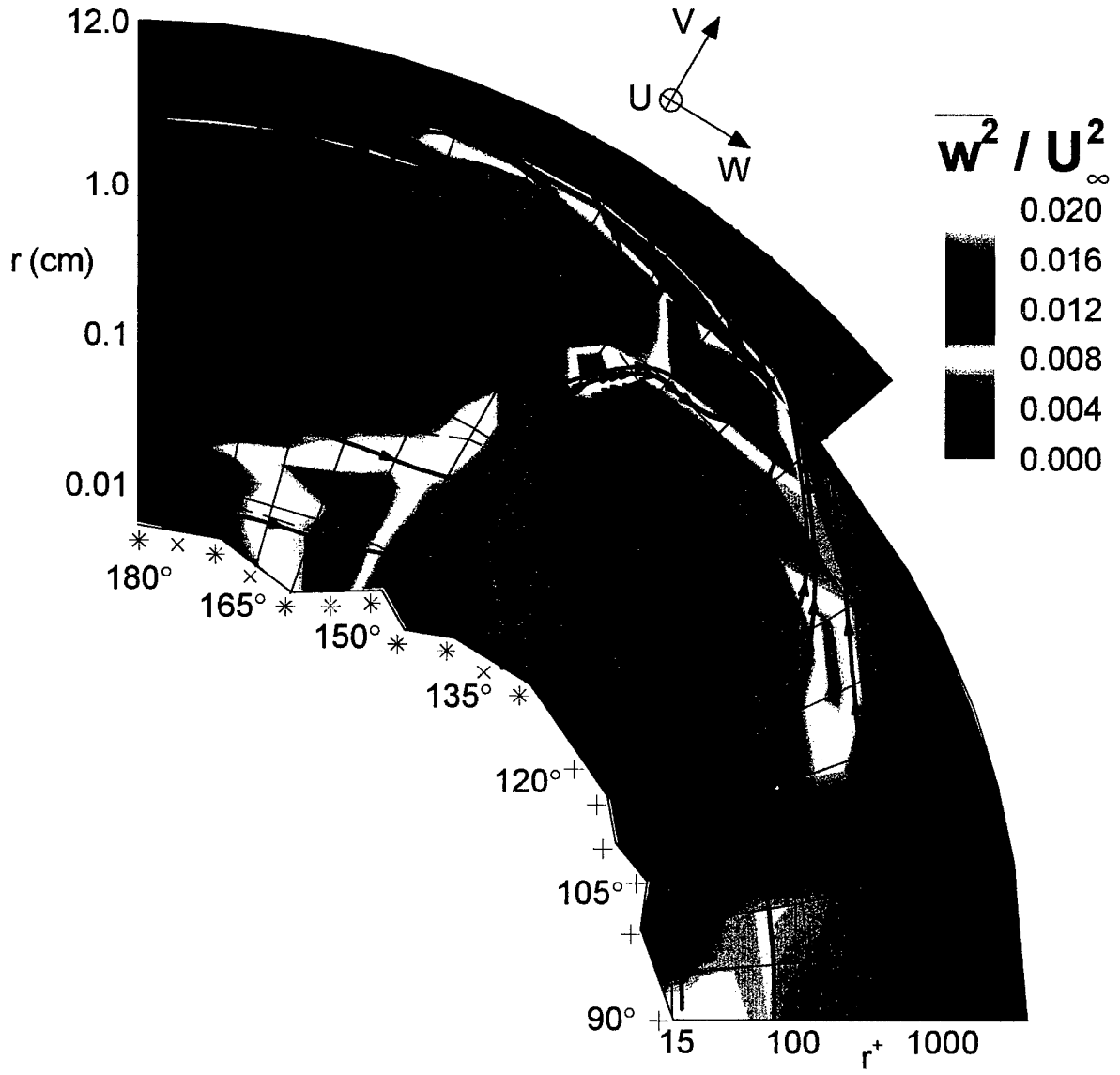

Figure 145. Secondary streamlines with contour levels of the fluctuating w-velocity component, $\alpha = 20°$, $x/L = 0.772$. The pluses (+) along the ϕ-axis denote the ϕ locations at which radial profiles of simultaneous velocity (LDV) and surface pressure measurements were carried out. The Xs (×) along the ϕ-axis denote the ϕ locations at which radial profiles of velocity were carried out using a 4-hot-wire probe. The asterisks (*) denote ϕ-locations at which velocity profiles were carried using both LDV and the 4-hot-wire probe. The radial coordinate (r) is plotted on a logarithmic scale and the dashed lines show lines of constant r^+. The irregular shape of the inner boundary is defined by the measurement locations nearest the model surface.

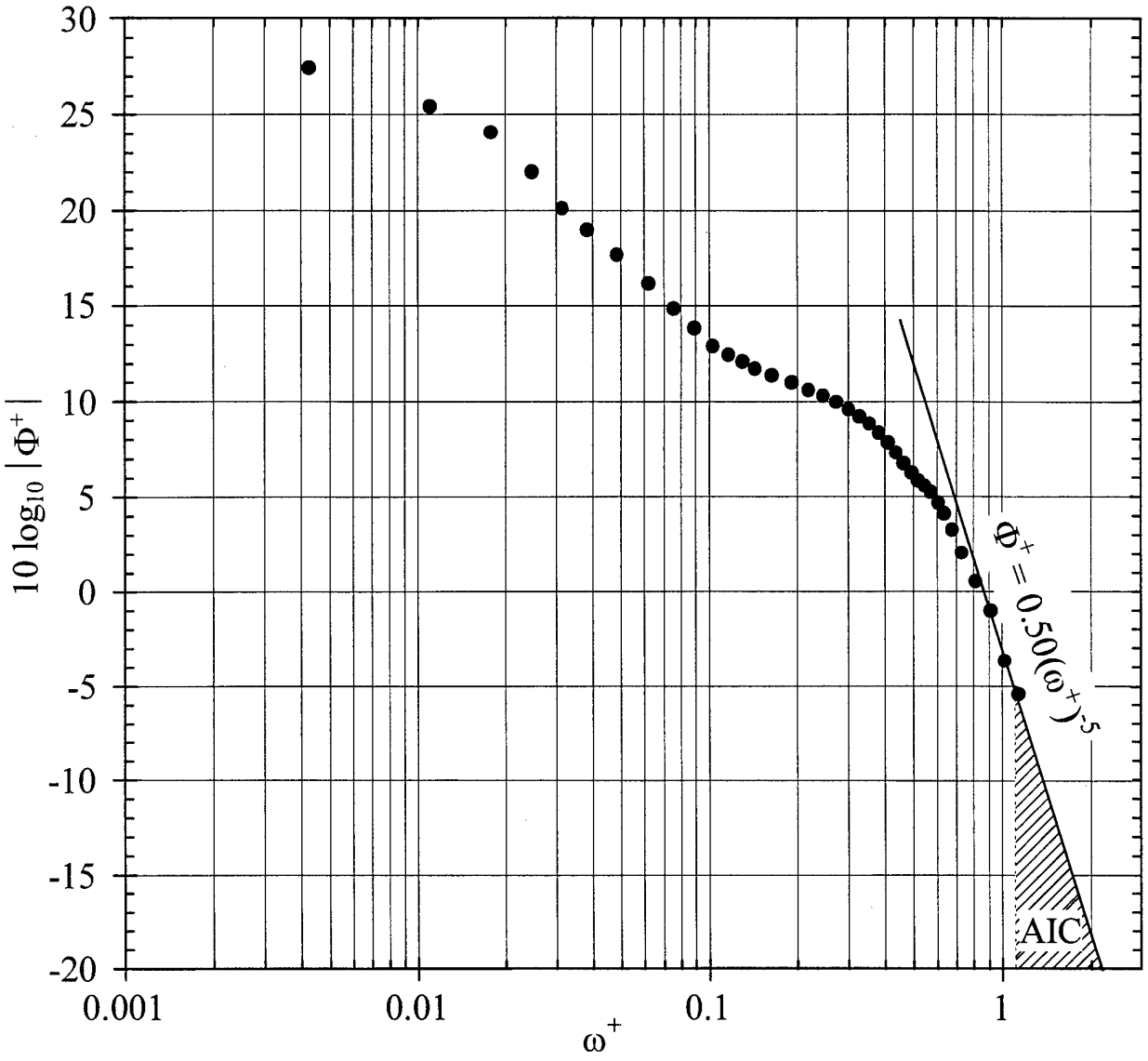

Figure 146. The power spectrum of surface pressure fluctuations at $\alpha = 10°$, $x/L = 0.772$, $\phi = 140°$ made non-dimensional using ν/u_τ^2 as the time scale and τ_W as the pressure scale. Also shown is the curve that bounds the Analytical Integral Contribution (AIC) to $\overline{p^2}$ at $\alpha = 10°$, $x/L = 0.772$, $\phi = 140°$.

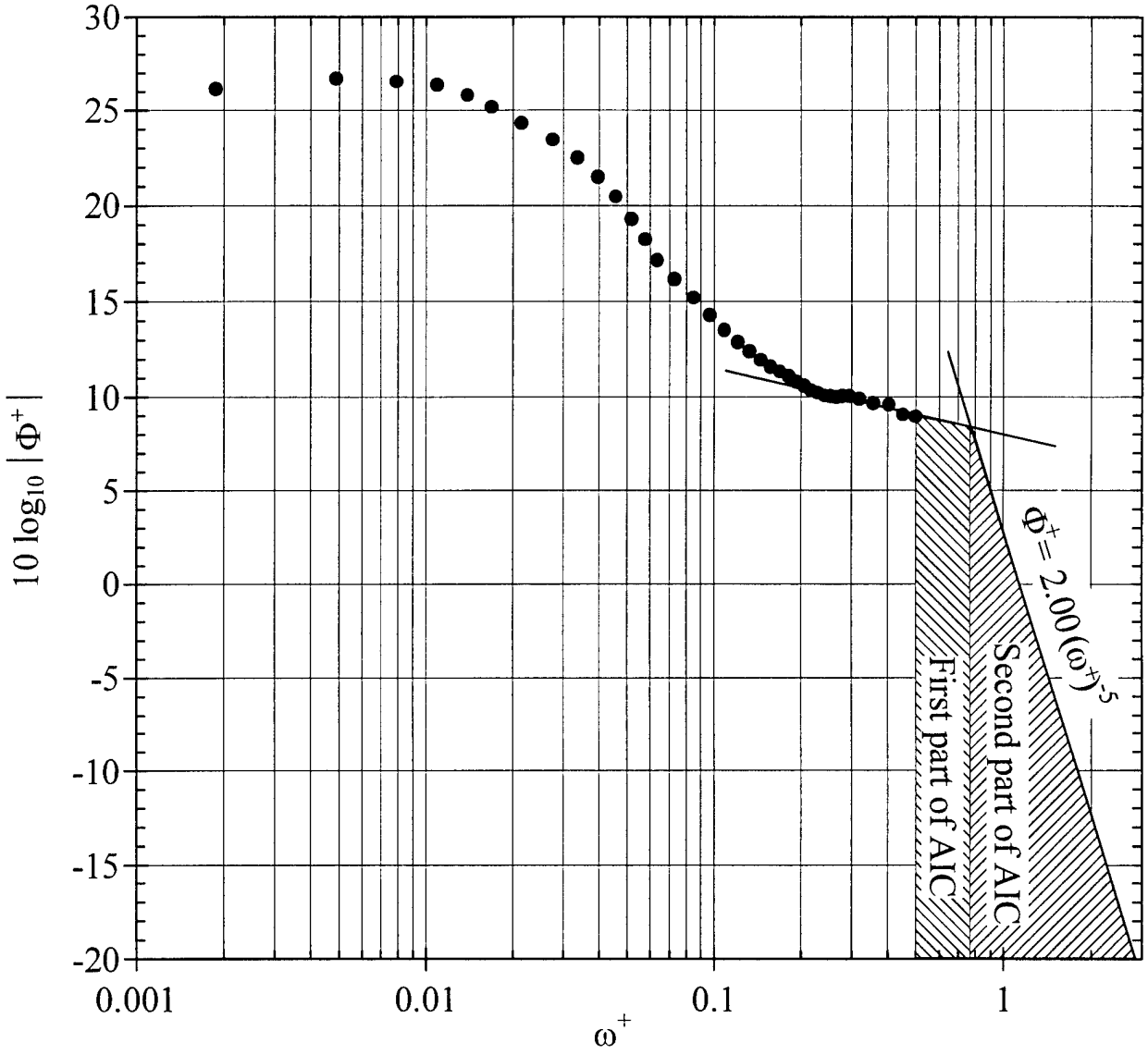

Figure 147. The power spectrum of surface pressure fluctuations at $\alpha = 20°$, $x/L = 0.772$, $\phi = 130°$ made non-dimensional using ν/u_τ^2 as the time scale and τ_W as the pressure scale. Also shown are the curves that bound the Analytical Integral Contribution (AIC) to $\overline{p^2}$ at $\alpha = 20°$, $x/L = 0.772$, $\phi = 130°$.

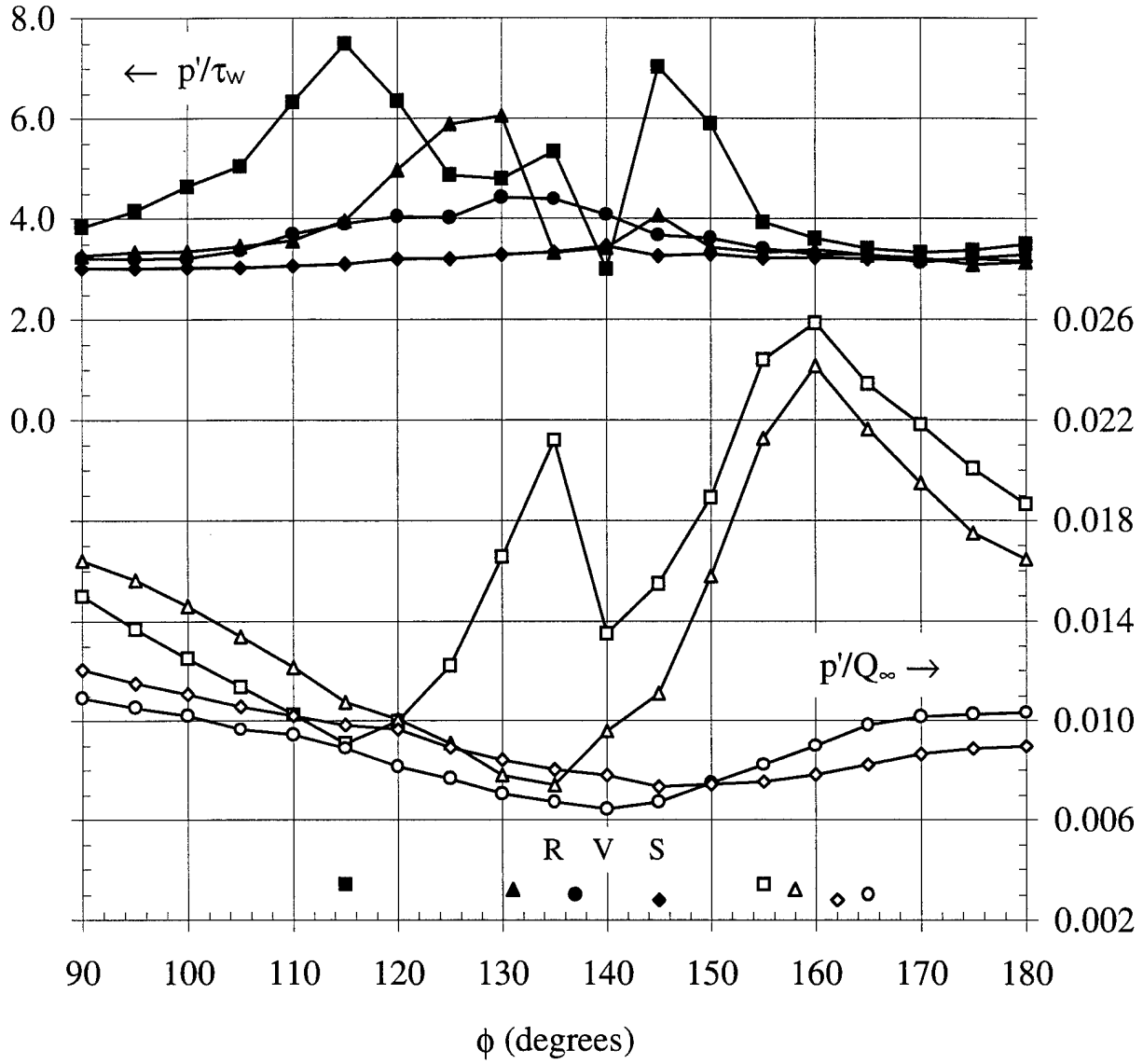

Figure 148. Variation of RMS wall pressure fluctuations with ϕ position: ◇, $\alpha = 10°$, $x/L = 0.600$; ○, $\alpha = 10°$, $x/L = 0.772$; Δ , $\alpha = 20°$, $x/L = 0.600$; □, $\alpha = 20°$, $x/L = 0.772$. The solid symbols immediately above the ϕ-axis denote the location of primary separation (Wetzel *et al.*, 1998). The open symbols immediately above the ϕ-axis denote the approximate location of the shed vortex core. The letters R, V, and S denote the location of reattachment, secondary vortex core, and secondary separation, respectively, for $\alpha = 20°$, $x/L = 0.772$.

A.1. Input Files

The program TIM-DLY.EXE is a program that was compiled using Watcom C/C^{++} v.10 to work in a DOS environment. It reads binary "raw" data files, applies a user-selected time delay, computes the power spectrum, and writes the result to an ASCII file. The time delay technique is described in §2.3.1. Since a given data set may consist of multiple data files, the program uses program line arguments so that large amounts of data can be processed in a "batch" format. The program line arguments are:

```
TIM-DLY.EXE <input file name> <log file name>
                  (required)          (optional)
```

An *input file* is required for program execution in order to specify user selected options. The log file is optional. If a *log file name* is provided, a copy of all screen I/O is written to the that file. An example input file is,

```
      Output Root Filename = E:\DATA\SPECTRUM
               Record Size = 8192
                     Shift = 8192
Number of Raw Data Files = 5
    E:\RAW-DATA\DATA1.RAW  27.01  20.31
    E:\RAW-DATA\DATA2.RAW  27.01  20.31
    E:\RAW-DATA\DATA3.RAW  27.01  20.31
    E:\RAW-DATA\DATA4.RAW  27.01  20.31
    E:\RAW-DATA\DATA5.RAW  27.01  20.31
```

In the above example, The *Output root filename* is used to construct the output file names. One output file is created for each data channel. The number of the data channel is appended as an extension to the text string given as the *Output root filename*. For example, using the above input file and raw data files that each contain two channels of data, two output files of power spectra would be created– `E:\DATA\SPECTRUM.P1` and `E:\DATA\SPECTRUM.P2`. The *Record Size* is the number of contiguous samples to use when computing the spectral power density and the *Shift* is the number of samples to use as the equivalent time delay. The actual time delay is calculated by multiplying the *Shift* by 1/(sample frequency of data acquisition). The *Number of Raw Data Files* is followed by a list of each "raw" data file name. The static sensitivity (at 0 Hz) of each data channel in the "raw" data file is specified (in Pa/V) following

each "raw" data file name. The frequency response of the transducer must be applied to the spectral power density, which is the output of TIM-DLY.EXE.

A.2. Output files

The primary output of TIM-DLY.EXE are several power spectra for each data channel (time series) in the "raw" data files. For example, using the above input file and raw data files that each contain two channels of data, two output files of power spectra would be created– `E:\DATA\SPECTRUM.P1` and `E:\DATA\SPECTRUM.P2`. An example output file is,

Freq	p1	p2	p1-p2	p1+p2
6.10352e+000	9.92157e-001	9.92038e-001	1.80845e+000	2.15994e+000
1.42415e+001	3.14360e-001	3.11584e-001	6.13420e-001	6.38468e-001
2.23796e+001	5.88380e-002	5.85823e-002	1.34346e-001	1.00495e-001
3.05176e+001	6.28321e-002	6.19110e-002	1.88205e-001	6.12808e-002
3.86556e+001	4.14870e-002	4.11076e-002	1.10290e-001	5.48988e-002
4.67936e+001	1.23961e-002	1.33300e-002	3.15965e-002	1.98557e-002

The first column (`Freq`) is the center frequency, in Hertz, of each spectral estimate (spectral level). The second column (`p1`) contains the spectral power density of the input time series *without* any time-delay applied. The third column (`p2`) contains the spectral power density of the time-delayed time series. For a perfectly stationary and ergodic time series, the values in `p1` and `p2` are equal. The fourth column (`p1-p2`) contains the spectral power density of the time-delayed and subtracted time series. The fifth column (`p1+p2`) contains the spectral power density of the time-delayed and added time series. The spectral power density due to the turbulent contributions can be separated from the spectral power density due to the coherent contributions (acoustic, vibration) using the method described in §2.3.1.

The other files created by this program are used to check the calculation. The first and last spectral value for each power density spectrum calculated by this program should be very near zero, since each time series is made to have zero mean by the program before the power density spectrum is calculated. This is done in order to prevent spectral energy from the mean value from *leaking* into (contaminating) the adjacent, low frequency spectral estimates (side-lobe leakage is discussed by Bendat and Piersol, 1986, pp. 393-400). The first and last spectral value are not written to the output files that contain the rest of the power density spectrum, since these two estimates should be zero. Therefore, the first and last spectral estimate from each record is

written to a separate file. Following the convention adopted for the power density spectrum output, the first and last spectral estimates for each data channel are written to a separate file. For example, using the above input file and raw data files that each contain two channels of data, two additional output files would be created– `E:\DATA\SPECTRUM.M1` and `E:\DATA\SPECTRUM.M2`. An example output file is,

```
Record     FirstEst        LastEst
     0   6.24075e-009   6.37123e-009
     1  -3.44704e-009  -3.55237e-009
     2  -1.11723e-009  -1.26382e-009
     3  -3.44646e-009  -3.36124e-009
     4   3.72054e-010   3.72128e-009
     5   8.98667e-009   8.88884e-009
     6  -6.51994e-009  -6.62983e-009
     7   2.18546e-009   2.15682e-009
```

A.3. Program Listings

The source code for TIM-DLY.EXE is split up into 8 files:

`TIM-DLY.C`	Main functions of the program
`DATHEAD.H`	Contains the definition of the "raw" data file header structure
`FILE-OPS.H` `FILE-OPS.C`	These two files contain utility functions used for file I/O
`LOG-OPS.H` `LOG-OPS.C`	These two files contain redefinitions of the functions `printf` and `scanf` in order to copy screen I/O to a log file, if one is open.
`REALFFT.H` `REALFFT.C`	These two files contain the REALFFT algorithm given on p. 513 of Press *et al.* (1994) modified to use double precision.

TIM-DLY.C

```
/*************************************************************************
*   THIS PROGRAM CALCULATES THE POWER SPECTRUM OF A SIGNAL AFTER APPLYING   *
*       A USER SELECTED TIME DELAY                                          *
*************************************************************************/
#include <stdio.h>
#include <stddef.h>
#include <stdlib.h>
#include <stdarg.h>
```

```
#include <math.h>
#include <ctype.h>
#include <conio.h>
#include <string.h>
#include <malloc.h>
#include <errno.h>
#include <graph.h>

#include "dathead.h"
#include "realfft.h"
#include "log-ops.h"
#include "file-ops.h"

#define NUM_SPEC    4

//
//      GLOBAL VARIABLES
//
DataHeader      h ;
FileInfo        LogF, IniF, DataF, OutF ;
char            OutRoot[80] ;
unsigned long   RecSize, Shift, BlockSize, TotalRecs, Bins, SampPerBlock,
                NumRecs, RecsDone ;
unsigned short  NumFiles, SampPerBank, ****Data ;
double          delF, ***avg, sens[16], **scratch, ***ms, ***power,
                ***FirstEst, ***LastEst ;


//
//      FUNCTION DECLARATIONS
//
          void ProcessArgs (int ArgCount, char **Arg) ;
unsigned short ReadConfig (void) ;
unsigned short GetNextDataFname (void) ;
          void WrapUp (void) ;
          void PrintConfig (void) ;
          void PrintGlobals (void) ;
unsigned short GetMem(void) ;
          void FreeMem (void) ;
unsigned short OpenDataFile (DataHeader *Header) ;
unsigned short ReadData (void) ;
          void PrintDataHeader (void) ;
          void CalcPowerSpectra (void) ;
unsigned short SaveSpec (void) ;


//
//      MAIN ROUTINE
//
void main (int ArgCount, char **Arg)
{ unsigned short    sp, ch, file, error ;
  unsigned long     bn ;

  _clearscreen(_GCLEARSCREEN) ;
  printf ("\n\n    STARTING TIME DELAY PROGRAM\n\n") ;
  if (ArgCount < 2)
   { printf ("  Usage : tim-dly <Ini Filename> <Log Filename>\n") ;
     printf ("                    (required)     (optional)\n\n") ;
   }
  atexit (WrapUp) ;
```

```
  ProcessArgs(ArgCount, Arg) ;
  if (!IniF.loaded) return ;
  LogFptr = LogF.ptr ;

//
//  THE INI (CONFIGURATION) FILE IS READ AND PRINTED TO THE SCREEN
//
  printf (" Reading Configuration ... ") ;
  error = ReadConfig() ;
  if (error)
   { printf ("ERROR %hu\n\n", error) ;
     return ;
   }
  printf ("O.K.\n") ;
  PrintConfig() ;
//
//  THE FIRST DATA FILE IS OPENNED AND THE HEADER IS READ AND DISPLAYED
//
  fscanf (IniF.ptr, "%s", DataF.name) ;

  error = OpenDataFile (&h) ;
  if (error) return ;

  for (ch=0; ch<h.Channels; ch++)  fscanf (IniF.ptr, "%lg", &sens[ch]) ;

  PrintDataHeader() ;
//
//  THESE GLOBAL PARAMTERS ARE CALCULATED BASED ON THE FIRST FILE HEADER
//      IT IS ASSUMED THAT THE OTHERS WILL BE THE SAME
//
  BlockSize = RecSize + Shift ;
  SampPerBank = h.Samples / h.Channels ;
  SampPerBlock = (unsigned long)SampPerBank * (unsigned long)h.Banks ;
  NumRecs = SampPerBank / BlockSize ;
  Bins = RecSize/2 ;
  TotalRecs = NumFiles * h.Blocks * NumRecs ;
  delF = 1e6 / ((double)RecSize * (double)h.SPeriod) ;
  PrintGlobals() ;
//
//  MEMORY IS ALLOCATED
//
  printf (" Allocating memory ... ") ;
  error = GetMem() ;
  if (error)
   { printf ("ERROR %hu\n\n", error) ;
     return ;
   }
  printf ("O.K.\n") ;

  RecsDone = 0L ;

  for (sp=0; sp<NUM_SPEC; sp++)
   for (ch=0; ch<h.Channels; ch++)
    for (bn=0; bn<Bins; bn++)
     power[sp][ch][bn] = 0.0 ;

//
//  THIS LOOPS THROUGH THE DATA FILES LISTED IN THE INI FILE
//
  for (file=0; file<NumFiles; file++)
```

```
    {//
     //  DATA IS READ IN FROM FILE
     //
      printf (" Reading Data ...  ") ;
      error = ReadData () ;
      if (error)
       { printf ("ERROR %hu\n\n", error) ;
         return ;
       }
      printf ("O.K.\n") ;
     //
     //  SPECTRA ARE CALCULATED
     //
      printf (" Calculating ...    ") ;
      CalcPowerSpectra () ;
      printf ("O.K.\n") ;
      CloseFile(&DataF) ;
     //
     //  THE NEXT DATA FILE IS OPENNED AND THE HEADER SKIPPED
     //
      if (file < (NumFiles-1))
       { GetNextDataFname() ;
         error = OpenDataFile(0L) ;
         if (error)
          { printf (" ***ERROR SKIPPING HEADER\n\n") ;
            return ;
    }  }  }
  CloseFile(&IniF) ;

  printf (" Saving spectra ...\n") ; fflush(stdout) ;
  error = SaveSpec() ;
  if (error)
   { printf (" *** ERROR %i\n\n", error) ;
     return ;
   }

  printf ("\n             MEAN SQUARES\n");
  printf ("            ************\n");
  for (ch=0; ch<h.Channels; ch++)
   { printf ("  Channel %02hu :  p1 = %-lg Pa%c\n", ch+1,ms[0][ch][0],253) ;
     printf ("                  p2 = %-lg Pa%c\n", ms[1][ch][0], 253) ;
     printf ("               p1-p2 = %-lg Pa%c\n", ms[2][ch][0], 253) ;
     printf ("               p1+p2 = %-lg Pa%c\n", ms[3][ch][0], 253) ;
   }
  return ;
}


/*************************************************************************
*   THIS FUNCTION PROCESSES PROGRAM ARGUMENTS                            *
*************************************************************************/
void ProcessArgs (int ArgCount, char **Arg)
{
  if (ArgCount > 2)
   { strcpy (LogF.name, Arg[2]) ;
     OpenFile (&LogF, "wt") ;
   }

  if (ArgCount > 1)
   { strcpy (IniF.name, Arg[1]) ;
     OpenFile (&IniF, "rt") ;
```

```
} }


/*************************************************************************
*   THIS FUNCTION READS CONFIGURATION INFO FROM A CONFIGURATION FILE      *
*************************************************************************/
unsigned short ReadConfig (void)
{
  GotoChar (&IniF, '=') ;  fscanf (IniF.ptr, "%s", OutRoot) ;
  GotoChar (&IniF, '=') ;  fscanf (IniF.ptr, "%lu", &RecSize) ;
  GotoChar (&IniF, '=') ;  fscanf (IniF.ptr, "%lu", &Shift) ;
  GotoChar (&IniF, '=') ;  fscanf (IniF.ptr, "%hu", &NumFiles) ;

  return 0 ;
}


/*************************************************************************
*   THIS FUNCTION READS THE NEXT DATA FILENAME IN THE INI FILE AND THE    *
*       ASSOCIATED SENSITIVITIES                                          *
*************************************************************************/
unsigned short GetNextDataFname (void)
{ unsigned short ch ;

  fscanf (IniF.ptr, "%s", DataF.name) ;
  for (ch=0; ch<h.Channels; ch++)  fscanf (IniF.ptr, "%lg", &sens[ch]) ;

  return 0 ;
}


/*************************************************************************
*   THIS FUNCTION FREES MEMORY AND CLOSES FILES.  IT IS CALLED WHEN PROGRAM *
*       EXECUTION TERMINATES                                              *
*************************************************************************/
void WrapUp (void)
{ FreeMem() ;
  flushall() ;
  fcloseall() ;
}


/*************************************************************************
*   THIS FUNCTION PRINTS THE CONFIGURATION INFORMATION                    *
*************************************************************************/
void PrintConfig (void)
{
  printf ("\n") ;
  printf ("    Output Filename Root : %s\n", OutRoot) ;
  printf ("           Record Length = %lu\n", RecSize) ;
  printf ("                   Shift = %lu\n", Shift) ;
  printf ("         Number of Files = %hu\n", NumFiles) ;
  printf ("\n") ; fflush(stdout) ;
}

/*************************************************************************
*   THIS FUNCTION PRINTS SOME GLOBAL VARIABLES                            *
*************************************************************************/
```

```
void PrintGlobals (void)
{
  printf ("\n") ;
  printf ("               BlockSize = %lu\n", BlockSize) ;
  printf ("            Samples/Bank = %hu\n", SampPerBank) ;
  printf ("           Samples/Block = %lu\n", SampPerBlock) ;
  printf ("                 NumRecs = %lu\n", NumRecs) ;
  printf ("                    Bins = %lu\n", Bins) ;
  printf ("               TotalRecs = %lu\n", TotalRecs) ;
  printf ("                    delF = %g\n", delF) ;
  printf ("\n") ; fflush(stdout) ;
}



/*************************************************************************
*   THIS FUNCTION ALLOCATES MEMORY FROM THE HEAP                         *
*************************************************************************/
unsigned short GetMem(void)
{ unsigned short  sp, ch, bl, ba ;

  scratch = (double **) calloc (NUM_SPEC, sizeof(double *)) ;
  avg     = (double ***)calloc (NUM_SPEC, sizeof(double **)) ;
  ms      = (double ***)calloc (NUM_SPEC, sizeof(double **)) ;
  FirstEst= (double ***)calloc (NUM_SPEC, sizeof(double **)) ;
  LastEst = (double ***)calloc (NUM_SPEC, sizeof(double **)) ;
  power   = (double ***)calloc (NUM_SPEC, sizeof(double **)) ;
  if (!scratch || !ms || !power)  return 1 ;

  for (sp=0; sp<NUM_SPEC; sp++)
   { scratch[sp] = (double *) calloc (RecSize, sizeof(double)) ;
     avg[sp]     = (double **)calloc (h.Channels, sizeof(double *)) ;
     ms[sp]      = (double **)calloc (h.Channels, sizeof(double *)) ;
     FirstEst[sp]= (double **)calloc (h.Channels, sizeof(double *)) ;
     LastEst[sp] = (double **)calloc (h.Channels, sizeof(double *)) ;
     power[sp]   = (double **)calloc (h.Channels, sizeof(double *)) ;
     if (!scratch[sp] || !ms[sp] || !power[sp])  return 2 ;

     for (ch=0; ch<h.Channels; ch++)
      { avg[sp][ch]   = (double *)calloc (TotalRecs, sizeof(double)) ;
        ms[sp][ch]    = (double *)calloc (TotalRecs, sizeof(double)) ;
        FirstEst[sp][ch] = (double *)calloc (TotalRecs, sizeof(double)) ;
        LastEst[sp][ch]  = (double *)calloc (TotalRecs, sizeof(double)) ;
        power[sp][ch] = (double *)calloc (Bins, sizeof(double)) ;
        if (!ms[sp][ch] || !power[sp][ch])  return 3 ;
   }  }

  Data = (unsigned short ****) calloc(h.Channels, sizeof(unsigned short ***));
  if (!Data)  return 4 ;

  for (ch=0; ch<h.Channels; ch++)
   { Data[ch]= (unsigned short ***)calloc(h.Blocks,sizeof(unsigned short **));
     if (!Data[ch])  return 5 ;

     for (bl=0; bl<h.Blocks; bl++)
      { Data[ch][bl] = (unsigned short **)calloc(h.Banks,
                                          sizeof(unsigned short *));
        if (!Data[ch][bl]) return 6 ;

        Data[ch][bl][0] = (unsigned short *)calloc(SampPerBlock,
```

```
                                                    sizeof(unsigned short)) ;
        if (!Data[ch][bl][0]) return 7 ;

        for (ba=1; ba<h.Banks; ba++)
          Data[ch][bl][ba] = Data[ch][bl][ba-1] + (unsigned long)SampPerBank ;
   }  }

  return 0 ;
}


/*****************************************************************************
*   THIS FUNCTION RETURNS MEMORY TO THE HEAP                                 *
*****************************************************************************/
void FreeMem (void)
{ unsigned short    sp, ch, bl ;

  for (ch=0; ch<h.Channels; ch++)
   { for (bl=0; bl<h.Blocks; bl++)
      { free (Data[ch][bl][0]) ;
        free (Data[ch][bl]) ;
      }
     free (Data[ch]) ;
   }
  free (Data) ;

  for (sp=0; sp<NUM_SPEC; sp++)
   { for (ch=0; ch<h.Channels; ch++)
      { free (avg[sp][ch]) ;
        free (ms[sp][ch]) ;
        free (FirstEst[sp][ch]) ;
        free (LastEst[sp][ch]) ;
        free (power[sp][ch]) ;
      }
     free (scratch[sp]) ;
     free (avg[sp]) ;
     free (ms[sp]) ;
     free (FirstEst[sp]) ;
     free (LastEst[sp]) ;
     free (power[sp]) ;
   }
  free (scratch) ;
  free (avg) ;
  free (ms) ;
  free (FirstEst) ;
  free (LastEst) ;
  free (power) ;
}


/*****************************************************************************
*   THIS FUNCTION OPENS A DATA FILE AND EITHER READS THE HEADER INFO (IF A   *
*       NON-ZERO POINTER IS PASSED) MOVES THE FILE POINTER PAST THE HEADER   *
*       INFO                                                                 *
*****************************************************************************/
unsigned short OpenDataFile (DataHeader *Header)
{ size_t    numr ;
  int       error ;

  error = OpenFile (&DataF, "rb") ;
```

```
  if (error) return 1 ;

  if (Header)
   { numr = fread (Header, sizeof(DataHeader), 1, DataF.ptr) ;
     if (numr != 1) return 2 ;
   }
  else
   { error = fseek (DataF.ptr, (long)sizeof(DataHeader), SEEK_SET) ;
     if (error) return 3 ;
   }

  return 0 ;
}


/*****************************************************************************
*   THIS FUNCTION READS RAW BINARY DATA FROM THE DATA FILE                   *
*****************************************************************************/
unsigned short ReadData (void)
{ unsigned short bl, ba, ch, DataPt ;
  unsigned long  numr, sa, n ;

  n=0L ;
  for (bl=0; bl<h.Blocks; bl++)
   for (ba=0; ba<h.Banks; ba++)
    {  switch (n%4)
        { case 0 : fprintf (stdout, "\b-");  break ;
          case 1 : fprintf (stdout, "\b\\"); break ;
          case 2 : fprintf (stdout, "\b|");  break ;
          case 3 : fprintf (stdout, "\b/");  break ;
        }
       fflush(stdout) ;
       n++ ;

       for (sa=0; sa<SampPerBank; sa++)
        for (ch=0; ch<h.Channels; ch++)
         { numr = fread (&DataPt, 2, 1, DataF.ptr) ;
           if (numr != 1) return errno ;
           Data[ch][bl][ba][sa] = DataPt ;
    }    }

  fprintf (stdout, "\b ");  fflush(stdout);
  return 0 ;
}


/*****************************************************************************
*   THIS FUNCTION PRINTS THE DATA FILE HEADER TO THE SCREEN                  *
*****************************************************************************/
void PrintDataHeader (void)
{ printf ("\n") ;
  printf ("                    DATA FILE HEADER\n") ;
  printf ("      Number of Channels = %-hu\n", h.Channels) ;
  printf ("           Sample Period = %-hu %cs\n", h.SPeriod, 230) ;
  printf ("        Number of Blocks = %-hu\n", h.Blocks) ;
  printf ("         Number of Banks = %-hu\n", h.Banks) ;
  printf ("        Samples per Bank = %-hu\n", h.Samples) ;
  printf ("              A/D offset = %-hu\n", h.ADoffset) ;
  printf ("               A/D slope = %-g\n\n", h.ADslope) ;
}
```

```
/*****************************************************************************
*   THIS FUNCTION CALCULATES THE POWER SPECTRA                                *
*****************************************************************************/
void CalcPowerSpectra (void)
{ unsigned short    ch, bl ;
  unsigned long     rec, sp, sa, bn, start ;
  double            raw[4] ;

  for (bl=0; bl<h.Blocks; bl++)
   for (rec=0; rec<NumRecs; rec++)
    {
    //  THIS JUST PRINTS A STATUS INDICATOR TO THE SCREEN
    //
      fprintf (stdout, "\b\b\b\b\b\b%031u   ", RecsDone) ;
      fflush (stdout) ;

      for (ch=0; ch<h.Channels; ch++)
       { for (sp=0; sp<NUM_SPEC; sp++)      //
          { avg[sp][ch][RecsDone] = 0.0 ;  //  ZERO STATISTICS ARRAYS
            ms[sp][ch][RecsDone]  = 0.0 ;  //
          }
    //
    //  THIS JUST PRINTS A STATUS INDICATOR TO THE SCREEN
    //
         fprintf (stdout, "\b\b%02hu", ch) ;
         fflush (stdout) ;

    //
    //  THE SCRATCH ARRAYS ARE FILLED AND THE AVERAGE IS CALCULATED
    //
         bn = 0 ;
         start = rec * BlockSize ;
         for (sa=start; sa<(start+RecSize); sa++)
          { raw[0] = (double)Data[ch][bl][0][sa] ;            //  p1
            raw[1] = (double)Data[ch][bl][0][sa+Shift] ;      //  p2
            raw[2] = raw[0] - raw[1] ;                        //  p1 - p2
            raw[3] = raw[0] + raw[1] ;                        //  p1 + p2

            for (sp=0; sp<NUM_SPEC; sp++)
             { scratch[sp][bn] = raw[sp] * (double)h.ADslope * sens[ch] ;
               avg[sp][ch][RecsDone] += scratch[sp][bn] ;
             }
            bn++ ;
          }
    //
    //  THE MEAN SQUARE, FFT, AND POWER SPECTRUM ARE CALCULATED
    //
         for (sp=0; sp<NUM_SPEC; sp++)
          { avg[sp][ch][RecsDone] /= (double)RecSize ;
            for (bn=0; bn<RecSize; bn++)
             { scratch[sp][bn] -= avg[sp][ch][RecsDone] ;
               ms[sp][ch][RecsDone] += scratch[sp][bn]*scratch[sp][bn] ;
             }
            ms[sp][ch][RecsDone] /= (double)RecSize ;

            drealft (scratch[sp]-1L, RecSize, 1) ;

            FirstEst[sp][ch][RecsDone] = scratch[sp][0] ;
```

```
            LastEst[sp][ch][RecsDone] = scratch[sp][1] ;
            for (bn=0; bn<Bins; bn++)
              power[sp][ch][bn] += scratch[sp][2*bn] * scratch[sp][2*bn] +
                                   scratch[sp][2*bn+1]*scratch[sp][2*bn+1] ;
       } }

      RecsDone++ ;
    }
  fprintf (stdout, "\b\b\b\b\b\b") ;
  printf ("%03lu %02hu ", RecsDone, ch) ;  fflush (stdout);
}


/*************************************************************************
*   THIS FUNCTION NORMALIZES THE COMPUTED POWER SPECTRA TO BE A SPECTRAL    *
*       POWER DENSITY.  IT THEN WRITES THIS TO FILE.                       *
*************************************************************************/
unsigned short SaveSpec (void)
{ unsigned short    sp, ch, error ;
  unsigned long     bn, rec ;
  char              OutExt[4] ;
  double            Denom, TrueAvg, Adjustment, Freq ;

  Denom = (double)RecSize*(double)RecSize*(double)RecsDone*delF / 2.0 ;

  for (ch=0; ch<h.Channels; ch++)
   {for (sp=0; sp<NUM_SPEC; sp++)
      {
      //    POWER SPECTRA ARE NORMALIZED SUCH THAT THEY INTEGRATE
      //        TO THE MEAN SQUARE
      //
        for (bn=0; bn<Bins; bn++)  power[sp][ch][bn] /= Denom ;
      //
      //    THE AVERAGE OF THE INDIVIDUAL BLOCK AVERAGES IS CALCULATED
      //
        TrueAvg = avg[sp][ch][0] ;
        for (rec=1; rec<RecsDone; rec++)  TrueAvg += avg[sp][ch][rec] ;
        TrueAvg /= (double)RecsDone ;
      //
      //    THE MEAN SQUARE IS CALCULATED FROM THE BLOCK MEAN SQUARES
      //        ACCOUNTING FOR THE BLOCK AVERAGES BEING DIFFERENT
      //
        Adjustment = avg[sp][ch][0] - TrueAvg ;
        ms[sp][ch][0] += Adjustment*Adjustment ;
        for (rec=1; rec<RecsDone; rec++)
         { Adjustment = avg[sp][ch][rec] - TrueAvg ;
           ms[sp][ch][0] += ms[sp][ch][rec] + Adjustment*Adjustment ;
         }
        ms[sp][ch][0] /= (double)RecsDone ;
      }
    //
    //   THE OUTPUT FILENAME IS CONSTRUCTED AND OPENNED
    //
      sprintf (OutExt, "p%-u", ch+1) ;
      _makepath (OutF.name, NULL, NULL, OutRoot, OutExt) ;
      error = OpenFile (&OutF, "wt") ;
      if (error) return 1 ;
    //
    //   COLUMN HEADINGS ARE WRITTEN TO THE OUTPUT FILE
    //
      fprintf (OutF.ptr, "      Freq      ") ;
```

```
      fprintf (OutF.ptr, "      p1      ") ;
      fprintf (OutF.ptr, "      p2      ") ;
      fprintf (OutF.ptr, "     p1-p2    ") ;
      fprintf (OutF.ptr, "     p1+p2\n") ;
    //
    //   ADJACENT BINS ARE AVERAGED AND WRIITEN TO FILE. THROUGH TRIAL AND
    //       ERROR IT WAS FOUND THAT THIS SIGNIFICANTLY SMOOTHED THE SPECTRUM
    //
      Freq = delF ;
      for (bn=1; bn<Bins; bn++)
       { fprintf (OutF.ptr, " % 13.5le", Freq) ;
         for (sp=0; sp<NUM_SPEC; sp++)
           fprintf (OutF.ptr, " % 13.5le", power[sp][ch][bn]) ;

         fprintf (OutF.ptr, "\n") ;
         Freq += delF ;
       }

      CloseFile (&OutF) ;

      sprintf (OutExt, "m%-u", ch+1) ;
      _makepath (OutF.name, NULL, NULL, OutRoot, OutExt) ;
      error = OpenFile (&OutF, "wt") ;
      if (error) return 1 ;
     //
    //   COLUMN HEADINGS ARE WRITTEN TO THE OUTPUT FILE
    //
      fprintf (OutF.ptr, "  Record ") ;
      fprintf (OutF.ptr, "   FirstEst   ") ;
      fprintf (OutF.ptr, "   LastEst\n") ;

      for (rec=0; rec<RecsDone; rec++)
       { fprintf (OutF.ptr, " % 6lu ", rec) ;
         fprintf (OutF.ptr, " % 13.5le", FirstEst[3][ch][rec]) ;
         fprintf (OutF.ptr, " % 13.5le\n", LastEst[3][ch][rec]) ;
       }
      CloseFile (&OutF) ;
    }
  return 0 ;
}
```

DATHEAD.H

```
#ifndef _DATHEAD_H_
#define _DATHEAD_H_
/*****************************************************************************
*   THIS FILE DEFINES THE DATA FILE HEADER STRUCTURE                         *
*****************************************************************************/
//
//  Data File Header Structure
//
typedef struct
 {  unsigned short  Channels,
                    SPeriod,
                    Blocks,
                    Banks,
                    Samples,
                    ADoffset ;
    float           ADslope ;
 }
DataHeader ;

#endif
```

FILE-OPS.H

```
#ifndef _FILE_OPS_H_
#define _FILE_OPS_H_
/*****************************************************************************
*   THIS FILE CONTAINS DEFINITIONS USED FOR FILE I/O                         *
*****************************************************************************/

#include <stdio.h>
#include <errno.h>

typedef struct
 { FILE             *ptr ;
   char             name[80] ;
   unsigned short   loaded ;
 }
FileInfo ;

extern unsigned short OpenFile (FileInfo *f, char *mode) ;
extern void CloseFile (FileInfo *f) ;
extern void GotoChar (FileInfo *f, char c) ;
extern void SkipLine (FileInfo *f) ;

#endif
```

FILE-OPS.C

```
/*************************************************************************
*   THIS FILE CONTAINS FUNCTION DECLARATIONS USED FOR FILE I/O           *
*************************************************************************/

#include "file-ops.h"

/*************************************************************************
*   THIS FUNCTION OPENS A FILE                                           *
*************************************************************************/
unsigned short OpenFile (FileInfo *f, char *mode)
{
  printf ("  Openning %s ... ", f->name) ;

  if ((f->ptr = fopen (f->name, mode)) == NULL)
   { printf ("ERROR #%i", errno) ;
     f->loaded = 0 ;
     return 1 ;
   }

 printf ("O.K.\n") ;
 f->loaded = 1 ;

 return 0 ;
}

/*************************************************************************
*   THIS FUNCTION CLOSES A FILE                                          *
*************************************************************************/
void CloseFile (FileInfo *f)
{
  fclose (f->ptr) ;
  f->loaded = 0 ;
}

/*************************************************************************
*   THIS FUNCTION MOVES THE GIVEN ASCII FILE POINTER TO THE GIVEN CHARACTER *
*************************************************************************/
void GotoChar (FileInfo *f, char c)
{ char format[] = "%*[^ ]%*[ ]" ;

  format[4] = format [9] = c ;
  fscanf (f->ptr, format) ;
}

/*************************************************************************
*   THIS FUNCTION ADVANCES THE FILE POINTER PAST THE NEXT LINE OF AN ASCII  *
*       FILE                                                             *
*************************************************************************/
void SkipLine (FileInfo *f)
{ char buffer[256] ;
  fgets (buffer, 256, f->ptr) ;
}
```

LOG-OPS.H

```
#ifndef _LOG_OPS_H_
#define _LOG_OPS_H_
/*************************************************************************
*   THIS FILE CONTAINS FUNCTION DECLARATIONS FOR LOGGING SCREEN I/O       *
*************************************************************************/

#include <stdio.h>
#include <stdarg.h>

extern FILE *LogFptr ;

extern int scanf (const char *format, ...) ;
extern int printf (const char *format, ...) ;

#endif
```

LOG-OPS.C

```
/*************************************************************************
*   THIS FILE CONTAINS FUNCTION DEFINITIONS FOR LOGGING SCREEN I/O       *
*************************************************************************/

#include "log-ops.h"

FILE *LogFptr = 0L ;

/*************************************************************************
*   THIS FUNCTION REMAPS THE SCREEN INPUT THAT IS TRANSFERRED USING SCANF *
*       TO ALSO PRINT A COPY TO THE LOGFILE IF ONE IS OPEN                *
*************************************************************************/
int scanf (const char *format, ...)
{ va_list   args ;
  char      buffer[80] ;
  int       result ;

  va_start (args, format) ;

  gets (buffer) ;
  result = vsscanf (buffer, format, args) ;
  va_end (args) ;

  if (LogFptr)
   { va_start (args, format) ;
     fprintf (LogFptr, "%s", buffer) ;
     fprintf (LogFptr, "\n") ;
     va_end (args) ;
     fflush (LogFptr) ;
   }

  return result ;
}
```

```
/*************************************************************************
*   THIS FUNCTION REMAPS THE SCREEN OUTPUT THAT IS TRANSFERRED USING PRINTF *
*       TO ALSO PRINT TO A LOG FILE IF ONE IS OPEN                        *
*************************************************************************/
int printf (const char *format, ...)
{ va_list   args ;
  int       result ;

  va_start (args, format) ;

  result = vprintf (format, args) ;
  va_end (args) ;

  if (LogFptr)
   { va_start (args, format) ;
     vfprintf (LogFptr, format, args) ;
     va_end (args) ;
     fflush (LogFptr) ;
   }

  return result ;
}
```

REALFFT.H

```
#ifndef _REALFFT_H_
#define _REALFFT_H_
/*************************************************************************
*   THIS IS THE HEADER FILE FOR FFT FUNCTIONS                            *
*************************************************************************/
#include <math.h>

extern void drealft (double data[], unsigned long nn, int isign) ;

#endif
```

REALFFT.C

```
#include "realfft.h"

#define SWAP(a,b) tempr=(a); (a)=(b); (b)=tempr

/*************************************************************************
*   This function calculates the fast Fourier Transform of a time series.    *
*     Taken from Numerical Recipes in C.                                  *
*************************************************************************/

void four1(double data[], unsigned long nn, int isign)
{
   unsigned long n,mmax,m,j,istep,i;
   long double wtemp,wr,wpr,wpi,wi,theta;
   double tempr,tempi;
```

```
    n=nn << 1;
    j=1;
    for (i=1;i<n;i+=2) {
        if (j > i) {
            SWAP(data[j],data[i]);
            SWAP(data[j+1],data[i+1]);
        }
        m=n >> 1;
        while (m >= 2 && j > m) {
            j -= m;
            m >>= 1;
        }
        j += m;
    }
    mmax=2;
    while (n > mmax) {
        istep=mmax << 1;
        theta=isign*(6.28318530717959/mmax);
        wtemp=sin(0.5*theta);
        wpr = -2.0*wtemp*wtemp;
        wpi=sin(theta);
        wr=1.0;
        wi=0.0;
        for (m=1;m<mmax;m+=2) {
            for (i=m;i<=n;i+=istep) {
                j=i+mmax;
                tempr=wr*data[j]-wi*data[j+1];
                tempi=wr*data[j+1]+wi*data[j];
                data[j]=data[i]-tempr;
                data[j+1]=data[i+1]-tempi;
                data[i] += tempr;
                data[i+1] += tempi;
            }
            wr=(wtemp=wr)*wpr-wi*wpi+wr;
            wi=wi*wpr+wtemp*wpi+wi;
        }
        mmax=istep;
    }
}
#undef SWAP


/*************************************************************************
*   This function uses FOUR1 to calculate the Fourier Transform of a set of  *
*     n real-valued data points.  Replaces this data by the POSITIVE          *
*     frequency half of its complex Fourier Transform.  The real-valued       *
*     first and last components of the complex transform are returned as      *
*     elements data[1] and data[2], respectively.                             *
*************************************************************************/

void drealft(double data[], unsigned long n, int isign)
{
    void four1(double data[], unsigned long nn, int isign);
    unsigned long i,i1,i2,i3,i4,np3;
    double c1=0.5,c2,h1r,h1i,h2r,h2i;
    long double wr,wi,wpr,wpi,wtemp,theta;

    theta=3.141592653589793/(long double) (n>>1);
    if (isign == 1) {
```

```
        c2 = -0.5;
        four1(data,n>>1,1);
    } else {
        c2=0.5;
        theta = -theta;
    }
    wtemp=sin(0.5*theta);
    wpr = -2.0*wtemp*wtemp;
    wpi=sin(theta);
    wr=1.0+wpr;
    wi=wpi;
    np3=n+3;
    for (i=2;i<=(n>>2);i++) {
        i4=1+(i3=np3-(i2=1+(i1=i+i-1)));
        h1r=c1*(data[i1]+data[i3]);
        h1i=c1*(data[i2]-data[i4]);
        h2r = -c2*(data[i2]+data[i4]);
        h2i=c2*(data[i1]-data[i3]);
        data[i1]=h1r+wr*h2r-wi*h2i;
        data[i2]=h1i+wr*h2i+wi*h2r;
        data[i3]=h1r-wr*h2r+wi*h2i;
        data[i4] = -h1i+wr*h2i+wi*h2r;
        wr=(wtemp=wr)*wpr-wi*wpi+wr;
        wi=wi*wpr+wtemp*wpi+wi;
    }
    if (isign == 1) {
        data[1] = (h1r=data[1])+data[2];
        data[2] = h1r-data[2];
    } else {
        data[1]=c1*((h1r=data[1])+data[2]);
        data[2]=c1*(h1r-data[2]);
        four1(data,n>>1,-1);
    }
}
```

B.1. Input Files

The program BIN-AV.EXE is a program that was compiled using Watcom C/C++ v.10 to work in a DOS environment. It reads an ASCII file that nominally contains a spectral power density. BIN-AV.EXE creates another ASCII file with the spectral estimates (data points) spaced differently. The program was written in order to decrease the data file size and to prevent the spectral estimates from being bunched together at high frequencies when plotted on a logarithmically-spaced frequency axis. It does this by making multiple passes through the data file. Each pass starts at a user-specified frequency. Adjacent spectral estimates at frequencies that are higher than the user-specified frequency are averaged. Then, the center frequency of the new, averaged spectral estimate is adjusted accordingly in order to satisfy Parseval's theorem and preserve the mean square integral. Since a given data set may consist of multiple data files, the program uses program line arguments so that large amounts of data can be processed in a "batch" format. The program line arguments are:

```
BIN-AV.EXE <input file name> <log file name>
                (required)          (optional)
```

An *input file* is required for program execution in order to specify user selected options. The log file is optional. If a *log file name* is provided, a copy of all screen I/O is written to the that file. An example input file is,

```
 Input data file = E:\DATA\P-SPEC.P1
Output data file = E:\DATA\P-SPEC.AV
        StartRow = 2
         NumRows = 8191
         NumCols = 5
         Key Col = 0
   NumBoundaries = 10
 Boundaries (Hz) =  50
                   100
                   300
                   500
                   700
                  1000
                  2000
                  4000
                  5000
                  7000
```

In the above example, the *Input data file* and *Output data file* are self-explanatory. The *StartRow* is the row number of the input ASCII data file that the program starts reading data from. In the above example, *StartRow* = 2. So, BIN-AV will transfer the first line of the input data file directly to the output data file, then start reading data values beginning at row 2 of the input data file. This feature is intended to handle column names or other header-type information. *NumRows* and *NumCols* specify the organization of the data. *NumRows* is the number of rows **of data**. For example, an input data file may have 8192 lines, however, if the first line contains column labels, then there are only 8191 rows of data. Therefore, *NumRows* would be 8191. *KeyCol* is the column number that contains the frequency of each spectral estimate. For the *KeyCol* **only**, the numbering starts with zero– the first column is column 0, the second column is column 1, etc. *KeyCol* specifies what column will be searched by BIN-AV in order to find the boundary values which are specified by *NumBoundaries* and *Boundaries (Hz)*. The *Boundaries (Hz)* values specify the start frequencies for each successive pass of BIN-AV through the input data file to average adjacent bins. Using the above input file, BIN-AV would first find the first spectral estimate that is at a frequency that is not less than 50. Then, adjacent spectral estimates at higher frequencies would be averaged. Next, BIN-AV would find the first spectral estimate that is at a frequency that is not less than 100, and adjacent spectral estimates at higher frequencies would be averaged. This process would be carried out for each *boundary* frequency.

B.2. Output files

The output data file is the only output file of this program. The format of the output data file is identical to the format of the input data file.

B.3. Program Listings

The source code for BIN-AV.EXE is split up into 5 files:

`BIN-AV.C`	Main functions of the program
`FILE-OPS.H` `FILE-OPS.C`	These two files contain utility functions used for file I/O

LOG-OPS.H
LOG-OPS.C

These two files contain redefinitions of the functions `printf` and `scanf` in order to copy screen I/O to a log file, if one is open.

BIN-AV.C

```
/*****************************************************************************
*   THIS PROGRAM PERFORMS A BIN AVERAGE ON AN INPUT ASCII SPECTRUM FILE.     *
*****************************************************************************/

#include <stdio.h>
#include <stdlib.h>
#include <string.h>
#include <malloc.h>
#include <graph.h>
#include <time.h>

#include "log-ops.h"
#include "file-ops.h"

#define MAX_LINE_SIZE   256

FileInfo        IniF, LogF, InSpecF, OutSpecF ;
unsigned long   StartRow, SkipLines, NumRows ;
unsigned short  NumCols, KeyCol, NumBoundaries ;
double          **InSpec, *Boundary ;
char            **SkipRow ;

void ProcessArgs (int ArgCount, char **Arg) ;
unsigned short ReadConfig (void) ;
void           PrintConfig (void) ;
unsigned short GetMem(void) ;
void           FreeMem (void) ;
unsigned short ReadInSpec (void) ;
unsigned long  MakeEven (unsigned long Number) ;
unsigned short DoAveraging (void) ;
unsigned short WriteOutSpec (void) ;

void main (int ArgCount, char **Arg)
{ unsigned short    error ;
  time_t            TheTime ;

  _clearscreen(_GCLEARSCREEN) ;
  printf ("\n\n    STARTING BIN AVERAGE PROGRAM\n\n") ;
  if (ArgCount < 2)
   { printf ("  Usage : bin-av <Ini Filename> <Log Filename>\n") ;
     printf ("                    (required)     (optional)\n\n") ;
   }
  atexit (FreeMem) ;

  ProcessArgs(ArgCount, Arg) ;
  if (!IniF.loaded) return ;
  LogFptr = LogF.ptr ;
```

```
  time (&TheTime) ;
  printf ("\n\n    STARTING BIN AVERAGE PROGRAM : %s\n\n", ctime(&TheTime)) ;

  printf (" Reading Configuration ... ") ;
  error = ReadConfig() ;
  if (error)
   { printf ("ERROR %hu\n", error) ;
     return ;
   }
  printf ("O.K.\n") ;
  PrintConfig() ;

  printf (" Allocating memory ... ") ;
  error = GetMem() ;
  if (error)
   { printf ("ERROR %hu\n", error) ;
     return ;
   }
  printf ("O.K.\n") ;

  printf (" Reading spectra ...\n") ;
  error = ReadInSpec () ;
  if (error)
   { printf (" READING ERROR %hu\n", error) ;
     return ;
   }
  printf ("\n") ;

  printf (" Calculating ... ") ;
  error = DoAveraging() ;
  if (error)
   { printf ("ERROR %hu\n", error) ;
     return ;
   }
  printf ("O.K.\n") ;

  printf (" Saving bin-averaged spectra ...\n") ;
  error = WriteOutSpec () ;
  if (error)
   { printf (" WRITING ERROR %hu\n", error) ;
     return ;
   }

  time (&TheTime) ;
  printf ("\n   SUCCESSFUL COMPLETION : %s", ctime(&TheTime)) ;
  printf ("                              New NumRows = %lu\n", NumRows) ;
}


/*************************************************************************
*   THIS FUNCTION PROCESSES PROGRAM ARGUMENTS                            *
*************************************************************************/
void ProcessArgs (int ArgCount, char **Arg)
{
  if (ArgCount > 2)
   { strcpy (LogF.name, Arg[2]) ;
     OpenFile (&LogF, "wt") ;
   }

  if (ArgCount > 1)
```

```
   { strcpy (IniF.name, Arg[1]) ;
     OpenFile (&IniF, "rt") ;
}  }


/*************************************************************************
*   THIS FUNCTION READS CONFIGURATION INFO FROM A CONFIGURATION FILE      *
*************************************************************************/
unsigned short ReadConfig (void)
{ unsigned short b ;

  GotoChar (&IniF, '=') ;  fscanf (IniF.ptr, "%s", InSpecF.name) ;
  GotoChar (&IniF, '=') ;  fscanf (IniF.ptr, "%s", OutSpecF.name) ;
  GotoChar (&IniF, '=') ;  fscanf (IniF.ptr, "%lu", &StartRow) ;
  GotoChar (&IniF, '=') ;  fscanf (IniF.ptr, "%lu", &NumRows) ;
  GotoChar (&IniF, '=') ;  fscanf (IniF.ptr, "%hu", &NumCols) ;
  GotoChar (&IniF, '=') ;  fscanf (IniF.ptr, "%hu", &KeyCol) ;
  GotoChar (&IniF, '=') ;  fscanf (IniF.ptr, "%hu", &NumBoundaries) ;

  SkipLines = StartRow - 1 ;

  Boundary = (double *)calloc(NumBoundaries, sizeof(double)) ;
  if (!Boundary)  return 1 ;

  GotoChar (&IniF, '=') ;
  for (b=0; b<NumBoundaries; b++)
    fscanf (IniF.ptr, "%lg", &(Boundary[b])) ;

  return 0 ;
}


/*************************************************************************
*   THIS FUNCTION PRINTS THE CONFIGURATION INFORMATION                   *
*************************************************************************/
void PrintConfig (void)
{ unsigned short b ;

  printf ("\n") ;
  printf ("\t\t       Input Filename : %s\n", InSpecF.name) ;
  printf ("\t\t      Output Filename : %s\n", OutSpecF.name) ;
  printf ("\t\t           Start Row = %lu\n", StartRow) ;
  printf ("\t\t       Number of Rows = %lu\n", NumRows) ;
  printf ("\t\t    Number of Columns = %hu\n", NumCols) ;
  printf ("\t\t           Key Column = %hu\n", KeyCol) ;
  printf ("\t\t Number of Boundaries = %hu\n", NumBoundaries) ;
  for (b=0; b<NumBoundaries; b++)
    printf ("\t\t          Boundary %02hu : %lg\n", b+1, Boundary[b]) ;
  printf ("\n") ; fflush(stdout) ;
}


/*************************************************************************
*   THIS FUNCTION ALLOCATES MEMORY FROM THE HEAP                         *
*************************************************************************/
unsigned short GetMem(void)
{ unsigned long     TotalSize = NumRows * NumCols ;
  unsigned short    row, col ;
```

```
  InSpec = (double **) calloc (NumCols, sizeof (double *)) ;
  if (!InSpec)  return 1 ;

  InSpec[0] = (double *) calloc (TotalSize, sizeof (double)) ;
  if (!InSpec[0])  return 2 ;

  for (col=1; col<NumCols; col++)
    InSpec[col] = InSpec[col-1] + NumRows ;

  if (SkipLines)
   { SkipRow = (char **) calloc (SkipLines, sizeof(char *)) ;
     if (!SkipRow)  return 3 ;

     SkipRow[0] = (char *) calloc (SkipLines*(MAX_LINE_SIZE+1), sizeof(char));
     if (!SkipRow[0])  return 4 ;

     for (row=1; row<SkipLines; row++)
       SkipRow[row] = SkipRow[row-1] + (MAX_LINE_SIZE+1L) ;
   }

  return 0 ;
}


/*************************************************************************
*   THIS FUNCTION RETURNS MEMORY TO THE HEAP                             *
*************************************************************************/
void FreeMem (void)
{ free (Boundary) ;
  free (InSpec[0]) ;
  free (InSpec) ;
  free (SkipRow[0]) ;
  free (SkipRow) ;
}


/*************************************************************************
*   THIS FUNCTION READS THE INPUT SPECTRA                                *
*************************************************************************/
unsigned short ReadInSpec (void)
{ unsigned long     line, row, numr ;
  unsigned short    error, col ;

  error = OpenFile (&InSpecF, "rt") ;
  if (error) return 1 ;

  for (line = 0; line < SkipLines; line++)
   if (fgets(SkipRow[line], MAX_LINE_SIZE, InSpecF.ptr) == NULL) return 2 ;

  for (row = 0; row < NumRows; row++)
   for (col = 0; col < NumCols; col++)
    { numr = fscanf (InSpecF.ptr, "%lg", &(InSpec[col][row])) ;
      if (numr != 1)  return 3 ;
    }

  CloseFile(&InSpecF) ;
  return 0 ;
}
```

```
/*************************************************************************
*   THIS FUNCTION IS PASSED A NUMBER.  IT TESTS IF THE NUMBER IS EVEN. IF   *
*       THE NUMBER IS NOT EVEN THE RETURNED VALUE IS THE NUMBER MINUS ONE   *
*       IN ORDER TO MAKE IT EVEN                                            *
*************************************************************************/
unsigned long MakeEven (unsigned long Number)
{ unsigned long Left, Right ;

  Left  = Number >> 1 ;
  Right = Left << 1 ;

  if (Right == Number) return Number ;

  return Number-- ;
}


/*************************************************************************
*   THIS FUNCTION DOES THE BIN AVERAGING                                  *
*************************************************************************/
unsigned short DoAveraging (void)
{
  unsigned short    avg, c ;
  unsigned long     r, FirstRow, NewNumRows, NewIndex ;

  NewNumRows = MakeEven(NumRows) ;

  for (avg=0; avg<NumBoundaries; avg++)
   { FirstRow = 0L ;
     while (InSpec[KeyCol][FirstRow] < Boundary[avg])
      { FirstRow++ ;
        if (FirstRow > NewNumRows)
         { printf ("%lu %lg ", NewNumRows, Boundary[avg]);
           return 1 ;
      }  }

     NewIndex = MakeEven(FirstRow) ;

     for (r=NewIndex; r < NewNumRows; r+=2L)
      { for (c=0; c<NumCols; c++)
         InSpec[c][NewIndex] = 0.5 * (InSpec[c][r] + InSpec[c][r+1L]) ;
        NewIndex++ ;
      }
     NewIndex-- ;
     NewNumRows = NewIndex ;
   }

  NewIndex = MakeEven(NumRows) ;
  if (NewIndex != NumRows)
   { for (c=0; c<NumCols; c++)
       InSpec[c][NewNumRows] = InSpec[c][NewIndex] ;
     NewNumRows++ ;
   }

  NumRows = NewNumRows ;
  return 0 ;
}
```

```
/*****************************************************************************
*   THIS FUNCTION WRITES THE OUTPUT SPECTRA                                  *
*****************************************************************************/
unsigned short WriteOutSpec (void)
{ unsigned long     row ;
  int               numw ;
  unsigned short    error, col ;

  error = OpenFile (&OutSpecF, "wt") ;
  if (error) return 1 ;

  for (row = 0; row < SkipLines; row++)
   { numw = fprintf (OutSpecF.ptr, "%s", SkipRow[row]) ;
     if (numw < 0)  return 2 ;
   }

  for (row = 0; row < NumRows; row++)
   { for (col = 0; col < NumCols; col++)
      { numw = fprintf (OutSpecF.ptr, " % 13.5le", InSpec[col][row]) ;
        if (numw < 0)  return 3 ;
      }
     fprintf (OutSpecF.ptr, "\n") ;
   }

  CloseFile(&OutSpecF) ;
  return 0 ;
}
```

FILE-OPS.H

```
#ifndef _FILE_OPS_H_
#define _FILE_OPS_H_
/*****************************************************************************
*   THIS FILE CONTAINS DEFINITIONS USED FOR FILE I/O                         *
*****************************************************************************/

#include <stdio.h>
#include <errno.h>

typedef struct
 { FILE             *ptr ;
   char             name[80] ;
   unsigned short   loaded ;
 }
FileInfo ;

extern unsigned short OpenFile (FileInfo *f, char *mode) ;
extern void CloseFile (FileInfo *f) ;
extern void GotoChar (FileInfo *f, char c) ;
extern void SkipLine (FileInfo *f) ;

#endif
```

FILE-OPS.C

```
/*************************************************************************
*   THIS FILE CONTAINS FUNCTION DECLARATIONS USED FOR FILE I/O           *
*************************************************************************/

#include "file-ops.h"

/*************************************************************************
*   THIS FUNCTION OPENS A FILE                                           *
*************************************************************************/
unsigned short OpenFile (FileInfo *f, char *mode)
{
  printf ("  Openning %s ... ", f->name) ;

  if ((f->ptr = fopen (f->name, mode)) == NULL)
   { printf ("ERROR #%i", errno) ;
     f->loaded = 0 ;
     return 1 ;
   }

 printf ("O.K.\n") ;
 f->loaded = 1 ;

 return 0 ;
}

/*************************************************************************
*   THIS FUNCTION CLOSES A FILE                                          *
*************************************************************************/
void CloseFile (FileInfo *f)
{
  fclose (f->ptr) ;
  f->loaded = 0 ;
}

/*************************************************************************
*   THIS FUNCTION MOVES THE GIVEN ASCII FILE POINTER TO THE GIVEN CHARACTER *
*************************************************************************/
void GotoChar (FileInfo *f, char c)
{ char format[] = "%*[^ ]%*[ ]" ;

  format[4] = format [9] = c ;
  fscanf (f->ptr, format) ;
}

/*************************************************************************
*   THIS FUNCTION ADVANCES THE FILE POINTER PAST THE NEXT LINE OF AN ASCII  *
*       FILE                                                             *
*************************************************************************/
void SkipLine (FileInfo *f)
{ char buffer[256] ;
  fgets (buffer, 256, f->ptr) ;
}
```

LOG-OPS.H

```
#ifndef _LOG_OPS_H_
#define _LOG_OPS_H_
/*****************************************************************************
*   THIS FILE CONTAINS FUNCTION DECLARATIONS FOR LOGGING SCREEN I/O          *
*****************************************************************************/

#include <stdio.h>
#include <stdarg.h>

extern FILE *LogFptr ;

extern int scanf (const char *format, ...) ;
extern int printf (const char *format, ...) ;

#endif
```

LOG-OPS.C

```
/*****************************************************************************
*   THIS FILE CONTAINS FUNCTION DEFINITIONS FOR LOGGING SCREEN I/O           *
*****************************************************************************/

#include "log-ops.h"

FILE *LogFptr = 0L ;

/*****************************************************************************
*   THIS FUNCTION REMAPS THE SCREEN INPUT THAT IS TRANSFERRED USING SCANF    *
*       TO ALSO PRINT A COPY TO THE LOGFILE IF ONE IS OPEN                   *
*****************************************************************************/
int scanf (const char *format, ...)
{ va_list   args ;
  char      buffer[80] ;
  int       result ;

  va_start (args, format) ;

  gets (buffer) ;
  result = vsscanf (buffer, format, args) ;
  va_end (args) ;

  if (LogFptr)
   { va_start (args, format) ;
     fprintf (LogFptr, "%s", buffer) ;
     fprintf (LogFptr, "\n") ;
     va_end (args) ;
   }

  return result ;
}
```

```
/*************************************************************************
*   THIS FUNCTION REMAPS THE SCREEN OUTPUT THAT IS TRANSFERRED USING PRINTF *
*       TO ALSO PRINT TO A LOG FILE IF ONE IS OPEN                        *
*************************************************************************/
int printf (const char *format, ...)
{ va_list   args ;
  int       result ;

  va_start (args, format) ;

  result = vprintf (format, args) ;
  va_end (args) ;

  if (LogFptr)
   { va_start (args, format) ;
     vfprintf (LogFptr, format, args) ;
     va_end (args) ;
   }

  return result ;
}
```

C.1. Input Files

The program `P-TERM.EXE` is a program that was compiled using Watcom C/C^{++} v.10 to work in a DOS environment. `P-TERM.EXE` computes approximations to some terms of the Poisson integral (equation 25, see §4.3) using experimental, wing-body junction flow, LDV velocity data. The calculations performed by this program were used to analyze the Poisson Ratio (equation 56) that is discussed in §4.3. Input to `P-TERM.EXE` is controlled through the header file `BL-DATA.H`. The program doesn't accept any command line arguments. Therefore, the source code must be recompiled in order to change the input information. The calculations were performed using two data sets. The control of which data set was used was handled using a C-compiler directive, `#define`, at the beginning of `P-TERM.C`. The directive `#define LOW_RE` causes the program to use the velocity data of Ölçmen and Simpson (1996, Re_θ= 7300(2-D), 5940(3-D)). The directive `#define HIGH_RE` causes the program to use the velocity data of Ölçmen *et al.* (1998, Re_θ= 23400(2-D), 23200(3-D)).

C.2. Output files

`P-TERM.EXE` creates 10 output files– one from 2-D velocity data and 9 from each velocity measurement station around the wing-body junction. Each output file contains 12 columns. Each column is a y^+-profile of a particular variable. Table C.1 shows the contents of each column of the output file.

For 2-D flow, $W = 0$. Therefore, $\partial W^+/\partial y^+$ (column 8, see table C.1) and $v^+(\partial W^+/\partial y^+)$ (column 11, see table C.1) should be identically zero. However, these terms were non-zero when calculated using the experimental data, due to the experimental uncertainty of the velocity data. Therefore, the output file contains non-zero values in columns 8 and 11 even when 2-D flow velocity data was used in the calculation. However, the quantity in column 12 (see table C.1) was

adjusted so as not to include non-zero W-velocity data. When 2-D flow velocity data is used in the calculation, column 12 contains

$$\left[\sqrt{\overline{\left(v^{+}\right)^{2}}}\left(\frac{\partial U^{+}}{\partial y^{+}}\right)+\left(\frac{\partial}{\partial y^{+}}\sqrt{\overline{\left(v^{+}\right)^{2}}}\right)\left(\frac{\partial V^{+}}{\partial y^{+}}\right)\right]^{2}$$

When 3-D, wing-body junction flow velocity data is used in the calculation, columns 4-12 each contain the term shown in table C.1 normalized by its value in a 2-D flow at comparable Re_{θ}. For example, when 3-D, wing-body junction flow velocity data is used in the calculation, column 4 contains

$$\frac{\left[\sqrt{\overline{\left(v^{+}\right)^{2}}}\right]_{3\text{-D}}}{\left[\sqrt{\overline{\left(v^{+}\right)^{2}}}\right]_{2\text{-D}}}$$

All derivatives are calculated using a 5-point parabola fit to the experimental data.

Column Number	Column Label	Variable contained
1	"yplus"	y^+
2	"y"	y-coordinate, units = meters
3	"ydstar"	y/δ^*
4	"v"	$\sqrt{\overline{(v^+)^2}}$
5	"vdy"	$\frac{\partial}{\partial y^+}\sqrt{\overline{(v^+)^2}}$
6	"dUdy"	$\frac{\partial U^+}{\partial y^+}$
7	"dVdy"	$\frac{\partial V^+}{\partial y^+}$
8	"dWdy"	$\frac{\partial W^+}{\partial y^+}$
9	"Uterm"	$\sqrt{\overline{(v^+)^2}}\left(\frac{\partial U^+}{\partial y^+}\right)$
10	"Vterm"	$\left(\frac{\partial}{\partial y^+}\sqrt{\overline{(v^+)^2}}\right)\left(\frac{\partial V^+}{\partial y^+}\right)$
11	"Wterm"	$\sqrt{\overline{(v^+)^2}}\left(\frac{\partial W^+}{\partial y^+}\right)$
12	"SumSq"	$\left[\sqrt{\overline{(v^+)^2}}\left(\frac{\partial U^+}{\partial y^+}+\frac{\partial W^+}{\partial y^+}\right)+\left(\frac{\partial}{\partial y^+}\sqrt{\overline{(v^+)^2}}\right)\left(\frac{\partial V^+}{\partial y^+}\right)\right]^2$

Table C.1. Contents of `P-TERM.EXE` output file.

C.3. Program Listings

The source code for P-TERM.EXE is split up into 8 files:

P-TERM.C	Main functions of the program
BL-DATA.H	Header file that contains the path and name of the LDV velocity data files and values for boundary layer parameters such as U_e, δ, δ^*, etc.
VELDATA.H VELDATA.C	These two files contain functions used to read the LDV data files
PARA-FIT.H PARA-FIT.C	These two files contain functions that fit a polynomial of order 2 or less to two data arrays using a least-squares fit
MYFILE.H MYFILE.C	These two files contain utility functions used for file I/O

P-TERM.C

```
/*****************************************************************************
*   THIS PROGRAM CALCULATES SOME TERMS OF THE POISSON EQN AND WRITES          *
*   THEM TO FILE.  VALUES AT 3D STATIONS ARE NORMALIZED BY CORRESPONDING      *
*   2D VALUES.  NOTE THAT ALTHOUGH dW/dy IS CALCULATED FOR THE 2D FLOW.  IT   *
*   SHOULD BE ZERO.                                                           *
*                                                                             *
*   TO RUN LOW RE(THETA)   #define LOW_RE                                    *
*                                                                             *
*   TO RUN HIGH RE(THETA)  #define HIGH_RE                                   *
*                                                                             *
*  MODIFIED 5/4/99 TO USE YPLUS-WALL-COORDINATES VELOCITY FILES               *
*                                                                             *
*****************************************************************************/
#define LOW_RE

#include "myfile.h"
#include "veldata.h"
#include "bl-data.h"
#include "para-fit.h"
#include <stdio.h>
#include <string.h>
#include <math.h>

#define ERR_LOW_Y       2
#define ERR_HIGH_Y      3
#define ERR_BAD_DERIV   4

void main(void)
{  FileInfo InF, OutF ;
   int      yloc, err, st ;
```

```
   double   dimY,
            v,      v2D[NUM_Y_LOCS],
            dvdy,   dvdy2D[NUM_Y_LOCS],
            dUdy,   dUdy2D[NUM_Y_LOCS],
            dVdy,   dVdy2D[NUM_Y_LOCS],
            dWdy,   Wterm,
            Uterm,  Uterm2D[NUM_Y_LOCS],
            Vterm,  Vterm2D[NUM_Y_LOCS],
            SumSq,  SumSq2D[NUM_Y_LOCS] ;
//
//  2D STATION - POISSON TERMS ARE STORED IN ORDER TO NORMALIZE POISSON TERMS
//      FOR 3D STATIONS
//
    //
    //  OPEN DATA FILE AND READ DATA
    //
   strcpy(InF.name, DataFname[0]) ;
   OpenFile (&InF, "rt") ;
   ZeroAllVelData() ;
   ReadVelData(InF.ptr) ;
   CloseFile(&InF) ;
    //
    //  CONVERT Ys TO METERS AND TAKE SQUARE ROOT OF NORMAL STRESSES
    //
//   CorrectYs() ;
   SqrtNormStresses() ;
    //
    //  OPEN OUTPUT FILE AND WRITE COLUMN LABELS
    //
   strcpy(OutF.name, OutFname[0]);
   OpenFile(&OutF, "wt");

   fprintf (OutF.ptr,"    \"yplus\"        \"y\"     ") ;
   fprintf (OutF.ptr,"   \"ydstar\"        \"v\"     ");
   fprintf (OutF.ptr,"     \"vdy\"       \"dUdy\"    ") ;
   fprintf (OutF.ptr,"    \"dVdy\"       \"dWdy\"    ") ;
   fprintf (OutF.ptr,"    \"Uterm\"      \"Vterm\"   ") ;
   fprintf (OutF.ptr,"    \"Wterm\"      \"SumSq\"\n") ;
    //
    //  FOR EACH y+
    //
   for (yloc=0; yloc<NUM_Y_LOCS; yloc++)
    {
        //
        //  CALCULATE POISSON TERMS
        //
            //  y+, y(m), y/d*
            //
      fprintf (OutF.ptr, "%13.4le", yplus[yloc]);
      dimY = yplus[yloc] ;
      fprintf (OutF.ptr, "%13.4le", dimY*nu[0]/utau[0]) ;
      fprintf (OutF.ptr, "%13.4le", dimY*nu[0]/utau[0]/delstar[0]) ;
            //
            //  v
            //
      err = CalcTerm(&v2D[yloc], dimY, &vv, 0) ;
      if (err)
       { printf (" ERR : yloc = %i, v2D CalcTerm returned %i\n", yloc, err);
         return ;
       }
      fprintf (OutF.ptr,"%13.4le", v2D[yloc]) ;
            //
```

```
            //  dv/dy
            //
        err = CalcTerm(&dvdy2D[yloc], dimY, &vv, 1) ;
        if (err)
         { printf (" ERR : yloc = %i, dvdy2D CalcTerm returned %i\n",yloc,err);
           return ;
         }
        fprintf (OutF.ptr,"%13.4le", dvdy2D[yloc]) ;
            //
            //  dU/dy
            //
        err = CalcTerm(&dUdy2D[yloc], dimY, &U, 1) ;
        if (err)
         { printf (" ERR : yloc = %i, dUdy2D CalcTerm returned %i\n",yloc,err);
           return ;
         }
        fprintf (OutF.ptr,"%13.4le", dUdy2D[yloc]) ;
            //
            //  dV/dy
            //
        err = CalcTerm(&dVdy2D[yloc], dimY, &V, 1) ;
        if (err)
         { printf (" ERR : yloc = %i, dVdy2D CalcTerm returned %i\n",yloc,err);
           return ;
         }
        fprintf (OutF.ptr,"%13.4le", dVdy2D[yloc]) ;
            //
            //  dW/dy
            //
        err = CalcTerm(&dWdy, dimY, &W, 1) ;
        if (err)
         { printf (" ERR : yloc = %i, dWdy2D CalcTerm returned %i\n",yloc,err);
           return ;
         }
        fprintf (OutF.ptr,"%13.4le", dWdy) ;
            //
            //  Uterm = (v)(dU/dy)
            //
        Uterm2D[yloc] = v2D[yloc]*dUdy2D[yloc] ;
        fprintf (OutF.ptr, "%13.4le", Uterm2D[yloc]) ;
            //
            //  Vterm = (dv/dy)(dV/dy)
            //
        Vterm2D[yloc] = dvdy2D[yloc]*dVdy2D[yloc] ;
        fprintf (OutF.ptr, "%13.4le", Vterm2D[yloc]) ;
            //
            //  Wterm = (v)(dW/dy)
            //
        Wterm = v2D[yloc]*dWdy ;
        fprintf (OutF.ptr, "%13.4le", Wterm) ;
            //
            //  SumSq = [ (v)(dU/dy) + (dv/dy)(dV/dy) ]^2
            //
        SumSq2D[yloc] = Uterm2D[yloc] + Vterm2D[yloc] ;
        SumSq2D[yloc] *= SumSq2D[yloc] ;
        fprintf (OutF.ptr,"%13.4le\n", SumSq2D[yloc]);
        fflush(OutF.ptr) ;
     }
    CloseFile (&OutF) ;
//
//  FOR EACH 3D STATION
//
```

```
   for (st=1; st<NUM_STATIONS; st++)
    {
        //
        //  OPEN DATA FILE AND READ DATA
        //
       strcpy(InF.name, DataFname[st]) ;
       OpenFile (&InF, "rt") ;
       ZeroAllVelData() ;
       ReadVelData(InF.ptr) ;
       CloseFile(&InF) ;
        //
        //  CONVERT Ys TO METERS AND TAKE SQUARE ROOT OF NORMAL STRESSES
        //
//#ifdef LOW_RE
//       if (st>7)        //  USE IF STATEMENT FOR LOW RE(THETA)
//#endif
//         CorrectYs() ;
       SqrtNormStresses() ;
        //
        //  OPEN OUTPUT FILE AND WRITE COLUMN LABELS
        //
       strcpy(OutF.name, OutFname[st]);
       OpenFile(&OutF, "wt");

       fprintf (OutF.ptr,"    \"yplus\"        \"y\"     ") ;
       fprintf (OutF.ptr,"   \"ydstar\"        \"v\"     ");
       fprintf (OutF.ptr,"     \"vdy\"       \"dUdy\"    ") ;
       fprintf (OutF.ptr,"    \"dVdy\"       \"dWdy\"    ") ;
       fprintf (OutF.ptr,"    \"Uterm\"      \"Vterm\"   ") ;
       fprintf (OutF.ptr,"    \"Wterm\"      \"SumSq\"\n") ;
        //
        //  FOR EACH yplus
        //
       for (yloc=0; yloc<NUM_Y_LOCS; yloc++)
        {
            //
            //  CALCULATE POISSON TERMS
            //
                //  y+, y(m), y/d*
                //
          fprintf (OutF.ptr, "%13.4le", yplus[yloc]);
          dimY = yplus[yloc] ;
          fprintf (OutF.ptr, "%13.4le", dimY*nu[st]/utau[st]) ;
          fprintf (OutF.ptr, "%13.4le", dimY*nu[st]/utau[st]/delstar[st]) ;
                //
                //  v
                //
          err = CalcTerm(&v, dimY, &vv, 0) ;
          if (err)
           { printf (" ERR : yloc = %i, v CalcTerm returned %i\n", yloc, err);
             return ;
           }
          fprintf (OutF.ptr,"%13.4le", v) ;
                //
                //  dv/dy
                //
          err = CalcTerm(&dvdy, dimY, &vv, 1) ;
          if (err)
           { printf (" ERR : yloc = %i, dvdy CalcTerm returned
%i\n",yloc,err);
             return ;
           }
```

```
          fprintf (OutF.ptr,"%13.4le", dvdy) ;
                //
                //  dU/dy
                //
          err = CalcTerm(&dUdy, dimY, &U, 1) ;
          if (err)
           { printf (" ERR : yloc = %i, dUdy CalcTerm returned
%i\n",yloc,err);
             return ;
           }
          fprintf (OutF.ptr,"%13.4le", dUdy) ;
                //
                //  dV/dy
                //
          err = CalcTerm(&dVdy, dimY, &V, 1) ;
          if (err)
           { printf (" ERR : yloc = %i, dVdy CalcTerm returned
%i\n",yloc,err);
             return ;
           }
          fprintf (OutF.ptr,"%13.4le", dVdy) ;
                //
                //  dW/dy
                //
          err = CalcTerm(&dWdy, dimY, &W, 1) ;
          if (err)
           { printf (" ERR : yloc = %i, dWdy CalcTerm returned
%i\n",yloc,err);
             return ;
           }
          fprintf (OutF.ptr,"%13.4le", dWdy) ;
                //
                //  Uterm = (v)(dU/dy)
                //
          Uterm = v*dUdy ;
          fprintf (OutF.ptr, "%13.4le", Uterm / Uterm2D[yloc]) ;
                //
                //  Vterm = (dv/dy)(dV/dy)
                //
          Vterm = dvdy*dVdy ;
          fprintf (OutF.ptr, "%13.4le", Vterm / Vterm2D[yloc]) ;
                //
                //  Wterm = (v)(dW/dy)
                //
          Wterm = v*dWdy ;
          fprintf (OutF.ptr, "%13.4le", Wterm) ;
                //
                //  SumSq = [ (v)(dU/dy) + (dv/dy)(dV/dy) + (v)(dW/dy) ]^2
                //
          SumSq = Uterm + Vterm + Wterm ;
          SumSq *= SumSq / SumSq2D[yloc] ;
          fprintf (OutF.ptr,"%13.4le\n", SumSq);
          fflush(OutF.ptr) ;
        }
       CloseFile (&OutF) ;
    }
   printf ("\n PROGRAM COMPLETED\n") ;
}
```

```
/*****************************************************************************
*   THIS FUNCTION REPLACES THE NORMAL STRESSES WITH THEIR SQUARE ROOT        *
*****************************************************************************/
void SqrtNormStresses(void)
{ int i ;

  for (i=0; i<uu.num; i++)  uu.dat[i] = sqrt(uu.dat[i]) ;
  for (i=0; i<vv.num; i++)  vv.dat[i] = sqrt(vv.dat[i]) ;
  for (i=0; i<ww.num; i++)  ww.dat[i] = sqrt(ww.dat[i]) ;
}


/*****************************************************************************
*   THIS FUNCTION CONVERTS THE Y VALUES FROM MICROMETERS TO METERS           *
*****************************************************************************/
void CorrectYs(void)
{ int i ;

  for (i=0; i<U.num; i++)   U.y[i] *= 1e-6 ;
  for (i=0; i<V.num; i++)   V.y[i] *= 1e-6 ;
  for (i=0; i<W.num; i++)   W.y[i] *= 1e-6 ;
  for (i=0; i<uu.num; i++)  uu.y[i] *= 1e-6 ;
  for (i=0; i<vv.num; i++)  vv.y[i] *= 1e-6 ;
  for (i=0; i<ww.num; i++)  ww.y[i] *= 1e-6 ;
  for (i=0; i<uv.num; i++)  uv.y[i] *= 1e-6 ;
  for (i=0; i<uw.num; i++)  uw.y[i] *= 1e-6 ;
  for (i=0; i<vw.num; i++)  vw.y[i] *= 1e-6 ;
}


/*****************************************************************************
*   THIS FUNCTION INTERPOLATES A VALUE OR ITS DERIVATIVE USING A 5 POINT     *
*       PARABOLA FIT GIVEN A "KEY" Y VALUE                                   *
*****************************************************************************/
int CalcTerm (double *term, double KeyValue, VelData *D, int Deriv)
{ int       r=0, StartRow, err ;
  double    A[3] ;

  while ((KeyValue > D->y[r]) && (r < D->num)) r++ ;

  if (r == 0)  return ERR_LOW_Y ;
  if (r == D->num)  return ERR_HIGH_Y ;

  StartRow = r - 2 ;
  if (StartRow < 0) StartRow = 0 ;
  if (StartRow > D->num-5) StartRow = D->num - 5 ;

  err = ParaFit(5, &(D->y[StartRow]), &(D->dat[StartRow]), A) ;
  if (err == ERR_UNDEF_COEFF)  return err ;

  switch (Deriv)
   { case 0 : *term = A[2]*KeyValue*KeyValue + A[1]*KeyValue + A[0] ; break ;
     case 1 : *term = 2.0*A[2]*KeyValue + A[1] ; break ;
//     case 2 : *term = 2.0*A[2] ; break ;
     default : return ERR_BAD_DERIV ;
   }

  return 0 ;
}
```

BL-DATA.H

```
#ifndef BL_DATA_H_
#define BL_DATA_H_
//
//  THESE ARE THE NON-DIMENSIONAL Y VALUES FOR THE OUTPUT PROFILE
//
#define NUM_Y_LOCS  14
  const double yplus[NUM_Y_LOCS] =
                 { 10.0, 20.0, 30.0, 40.0, 50.0, 62.8, 69.1, 75.4,
                   81.7, 88.0, 94.2, 100.5, 106.8, 113.1 };

//
//  THESE ARE THE FILE NAMES OF DATA AND OUTPUT FILES
//
#define NUM_STATIONS    10

/*************************************************************************
*   CONTROL OF VARIABLE INITIALIZATION (LOW RE(THETA) OR HIGH RE(THETA)) IS *
*       THROUGH #define LOW_RE STATEMENT AT BEGINNING OF p-term.c          *
*              ^^^^^^^^^^^^^^                                             *
*************************************************************************/

#ifdef  LOW_RE
        //  RE(THETA) = 5940

  const char   DataFname[NUM_STATIONS][80] =
                {"E:\\LDV-BL\\RE7000\\2DDER\\TC\\YPLUS\\2D1.UT",
                 "E:\\LDV-BL\\RE7000\\ST1\\WC\\YPLUS\\ST11.UT",
                 "E:\\LDV-BL\\RE7000\\ST2\\WC\\YPLUS\\ST21.UT",
                 "E:\\LDV-BL\\RE7000\\ST3\\WC\\YPLUS\\ST31.UT",
                 "E:\\LDV-BL\\RE7000\\ST4\\WC\\YPLUS\\ST41.UT",
                 "E:\\LDV-BL\\RE7000\\ST5\\WC\\YPLUS\\ST51.UT",
                 "E:\\LDV-BL\\RE7000\\ST6\\WC\\YPLUS\\ST61.UT",
                 "E:\\LDV-BL\\RE7000\\ST7\\WC\\YPLUS\\ST71.UT",
                 "E:\\LDV-BL\\RE7000\\STATION8\\WC\\YPLUS\\S81.UT",
                 "E:\\LDV-BL\\RE7000\\STATION9\\WC\\YPLUS\\S912.UT" } ;

  const char   OutFname[NUM_STATIONS][80] =
                {"E:\\LDV-BL\\RE7000\\POISSON\\LO2D-P.DAT",
                 "E:\\LDV-BL\\RE7000\\POISSON\\LOS1-PN.DAT",
                 "E:\\LDV-BL\\RE7000\\POISSON\\LOS2-PN.DAT",
                 "E:\\LDV-BL\\RE7000\\POISSON\\LOS3-PN.DAT",
                 "E:\\LDV-BL\\RE7000\\POISSON\\LOS4-PN.DAT",
                 "E:\\LDV-BL\\RE7000\\POISSON\\LOS5-PN.DAT",
                 "E:\\LDV-BL\\RE7000\\POISSON\\LOS6-PN.DAT",
                 "E:\\LDV-BL\\RE7000\\POISSON\\LOS7-PN.DAT",
                 "E:\\LDV-BL\\RE7000\\POISSON\\LOS8-PN.DAT",
                 "E:\\LDV-BL\\RE7000\\POISSON\\LOS9-PN.DAT" } ;

#else
        //  RE(THETA) = 23200

  const char   DataFname[NUM_STATIONS][80] =
                {"E:\\LDV-BL\\RE23000\\WC\\2D61.UT",
                 "E:\\LDV-BL\\RE23000\\WC\\S1H12.UT2",
                 "E:\\LDV-BL\\RE23000\\WC\\S2H15.UT2",
                 "E:\\LDV-BL\\RE23000\\WC\\S3H12.UT",
                 "E:\\LDV-BL\\RE23000\\WC\\S4H13.UT",
                 "E:\\LDV-BL\\RE23000\\WC\\ST5HL1.UT2",
```

```
                "E:\\LDV-BL\\RE23000\\WC\\S6H13.UT",
                "E:\\LDV-BL\\RE23000\\WC\\S7H12.UT",
                "E:\\LDV-BL\\RE23000\\WC\\S8H12.UT",
                "E:\\LDV-BL\\RE23000\\WC\\S9H12.UT" } ;

  const char   OutFname[NUM_STATIONS][80] =
                {"E:\\LDV-BL\\RE23000\\POISSON\\HI2D-P.DAT",
                 "E:\\LDV-BL\\RE23000\\POISSON\\HIS1-PN.DAT",
                 "E:\\LDV-BL\\RE23000\\POISSON\\HIS2-PN.DAT",
                 "E:\\LDV-BL\\RE23000\\POISSON\\HIS3-PN.DAT",
                 "E:\\LDV-BL\\RE23000\\POISSON\\HIS4-PN.DAT",
                 "E:\\LDV-BL\\RE23000\\POISSON\\HIS5-PN.DAT",
                 "E:\\LDV-BL\\RE23000\\POISSON\\HIS6-PN.DAT",
                 "E:\\LDV-BL\\RE23000\\POISSON\\HIS7-PN.DAT",
                 "E:\\LDV-BL\\RE23000\\POISSON\\HIS8-PN.DAT",
                 "E:\\LDV-BL\\RE23000\\POISSON\\HIS9-PN.DAT" } ;
#endif
//
//  THESE ARE BOUNDARY LAYER VARIABLES USED TO NON-DIMENSIONALIZE
//
#ifdef LOW_RE
        //  RE(THETA) = 5940

   double nu[NUM_STATIONS] =
                { 1.67e-5, 1.65e-5, 1.65e-5, 1.65e-5, 1.65e-5,
                  1.67e-5, 1.68e-5, 1.68e-5, 1.67e-5, 1.68e-5 } ;
   double utau[NUM_STATIONS] =
                { 0.980, 0.864, 0.865, 0.957, 1.110,
                  1.150, 1.160, 1.200, 1.024, 1.011 } ;
   double Ue[NUM_STATIONS] =
                { 27.1, 24.9, 24.8, 25.3, 27.3,
                  29.5, 30.5, 31.0, 30.9, 30.5 } ;
   double del[NUM_STATIONS] =
                { 39.1e-3, 39.2e-3, 40.2e-3, 39.3e-3, 39.0e-3,
                  39.6e-3, 39.2e-3, 38.8e-3, 38.4e-3, 40.7e-3 } ;
   double delstar[NUM_STATIONS] =
                { 6.20e-3, 6.90e-3, 7.54e-3, 6.86e-3, 5.53e-3,
                  5.37e-3, 5.24e-3, 5.20e-3, 5.08e-3, 5.68e-3 } ;
#else
        //  RE(THETA) = 23200

   double nu[NUM_STATIONS] =
                { 1.68e-5, 1.67e-5, 1.67e-5, 1.67e-5, 1.67e-5,
                  1.68e-5, 1.67e-5, 1.66e-5, 1.69e-5, 1.67e-5 } ;
   double utau[NUM_STATIONS] =
                { 1.030, 0.910, 0.916, 1.094, 1.240,
                  1.208, 1.208, 1.304, 1.128, 1.104 } ;
   double Ue[NUM_STATIONS] =
                { 31.31, 28.31, 28.71, 29.03, 31.14,
                  33.02, 34.66, 35.48, 35.17, 34.30 } ;
   double del[NUM_STATIONS] =
                { 13.42e-2, 13.64e-2, 13.51e-2, 13.68e-2, 13.19e-2,
                  12.33e-2, 12.86e-2, 12.90e-2, 13.35e-2, 13.46e-2 } ;
   double delstar[NUM_STATIONS] =
                { 15.80e-3, 22.78e-3, 18.37e-3, 16.84e-3, 17.28e-3,
                  13.72e-3, 17.17e-3, 12.87e-3, 12.99e-3, 13.51e-3 } ;
#endif
#endif
```

VELDATA.H

```
#ifndef _VELDATA_H_
#define _VELDATA_H_

#include <stdio.h>
#include <string.h>
#include <stdlib.h>

#define MAX_V_ROWS  40

typedef struct
 { int      num ;
   double   y[MAX_V_ROWS] ;
   double   dat[MAX_V_ROWS] ;
 }
VelData ;

extern VelData U, V, W, uu, vv, ww, uv, uw, vw ;

extern int  ReadVelData (FILE *Fptr) ;
extern void ZeroAllVelData (void) ;
extern void ZeroVelData (VelData *D) ;
extern int  ReadField (FILE *Fptr, double CurrY, VelData *D) ;

#endif
```

VELDATA.C

```
/*****************************************************************************
*   THIS FILE CONTAINS FUNCTIONS TO READ VELOCITY PROFILE DATA FILES.  IT    *
*       PROPERLY HANDLES ENCOUNTERING "M" WHICH DENOTES A MISSING DATA       *
*       POINT                                                                *
*****************************************************************************/

#include "veldata.h"

VelData U, V, W, uu, vv, ww, uv, uw, vw ;

int ReadVelData (FILE *Fptr)
{ double    CurrY ;
  int       err, i ;

  for (i=0; i<MAX_V_ROWS; i++)
   { //
     // Column 1 = y
     //
     err = fscanf(Fptr, "%lg", &CurrY);
     if (err == EOF) return 0;

     ReadField (Fptr, CurrY, &U) ;
     ReadField (Fptr, CurrY, &V) ;
     ReadField (Fptr, CurrY, &W) ;
     ReadField (Fptr, CurrY, &uu) ;
     ReadField (Fptr, CurrY, &vv) ;
     ReadField (Fptr, CurrY, &ww) ;
     ReadField (Fptr, CurrY, &uv) ;
```

```
      ReadField (Fptr, CurrY, &uw) ;
      ReadField (Fptr, CurrY, &vw) ;
    }
  return 0 ;
}


void ZeroAllVelData (void)
{ ZeroVelData (&U) ;
  ZeroVelData (&V) ;
  ZeroVelData (&W) ;
  ZeroVelData (&uu) ;
  ZeroVelData (&vv) ;
  ZeroVelData (&ww) ;
  ZeroVelData (&uv) ;
  ZeroVelData (&uw) ;
  ZeroVelData (&vw) ;
}


void ZeroVelData (VelData *D)
{ int i ;

  D->num = 0 ;
  for (i=0; i<MAX_V_ROWS; i++)
   { D->y[i]   = 0.0 ;
     D->dat[i] = 0.0 ;
}  }


int ReadField (FILE *Fptr, double CurrY, VelData *D)
{ char strfield[50] ;

  fscanf (Fptr, "%*[^0123456789EeM.+-]%[0123456789EeM.+-]", strfield) ;
  if (strcmp(strfield, "M"))
   { D->y[D->num] = CurrY ;
     D->dat[D->num] = atof(strfield) ;
     D->num++ ;
    }

  return 0 ;
}
```

PARA-FIT.H

```
#ifndef _PARA_FIT_H_
#define _PARA_FIT_H_
/*************************************************************************
*   HEADER FILE FOR para-fit.c WHICH FITS A PARABOLA TO THE GIVEN X AND Y   *
*       ARRAYS USING A LEAST SQUARES FIT                                    *
*************************************************************************/

#define SMALL           1e-30
#define ERR_UNDEF_COEFF 1

extern int    ParaFit (int Npts, double *X, double *Y, double *A) ;
extern double Deter33 (double A[3][3]) ;

#endif
```

PARA-FIT.C

```
/*****************************************************************************
*   THIS FUNCTION FITS A PARABOLA TO THE GIVEN X AND Y ARRAYS USING A LEAST *
*       SQUARES FIT                                                          *
*****************************************************************************/

#include "para-fit.h"
#include <stdio.h>

int ParaFit (int Npts, double *X, double *Y, double *A)
{ int       i, r, c, cc ;
  double    C[3][3], TempMat[3][3], D[3], CoeffDet ;

  for (r=0; r<3; r++)
   { D[r] = 0.0 ;
     for (c=0; c<3; c++)
      C[r][c] = 0.0 ;
   }

  for (i=0; i<Npts; i++)
   { C[0][1] += X[i] ;
     C[0][2] += X[i]*X[i] ;
     C[1][2] += X[i]*X[i]*X[i] ;
     C[2][2] += X[i]*X[i]*X[i]*X[i] ;
        D[0] += Y[i] ;
        D[1] += Y[i]*X[i] ;
        D[2] += Y[i]*X[i]*X[i] ;
   }
  C[0][0] = (double)Npts ;
  C[1][0] = C[0][1] ;
  C[1][1] = C[2][0] = C[0][2] ;
  C[2][1] = C[1][2] ;

  CoeffDet = Deter33(C) ;
  if (CoeffDet < SMALL) return ERR_UNDEF_COEFF ;

  for (cc=0; cc<3; cc++)
   { for (r=0; r<3; r++)
      { for (c=0; c<3; c++)
         TempMat[r][c] = C[r][c] ;
        TempMat[r][cc] = D[r] ;
      }

     A[cc]  = Deter33(TempMat) ;
     A[cc] /= CoeffDet ;
   }

  return 0 ;
}
```

```
/*****************************************************************************
*   THIS FUNCTION COMPUTES THE DETERMINANT OF A 3X3 MATRIX                   *
*****************************************************************************/
double Deter33 (double A[3][3])
{ double   det ;

  det  = A[0][0] * A[1][1] * A[2][2] ;
  det += A[0][1] * A[1][2] * A[2][0] ;
  det += A[2][1] * A[1][0] * A[0][2] ;
  det -= A[0][2] * A[1][1] * A[2][0] ;
  det -= A[1][0] * A[0][1] * A[2][2] ;
  det -= A[2][1] * A[1][2] * A[0][0] ;

  return det ;
}
```

MYFILE.H

```
#ifndef _MYFILE_H_
#define _MYFILE_H_

#include <stdio.h>
#include <string.h>
#include <errno.h>

typedef struct
 { FILE             *ptr ;
   char             name[80] ;
 }
FileInfo ;

extern int  OpenFile (FileInfo *F, char *mode) ;
extern void CloseFile (FileInfo *F) ;

#endif
```

MYFILE.C

```
#include "myfile.h"

/*************************************************************************
*   THIS FUNCTIONS OPENS A FILE AND PRINTS STATUS INFO TO THE SCREEN      *
*************************************************************************/
int OpenFile (FileInfo *F, char *mode)
{
 printf (" Openning %s ... ", F->name) ;
 if ((F->ptr=fopen (F->name, mode)) == NULL)
  { printf ("\n  ERROR %i : %s\n", errno, strerror(errno)) ;
    return errno ;
  }
 printf ("O.K.\n") ;
 return 0 ;
}


void CloseFile (FileInfo *F)
{
  fclose (F->ptr) ;
}
```